



UNIVERSITÀ DEGLI STUDI DI ROMA "TOR VERGATA"

Department of Civil Engineering and Computer Science
PhD Thesis

XXVI Cycle

Archaeological Prospection using Spaceborne Synthetic Aperture Radar

Christopher Stewart

A.A. 2010/11
Submitted: January 2017

Supervisor: Prof. Giovanni Schiavon

ABSTRACT

Population growth accompanies a corresponding increase in the demand for resources, the short term satisfaction of which is often to the detriment of irreplaceable historical evidence. Efficient prospection is the first step in the preservation and management of the archaeological record. In the present era of Big Data we are witnessing an unprecedented rate of development in SAR sensors, processing platforms and algorithms. As the movement of Open Science gains momentum, SAR data and tools for its exploitation are becoming increasingly accessible. Given the mutual lack of awareness amongst SAR remote sensing scientists and cultural heritage experts of their respective capabilities and requirements, these developments have largely sidelined the archaeological community. The aim of this PhD research is to harness recent advances in SAR remote sensing for the benefit of archaeological prospection. This is carried out through case studies on the utilisation of SAR sensors and processing techniques for archaeological survey over the types of land and water surfaces corresponding to the greatest need for prospection and where SAR techniques may yield a promising and unique contribution. The PhD attempts to exploit to the maximum extent the availability of SAR sensors in various frequencies and polarisations. It aims to extract the most information possible from both the SAR intensity and phase, while utilising large time series of data.

Results reveal for the first time the potential to detect proxy surface residues of archaeological structures buried beneath vegetated soils in Central Italy in coherence images. The benefit of a large time series is demonstrated to greatly improve the direct detection capability of structures obscured by sand, or the indirect exposure of features through soil or vegetation proxies, using filtered SAR intensity. The identification of topographic traces of buried structures exploiting repeat pass interferometry, and the Small Baseline Subsets technique, is proved possible. Novel extraction algorithms are devised to automatically detect anthropogenic features in the North Sinai Desert, taking the multitemporal speckle filtered intensity or the average coherence as input. A recent and efficient bathymetric inversion algorithm is applied for the first time on Sentinel-1 imagery over the North Sea and the resulting bathymetric map compared with an existing map of the North Sea palaeolandscape. The utility of SAR bathymetry as an input to the regular mapping of extensive submerged palaeolandscapes is discussed.

The research has been published in five peer reviewed articles, in a number of edited book chapters and conference proceedings. The work has been further disseminated through the co-organisation of workshops, and presentations at conferences and symposia. Collaboration with the research, operational and user community has taken place through the participation, at various levels, in research and demonstration projects. Throughout the PhD, knowledge acquired as a result of the research has been communicated through the delivery of training events targeted at a broad range of users worldwide.

“It’s not what you find, it’s what you find out.”

David Hurst Thomas

CONTENTS

Abstract	i
Contents	iii
Acronyms	viii
1 Introduction	1
1.1 Justification	1
1.2 Motivation.....	5
1.3 Structure of Thesis	6
2 Principles of Synthetic Aperture Radar	8
2.1 Electromagnetic Radiation.....	8
2.2 Microwaves.....	9
2.3 Radar	10
2.4 The radar equation	10
2.5 Real Aperture Radar.....	11
2.6 Synthetic Aperture Radar.....	13
2.7 Speckle	14
2.8 SAR calibration	16
2.9 SAR Geometric Distortions.....	17
2.10 SAR images.....	18
2.10.1 Single Look Complex	18
2.10.2 Multi Look Detected.....	18
2.11 SAR acquisition modes.....	19
2.12 PolSAR	19
2.12.1 Stokes Vector	21
2.12.2 Poincaré sphere	21
2.12.3 Jones vector	22
2.12.4 Polarimetric basis and change of basis	22
2.12.5 Scattering Matrix.....	23
2.12.6 Covariance matrix and coherency matrix	23
2.12.7 Polarimetric decompositions	24

2.13	InSAR	26
2.13.1	Altitude of Ambiguity	28
2.13.2	Critical Baseline	28
2.13.3	Range Spectral Shift Filtering	28
2.13.4	Azimuth Common Band Filtering	28
2.13.5	DEM creation	28
2.13.6	Coherence	29
2.13.7	DEM error sources	30
2.13.8	Small BAseLine Subsets (SBAS)	30
2.14	Interaction of microwaves with surface materials	31
2.14.1	Scattering from rough surfaces.....	31
2.14.2	Bragg scattering	32
2.14.3	Volume scattering	33
2.14.4	Signal transmission and attenuation	33
3	Review of Literature on the Use of SAR for Archaeological Prospection.....	35
3.1	Origins	35
3.2	Prospection through topographic analysis	36
3.2.1	SAR intensity analysis of surface topography and roughness	37
3.2.2	Prospection using DEMs	39
3.3	Identification through sand volume transmission.....	41
3.4	Identification through vegetation and soil proxies.....	47
3.4.1	Crop Marks in Temperate Regions.....	48
3.4.2	Soil Marks in Temperate Regions.....	52
3.4.3	Remote Sensing of crop and soil marks in temperate regions	53
3.5	Identification under water	55
3.5.1	Physical mechanisms.....	55
3.5.2	Application of Remote Sensing for Archaeological Prospection Underwater	61
4	Archaeological Prospection Using SAR in Agricultural Crop and Grassland Around Rome	63
4.1	Study Areas	64
4.1.1	Portus	67
4.1.2	Ostia	68
4.1.3	Appia	69

Contents

4.1.4	Prenestina	71
4.1.5	Salaria.....	73
4.1.6	Veii	74
4.2	SAR Data.....	75
4.2.1	CSK Data	75
4.2.2	R2 Data.....	76
4.2.3	ALOS PALSAR Data	77
4.3	Methodology.....	78
4.3.1	Multitemporal speckle filtered σ^0 backscatter	78
4.3.2	Interferometric coherence.....	80
4.3.3	DEM.....	80
4.3.4	Polarimetric Analysis.....	84
4.3.5	Analysis of Features	86
4.4	Results.....	89
4.4.1	Portus.....	89
4.4.2	Prenestina CSK	96
4.4.3	Prenestina R2	109
4.4.4	Salaria.....	120
4.5	Discussion.....	125
4.5.1	Filtered σ^0 backscatter	126
4.5.2	Coherence	127
4.5.3	DEM.....	128
4.6	Conclusions	128
5	Archaeological Prospection Using SAR in North Sinai Desert	130
5.1	Study Area.....	130
5.1.1	North Sinai Geography, Geology and Climate	130
5.1.2	North Sinai Archaeology	133
5.2	PALSAR-1 Data	134
5.3	PALSAR-2 Data	136
5.4	Methodology.....	137
5.4.1	PALSAR-1 Mosaic of North Sinai	138
5.4.2	Extraction of Linear Features of High Backscatter over AOI 1.....	140

Contents

5.4.3	Analysis of Geometric Features of Low Backscatter in AOI 2	144
5.5	Results	145
5.5.1	Mosaic	145
5.5.2	Focus on AOI 1 (Region East of Wadi Tumilat and West of Gebel Maghara)	147
5.5.3	Focus on AOI 2 (Area of Tell El-Farama, Tell El-Mahzan, and Tell El-Kanais)	151
5.5.4	Image Artefacts	167
5.6	Conclusions	169
6	Archaeological Prospection of the North Sea Palaeolandscape Using SAR	171
6.1	The Palaeolandscape of the North Sea	172
6.2	Sentinel-1 Bathymetry Retrieval	173
6.2.1	SAR data	173
6.2.2	Ancillary data for bathymetry retrieval	174
6.2.3	Methodology	176
6.2.4	Results	183
6.3	SAR Support to the Mapping and Monitoring of Palaeolandscape Features	186
6.4	Conclusions	188
7	Overall Conclusions	190
7.1	Prospection over vegetated areas	190
7.2	Prospection over sand covered areas	191
7.3	Prospection under water	192
7.4	PhD activities	194
7.5	Final remarks	195
	Acknowledgements	196
APPENDIX A	Image Data Scene IDs	199
APPENDIX B	CSK SBAS Connections	205
Appendix B.1	Stripmap Prenestina AOI	205
Appendix B.2	Spotlight Prenestina AOI	213
APPENDIX C	Communication and Dissemination Activities	217
Appendix C.1	Workshop: Advances in Remote Sensing for Cultural Heritage	217
Appendix C.2	Training Courses	223
Appendix C.2.1	Co-organised training events	223
Appendix C.2.2	Externally organised training	238

Contents

Appendix C.3	Project participation	239
Appendix C.3.1	WHERE	239
Appendix C.3.2	ITACA	240
Appendix C.3.3	PRIN “The Seven Plagues”	240
Appendix C.3.4	ArchEO	241
Appendix C.4	Conference, symposium and workshop presentations	242
APPENDIX D	Publications	245
Appendix D.1	Peer Reviewed Journal Articles.....	245
Appendix D.1.1	Paper 1	245
Appendix D.1.2	Paper 2	245
Appendix D.1.3	Paper 3	246
Appendix D.1.4	Paper 4	247
Appendix D.1.5	Paper 5	248
Appendix D.2	Edited Book Chapters.....	249
Appendix D.2.1	AHMES Volume 2, Chapter 14.....	249
Appendix D.2.2	AHMES Volume 2, Chapter 13.....	249
Appendix D.2.3	AHMES Volume 2, Chapter 12.....	250
Appendix D.2.4	Remote Sensing Survey of Saddina	251
Appendix D.3	Conference Proceedings	251
Appendix D.3.1	Proceedings: 2 nd International Conference of Aerial Archaeology	251
Appendix D.3.2	Proceedings: International Workshop “Italian Days in Aswan”	252
Appendix D.3.3	Proceedings: Cultural Heritage Workshop – Euromed2014	252
Appendix D.3.4	Proceedings: 4 th EARSeL Workshop on Cultural and Natural Heritage	254
Appendix D.4	Poster Presentations	256
References.....	260

ACRONYMS

ABE	Action Balance Equation
AD	Anno Domini
AHMES	Archaeological Heritage & Multidisciplinary Egyptological Studies
ALSF	Aggregates Levy Sustainability Fund
ALOS-1, 2	Advanced Land Observing Satellite 1 and 2
AOI	Area Of Interest
ARSIAL	Agenzia Regionale per lo Sviluppo e l'Innovazione dell'Agricoltura del Lazio
ASAR	Advanced SAR
ASCAT	Advanced SCATerometer
ASCII	American Standard Code for Information Interchange
ASI	Agenzia Spaziale Italiana (Italian national space agency)
ASIB	Air-Sea Interaction Drift Buoy
ASTER	Advanced Spaceborne Thermal Emission and Reflection Radiometer
BABEL	Bathymetry Assessment Demonstration off the Belgian Coast
BAS	Bathymetric Assessment System
BC	Before Christ
BGS	British Geological Survey
BSA	Backscatter Alignment
BSR	British School at Rome
CAS	Chinese Academy of Sciences
CNES	Centre National d'Études Spatiales (French national space agency)
CNR	Consiglio Nazionale delle Ricerche (Italian National Research Council)
CONAE	Argentinian Space Agency
CoV	Coefficient of Variation

Acronyms

CSG	COSMO SkyMed Second Generation
CSK	COSMO SkyMed
dB	Decibel
DEM	Digital Elevation Model
DInSAR	Differential SAR Interferometry
DTM	Digital Terrain Model
DUE	Data User Element (ESA)
EARSeL	European Association of Remote Sensing Laboratories
EGU	European Geosciences Union
EC	European Commission
EM	Electromagnetic
EMODnet	European Marine Observation and Data Network
ENL	Equivalent Number of Looks
EO	Earth Observation
ERS-1, 2	European Remote Sensing Satellite 1 and 2
ESA	European Space Agency
ESRIN	European Space Research Institute
EU	European Union
EW	Extra Wide Swath (Sentinel-1 sensor mode)
FBD	Fine Beam Dual Polarisation (PALSAR-1 sensor mode)
FBS	Fine Beam Single Polarisation (PALSAR-1 sensor mode)
FC	Field Capacity
FFT	Fast Fourier Transform
FP7	Seventh Framework Programme (of the EU)
FQ	Fine Quad (Radarsat-2 sensor mode)

Acronyms

FR	Full Resolution
GCP	Ground Control Points
GDEM	Global DEM
GHz	Gigahertz
GIS	Geographic Information System
GPR	Ground Penetrating Radar
HH	Horizontal transmit, Horizontal receive (polarisation)
HIST	International Centre on Space Technologies for Natural and Cultural Heritage
HR	High Resolution
HV	Horizontal transmit, Vertical receive (polarisation)
IAF	International Astronautical Federation
ICOMOS	International Council on Monuments and Sites
IDL	Interactive Data Language
IF	Impact Factor
IBAM	CNR institute of Archaeological and Monumental Heritage
IMAA	CNR institute of Methodologies for Environmental Analysis
INGV	Istituto Nazionale di Geofisica e Vulcanologia (Italian national institute for geophysics and volcanology)
InSAR	Interferometric SAR
IoT	Internet of Things
ISMA	CNR Institute for Ancient Mediterranean Studies
ITACA	Innovative Technologies and Applications for Coastal Archaeological sites
ITU	International Telecommunication Union
IW	Interferometric Wide Swath (Sentinel-1 sensor mode)
JAXA	Japan Aerospace Exploration Agency
JERS-1	Japanese Earth Resources Satellite 1

Acronyms

JPL	Jet Propulsion Laboratory
KML	Keyhole Markup Language
KNIR	Royal Netherlands Institute in Rome
LiDAR	Light Detection And Ranging
NASA	National Aeronautics and Space Administration
NIR	Near-Infrared
NOC	National Oceanography Centre
NRCS	Normalised Radar Backscattering Cross Section
NSPP	North Sea Palaeolandscapes Project
LAI	Leaf Area Index
LIA	Local Incidence Angle
LPS	ESA Living Planet Symposium
MAST	Marine Science and Technology (programme of the EC)
MEM	CNR Multidisciplinary Egyptological Mission
MERIS	Medium Resolution Imaging Spectrometer
MHz	Megahertz
MIUR	Italian Ministry of Education, Universities and Research
MLD	Multi Look Detected
MoD	Ministry of Defence
MRD	Mean Ratio Detector
NEST	Next ESA SAR Toolbox
ONERA	French Aerospace Research Agency
OS	Open Source
OSL	Optically Simulated Luminescence
PALSAR-1, 2	Phased Array type L-band SAR 1 and 2

Acronyms

PDF	Probability Density Function
PDF	Portable Document Format
PGS	Petroleum Geo-Services
POLIMI	Politecnico di Milano
POLinSAR	International Workshop on Science and Applications of SAR Polarimetry and Polarimetric Interferometry
PoSAR	Polarimetric SAR
PoSARpro	ESA OS toolbox for polarimetric SAR data processing and education
PRIN	Progetti di ricerca di Rilevante Interesse Nazionale (Italian research projects of national interest)
PRISM	Panchromatic Remote-sensing Instrument for Stereo Mapping
PSMD	Potential Soil Moisture Deficit
PSMS	Potential Soil Moisture Surplus
PWP	Permanent Wilting Point
QGIS	Quantum GIS
R2	Radarsat-2
RADAR	Radio Detection And Ranging
RAF	British Royal Air Force
RAR	Real Aperture Radar
RCM	Radarsat Constellation Mission
RFI	Radio Frequency Interference
RSAC	Remote Sensing Applications Consultants
SAR	Synthetic Aperture Radar
SatER	Satellite Remote Sensing in Support to Egyptological Research
SBAS	Small Baseline Subsets
SfM	Structure from Motion

Acronyms

SIR-A, B, C	Shuttle Imaging Radar A, B and C
SLAR	Side Looking Airborne Radar
SLC	Single Look Complex
SM	Stripmap (Sentinel-1 sensor mode)
SMD	Soil Moisture Deficit
SME	Small and Medium Enterprises
SMOS	Soil Moisture and Ocean Salinity Mission
SMS	Soil Moisture Surplus
SNAP	Sentinels Application Platform
SNR	Signal to Noise Ratio
SOAR	Science and Operational Application Research
SRTM	Shuttle Radar Topography Mission
STACH I	Italian - Egyptian Workshop on Sciences and Technologies applied to Cultural Heritage I
TIR	Thermal-Infrared
TOPS	Terrain Observation through Progressive Scans
TPM	ESA Third Party Mission
UAV	Unmanned Aerial Vehicle
UN	United Nations
UNESCO	United Nations Educational, Scientific and Cultural Organization
URL	Uniform Resource Locator
USGS	United States Geological Survey
UTC	Coordinated Universal Time
UTM	Universal Transverse Mercator
UV	Ultraviolet
VH	Vertical transmit, Horizontal receive (polarisation)

Acronyms

VHR	Very High Resolution
VSE	Volterra Series Expansion
VV	Vertical transmit, Vertical receive (polarisation)
WGS84	World Geodetic System 1984
WHERE	World HEritage monitoring by REmote sensing
WMS	Web Map Service

1 INTRODUCTION

1.1 Justification

The value of history justifies the need for archaeology. The excavation of Old Kingdom Egyptian structures during the Egyptian New Kingdom (Lehner 1992) testifies to the endurance of archaeological practice and suggests that historical interest is no recent phenomenon. Such interest can stimulate extensive societal changes. The rediscovery and re-evaluation of the classical world in the Renaissance (Highet 1949, Kristeller 1979, Jensen 1992) illustrates how progress in all spheres is not always directly proportional with time. If we wish to see positive development, we need history to understand how past deeds should not be repeated, and the extent of their consequences in the present. This is the case not only of political actions, a reason for which we study former conflicts, but also of past human modifications of our landscape and environment. Having emerged from the industrial revolution, for example, we now debate the extent of anthropogenic influence on climate change (Meehl et al. 2007, Poortinga et al. 2011). Historical interest changes our perception of the past, affects policy decisions today, and shapes the history of tomorrow.

The emergence of archaeology as a study of the human past through tangible evidence, epitomised by the antiquarian Sir Richard Colt Hoare “We speak from facts not theory” (Piggott 1937), is a recognition of the importance of the archaeological record as a fingerprint of humanity. However, the perceived value of this archaeological record often varies, especially when confronted with conflicting interests. For many, the search for cultural artefacts is synonymous with treasure hunting, and looting of archaeological sites is carried out for economic gain with little regard for historical worth (Lasaponara et al. 2014). Population growth accompanies a corresponding increase in the demand for resources, the short term satisfaction of which is often to the detriment of irreplaceable historical evidence (Jones 1984). The recognition of this has led to the concept of “rescue archaeology” as the definition of the pre-emptive identification, documentation and preservation of archaeological finds proceeding a development project which may endanger them (Jones 1984, Gibson 2016). In heavily occupied areas, most surface traces of past human activities have been obliterated and remain only underground or under water (Scollar et al. 1990). It can be argued that tangible cultural heritage, hidden from view, sealed in a protective medium and preserved in the context of its surroundings should remain so for future generations. However, if it is not known to exist, protection is far from guaranteed given the threats of looting, accidental or wanton destruction (Gibson 2016).

What is the best method for archaeological prospection? Excavation sheds light on tangible cultural heritage, long kept in the dark; but even if un-earthed structures can be subsequently re-interred, this technique is invasive, and the risk of damage to archaeological finds and the destruction of the overlying landscape is inevitable. Moreover, excavation can be costly and time consuming (Scollar et al. 1990). Ground based geophysical prospection techniques exist, such as Ground Penetrating Radar (GPR), magnetometry and resistivity (Wynn 1986). These are capable of identifying buried structures in a manner that is neither destructive nor invasive (Keller and Frischknecht 1966, Jones 2008). However, as with excavation, their application over large areas can be expensive and inefficient. Aside from the

1. Introduction

drawbacks of cost and time in the application of large scale ground survey, even over small areas it may not be feasible if such areas are inaccessible. This may be for geographic reasons if they are situated in remote or inhospitable terrain, or for reasons of security, if they are located in conflict zones (Parcak 2009, Lasaponara and Masini 2012b).

Techniques operated remotely offer the advantages of providing a synoptic view, covering large areas, frequently and at low cost (Parcak 2009, Lasaponara and Masini 2012b). Just as the best perspective from which to see the proverbial wood from the trees may be remote, traces of buried features can often only be seen from afar (Wilson 2000). Archaeologists now have an increasing choice of remote platforms from which to base their measurements, from low altitude Unmanned Aerial Vehicles (UAVs) and high altitude airborne platforms, to spaceborne satellites orbiting the Earth (Wilson 2000, Lin et al. 2011). Some archaeological traces are notoriously ephemeral and appear only briefly on the occasions of rare ground and atmospheric conditions. This is often the case with archaeological crop marks, which may require a high acquisition frequency to capture a moment when such features emerge (Jones and Evans 1975, Agapiou et al. 2013).

Remote sensing instruments commonly seek information about a target by measuring its interaction with electromagnetic radiation. Different wavelength regions of the electromagnetic (EM) spectrum are already utilised for remote prospection in a wide range of geographical regions, over both land and water (Wiseman and El-Baz 2007, Parcak 2009). The visible region of the EM spectrum can penetrate clear water and be reflected by objects on the sea-bed (Sandidge and Holyer 1998, Lyzenga et al. 2006). Over land, subtle differences in the characteristics of surface materials due to the presence of buried structures may not be apparent to the naked eye, but may display a characteristic spectral signature when analysing their spectral response in multiple wavelength regions from the visible to the infrared (Agapiou et al. 2013). In areas of green vegetation, the strong reflectance in the near-infrared by chlorophyll is particularly exploited to detect such subtle variations (Lasaponara and Masini 2012b). Sensors operating in the thermal infrared can detect heat signatures of buried structures (Ben-Dor et al. 2013). While these are all achieved with passive sensors that measure the response of reflected solar or emitted terrestrial radiation, active sensors operating in the same wavelength regions can be employed in innovative ways to disclose hidden objects beneath dense and seemingly impenetrable layers. LiDAR (Light Detection and Ranging), for example, operating in the near-infrared, can detect subtle topographic relief variations caused by structures, even when buried beneath a dense forest canopy (Gallagher and Josephs 2008). LiDAR operating in the visible green region can penetrate deep into clear water to detect similar subtle topographic relief of structures on the sea-bed (Doneus et al. 2013). Active sensors in the microwave region can detect moisture anomalies, surface roughness and texture differences, which may indicate the presence of archaeological objects. These may even be buried beneath a layer of sand (Wiseman and El-Baz 2007). (A complete literature review of SAR remote sensing techniques is provided in Chapter 3.)

The many instruments that are available, and the many techniques that are continuously being developed for the exploitation of their data, have often been devised for applications other than archaeological research. As such, they inevitably have limitations. For example the choice of spectral channels in multispectral or hyperspectral imagers, or the geometric configuration of active sensors,

1. Introduction

which may have been conceived for certain core applications, such as disaster mapping, forestry and agricultural monitoring, may not be the most suitable for archaeology. There are sensor types and wavelength regions the utility of which for archaeological applications has not been significantly researched. Archaeologists are often not remote sensing scientists (Parcak 2009). Certain techniques or instruments which may be considered too technical and specialised can thus easily be ignored. SAR fits into this category given its uniqueness and complexity. This is exacerbated by the fact that SAR data availability and access has until recently been fairly prohibitive. There were no Very High Resolution (VHR) SAR missions prior to 2007. Even with the advent of the “golden age” of SAR heralded by the launch of COSMO SkyMed, TerraSAR-X and Radarsat-2, all in 2007, data from these missions has often been costly and restrictive. This is particularly problematic for the cultural heritage community, which habitually operates under very tight budgets. This is beginning to change, with increasing data availability and progressively free and open access policies, opening up new opportunities for the exploitation of little used sensors, such as SAR, which may reveal great promise for archaeological applications.

We are currently in the era of Big Data, characterised by an unprecedented increase in the volume, velocity and variety of information being acquired by sensors, both remote and in-situ (Manyika et al. 2011). While this provides unparalleled opportunities for monitoring, it also presents challenges associated with data processing and management. Cloud computing becomes a necessity as the processing power and storage capacity of desktop computers struggles to keep up with the demands of Big Data management (Hashem et al. 2015). Processing is increasingly automated with data mining becoming a key research area (Han et al. 2011). Where manual intervention is required, crowd sourcing applications and “citizen science” are ever more popular, and commonly take advantage of input from social networks (Brabham 2013). The explosive number of sensors are progressively interconnected. This phenomenon is referred to as the “Internet of Things” (IoT) (Gubbi et al. 2013). In-situ sensors are increasingly coupled with satellite Earth Observation (EO) measurements for validation and modelling.

In parallel with increasing data acquisition we are experiencing a positive trend in the availability, accessibility and openness of scientific data and results. This is referred to as “Open Science” or “Science 2.0”, given its close relationship with Web 2.0 (Waldrop 2008). Scientific research is changing with new ways of collaboration through such tools as wikis and blogs. The dissemination of results is facilitated through social media and Open Access publications. Formerly expensive satellite Earth Observation (EO) data is becoming free and accessible to an ever wider user community (Harris and Baumann 2015). Perhaps the best and most recent example of this is the recently launched Copernicus programme, the most ambitious EO programme to date, which foresees the launch of an array of satellite constellations to provide reliable, long term monitoring with instruments operating from the visible to the microwave parts of the electromagnetic spectrum for operational applications. The data from all these satellite missions are free and open (Aschbacher and Milagro Perez 2014, Harris and Baumann 2015).

The purpose of this PhD research is to assess the possibility of harnessing these developments for the benefit of archaeological science. In particular, developments in SAR remote sensing are considered, given that there is a clear discrepancy between the rate of advancement in SAR remote sensing and the pace of its uptake by the archaeological community. These developments include the launch of new

1. Introduction

sensors, most recently Sentinel-1 and ALOS-2, and the prospect of new missions, such as the Radarsat Constellation Mission (RCM) and COSMO SkyMed Second Generation (CSG). They include also new techniques furthering the capabilities in areas such as InSAR and PolSAR. And finally they include new data access policies, which are seeing a trend towards becoming increasingly open and free.

Only archaeological prospection is considered, even if this is only one aspect of the study of tangible cultural heritage. Other fundamental aspects include its preservation, interpretation, documentation, monitoring, management and valorisation (Lozny 2006, Timothy 2007). Moreover, each can be broken down into further categories. The monitoring of archaeological sites for example may entail structural monitoring of monuments to detect signs of crumbling or cracking that may be caused by small scale displacement effects. These may result from external anthropogenic or natural causes. Anthropogenic causes may be related to nearby constructions, such as a newly built subway (Cigna et al. 2014). Natural causes may be related to slope instability, or to gradual, but continuous subsidence, (Catalao et al. 2011, Fanti et al. 2013). Another type of monitoring may be carried out for security reasons, such as to detect possible looting or vandalism of archaeological sites (Tapete et al. 2016). A third type of monitoring may be carried out to detect possible atmospheric degradation of archaeological structures (Folegani et al. 2013). Remote sensing can benefit many of these applications related to cultural heritage, and in many cases is already applied operationally, (Barnes 2003, Stubbs and McKee 2006). It was chosen to focus on the prospection of tangible cultural heritage given primarily the lack of previous research on the use of SAR techniques for this application, and the potential that SAR remote sensing may reveal. Another aspect where SAR can greatly benefit the cultural heritage sector is in the structural monitoring of archaeological sites. However, this is already well established and is applied operationally through InSAR techniques (Tapete et al. 2012).

This PhD research takes the form of three case studies in which various SAR techniques using multiple sensors are applied for direct archaeological prospection in three completely different areas.

The first case study focuses on the use of multi-frequency, HR and VHR polarimetric and interferometric SAR for archaeological prospection through the detection of vegetation and soil proxies in a temperate region. The primary purpose of this research is to fully exploit the SAR phase in addition to the amplitude. While some tentative attempts have been made in the past to use the SAR amplitude for archaeological prospection over similar areas, none have successfully exploited the phase. A more complete review of literature and justification of this research is provided in Section 3.4.3. The region of interest includes a series of small areas surrounding the city of Rome in Italy. These are chosen for the quantity of archaeological structures, ease of access (I live in Rome), and lack of previous research. The sensors employed in the analysis include COSMO-SkyMed, Radarsat-2 and PALSAR-1.

The second case study assesses the potential of HR and VHR L-band SAR to detect archaeological structures buried or obscured by sand. While the use of SAR has long been proven to detect subsurface features, these have mainly been for geological or hydrological applications. In some cases SAR has been applied for archaeological prospection in sandy areas, but mostly indirectly through the detection of palaeolandscape features. Moreover, previous studies tend to be serendipitous, and not systematic (see Section 3.3). In this case study an attempt is made to directly and systematically detect

1. Introduction

anthropogenic features, and to extract them over a large area. The region includes the North Sinai Desert. This area was chosen for its relatively homogenous sand cover, and for the density of archaeological structures known to exist in the area. The sensors employed include PALSAR-1 and 2.

The third case study aims to determine the extent to which SAR data can be systematically used for the detection and monitoring of submerged palaeolandscapes. While SAR bathymetry has long been studied and even operationally applied, its use for the study of submerged palaeolandscapes has not yet been the subject of any research (see Section 3.5). The area of interest chosen for the analysis includes a region of the southern North Sea where the North Sea Palaeolandscapes Project (NSPP) mapped the submerged palaeolandscape using datasets which do not include SAR. The results of the NSPP were compared with the results of the SAR analysis. Sentinel-1 SAR data was used in this case study.

The areas and SAR techniques selected for this PhD research are by no means exhaustive. Many different types of terrain could have been selected, such as various types of forest, ice, snow, permafrost, or even beneath built-up areas. Archaeological prospection under ice and snow using SAR may yield unique information given the penetration capability of SAR in ice and dry snow (Rignot et al. 2001). However, identifying areas likely to contain archaeological material, and where validation can be carried out, is particularly challenging. It may be that in built-up areas, archaeological structures are identifiable beneath the urban fabric using SAR techniques. In the city of Rome for example, a major problem facing urban authorities is the danger posed by subterranean quarries, particularly Roman quarries of tuf. These frequently cause sink holes to appear in overlying structures, such as roads, especially following periods of rain (Nisio and Ciotoli 2016). It may be that InSAR techniques are able to provide information to locate areas where quarries may exist before the destruction of the urban landscape. Other areas, such as forests, contain many archaeological structures, and some attempts have already been made using SAR in these regions (Yakam-Simen et al. 1998) (see Section 3). However, other techniques, such as LiDAR, are already routinely used in such regions, and with great effect (Gallagher and Josephs 2008), even if airborne LiDAR may come at a cost disadvantage when compared to satellite techniques. Given the constraints of time, it was decided to focus on the surface types where there appears to be a greater need for archaeological prospection, given the pressure of urbanisation and development, and where it is deemed that SAR techniques can provide a unique contribution.

1.2 Motivation

The merging of two seemingly unrelated subjects is not new to me. Having studied mathematics with Spanish as an undergraduate, I have always sought to broaden the scope of my learning. The idea of combining archaeology with remote sensing comes from a deep seated interest in the humanities, particularly history, while recognising the real world potential of the sciences. Ultimately it was this that brought me to Rome, a city steeped in history, to work at the European Space Research Institute (ESRIN) of the European Space Agency (ESA). At ESRIN, in the Earth Observation Programmes directorate, I have supported the management of research, demonstration and fully operational projects in applications ranging from disaster management, to food security, water resources management and archaeological prospection. In addition I have been heavily involved in education, training and capacity building activities, and have supported the organisation of training courses in many applications targeted to

participants at all levels and backgrounds. These include general remote sensing courses delivered to PhD students and post-docs, to courses intended for service providers in a specific sector. In this capacity it has been possible for me to gain the widest possible exposure to EO science and applications and to attain a thorough familiarity with research and operational activities in this field.

The decision to focus on the application of SAR for archaeological prospection was made following long deliberation on the most suitable topic that is of particular interest to me, where there is a clear need for further research, and which provides the flexibility to apply a wide range of processing methods over an extensive variety of surface types. Rome is an ideal situation from which to work on such a topic, given its abundance of cultural heritage and the advancement of research in Italian universities, research institutes, and foreign academies, several of which are based in or near Rome. Moreover, Italy has a significant heritage in SAR research. This is apparent particularly in universities such as the Politecnico di Milano (POLIMI); in research institutes, such as the Istituto Nazionale di Geofisica e Vulcanologia (INGV); and in successful spin-off companies, such as TRE, which later merged with Altamira Information. Moreover, Italy has invested significantly in SAR missions and has one of the most advanced SAR satellite constellations, COSMO SkyMed, which is jointly funded by the Italian Space Agency (ASI) and the Italian Ministry of Defence (Covello et al. 2010).

1.3 Structure of Thesis

The thesis is structured in the following way:

- Chapter 1 is the introduction, providing a justification and a motivation for this research.
- Chapter 2 provides an overview of the principles and techniques of Synthetic Aperture Radar that are most relevant to the research described in this thesis.
- Chapter 3 is a review of the literature, and outlines the state of the art in the use of SAR for archaeological prospection. The chapter is broken down into sections, each of which focusses on a specific type of prospection which may be relevant to particular surface types.
- Chapters 4, 5 and 6 comprise the case studies of research carried out in the framework of the PhD. Each of these three chapters provides an introduction, justifying the choice of the particular case study, including the decision regarding area, processing techniques and sensors employed. This is followed by a description of the study area and the data. The methodology is then outlined. The derived results are described in depth. Finally, the conclusions of the research are detailed. The three chapters each focus on a different prospection technique over a particular area. These include:
 - prospection through the detection of archaeological vegetation and soil proxies over temperate vegetated areas around Rome (Chapter 4)
 - prospection through the direct detection of structures in sandy areas of North Sinai (Chapter 5)
 - prospection under water in a region of the North Sea (Chapter 6).
- Chapter 7 provides the overall conclusions of the PhD research, which summarises the conclusions of Chapters 4, 5 and 6.
- An acknowledgements section follows Chapter 7.

1. Introduction

- Four appendices are included:
 - Appendix A provides the scene IDs of all imagery used in the analyses.
 - Appendix B provides details on the SBAS connections for the CSK data, used in the analysis described in Chapter 4.
 - Appendix C describes the activities carried out in the framework of the PhD, including the organisation of workshops and training events, project participation and attendance at workshops, conferences and symposia.
 - Appendix D lists all publications resulting from the PhD research, including peer reviewed papers, book chapters and conference proceedings.
- The thesis concludes with a list of references.

2 PRINCIPLES OF SYNTHETIC APERTURE RADAR

2.1 Electromagnetic Radiation

While the origins of a topic are often subject to debate, a suitable beginning in the history of microwave remote sensing could begin with James Clark Maxwell's mathematical derivation of electromagnetic waves in 1862-4. Maxwell unified a set of known experimental laws on electricity and magnetism (Gauss' Law, Gauss' Magnetism Law, Faraday's Law, Ampere's Law) into a symmetric coherent set of equations. In doing so, he was one of the first to discover that the speed of propagation of electromagnetic waves is the same as the speed of visible light, and therefore to conclude that they were the same phenomenon (Maxwell 1865, Maxwell 1881). Maxwell's equations are the following:

$$\nabla \times \mathbf{E} = -\frac{\partial \mathbf{B}}{\partial t} \quad 2.1$$

$$\nabla \times \mathbf{H} = \frac{\partial \mathbf{D}}{\partial t} + \mathbf{J} \quad 2.2$$

$$\nabla \cdot \mathbf{D} = \rho \quad 2.3$$

$$\nabla \cdot \mathbf{B} = 0 \quad 2.4$$

where

$$\mathbf{D} = \varepsilon \mathbf{E} \text{ and } \mathbf{B} = \mu \mathbf{H}$$

In these equations \mathbf{E} is the electric field, \mathbf{B} the magnetic induction, \mathbf{H} the magnetic field, \mathbf{D} the electric displacement, \mathbf{J} the conduction current density, t time, ρ the electric charge density, ε and μ the permittivity and permeability of the medium respectively. The operator $\nabla \times$ describes curl, and $\nabla \cdot$ divergence (Ulaby et al. 1981).

These equations include almost all there is to know about electromagnetic waves: including how electric and magnetic fields propagate, interact, and how they are influenced by objects (Woodhouse 2005). From these equations, the electromagnetic wave equation can be derived in the following way, assuming the wave is propagating through an environment such as a vacuum, where both $\mathbf{J} = 0$ and $\rho = 0$:

$$\psi(z, t) = A \sin(kz - \omega t + \varphi_0) \quad 2.5$$

where z is the direction of travel of the wave (we assume the x and y directional components are both zero), t is time, A is amplitude, $k = \frac{2\pi}{\lambda}$ is the wavenumber (for a wavelength λ), $\omega = kv$ is the angular frequency (for a propagation speed v , which in a vacuum is the speed of light, c), and φ_0 is the initial phase (Woodhouse 2005, Lee and Pottier 2009).

Equation 2.5 provides a complete sinusoidal description of a monochromatic wave travelling in a vacuum. An electromagnetic wave may have different polarisations, this is described in more detail in section 2.12. Another, more compact, way to describe the wave is in the complex notation (Lee and Pottier 2009).

$$\psi(z, t) = Ae^{i(kz - \omega t + \phi_0)} = Ae^{i\phi} = A(\cos \phi + i \sin \phi) \quad 2.6$$

This can be graphically represented in Figure 2.1. The real part of the wave is given by $z_1 = A \cos \phi$ (called the in-phase channel). The imaginary part is given by $z_2 = Ai \sin \phi$ (called the quadrature channel). The amplitude is therefore $A = \sqrt{(z_1^2 + z_2^2)}$. In practice, an antenna will measure the power, defined as energy per unit time, also known as intensity. The intensity is given by $I = A^2$ (Ulaby et al. 1981).

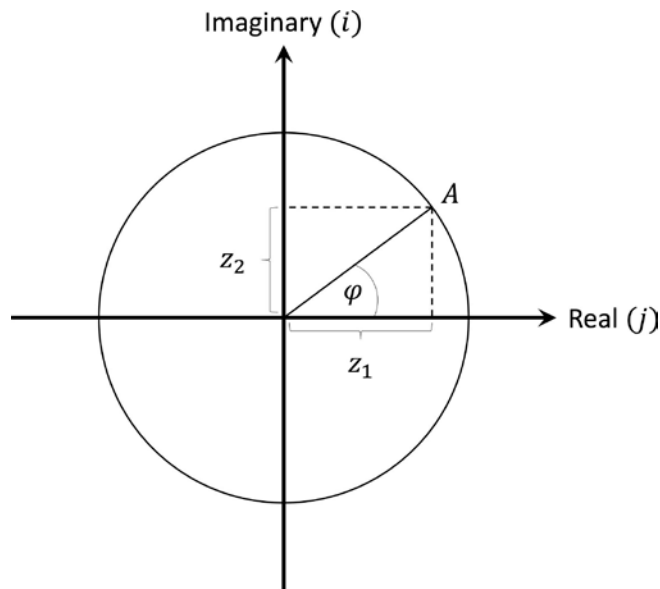


Figure 2.1. Graphical representation of complex electromagnetic wave.

2.2 Microwaves

Given the continuous nature of the electromagnetic spectrum, the precise boundary between radio waves to microwaves, or microwaves to infrared, is ambiguous. However, generally microwaves cover the region of the electromagnetic spectrum from around 1 to 300 gigahertz (GHz), or about 300 to 1 millimeters (Ulaby et al. 1981, Woodhouse 2005).

In this region of the spectrum the Earth's atmosphere is almost transparent, although at the shortest wavelength end, the similarities in the sizes of hydrometeors (rainfall and cloud liquid water) can be similar to the wavelength, and interaction between the two can occur.

Passive and active microwave instruments have been developed to sound the atmosphere and measure planetary surface properties of the Earth and other celestial bodies, either from spaceborne platforms, or from instruments on the Earth's surface (Woodhouse 2005).

2.3 Radar

Radar (Radio Detection and Ranging) is an active technique that uses the principle of echolocation to measure the portion of an emitted microwave signal that returns to a receiving antenna. Radar was first developed for locating and ranging objects such as ships and aircraft, taking advantage of the transmissivity of cloud and fog to microwaves and the ability for use at night given its active nature. Later development has led to radar becoming a fundamental remote sensing instrument, able to provide unique information on surface properties such as moisture content, salinity and physical characteristics (shape, size and geometry), at very small scales and with high accuracy (Ulaby et al. 1982, Oliver and Quegan 1998, Woodhouse 2005).

The frequencies used by radar imaging systems are grouped into bands (Table 2-1) that formerly related to the various instruments used to transmit and receive signals at these frequencies. The names of these bands were given during a time of war and deliberately coded to prevent easy interpretation (Woodhouse 2005). The most commonly used frequency bands by spaceborne imaging radar systems are X, C and L band (Moreira et al. 2013).

Table 2-1. Commonly used frequency bands for SAR systems (from Moreira et al. (2013)).

Frequency Band	Frequency (GHz)	Wavelength (cm)
Ka	40-25	0.75-1.2
Ku	17.6-12	1.7-2.5
X	12-7.5	2.5-4
C	7.5-3.75	4-8
S	3.75-2	8-15
L	2-1	15-30
P	0.5-0.25	60-120

2.4 The radar equation

The radar equation describes the relation between the power of the incident electromagnetic wave emitted by an instrument, which is intercepted by an object, and the power of the electromagnetic wave that returns from this object to the instrument (Mott 1992, Lee and Pottier 2009).

$$P_R = \frac{P_T G_T \sigma A_R}{(4\pi)^2 R^4} \quad 2.7$$

where P_R is the power detected at the receiving antenna, P_T the power transmitted, G_T the transmitting antenna gain, A_R the effective aperture of the receiving antenna, R the distance between the transmitting antenna and the target, and σ the radar cross section. σ determines the effect the target

itself has on the incident radiation and is defined as the cross section of an equivalent idealised isotropic scatterer that produces the same scattered power density as the object in the observed direction (Lee and Pottier 2009)

Equation 2.7 shows how quickly the signal drops with range (by a factor of $1/R^4$). This puts a limit on the transmitting power of a radar system to ensure the received signal is greater than the instrument noise, N_0 . It is therefore useful to write the radar equation as a Signal to Noise Ratio (SNR)

$$\frac{P_R}{N_0} = \frac{P_T G_T \sigma A_R}{(4\pi)^2 R^4 N_0} \quad 2.8$$

The only term in 2.7 which is dependent on the target is σ . All other parameters depend on the instrument and should be known. σ can be calculated from equation 2.7 as follows:

$$\sigma = \frac{P_R (4\pi)^2 R^4}{P_T G_T \sigma A_R} \quad 2.9$$

The radar cross section of an object is a function of many parameters. Some of these are connected with the imaging system:

- Frequency
- Polarisation
- Imaging configurations: azimuth and elevation angles of both incident and scattering directions

Others are associated with the target:

- Geometric structure
- Dielectric properties

In Earth Observation, the target is usually a distributed area, rather than a discrete object. It is therefore more appropriate to normalise the radar cross section to a unit area, A_0 . This normalised radar cross section is also referred to as the backscattering coefficient, σ_0 :

$$\sigma_0 = \frac{\sigma}{A_0} \quad 2.10$$

(Lee and Pottier 2009)

2.5 Real Aperture Radar

Early imaging radar systems were known as Side Looking Airborne Radar (SLAR). These were mounted on airborne platforms and would measure the return signal from a sequence of pulses emitted from a side looking geometry, perpendicular to the line of flight, as shown in Figure 2.2.

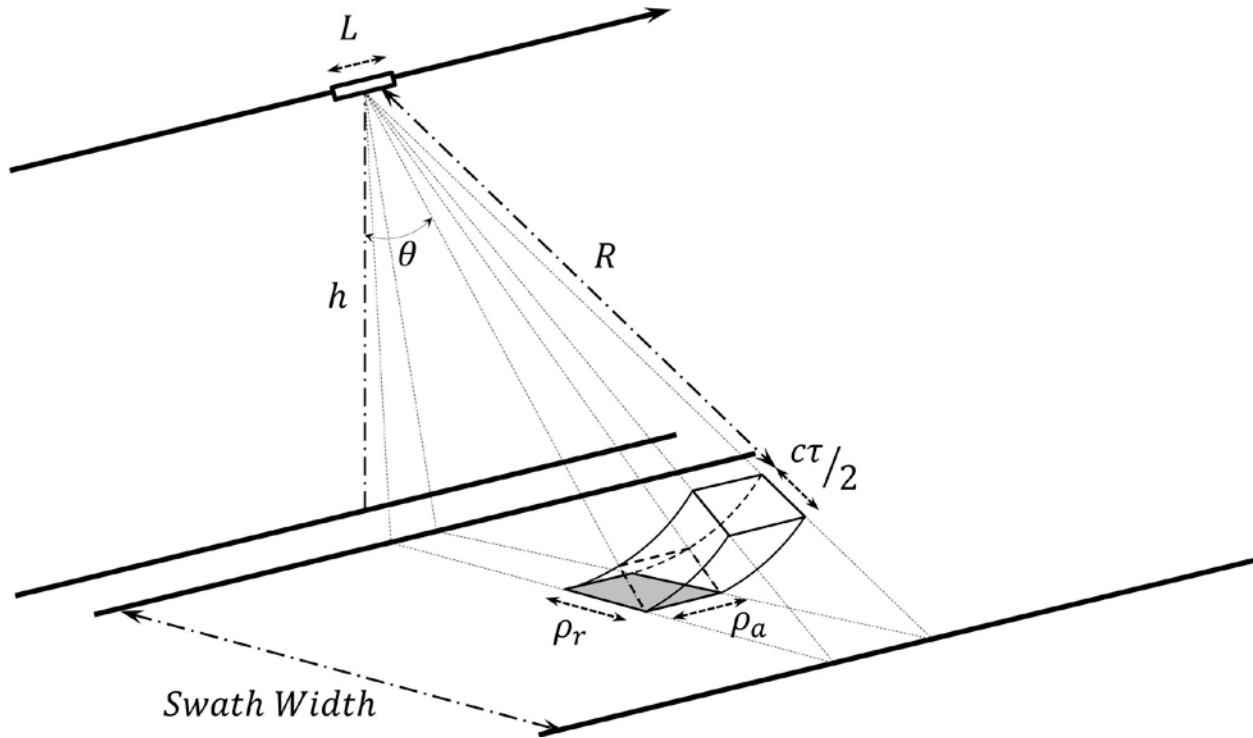


Figure 2.2. RAR geometry. τ is the radar pulse duration, θ the incidence angle, ρ_r the range resolution and ρ_a the azimuth resolution.

The limit of the range resolution of a SLAR system can be defined as the ability to distinguish (in time) the return pulses from two point targets (Woodhouse 2005).

$$\rho_r = \frac{c\tau}{2} \quad 2.11$$

The range resolution is therefore limited by the length of the pulse, τ . However, the shorter the pulse, the weaker the power that a transmitter can generate. To avoid reducing the pulse length, while optimising range resolution, a frequency modulated pulse is used. The range resolution then depends on the pulse beamwidth, B_p , such that:

$$\rho_r = \frac{c}{2B_p} \quad 2.12$$

The ground range resolution is the range resolution (which is in slant range) projected onto a ground reference surface. It is given by:

$$\rho_g = \frac{c}{2B_p \sin \theta_i} \quad 2.13$$

where θ_i is the local incidence angle (the angle between the line of sight and the normal to the reference surface).

2. Principles of Synthetic Aperture Radar

The azimuth resolution depends on the width of the beam on the ground, which in turn depends on the antenna length, L , and the range:

$$\rho_a \approx \frac{\lambda R}{L} \quad 2.14$$

The resolution that this would provide from airborne platforms may be reasonable. However, from a spaceborne platform, only a very low azimuth resolution would be feasible, given the impracticalities of constructing such a large antenna to compensate for the high range. An alternative is therefore required to improve the azimuth resolution. This is achieved through aperture synthesis (Ulaby et al. 1981, Woodhouse 2005).

2.6 Synthetic Aperture Radar

Synthetic Aperture Radar (SAR) improves the azimuth spatial resolution taking advantage of the Doppler frequency shift that occurs as the relative velocities change between the ground in the footprint, along the azimuth axis, and the instrument as it moves along its orbital path. The length of this “synthetic aperture” is approximately equal to the beam width provided by the actual antenna. Pulses are transmitted from a small antenna over a series of broad overlapping footprints as the antenna moves in azimuth. Through azimuth compression the phase histories of targets on the ground from pulses emitted in different positions along the track are then used to improve considerably the azimuth spatial resolution, the theoretical limit of which is now given by:

$$\rho_a = \frac{L}{2} \quad 2.15$$

The azimuth resolution for SAR still depends on the antenna length, but remarkably, the smaller the antenna, the higher the resolution. Also, the resolution no longer depends on the range (Ulaby et al. 1981, Woodhouse 2005). Figure 2.3 illustrates the SAR technique.

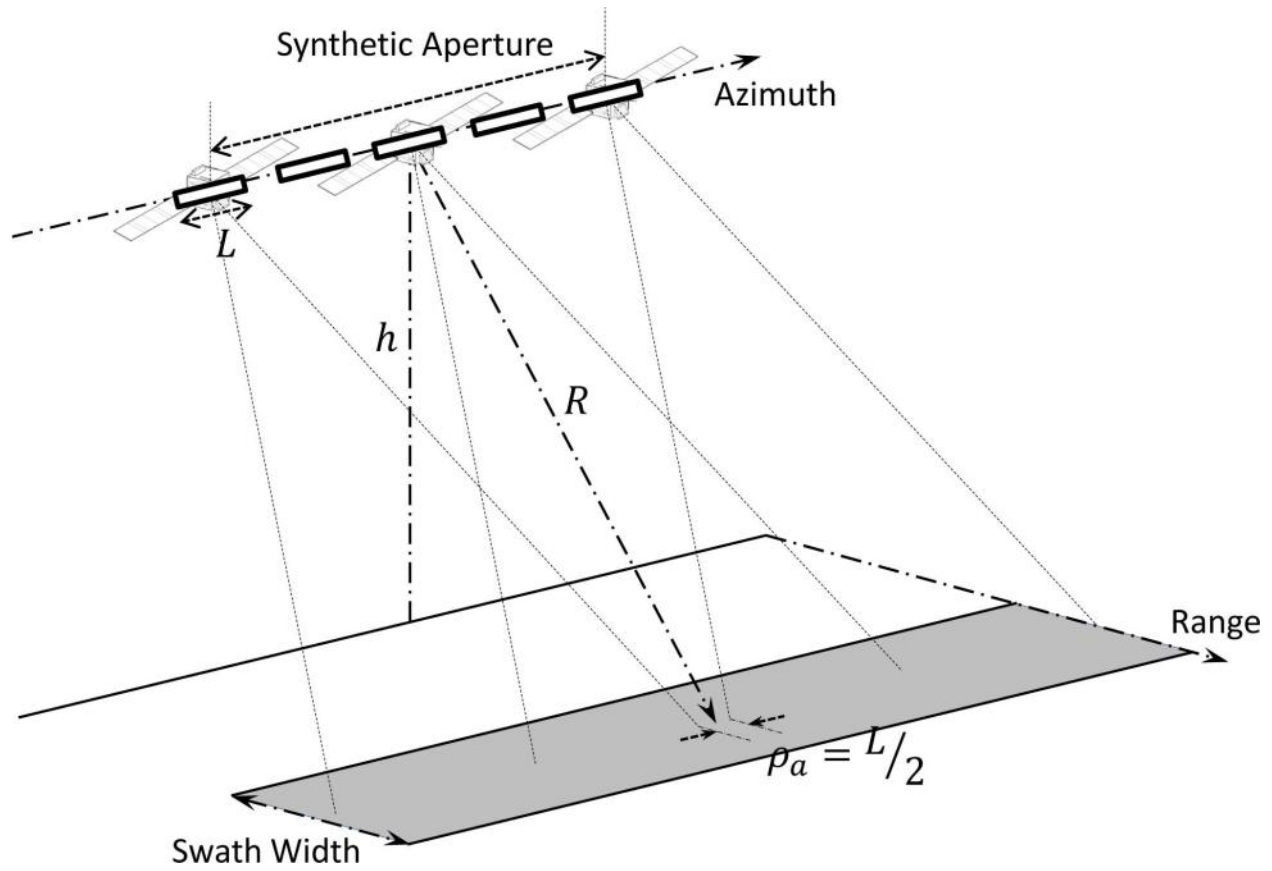


Figure 2.3 SAR imaging geometry.

2.7 Speckle

A characteristic of coherent imaging systems, such as SAR, is speckle. Speckle looks like “salt and pepper” noise, due to the seemingly random grainy appearance of the imagery. Speckle however is not, strictly speaking, noise, given that it is a deterministic and repeatable phenomenon. It is caused by interference among the coherent signals of individual scatterers within a resolution cell (Woodhouse 2005).

The speckle phenomenon can be described in vector form in Figure 2.4. i corresponds to the imaginary and j corresponds to the real part of the complex signal. A is the signal amplitude and θ the phase. The phase and amplitude from many individual scatterers within two seemingly similar pixels will combine coherently to produce measured phases and amplitudes that may be very different between the two pixels (Moreira et al. 2013).

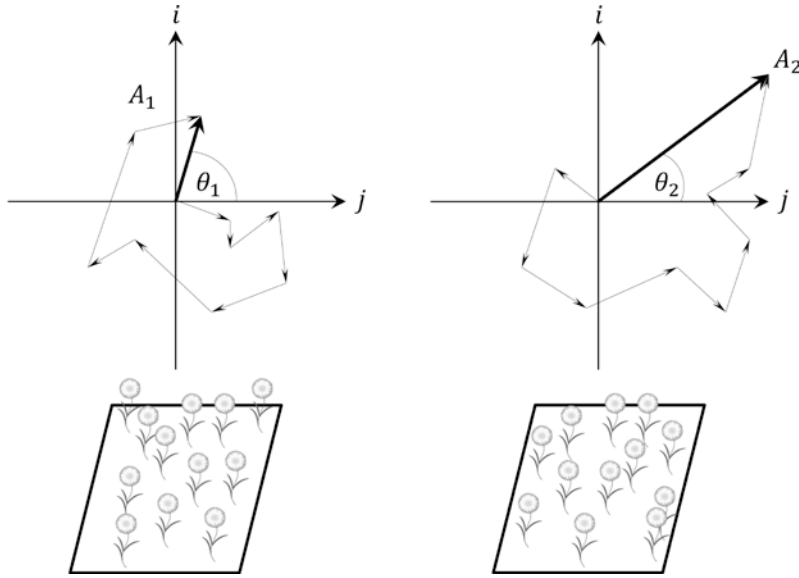


Figure 2.4. Characteristics of image speckle. Two pixels are shown with similarly vegetated land cover (below left and right). The final backscatter, derived from the coherent sum of individual point targets, is very different for each pixel, as shown by the graphical representation of each (above left and right).

Speckle is considered fully developed when in each resolution cell there is a large number of randomly distributed scatterers, statistically independent of each other, without any dominant scatterers, and with uniformly distributed phases (Henderson and Lewis 1998).

In the case of fully developed speckle, both the real and imaginary components will be Gaussian distributed with a mean of zero and a variance of $\sigma^2/2$, which depends on the amplitudes of individual scatterers. The Probability Density Function (PDF) of any real, z_i , and imaginary, z_j , values occurring in a wave is given by:

$$P(z_i, z_j) = \frac{1}{\pi\sigma} e^{-\left(\frac{z_i^2 + z_j^2}{\sigma}\right)} \quad 2.16$$

Here the phase is uniformly distributed across the 2π range.

The PDF of the amplitude, A , is given by the Rayleigh distribution:

$$P(A) = \frac{2A}{\sigma} e^{-\left(\frac{A^2}{\sigma}\right)}, \quad A \geq 0. \quad 2.17$$

The mean value of A is $\frac{1}{2}\sqrt{\pi\sigma}$. However, it is the power (or intensity) that is of interest, given that it is directly related to the definition of the radar cross section in the radar equation. The PDF of the intensity has a negative exponential distribution given by:

$$P(I) = \frac{1}{\sigma} e^{-\left(\frac{I}{\sigma}\right)}, \quad I \geq 0. \quad 2.18$$

Here both the mean and standard deviation are equal to σ .

An improved estimate of σ can be obtained by taking an incoherent average of a number of independent estimates of the same target. This is referred to as multilooking. It is important to take an incoherent rather than a coherent average given that it is the average power that is of interest. Taking a coherent average, including the phase, the statistics of the intensity would merely be the same as in Equation 2.18. With N independent measurements of a uniform distributed scatterer, the PDF of the intensity is now

$$P(I) = \frac{1}{\Gamma(N)} \left(\frac{N}{\sigma}\right)^N I^{N-1} e^{-NI/\sigma}, \quad I \geq 0. \quad 2.19$$

Where $\Gamma(N) = (N - 1)!$ is the gamma function. The variance of the intensity is given by σ^2/N . This may be used to provide an Equivalent Number of Looks (ENL), given by,

$$ENL = \frac{\text{mean}^2}{\text{variance}} \quad 2.20$$

(Oliver and Quegan 1998)

This ENL is useful to estimate the true value of N over a part of an image where it can be applicable, as it may not be known due for example to spatial filtering, or resampling following geometric correction (Woodhouse 2005).

2.8 SAR calibration

Radar backscatter, β , is expressed as a ratio between the scattered power, P_s , and incident power, P_i , at ground level, such that $\beta = P_s/P_i$. The backscatter coefficient is the backscatter ratio estimate per given reference area (Small 2011).

In the simplest case, the SAR system measures the radar brightness per unit area in slant range. This is referred to as β^0 , and is given by,

$$\beta^0 = \frac{\beta}{A_\beta} \quad 2.21$$

If this is projected onto the ground range, the backscatter coefficient is referred to as σ^0 . This can be calculated for a ground area of a reference ellipsoid, in which case θ refers to the incidence angle, or it can be calculated taking into account the local terrain, such as that derived from a DEM. In this case, θ corresponds to the local incidence angle of the relief.

$$\sigma^0 = \frac{\beta^0}{\sin \theta} \quad 2.22$$

Many surface features act like volume scatterers, scattering energy in all directions. In this case the value of σ^0 varies only in proportion to the projected area of the incident energy, and it is convenient to normalise the σ^0 by the cosine of the local incidence angle. This is referred to as γ^0 , and is given by,

$$\gamma^0 = \frac{\sigma^0}{\cos \theta} \quad 2.23$$

Figure 2.5 illustrates the various ways to express the backscattering coefficient according to the various reference areas.

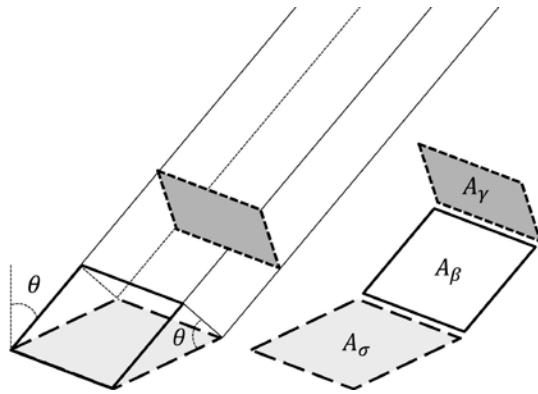


Figure 2.5 Diagram showing SAR normalisation areas of A_β , A_σ and A_γ corresponding to the respective SAR calibration of β^0 , σ^0 and γ^0 . Based on diagram in (Small 2011).

(Small 2011)

2.9 SAR Geometric Distortions

The side looking geometry of SAR and the fact that it is an active ranging instrument means that geometric distortion will take place over areas of topography. This is illustrated in Figure 2.6, which shows various points on a surface with varying topography and their corresponding points on the SAR image plane.

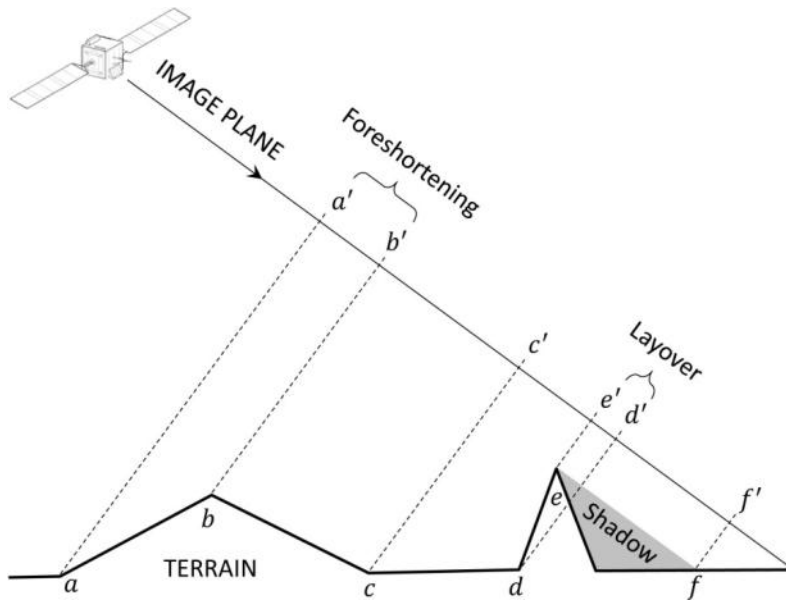


Figure 2.6. Diagram showing distortion effects on SAR images due to terrain.

Foreshortening occurs if the terrain slope is oriented towards the instrument, but not so much as to exceed the point where the surface is perpendicular to the SAR pulse. In this case, objects on the ground surface will appear closer to each other in the SAR image plane. If the terrain slope is oriented towards the instrument and exceeds the point where the surface is perpendicular to the SAR pulse, layover occurs. In this case, objects on the ground appear flipped in the SAR image plane, due to backscatter being received from the top of the slope prior to the bottom. In areas of steep topography, the SAR pulse may be blocked in its path, and some areas of the surface are therefore not visible. These areas are referred to as radar shadow (Massonnet and Souyris 2008).

2.10 SAR images

Only after techniques called range and azimuth compression is an image obtained with the SAR backscatter contained in discrete pixels representing spatial areas (Moreira et al. 2013).

2.10.1 Single Look Complex

In Single Look Complex (SLC) images, each pixel contains both the phase and amplitude of the backscatter with a single look and in slant range geometry. In single look data the azimuth compression has been carried out using the full azimuth bandwidth of the sensor. This produces the highest azimuth spatial resolution, but at the cost of higher speckle. The image pixels are usually not square, given that the range and azimuth resolutions are not the same. SLC images are required for applications that use the phase, such as interferometry (Oliver and Quegan 1998, Massonnet and Souyris 2008).

2.10.2 Multi Look Detected

For applications that do not require the phase, it is often more convenient to use Multi Look Detected (MLD) images. MLD images have been multilooked, usually to produce pixels of equal dimensions in

range and azimuth. As the multilook process is done by incoherent averaging, the phase information is lost (Woodhouse 2005).

2.11 SAR acquisition modes

SAR systems operate at various different imaging modes. The most fundamental mode is stripmap, where the SAR system images a single continuous strip. The scanSAR mode is able to increase the swath width through successive steering of the antenna to different elevation angles. In the case of the Terrain Observation through Progressive Scans (TOPS) mode, the antenna is also steered in azimuth while scanning each sub-swath. With the increased swath width there is usually a trade-off with resolution given that less time can be spent scanning each area. With spotlight modes the opposite effect is achieved. A higher resolution image can be acquired, but at the expense of area coverage. In this case the antenna is steered in azimuth towards a fixed point to achieve a longer illumination time. The drawback of this technique is that only discontinuous areas can be imaged, rather than a continuous swath (Moreira et al. 2013). Figure 2.7 illustrates the SAR acquisition modes of stripmap, ScanSAR and spotlight.

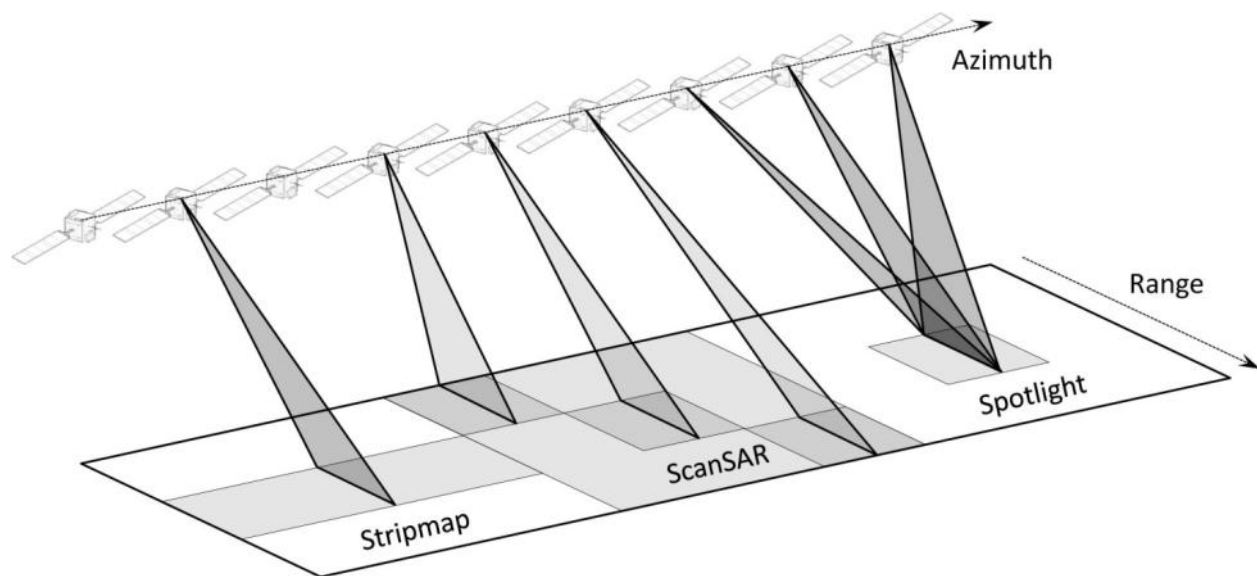


Figure 2.7. Common SAR image acquisition modes.

2.12 PolSAR

Polarimetric SAR (PolSAR) seeks to obtain information not only about the amplitude and phase of electromagnetic waves, but also of the shape and orientation of the electric field vector. The polarisation of a wave, and the relative phase and amplitude differences between waves of different polarisation, can provide much information about the nature of a scattering object (Lee and Pottier 2009).

Polarised waves can be described by two orthogonal components of the electric field vector combined in a wave vector, which propagates in the third component of a Cartesian coordinate system:

$$\mathbf{E}(r, t) = \begin{bmatrix} E_x \cos(\omega t - kz + \varphi_x) \\ E_y \cos(\omega t - kz + \varphi_y) \\ 0 \end{bmatrix} \quad 2.24$$

The polarisation of a wave can be visualised in a polarisation ellipse (Figure 2.8), which describes the shape of a polarised wave with the following parameters:

Amplitude, A , given by,

$$A = \sqrt{E_x^2 + E_y^2} \quad 2.25$$

Orientation angle, $\phi \in \left[-\frac{\pi}{2}, \frac{\pi}{2}\right]$, given by,

$$\tan 2\phi = 2 \frac{E_x E_y}{E_x^2 - E_y^2} \cos \varphi, \text{ with } \varphi = \varphi_y - \varphi_x \quad 2.26$$

Ellipticity, $\tau \in \left[0, \frac{\pi}{4}\right]$, given by,

$$|\sin 2\tau| = 2 \frac{E_x E_y}{E_x^2 - E_y^2} |\sin \varphi| \quad 2.27$$

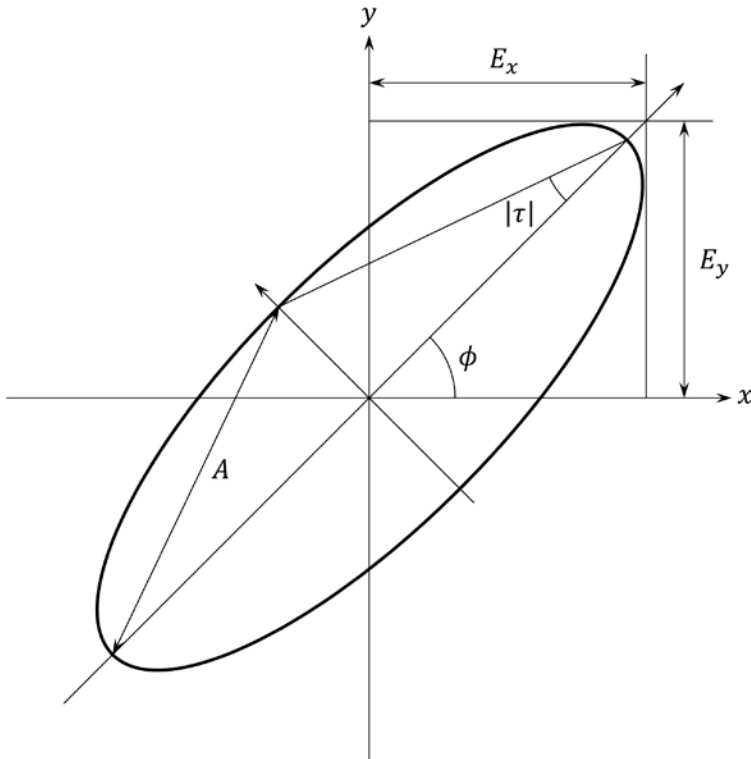


Figure 2.8. Polarisation ellipse.

(Woodhouse 2005, Lee and Pottier 2009)

2.12.1 Stokes Vector

A more practical description of a polarised wave is given by the Stokes vector, which is composed of four elements: I_0 , Q , U and V . The first term, I_0 , is proportional to the total intensity of the wave. The other three terms correspond to the state of polarisation of the wave: Q describes the extent to which the wave is vertical ($Q < 0$) or horizontal ($Q > 0$), assuming a horizontal and vertical basis is chosen; U describes the extent to which the wave is polarised at $+45^\circ$ ($U > 0$) or -45° ($U < 0$); V describes the direction of propagation, whether to the right ($V < 0$) or to the left ($V > 0$). The Stokes vector is given by,

$$\mathbf{g} = \begin{bmatrix} I_0 \\ Q \\ U \\ V \end{bmatrix} = \begin{bmatrix} |E_y|^2 + |E_x|^2 \\ |E_y|^2 - |E_x|^2 \\ 2\Re(E_y E_x^*) \\ -2\Im(E_y E_x^*) \end{bmatrix} = I_0 \begin{bmatrix} 1 \\ \cos 2\phi \cos 2\tau \\ \sin 2\phi \cos 2\tau \\ \sin 2\tau \end{bmatrix} \quad 2.28$$

where * represents the complex conjugate. From this, the following can be established,

$$I_0 = Q + U + V \quad 2.29$$

This means that out of the four Stokes parameters, there are only three which are independent (Lee and Pottier 2009).

2.12.2 Poincaré sphere

A convenient way to visualise the three independent Stokes parameters is with the Poincaré sphere (Figure 2.9). This is a spherical representation with the radius corresponding to I_0 , degrees of longitude to the orientation angle, ϕ , and degrees of latitude to the ellipticity, τ . The angle, α , corresponds to the absolute phase (Lee and Pottier 2009).

2.12.5 Scattering Matrix

The backscatter from fully polarimetric SAR systems can be described by the scattering matrix (or Sinclair matrix), which for the linear horizontal and vertical basis can be described by,

$$\mathbf{E}^s = \frac{e^{-ikR}}{R} \begin{bmatrix} S_{HH} & S_{HV} \\ S_{VH} & S_{VV} \end{bmatrix} \mathbf{E}^i \quad 2.31$$

where \mathbf{E}^i and \mathbf{E}^s are the incident and scattered Jones vectors, and e^{-ikR}/R takes into account propagation effects (where k is the wavenumber and R is the slant range distance). The matrix elements S_{HH} , S_{HV} , S_{VH} and S_{VV} are the complex scattering coefficients in the respective configurations of horizontal transmit and horizontal receive (HH), horizontal transmit and vertical receive (HV), vertical transmit and horizontal receive (VH) and vertical transmit and vertical receive (VV).

For a SAR operating in the monostatic Backscatter Alignment (BSA) configuration, using the same antenna for both transmission and reception, reciprocity can be assumed. This implies that S_{HV} is identical to S_{VH} , which reduces the matrix elements to 3 instead of 4, and the number of independent parameters of the scattering matrix from 7 to 5: including three amplitudes, two relative phases and one absolute phase.

(Lee and Pottier 2009)

2.12.6 Covariance matrix and coherency matrix

The scattering matrix is only able to describe coherent targets, or “pure” targets, characterised by one dominant scattering mechanism. In reality, most resolution cells cover regions characterised by distributed targets of mixed scattering mechanisms. Second order polarimetric representations are therefore required that can analyse distributed scatterers that contribute to the speckle effect in SAR data. Such second order descriptors include the covariance matrix \mathbf{C}_3 and coherency matrix \mathbf{T}_3 .

The covariance matrix is formed by multiplying the vectorised scattering matrix with its transpose. The vectorised scattering matrix can be given by,

$$\mathbf{k}_{3L} = [S_{HH} \ \sqrt{2}S_{HV} \ S_{VV}]^T \quad 2.32$$

The covariance matrix is then given by,

$$\mathbf{C}_3 = \mathbf{k}_{3L} \mathbf{k}_{3L}^{*T} = \left\langle \begin{bmatrix} |S_{HH}|^2 & \sqrt{2}S_{HH}S_{HV}^* & S_{HH}S_{VV}^* \\ \sqrt{2}S_{HV}S_{HH}^* & |S_{HV}|^2 & \sqrt{2}S_{HV}S_{VV}^* \\ S_{VV}S_{HH}^* & \sqrt{2}S_{VV}S_{HV}^* & |S_{VV}|^2 \end{bmatrix} \right\rangle \quad 2.33$$

(Lee and Pottier 2009).

The coherency matrix is formed by multiplying the Pauli vectorisation with its transpose (Woodhouse 2005). The Pauli vectorisation is given by,

$$\mathbf{k}_{3P} = \frac{1}{\sqrt{2}} [S_{HH} + S_{VV} \quad S_{HH} - S_{VV} \quad 2S_{HV}]^T \quad 2.34$$

The coherency matrix is thus,

$$\mathbf{T}_3 = \mathbf{k}_{3P} \mathbf{k}_{3P}^{*T} \quad 2.35$$

$$\mathbf{T}_3 = \left\langle \begin{bmatrix} |S_{HH} + S_{VV}|^2 & (S_{HH} + S_{VV})(S_{HH} + S_{VV})^* & 2(S_{HH} + S_{VV})S_{HV}^* \\ (S_{HH} - S_{VV})(S_{HH} + S_{VV})^* & |S_{HH} - S_{VV}|^2 & 2(S_{HH} - S_{VV})S_{HV}^* \\ 2S_{HV}(S_{HH} + S_{VV})^* & 2S_{HV}(S_{HH} - S_{VV})^* & 4|S_{HV}|^2 \end{bmatrix} \right\rangle \quad 2.36$$

(Lee and Pottier 2009)

2.12.7 Polarimetric decompositions

Polarimetric decompositions attempt to express the radar backscatter from an object as a combination of scattering responses from a number of simpler objects with known backscatter characteristics. These simple objects could include a plane, diplane, sphere, helix, etc. In some cases, rather than referring to objects, decompositions specify scattering mechanisms, such as single, double and volume scattering.

Polarimetric decompositions can be divided between those which assume coherent, simple targets, which have a clearly defined dominant scattering mechanism (coherent decompositions), and those which assume the target is diffuse and incoherent (incoherent decompositions). Coherent decompositions are based on the scattering matrix, $[S]$, as measured by the SAR instrument. They attempt to express $[S]$ as the combination of the scattering matrices of simpler objects, such that,

$$[S] = \sum_{i=1}^k c_i [S]_i \quad 2.37$$

where $[S]_i$ is the scattering matrix of each simple object (also known as canonical objects), and c_i is the weight of contribution of each to the final scattering matrix (Lee and Pottier 2009).

Some common coherent decompositions include the Pauli (Cloude and Pottier 1996), Krogager (Krogager 1990) and Cameron (Cameron and Leung 1990) decompositions. Incoherent decompositions are based on the covariance or coherency matrices. They include, amongst many others, the Freeman (Freeman and Durden 1998), Huynen (Huynen 1982), Barnes (Barnes 1988) and H,A,alpha decompositions (Cloude and Pottier 1996). The latter include an analysis of the degree of polarimetric coherence of a target (entropy), which determines the extent to which a target is dominated by a single scattering mechanism. The Touzi criterion (Touzi and Charbonneau 2002) seeks to identify whether a

particular scene is composed of pure targets, over which therefore coherent decompositions can be applied, or whether incoherent decompositions are more appropriate.

2.12.7.1 Pauli decomposition

One of the most common coherent decompositions is the Pauli decomposition. In the conventional linear horizontal/vertical basis, the Pauli decomposition expresses the scattering matrix as a combination of the following,

$$[S]_a = \frac{1}{\sqrt{2}} \begin{bmatrix} 1 & 0 \\ 0 & 1 \end{bmatrix} \quad 2.38$$

$$[S]_b = \frac{1}{\sqrt{2}} \begin{bmatrix} 1 & 0 \\ 0 & -1 \end{bmatrix} \quad 2.39$$

$$[S]_c = \frac{1}{\sqrt{2}} \begin{bmatrix} 0 & 1 \\ 1 & 0 \end{bmatrix} \quad 2.40$$

$$[S]_d = \frac{1}{\sqrt{2}} \begin{bmatrix} 0 & -1 \\ 1 & 0 \end{bmatrix} \quad 2.41$$

Assuming reciprocity, where $S_{HV} = S_{VH}$, which is the case for a monostatic system, the Pauli basis can be reduced to,

$$\{[S]_a, [S]_b, [S]_c\} \quad 2.42$$

These are the scattering mechanisms of simple, canonical objects: $[S]_a$ is that of a plane, or trihedral, or any surface characterised by odd bounce scattering; $[S]_b$ is the scattering matrix of a dihedral oriented at 0 degrees, characterised by double bounce scattering; $[S]_c$ represents the scattering matrix of a diplane oriented at 45 degrees. This last contribution changes the orientation of the incident wave (the object returns a wave with a polarization orthogonal to the incident one). This is characteristic of many randomly oriented targets, such as that of a vegetation canopy. It is therefore commonly associated with volume scattering.

A measured scattering matrix can then be expressed as,

$$[S] = \begin{bmatrix} S_{HH} & S_{HV} \\ S_{VH} & S_{VV} \end{bmatrix} = k_1[S]_a + k_2[S]_b + k_3[S]_c \quad 2.43$$

where

$$k_1 = \frac{S_{HH} + S_{VV}}{\sqrt{2}} \quad 2.44$$

$$k_2 = \frac{S_{HH} - S_{VV}}{\sqrt{2}} \quad 2.45$$

$$k_3 = \sqrt{2}S_{HV} \quad 2.46$$

From equations 2.44, 2.45 and 2.46 it can be shown that the span of $[S]$ can be derived as follows,

$$SPAN = |S_{HH}|^2 + |S_{VV}|^2 + 2|S_{HV}|^2 = |k_1|^2 + |k_2|^2 + |k_3|^2 \quad 2.47$$

where $|k_1|^2$, $|k_2|^2$ and $|k_3|^2$ are the power scattered by targets characterised by the $[S]_a$, $[S]_b$ and $[S]_c$ scattering matrices respectively.

The Pauli decomposition of a SAR image therefore produces separate image channels representing the contributions of $|k_1|^2$, $|k_2|^2$ and $|k_3|^2$. These are commonly displayed as a 3 colour composite with $|k_1|^2$ (odd bounce) displayed as red, $|k_2|^2$ (double bounce) as blue, and $|k_3|^2$ (volume scattering) as green.

(Lee and Pottier 2009)

2.13 InSAR

Interferometric SAR (InSAR) is a technique that makes use of the coherent properties of SAR images to compare signals. The absolute phase of an electromagnetic wave is very difficult to measure, and in itself, would provide little information. However, the relative phase difference between two or more coherent waves can be measured and utilised to provide unique information, including centimetric, or even millimetric, surface displacements from space. The correlation of the subtle pattern of phase differences over an area can also provide a distinctive indication of the spatial variability and randomness of the individual scatterers in a resolution cell (Ferretti et al. 2007).

For a phase difference to exist, more than one measurement obtained separately in either space or time is required. The spatial separation of measurements for InSAR applications relevant to this thesis is in the across track direction, perpendicular to the orbital path. This is referred to as across track interferometry. Multiple measurements can be made simultaneously from a single platform with two receiving antennas with a particular baseline of separation (single pass interferometry), or they can be made separately from an instrument with a single receiving antenna, but from different orbital cycles (repeat pass interferometry) (Woodhouse 2005).

Figure 2.10 shows the interferometric configuration for two antennas separated by a baseline, B . There are various ways to describe the baseline of separation, the most common, and relevant to this discussion, being the perpendicular baseline, B_{\perp} . Another way to describe the baseline is by its parallel component, B_{\parallel} . h is the height of the reference antenna above a reference surface, R is the slant range of the reference signal and θ is the incidence angle between the reference range and normal to the reference surface. a and b refer to two points on the surface (Woodhouse 2005, Ferretti et al. 2007).

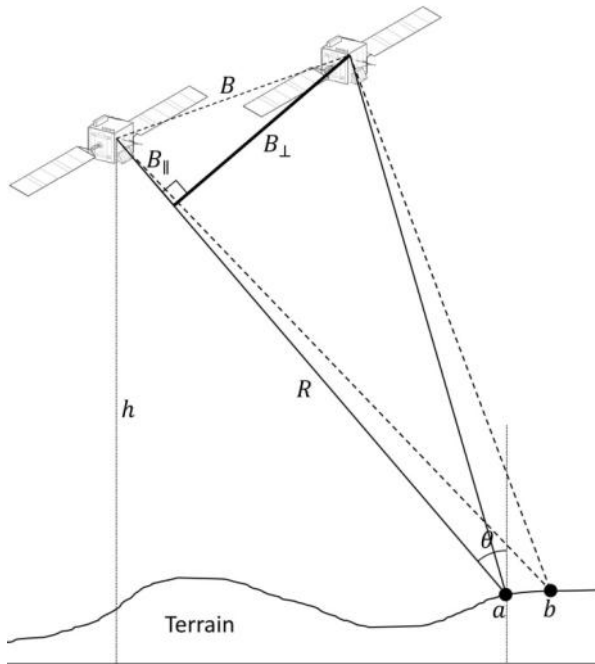


Figure 2.10. InSAR acquisition configuration.

The difference in the relative phases between two signals received from the same point on the surface varies from one point (such as point a in Figure 2.10) to another (such as point b). This phase difference is given by,

$$\Delta\phi = \frac{2\pi\Delta r}{\lambda} \quad 2.48$$

where Δr is the path difference variation between the pairs of signals received at each point. $\Delta\phi$ can be expressed in relation to the perpendicular baseline, the slant range displacement (ΔR) and the height variation (Δh) between the two points, given by,

$$\Delta\phi = -\frac{4\pi}{\lambda} \frac{B_{\perp}\Delta h}{R \sin \theta} - \frac{4\pi}{\lambda} \frac{B_{\perp}\Delta R}{R \tan \theta} \quad 2.49$$

The perpendicular baseline can be calculated from precise knowledge of the antenna orbital positions. The slant range phase variation can be computed and subtracted in a step referred to as interferogram flattening, leaving the phase variation due to topography.

(Ferretti et al. 2007)

2.13.1 Altitude of Ambiguity

The value of Δh that generates an interferometric phase change of 2π after interferogram flattening is referred to as the altitude of ambiguity, h_a , and can be expressed as,

$$h_a = \frac{\lambda R \sin \theta}{2B_{\perp}} \quad 2.50$$

The altitude of ambiguity is therefore inversely proportional to the perpendicular baseline. In theory, the higher the baseline, the more accurate the altitude measurement, given that the phase noise is equivalent to a smaller altitude noise. However, the higher the baseline, the denser the fringes of topography induced phase variation and the harder it is to translate “unwrap” the fringes into height measurements (Ferretti et al. 2007).

2.13.2 Critical Baseline

There is also an upper limit to the perpendicular baseline, beyond which the interferometric signals decorrelate, this is a function of the instrument band width, B_{bw} , height, incidence angle and frequency, f , and is given by,

$$B_{cr} = \frac{B_{bw} h \sin \theta}{f \cos^2 \theta} \quad 2.51$$

This upper limit to the perpendicular baseline is referred to as the “critical baseline” (Rodriguez and Martin 1992, Ferretti et al. 2007).

2.13.3 Range Spectral Shift Filtering

The difference in antenna look angles between InSAR acquisition configurations results also in a difference in the portion of range spectra received from each point on the ground, this is known as the Spectral Shift Principle and affects the Critical Baseline. Range Spectral Shift Filtering is the process of removing the non-overlapping portions of range spectra caused by the Spectral Shift Principle in order to improve the interferometric coherence. (Ferretti et al. 2007).

2.13.4 Azimuth Common Band Filtering

Similar to the Range Spectral Shift Filtering, also in azimuth there can be differences in the spectral portion received from a given area on the ground. This can be due to differences in the antenna pointing such as would result in different Doppler Centroids of two InSAR acquisitions. Azimuth Common Band Filtering removes non-overlapping azimuth spectra to improve interferometric coherence (Ferretti et al. 2007).

2.13.5 DEM creation

The processing steps to create a DEM from an InSAR configuration (such as that illustrated in Figure 2.10) include the following:

1. Coregistration

The two complex images need to be coregistered to an accuracy of around 1/10 of the resolution, or better.

2. Range Spectral Shift and Azimuth Common Band Filtering

See Sections 2.13.3 and 2.13.4.

3. Interferogram generation

The interferogram is generated by multiplying one coregistered and spectral-shift-filtered image E_1 with the complex conjugate of the other E_2^* ,

$$Int = E_1 E_2^* \quad 2.52$$

4. Interferogram flattening

Removal of fringes induced by systematic slant range variation.

5. Phase filtering

To aid phase unwrapping, it is common practice to apply a filter to reduce fringe noise.

6. Phase unwrapping

Phase unwrapping removes the 2π ambiguity of fringes.

7. Phase to height conversion

The unwrapped fringes are converted to height values.

8. Geometric correction

The final DEM is then produced following geometric correction onto a map system.

(Ferretti et al. 2007)

2.13.6 Coherence

If a target area is stable enough to produce phase differences that vary gradually over a given area, the phase differences are said to be coherent. If the phase differences are random, due for example to heterogeneous movement of individual point targets within resolution cells between image acquisitions, they are said to be incoherent. A measure of coherence for an N sample window of pixels is given by the following:

$$\gamma = \frac{|\sum_N E_1(x) E_2^*(x)|}{\sqrt{\sum_N |E_1(x)|^2 \sum_N |E_2(x)|^2}} \quad 2.53$$

where $E_1(x)$ and $E_2(x)$ are the Single Look Complex (SLC) pixel values (Ferretti et al. 2007).

This measure of coherence, which ranges from 0 (the pattern of phase differences over the N pixels are completely uncorrelated) to 1 (the phase differences are completely correlated), can provide useful

information about the target. There are many reasons for loss in coherence. The main causes due to target properties include temporal decorrelation and volume decorrelation (Woodhouse 2005).

2.13.6.1 Temporal decorrelation

If loss in coherence occurs due to small scale random movement of scattering elements, such as wind blown leaves in a vegetated area, or wind driven waves on water, this is referred to as temporal decorrelation (Woodhouse 2005).

2.13.6.2 Volume decorrelation

If there is transmission of the microwave signal in a volume, such as dry sand, there is greater probability that loss in coherence will occur. This loss in coherence may be simply due to attenuation of the signal, or it may be caused by the individual scatterers within the volume altering randomly the phase between image acquisitions. Even if these individual scatterers remain constant over time, due to the complexity of scattering within the volume, any slight change in the instrument configuration and geometry between acquisitions may randomly produce a different phase. This loss in coherence due to scattering within a volume is referred to as volume decorrelation (Woodhouse 2005).

2.13.7 DEM error sources

There are several sources of error that can affect InSAR DEM accuracy. Some of the main ones include:

- Phase unwrapping errors
- Phase noise
- Atmospheric effects
- Orbit indetermination (baseline errors)

In DEM generation, the use of multiple interferograms can mitigate some of these errors, and can help fill gaps in areas where coherence may be low (Ferretti et al. 2007).

2.13.8 Small BAseline Subsets (SBAS)

The use of interferometry for monitoring displacement (Differential Interferometry or DInSAR) is outside the scope of this research, given that it is less relevant than other techniques for the type of archaeological prospection discussed here. However, the DInSAR technique of Small Baseline Subsets (SBAS) is applicable, given that it can also be used to generate DEMs. The main concept of SBAS is to generate from a large time series of SLC data, interferograms that are selected to minimise the spatial (for displacement velocities, but not necessarily for DEM generation) and temporal baselines between acquisitions, thus avoiding decorrelation effects (Berardino et al. 2002, Lanari et al. 2007).

The SBAS algorithm is very computationally demanding given that the interferometric workflow is carried out on multiple image pair combinations in, usually large, time series of SLC data. The steps for SBAS DEM generation are given in Figure 2.11. An initial input DEM is required, but even a low resolution *a-priori* DEM is sufficient (Berardino et al. 2002).

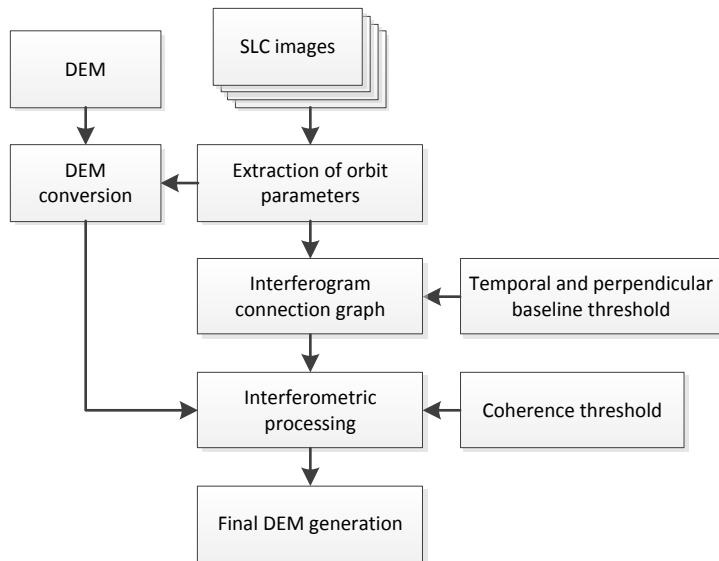


Figure 2.11. Main steps of the SBAS algorithm.

2.14 Interaction of microwaves with surface materials

The interpretation of SAR imagery has to be made with an understanding of the nature of microwave interaction with materials. This interaction depends above all on the dielectric properties of the material; and on its size, shape and density in proportion to the microwave wavelength.

For most applications of Earth Observation with SAR, Earth's atmosphere can be considered transparent to microwaves, given that atmospheric constituents generally have particle sizes that are significantly smaller than most SAR wavelengths. Some exceptions are in cases of heavy rainfall, that may scatter short wavelength SAR signals, and in interferometric applications, where very precise phase differences are measured and can be influenced by atmospheric effects (Woodhouse 2005, Massonnet and Souyris 2008).

The surface of the Earth can be considered a boundary layer on which various types of scattering can be observed. These are described in the following sections.

2.14.1 Scattering from rough surfaces

Given the side looking geometry of a SAR system. Over a smooth flat surface with a local incidence angle less than $\pi/2$, no backscatter is received by the sensor due to specular reflection, which directs the backscatter away from the sensor. Backscatter is observed when the surface is rough, or the geometry orientates the backscatter in the direction of the sensor. Roughness can be described in relation to the SAR wavelength, a definition is provided by the Rayleigh criterion that states that a surface is smooth with respect to a particular wavelength if the root mean square height deviation, h_s , of a surface satisfies the following condition

$$h_s < \frac{\lambda}{8 \cos \theta} \quad 2.54$$

If this condition is not satisfied, a surface is considered rough. The backscatter over surfaces of varying roughness is illustrated in Figure 2.12. In the roughest case, the backscatter is almost entirely diffuse, and does not vary significantly with incidence angle.



Figure 2.12. Backscatter behaviour over surfaces of varying roughness relative to the incident wavelength.

(Ulaby et al. 1982, Massonnet and Souyris 2008)

2.14.2 Bragg scattering

A special case of roughness is when the surface height deviation is not random, but periodic. This results in a coherent addition (resonance) of return waves (Holt 2004), causing high backscatter. This case is referred to as Bragg scattering and is illustrated in Figure 2.13. The wavelength of Bragg waves, λ_B , is given by

$$\lambda_B = \frac{\lambda}{2 \sin \theta} \quad 2.55$$

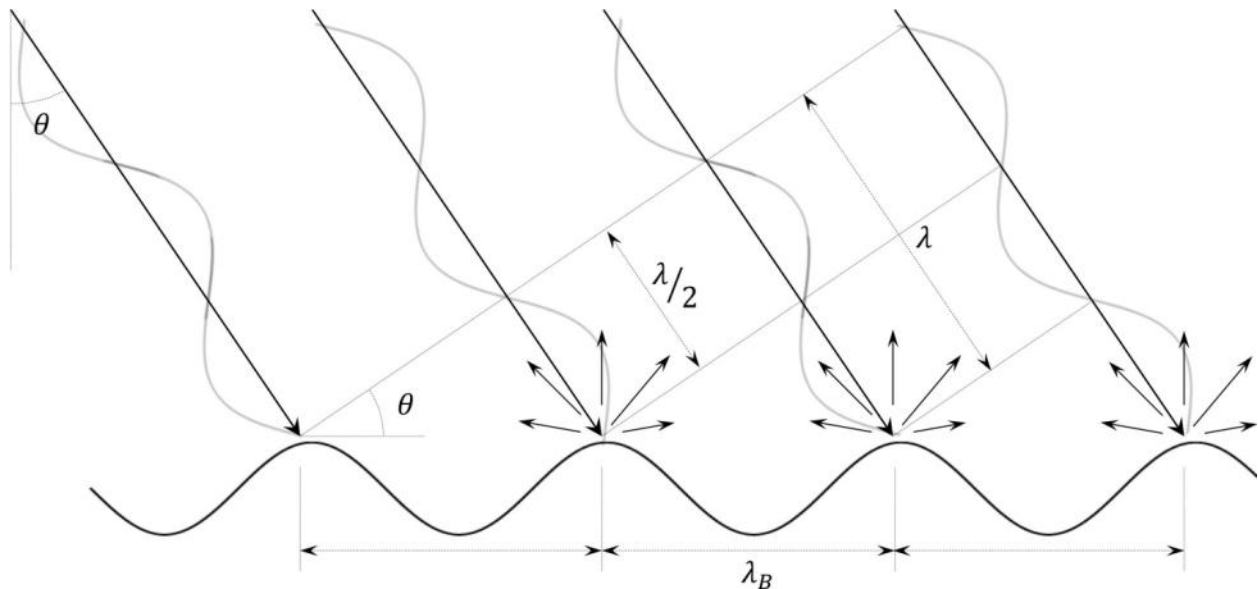


Figure 2.13. Bragg scattering mechanism.

SAR backscatter of sea surfaces is particularly characterised by Bragg scattering (Holt 2004), due to small wind driven capillary waves, or short gravity waves (Woodhouse 2005). Bragg scatter also applies to some land surfaces (Holt 2004).

2.14.3 Volume scattering

In addition to scattering at the surface, electromagnetic waves may interact within the volume of materials such as a vegetation canopy, dry snow and ice, and dry sand (Woodhouse 2005).

Volume scattering occurs in inhomogenous media, such as a vegetation canopy, and is caused mainly by dielectric discontinuities within the volume (Ulaby et al. 1982), which is composed of randomly distributed discrete elements with significant cross-sections.

2.14.4 Signal transmission and attenuation

The penetration of microwave signals in a medium can be described by the following relations.

We can use the following formula to express the intensity at depth z ,

$$I(z) = I_0 \exp \left[- \int_0^z k_e(z') dz' \right] \quad 2.56$$

Where I_0 is the intensity just below the surface, and k_e is the extinction coefficient (Ulaby et al. 1981).

The penetration depth δ_p of an electromagnetic wave inside a material can be defined as the depth z at which,

$$\int_0^{\delta_p} k_e(z) dz = 1 \quad 2.57$$

Or, inserting this into Equation 2.56,

$$I(\delta_p) = I_0 e^{-1} \quad 2.58$$

The penetration depth is therefore defined as the depth at which the intensity of the electromagnetic wave reduces to $1/e$, or to about 36.8% of the intensity of the electromagnetic field immediately beneath the surface (Feynman 2005).

If the assumptions can be made that scattering in the soil volume can be ignored and that the extinction coefficient is constant with depth, then we can re-write equation 1 as follows (Farr et al. 1986),

$$I(z) \cong I_0 \exp \left(-2\alpha \int_0^z dz' \right) \quad 2.59$$

where α is the field attenuation coefficient and can be described accordingly,

$$\alpha = \frac{2\pi}{\lambda} |\text{Im}[\sqrt{\varepsilon}]| \quad 2.60$$

where λ is the wavelength in free space and $\varepsilon = \varepsilon' - j\varepsilon''$ is the relative complex dielectric constant of the material medium.

The penetration depth can be characterised according to α in the following way (Ulaby et al. 1981),

$$\delta_p = \frac{1}{2\alpha} \quad 2.61$$

The penetration depth is therefore directly proportional to the wavelength of the signal and indirectly proportional to the modulus of the imaginary part of the relative complex dielectric constant.

This implies that, in theory, the longer the wavelength of the SAR system, the greater the penetration capability. It also implies that materials that have a very low dielectric constant, such as dry sand, are more inclined to be transparent to microwaves.

3 REVIEW OF LITERATURE ON THE USE OF SAR FOR ARCHAEOLOGICAL PROSPECTION

This chapter outlines the knowledge to date on the scientific principles, techniques and the most significant previous results of the use of spaceborne SAR for archaeological prospection. After a brief discussion and justification of the origins of the subject in Section 3.1, the chapter is divided into four main sections, each focussing on a particular technique applicable to different surface types most relevant for archaeological research. These sections include: prospection through topographic analysis (Section 3.2); prospection through sand volume transmission (Section 3.3); prospection through vegetation and soil proxies (Section 3.4); and prospection under water (Section 3.5). Each section includes literature reviews of both the SAR technique, or the underlying physical principle, and its application for archaeological prospection. In many cases a particular archaeological feature may be identified through a range of the techniques outlined above. For example, buried archaeological structures may leave a topographic trace at the surface and also alter overlying vegetation. These features may therefore be identified in topographic images or through analysis of the vegetation characteristics. The latter may in turn alter the backscatter through differences in the relative permittivity (moisture) or differences in geometric roughness (differential vegetation height) with respect to areas surrounding the buried feature. Many of the previous studies referred to in the sections below employ a range of techniques, these may therefore be cited multiple times.

3.1 Origins

A literature review should summarise past developments in a certain topic and provide the current state of advancement. But how far back should one go? This particular topic is a marriage of two separate disciplines: archaeology and Synthetic Aperture Radar. The only real similarity between the two is that they could both be considered a scientific discipline, however, archaeologists often consider themselves more humanitarians than scientists.

To provide a review of developments of each topic separately would exacerbate the dilemma of where to begin. Synthetic Aperture Radar (SAR) is an ingenious technique of synthesising a larger aperture to improve the spatial resolution of imaging radar. However, advancement in SAR technology follows developments in our understanding of electromagnetism, which is still very much in its infancy. Progress in our comprehension of the subject can be traced almost to the beginning of recorded history, with evidence of early perception of electricity documented on ancient Egyptian murals from around 2750 BC depicting electric catfish next to the symbol for lightning (Kramer 2012).

Similarly, debates on the origins of archaeological research vary widely. Some may argue that its roots lie with antiquarianism: the study of history through analyses of physical objects, such as artifacts, manuscripts and monuments. This saw particular progress during the age of Enlightenment in the 17th and 18th centuries and eventually lead to the development of the five pillars of archaeology in the late 19th and early 20th centuries (Stiebing 1993). However, it can also be argued that we have always been interested in traces testifying to the activity of our ancestors. Some of the earliest documented

3. Review of Literature on the Use of SAR for Archaeological Prospection

excavations date back to the Egyptian New Kingdom, when Thutmose IV excavated the Great Sphinx of Giza around 1400 BC, as testified by the “Sphinx Stele of Thutmose IV” (Lehner 1992).

Remote sensing is conventionally considered to originate in 1858, when Gaspar Felix Tournachon, known as “Nadar” acquired the first aerial photograph from a balloon over Paris (Estes et al. 1977). However, it has been argued that this event had very little impact on developments in microwave remote sensing. Advances in photography in the 19th century ran parallel with and almost completely separate to progress in electricity and magnetism in the same period (Woodhouse 2005). Perhaps a more relevant origin of microwave remote sensing is the publication of Maxwell’s theory of the electromagnetic field in 1865 (Maxwell 1865) when the equations governing the behaviour of electromagnetic waves were finally understood, revealing that electromagnetic waves and light were the same phenomena.

Here, the starting point for discussion in each section is when SAR remote sensing was first actually applied for a particular archaeological prospection technique, although to set the context, references are sometimes made to historical milestones in the use of other parts of the electromagnetic spectrum for the same technique.

The use of radar for archaeological applications was first discussed by Gumerman and Lyons (1971), who compared different parts of the electromagnetic spectrum and concluded that radar was inadequate for most archaeological purposes. Since then however, technological advancements have brought SAR to the forefront of research in the application of remote sensing for archaeological prospection.

3.2 Prospection through topographic analysis

The sensitivity of SAR to roughness can be exploited to detect hidden archaeological features, either buried or at the surface. If an archaeological structure has a particular topographic or textural signature that causes a different radar backscatter with respect to surrounding areas it may be visible in SAR intensity images. This would depend on the geometry of the micro-relief or roughness pattern of the archaeological structure and surrounding areas, in relation to the SAR wavelength and configuration of image acquisition.

The first spaceborne SAR systems had spatial resolutions which reduced their utility for direct archaeological prospection. Nonetheless, geological mapping of the wider environmental context using images of SAR intensity have been used to more efficiently target archaeological survey.

Section 3.2.1 provides a review of the literature to date on the use of SAR intensity to directly detect archaeological structures, or to indirectly detect them through geological mapping, due to surface roughness and topography.

Buried features often leave a topographic trace on the surface. These traces can be very subtle and in some cases only visible on DEMs of very high vertical accuracy and spatial resolution. They can be enhanced by artificially illuminating the surface to create a shaded relief. Archaeological structures which are not buried, but are perhaps obscured by their environmental context, such as tracks in a

desert landscape, or structures within a forest canopy, may also have relief characteristics. These also may be detectable through topographic analysis.

Archaeological prospection is often assisted by analysis of the wider environmental setting. For this, DEMs of low vertical accuracy and coarse spatial resolution, but covering a large area, even if not used directly for archaeological prospection, are useful to better understand the landscape and to provide an input for ancient landscape reconstruction and modelling. This can help determine possible areas that may have been favourable for settlement taking into account factors such as ancient flood plains and strategic areas of high ground.

A review of studies carried out to date on the use of SAR derived DEMs for direct archaeological prospection, or indirect prospection through topographic mapping of the wider geographical context, is provided in section 3.2.2.

3.2.1 SAR intensity analysis of surface topography and roughness

Without actually measuring the height of terrain, topographic variations caused by archaeological structures on the surface or underground can be detected by both passive and active remote sensing techniques. Relief can be enhanced by shadows in passive optical imagery, especially if acquired with a high incidence angle and high solar zenith angle. In SAR imagery, the roughness in relation to the SAR wavelength and the geometric shape and orientation of terrain effect the SAR backscatter, with the result that small alterations at the surface caused by archaeological structures can be enhanced in imagery of SAR backscatter intensity.

One of the first uses of SAR intensity for archaeological prospection was in Belize and the Peten area of Guatemala in the late 1970s. A modified version of SAR designed for imaging Venus was provided by NASA JPL for an experimental aerial survey of these areas in 1977 and 1978. Archaeological sites including ancient cities, raised roads, edges of extensive paved zones, and canals were detected using the SAR imagery. Ground survey carried out in 1980 confirmed these finds, in particular a linear canal network in the swamplands. The author states that the finds may have confirmed the advanced state of the Maya civilisation in which intensive agriculture was practiced, wetlands managed and centralised control exercised (Adams 1980). SAR intensity data from airborne platforms has continued to be used for direct archaeological prospection since. Comer and Blom (2006) used two airborne SAR systems (AIRSAR and GeoSAR) with multiple SAR frequencies and polarisations, together with other remote sensing and ground based datasets, to develop protocols to increase the efficiency of archaeological survey. A test area was chosen on the San Clemente Island, off the coast of California, characterised by a wide variety of archaeological sites and environmental zones.

Given that the spatial resolution of early spaceborne SAR systems was coarse in relation to the size of most man-made structures, more often these systems were used for archaeological research through indirect analysis of the wider environmental context. In particular, geological and hydrological mapping to detect lineaments, predict the location of groundwater aquifers and locate specific raw materials which may have been exploited by humans at various time periods, e.g. (Wendorf et al. 1987, McHugh et al. 1988b, El-Baz 1999, Abdelsalam et al. 2000, Holcomb 2001).

3. Review of Literature on the Use of SAR for Archaeological Prospection

There were however some early successes in the direct application of spaceborne SAR intensity imagery of surface roughness for archaeological prospection. Research on the Maya civilisation over the same area in Belize and Guatemala studied by Adams (1980), and additionally in parts of Mexico, was continued by Pope and Dahlin (1989) using SAR imagery from the Seasat satellite, which acquired data in 1978. Blom and Hedges (1997) tasked the SIR-B SAR system, during the 1984 shuttle flight, to acquire imagery over a region of Oman to assist in the search of the lost city of Ubar, an ancient caravansary that supported incense trade. While the SAR data was not the primary dataset used in the research, it proved capable of identifying linear features, including ancient tracks which, if complete coverage had been available, would have shown to converge on a suspected site for Ubar. Huadong (1997) discovered a part of the Great Wall of China through analysis of multi-frequency and multi-polarisation SAR intensity imagery from SIR-C. Moore et al. (2007) used SIR-C/X-SAR and AIRSAR data to detect manmade features (curvilinear features) to understand the environmental context and influence in the rise of Angkor. Polarimetric data was used to distinguish features by their particular scattering mechanisms.

Even in recent times, despite the availability of VHR SAR sensors, SAR intensity data from instruments operating at HR spatial resolutions of over 10 meters still continue to be used for archaeological prospection, taking advantage of their wide swath coverage, choice of frequency and polarisation, or ease of data access. Some examples include the detection of ancient aqueduct systems (*puquios*) in Nasca, Peru, using ENVISAT ASAR (C-band) data of 30m spatial resolution (Tapete et al. 2013). In the context of this PhD, PALSAR (L-band) data of 10 and 15 meter resolution was used to detect man-made surface features (as well as features buried beneath the sand) in the desert region of North Sinai (Stewart et al. 2015a, Stewart et al. 2016a). Fully polarimetric PALSAR data at around 20m resolution was used to identify archaeological structures in Samarra, Iraq, and Djebel Barkal, Sudan, at the surface and possibly also buried underground, by characterising their scattering mechanisms (Dore et al. 2013).

A “golden era” in SAR remote sensing began in 2007, with the advent of VHR SAR systems including COSMO SkyMed, TerraSAR-X and Radarsat-2, all launched in 2007. This marked a renewed interest in remote sensing for archaeology. Later VHR SAR in L-band was available with the launch of PALSAR-2 in 2014. Some examples of the utility of these satellite missions are summarised here: Linck et al. (2011) used TerraSAR-X data to survey both upstanding and buried structures in the archaeological site of Palmyra in Syria. Patruno et al. (2013) used fully polarimetric Radarsat-2 and ALOS PALSAR data to detect surface and buried archaeological features in two UNESCO Cultural Heritage sites: Samarra, in Iraq, and Gebel Barkal, in Sudan. Both were inaccessible to ground survey for security reasons. The polarimetric data was used to distinguish archaeological structures at the surface from surrounding areas by their backscatter signature related to their geometric and topographic characteristics. Chen et al. (2015) successfully applied COSMO SkyMed intensity data for archaeological prospection through analysis of roughness and microtopography (as well as soil and vegetation marks) over a number of sites characterised by different types of land cover, including Luoyang city in China, Sabratha in Libya, and Metapontum in Italy. Gade and Kohlus (2015) used the high resolution TerraSAR-X Staring Spotlight acquisition mode, with a pixel size of 0.3m, to detect archaeological structures in the intertidal flats of the Wadden Sea, in the German North Sea coast. The structures identified include remnants of building foundations and a former system of ditches dating from the 14th to 17th centuries.

3.2.2 Prospection using DEMs

DEMs at various scales are now standard tools for archaeological prospection. At the micro scale, DEMs of very high vertical accuracy and spatial resolution can resolve very subtle changes in surface relief caused by buried structures, which to an observer on the ground may be invisible. At the other end of the scale, DEMs with low vertical accuracy and low spatial resolution, but covering large areas, can indirectly aid archaeological prospection. Slope and elevation, for example, can contribute as input data in predictive modelling to locate potential archaeological sites and migration routes (Evans and Farr 2006).

Various techniques exist for producing DEMs, using ground based as well as active and passive remote sensing methods. The most common passive remote sensing methods include optical photogrammetry and Structure from Motion (SfM), while standard active techniques are Light Detection And Ranging (LiDAR), InSAR and Radargrammetry. Of the active SAR techniques, InSAR is capable of producing more accurate results than radargrammetry, but is limited in cases where phase decorrelation takes place. Radargrammetry does not suffer from phase decorrelation. While the principles of photogrammetry and radargrammetry are similar, the nature of SAR acquisition poses an added challenge for radargrammetry and makes it less accurate than photogrammetry. However, there are situations in which radargrammetry can be applied where photogrammetry cannot, such as in the case of cloud cover, or night time acquisition.

At the micro scale, passive optical instruments mounted on manned airborne or Unmanned Aerial Vehicle (UAV) platforms are becoming increasingly accurate and cost-effective techniques for archaeological prospection over small areas (such as agricultural fields and urban parklands). Active instruments, while more expensive to operate due to their increased weight and power consumption, also provide highly accurate information on micro-relief and have proven an invaluable tool for archaeological prospection. LiDAR has the added advantage of being able to map micro-relief beneath a forest canopy, which is particularly interesting given that many archaeological sites are preserved and unhindered by human development in forested areas. From spaceborne platforms, the passive optical technique of photogrammetry and the active SAR techniques of InSAR and radargrammetry are becoming increasingly accurate and applicable for micro-scale archaeological prospection. However, unlike from airborne platforms, they cannot yet resolve very small scale structures which would not be evident on the ground, but they may identify spatial relief patterns clearer from a remote perspective. Moreover, in large or inaccessible areas where access on the ground is not feasible, spaceborne systems may directly resolve even small scale structures that may otherwise not be identified. The capability of spaceborne systems to survey large areas globally and at low cost make them very efficient in archaeological surveys of extended areas. Spaceborne LiDAR is not yet feasible for archaeological prospection and current systems are mainly developed for atmospheric applications.

A standard technique to enhance visibility of relief is to artificially illuminate the terrain mapped by a DEM to create shadow marks, this technique is referred to as hill shade analysis.

DEMs of low vertical accuracy and spatial resolution are extensively used in archaeological surveys to better understand the environmental context. A number of freely available near global DEM datasets

3. Review of Literature on the Use of SAR for Archaeological Prospection

exist, such as the Advanced Spaceborne Thermal Emission and Reflection Radiometer (ASTER) Global DEM (GDEM), and the Shuttle Radar Topography Mission (SRTM) DEM. The ASTER GDEM was derived from spaceborne optical photogrammetry while the SRTM DEM is from single pass InSAR. Both have a spatial resolution of 30 meters and vertical accuracies of around 10 meters. Data for the SRTM DEM was acquired from the Shuttle Imaging Radar (SIR-C) and X-SAR instruments, operating respectively at C and X bands, and mounted on NASA's Space Shuttle Endeavour. The system included two receiving antennas separated by a 60 meter mast. The mission took place over 11 days in February 2000 (NASA 2016). A DEM was produced over the land surface of the Earth between about 60 degrees north and 56 degrees south latitude (Evans and Farr 2006). In 2010, a significant advancement came with the launch of a twin satellite (TanDEM-X) to accompany the TerraSAR-X mission. The two satellites fly in close formation, thus acting as single pass SAR interferometers. The primary goal of this system is the generation of a global DEM at 12 meter spatial resolution, and with a relative vertical accuracy of 2 to 4 meters (Krieger et al. 2007). The system operates in X-band and is currently in orbit.

There are many cases in which SAR derived DEMs have successfully been used for archaeological prospection. Some selected examples are given below.

In 1998, the legendary lost city of "Ciudad Blanca" was located in the Honduran tropical forest using data from the European Remote Sensing (ERS-1) satellite and Japanese Earth Resource Satellite (JERS-1). The extended region of cloud covered rain forest had not previously been fully mapped. To create a DEM, repeat pass InSAR techniques could not have been applied due to temporal decorrelation from the forest canopy between satellite acquisitions (neither instrument had single pass interferometry capability). A DEM was therefore created from radargrammetry. Structures beneath the forest canopy that changed the topography of the canopy top were identified on the DEM. Images of SAR intensity acquired by both satellites were also used to detect roughness anomalies of the vegetation canopy induced by underlying archaeological structures (Yakam-Simen et al. 1998).

Sever and Irwin (2003) used DEM data derived from an airborne InSAR system (STAR-3i) to locate elevated archaeological sites in and around large seasonal swamplands (bajos) in the Peten, Guatemala. Over 70 of these sites were visited in the field and all contained archaeological material. Also in Guatemala, Garrison et al. (2011) used airborne InSAR DEM data from the AIRSAR sensor to detect Mayan structures in forested areas. Data acquired in L and P band allowed some penetration of the forest canopy.

Comer and his colleagues used InSAR derived DEMs from two airborne SAR systems: AIRSAR (C-band) and GeoSAR (X-band). The DEMs were used to generate information on slope, slope inflection (rate of change of slope), distance to abrupt slope, aspect and viewshed. All these were used as input to a predictive model to detect archaeological sites (Comer and Blom 2006).

Mounding is a characteristic property of settlement sites in the Near East (Menze and Ur 2012). The SRTM DEM was a key dataset used to map settlement sites in north-eastern Syria. Both low and high mounded settlements were identified. The high mounded sites (tells) were mapped automatically via a topography based classifier using the SRTM DEM. The results were tested in an archaeologically

surveyed area where an 85 % success rate was found for tells that were 5 to 6 meters or higher. Lower tells were identified using multispectral images to detect anthrosols. In total around 14,000 settlement sites in a 23,000 km² area were mapped (Menze et al. 2006, Menze and Ur 2012). In Southeast Asia, in addition to the polarimetric datasets mentioned in section 3.2.1, Moore et al. (2007) also used airborne InSAR DEM data from the AIRSAR sensor in their archaeological analysis of Angkor in Cambodia. The data contributed in identifying elevated sites and characterising their environmental context.

River systems are one of the best predictors of cultural boundaries and one of the most reliable indicators of site location (Evans and Farr 2006). Hritz (2010) used the SRTM DEM, together with other datasets, to extend archaeological surveys into previously unsurveyed areas where the Tigris river was hypothesised to flow in antiquity. The SRTM DEM was used to locate relict river and channel levees (Hritz and Wilkinson 2006, Hritz 2010, 2014). A more recent study used experimental TanDEM-X data in Stripmap and High Resolution Spotlight modes to reconstruct a suspected palaeochannel in the alluvial plain of Cilicia, Turkey (Erasmı et al. 2014).

3.3 Identification through sand volume transmission

As described in section 2.14.4, a significant factor which influences the interaction and transmission of microwaves in a medium is the relative permittivity (also known as dielectric constant) of the medium. In materials with very low relative permittivity, such as dry sand, microwave signals are capable of some degree of penetration. While this property had been previously studied and applied successfully for geologic subsurface sounding (Roth and Elachi 1975), the real interest in the use of SAR remote sensing for geoarchaeological applications followed the Shuttle Imaging Radar (SIR-A) discovery of buried palaeorivers in the Sahara in November 1981 (McCauley et al. 1982). SIR-A operated at L-band (24cm), HH polarisation and had an incidence angle of 47° at the surface. It was flown on the space shuttle Columbia and acquired surface images with a 40m spatial resolution. The imagery acquired over the Selima Sand Sheet, and drift sand of the eastern Sahara, revealed previously unknown buried valleys and geologic features (McCauley et al. 1982).

Figure 3.1 shows a part of the area first imaged by SIR-A, revisited with Sentinel-1 and Sentinel-2. Even at the shorter frequency of C-band, the palaeorivers of the Bir Safsaf area of the Eastern Sahara are clearly visible.

3. Review of Literature on the Use of SAR for Archaeological Prospection

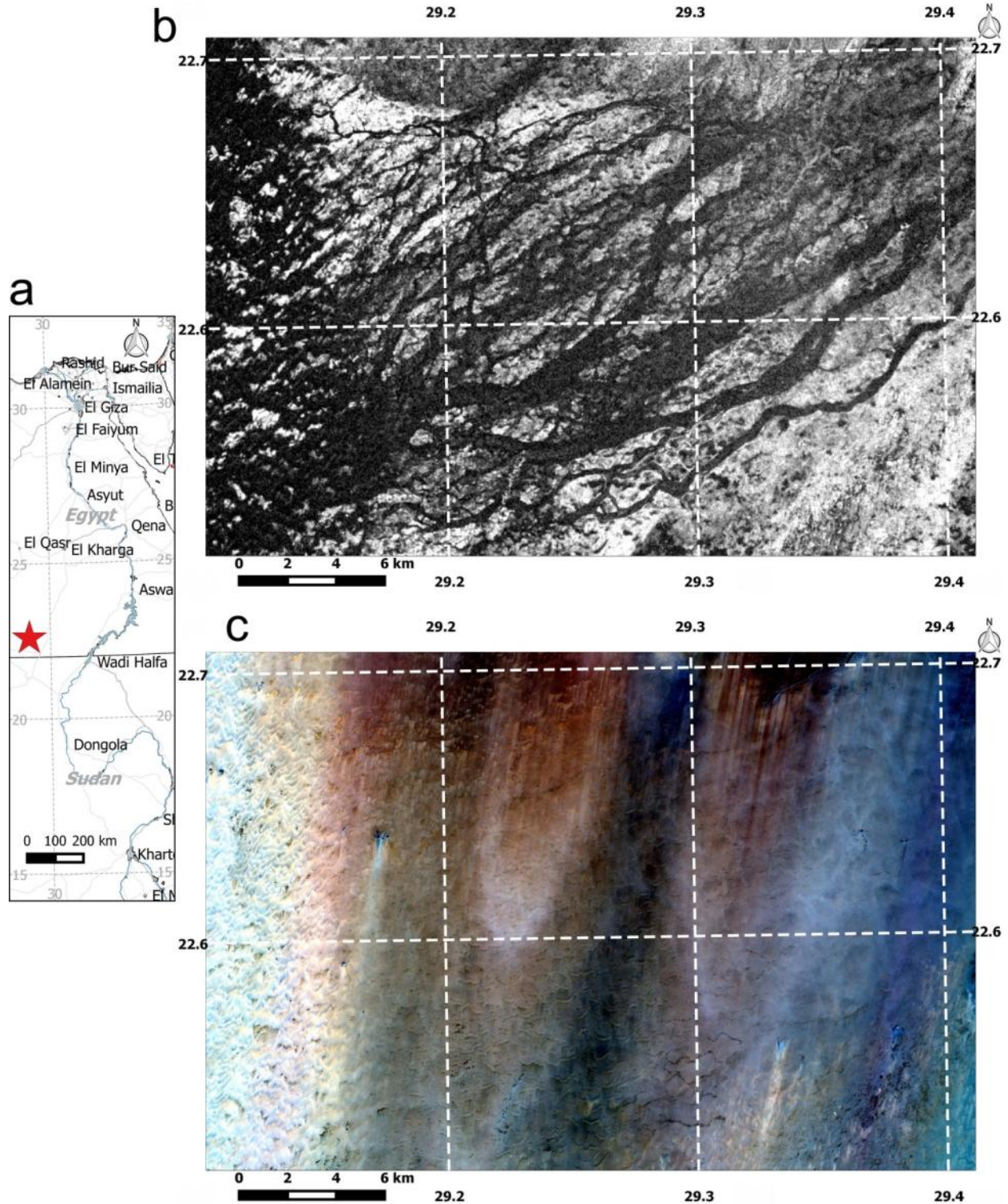


Figure 3.1. a) Map of the Bir Safsaf area where the images in b) and c) were acquired. b) Sentinel-1A IW GRD VV σ^0 backscatter (in dB) image acquired on 11 February 2016. c) Sentinel-2A L1C image acquired on 20 March 2016 corresponding to the same area as in b). Displayed as a true colour combination of band 4 (red), band 3 (green) and band 2 (blue). Contains modified Copernicus Sentinel data 2016.

3. Review of Literature on the Use of SAR for Archaeological Prospection

The discovery of the “radar rivers” sparked a great interest in the use of spaceborne SAR for subsurface imaging in sand covered regions and prompted many further studies on the subject in areas with similar land cover, e.g. in the Mojave Desert of California using SEASAT imagery (also L-band SAR) acquired in 1978 (Blom et al. 1984); over the Al-Labbah Plateau, Saudi Arabia, using L-band SIR-B data (Berlin et al. 1986); in the Alashan Plateau of north-central China using SIR-A and SIR-B (Huadong et al. 1986); in the Badain Jaran Desert of Inner Mongolia, China, using SIR-A (Walker et al. 1987) and in the Taklamakan Desert of China using SIR-A (Holcomb 1991).

In many cases, laboratory measurements and field studies were carried out to determine the depth of SAR penetration and the SAR acquisition parameters that are most suited to subsurface imaging. Following the SIR-A discovery of palaeochannels in the Selima Sand Sheet, the depth of radar penetration was calculated by laboratory measurements of the electrical properties of samples of dry sand and granules taken from the same area. From this, the penetration depth was determined to be at least 5 meters. Field studies carried out in Egypt verified SIR-A signal penetration depths of at least 1 meter in the Selima Sand Sheet and in drift sand and 2 or more meters in sand dunes (McCauley et al. 1982). Blom et al. (1984) observed a backscatter response in SEASAT imagery from rough and dihedral shaped igneous dikes buried at a depth of at least 2m in the alluvium of the Mojave Desert of California, where the soil moisture was assumed to be beneath 1%. Berlin et al. (1986) compared the backscatter response in SIR-B images over varying depths of sand with depth measurements of more than 80 test holes. It was found that a backscatter response was received from carbonate rocks buried beneath a thin layer of fine to medium grained low density quartz sand of around 0.2% moisture, a maximum measured thickness of 1.24m, an average dielectric constant of 2.503, and average loss tangent of 0.0066. Over a thicker sand hill on the other hand, with a minimum thickness thought to be around 3.1m, only negligible backscatter was received. Farr et al. (1986) measured microwave attenuation as a function of soil moisture in situ, using receivers buried in the Nevada desert to receive signals from SIR-B. Results agreed closely with laboratory measurements of attenuation and penetration depths from 0.28m to 0.85m. Various field expeditions were undertaken in the Eastern Sahara in the early 1980's where palaeochannels were identified in SIR-A imagery, and laboratory measurements were made of the physical and chemical properties of the surface materials. The radar imaging depth, defined by Schaber et al. (1986) as the depth of the signal penetration that results in a recorded backscatter, was documented (empirically) to reach a maximum of 1.5m over the sand sheet sediment test areas, or 0.25 of the calculated skin depth of the materials, and was estimated to be between 2 and 3m in active sand dune materials in the study area (Schaber et al. 1986).

The incidence angle was shown to have an effect on signal penetration. Elachi et al. (1984) showed that an overlying sand layer could enhance the capability to image subsurface features, due to the refraction at the air-sand interface given by Snell's Law. The refraction results in a smaller effective incidence angle and a stronger backscatter which can in part compensate both for the losses due to absorption in the sand layer and the reflection at the air-sand interface. This was found to be more pronounced in HH polarisation and at large incidence angles (Elachi et al. 1984). Through an analysis of SIR-A and SIR-B imagery of sand dunes in the Alashan Plateau of China, Huadong et al. (1986) noted that radar illumination direction is an important factor which results in changes in backscatter intensity for the

3. Review of Literature on the Use of SAR for Archaeological Prospection

same type and size of sand dunes. The sand dunes in which the slipfaces were oriented to the radar beam were characterised by high backscatter while the dunes in which the gentle slopes faced the radar beam had a low backscatter response. Blom and Elachi (1987) also noted that at small incidence angles, peak backscatter usually occurs at the incidence angle equal to the angle of repose of sand dunes.

The influence of microwave frequency and polarisation on signal penetration was studied particularly from 1994, when the SIR-C/X-SAR instrument was flown on the Space Shuttle Endeavor. SIR-C operated at L, C and X band, and was fully polarimetric, functioning in HH, HV, VH and VV for L and C bands, and VV in X-band (Evans et al. 1994). Abdelsalam and Stern (1996) used SIR-C/X-SAR imagery for mapping geologic structures obscured by Aeolian cover in the Sahara Desert of NE Sudan. Structures were best revealed by longer wavelengths, in order (best to worst): L-band, C-band, X-band. They also determined that cross pol enhances penetration of C-band. Schaber et al. (1997) compared frequency and polarisations of SIR-C/X-SAR over Bir Safsaf, Egypt, and provided suggestions for optimal configurations. For the Safsaf site, an overall ranking of the utility of the SIR-C/X-SAR frequency bands and polarizations for general geologic mapping below the blow sand cover was provided. This is, in order of decreasing priority: LHV, LHH(VV), CHV, CHH(VV), and XVV. This reflects the increased radar imaging depth with decreasing frequency. Dabbagh et al. (1997) used SIR-C/X-SAR to map palaeo-drainage features in the Arabian Peninsula. A comparison of the SAR imagery at L and C band over test areas where pits were dug in the eolian deposits revealed that the L-band (HH) signal was able to penetrate sand up to 4m thick, while the C band signal did not reveal any penetration in the same areas. The complex, relative dielectric permittivity ϵ of dry desert sand, collected at the Grand Erg Oriental in Tunisia in October 1994, was measured with microwave resonators at frequencies between 0.245 and 6 GHz. It was discovered that the real part of the signal ϵ' is nearly independent of frequency, while the imaginary part ϵ'' steadily decreases with increasing frequency. The measurements could be fitted to a Debye relaxation spectrum with a relaxation frequency of around 0.27 GHz, leading to a nearly frequency-independent penetration depth of about 1 m over the range from 1–10 GHz. Maxwell–Wagner losses of semiconducting spheres embedded in a nonconducting sand medium could explain the spectrum (Matzler 1998).

Further research was carried out with later sensors. The Canadian C-band RADARSAT for example was used to reveal fluvial features in northwestern Sudan, buried beneath low-amplitude chevron sand dunes and megaripples of 10 to 30 cm height (Robinson et al. 1999). Holcomb (2001) also used a mosaic of RADARSAT imagery to detect lake strand-lines covered by sand in the Valley of Lakes in the Gobi Desert in Mongolia. Given the increased penetration capability in proportion to increasing wavelength, there has been significant interest in low frequency SAR systems for subsurface imaging applications. Certain limitations have prevented the development of spaceborne Earth Observation SAR imaging instruments which operate at wavelengths longer than L-band. One limitation includes interference that can take place in the ionosphere causing phase dispersion, scintillation and Faraday rotation (Snoeij et al. 2001). Phase dispersion results in corruption of the slant range measurement. Scintillation results in defocusing of the radar impulse response function, particularly in azimuth. Faraday rotation causes a rotation of the plane of polarisation in proportion to the magnetic field in direction of propagation (Snoeij et al. 2001). Another limitation is the constraint imposed by the International

3. Review of Literature on the Use of SAR for Archaeological Prospection

Telecommunication Union (ITU) on the frequency and bandwidth (Heliere et al. 2009). Finally, at the crowded long wave frequency bands, SAR systems are highly vulnerable to Radio Frequency Interference (RFI) that can cause image artefacts (Rosen et al. 2008, Meyer et al. 2013). The only P-band spaceborne EO mission that is currently planned is the ESA BIOMASS Earth Explorer mission. However, the narrow bandwidth will impose a limitation on the spatial resolution, which is planned to be around 50m (Heliere et al. 2009). The current launch date for BIOMASS is 2020. While there is a lack of P-band spaceborne SAR missions, there are however a number of airborne SAR systems that operate at P-band, some of which include: AIRSAR, of the United States (US) National Aeronautics and Space Administration, Jet Propulsion Laboratory (NASA JPL); and RAMSES, of the French Aerospace Research Agency (ONERA).

The subsurface imaging capability of SAR was significantly researched and applied using airborne sensors. Schaber (1999) and Schaber and Breed (1999) used multi frequency (C, L and P band) and polarimetric data from AIRSAR to detect buried, metallic military ordnance in the Yuma Desert of Arizona. Greater depths of penetration were observed with increasing wavelength, and the cross pol (HV) channel proved better at distinguishing buried features given the greater contrast between target and low SNR background. Several studies were also carried out with the fully polarimetric multi-frequency (including P-band) RAMSES airborne SAR system. An attempt was made at detecting buried archaeological structures through signal transmission outside the desert environment, in the temperate region of Bordeaux, France, using RAMSES. The test areas were two Gallo-Roman sites, buried at 30-40 cm, including Brion, near St Germain d'Esteuil, Gironde, and Moulin du Fâ at Barzan, Charente Maritime. No penetration was evident, not even at P-band. However, the flight was performed at the end of April, after and during a very wet period, so the ground was saturated with water. Also, it is likely that the main component of the observed volume scattering came from the dense grass over one test site, and growing cereals over the other. Over the same areas, GPR at 500 MHz revealed archaeological and other structures beneath the ground (Chapoulie et al. 2002). This research formed a part of a wider project analysing low frequency signal penetration with instruments mounted on RAMSES, most of which was carried out over the Pyla Dune in Bordeaux, the so-called "PYLA'01 experiment" of the "low frequency radar working group" set up by the French space agency CNES in order to explore potentials of low frequency radar for sub-surface moisture detection, biomass evaluation, mapping of the ocean bathymetry, mapping of ocean salinity and for archaeological prospection (Grandjean et al. 2001, Paillou et al. 2003). Several flights were performed over the Bordeaux region during April and May 2001. One experiment carried out over the Pyla Dune was to determine the penetration capabilities of the L-band SAR on RAMSES for the mapping of subsurface moisture. It was discovered that an HH and VV phase difference of 25° correlated with the presence of wet palaeosoils, buried at a depth of up to 6.5m, far beyond which any HH and HV backscatter amplitude is observed, i.e. 2.5m deeper. This confirmed fieldwork measurements and fit the semi-empirical model of Oh et al. (1993), (Paillou et al. 2003).

Remote SAR laboratory measurements have also been carried out to determine the subsurface penetration capability of SAR and its utility for archaeological prospection. Morrison (2013) developed a model to distinguish between surface and subsurface features buried under sand using a C-band VV polarisation remote SAR instrument in a laboratory. The SAR amplitude and phase of repeated

3. Review of Literature on the Use of SAR for Archaeological Prospection

measurements were taken over a basin of sand in which a trihedral and stones were buried. Various amounts of soil moisture were added between acquisitions. A linear relationship was discovered between soil moisture and the difference in phase between images acquired over time, and this was found to be independent of incidence angle. Morrison proposed that with DInSAR measurements (even from airborne or spaceborne platforms) the differing phase histories between surface and subsurface features, and their independence of incidence angle could be exploited for archaeological prospection in sandy areas. He also suggested that if the soil moisture is known, the depth of burial could be estimated (Morrison 2013).

In the early days, the main applications of subsurface imaging using spaceborne SAR had been for geological and hydrological mapping, which benefit from large scale and low resolution imagery, e.g. (McCauley et al. 1986, Stern and Abdelsalam 1996, El-Baz 1999). In some cases the implications for archaeological prospection had been discussed, e.g. McCauley et al. (1982) recognised the potential of the newly discovered palaeochannels in the Sahara to be Stone Age occupation sites. Archaeological prospection had also in many cases been directed in the proximity of possible ancient natural resources that were mapped using the subsurface imaging capability of SAR. Walker et al. (1987) noted that the playa in the Badain Jaran Desert of China appeared to cover a significantly larger area in SIR-A imagery than in optical Landsat imagery. Archaeological evidence suggested that prehistoric and historic human activity took place in the playa which may have been a considerably larger inland lake (Walker et al. 1987). Ground surveys carried out in the Southern Eastern Sahara revealed Acheulean artefacts and the presence of Neolithic sites in the proximity of the ancient drainage channels first mapped by SIR-A (McHugh et al. 1988a, McHugh et al. 1988b, McHugh et al. 1989). Areas that may have contained archaeological sites had been assessed through the detection of ancient waterways buried beneath the sand of the Taklamakan Desert in China using SIR-A data (Holcomb 1991). Holcomb (2001) carried out archaeological ground survey and successfully located Palaeolithic cultural artefacts in the proximity of multiple ancient lake strand lines buried beneath the sand of the Gobi Desert of Mongolia using RADARSAT data. The study of ancient settlement patterns by analysing the evolution of former natural resources mapped using spaceborne SAR has been demonstrated by Conesa et al. (2014). He and his team established a correlation between Mid-Holocene settlement patterns obtained from archaeological data, and seasonal flood prone areas in the semi-arid region of North Gujarat, India, mapped using the C-band Advanced SAR (ASAR) sensor on-board the ENVISAT satellite.

In the 1990's and late 2000's, regularly acquired L-band SAR data was available globally through the Japanese satellite missions of the Japanese Earth Resources Satellite (JERS-1) and the Advanced Land Observing Satellite (ALOS) with its Phase Array type L-band SAR (PALSAR) instrument. JERS-1 operated from 1992 to 1998. It had a spatial resolution of 18m, operated in HH polarisation and had an off-nadir angle of 35 degrees. PALSAR operated from 2006 to 2011, had fully polarimetric capability and functioned at variable off-nadir angles from 8 to 60 degrees. The maximum spatial resolution was around 7m. Through the SAHARASAR project, a first fine resolution (50 m), regional-scale radar mosaic of East Sahara (Egypt, northern Sudan, eastern Libya, northern Chad), compiled from existing archives of JERS-1 L-band SAR data, was realized (Paillou and Rosenqvist 2003). Later, within the framework of the

3. Review of Literature on the Use of SAR for Archaeological Prospection

Kyoto & Carbon Initiative of the Japanese Space Agency (JAXA), JERS-1 and ALOS PALSAR radar images were used to build even larger regional and continental scale mosaics of the Sahara (Paillou et al. 2010).

The low frequency signal and high resolution of ALOS PALSAR, and the possibility for repeated acquisitions globally, made it suitable to be applied directly for archaeological prospection. Apart from some attempts mentioned above using airborne SAR e.g. (Chapoulie et al. 2002), direct archaeological prospection of cultural artefacts through subsurface imaging using SAR was carried out for the first time with PALSAR, mostly in the framework of this PhD research. Stewart et al. (2013b) detected possible ancient man-made structures over the archaeological site of Pelusium, in the Northeast Sinai region of Egypt. These were further analysed and compared with the results of previous ground survey (Stewart et al. 2016b). This work is the subject of Chapter 5 of this PhD thesis. At the same time, Gaber et al. (2013) also used PALSAR and GPR data to detect a suspected buried foundation in the Western Desert of Egypt.

The new generation of VHR spaceborne missions that began in 2007 with the launch of TerraSAR-X, COSMO SkyMed and Radarsat-2 heralded a renewed interest in the direct application of spaceborne SAR signal transmission for archaeological prospection. Linck et al. (2011) and Linck et al. (2013b) used TerraSAR-X data to attempt to distinguish buried archaeological structures in the archaeological site of Palmyra, Syria. Patruno et al. (2013) applied Radarsat-2 data for archaeological prospection over two sites, including Djebel Barkal, Sudan, and Samarra, Iraq. Existing surface features were mapped, and a possible subsurface structure was detected. Chen et al. (2015) used COSMO SkyMed data for archaeological prospection over a number of sites of different land cover, some of which were in desert environments. Several archaeological structures and palaeoenvironmental features were identified through dielectric anomalies.

The first spaceborne VHR SAR sensor operating at a low frequency signal (L-band) was launched on 24 May 2014 (Kankaku et al. 2014). This is perhaps the most interesting and relevant mission to date for archaeological prospection through surface penetration given its high spatial resolution (up to 1x3m in Spotlight Mode) and long wavelength (around 24 centimetres) (Arikawa et al. 2014). Research on the application of PALSAR-2 for archaeological prospection in a coastal region of North Sinai was carried out by Stewart et al. (2016b), and is the subject of Chapter 5 of this PhD thesis.

3.4 Identification through vegetation and soil proxies

Archaeological structures buried under land that leave no direct topographical trace on the surface can nonetheless interact with overlying material, such as the soil itself, vegetation growing in the soil, or snow covering both soil and vegetation (Jones and Evans 1975, Stanjek and Fassbinder 1995, Wilson 2000, Lasaponara and Masini 2012b). When this takes place, the overlying materials that have been modified can be referred to as proxy indicators of buried archaeological structures (Beck 2007). Proxy indicators can reveal locations of man-made constructions from materials, such as paved roads, buildings made of brick, stone or wood, and other such structures; and they can also reveal man-made modifications of the landscape, such as ditches, canals, pits, mounds and other earthworks (Wilson 2000, Gojda and Hejcman 2012, Lasaponara and Masini 2012b). The extent to which materials overlying

archaeological structures are modified sufficiently to be detectable depends on many factors including the depth of the materials, the composition of buried archaeological structures, meteorological and other influencing elements (Kaimaris et al. 2012, Agapiou et al. 2013, Agapiou et al. 2014).

This chapter describes the main physical mechanisms responsible for the formation of vegetation and soil archaeological proxy indicators in temperate regions and provides a summary of studies carried out so far for the detection of these using remote sensing data. The focus is limited only to short vegetation (crop and grassland) and soil proxies, and only in temperate regions, as these are common sources of archaeological proxies in European soils. There are other proxies, such as snow or thaw marks caused by differential thawing over buried archaeological structures (Stanjek and Fassbinder 1995). However, given the transmission of microwave radiation in snow (Ulaby et al. 1982) SAR remote sensing of these may not be appropriate. Vegetation and soil proxies also exist outside temperate regions. For example in the tropical Petén region of Guatemala, Saturno et al. (2006) used remote sensing data to identify vegetation proxies above buried Mayan structures. These are believed to be caused by limestone and lime plasters used in construction by the Maya decomposing over the centuries and affecting the surface vegetation (Saturno et al. 2006). Due to constraints of time and data access, only agricultural and grassland vegetation (crop marks) and European soils are considered here.

3.4.1 Crop Marks in Temperate Regions

Significant research on crop marks in temperate regions was carried out in the 1970s, particularly by (Jones and Evans 1975) and (Evans and Jones 1977). Much of the present literature refers to these studies. Researchers have recently questioned the continuing validity of these studies and have suggested more up to date research is necessary (Rączkowski 2011), particularly since cereal crops of the 1970's and earlier are very different to the modern varieties (Evans 2007).

Plants convert solar energy, water and soil nutrients into vegetative matter, this is what governs their growth. The chlorophyll of green plants absorbs light, which provides energy for the photosynthesis of carbon dioxide and water. This produces carbohydrate which is used to create plant cells (Jones and Evans 1975, Berry and Downton 1982, Lambers et al. 2008).

The main factors influencing crop growth are related to climate, soil moisture and soil properties. The climate factors include: solar radiation, temperature and precipitation (Hogg 1971, Lambers et al. 2008). The soil factors can be further subdivided into physical properties including depth, porosity, consistence, degree of compaction, stoniness, structure and particle size; and chemical properties including the mineral fraction, type and quantity of organic matter and nutrients (Jones and Evans 1975, Lambers et al. 2008).

3.4.1.1 Influence of Soil Moisture Deficit on Vegetation Growth

Differences in crop growth on a field scale are commonly caused by variations in available soil moisture. Soil moisture available for plant growth is a function of precipitation, water holding capacity of the soil, availability of ground water, evaporation and transpiration (Jones and Evans 1975). Water stress affects first the growth of leaves, followed by stems, followed by roots. When water is replenished, the order of growth is reversed, with roots growing first and leaves last (May and Milthorpe 1962).

Both a Soil Moisture Surplus (SMS) and a Soil Moisture Deficit (SMD) can inhibit plant growth. In the case of SMS, excess water in the soil leads to a lack of oxygen in the rooting zone, given that waterlogged soil is anaerobic (Leysdon and Sheard 1974). This suppresses many of the oxygenated processes needed for plant growth. Stomatal opening is inhibited as a result of which respiration and photosynthesis is reduced (Wright 1972). In the case of SMD, growing plants begin to extract available water stored in the soil. The amount of water available in the soil (usually in mm per cm of soil) is calculated as the difference between the volume of water held per cm at field capacity (FC) and at the permanent wilting point (PWP) (Russell 1961, Salter and Haworth 1961). When all water available at a certain soil depth has been extracted, different plants react in varying ways and according to their state of growth: Some will wilt while others stop growing but continue to transpire at a significantly lower rate (May and Milthorpe 1962, Bingham 1966); cereals require significantly more water, and are therefore more inclined to wilt, before heading than after; crops may avoid wilting by extracting water at greater depths (between 60 and 90 cm) through deep tap roots (May and Milthorpe 1962). Deep tap roots often ensure only plant survival, rather than maximum growth. According to Jones and Evans (1975) given that most roots and nutrients are in the top 40 cm, the depletion of soil moisture to this depth probably stops the growth of most temperate crops.

Water retention varies in different types of soil. The rate of release of water also varies. In coarse sand, water is released rapidly, and plants may grow quickly until they exhaust the available supply of water and encounter a sudden deficit when all is transpired. In heavy clay, water is withheld at increasing tension as water is depleted (May and Milthorpe 1962). This means that growth can become more gradual (Jones and Evans 1975).

Once a crop has ripened or become senescent, transpiration is negligible and SMD has little effect on the state of the plant (Jones and Evans 1975).

3.4.1.2 Influence of Soil Properties on Vegetation Growth

Physical soil properties including particle size, structure, composition, compaction and depth affect the development of roots in the soil medium and, more importantly for differential crop growth, affect also the water and nutrients available to plants. For plant roots to absorb nutrients there has to be an adequate supply in the soil, the roots must be able to penetrate through the soil, and there has to be enough water to permit the transfer of nutrients both to the root surface and within the plant (Jones and Evans 1975).

A number of macro nutrients affect the growth of plants, these include nitrogen, phosphorus, potassium, calcium, magnesium, and sulphur. Trace elements of other nutrients (micro nutrients) may also have an effect on crop growth, but to a lesser extent. These include iron, manganese, zinc, copper, boron, and molybdenum. Nitrogen is used by plants to produce dry matter and determines the greenness of the plant. Excess nitrogen can cause crop lodging, when plants collapse due to excessive and rapid growth. Phosphorus is required for metabolic processes and affects the growth and colour of plants. Variations in pH can have an effect on the availability of nitrogen and phosphorus (Jones and Evans 1975). Calcium is a constituent of the cell wall of plants. It controls acidity, indirectly influences processes such as nitrogen fixation and affects the activity of earthworms, which improve aeration and

structure of the soil medium around the roots (Russell 1961). Magnesium is important as a constituent of chlorophyll (Salmon 1963).

Macro nutrients exist mainly in the top 30 cm of soils, due to weathering and the application of fertilisers (Viets 1972). Cereal roots are primarily found in the top 30 cm of soils corresponding to the availability of nutrients (Cannell and Drew 1973).

3.4.1.3 Formation of vegetation marks

Any impediment in the soil that prevents adequate rooting in a particular area, such as a buried wall, may cause differential crop growth. Conversely, any exception to an impediment that allows better rooting and uptake of moisture and nutrients can also cause differential crop growth, such as deeper soil in a former ditch or post hole. An archaeological feature that causes an impediment to crop growth is referred to as a negative archaeological crop mark, while one that causes more abundant crop growth is labelled as a positive crop mark (Wilson 2000) (see Figure 3.2).

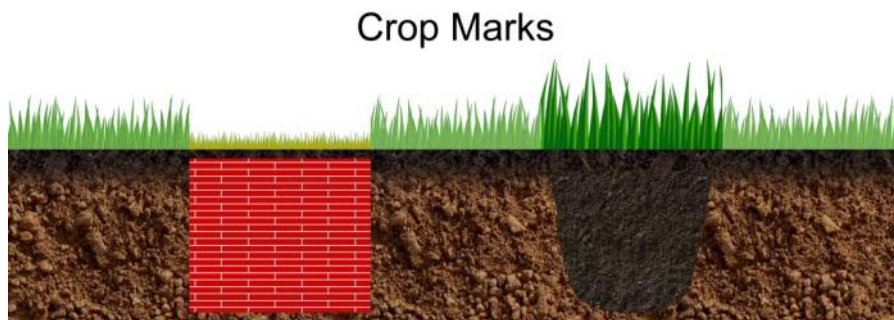


Figure 3.2. Formation of negative and positive crop marks caused respectively by a buried wall (left) and a buried ditch (right).

The first detailed analysis of the physical conditions that cause the appearance of vegetation marks was undertaken by Jones and Evans (1975), who reported results of a comparison between air photos of natural and archaeological vegetation marks with ground data obtained over sites distributed throughout the UK. Results of this analysis were reported for a number of influencing factors, including the depth and type of soil, soil moisture deficit, crop type, and plant nutrients.

For soil depth it was found that most vegetation marks existed over soils with a rooting depth between 30 and 60 cm. The depth of the overlying soil was a more significant influencing factor in the development of vegetation marks than soil particle size, but most vegetation marks were recorded in loamy soils. Given the increased water retention in soils of small particle size, such as clay, and the correspondingly slower growth rate of crops in these soils, crop marks due to differential crop growth are less evident in these soils (Jones and Evans 1975).

For SMD, Jones and Evans (1975) describe the application of a model to calculate the “potential soil moisture deficit” (PSMD). The PSMD is a measure of the SMD but taking only meteorological data as input. It is derived by subtracting rainfall from the “potential transpiration” rate of a crop. The potential

3. Review of Literature on the Use of SAR for Archaeological Prospection

transpiration, given by Penman (1948), is a calculation of the rate of water use by an extended area of green crop, growing actively, shading the ground completely, and with an adequate supply of water at the roots. The required input for this model includes mean air temperature, mean dewpoint, mean wind velocity at a standard height, and mean duration of sunshine. Potential transpiration measurements showed good agreement when compared with other data sources over various sites in the USA, Europe and India (Penman 1948). The PSMD at any given time is an accumulation of a time series of PSMD measurements. Given the difficulties in calculating the actual SMD, the PSMD is a practical alternative. Following experiments on irrigation requirements in Woburn, UK, Penman (1970a) discovered that the growth of grass and arable crops is restricted when a PSMD of 50 mm is reached. In many soils 50 mm equates to the available water in the top 30-40 cm. Penman concludes that this is the case in a wide range of soils, and is due to the rooting depths of plants and the depth of available nutrients in the soil. Jones and Evans (1975) found that over the vast majority of crop marks studied there was a high PSMD, and that the clearest marks were due to differential depletion of available soil moisture. However, a small number of crop marks were presumed to be due to a Potential Soil Moisture Surplus (PSMS), where water saturation of shallow soils over an impermeable layer prevented growth, while in surrounding deeper soil, vegetation growth was less inhibited. Later invasions of weeds can enhance the difference (Jones and Evans 1975).

For crop type, it was found that vegetation marks are most common in cereals (barley, wheat, oats), less so in sugar beet and grass, and only seldom in potatoes (Jones and Evans 1975, Evans and Jones 1977, Riley 1979). In grass, marks appear only when PSMD is 10-40 mm more than that which would cause marks to appear in cereals. The reasons for this are not fully understood, but may be partly due to the increased variety of grass species when compared with a cereal stand, the increased water holding capacity of an uncultivated soil layer, and grazing in areas of higher growth hiding differential growth patterns (Evans and Jones 1977). In cereals, marks can be obscured due to tillering in the event of heavy rain following the differential crop growth (Rackham 1972). The time before ear emergence is when moisture stress in cereals most affects growth (Penman 1970a, b, c). Jones and Evans (1975) referring to conditions in the UK, report that the period from late May to early July is therefore when differential crop growth in cereals due to moisture stress is most likely to take place. Marks due to moisture stress are more visible in barley than in wheat, given its larger leaf area index, and correspondingly greater differential growth. Marks only seldom appear in potato fields, due to a reduced leaf area index from the time (mid-July) when PSMD is more likely to be high (Jones and Evans 1975).

Natural and archaeological vegetation marks can also be caused by local differences in plant nutrients. The uneven application of nitrogen fertilizer often causes differences in crop greenness, leaf area index (LAI) and stem height. Greater quantities of soluble nitrogen and soil moisture in areas of deeper soil (such as an infilled ditch or post hole) also produce the same effect in plants, which additionally produce more tillers and grow for longer periods than plants in surrounding shallower soils with less nitrogen availability. The opposite effect is observed in shallow or dryer areas with less nitrogen availability. Differential crop growth can be stimulated by calcium that may be provided by the mortar in a buried wall (Jones and Evans 1975).

Evans and Jones (1977) discovered that once differential growth has taken place, growth differences frequently remain, even if water subsequently becomes available for continued growth.

Many other factors may lead to the emergence of crop marks. Such factors often depend on local conditions making the prediction across large areas difficult (Rączkowski 2011). Czajlik (2009) noted that crop marks were more visible in true colour optical aerial surveys in Hungary where the subsoil water level is high. Over these areas crop marks formed from differences in soil type (emergence of sandier soils) and water level affecting local crop growth. In an aerial archaeological survey of Poland in 2011, Rączkowski (2011) discovered that in some areas crop marks appeared very clearly in true colour air photos soon after a period of rainfall in early July that followed a longer period of drought. The crop marks appeared as dark brown to black marks in the crops. The cause of these marks was attributed to the early July rainfall creating suitable conditions for an increase in diseases and molds (in particular the saprotrophic black mold) that covered the stalks and leaves of the drought weakened crops in some areas. In other areas, crops only a little healthier (positive crop marks) were able to better defend themselves, and were consequently not covered by the mold (Rączkowski 2011).

3.4.2 Soil Marks in Temperate Regions

Archaeological structures, such as earthworks, ditches, pits, former moats and canals, may contain soil that differs in its chemical properties, or in the amount and nature of organic matter and anthrosols contained within them. These may be indistinguishable due to an overlying layer of modern topsoil. However, ploughing activity may extract and upend the topsoil at a sufficient depth to reveal traces of the underlying soil infilling archaeological structures, which thus become visible as soil marks (Jones and Evans 1975, Stanjek and Fassbinder 1995, Wilson 2000).

In some cases traces of pottery and building material can also be seen in soils. Ploughing may bring up traces of buried material (Lasaponara and Masini 2012a). Also frost action moves stones to the surface (Corte 1966). Rain and weathering can then remove soil adhering to them (Jones and Evans 1975). The depth and direction of ploughing effects the emergence and clarity of soil marks (Jones and Evans 1975).

Figure 3.3 is a diagram demonstrating the effect of ploughing in revealing traces of buried archaeological structures.



Figure 3.3. Archaeological soil marks revealing the presence of a buried wall (left) and a buried ditch (right), traces of which have been brought to the surface by ploughing.

3.4.3 Remote Sensing of crop and soil marks in temperate regions

The first known crop and soil marks have been discovered in panchromatic air photographs acquired from remote platforms, such as balloons and aircraft, since the beginning of the 20th century (Wilson 2000). Their potential for archaeological research was soon recognised. One of the first to study them in detail was O. G. S. Crawford, the first Archaeological Officer of the British Ordnance Survey (Crawford 1923). Following his discovery of crop marks of the Stonehenge Avenue on British Royal Air Force (RAF) photographs, he undertook campaigns of air photography dedicated to archaeological prospection, carried out excavations of identified sites and founded the journal *Antiquity*, in which many of the air photos were published (Wilson 2000).

The Second World War brought many technological advancements in remote sensing instruments and airborne platforms, and had a large impact on archaeologists (Parcak 2009). A momentum was created and shortly after the war experiments were undertaken on remote sensing of archaeological crop and soil marks in wavelength regions other than the visible. Edeine (1956) discussed for the first time the use of airborne infrared film for archaeological prospection. The high reflection of near-infrared radiation by the cell structure of healthy green plants (Knipling 1970) can be exploited to enhance archaeological vegetation marks. The thermal infrared (TIR) part of the spectrum has also been used to detect buried structures due to their heat signature (Ben-Dor et al. 2013), which can be enhanced through calculations of the day-night thermal inertia (McManus and Donoghue 2002). In 1971 the application of multispectral remote sensing for the detection of archaeological residues was described by Gumerman and Lyons (1971). The results of airborne remote sensors operating in different parts of the electromagnetic spectrum from the visible to the infrared were compared. While not actually applied, the utility of active microwave and passive UV for archaeological prospection were also discussed. However, it was suggested that these were less appropriate for archaeological applications than the visible and infrared parts of the spectrum. Later, remote sensing in both the UV and microwave regions of the spectrum were successfully used for archaeological prospection of proxy indicators. In the case of UV, Verhoeven and his team successfully demonstrated the utility of UV remote sensing to detect archaeological residue marks in vegetated areas. This is only possible from low altitude airborne platforms given the strong Rayleigh scattering at such short wavelengths (Verhoeven and Schmitt 2010).

One of the first examples of the successful application of SAR for the detection of vegetation proxy indicators of archaeological sites was over the Maya Lowlands of the Yucatan Peninsula in the late 1970s and early 1980s. Using an experimental airborne SAR provided by the Jet Propulsion Laboratory (JPL), which was originally designed for scanning the surface of Venus, Adams (1980) discovered a large network of former agricultural and drainage canals, which were identified due to differential vegetation height and density. This greatly furthered understanding of Maya agricultural practices and the extent to which it was applied (Adams 1980, 1982). Further studies on the distribution of ancient Mayan canal systems and their environmental context was carried out with a combination of SEASAT and Landsat data by Pope and Dahlin (1989), and later still with airborne AIRSAR and STAR-3i SAR data, together with optical imagery from Landsat, QuickBird and IKONOS by Saturno et al. (2006).

3. Review of Literature on the Use of SAR for Archaeological Prospection

In the early 1980s similar studies were carried out by Payson Sheets and his team in the Arenal area of Costa Rica to detect ancient paths dug by Native Americans. A fully polarimetric L-band SAR system was flown on a NASA aircraft to acquire data at 30 and 10 meter resolutions. Many linear anomalies were detected in uncut tropical rainforest, in secondary regrowth and in pastures. Following ground truthing, many of these were discovered to be historical, and a few to be ancient footpaths, verified by excavations and stratigraphic interpretations. Interpretation of the radar data was difficult, especially given the unsuccessful attempts to reduce noise, partly due to the use of a substitute antenna following damage to the primary antenna prior to data acquisition. The substitute antenna generated only uncalibrated data (Sheets and Sever 2006).

A comprehensive study of the archaeological site of Angkor Watt in Cambodia was undertaken from the early 1990s with multi-frequency and polarimetric SAR data, initially from the SIR-C mission flown on the Space Shuttle Endeavor in 1994, and later from the AIRSAR TopSAR airborne SAR, flown in 1996 over the area. The AIRSAR instrument operated at C, L and P band, and was also polarimetric (Moore et al. 2007). The fully polarimetric data was used to produce decompositions of elementary scattering mechanisms of the area, such as double bounce, volume scatter and Bragg scatter displayed respectively as red, green and blue. This was performed at various frequencies and allowed better discrimination of landcover differences which helped to understand terrain and hydrological preferences of ancient settlements and water management structures. The P-band SAR on AIRSAR allowed better penetration of the forest canopy. A number of circular sites surrounded by moats were identified on the SAR data due to slight moisture and vegetation differences, which were not evident on the ground or in the available optical imagery (Moore et al. 2007).

A number of protocols for archaeological prospection over large areas were described by Comer and Blom (2006). These were developed during a research project which took place from 2002 to 2005 on San Clemente Island, California, and was funded by the United States Department of Defence. Airborne, fully polarimetric AIRSAR data at P, L and C band, and GeoSAR data at P band dual pol (HH, HV) and X band single pol (VV) were used at various incidence angles, flight directions and height configurations to detect archaeological structures dating back to almost 10,000 years. Some of these archaeological structures were buried underground beneath shrubs or grasses and distinguished by positive crop marks, i.e. taller and denser vegetation over the buried archaeological structures. L-band was found to be most sensitive to the differential densities due to the buried archaeology, and VV polarisation was found to more strongly reflect the taller and more abundant grass stalks at the centre of the areas in which buried structures were located (Comer and Blom 2006).

An attempt was made to detect surface residues of buried features over the archaeological site of Vulci in Italy using polarimetric ALOS PALSAR data. A red, green and blue composite of the Eigenvector-Eigenvalue decomposition (with red displayed as eigenvalue 1, green as eigenvalue 2 and blue as eigenvalue 3) appeared to display a signal of a buried moat around the ancient city of Vulci. However, the precise cause of this anomaly feature was not determined (Patrino et al. 2009, Dore et al. 2010).

An analysis of the potential to detect archaeological residues using X-band SAR data (COSMO SkyMed) was undertaken over a number of sites, including both desert and (albeit sparsely) vegetated areas. The

vegetated areas included Luoyang city in China, and Metapontum in southern Italy. Some success was achieved in identifying archaeological crop, soil and moisture marks in images of SAR backscatter amplitude (Chen et al. 2015).

The potential to exploit both polarimetric and interferometric information from the new generation of VHR SAR sensors (in particular, COSMO SkyMed and Radarsat-2), to detect archaeological residues over vegetated sites in the temperate region of central Italy has been undertaken by Stewart et al. (2013a), Stewart et al. (2014) and (Stewart 2017). This constitutes the first use of the SAR phase in the form of coherence images to detect crop and soil marks, and the first use of a large SAR time series to produce images of filtered intensity and DEMs from repeat pass interferometry to detect surface residues of buried archaeological structures. This is the subject of Chapter 4 of this PhD thesis.

3.5 Identification under water

3.5.1 Physical mechanisms

Many techniques exist for remotely obtaining information about the surface or subsurface of the sea-bed. Those that operate through a body of water could be considered remote sensing devices, given that they are not in physical contact with the material being sensed. Such methods commonly use acoustic sounding, such as echo-sounders (to detect objects directly beneath a sounding device), sonar (for wider mapping of the surface of the sea-bed surrounding the sensing device), and seismic profiling (to map the subsurface of the sea-bed) (Trabant 2013). Electromagnetic geophysical methods commonly employed for land surveys can be adapted for prospection of the sea-bed, such as electrical resistivity techniques, magnetometry and ground penetrating radar (Constable and Srnka 2007, Constable 2013).

Both active and passive electromagnetic techniques for underwater mapping can also be applied from remote platforms which are not in contact with the water medium. These more commonly use wavelengths outside the microwave region, in the short wave visible region which can penetrate clear water to a certain depth. Active techniques include LiDAR (Light Detection And Ranging), which transmit both green and infrared light. The green light penetrates the water while the infrared is reflected from the surface. It is possible with LiDAR techniques to reach a vertical accuracy of down to around 10 to 15cm at a spatial resolution greater than one elevation measurement per square meter, and can collect data down to depths of about three times the Secchi depth (Klemas 2011). In exceptionally clear waters, information can be retrieved down to a depth of around 70 m (Gao 2009).

Passive techniques include optical imaging, and can be applied from spaceborne platforms. The response of the reflected signal depends on illumination conditions, atmospheric radiative transfer, water depth, sea-bed albedo and inherent optical properties of the water column (scattering, absorption, and fluorescence) (Sandidge and Holyer 1998, Gao 2009). Multispectral or hyperspectral data are used to extract information about these parameters by providing multiple measurements in different wavelength regions from the visible to infrared (Sandidge and Holyer 1998, Lyzenga et al. 2006). As with LiDAR techniques, the depth of water through which topographic sea-bed mapping can be achieved depends on the Secchi depth, and is usually limited to 20m (Gao 2009).

3. Review of Literature on the Use of SAR for Archaeological Prospection

Electromagnetic waves emitted by spaceborne SAR systems penetrate into seawater only to a depth that is small in comparison to the radar wavelength (Alpers and Hennings 1984). Nonetheless, through indirect processes, topographic features on the seabed can sometimes be visible in SAR imagery.

The first observation of sea bottom topography with imaging radar was made in 1969 by de Loor and his co-workers. The phenomena was observed while studying the possibilities of detecting seawave and swell directions over the North Sea using Side Looking Airborne Radar (SLAR). It took some time to find the explanation. At first it stimulated little interest, and was even considered a hindrance to the detection of other phenomena. With the launch of SEASAT in 1978 much attention was given to SAR bathymetry when it was observed on a global scale in imagery acquired by the satellite's SAR sensor (De Loor 1981).

Alpers and Hennings (1984) published a theory of the imaging mechanism of seabed topography by SLAR and SAR. This imaging mechanism, illustrated in Figure 3.4, can be summarised as follows:

1. The seabed topography induces current variations. This interaction is described by the continuity equation.
2. The current variations modulate the short-scale sea surface roughness. This interaction is described by weak hydrodynamic interaction theory in the relaxation time approximation.
3. The modulation of the short-scale sea surface roughness gives rise to changes in the radar reflectivity.

Velocity bunching, caused by Doppler differences due to the motion of the waves, was also shown to contribute to the radar imaging mechanism. Although it was shown that in general the contribution is small in comparison to the hydrodynamic modulation (Alpers and Hennings 1984).

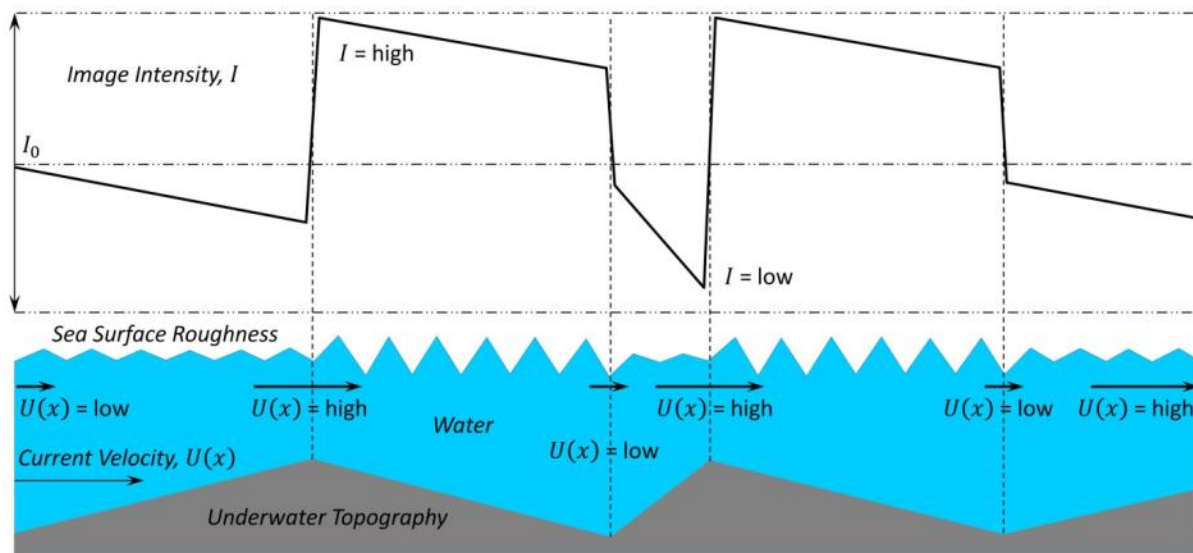


Figure 3.4. Schematic plot showing imaging mechanism of underwater bottom topography.

3. Review of Literature on the Use of SAR for Archaeological Prospection

Various similar models were published in the following years, such as by Shuchman et al. (1985) and Holliday et al. (1986, 1987). Vogelzang (1989) and Hennings (1990) showed the significance of advection to the modelling of underwater topography. The accuracy of these models was tested with data acquired by airborne SLAR systems over a number of sites, such as the Dutch Coast, (Vogelzang et al. 1992), and the Phelps Bank, near Nantucket Island, USA, (Cooper et al. 1994). Kooij et al. (1995) extended the hydrodynamic modelling to take into account the specific shape of underwater sand waves.

Improved understanding of the theoretical mechanisms stimulated the use of SAR for operational bathymetric mapping. Hesselmanns et al. (1995) and Calkoen et al. (2001) described an algorithm called the Bathymetric Assessment System (BAS) to operationally map underwater topography by means of data assimilation. The algorithm applies a series of models, developed by Delft Hydraulics, to simulate a radar image from known (coarse) bathymetry and other measured parameters. Each model corresponds with a step in the imaging mechanism. They include: a current model, a short wave spectral model and a radar backscatter model. The algorithm can be summarised as follows:

1. A SAR image is simulated from the first-guess depth map using the imaging models.
2. The simulated SAR image is compared with the measured SAR image by evaluating a penalty function. This penalty function also compares the model depths with the coarse, measured bathymetry.
3. The first-guess depth map is adjusted by minimizing the penalty function.
4. After several iterations of the procedure, the resulting model depth map is the best estimate for the real depth.

This algorithm has been used operationally as a commercial service by the company ARGOSS to support bathymetric surveys. From 1999 to 2000 an ESA Data User Element (DUE) project took place called BABEL (Bathymetry Assessment Demonstration off the Belgian Coast). The objective of BABEL was to demonstrate the BAS for mapping bathymetry using ERS SAR observations in Belgian coastal waters (Calkoen et al. 2000). The BAS has used SAR data from various sensors, such as ERS SAR and RADARSAT. While the system requires a-priori bathymetry, the added value is that only sparsely sampled depth measurements are required, and the BAS is able to interpolate the measurements to produce higher resolution maps at a more affordable cost than would be possible with higher sampling ship-based surveys (Hesselmanns et al. 1995, Calkoen et al. 2001).

In the meantime, research continued on the theory of SAR bathymetry. Some of these compared the response of different SAR frequencies. Greidanus et al. (1997) compared the results of several models with multifrequency SAR data over a submerged reef with greatly varying underwater topography. All models were found to underestimate the measured bathymetric contrasts. L-band was found to be more suited to bathymetric applications than C or X band. Vogelzang (1997) and Vogelzang et al. (1997) carried out measurements with the P, L and C band Airborne Imaging Radar (AIR) over an area of sand waves off the Dutch coast. An improved model was proposed following the results of the multi-frequency bathymetric analysis.

3. Review of Literature on the Use of SAR for Archaeological Prospection

Romeiser et al. (1997) published an improved composite surface model for the normalised radar backscattering cross section (NRCS) of the ocean surface. Romeiser and Alpers (1997) followed this up with another paper on the response of this model to surface roughness variations and the radar imaging of underwater topography. The model takes into account the impact of a two-dimensional ocean wave spectrum on the radar backscatter. It was shown to reproduce measured absolute NRCS values for a variety of radar configurations and wind speeds satisfactorily after some tuning of the input ocean wave spectrum. The composite surface model was reported to yield comparable radar signatures at high (X band) and low (L band) radar frequencies, which is in much better agreement with experimental results than the predictions of a first-order Bragg scattering model (Romeiser and Alpers 1997).

Mei-bing et al. (1998) published a simulation model of bathymetric features identified on SAR images, and showed the results of an inversion model to derive bathymetric maps from SEASAT imagery of the Southern North Sea.

The progress both in understanding the theory of SAR bathymetric imaging, and the practical application of this to deliver services, stimulated Hennings (1998) to write a review paper on the subject.

Up to this point in time, attention was devoted to the current modulation technique of SAR bathymetry. Wackerman et al. (1998) presented two algorithms to estimate near shore bathymetry. These follow a completely different approach from previously published methods, even if some of the ideas behind them are reported to date back to before World War II. The algorithms can be summarised as follows:

1. The first algorithm uses the kinematics of shoaling waves to extract depths. This assumes no significant current in the direction of wave propagation. The algorithm uses the following formula:

$$d = \frac{1}{k} \tanh^{-1} \left[\frac{w^2}{gk} \right] \quad 3.1$$

where d is the water depth, k is the wavenumber of the shoaling (equal to $2\pi/\lambda$ where λ is the wavelength), w is the frequency of the shoaling wave (equal to $2\pi/T$, where T is the period of the wave), and g is the gravitational constant.

The algorithm takes as input a time series of spotlight airborne SAR data acquired over the same area at short regular intervals. Fourier analysis is carried out on small subsets of this time series to obtain measurements of k and w and solve the equation for depth.

2. The second algorithm calculates water depth within the surf zone, where a significant amount of wave breaking takes place. This is estimated by using two sets of relationships:
 - a. Between the radar cross section and the rate of wave energy dissipation due to breaking
 - b. Between the wave height (or energy density), the water depth and the rate of energy dissipation.

3. Review of Literature on the Use of SAR for Archaeological Prospection

These techniques are complementary in that the first measures the water depth in the region outside the surf zone, while the second measures depth in the surf zone (Wackerman et al. 1998).

In the meantime, research continued on the practical derivation of bathymetry from SAR data based on the more established current modulation technique. Vogelzang (2001) compared various model predictions with measured signatures of submarine reefs near Heligoland in the North Sea, observed in multi-frequency (L, C and X band) airborne radar images. Huang et al. (2001) derived water depths off the east coast of Jingsu province, China, using a model based on current modulations with ERS-1 SAR imagery. Very good agreement was found between the SAR derived bathymetry and a sea chart of the same area. A root mean square difference of 0.42m was achieved. Xia and Yuan (2002) also successfully applied an inversion model proposed by Jin and Yuan (1997a, b) using a Radarsat image over the Tangu Sea to derive the bathymetry.

Inglada and Garello (1999b), Inglada and Garello (2002) proposed the use of a Volterra series expansion as a tool for obtaining an input-output relationship between the current and the SAR image pixel. An algorithm for the estimation of underwater bottom topography from SAR images using the Volterra series expansion was devised (Inglada and Garello 1999a). This algorithm has three steps:

1. Smooth the SAR image using the anisotropic diffusion approach
2. Estimate surface current gradients by inversion of the linear kernel of the Volterra model of the forward imaging mechanism
3. Obtain depth values by means of a continuity equation

The algorithm was reported to perform well, but *a-priori* information about the mean surface current, wind speed and other parameters is required to obtain a calibrated depth map.

The optimal conditions for current based SAR bathymetry were investigated by Huang et al. (2000), who studied the relationship between tidal currents, sea surface winds and SAR mapping of underwater bottom topography using a simulation model for the radar backscattering cross section of the sea surface. It was found that bathymetric features in SAR data are best observed when the current direction is perpendicular to topographic variation on the sea bed and least noticeable with the current direction parallel to the topographic variation. The optimal range of wind speeds for SAR bathymetry is between 3 and 9 m/s. It was also found that the wind directions between 30 and 89 degrees are preferred, although the effect of the wind direction on SAR bathymetry was found to be non-trivial.

A significant parameter that affects current based SAR bathymetry is the response time of the wave system to current variations, known as the relaxation rate (Alpers and Hennings 1984, Renga et al. 2013). During a field experiment carried out in the framework of the Marine Science and Technology (MAST) programme of the European Commission (EC), an Air-Sea Interaction Drift Buoy (ASIB) was set-up to measure in-situ parameters. These were compared with SAR data. The relaxation rate dependence on several parameters was determined as a function of various SAR frequency Bragg waves, in different wind speed conditions (Hennings et al. 2001).

3. Review of Literature on the Use of SAR for Archaeological Prospection

Further studies on the optimal conditions for current based SAR bathymetry were carried out by Fan et al. (2008a), who simulated the relationship between normalized radar backscattering cross-section and currents, winds, wave length, incidence angle and polarization to determine the optimal conditions for shallow water SAR bathymetry. Fan et al. (2008b) also wrote a review paper on remote sensing of the shallow sea bottom topography using SAR.

Up to the early 2000's, SAR bathymetry models based on current modulation largely assumed a homogenous current flow. Zheng et al. (2006) developed a model for a vertically stratified water body. The need for a more complex model was also recognised and addressed by Li et al. (2009), who observed submerged sand banks aligned parallel to the tidal current on RADARSAT-1 and ENVISAT SAR data. The observation could not be explained by existing models that require topographic features to be aligned perpendicular to currents. A similar observation of flow parallel to corrugated topography was made by Zheng and his colleagues, who studied the phenomena in the region of the Gulf Stream (Zheng et al. 2012a), and in the Bohai Sea (Zheng et al. 2012b). They explained the physical mechanism as the influence of a complex combination of horizontal and vertical shear current flow on surface roughness (Zheng et al. 2012b).

The arrival of the “golden age” of VHR spaceborne SAR sensors, with the launch of TerraSAR-X, COSMO-SkyMed and Radarsat-2, all in 2007, stimulated a number of studies on the use of these sensors for SAR bathymetry. Hennings and Herbers (2007), for example, proposed an improved radar imaging theory applicable to TerraSAR-X.

A new methodology for SAR bathymetry was devised by Brusch et al. (2011) and applied to TerraSAR-X data. This is based on the principle of the refraction and shoaling of long swell waves due to underwater bottom topography in shallow areas. The depths are derived using the dispersion relation. This method was applied over the entrance of Port Phillip near Melbourne (Australia) and the Duck Research Pier in North Carolina (USA).

The method can be summarised as follows:

1. Compute FFT of subimage. The peak in the 2D spectrum marks the mean wavelength and mean wave direction of all waves in the subimage. The peak wavelength and peak wave directions can be calculated as follows,

$$L = \frac{2\pi}{\sqrt{k_x^2 + k_y^2}} \quad 3.2$$

$$\varphi = \tan^{-1}\left(\frac{k_y}{k_x}\right) \quad 3.3$$

where L is the peak wavelength, φ is the peak wave direction, k_x and k_y are the peak coordinates in the wave number space.

2. The FFT window is then moved by one wavelength, a new FFT is computed, and step 1 is repeated. This continues until the edge of the FFT window reaches the shoreline. The change in wavelength and direction can thus be tracked as the wave propagates.
3. The depth is then derived using the linear dispersion relation for ocean gravity waves:

$$d(L, \omega) = \frac{L}{2\pi} a \tanh\left(\frac{\omega^2 L}{2\pi g}\right) \quad 3.4$$

where g is the acceleration due to gravity and ω is the angular wave frequency (Brusch et al. 2011).

Pleskachevsky et al. (2011) also applied the principle of refraction and shoaling of waves due to topographic features on the seabed. The authors produced a depth map of the area of Rottneest-Island, Australia. Optical techniques were additionally applied to the same area. It was reported that optical techniques could provide depth information up to about 20m, while SAR techniques are suitable from around 10 to 70m depth, depending on sea state and acquisition quality. This leaves an overlapping area of 10 to 20m depths where both techniques can be applied (Pleskachevsky et al. 2011).

A project, SAR4BAT, funded by the Italian Space Agency (ASI) is currently on-going with the objective of applying state of the art SAR-based bathymetric techniques to the Mediterranean Sea. The tidal currents are generally weaker than most other areas where current based SAR bathymetric techniques have been applied. SAR4BAT aims to use SAR data for coastal bathymetry and the documentation of underwater archaeological sites (Renga et al. 2012).

In the framework of SAR4BAT, Renga et al. (2012) published a review of state of the art techniques for SAR bathymetry. The same team went on to propose an algorithm for SAR bathymetric DEM retrieval that could be applied in Mediterranean areas. This algorithm, which is based on the current modulation technique, was applied on COSMO-SkyMed and ALOS-1 PALSAR data over the Gulf of Naples (Renga et al. 2013, 2014). It is described in detail in section 6.2.3.6. The main difference between this and similar current-based techniques is that it requires very little ancillary data, such as currents, winds and other parameters. All that are required are some bathymetric measurements over one SAR image range line to tune the algorithm and estimate correctly the relaxation rate, current velocity and depth corresponding to “equilibrium” conditions (i.e. unperturbed current and flat topography) (Renga et al. 2014). This would make the algorithm practically feasible to implement using only satellite data, and without the need for in-situ measurements, provided some initial coarse estimate is available over a part of the area to be mapped. The potential for applying this algorithm for submerged palaeolandscape mapping and monitoring is the subject of Chapter 6 of this PhD thesis.

3.5.2 Application of Remote Sensing for Archaeological Prospection Underwater

Many studies have applied remote underwater mapping techniques for archaeological prospection and submerged palaeolandscape studies. Some have used geophysical techniques directly through the water

3. Review of Literature on the Use of SAR for Archaeological Prospection

column to detect archaeological structures (e.g. Missiaen (2015)). Others have applied active (LiDAR) techniques from remote airborne platforms (e.g. Doneus et al. (2013)). Several have also used passive techniques, including from spaceborne platforms, to detect archaeological objects, such as historical ship wrecks (e.g. Di Iorio et al. (2015)). However, the successful applications to date of optical remote sensing techniques have been limited to areas with very clear waters, such as in the Mediterranean.

Research on the application of SAR bathymetry for underwater archaeology and palaeolandscape analysis was first carried-out by the author of this PhD research, using Sentinel-1 data (Stewart et al. 2016c). This research also constituted the first use of Sentinel-1 for bathymetric mapping. A description of this work is the subject of chapter 6 of this PhD research.

The feasibility of using satellite techniques for underwater archaeology was also the subject of a recent project funded by the European Union (EU) Seventh Framework Programme (FP7) called Innovation Technologies and Applications for Coastal Archaeological sites (ITACA). ITACA kicked-off in November 2013 and the final conference took place in June 2016. The aim of the project was to apply both optical and SAR remote sensing techniques for the detection and monitoring of underwater archaeological structures. In particular, ITACA attempted to achieve the following objectives:

- Search and location of ancient ship wrecks;
- Monitoring of ship wrecks, ruins and historical artefacts that are now submerged;
- Integration of resulting search and monitoring data with onsite data into a management tool for underwater sites;
- Demonstration of the system's suitability for a service.

These objectives were applied in coastal areas in Greece and Italy. For the SAR bathymetry, the algorithm of Renga et al. (2013, 2014) was employed using COSMO SkyMed Stripmap and Spotlight, TerraSAR-X Stripmap and Sentinel-1 Interferometric Wide Swath imagery. Over the Greek test sites, no topographic maps were derived from the SAR data due to a lack of currents and significant topography. However, over two of the Italian test sites, the locations of known shipwrecks may have corresponded to artifacts visible in some of the SAR imagery. Without prior knowledge of the locations of these features it may have been difficult to identify them in the SAR data given the presence of atmospheric artifacts in one case and due to geolocation inaccuracies in the other (Di Iorio et al. 2015, Tusa 2016). More details on the project are provided in Appendix C.3.2.

4 ARCHAEOLOGICAL PROSPECTION USING SAR IN AGRICULTURAL CROP AND GRASSLAND AROUND ROME

Published in Papers 1 & 4 (See Appendix D.1)

The aim of this chapter is to assess the use of both the polarimetric amplitude and the phase of the SAR signal to detect surface residues of buried archaeological structures in a temperate vegetated region. A number of sites have been selected surrounding the area of Rome where archaeological survey data exists. Analyses have been carried out to determine the potential of using filtered polarimetric SAR backscatter, coherence and an interferometric time series for archaeological prospection in this area. Prospection would be through the detection of residues, which are likely to be indirect proxy indicators of buried structures (as described in section 3.4), given the amount of water in the soil and the vegetated state of the study areas.

Over the study areas 77 COSMO SkyMed (CSK) Stripmap, 27 CSK Spotlight, 20 Radarsat-2 (R2) Fine Quad (FQ), 10 PALSAR-1 Fine Beam Dual Polarisation (FBD) and 3 PALSAR-1 Fine Beam Single Polarisation (FBS) imagery have been procured. The primary dataset comprises the CSK data. This was procured for the following reasons: 1) to have as large as possible a time series in order to cover a range of environmental and ground conditions; 2) to have data at the highest available spatial resolution, to resolve small scale features corresponding to recognisable archaeological structures; 3) to have the highest possible frequency of acquisition, to be able to perform coherence and InSAR DEM calculation, without complete loss of coherence. The rationale for the use of R2 FQ data is to determine the sensitivity of fully polarimetric backscatter to surface residues. The PALSAR-1 data was chosen to assess whether the longer (L-band) wavelength is any more likely to detect surface (or even subsurface) residues due to increased signal transmission in the vegetation or soil. The fact that these three SAR sensors operate in three respective SAR frequencies of X-band (CSK), C-band (R2) and L-band (PALSAR) would suggest that a comparison of frequency could be carried out, and an assessment made of that which may be most suitable for archaeological prospection in this area. However, the differences in imaging geometry, spatial resolution, mode of acquisition and instrument characteristics prevented an un-biased comparison of frequency alone. Interferometry was not carried out with the R2 and PALSAR-1 data. The long temporal baselines in the R2 and PALSAR-1 time series meant that coherence would likely have been lost very soon, and the varying temporal and spatial baselines in both time series meant that a comparison of coherence over time would have been difficult. Some initial attempts supported this conclusion.

Processing included multitemporal filtering of backscatter, calculation of coherence between consecutive CSK image acquisitions and SBAS DEM generation from the CSK data over each subset area. Surface residues of buried structures have been found in the filtered CSK backscatter, coherence and DEM. No conclusive evidence of archaeological structures were found in the processed R2 or PALSAR data. This is likely due to the coarse resolution, combined with the lack of detail in the available ground truth data. In an attempt to understand the mechanisms and conditions responsible for the appearance of residues in each layer in which they were present, an analysis of results has been carried out with CSK

interferometric coherence and Potential Soil Moisture Deficit (PSMD) data (calculated from rainfall and potential evapotranspiration).

4.1 Study Areas

The Areas Of Interest (AOIs) chosen for this study comprise a number of small (most no more than 10 km²) rural sites situated just outside the metropolitan area of Rome (see Figure 4.1). The land cover of each is mainly agricultural or pastoral. The geology of the region is characterized by volcanic deposits (mainly pyroclastic tuff) from the Albano volcano district to the southeast and the Sabatino volcano district to the northwest, with alluvial sediments along the Tiber valley in between the two (Funciello et al. 2006). Figure 4.2 is a DEM of the area from the Shuttle Radar Topography Mission (SRTM). The topography gradually decreases from these two volcanic districts towards the Tiber, with valleys carved by fluvial erosion. The AOIs of Appia and Prenestina are located on the volcanic deposits of the Albano volcano, with undulating eroded valleys. The AOI of Veii is the site of an ancient Etruscan city perched on an area of volcanic deposits from the Sabatino district, in between valleys carved out from the tuff by fluvial erosion. The remainder of the AOIs are in the alluvial deposits of the Tiber, characterized by very flat topography: Salaria is in the Tiber valley, while Portus and Ostia are in the Tiber delta.

The climate of the AOIs is warm and temperate (Mediterranean), with cool winters and warm to hot summers. Figure 4.3 is a graph of rainfall and temperature in the time period of the CSK image acquisitions. In this time period, the temperature almost every summer reached above 35 degrees centigrade, and in winters it seldom dropped below 5 degrees, and never reached 0. The monthly rainfall was particularly high in November 2010 and November 2013, when it reached beyond 250 mm. In July and August of most years in the time period there was negligible rainfall (Regione Lazio 2016).

All the AOIs are known to contain buried archaeological structures, mainly from the Roman to medieval periods. Some of these structures, perhaps not all, have been documented at various levels of detail following archaeological surveys including geophysical prospection, field walking or airborne or spaceborne optical remote sensing analysis. A detailed description of the archaeology in each AOI is described in subsections 4.1.1 to 4.1.6.

4. Archaeological Propection Using SAR in Agricultural Crop and Grassland Around Rome

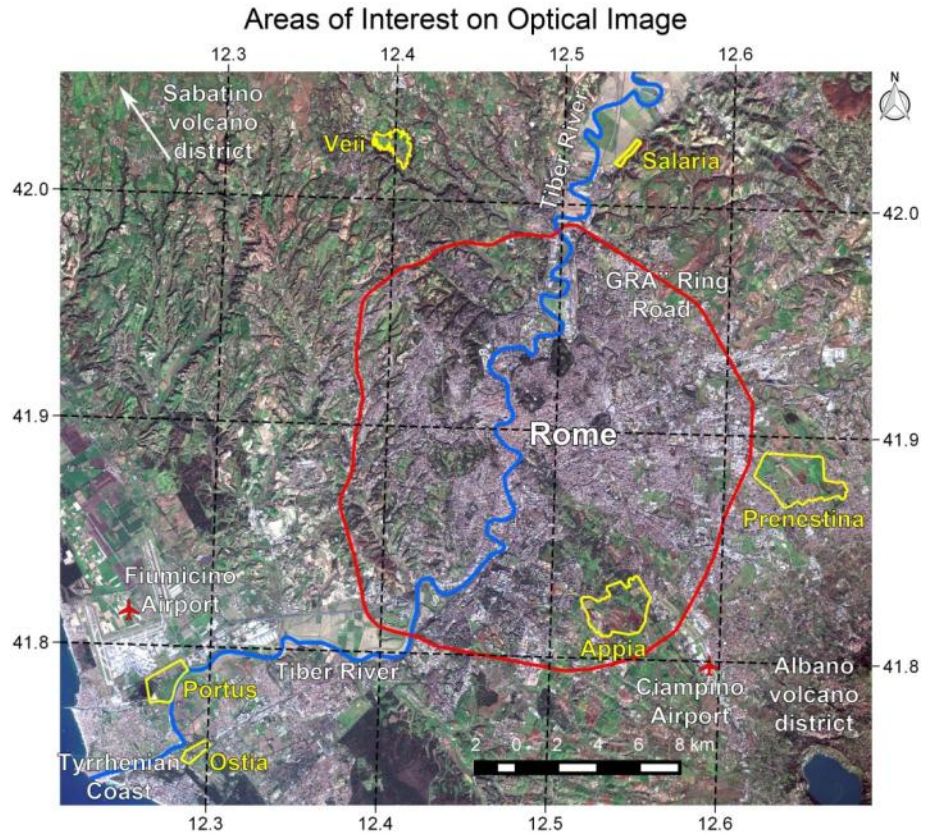


Figure 4.1 AOIs shown as yellow polygons on true colour, 10 meter resolution Sentinel-2 image acquired on 28 December 2015 (bands 4, 3 and 2 displayed as red (R), green (G) and blue (B) respectively). Contains modified Copernicus Sentinel data 2016.

4. Archaeological Propection Using SAR in Agricultural Crop and Grassland Around Rome

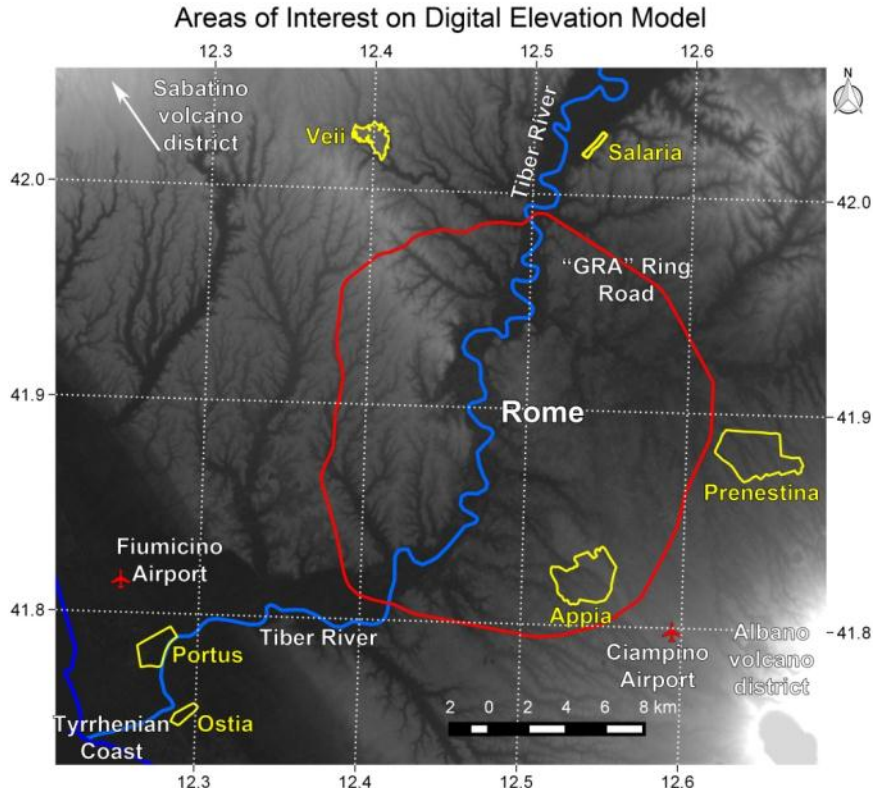


Figure 4.2 SRTM DEM at a spatial resolution of 1 arc-second (30m) with AOIs (yellow polygons) overlain. SRTM data courtesy of the United States Geological Survey (USGS, 2006).

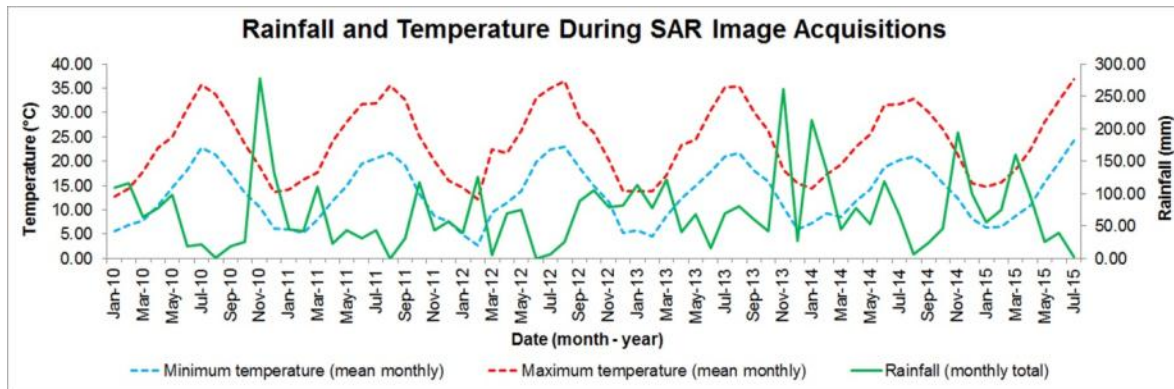


Figure 4.3 Graph showing rainfall and temperature in time period of CSK SAR image acquisitions (Regione Lazio 2016).

Each AOI is described in sections 4.1.1 to 4.1.6 below. In each section, the AOI is shown on a near-infrared (NIR), red (R) and green (G) colour composite of an optical satellite image, to highlight the vegetation characteristics of each area.

4.1.1 Portus

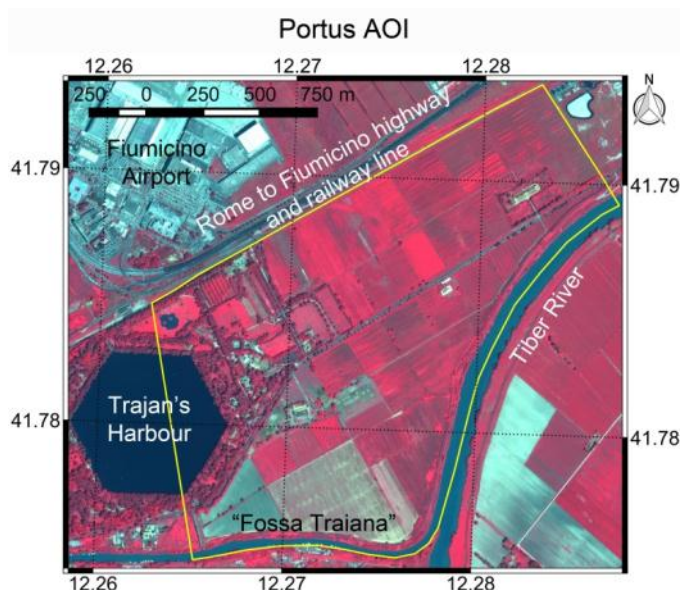


Figure 4.4 Portus AOI shown as yellow polygon on Pleiades image acquired on 8 May 2014. The image was pan-sharpened to 0.5 m spatial resolution, and is displayed as NIR, R and G respectively as R, G and B. Pleiades data provided by the European Space Agency.

The AOI of Portus is located between the hexagonal harbour of Trajan to the west, the Tiber river to the east, the “Fossa Traiana” to the south and the A91 Rome to Fiumicino highway and railway line to the north. Being in the Tiber delta, the area is very flat with an alluvial substrate (Modigliani 2008d). Today the AOI is in a region comprising irrigated fields of arable crops (Keay et al. 2005, Modigliani 2008b). It is traversed by a number of roads and there are some isolated farm buildings. To the west the area is more built-up and there are a greater number of trees.

The archaeology of the area is dominated by the presence of the ancient port of Rome, in particular, the hexagonal harbour of Trajan. Construction of Trajan’s harbour began in 100 AD as an enlargement of the artificial harbour initiated by Claudius in 42 AD and continued by Nero. The harbour complex, known as Portus, replaced Ostia as the principal port for the city of Rome up to the Byzantine period. While the coastline remained stable throughout the Roman period, it has since migrated seawards by several kilometres due to a combination of neotectonic movements, sea-level changes and sediment load variations of the Tiber river. The harbour of Portus would have silted up in post-Roman times (Keay et al. 2005, Keay et al. 2014).

Much archaeological research in this area has been carried out over the years, particularly by Lanciani (1868), Lugli and Filibeck (1935), Testaguzza (1970), and more recently, by the Portus Project. The Portus Project involves extensive non-destructive archaeological survey of Portus including geophysical prospection, air photo interpretation and systematic surface collection. The project began in 1997 and is on-going. The work is undertaken by the Soprintendenza per I Beni Archeologici di Ostia, the British School at Rome, and the Universities of Southampton, Durham and Cambridge (Keay et al. 2005, Keay et

al. 2014). It is primarily the results of this project (which integrates also the results of previous research) that has been used to compare with the results of the SAR data analysis.

4.1.2 Ostia

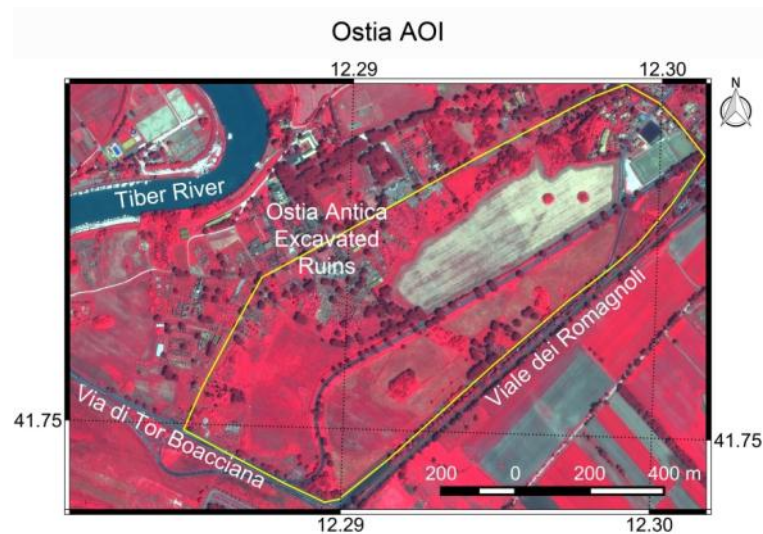


Figure 4.5 Ostia AOI shown as yellow polygon on Pleiades image acquired on 8 May 2014. The image was pan-sharpened to 0.5 m spatial resolution, and is displayed as NIR, R and G respectively as R, G and B. Pleiades data provided by the European Space Agency.

The AOI of Ostia is bordered to the north and west by the excavated part of the ancient Roman port city of Ostia, to the east by the Viale dei Romagnoli, and to the south west by the Via di Tor Boacciana (which also traverses the centre of the AOI). It is situated very close to the Portus AOI, and is also in the Tiber delta, thereby characterised by very flat topography and alluvial substrate (Modigliani 2008d). The area today comprises fields of grass, dotted with the occasional tree. The soil is of class 3, with notable limitations mainly due to stoniness and shallow depth (as a result of the buried structures), and possibly also to poor texture or chemistry (Modigliani 2008a).

The ancient city of Ostia predates Portus. Historical accounts state the city was founded, as a colony of Rome, in the seventh century BC. However, the oldest archaeological remains date back only to the fourth century BC (Bellotti et al. 2011). Following the construction of Portus, Ostia gradually fell into decline and was eventually abandoned in the 9th century AD (Meiggs 1973).

Extensive excavations were carried out in Ostia from 1938 to 1942 for the World Exhibition of 1942 in Rome. However, around 50 to 60 per cent of the area remains unexcavated (Becker 2015). In the fields of the AOI, buried streets and buildings continuing from the excavated part of Ostia have been identified as crop marks in air photos and in geophysical surveys carried out by Becker and his team (Becker 2015). An attempt was made by Linck et al to identify archaeological residues over the same area surveyed by Becker and his team using TerraSAR-X Spotlight (1 meter resolution) data acquired in October 2012 in the experimental 300 MHz bandwidth. Only a few faint traces of buried structures were visible (Linck et al. 2013a).

4.1.3 Appia

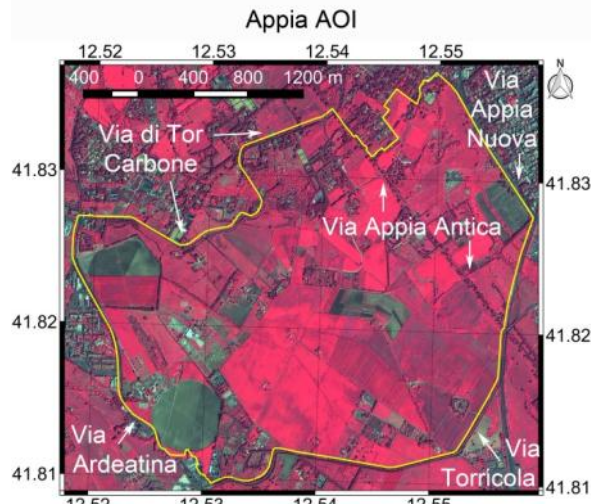


Figure 4.6 Komsat-2 image of the Appia AOI (shown in yellow polygon) acquired on 21 April 2011, pansharpned to 1m spatial resolution. False colour composite of NIR, R and G displayed as R, G and B respectively. Komsat-2 data provided by the European Space Agency.

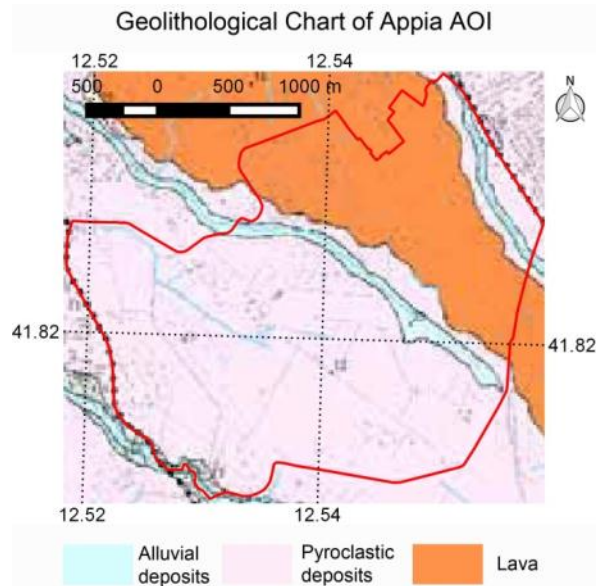


Figure 4.7 Geolithological chart of Appia AOI (shown in red polygon), last updated in 2007, courtesy of the Comune di Roma (Modigliani 2008d).

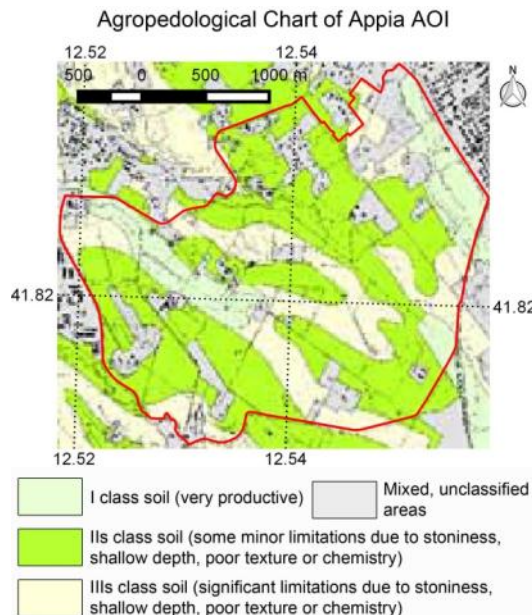


Figure 4.8 Agropedological chart of Appia AOI (shown in red polygon), last updated in 2007, courtesy of the Comune di Roma (Modigliani 2008c).

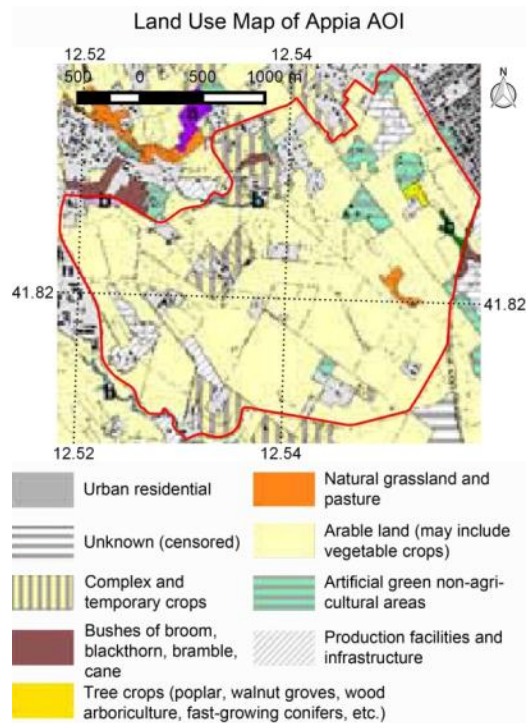


Figure 4.9 Land use map of Appia AOI (shown in red polygon), last updated in 2007, courtesy of the Comune di Roma (Modigliani 2008b).

The AOI of Appia comprises the area selected by the project “Mapping the Via Appia”. This area surrounds a part of the ancient Appian Way at the 5th Roman mile from its origin in Rome. It is bordered

to the north by the Via di Tor Carbone, to the south by the Via Torricola, to the east by the Via Appia Nuova and to the west by the Via Ardeatina. The AOI is within the “Parco Regionale dell’Appia Antica”. This is one of the larger AOIs. Figure 4.6 shows the location of the AOI on a near-infrared colour composite image. Figure 4.7 is a geolithological chart of the AOI, which shows the lava tongue on which the ancient Appia road was built, and from which the basalt paving stones of the road were quarried. The majority of the surrounding geolithology is also volcanic and comprises pyroclastic deposits, including tuff (Modigliani 2008d). Figure 4.8 shows the agropedology of the area, which comprises soils of class 1, 2 and 3. The limitations of the class 2 and 3 soils are mainly due to stoniness, shallow depth, poor texture or chemistry (Modigliani 2008a). Figure 4.9 is a land use map of the area, with particular attention given to vegetation classes. Most of the AOI is taken up by arable land (Modigliani 2008b).

The archaeology of the area is dominated by the Appian Way, the construction of which began in 312 BC (Della Portella et al. 2004, Mols 2014). Many structures were built in proximity to the road in antiquity, particularly tombs, but also inns, workshops and villas (Della Portella et al. 2004, Mols 2014). The AOI was chosen by the Mapping the Via Appia project due to its lack of modern development and the abundance of structures that were known to exist here in antiquity, and many of which are no longer present on the surface. These structures have been identified in various ancient sources: These include maps, such as from Carlo Labruzzi (1748-1817); etchings, such as those of Giovanni Battista Piranesi (1720-1778), and other sources. Various prospection techniques have been applied in the area by the Mapping the Via Appia project, including geophysical prospection (magnetometry, georadar and resistivity), analyses of historical air-photos and satellite imagery, and excavation. The results of these have been inserted into a project GIS (Mols 2014). This GIS has been used as a source of comparison for the SAR analysis.

4.1.4 Prenestina

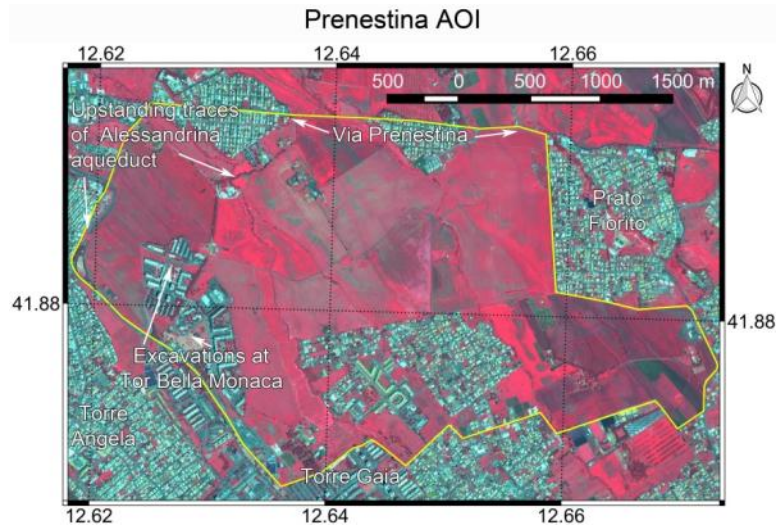


Figure 4.10 Pleiades image of the Prenestina AOI (shown in yellow polygon), acquired on 20 April 2014, pan-sharpened to 0.5m spatial resolution and displayed as a false colour composite of NIR, R and G displayed as R, G and B.

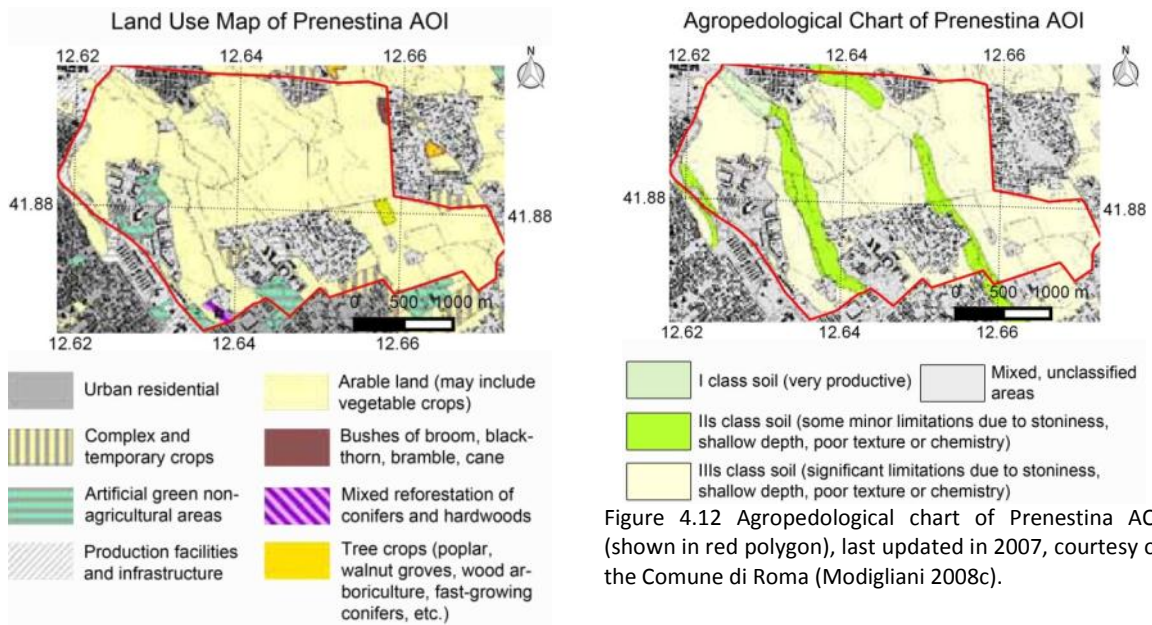


Figure 4.12 Agropedological chart of Prenestina AOI (shown in red polygon), last updated in 2007, courtesy of the Comune di Roma (Modigliani 2008c).

4. Archaeological Prospection Using SAR in Agricultural Crop and Grassland Around Rome

Figure 4.11 Land use map of Prenestina AOI (shown in red polygon), last updated in 2007, courtesy of the Comune di Roma (Modigliani 2008b).

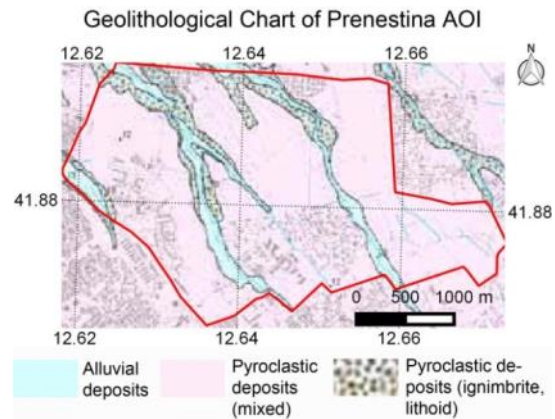


Figure 4.13 Geolithological chart of Prenestina AOI (shown in red polygon), last updated in 2007, courtesy of the Comune di Roma (Modigliani 2008d).

The AOI of Prenestina comprises an isolated rural area situated south of the modern Via Prenestina, and between the urban areas of Prato Fiorito (to the east), Torre Gaia (to the south) and Torre Angela (to the west). Most of the AOI is occupied by arable fields of non-irrigated crops (Modigliani 2008b) (see Figure 4.11). The topography throughout the area is undulating. The soil is mainly of class 3. Its suitability for cultivation may be hindered by stoniness, shallow depth, poor texture or inferior chemical composition (Modigliani 2008a) (see Figure 4.12). The substrate is mainly pyroclastic, from the Albano volcano district, with some alluvial material in the valleys (Modigliani 2008d) (see Figure 4.13). This is one of the two largest AOIs (together with the Appia).

The AOI lies approximately half way between the ancient cities of Rome and Gabii. It was traversed in antiquity by a number of Roman roads, including, amongst others, the Via Gabina, which then became the Via Prenestina. The Alessandrina aqueduct also crossed the area. Numerous other archaeological structures have been, to varying degrees of accuracy, identified in the area, including villas, tombs, wells and cisterns, and even small settlements (Quilici 1974). A few structures have been excavated in the course of urban development. During the construction of Tor Bella Monaca in the 1980's, a part of the Via Gabina was excavated, revealing basalt paving stones. Part of the bath complex of a villa, in use from the fourth century BC, was also excavated, and the remains of a portico belonging to a Roman farmhouse (De Franceschini 2005). Some structures are still upstanding, including some of the arches of the Alessandrina aqueduct. Most of the AOI has been un-touched by excavation and many archaeological features have been interpreted from scarce fragments of material at the surface following ploughing, such as ceramic, brick and stone (Quilici 1974).

The area in which the AOI is situated has, since the late 1950's, seen rapid and extensive urban development as a vast expansion of suburban Rome, as a result of which many archaeological sites have been destroyed (Quilici 1974). The fast pace of development stimulated Lorenzo Quilici, in 1969, to begin a massive archaeological survey of an area of just over 10 x 10 km surrounding, and including, the AOI. This survey reports on the results of field walking, air photo interpretation and excavation,

wherever these were undertaken. It provides a comprehensive description of all finds, including photos. It summarises the results of previous research in the area, such as that carried out by Pietro Rosa, Rodolfo Lanciani, Thomas Ashby and Jean Coste (Quilici 1974). The 938 page volume was published in 1974, and this is the source used to validate archaeological residues identified in the SAR imagery of the area.

4.1.5 Salaria

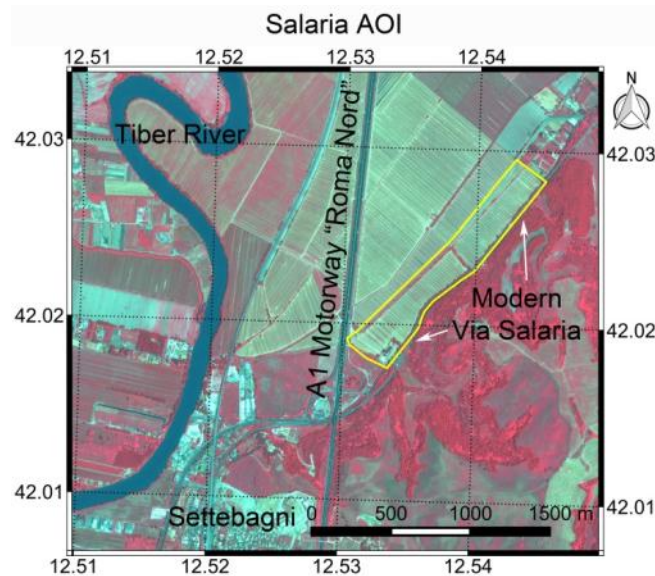


Figure 4.14 Pleiades image of the Salaria AOI (shown in yellow polygon) acquired on 22 May 2014, pansharpenered to 0.5m spatial resolution and displayed as a false colour composite of NIR, R and G respectively as R, G and B. Pleiades data provided by the European Space Agency.

The AOI of Salaria is the smallest AOI. It includes two fields of irrigated arable crops (Modigliani 2008b) traversed by the ancient Via Salaria ten Roman miles from its origin (Quilici and Gigli 1980). The area is situated on the edge of the flat lands of the Tiber valley, north of the settlement of Settebagni and in between the modern Via Salaria (to the right) and the A1 “Roma Nord” motorway (see Figure 4.14). The substrate is alluvial (Modigliani 2008d) and the soils of the fields are of class 2, with only minor limitations for cultivation due to stoniness and excess water, either in the form of stagnant water in the soil or possible flooding (Modigliani 2008a).

The ancient Roman Via Salaria is believed to have been constructed as a paved road from the beginning of the 3rd century BC (Wiseman 1970). No trace of the ancient Via Salaria is visible on the surface of the fields, but the line of the road has been identified as crop marks in optical air photos (e.g. by Quilici and Quilici Gigli in the 1970’s (Quilici and Gigli 1980)) and in optical satellite imagery (e.g. by Panu Hyppönen in 2014 (Hyppönen 2014)). In 1977, a cylindrical stone was found in the area, which is believed to be the 10th milestone. It was discovered at a depth of around 70 cm, during ploughing, at around kilometre 17.7 of the modern via Salaria (see Figure 4.14) (Quilici and Gigli 1980, Hyppönen 2014). The standard width of “viae publicae” (public roads) constructed from the 3rd century BC was generally around 4.2

meters, which was sufficient to allow two way traffic (Quilici 1992), this corresponds with the width of crop marks over the road in the AOI.

4.1.6 Veii

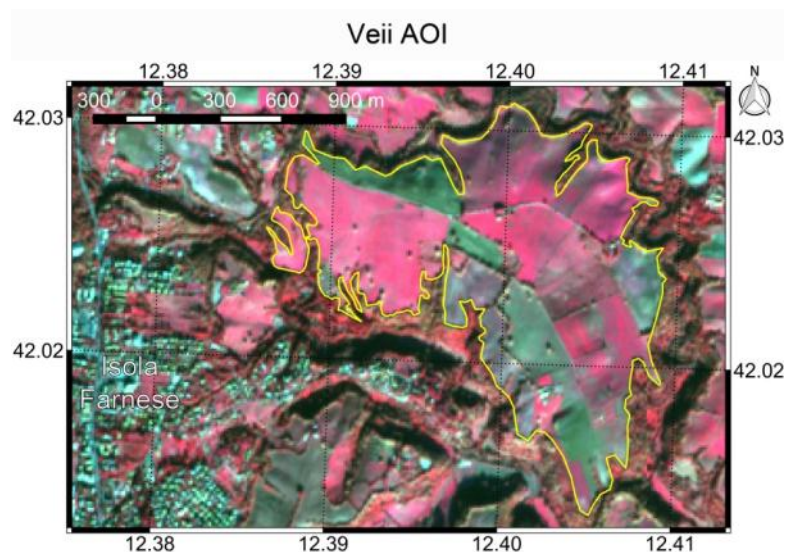


Figure 4.15 Sentinel-2 image of the Veii AOI (shown in yellow polygon), acquired on 28 December 2015. 10m spatial resolution. Displayed as band 8 (NIR), band 4 (R) and band 3 (G) respectively as R, G and B. Pleiades data provided by the European Space Agency.

The AOI of Veii is situated in the rolling countryside between the Tiber valley and the Sabatino volcano district, on a raised plateau of tuff from the pyroclastic deposits of the Sabatino volcanic eruptions (Modigliani 2008d). It is located to the east of the small settlement of Isola Farnese (see Figure 4.15). The landscape comprises arable fields and permanent pasture (Modigliani 2008b). The soils include class 1 (very productive) to class 2 (some minor limitations for cultivation) and class 3 (more significant limitations for cultivation). The limitations of the class 2 and 3 soils are mainly due to stoniness, shallow depth, poor texture or chemistry (Modigliani 2008a).

The area was the site of the ancient Etruscan city of Veii, the richest city of the Etruscan League. It prospered until its defeat by Rome in 396 BC. It continued to be occupied under the Romans, but its eminence declined until the city was eventually abandoned (Ward-Perkins 1961). From the 19th century, the site was studied by many scholars, including Gell, Nibby, Canina, Dennis, Stefani, Lanciani, Colini and Giglioli. After the Second World War, significant archaeological research in Veii was carried out by John Ward-Perkins of the British School at Rome (Ward-Perkins 1961). More recently, the La Sapienza University of Rome carried out an extensive survey of the area as part of the “Veii Project”. This includes analysis of a large archive of air photos and large scale geophysical (magnetometry) prospection. The magnetometry survey has covered almost the entire plateau and has revealed a dense network of buried streets and buildings (Campana 2016). This dataset has been used to compare with the SAR data.

4.2 SAR Data

4.2.1 CSK Data

The CSK data used for this part of the analysis included 77 CSK Stripmap and 27 CSK Spotlight imagery. This data was provided by the Italian Space Agency (ASI): 25 Stripmap and 8 Spotlight images were procured for the ASI World Heritage Monitoring by Remote Sensing (WHERE) project, an experimental component of which included research on the use of SAR for prospection of archaeological vegetation and soil residues. This component constitutes the research reported in this paper.

A further 52 Stripmap and 19 Spotlight CSK images were provided by ASI for an advanced SAR remote sensing training event provided to the Italian Ministry of Defense and ASI, and hosted by ESA. The two week course took place from 9 to 20 November 2015. The processing reported in this paper constituted a part of the practical exercises of the course.

Table 4-1 shows the characteristics of the CSK data. The CSK Stripmap images are all ascending pass, with a scene center incidence angle of 34 degrees and a polarization of Horizontal transmit and Horizontal receive (HH). 77 images were available in the e-geos catalogue with these characteristics over the AOIs at the time of the analyses. These were procured as they constituted the largest possible CSK Stripmap time series, with consistent geometry and polarization, that covered all AOIs.

The 27 Spotlight images also comprised the largest possible time series of CSK Spotlight data over any of the AOIs. Perhaps the reason so many CSK Spotlight images were available over this particular area is that it includes the headquarters of ASI. For the CSK Spotlight coherence analysis, only the HH images were used since InSAR is very sensitive to differences in polarisation and a consistent dataset was required. For the CSK intensity time series analysis on the other hand, both the HH and Vertical transmit and Vertical receive (VV) images were used, since this analysis is less sensitive to changes in polarisation. For more precise characteristics of all data, including individual scene record numbers, see Table A-1 in APPENDIX A .

Figure 4.16 shows the coverage of the CSK Stripmap data. Most scenes cover all AOIs. Figure 4.17 shows the coverage of the CSK Spotlight data, which includes only the Prenestina AOI.

Table 4-1. CSK data characteristics. For precise characteristics of all data, see Table A-1 in APPENDIX A .

Number of scenes	Sensor mode	Acquisition date range (year/month)	Polarisation	Pass	Scene Center Incidence Angle
27	ENHANCED Spotlight	2010/06 to 2012/08	24 x HH 3 x VV	Asc	25.25
77	Stripmap HIMAGE	2011/03 to 2015/07	HH	Asc	33.95

4. Archaeological Propection Using SAR in Agricultural Crop and Grassland Around Rome

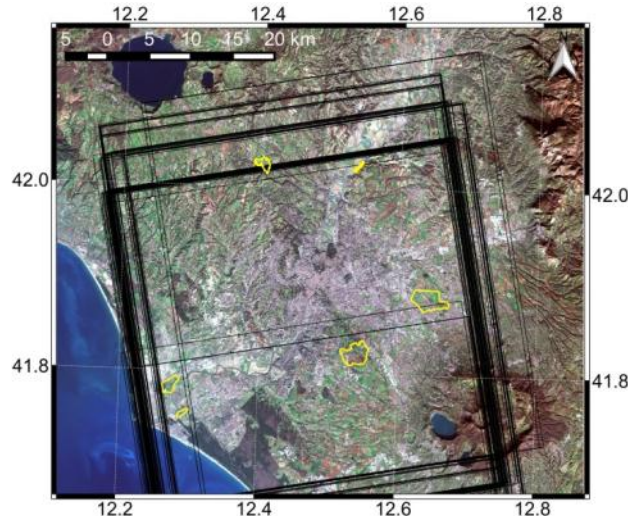


Figure 4.16 Footprints of CSK Stripmap data (in black) overlain on Sentinel-2 image. AOIs shown in yellow. Contains modified Copernicus Sentinel data 2016.

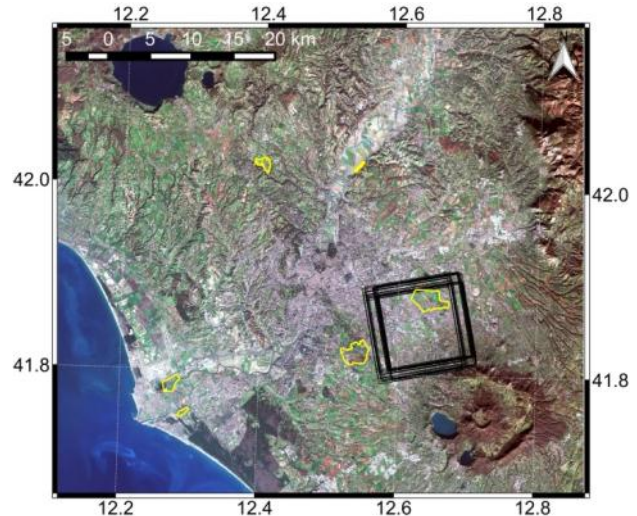


Figure 4.17 Footprints of CSK Spotlight data (in black) overlain on Sentinel-2 image. AOIs shown in yellow. Contains modified Copernicus Sentinel data 2016.

4.2.2 R2 Data

20 Radarsat-2 Fine Quad (FQ) images were obtained from the SOAR (Science and Operational Application Research) project 1488 and the SOAR-EU project 6795 through the University of Tor Vergata. The data was obtained in SLC (Single Look Complex) format. 10 of the scenes are ascending pass, acquired at around 16:50 local time, and 10 are descending, acquired at around 05:20 local time. All ascending pass images were acquired over the same track and frame, as were the descending pass images. (See Table 4-2 for image characteristics and Table Table A-2 in APPENDIX A for more complete information.)

Figure 4.18 shows the coverage of the R2 data. The ascending dataset includes both the Prenestina and Appia AOIs, while the descending dataset includes only the Prenestina AOI.

Table 4-2. R2 data characteristics. All images were acquired in 2008. For precise characteristics of all data, see Table A-2 in APPENDIX A .

Number of scenes	Antenna Beam Number	Acquisition date range (mm/dd)	Scene Center Incidence Angle	Pass	Nominal range resolution (m)	Nominal azimuth resolution (m)
10	FQ2	05/07 to 12/09	20.9	Asc	14.6	7.6
1	FQ4	08/25	23.1	Des	13.3	7.6
4	FQ9	18/08 to 11/12	28.9	Des	10.8	7.6
3	FQ14	09/08 to 12/13	34.3	Des	9.3	7.6
2	FQ19	09/15 to 10/09	39.1	Des	8.3	7.6

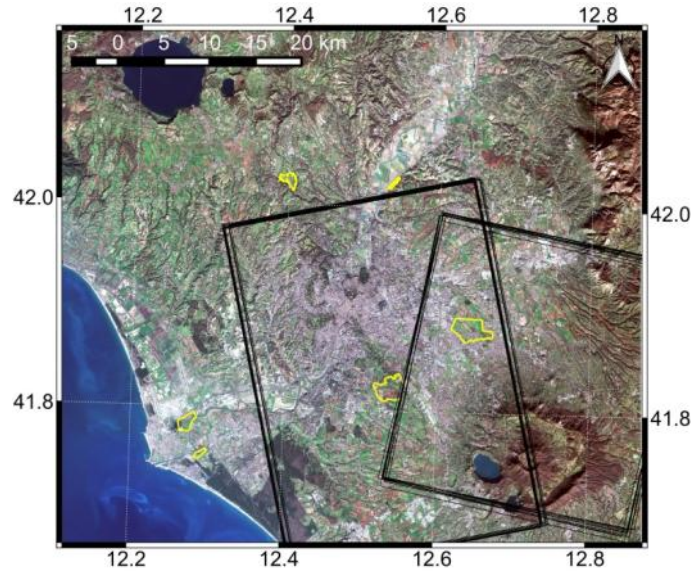


Figure 4.18 Footprints of R2 data (in black) overlain on Sentinel-2 image. AOIs shown in yellow. Contains modified Copernicus Sentinel data 2016.

4.2.3 ALOS PALSAR Data

13 ALOS PALSAR images were obtained from the ESA Category-1 (research) project C1F.11458. Of these, 10 are dual pol and 3 are single pol. All dual pol images were acquired over the same track and frame, as were the single pol images. All images are ascending pass, acquired at around 21:30 local time. (See Table 4-3 for image characteristics and Table A-3 in APPENDIX A for full details.)

Figure 4.19 and Figure 4.20 show the coverages of the PALSAR-1 FBD and FBS data respectively. Both datasets cover all AOIs except Ostia, although Portus is fully covered only by some images in each time series.

Table 4-3. PALSAR data characteristics. For precise characteristics of all data, see Table A-3 in APPENDIX A .

Number of scenes	Sensor mode and polarisation	Acquisition date range (yy/mm/dd)	Scene Center Incidence Angle	Pass
10	FBD (HH/HV)	2007/06/19 to 2010/08/12	38.7	Asc
3	FBS (HH)	2007/12/20 to 2010/12/28	38.7	Asc

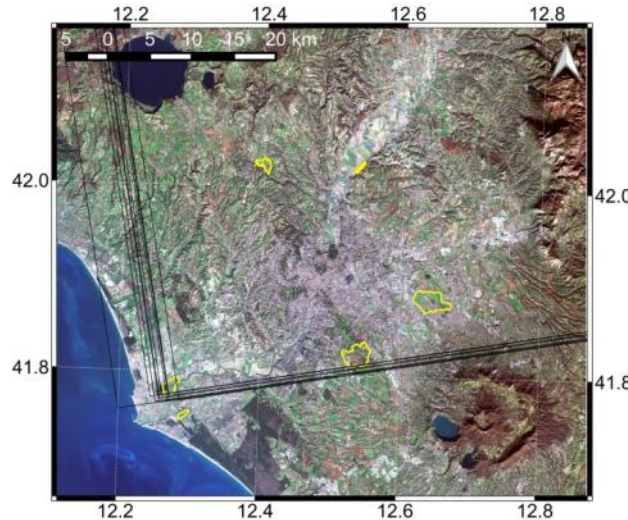


Figure 4.19 Footprints of PALSAR-1 FBD data (in black) overlain on Sentinel-2 image. AOIs shown in yellow. Contains modified Copernicus Sentinel data 2016.

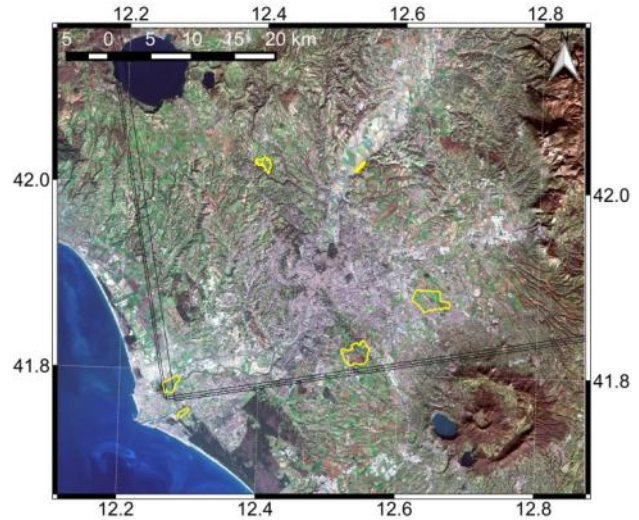


Figure 4.20 Footprints of PALSAR-1 FBS data (in black) overlain on Sentinel-2 image. AOIs shown in yellow. Contains modified Copernicus Sentinel data 2016.

4.3 Methodology

All images from each sensor were processed to derive the multitemporal speckle filtered σ^0 backscatter for each polarisation. In addition to this, from the CSK data, interferometric processing was carried out to obtain the coherence and attempt to produce DEMs using the SBAS technique for each AOI. From the R2 data, additional polarimetric layers were derived. These include decompositions and images of covariance matrix elements with various polarimetric bases chosen as a result of analyses of the scattering signatures of a number of anomaly features. All processed images were compared with available ground truth to determine whether any surface residues of buried archaeological structures were detected. Wherever detections occurred, these were analysed in detail.

The methodologies for deriving the multitemporal speckle filtered backscatter from the data of each sensor is described in section 4.3.1. The interferometric coherence processing from the CSK data is described in section 4.3.2. The CSK DEM processing chain is outlined in section 4.3.3. The methodology employed for the polarimetric analysis is described in section 4.3.4.

Detections occurred only on the CSK derived data. These were analysed with meteorological data and interferometric coherence in an attempt to determine the cause of the appearance of features in the various SAR layers. The methodology of this is described in section 4.3.5.

4.3.1 Multitemporal speckle filtered σ^0 backscatter

4.3.1.1 CSK

All 77 CSK Stripmap images in SLC format were subsetting for each AOI and the 27 Spotlight SLC images were subsetting for the Prenestina AOI. The stacks over each AOI were then coregistered with the aid of the SRTM 1 arc-second (30m) DEM. Over Prenestina each CSK image mode was coregistered separately.

The images were then multilooked by a factor of 1x1 (CSK pixel dimensions are square at SLC), only to remove the phase component and convert the images from SLC to detected.

Multitemporal De Grandi speckle filtering was then applied to each stack. Conceptually, the De Grandi filter works by averaging in the temporal domain parts of images that are statistically homogenous. If such an area is interrupted by the appearance of a feature in one or more images, the areas to be averaged are divided to exclude this feature (De Grandi et al. 1997). The De Grandi filter preserves the spatial resolution of the input images. Small scale structures in individual images are retained, making it suitable for identifying small anomaly features with only slight variations in backscatter from surrounding areas (De Grandi et al. 1997, Stewart et al. 2016b).

The speckle filtered imagery was then geocoded to the Universal Transverse Mercator (UTM) projection (Zone 33 North), with the World Geodetic System 1984 (WGS 84) datum. Terrain correction was performed with the SRTM 1 arc-second DEM. The pixel spacing of the CSK Stripmap imagery was set to 2.5m and the CSK Spotlight to 1m.

The imagery was calibrated to σ^0 and converted to decibel (dB).

4.3.1.2 R2

The same processing as described in Section 4.3.1.1 was carried-out on the R2 data, only different multi-look factors and pixel spacing were applied.

For the ascending stack, the pixel spacing of the SLC imagery is 4.7m in slant range and 4.7m in azimuth. The pixel spacing in ground range can be calculated from the following formula:

$$P_g = P_s / \sin \theta \quad 4.1$$

where P_g is the ground range pixel spacing, P_s is the slant range pixel spacing and θ is the scene center incidence angle (Massonnet and Souyris 2008). The ground range pixel spacing was calculated as 13.34m. A multilook factor of 3 in azimuth produced an azimuth pixel spacing of 14.6. To preserve the resolution, the pixel spacing was chosen as 14.6m.

For the descending stack, the slant range pixel spacing varied according to the various incidence angles of the R2 FQ modes from FQ4 to FQ19 (see Table 4-2). The imagery with the highest incidence angle, and therefore highest pixel spacing in range, are those acquired in the FQ19 mode. The FQ19 imagery has a ground range pixel spacing of 7.5m. A multi-look factor of 2 in azimuth produced an azimuth pixel spacing of 9.5m. To preserve the spatial resolution of the FQ19 imagery, all imagery in the descending stack were resampled to 9.5m.

The R2 ascending imagery included both the Prenestina and Appia AOIs, and processing was therefore carried out over both AOIs. The R2 descending imagery included only the Prenestina AOI, and processing was thus confined to this AOI.

4.3.1.3 PALSAR-1

As with the R2 data, the same processing as described in Section 4.3.1.1 was carried-out on the PALSAR-1 data, only different multi-look factors and pixel spacing were applied.

The PALSAR-1 imagery all have an incidence angle of around 38.7 degrees. The FBD imagery have a slant range pixel spacing of 9.4, a ground range pixel spacing of 15.0 and an azimuth pixel spacing of 3.1. Multi-looked by 5 in azimuth produced an azimuth pixel spacing of 15.3. The pixel spacing was therefore selected as 15m.

The FBS imagery have a slant range pixel spacing of 4.7, a ground range pixel spacing of 7.5 and an azimuth pixel spacing of 3.1. Multi-looked by 3 in azimuth produced an azimuth pixel spacing of 9.2. The pixel spacing was therefore selected as 9m.

The PALSAR-1 data was processed over all AOIs with the exception of Ostia and Portus, which were outside the coverage of the data.

4.3.2 Interferometric coherence

The interferometric coherence was calculated between consecutive CSK image acquisitions covering each AOI that have a temporal baseline of 16 days. In the case of the CSK Spotlight data, coherence was calculated between images with temporal baselines of 16 days and 1 day.

Prior to coherence generation, each SLC image pair was coregistered with the aid of a DEM (SRTM 1 arc-second). The coherence was then calculated over a window size of 5x5 pixels. Given the low resolution of the DEM compared to the CSK data, the local topographic phase was estimated in a 7x7 window and removed before coherence calculation.

The coherence images were then geocoded in the same way as that described in section 4.3.1.

Coherences were plotted against the acquisition dates of both the master and slaves in all coherence charts displayed in the results (section 4.4).

4.3.3 DEM

Over vegetated areas, often temporal decorrelation prohibits the use of repeat pass InSAR for DEM generation (Woodhouse 2005). However, with a large time series of data, this limitation can be overcome with techniques such as Small Baseline Subsets (SBAS). The SBAS technique generates interferograms that are selected to minimise the spatial (for displacement velocities) and temporal baselines between acquisitions, thus avoiding decorrelation effects (Berardino et al. 2002). While SBAS is primarily a technique for displacement measurement, it can also be used for DEM generation.

Over each AOI, an attempt was made to generate a DEM using the SBAS technique with the available CSK data. Given the high proportion of vegetation in all AOIs, the technique only worked well over the Prenestina AOI. However, over the Salaria AOI, despite the low coherence affecting most interferograms and / or the excessively small or large baselines, one interferogram (albeit noisy) clearly revealed the

ancient Via Salaria. A DEM was therefore created from this pair alone using standard InSAR, without the need for SBAS processing.

The SBAS processing was carried out using the ENVI SARscape software (version 5.2), the processing chain is shown in Figure 4.21. The processing is described in more detail for the Prenestina AOI in subsection 4.3.3.1, and for the Salaria AOI in subsection 4.3.3.2.

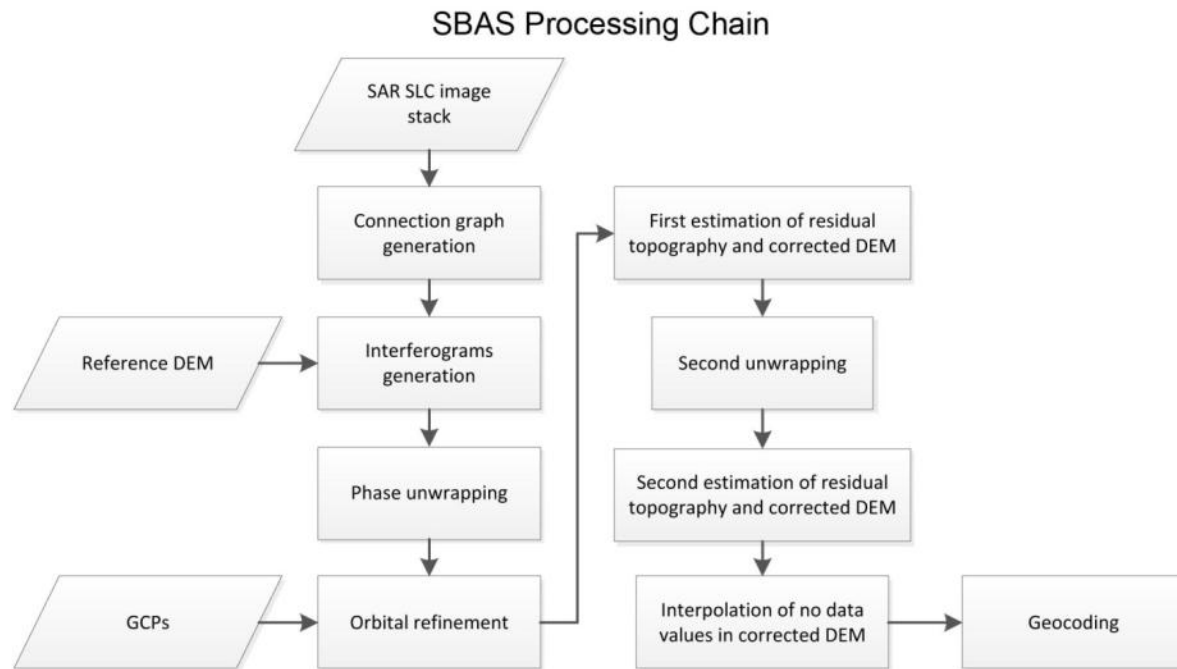


Figure 4.21 Flow chart showing the SBAS processing chain. This was implemented for both the CSK Stripmap and Spotlight time series using the SARscape software (version 5.2).

4.3.3.1 SBAS DEM: Prenestina AOI

With the availability of a time series of both Stripmap and Spotlight CSK data over the Prenestina AOI, two SBAS DEMs were created: the first using the Stripmap data, with the SRTM 1 arc-second DEM as a reference; the second using the Spotlight data, with the Stripmap SBAS DEM as a reference.

The first step in the SBAS process is to determine which image pairs to utilise to create interferograms. This can be displayed graphically as a two dimensional plot showing the temporal and spatial baselines of the interferometric pairs. Figure 4.22 shows the connection graph of the Stripmap acquisitions and Figure 4.23 the connection graph of the Spotlight acquisitions. For both the Stripmap and Spotlight SBAS processing, image pairs were connected only if their perpendicular baselines were from 0 to 35 percent of the critical baseline, and if their temporal baselines were from 0 to 17 days. Disconnected blocks were permitted given that calculation of displacement velocities was not required. For the Stripmap stack, 63 out of the 74 images were connected yielding a total of 54 interferometric pairs with 31 master images. The super master was automatically selected as the image acquired on 21 July 2010. More detail regarding the baselines and other characteristics of each connection is provided in Appendix B.1. For the Spotlight stack, the 3 VV images were removed leaving only the 24 remaining HH images. Out of these,

4. Archaeological Prospection Using SAR in Agricultural Crop and Grassland Around Rome

17 were connected yielding a total of 15 interferometric pairs with 10 master images. The super master was automatically selected as the image acquired on 16 December 2010. More detail regarding the baselines and other characteristics of each connection is provided in Appendix B.2.

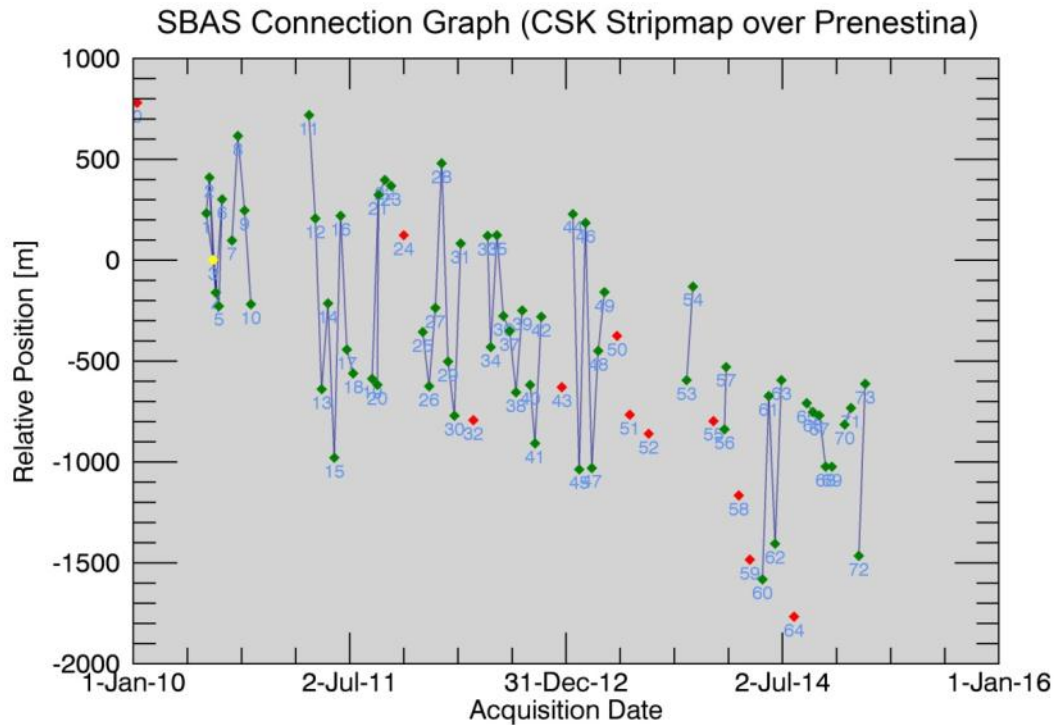


Figure 4.22 SBAS connection graph for the CSK Stripmap data. Selected and discarded images are displayed respectively as green and red points. The yellow point shows the super master image. More detail regarding the baselines and other characteristics of each connection is provided in Appendix B.1.

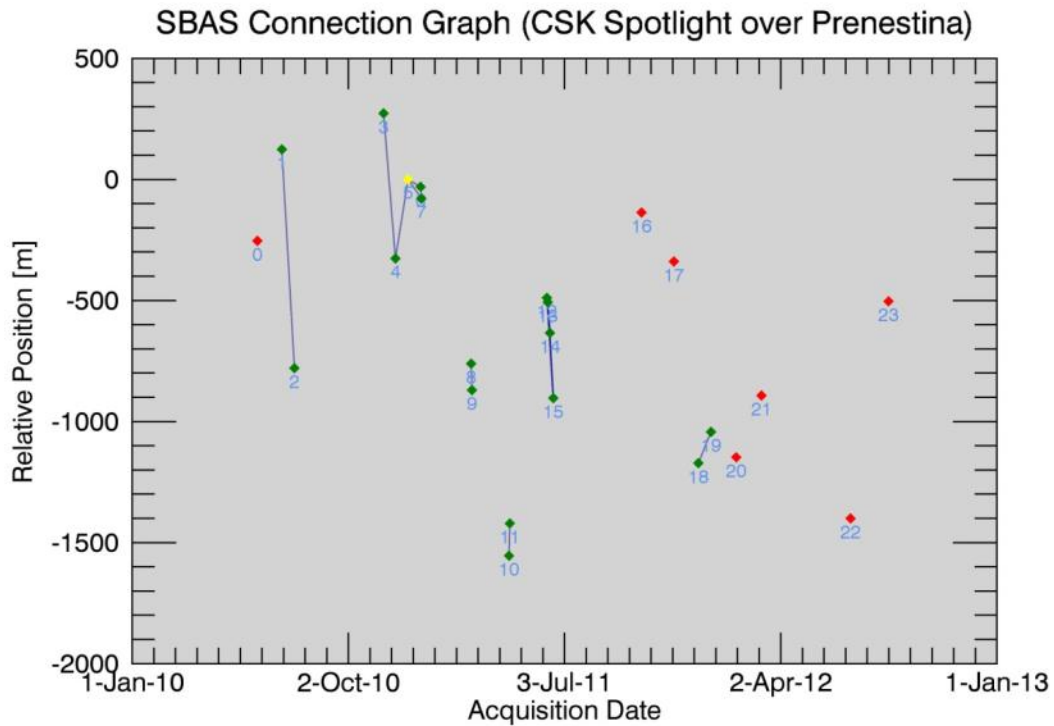


Figure 4.23 SBAS connection graph for the CSK Spotlight data. Selected and discarded images are displayed respectively as green and red points. The yellow point shows the super master image. More detail regarding the baselines and other characteristics of each connection is provided in Appendix B.2.

Interferometric processing was then carried out for each connected image pair. This included DEM assisted coregistration, interferogram generation, interferogram filtering (Goldstein), coherence calculation and phase unwrapping (Minimum Cost Flow). A reference DEM was required for the DEM assisted coregistration and for topographic fringe removal to assist with the phase unwrapping. For the Stripmap data the SRTM (1 arc-second) DEM was used, while for the Spotlight data the Stripmap SBAS DEM was used.

The unwrapped interferograms were inspected. Connections yielding very noisy results were removed. In some cases the unwrapping was repeated with the unwrapping coherence threshold readjusted.

On the selected remaining unwrapped phase images, Ground Control Points (GCPs) were placed over stable areas (mainly roads) and the unwrapped phases re-flattened to remove phase ramps due to orbit inaccuracies.

A first inversion was applied to the re-flattened, unwrapped interferograms to obtain the residual topography. Following this, a second unwrapping was performed as a further refinement. These final unwrapped interferograms were then used as input to a second inversion. The final DEM in slant range was produced following the second inversion.

The slant range DEM was geocoded to UTM zone 33 N, WGS 84. Some gaps in the DEM where the coherence was below the threshold for the phase unwrapping were interpolated.

4.3.3.2 InSAR DEM: Salaria AOI

During the SBAS process for the Salaria AOI, for all the interferometric pairs but one, either the coherence was very low, or the baselines were too large or small to permit DEM generation. However, during the inspection of the flattened interferograms, the trace of the ancient Via Salaria was very clearly visible in one flattened interferogram produced from the image pair acquired on the 10th and 26th of August 2012. Even this interferogram had low coherence throughout most of the image, but less so than most of the other interferograms. The perpendicular baseline was 307m and the altitude of ambiguity 21.6m. It was decided therefore to produce a DEM over the Salaria AOI with only this image pair as a standard InSAR procedure, rather than using SBAS with the entire time series.

Due to the low coherence, the final DEM was very noisy, and no accurate absolute or relative heights could be derived from it. However, as a purely qualitative result, it was nonetheless possible to trace the line of the ancient Via Salaria in the DEM. This is discussed further in the results, section 4.4.

4.3.4 Polarimetric Analysis

The polarimetric processing that was carried-out with the R2 data is described here. This was undertaken over the Prenestina AOI only, given that it was the only AOI in the coverage of both the ascending and descending R2 datasets.

Subsets of the Prenestina AOI were extracted from the SLC R2 imagery. These were coregistered with the other imagery from the same track and frame. In the end, coregistered stacks were obtained for each of the ascending and descending Radarsat-2 time series.

The four polarimetric channels of each coregistered image corresponds to the measured Scattering Matrix (see equation 2.31). From these, the Covariance Matrix (see equation 2.33) was calculated. This enabled the extraction of coherent decompositions (based on the Scattering Matrix), and model-based, incoherent decompositions (based on the Covariance Matrix), which are more suitable for distributed scatterers. The extracted coherent decompositions included: Pauli (surface, double bounce and volume scattering) (Cloude and Pottier 1996), and Krogager (sphere, diplane and helix scattering) (Krogager 1990). The extracted incoherent decompositions included: Freeman (surface, double bounce and volume scattering) (Freeman and Durden 1998) and Yamaguchi 4 components (surface, helix, double bounce and volume scattering) (Yamaguchi et al. 2005).

As the single scenes were far too speckled to be able to distinguish any features that may be of archaeological interest, multitemporal De Grandi speckle filtering was applied to the images in each coregistered stack after the polarimetric processing described above had been performed. This reduced greatly the image speckle. The average of each polarimetric image was also calculated for each ascending and descending stack.

An analysis was carried out to determine whether any anomaly features, present in all the time series, appear in any of the polarimetric products that may correspond to archaeological structures.

Further polarimetric analysis was then carried out on the ascending pass imagery. This involved identifying the typical polarimetric signature of possible anomaly features. From this polarimetric signature, the polarimetric orientation angle and ellipticity angle that yield the greatest backscatter were identified. The polarimetric basis was then changed for each image in the time series to this ellipticity and orientation angle and the images reprocessed with this polarimetric basis. The reprocessed imagery would thus show the anomaly feature enhanced, and potentially revealed other features of interest with the same scattering characteristics.

This processing was initially applied using Open Source (OS) software for SAR processing developed under ESA contract. This included the Next ESA SAR Toolbox (NEST) (for SAR processing) and PolSARPro (for polarimetric processing). At the time the processing was carried out, no multitemporal speckle filter was implemented in either software, so the only method of speckle filtering while preserving spatial resolution was to average the imagery. However, multitemporal De Grandi speckle filtering was subsequently carried out with the SARscape software. Figure 4.24 shows the processing chain applied to the data using NEST and PolSARPro.

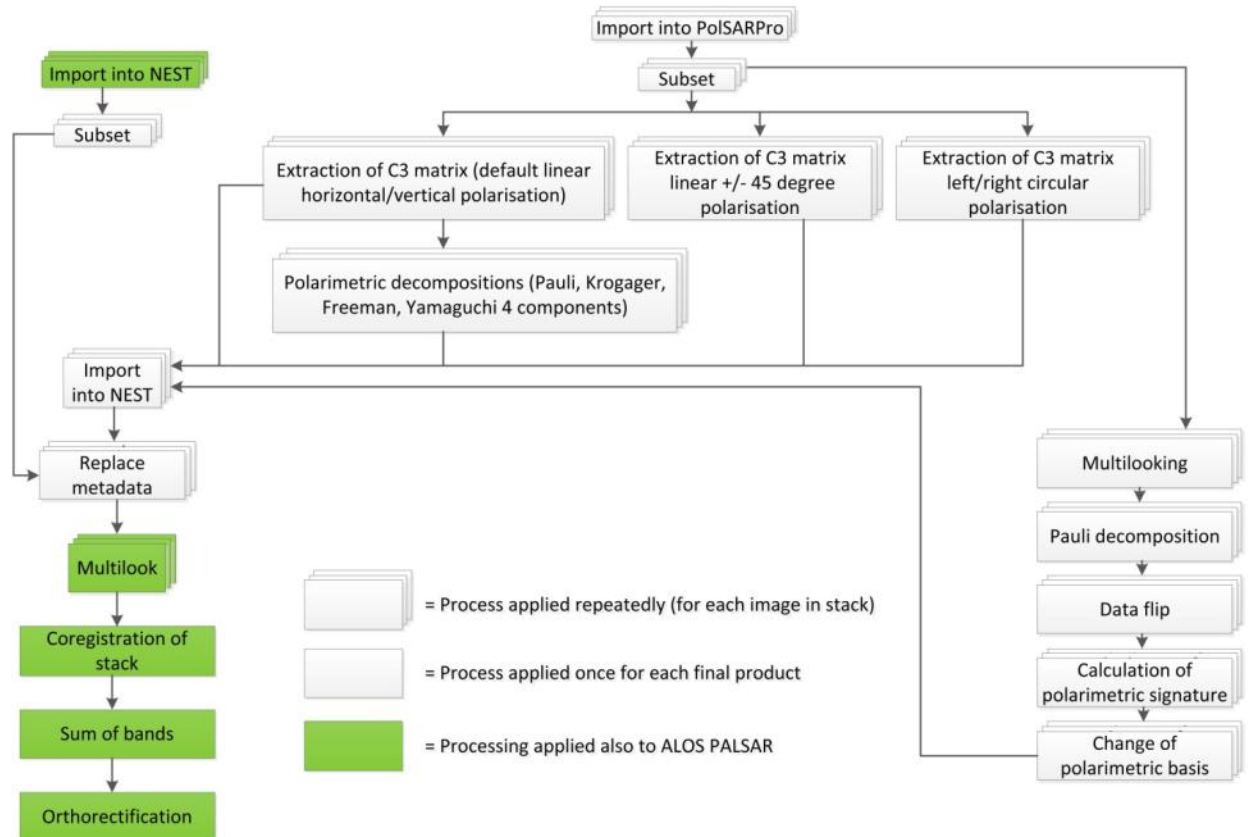


Figure 4.24 Processing chain applied to the R2 and PALSAR-1 data using NEST and PolSARPro. Subsequently the step “Sum of bands” was replaced by multitemporal De Grandi speckle filtering carried out with the SARscape software.

4.3.5 Analysis of Features

Having identified surface residues in the SAR data over locations in which buried archaeological structures are known, or suspected, to exist, the next step involved an in-depth analysis of these to attempt to understand why, and under what conditions, these residues are visible (or not visible) in the various SAR derived products of filtered σ^0 backscatter, coherence and DEM. To achieve this, first the clarity (contrast) of identified features was quantified. This enabled the quality of archaeological residues to be compared in SAR products over time, and to be correlated with possible contributing factors relating to meteorological, vegetation and soil conditions.

4.3.5.1 GIS

All SAR products were imported into a Geographic Information System (GIS) (using the software QGIS version 2.8.1) and compared with archaeological charts, optical images and DEMs.

Both the interpretation of the magnetometry survey published by (Keay et al. 2005) over the Portus AOI, and the map showing documented archaeological features by (Quilici 1974) in the Prenestina AOI, were manually geometrically corrected by the author by collecting GCPs using the geocoded Pleiades imagery as a reference, and resampling the images using a first order polynomial. These could subsequently be superimposed on the SAR images in the GIS for comparison.

4.3.5.2 Mean Ratio Detector

To quantify the clarity of the identified archaeological residues, the standard Mean Ratio Detector (MRD) method was applied, as described in (Inglada and Mercier 2007). The MRD calculates the ratio of the local means of two areas as a measure of their difference in backscatter intensity according to the following expression:

$$r_{\text{MRD}} = 1 - \min\left\{\frac{\mu_X}{\mu_Y}, \frac{\mu_Y}{\mu_X}\right\} \quad 4.2$$

where μ_X and μ_Y are the mean values of two subset regions (Inglada and Mercier 2007). The subset regions in this case comprise a region over the archaeological residue and a region outside but nearby (in some cases an average of two regions on either side of the archaeological residue). In the case of the σ^0 backscatter images, the subset regions were extracted from the non-filtered images in linear scale.

4.3.5.3 Potential Soil Moisture Deficit (PSMD)

As described in section 3.4.1.1, a key contributing factor in the formation of many archaeological crop marks is moisture, in particular a moisture deficit which may exacerbate differential crop growth (Jones and Evans 1975, Wilson 2000, Lasaponara and Masini 2007, Rączkowski 2011). Given the sensitivity of SAR to soil moisture (as variations of relative permittivity) (Ulaby et al. 1982) and roughness that may be affected by differential vegetation growth, it is hypothesised that there may be a correlation between archaeological residues in the SAR data and soil moisture. To test this hypothesis, the “Potential Soil Moisture Deficit” (PSMD), as described by Jones and Evans, 1975 (Jones and Evans 1975), was calculated over each AOI and for each day from a month prior to the first CSK image acquisition to the date of the last CSK acquisition. The PSMD is a measure of the water available to plants. It is calculated as a difference between potential evapotranspiration and rainfall and is an approximation of actual Soil Moisture Deficit (SMD), which requires knowledge of soil and plant parameters. PSMD, on the other hand, is purely a meteorological concept (Jones and Evans 1975). Here it is calculated as the difference between local potential evapotranspiration using the Penman-Monteith formula (Monteith and Unsworth 2007), and local rainfall for each AOI individually.

Soil moisture datasets are available, such as those derived from the Advanced Scaterometer (ASCAT) of the Metop satellite (Bartalis et al. 2007), and from Soil Moisture and Ocean Salinity (SMOS) satellite mission (Kerr et al. 2001), but the spatial resolution of the data (25km for ASCAT and 50km for SMOS) was deemed too coarse for such high resolution analysis. It may have been possible to derive soil moisture directly from the CSK SAR data, but accurate SAR derived soil moisture retrieval is particularly challenging given the difficulty in separating backscatter variations due to dielectric differences from those due to roughness, with the latter usually exerting a greater influence (Pathe et al. 2009). It was decided therefore to derive information on soil moisture from calculations of PSMD using data from the extensive local network of weather stations maintained by the Italian Hydrographic Office of the Lazio region (Ufficio Idrografico e Mareografico) and the Italian Agricultural Innovation and Development Agency for the Lazio region, ARSIAL (Agenzia Regionale per lo Sviluppo e l'Innovazione dell'Agricoltura del Lazio).

Calculation of PSMD requires measurements of potential evapotranspiration and rainfall. The potential evapotranspiration data, in mm per day, was obtained on request from ARSIAL. Data was obtained from several stations, including: Fiumicino, Maccarese (UTM 33N (X): 271.379, (Y): 4.633.596); Roma, Via Lanciani 38 (UTM 33N (X): 294.721, (Y): 4.644.111); and Roma, Ponte di Nona (UTM 33N (X): 305.016, (Y): 4.641.204). For each AOI, data from the station nearest the AOI was selected, and where there were gaps, these were filled by data from the next nearest station.

The rainfall data was obtained from the Italian Hydrographic Office of the Lazio region. Daily rainfall data is available from a dense network of stations through their website (Regione Lazio 2016). The data, in mm per day, was procured from the following weather stations: Isola Sacra, Ostia, Maccarese, Tor Vergata, Salone, Capannacce, Castelgiubileo, Fidene, Roma Nord and Monterotondo. The locations of these are shown on the Lazio Hydrographic Office website (Regione Lazio 2016). As with the evapotranspiration data, for each AOI, the rainfall data from the weather station nearest to the AOI was obtained, and where there were gaps, these were filled by data from the next nearest station.

To calculate the PSMD, first the daily potential evapotranspiration was subtracted from daily rainfall, then the sum of this difference for the last 30 days was calculated. This was done for each day in the time period of CSK image acquisitions. Negative values correspond to PSMD while positive values correspond to a Potential Soil Moisture Surplus (PSMS).

Finally, the PSMD was correlated with the clarity of archaeological residues in the various SAR products, and over time (see Section 4.4).

4.3.5.4 Coherence

Another key factor in the formation of archaeological residues in the SAR data products includes the state of vegetation. It may be that the archaeological residues in the SAR data are soil marks in fallow fields, or crop marks. Lacking precise information on the type of vegetation in each field of each AOI, an attempt was made to extract some information on the state of vegetation from the interferometric coherence. The temporal baseline between most of the consecutive CSK Stripmap acquisitions was 16 days, while for the Spotlight data, the most common temporal baselines were 16 days and 1 day.

Studies have shown inverse relationships between vegetation height and temporal decorrelation at various SAR frequencies, including at X-band and with COSMO SkyMed (Zalite et al. , Zalite et al. 2014). However, with X-band, complete temporal decorrelation is soon reached with vegetation growth and short temporal baselines are necessary to derive quantitative information on crop height (Zalite et al. , Zalite et al. 2014). Moreover, the rate of temporal decorrelation depends on many factors, such as crop type, moisture and wind (Engdahl et al. 2001). Another factor to take into account is the perpendicular baseline (Ferretti et al. 2007), which in the case of COSMO SkyMed, can vary considerably between image acquisitions. Given the complexity in establishing a quantitative relationship between coherence and crop height that takes into account these variables, and given primarily the long temporal baselines (16 days for the Stripmap data), the coherence calculated here provided only a rough qualitative idea of the ground conditions. For example, if very high coherence is observed in a particular field, this may be interpreted in different ways through analysis of the time series: it may coincide with a period in which

the field is fallow, or if the high coherence is observed over a longer time period, the field may be occupied by a crop or structure characterized by little random movement (such as beanstalks tied to poles). To obtain consistent datasets, for the Stripmap data only the coherence between InSAR pairs with 16 day baselines were considered, while for the Spotlight data, both 1 and 16 day baseline pairs were considered as separate datasets.

4.4 Results

Comparison of the SAR data with the archaeological charts over all AOIs revealed archaeological residues in Portus, Prenestina and Salaria. No archaeological residues were identified in Appia or Veii. Over Ostia only very faint traces were observed which were difficult to quantify. An in-depth analysis of the residues identified in Portus, Prenestina and Salaria is provided in this section. In Prenestina, the same residues were observed in both the CSK Spotlight and Stripmap data. Given that the clarity of these in all the SAR product types of filtered σ^0 backscatter, coherence and DEM was enhanced in the Spotlight data, the analyses for Prenestina is limited to the Spotlight data.

4.4.1 Portus

The most extensive recent archaeological survey of this area has been undertaken by the Portus Project, in particular using magnetometry geophysical prospection (Keay et al. 2005). Many archaeological structures are situated near the hexagonal harbour of Trajan (see Figure 4.4). In the open fields between the lake and the Tiber, the most significant buried structures identified to date include a canal to the north, referred to as the Northern Canal, and a canal to the south, along which ran a gravel road, aqueduct and various buildings. Near to the Tiber, the aqueduct changed direction and ran parallel to the Tiber. The region between the aqueduct and the Tiber appears to have been densely developed (Keay et al. 2005).

Many of the larger buried archaeological structures mapped by the survey are also visible as residues in the filtered σ^0 backscatter images. These include the Northern Canal and the built-up area in between the road and canal to the south, and in between the aqueduct and the Tiber river. No residues are present on the coherence images. The Northern Canal and built-up area to the south are treated as two subset areas, as shown in Figure 4.25. It is difficult to derive any information on buried structures from the SAR data near the hexagonal harbour of Trajan due to the high density of trees and buildings in this area.

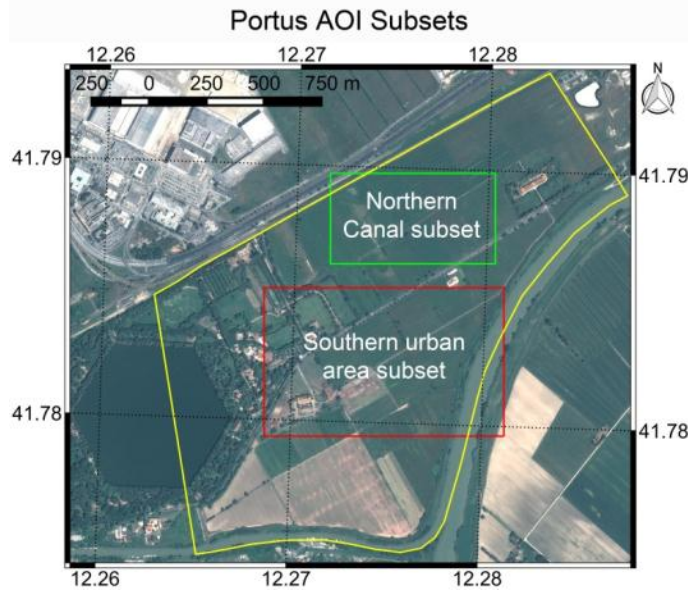


Figure 4.25 True colour Pleiades image acquired on 8 May 2014 over the Portus AOI (shown in yellow polygon). The Northern Canal subset is shown by the green rectangle and the subset over the southern urban area is shown by the red rectangle. The image has been pan sharpened to 0.5m. Pleiades data provided by the European Space Agency.

4.4.1.1 Portus Northern Canal

The Northern Canal is recorded in an inscription as having been constructed under the Emperor Claudius for flood relief. It was cut into the natural alluvium and had earth embankments. It connected the Tiber river to the sea. The width of the canal, as measured in the survey of Keay et al 2005, seems to vary between 20 and 35m (Keay et al. 2005).

Figure 4.26a shows a residue of the Northern Canal on an image of filtered σ^0 backscatter acquired on 16 November 2011. This is one of the clearest images of this residue on the σ^0 images. Figure 4.26b shows the same image with the interpretation of the magnetometer survey in (Keay et al. 2005) superimposed. Figure 4.27 is an optical Pleiades satellite image, covering the same extent as in Figure 4.26. It has been pan sharpened to 0.5 m spatial resolution, and displayed as a NIR, R and G colour composite. The yellow arrow points to the location and direction from which the photograph in Figure 4.28 was acquired. All residues of this feature appear in higher backscatter than surrounding areas. No traces of the feature are evident on the ground, as observed on 24 May 2013 (see photo acquired on that date in Figure 4.28). Traces are sometimes visible on optical air photos and satellite imagery. These are enhanced in the NIR (as in Figure 4.27).

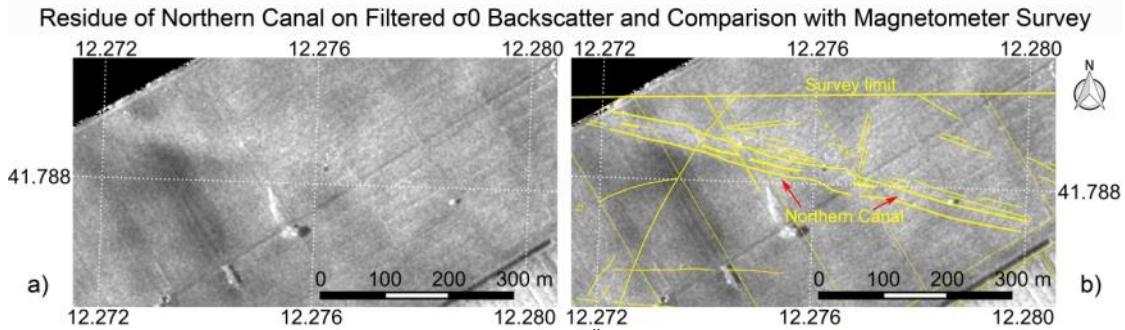


Figure 4.26 a) Residue of Northern Canal on image of filtered σ^0 backscatter acquired on 16 November 2011. b) Overlay with features interpreted by magnetometry survey published by Keay et al, 2005 (Keay et al. 2005). COSMO SkyMed data provided by the Italian Space Agency.

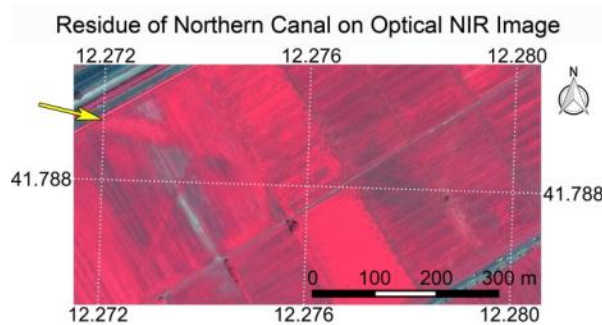


Figure 4.27 Residue of Northern Canal on Pleiades image acquired on 8 May 2014, pan-sharpened to 0.5m spatial resolution. NIR, R and G displayed as R, G and B respectively. Yellow arrow shows direction and location from which photo in Figure 4.28 was acquired. Pleiades data provided by the European Space Agency.



Figure 4.28 Photo acquired over site of Northern Canal on 24 May 2013 at 18:45. No traces are evident of the Northern Canal. The shadow of the photographer in the center shows the direction of the sun. The location and direction from which the photo was acquired is shown in Figure 4.27.

4.4.1.2 Portus Southern Urban Area

This area is also crossed by a canal, which was constructed under Trajan. It was approximately 35m wide and the magnetic survey of Keay et al, 2005 reveals that it was probably flanked by wide walls, about 3 or 4m wide, that may have acted as towpaths. The canal connected the Fossa Traiana with the Tiber (see Figure 4.4) and was probably used for navigation. To the north of the canal was a road, about 15m wide. However, the magnetic survey only noted the kerbs of this road. It is likely therefore that it had only a gravel surface rather than stone paving. To the north of the road passed an aqueduct, which was carried on piers. The geophysical survey revealed two phases of development of the aqueduct: the first phase predated the canal and road, while the second took place in the Trajanic period, probably at the same time as the canal and road were built. In between the canal and the road a series of buildings have been detected by the geophysical survey. Also, as the aqueduct changes direction and travels alongside the Tiber, the area in between the Tiber and the aqueduct seems to have been densely developed. Surface ceramics from these areas suggest construction began primarily from the second century onwards. Development was thought to have been stimulated by the presence of the canal and road (Keay et al. 2005).

4. Archaeological Prospection Using SAR in Agricultural Crop and Grassland Around Rome

Figure 4.29a is a subset of a filtered σ^0 backscatter image acquired on 9 July 2012. This is one of the images that best reveals residues of the buried urban structures in this area. These buried urban structures are between the canal (to the south) and the gravel road and aqueduct (to the north), and between the aqueduct, further to the north, and the Tiber river. Other structures, such as the canal, road and aqueduct, do not appear as residues in any of the SAR images. In all images in which traces of these urban structures are visible, they are visible as areas of lower backscatter relative to surrounding areas. Figure 4.29b shows the interpretation of the archaeological survey of Keay et al (Keay et al. 2005) overlain. The vast majority of the features identified in this survey were from magnetometry prospection, but a few structures were identified in crop marks on air photos, such as the isolated building to the west of the aqueduct as it travels parallel to the Tiber. Figure 4.30 is another subset of the same Pleiades image as in Figure 4.27, also pan-sharpened and displayed in the same band combination. Some of these structures are also faintly visible in this Pleiades image.

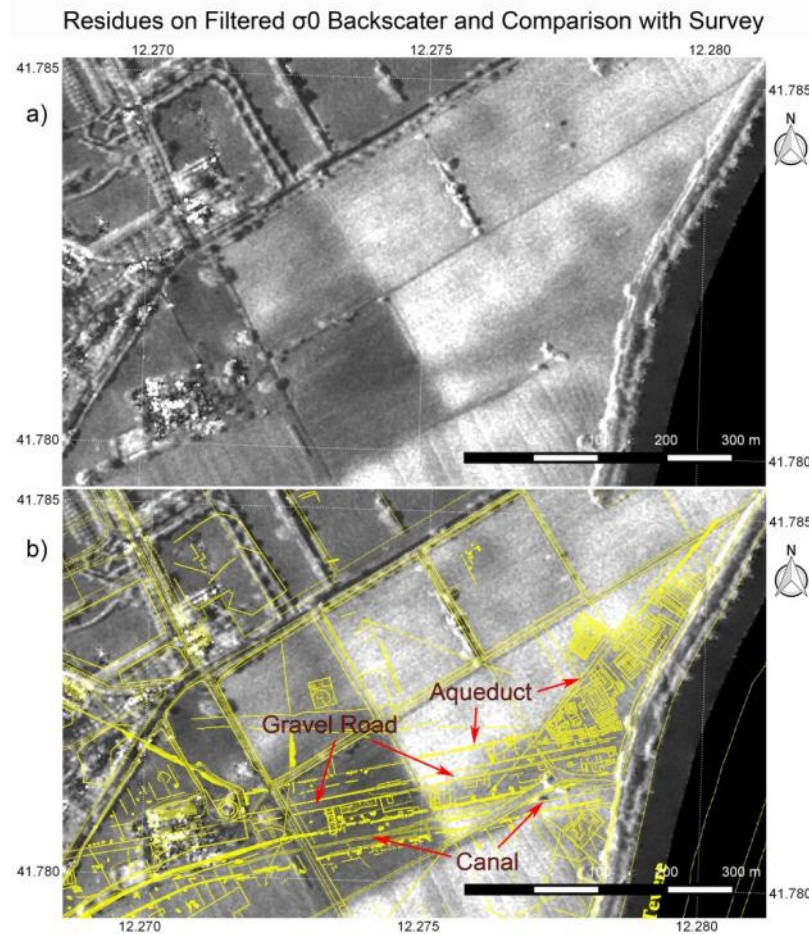


Figure 4.29 a) Residue of buried buildings on image of filtered σ_0 backscatter acquired on 9 July 2012. b) Interpretation by Keay et al, 2005 of integrated archaeological survey (mainly magnetometry) published in (Keay et al. 2005) overlain. The residues in the SAR image correspond to the built-up areas, not to the canal or the gravel road. COSMO SkyMed data provided by the Italian Space Agency.

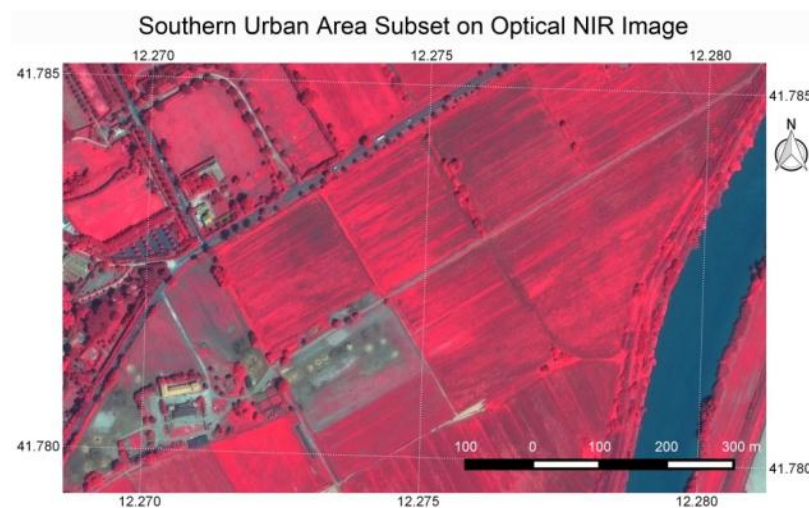


Figure 4.30 Southern urban area subset of Portus AOI (same extent as Figure 4.30) on Pleiades image acquired on 8 May 2014, pan-sharpened to 0.5m spatial resolution. NIR, R and G displayed as R, G and B respectively. Pleiades data provided by the European Space Agency.

4.4.1.3 Portus features analysis

Figure 4.31 shows the location of subset areas extracted over and outside of each of the residue areas in the Portus AOI for the MRD contrast analysis. Figure 4.32 shows the contrast of the residues in the σ^0 backscatter over time, and plotted with PSMD. No clear correlation in the clarity of the two features over time is present. Perhaps this is not surprising, given that the two residues are of a completely different nature (possibly manifestations of positive and negative crop marks respectively). The contrast of neither residue appears to correlate with PSMD. However, this may not play a role if the residues are situated in irrigated fields (Modigliani 2008b).

Figure 4.33 shows the contrast of residues in the σ^0 backscatter with residue coherence over time, while Figure 4.34 compares them in a scatter plot. Over the Northern Canal residue, in most cases, high contrast in the σ^0 backscatter is observed with high coherence. The image pair acquired between 22 April and 8 May 2011, for example, has a coherence of 0.68 over a temporal baseline of 16 days. In both images the Northern Canal residue appears clearly (see Figure 4.35). The coherence prior to this date is unknown, as there is a gap in the interferometric time series of six months. However, in the following interferometric pair (from 8 May to 24 May 2011), the coherence drops to 0.31 (approximately the same coherence value as in the surrounding fields), and the canal contrast also drops in the σ^0 backscatter. As mentioned in section 4.3.5.4, very high coherence may be observed over a fallow field, or over a field of crops characterized by very little movement, such as dried stems or crops tied to poles. In both cases, it is possible that the cause of the residue is in the soil. It may be therefore that the residues of the Northern Canal in the images acquired on 22 April and 8 May 2011 are soil marks. Between the image pair acquired on 13 and 29 October 2012 there is also a high coherence of 0.52 over the Northern Canal residue. Also in this case the residue is clearly present in the σ^0 backscatter of both images. Before and after this image pair, the contrast of the residue rapidly declines, as does the coherence. Where there is low coherence and high residue clarity, the residue may still be a soil mark, only there may have been some change to the field, such as rainfall, strong winds or human activity sufficient to reduce the coherence.

Over the southern feature, the residues appear with greatest clarity at times of low coherence. The fact that the residues appear as areas of lower than surrounding backscatter (in contrast to the Northern Canal) may be a result of negative crop marks. This could be explained by the buried urban structures hindering vegetation growth, as described in section 3.4.1.3.

4. Archaeological Prospection Using SAR in Agricultural Crop and Grassland Around Rome

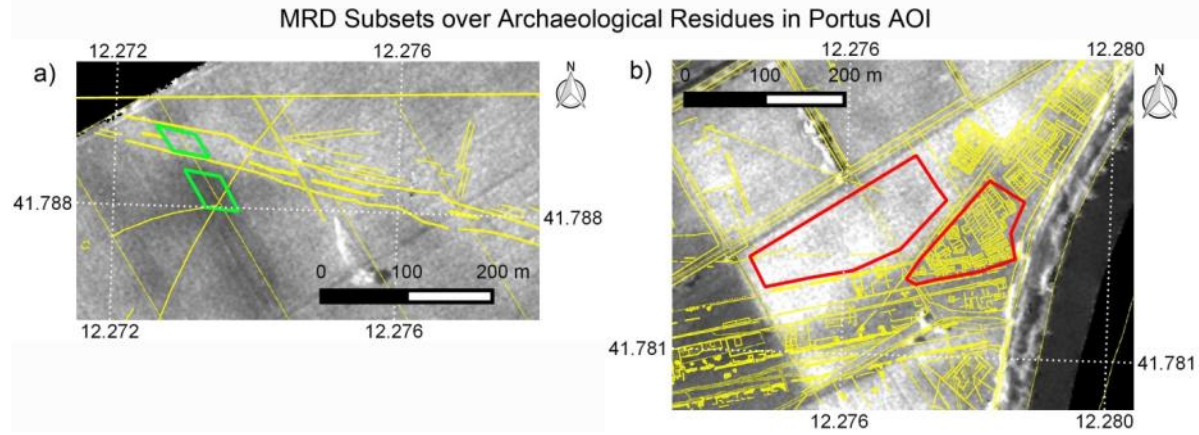


Figure 4.31 Subset areas used for MRD contrast analysis shown as: a) green polygons, over and outside of a part of the Northern Canal residue; and b) red polygons, over and outside of a part of the southern urban area residues. Polygons are overlain on the image of filtered σ^0 backscatter acquired on 16 November 2011. COSMO SkyMed data provided by the Italian Space Agency.

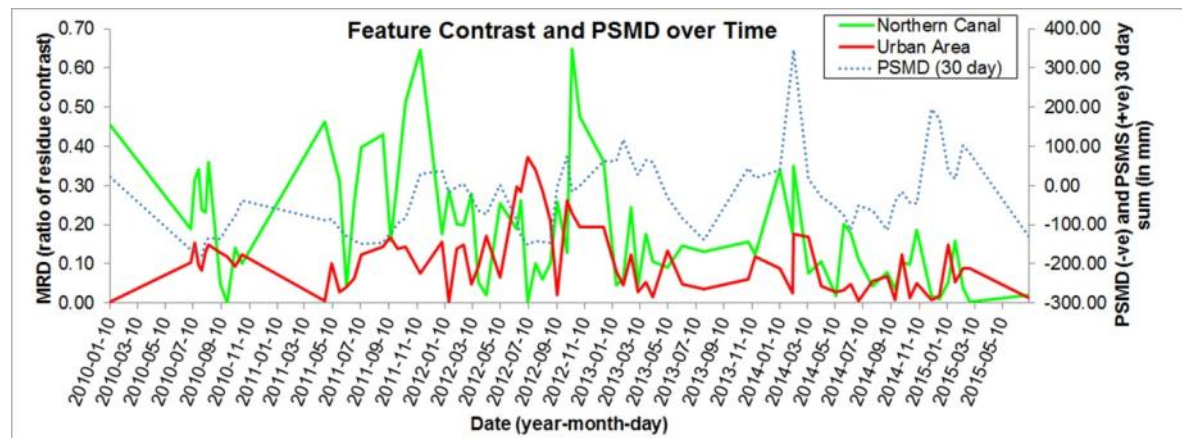


Figure 4.32 Graph showing clarity (contrast) of the two archaeological residues of the Northern Canal (in green) and the southern urban area (in red), plotted over time and with PSMD. The clarity of residues is quantified as a ratio (MRD). For the PSMD, negative values correspond to high PSMD (dry conditions), while positive values correspond to high PSMD (wet conditions).

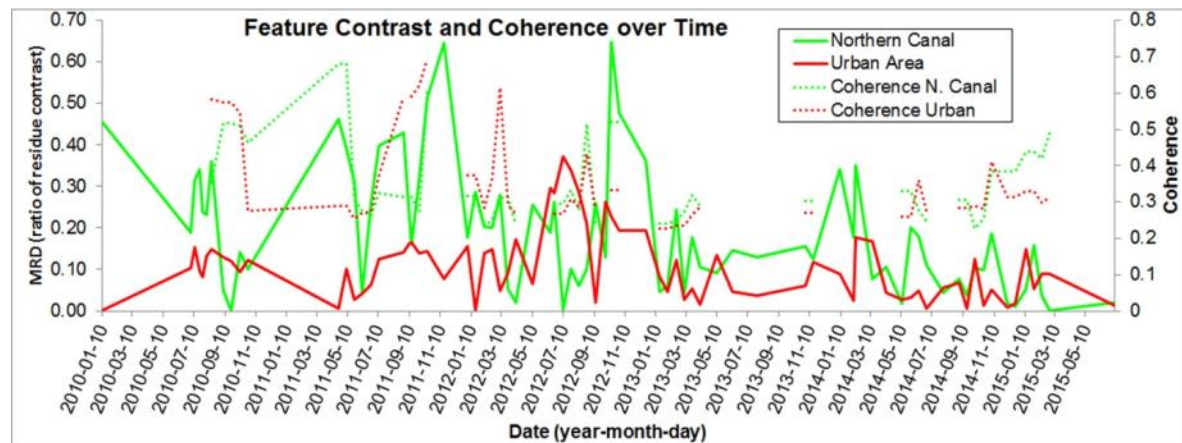


Figure 4.33 Graph showing contrast, quantified by means of MRD, of the two archaeological residues of the Northern Canal (in green) and the southern urban area (in red), plotted with their respective coherences (dotted lines) over time. The coherence values are provided both for the master and the slaves of InSAR pairs. Where a master is also a slave, it

takes the value of the slave.

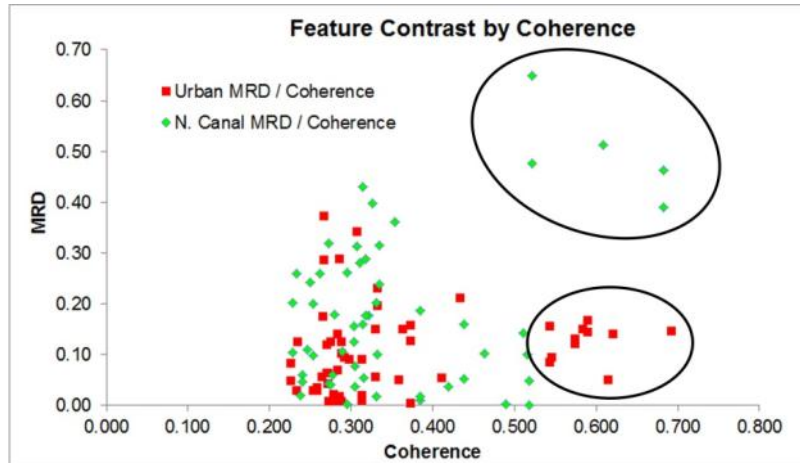


Figure 4.34 Graph showing contrast, quantified by means of MRD, of the two archaeological residues of the Northern Canal (in green) and the southern urban area (in red), plotted against their respective coherences. Where high coherence is observed, the contrast of the Northern Canal residue is often high, while the contrast of the southern urban area is consistently low. These patterns are shown in black ellipses.

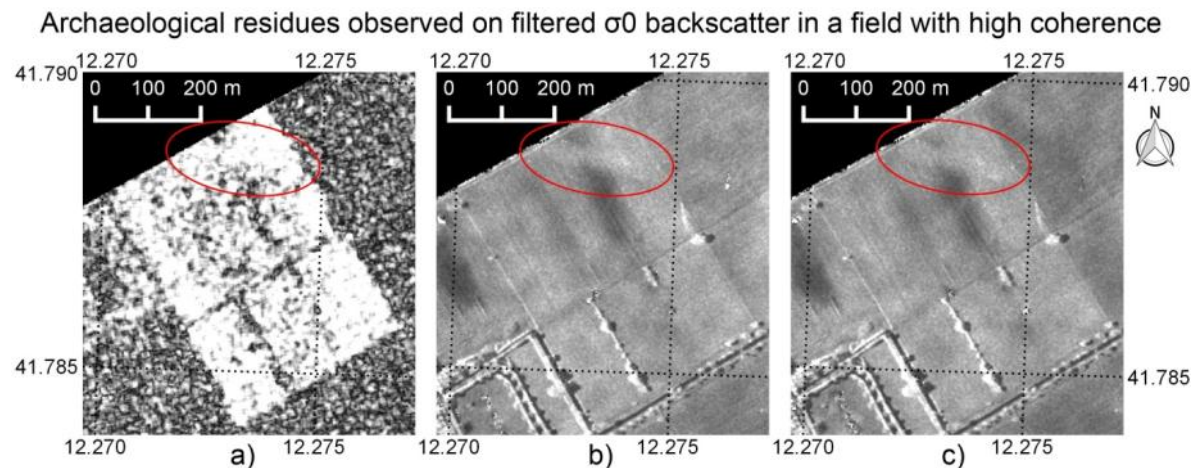


Figure 4.35 Example of a case in which very high coherence is observed over some fields in the CSK Stripmap pair with a temporal baseline of 16 days: from 22 April to 8 May 2011 (left). Residues of the buried Northern Canal are visible in the filtered σ^0 backscatter of both images of the pair, shown as red ellipse on filtered σ^0 image acquired on 22 April (centre) and 8 May (right). COSMO SkyMed data provided by the Italian Space Agency.

4.4.2 Prenestina CSK

Over the Prenestina AOI, archaeological residues were identified in all three SAR product types, and in both the Stripmap and Spotlight data. Results are reported here only of the Spotlight data processing given that the residues are generally clearer and more often present in all the product types of the Spotlight times series. This is probably due to the enhanced resolution, and the availability of 1-day as well as 16-day InSAR pairs.

Figure 4.36 shows one of the CSK Spotlight filtered σ^0 backscatter images, acquired on 25 July 2010. Figure 4.37 shows one of the Spotlight coherence images, derived from the InSAR couple acquired on 9 and 25 July 2010 (16 day temporal baseline). Figure 4.38 shows the DEM derived from the Stripmap data, and Figure 4.39 the DEM produced with the Spotlight imagery, both using the SBAS technique. Figure 4.40 shows the subset covering the AOI of the map showing all the archaeological structures documented by Quilici, 1974 (Quilici 1974). Figure 4.41 shows a Pleiades image over the AOI acquired on 20 April 2014 as a colour composite of NIR, R and G displayed respectively as R, G and B.

On each of Figure 4.36 to Figure 4.41 archaeological residues are highlighted in yellow. These are named according to their catalogue number in the archaeological chart of Quilici (Quilici 1974). Their clarity differs between the various SAR products. The residues are all of roads. Most other structures recorded in this area in Quilici (Quilici 1974) have been interpreted from scant surface fragments, and they may not have a coherent form.

4.4.2.1 Road 384

In the archaeological chart of Quilici, 1974 (Quilici 1974), a road has been recorded that traversed the AOI horizontally, to the south of, and parallel to, the modern Via Prenestina. The road (with catalogue number 384) was also identified in parts by scholars such as Rodolfo Lanciani and Thomas Ashby. Traces of it are visible in air photos as crop marks (Quilici 1974). A part has been excavated at Tor Bella Monaca Figure 4.42, revealing the basalt paving stones of two phases of development. This excavated part continues for no longer than around 245 m. Elsewhere in the AOI the only traces at the surface are topographic. In some cases as a very narrow trough Figure 4.43, and in others as a wider valley Figure 4.44. The road has been identified as the Via Gabina, which then became the Via Prenestina (De Franceschini 2005). However, for consistency, here it will be referred to by its catalogue number in Quilici as “Road 384”.

This feature is visible in all the SAR product types: in the filtered σ^0 backscatter images the centre is most visible (where there is a narrow trough), in the coherence images the parts of the road that continue along wider valleys appear clearest, while in the DEMs (especially the Spotlight DEM), most sections are visible. It is likely that the topography itself is the cause of the residues in all SAR products. The filtered σ^0 backscatter is sensitive to the narrow trough probably due to its geometry, the sides of which possibly act as corner reflectors. This would explain why this segment of the road is visible in all the images of filtered σ^0 backscatter, as the geometry is less ephemeral than a crop or soil mark. The coherence residue, which is always distinguished by lower coherence over the feature with respect to surrounding areas, is likely due to increased crop growth at the bottom of the wider valleys where water would collect. The best example of the coherence residue is in the 9 and 25 July 2010 pair (16 day temporal baseline).

4.4.2.2 Road 492

This road is recorded in Quilici (Quilici 1974) as having been identified by Pietro Rosa in the late 19th century (Rosa 1870) as surface remains in open fields which are now occupied by modern urban development. The road was also observed as crop or soil marks in air photos, and pieces of stone

4. Archaeological Prospection Using SAR in Agricultural Crop and Grassland Around Rome

paving, brought to the surface by ploughing, can be found occasionally throughout the course of the road (Quilici 1974). In this short stretch between the urban areas of Valle Fiorita and Tor Bella Monaca, it appears clearly on the DEMs and in the same coherence images in which the residue of Road 384 appears as it crosses the same field. It is much less evident in the images of filtered σ^0 backscatter.

4. Archaeological Propection Using SAR in Agricultural Crop and Grassland Around Rome

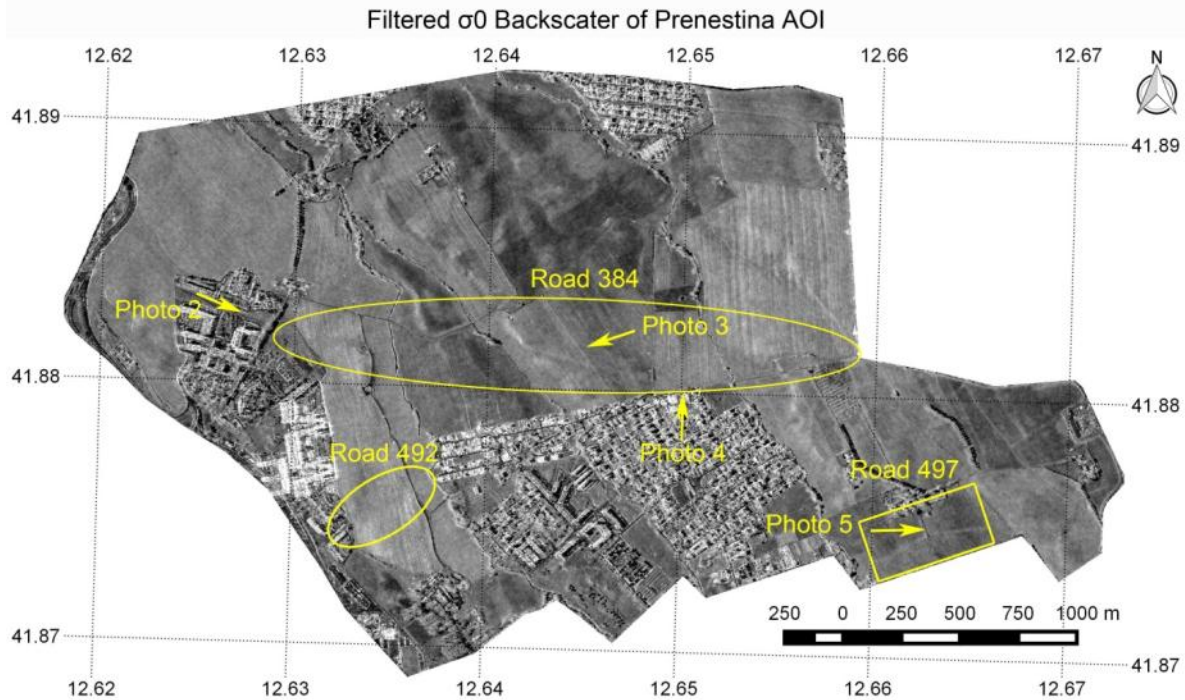


Figure 4.36 Image of filtered σ^0 backscatter over the Prenestina AOI acquired on 25 July 2010. Annotations in yellow show the locations of residues and the locations and directions from which photographs were acquired on the ground. COSMO SkyMed data provided by the Italian Space Agency.

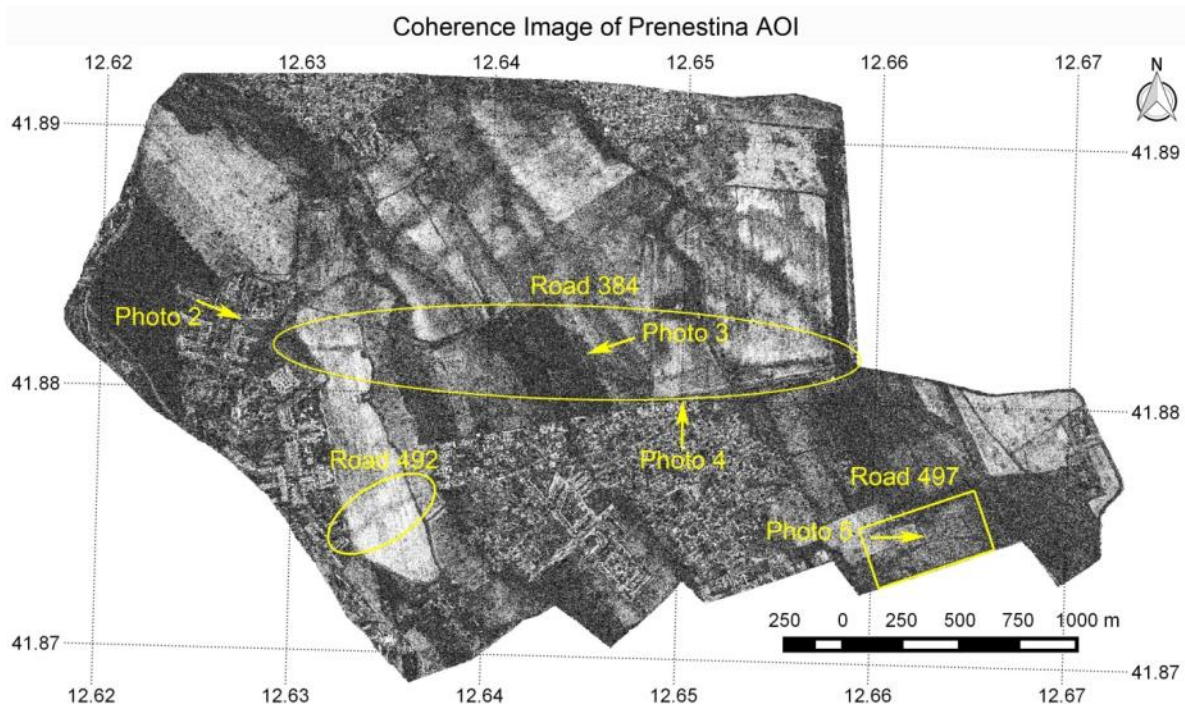


Figure 4.37 Coherence image from CSK Spotlight InSAR pair acquired on 9 and 25 July 2010 over the Prenestina AOI. Annotations in yellow show the locations of residues and the locations and directions from which photographs were acquired on the ground. COSMO SkyMed data provided by the Italian Space Agency.

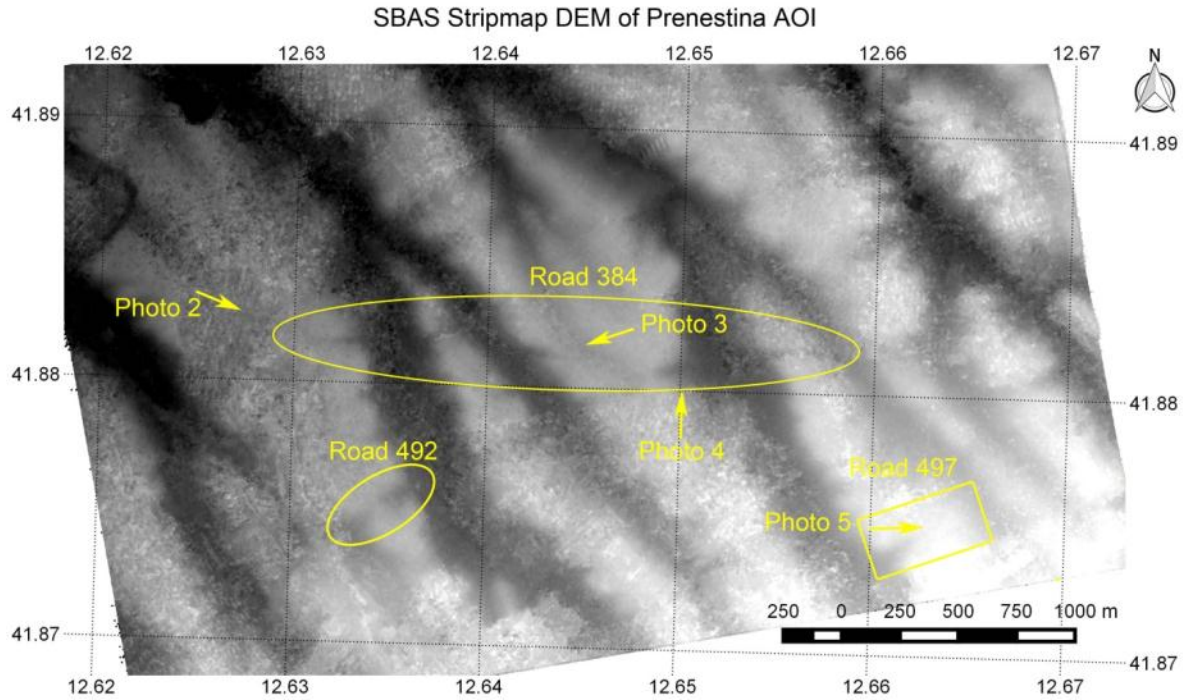


Figure 4.38 SBAS DEM produced from CSK Stripmap imagery over the Prenestina AOI. Annotations in yellow show the locations of residues and the locations and directions from which photographs were acquired on the ground. COSMO SkyMed data provided by the Italian Space Agency.

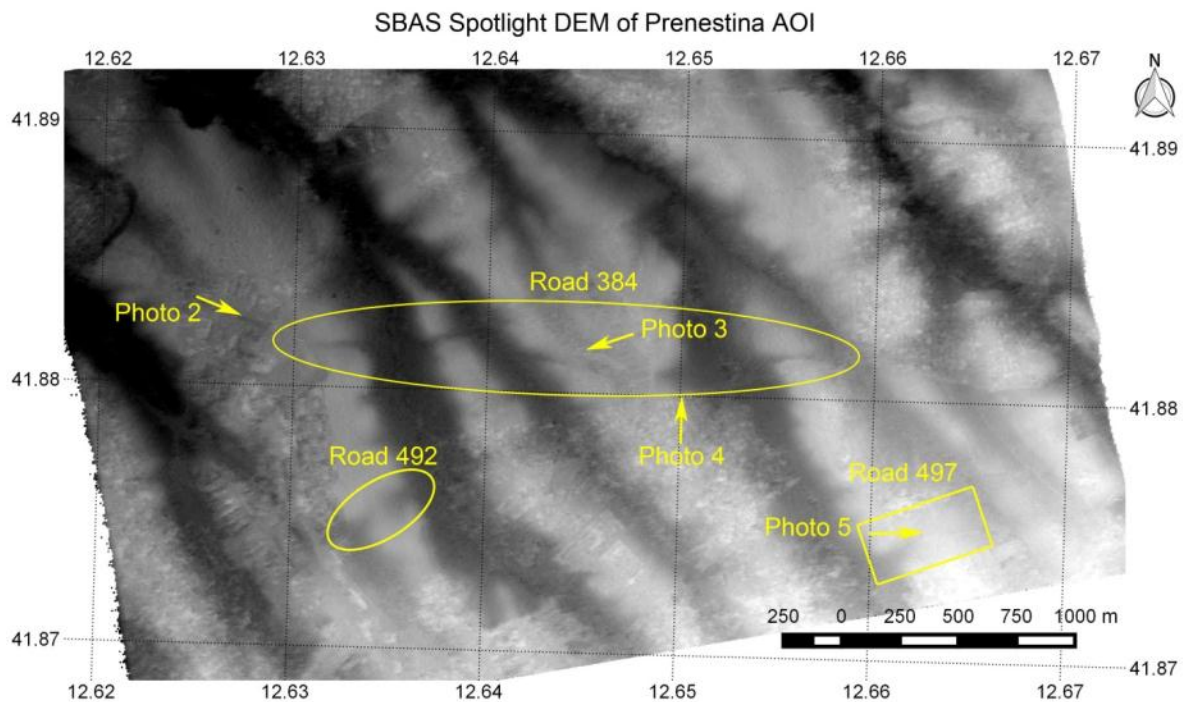


Figure 4.39 SBAS DEM produced from CSK Spotlight imagery over the Prenestina AOI. Annotations in yellow show the locations of residues and the locations and directions from which photographs were acquired on the ground. COSMO SkyMed data provided by the Italian Space Agency.

4. Archaeological Prospection Using SAR in Agricultural Crop and Grassland Around Rome

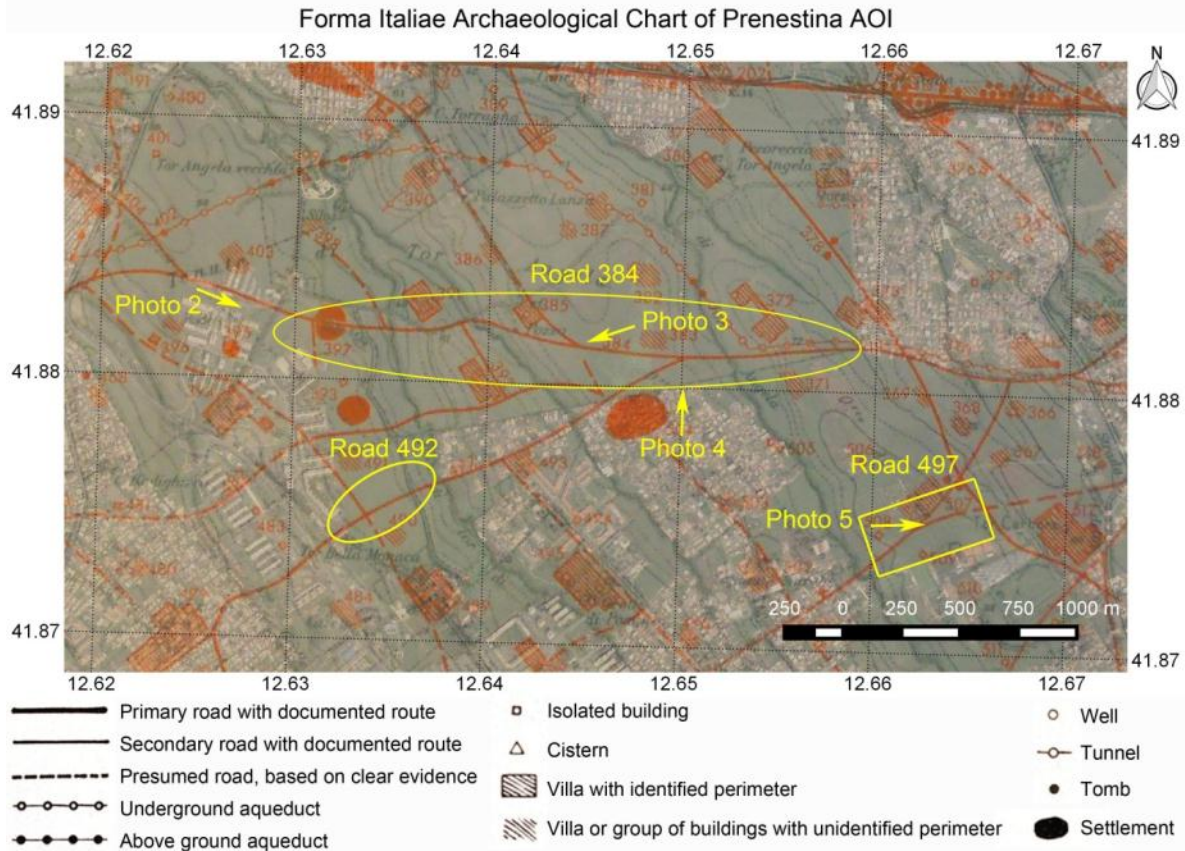


Figure 4.40 Subset of archaeological chart over the Prenestina AOI taken from Quilici, 1974 (Quilici 1974) and published as part of the Forma Italiae series. Annotations in red show documented archaeological structures, annotations in yellow show the locations of residues and the locations and directions from which photographs were acquired on the ground.

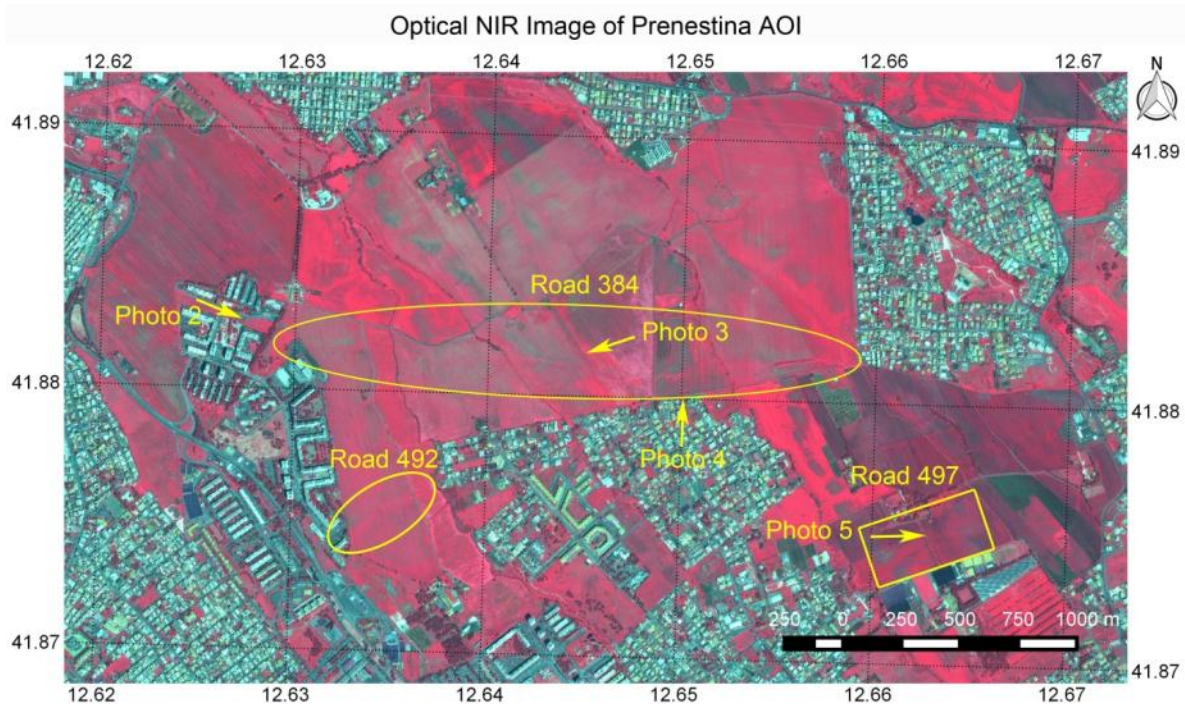


Figure 4.41 Pleiades image acquired on 20 April 2014 over the Prenestina AOI, pan-sharpened to 0.5m spatial resolution.

4. Archaeological Prospection Using SAR in Agricultural Crop and Grassland Around Rome

NIR, R and G displayed as R, G and B respectively. Pleiades data provided by the European Space Agency.



Figure 4.42 Photograph acquired of the part of Road 384 that was excavated during the construction of Tor Bella Monaca in the 1980's. Two phases of development can be seen from the two layers of paving and different widths. The photograph was acquired on 16 March 2013 at 18:27.



Figure 4.43 Photograph acquired of the location of a part of Road 384, evident as a narrow trough in the center of a broad valley. The photograph was acquired on 16 March 2013 at 17:01.



Figure 4.44 Photograph acquired of the location of a part of Road 384, situated in the center of the broad valley. The photograph was acquired on 6 October 2015 at 12:36.

4.4.2.3 Road 497

This road, which connected the settlement of Osteria dell'Osa with the Via Casilina, was still in use in the first decades of the 20th century. The segment of this road highlighted in Figure 4.36 to Figure 4.41 shows on the archaeological chart of Quilici (Figure 4.40) as a continuous line followed by a dashed line (after a fork in the road). The line becomes dashed as no physical traces remained of the segment at the time the archaeological chart was published. However, based on evidence elsewhere along its course, it was suspected to have continued along the route of the dashed line (Quilici 1974).

Parts of this road are visible in some of the images of filtered σ^0 backscatter (see Figure 4.45a), and coherence (see Figure 4.45b). Along the dashed line there is no longer any topographic trace in the Spotlight DEM (see Figure 4.45c). On 6 October 2015 a UAV was flown over this part of the feature and a very high resolution photogrammetric DEM was produced, with a spatial resolution of 12 x 12

centimeters (see Figure 4.45d). In this DEM a trace of the road is visible where it is suspected to continue. It is also visible in the UAV orthophoto that was used as input to the DEM (see Figure 4.45e). It is partly visible in a Pleiades image acquired on 20 April 2014, displayed as a colour composite of NIR, R and G displayed respectively as R, G and B in Figure 4.45f. A subset of this area in the archaeological chart of Quilici is shown in Figure 4.45g. No topographic or other traces are visible on the ground (see photo 5 in Figure 4.45h).

The archaeological chart of Quilici documents the presence of other roads, and a villa with unknown perimeter, in the same area as the segment of Road 497 discussed here (see Figure 4.45g). None of these have been identified in any of the imagery, SAR or optical. From extensive surface finds, the villa is thought to be at the centre of a vast archaeological area (Quilici 1974). Perhaps the remains of these features are scattered, due to damage or looting, to the extent that they no longer have a coherent shape that may be detectable on remotely sensed imagery.

Analysis of Road 497 Subset

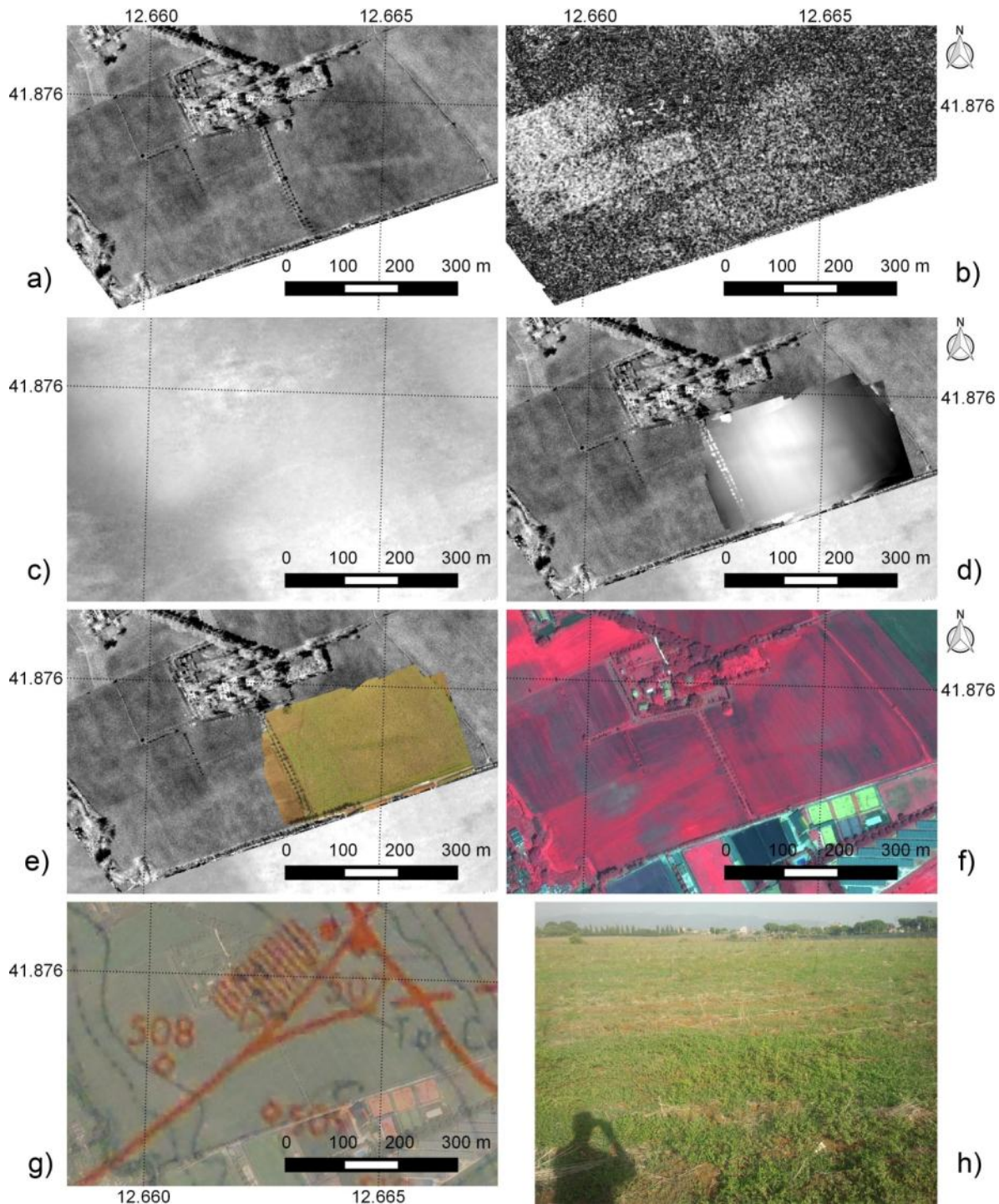


Figure 4.45 Subsets of Road 497, as shown in yellow rectangle in Figure 4.36 to Figure 4.41: a) CSK Spotlight image of filtered σ^0 backscatter, acquired on 25 July 2010. b) CSK Spotlight coherence image with 16 day temporal baseline from image pairs acquired on 9 and 25 July 2010. c) SBAS DEM produced from CSK Spotlight time series. d) DEM derived from UAV photogrammetric imagery acquired on 6 October 2015, overlain on imagery in part a). e) Orthophoto acquired by UAV on 6 October 2015, overlain on imagery in part a). f) Pleiades image acquired on 20 April 2014, pan-sharpened to 0.5m spatial resolution. NIR, R and G displayed as R, G and B respectively. g) Archaeological chart of Quilici, 1974 (Quilici 1974) overlain on true colour Pleiades image acquired on 20 April 2014. h) Photo 5. Acquired on 19 September 2015 at 17:03. The location and direction from which the photo was taken is shown in Figure 4.36 to Figure 4.41. COSMO

SkyMed data provided by the Italian Space Agency. Pleiades data provided by the European Space Agency.

4.4.2.4 Prenestina features analysis

The contrast of the archaeological residues in the various SAR images were quantified and compared over time. They were also correlated with PSMD and coherence, as described in section 3. Figure 4.46a shows the MRD subsets over a western part (green) and an eastern part (red) of Road 384 overlain on one of the clearest images on which these residues appear: the coherence image from the CSK Spotlight pair acquired on 9 and 25 July 2010. Figure 4.46b shows the MRD subsets over Road 497 overlain on the clearest image on which this residue appears: the CSK Spotlight image of filtered σ^0 backscatter, acquired on 25 July 2010. Figure 4.47a shows the areas where profile plots were produced from the Spotlight SBAS DEM of the topographic residues of Road 384. Figure 4.47b shows the area where a profile plot was produced from the UAV DEM of the topographic residue of Road 497.

The reason for selecting two areas for MRD calculation along this road is that they are both in different fields and the similarity in the contrast of the two archaeological residues are not the same in all images. In addition, no analysis was done of Road 492 due to the fact that the archaeological residue over the western part of Road 492 lies in the same field as the residue of road 384, and the difference in the clarity of each is the same for every image (the residue of Road 384 is always a little clearer than that of the western part of Road 492).

Figure 4.48 compares the clarity of each of the archaeological residues in each of the Spotlight SAR products (filtered σ^0 backscatter, 1 and 16 day coherence), plotted over time and with PSMD. The DEM is not included as this was calculated using the entire time series. The chart shows that the coherence residues over the eastern and western parts of Road 384 and over Road 497 all have similar contrast changes over time. The clearest coherence residues are in the 16 day coherence imagery from July 2010, in particular for the western part of Road 384. The σ^0 residues over the three features do not vary consistently over time as do the coherence residues. However, in the case of the σ^0 residues over Road 384, the residues seem more to be due to a geometric effect of the topography (the eastern part revealing no significant residue, while the western part a little more, but still not varying significantly over time). The σ^0 residue over Road 497 on the other hand may more likely be a crop or soil mark than a geometric effect of the topography, and the peak residue contrast coincides with the peak coherence contrast in July 2010.

There does not appear to be any correlation between the σ^0 residues and PSMD, although the time of peak visibility of the σ^0 residue over Road 497 coincides with the time of greatest soil moisture deficit. This supports the argument that the σ^0 residue over Road 497 may be a crop mark, given that archaeological crop marks caused by differential crop growth often occur at times of drought (see section 1.1). In contrast, there does seem to be some correlation between PSMD and the coherence residues, which appear with greater contrast at times of high soil moisture deficit, and less with high soil moisture surplus. This also supports the argument that the coherence residues are crop marks. The fact that all the coherence residues are due to lower coherence than surrounding areas leads further to interpret the features as positive crop marks.

Figure 4.49 compares the contrast of the three coherence residues with the coherence of each respective residue (calculated over the subsets including the residues only). Interestingly, for the 16 day coherences there seems to be a proportional relationship between residue contrast and coherence, while over the 1 day coherences there appears to be an inversely proportional relationship. Given that coherence is entirely lost over the vegetated areas in most of the 16 day coherence images, it is not surprising that low residue contrast coincides generally with low coherence. However, the coherence is never entirely lost over the vegetated areas in any of the 1 day coherence images, as a consequence of which the relationship has more significance. The lower coherence may be a result of higher vegetation and a greater sensitivity to differential vegetation growth. The lower coherence may of course be due to other factors, such as rainfall, but the high contrast in 1-day coherence residues also coincide with greater soil moisture deficit (see Figure 4.48).

Figure 4.50 compares the contrast of the σ^0 residues over time with coherence over the residues. No particular correlation is observable between the residues over Road 384 and their coherences, but as stated above, these residues are likely to be geometric and due to a lesser extent to environmental or vegetation factors. Over the σ^0 residue of Road 497, while there is little observable correlation in the absolute values (exacerbated by the difference between 1 and 16 day coherences), there is nonetheless some similarity in their patterns over time, with highest coherence observed at times of highest σ^0 residue contrast.

Figure 4.51 compares the contrast of the σ^0 residue with the 1 and 16 day coherence residues of Road 497. Some correlation can be observed with the 16 day coherence residues, supporting the argument that these are manifestations of positive crop marks on both the σ^0 and coherence images. No significant correlation exists with the 1 day coherence residues, although residues were identified over Road 497 neither in the 1 day coherence images, nor in the σ^0 images on the dates of the 1-day coherence acquisitions.

Figure 4.52 shows the topographic profile of the eastern and western residues of Road 384 on the DEM derived from the SBAS processing on the Spotlight data, and the topographic profile of the residue of Road 497 on the DEM produced by the optical UAV photogrammetry. The residues of Road 384 show clear valleys of differing widths. The residue of Road 497 shows a very slight topographic trace, but this is negligible compared to surrounding topography, and is not visible on the ground.

4. Archaeological Prospection Using SAR in Agricultural Crop and Grassland Around Rome

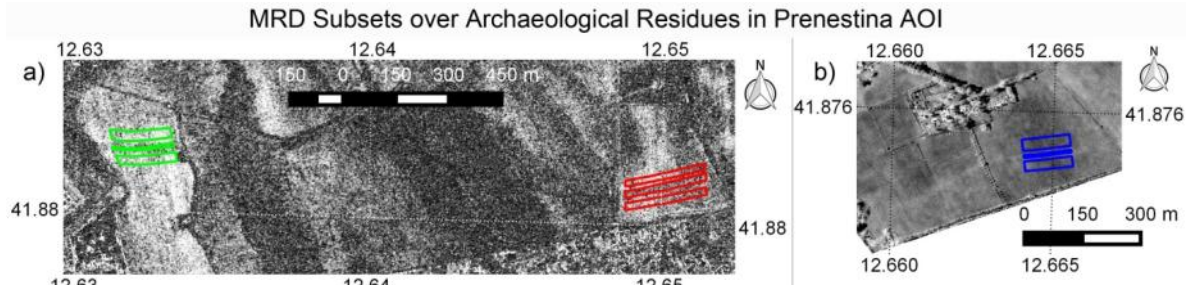


Figure 4.46 Subset areas shown as coloured polygons over and outside of residues used for MRD contrast analysis: a) Green and red polygons over and outside of residues of Road 384. Polygons are overlain on CSK Spotlight coherence image from InSAR pair acquired on 9 and 25 July 2010. b) Blue polygons over and outside of residue of Road 497. Polygons are overlain on σ^0 image acquired on 25 July 2010. COSMO SkyMed data provided by the Italian Space Agency.

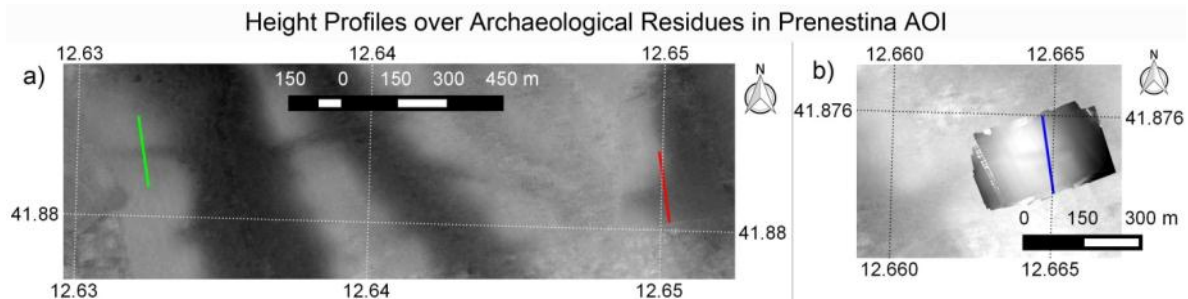


Figure 4.47 Profiles over residues in Prenestina AOI. Height measurements along the profiles in the various DEMs are plotted in Figure 4.52. a) Profiles (in green and red) over residues of Road 384 overlain on SBAS DEM produced from CSK Spotlight time series. COSMO SkyMed data provided by the Italian Space Agency. b) Profile (in blue) of residue of Road 497 overlain on DEM derived from UAV photogrammetry.

4. Archaeological Prospection Using SAR in Agricultural Crop and Grassland Around Rome

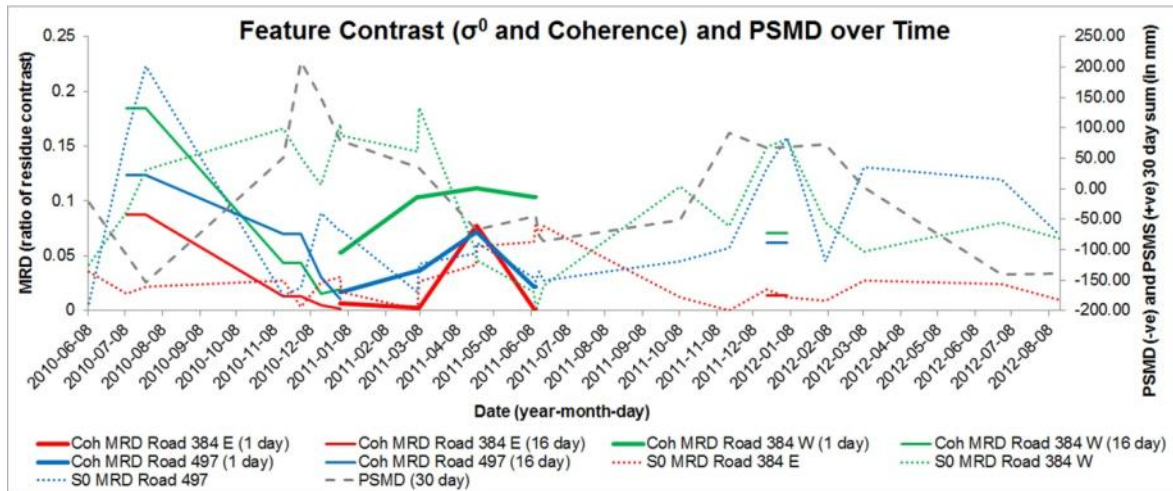


Figure 4.48 Graph showing clarity (contrast) of the archaeological residues in Prenestina: eastern part of Road 384 in red, western part of Road 384 in green and Road 497 in blue. Residues in the filtered σ^0 images are shown as dotted lines, in the 16-day coherence images as continuous lines, and in the 1-day coherence images as bold continuous lines. The clarity of residues is quantified as a ratio (MRD). PSMD and PSMS plotted as a grey dashed line. Negative values correspond to high PSMD (dry conditions), while positive values correspond to high PSMS (wet conditions).

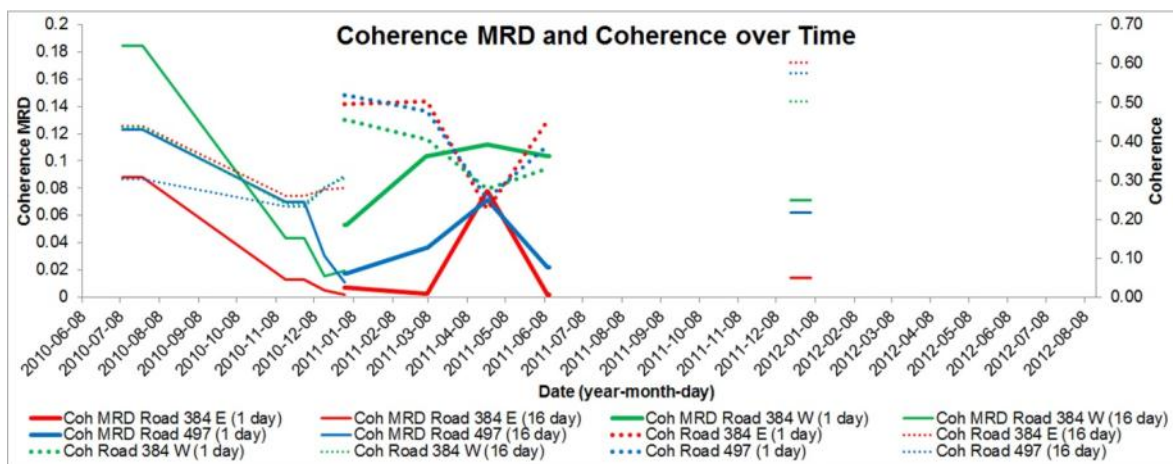
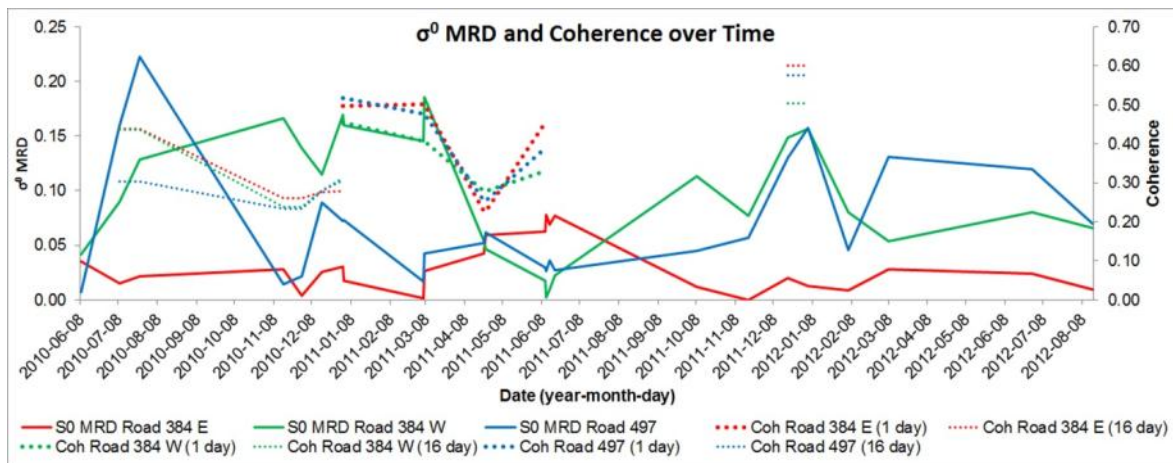


Figure 4.49 Graph showing contrast of coherence residues, as described in Figure 4.48, and coherence over each residue (in dotted lines). The coherence values are provided both for the master and the slaves of InSAR pairs. Where a master is also a slave, it takes the value of the slave.



4. Archaeological Prospection Using SAR in Agricultural Crop and Grassland Around Rome

Figure 4.50 Graph showing contrast of σ^0 residues, as described in Figure 4.48, and coherence over each residue (in dotted lines). The coherence values are provided both for the master and the slaves of InSAR pairs. Where a master is also a slave, it takes the value of the slave.

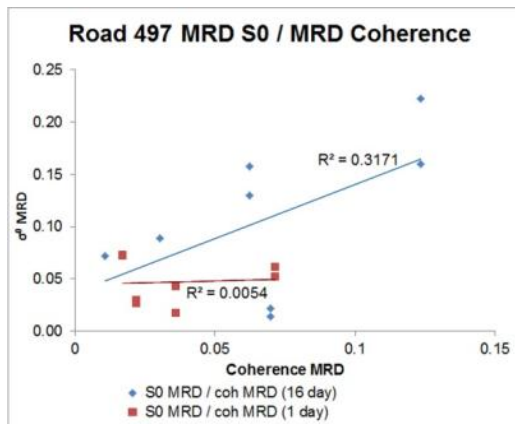


Figure 4.51 Graph showing clarity of σ^0 residue of Road 497, plotted against clarity of 16-day (blue) and 1-day (red) coherence residues of the same feature. Linear trend lines and R^2 values are shown in blue for the 16-day coherence / σ^0 plot, and red for the 1-day coherence / σ^0 plot. A better correlation can be seen for the 16-day coherence / σ^0 plot.

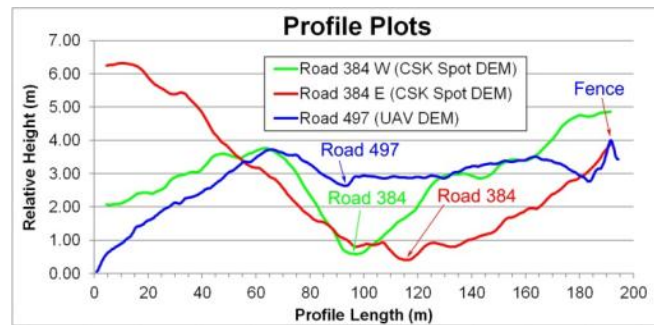


Figure 4.52 Graph showing height profiles over archaeological residues: western (green) and eastern (red) parts of Road 384, both taken from SBAS DEM derived from CSK Spotlight data, and Road 497 (blue), taken from DEM derived from UAV photogrammetry. Annotations for each profile are shown in their respective colours.

4.4.3 Prenestina R2

Interpretation of the results of the polarimetric analysis is very difficult given primarily the coarse resolution of the Radarsat-2 data combined with the lack of detail of the archaeological chart. In none of the processed imagery is it possible to say whether residues of buried archaeological structures are present. However, results are nonetheless shown in this section which are more a demonstration of the methodological approach than an assessment of its utility for archaeological prospection.

Having extracted the various decompositions, these were analysed and compared with the archaeological chart and optical imagery. Many features were present in both the averaged and the multitemporal speckle filtered time series. However, none of these could be stated to correspond clearly with archaeological structures. Some of these are shown in Figure 4.53 to Figure 4.58 below. Figure 4.53 shows a three colour composite of odd bounce, volume scattering and double bounce components of the Yamaguchi four components decomposition (Yamaguchi et al. 2005), displayed respectively as red, green and blue. This is one of the visualisations in which the contrast of features is greatest. Figure 4.54 is a colour composite of the C11, C22 and C33 elements of the covariance matrix (see equation 2.33) displayed respectively as red, green and blue. In this visualisation also, the contrast of features is enhanced. Some examples of features evident in all the Radarsat-2 ascending time series, but which are not evident in other data, are highlighted and labeled as “Anomaly 1” and “Anomaly 2” in Figure 4.53 to Figure 4.58. In the same figures, an example of an anomaly visible in all the Radarsat-2 descending time series is highlighted and labeled as “Anomaly 3”.

Anomaly 1 includes a rectangular feature closed on three sides. It is situated in an open field near to a broad valley. The nearest archaeological structure shown on the chart of Quilici includes what was believed to be a vast villa, the perimeter of which is undefined. The evidence for this includes many blocks of mosaic, tile, pieces of marble sculpture, and other such material from Roman republican to imperial age, stretched over a large area (Quilici 1974). Anomaly 2 is a circular feature close by, and to the south of, Anomaly 1. During the construction of an electrical plant to the east of Anomaly 2 and to the north of Anomaly 3, much archaeological material has been found in the form of building material and, in some cases, well preserved objects, such as a basin for harvesting oil made from *peperino* stone and with an inscription (Quilici 1974). Anomaly 2 is situated in an area of flat topography. Anomaly 3 roughly follows topographic contour lines and may therefore be related to the topography. It is also visible in the Pleiades infrared colour composite (see Figure 4.59).

From the polarimetric decompositions, Anomaly 2 appears to be in a small region characterised on average by volume scattering, while Anomalies 1 and 3 are in regions dominated on average by odd bounce scattering. The polarimetric signatures were analysed over the anomalies and over areas surrounding them in all images: In the case of Anomalies 1 and 2 in the ascending data, it was found that in the 7 May acquisition, most of the region not occupied by buildings is dominated by volume scattering. In the 24 June acquisition, volume scattering still dominates, but odd bounce scattering is now present in the area of Anomaly 1. In all other images, from 18 July until 9 December, odd bounce dominates the centre of the image where the features are present. The transition from volume scattering to odd bounce may be due to agricultural activity.

The method of identifying the polarimetric basis at which a particular feature produces greatest backscatter, and then reprocessing the data with this synthesised polarimetric basis to highlight similar features, was performed for Anomaly 1. Over a pixel of this feature the polarimetric signatures are shown in Figure 4.55 for a number of images in the ascending FQ2 time series. The polarimetric basis that yields highest backscatter for this feature is approximately that with an ellipticity of 15 degrees and an orientation angle of 80 degrees. The polarimetric basis was therefore changed to this for all images in the Radarsat-2 FQ2 ascending time series. The C11, C22 and C33 covariance matrix elements of the average of the time series converted to this basis is shown in Figure 4.56. In this image features with a similar polarimetric signature as Anomaly 1 are therefore highlighted.

In the case of Anomaly 3 in the descending data, throughout the time series, the contrast of the anomaly becomes progressively greater as the dominant scattering mechanism in the field in which it is situated tends increasingly to single bounce from the date of the first acquisition on 8 August 2008 (see De Grandi filtered Pauli decomposition in Figure 4.57) to the last acquisition on 13 December 2008 (see De Grandi filtered Pauli decomposition in Figure 4.58). The archaeological chart of Quilici reveals the presence of what has been interpreted as a villa from material evidence found on site which mainly comprises pottery pieces and building material from the 4th to 3rd centuries BC (Quilici 1974).

Figure 4.59 is a Pleiades image of the Prenestina AOI, acquired on 20 April 2014. It was pan-sharpened to 0.5m spatial resolution and is a colour combination of NIR, R and G displayed as R, G and B respectively. Figure 4.60 is a subset of the archaeological chart of Quilici (1974). Figure 4.61 shows the

4. Archaeological Prospection Using SAR in Agricultural Crop and Grassland Around Rome

SBAS DEM produced from the CSK Spotlight imagery. Annotations in yellow on these figures show the locations of the anomaly features, and the locations and directions from which photographs were acquired on the ground. These photographs are shown in Figure 4.62, Figure 4.63 and Figure 4.64.

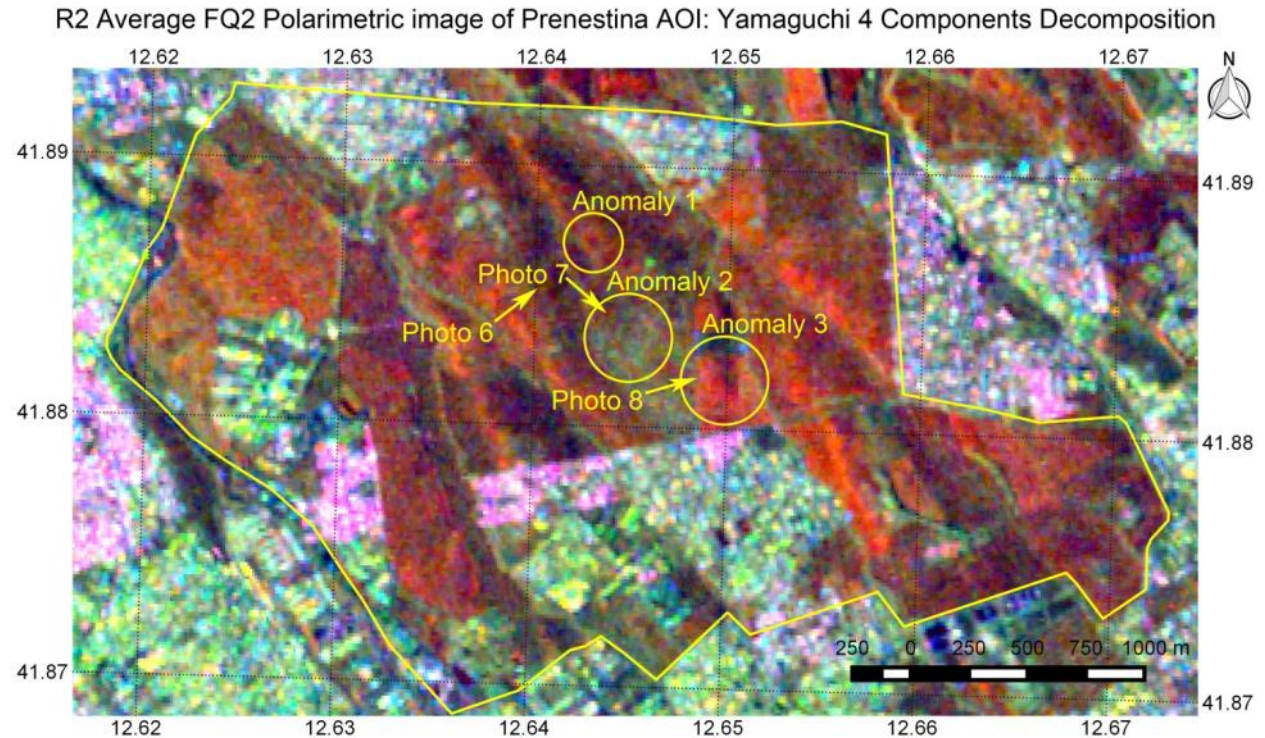


Figure 4.53. Average of Radarsat-2 FQ2 time series of colour composite of odd, volume and double bounce scattering mechanisms displayed as red, green and blue respectively. Annotations in yellow show the boundary of the Prenestina AOI, the locations of anomaly features and the locations and directions from which photographs were acquired on the ground.

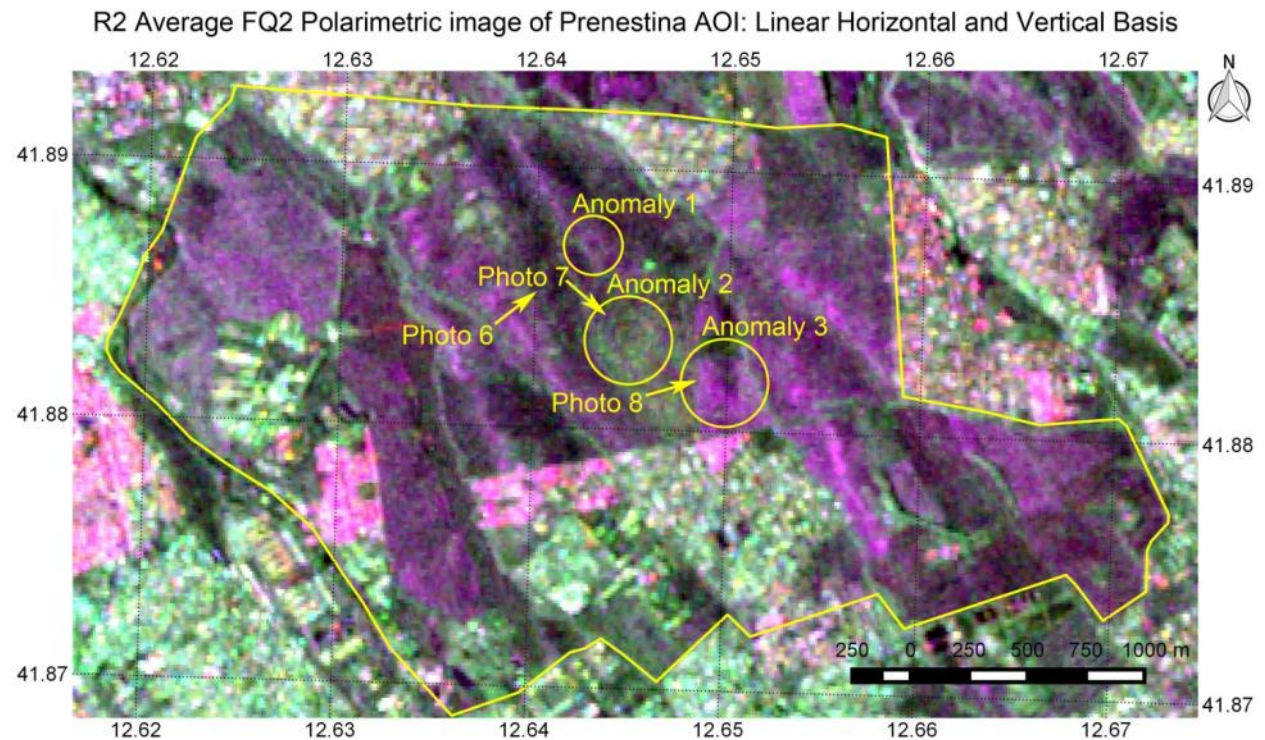


Figure 4.54. Average of Radarsat-2 FQ2 time series of colour composite of C11, C22 and C33 elements of covariance matrix (see equation 2.33) displayed as red, green and blue respectively. The polarimetric basis is linear horizontal/vertical. Annotations in yellow show the boundary of the Prenestina AOI, the locations of anomaly features and the locations and directions from which

4. Archaeological Prospection Using SAR in Agricultural Crop and Grassland Around Rome

photographs were acquired on the ground.

4. Archaeological Propection Using SAR in Agricultural Crop and Grassland Around Rome

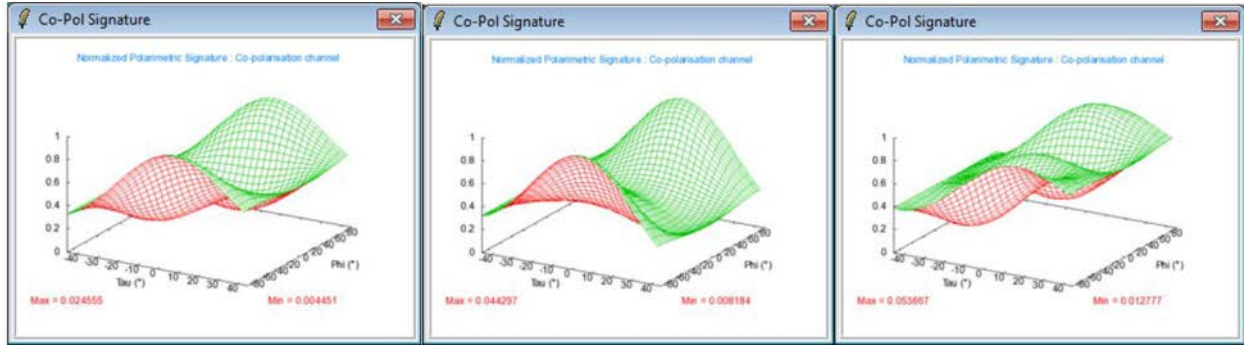


Figure 4.55 Co-polarised polarimetric signature of pixel belonging to Anomaly 1 in Radarsat-2 FQ2 image acquired on 28 September (left), 15 November (centre) and 9 December 2008 (right).

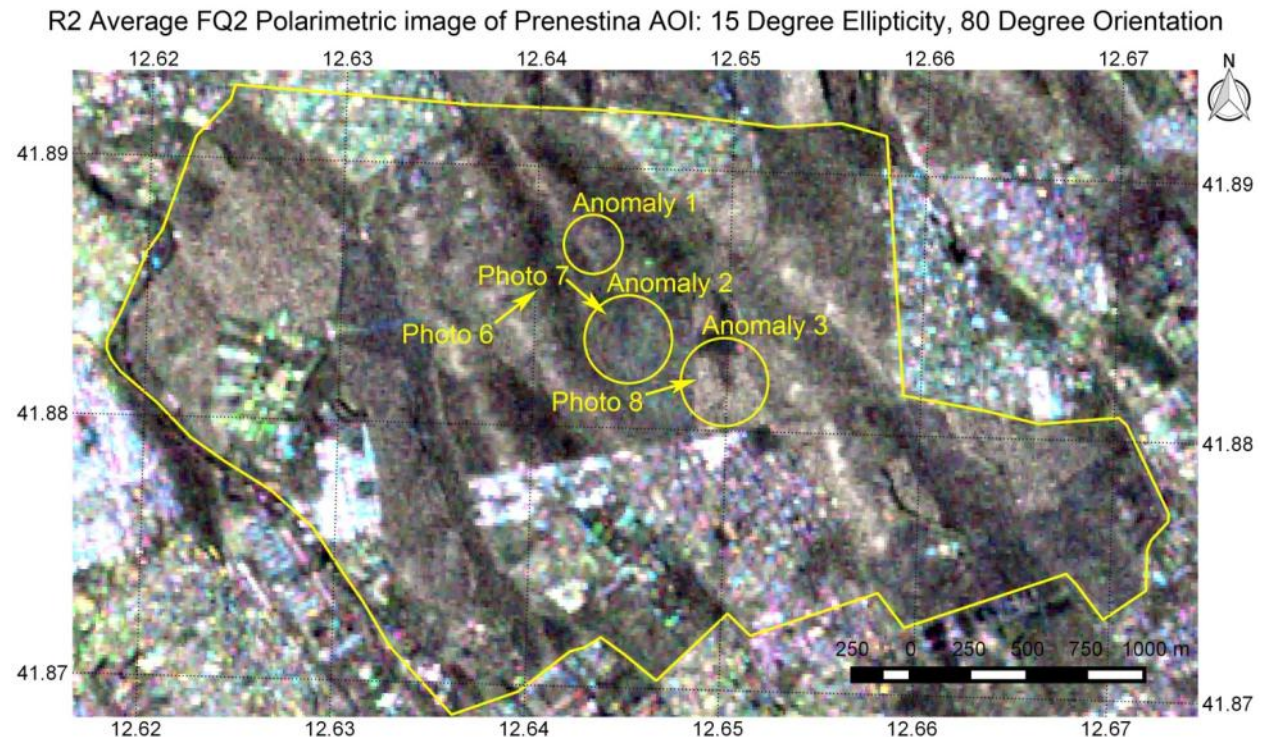


Figure 4.56 Average of Radarsat-2 FQ2 time series of colour composite of C11, C22 and C33 elements of covariance matrix (see equation 2.33) displayed as red, green and blue respectively. The polarimetric basis is 15° elliptical, with an 80° orientation angle. Annotations in yellow show the boundary of the Prenestina AOI, the locations of anomaly features and the locations and directions from which photographs were acquired on the ground.

4. Archaeological Prospection Using SAR in Agricultural Crop and Grassland Around Rome

De Grandi Filtered R2 FQ9 Polarimetric image of Prenestina AOI: Pauli Decomposition 2008/08/08

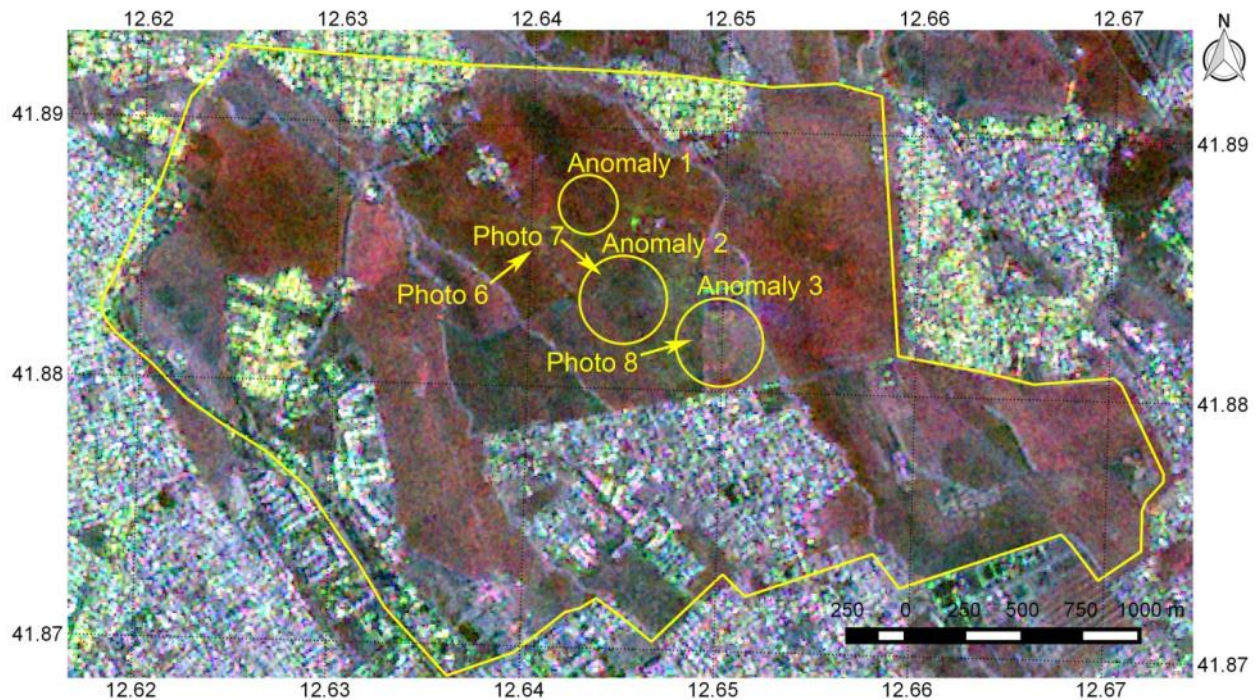


Figure 4.57 Colour composite of Pauli decomposition of R2 FQ9 descending pass image acquired on 8 August 2008. Red corresponds to K1, green to K2 and blue to K3 (see Section 2.12.7.1). The image has been multitemporal speckle filtered with the time series of descending pass images. Annotations in yellow show the boundary of the Prenestina AOI, the locations of anomaly features and the locations and directions from which photographs were acquired on the ground.

De Grandi Filtered R2 FQ14 Polarimetric image of Prenestina AOI: Pauli Decomposition 2008/12/13

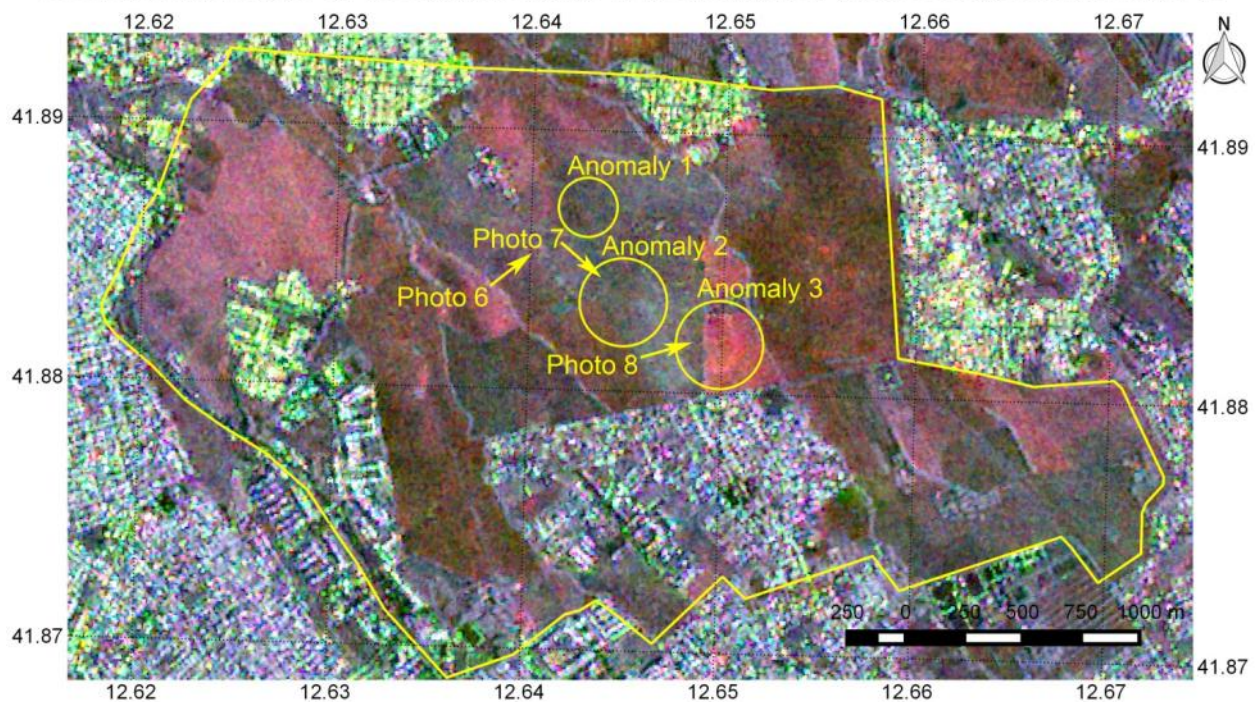


Figure 4.58 Colour composite of Pauli decomposition of R2 FQ14 descending pass image acquired on 13 December 2008. Red corresponds to K1, green to K2 and blue to K3 (see Section 2.12.7.1). The image has been multitemporal speckle filtered with

4. Archaeological Prospection Using SAR in Agricultural Crop and Grassland Around Rome

the time series of descending pass images. Annotations in yellow show the boundary of the Prenestina AOI, the locations of anomaly features and the locations and directions from which photographs were acquired on the ground.

4. Archaeological Prospection Using SAR in Agricultural Crop and Grassland Around Rome

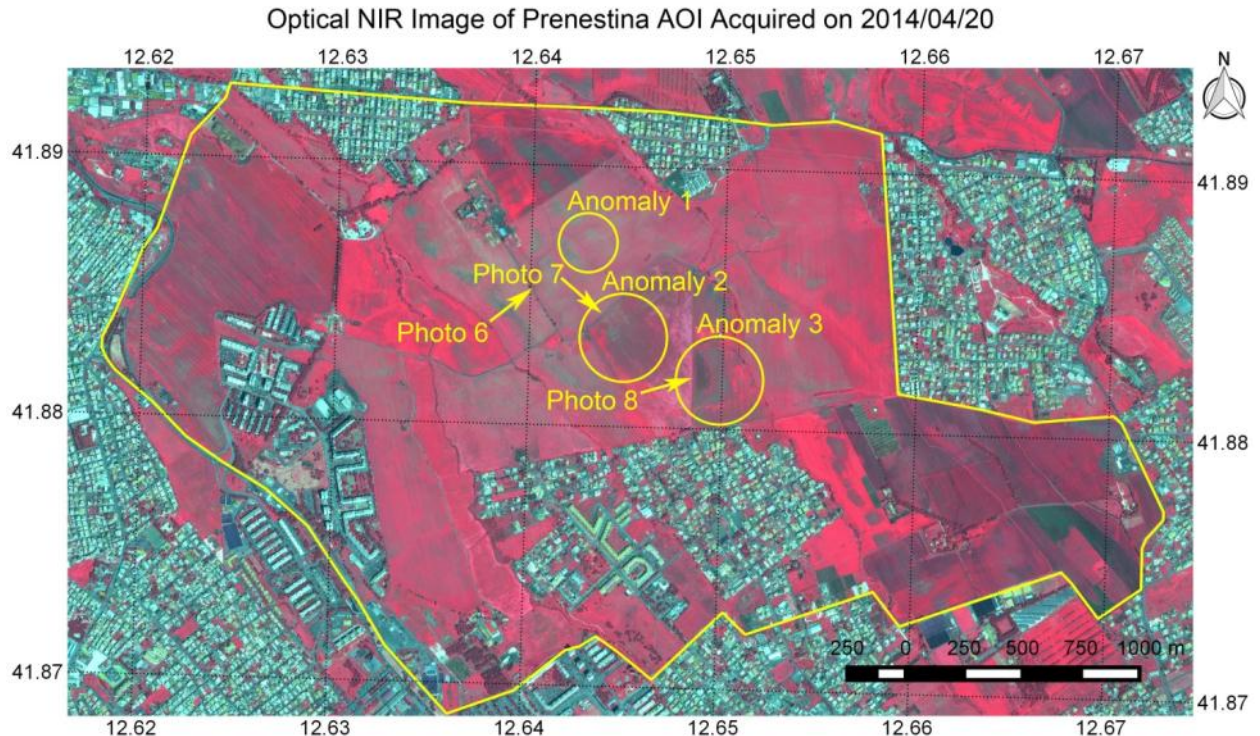


Figure 4.59 Pleiades image acquired on 20 April 2014 over the Prenestina AOI, pan-sharpened to 0.5m spatial resolution. NIR, R and G displayed as R, G and B respectively. Annotations in yellow show the boundary of the Prenestina AOI, the locations of anomaly features and the locations and directions from which photographs were acquired on the ground. Pleiades data provided by the European Space Agency.

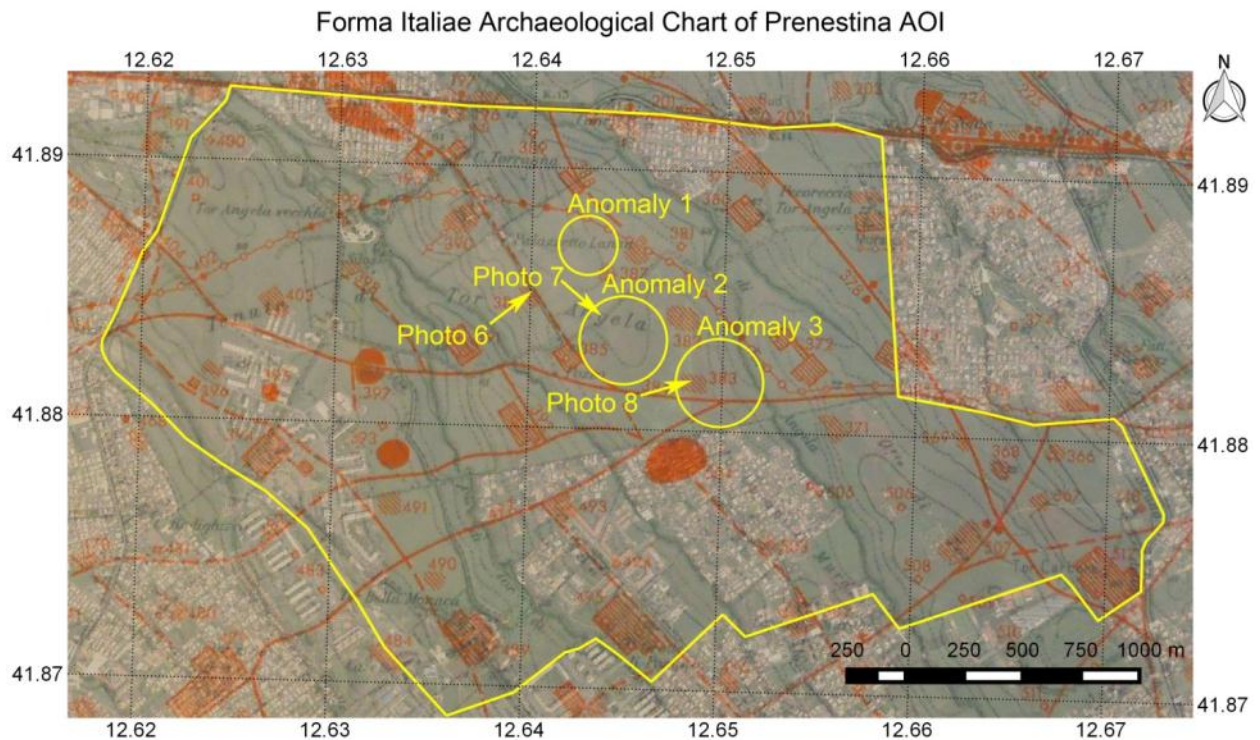


Figure 4.60 Subset of archaeological chart over the Prenestina AOI taken from Quilici (1974) and published as part of the Forma Italiae series. Annotations in red show documented archaeological structures. For the legend, see Figure 4.40. Annotations in

4. Archaeological Prospection Using SAR in Agricultural Crop and Grassland Around Rome

yellow show the boundary of the Prenestina AOI, the locations of anomaly features and the locations and directions from which photographs were acquired on the ground.

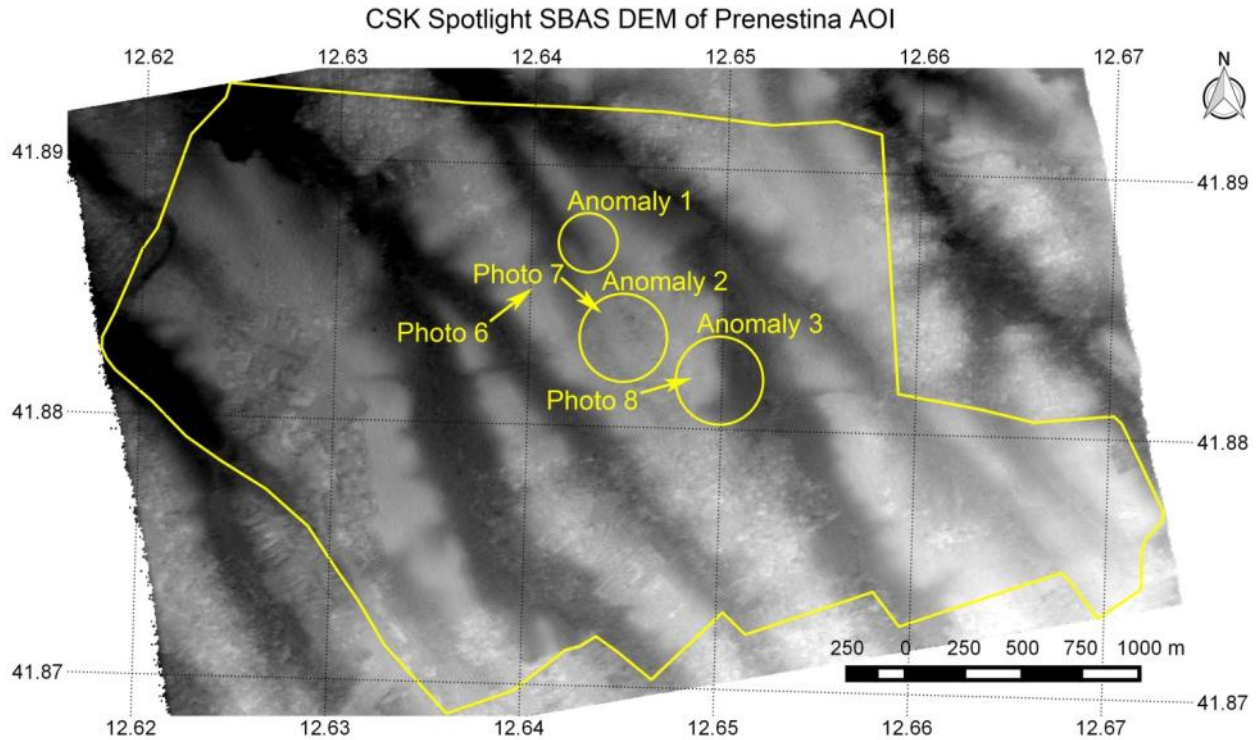


Figure 4.61. SBAS DEM produced from CSK Spotlight imagery over the Prenestina AOI. Annotations in yellow show the boundary of the Prenestina AOI, the locations of anomaly features and the locations and directions from which photographs were acquired on the ground. COSMO SkyMed data provided by the Italian Space Agency.

Photo 6



Figure 4.62. Photograph acquired on 16 March 2013 at 16:56. Location and direction of photographer shown in Figure 4.53 to Figure 4.61.

Photo 7



Figure 4.63. Photograph acquired on 16 March 2013 at 16:49. Location and direction of photographer shown in Figure 4.53 to Figure 4.61.

Photo 8



Figure 4.64. Photograph acquired on 6 October 2015 at 12:51. Location and direction of photographer shown in Figure 4.53 to Figure 4.61.

4.4.4 Salaria

Figure 4.65 is a Pleiades image of the Salaria AOI acquired on 22 May 2014 and displayed as a colour composite of NIR, R and G as R, G and B respectively. Figure 4.66 shows the AOI on a filtered σ^0 backscatter image acquired on 7 April 2013. This is the filtered σ^0 image on which the residue of the ancient Via Salaria appears clearest as a line of low backscatter traversing the field adjacent to the modern Via Salaria. All the residues on the filtered σ^0 images appear as areas of lower backscatter relative to surrounding areas. No residues were identified in any of the coherence images.

Figure 4.67 shows the DEM produced from the image pair acquired on 10th and 26th of August 2012. The result is very noisy given the low coherence, but the ancient Via Salaria can be seen very clearly as a valley or ditch traversing the fields. This was one of the few image pairs from which it was possible to derive a DEM (albeit noisy) and the only one on which the Via Salaria is visible.

Figure 4.68 is a photo acquired of the area on 1 October 2016. No topographic, or any other, trace of the ancient Via Salaria is visible. Figure 4.69 shows the best available example of the ancient Via Salaria as a straight negative crop mark surrounded by positive crop marks, in an optical image available on Google Earth, acquired on 11 September 2009. The location and direction from which the photo in Figure 4.68 was acquired is shown as a yellow arrow on this image.

4. Archaeological Propection Using SAR in Agricultural Crop and Grassland Around Rome

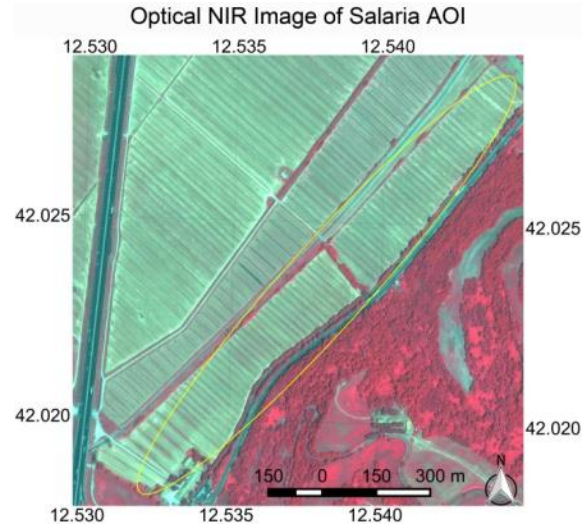


Figure 4.65 Pleiades image acquired on 22 May 2014 over the Salaria AOI, pan-sharpened to 0.5m spatial resolution. NIR, R and G displayed as R, G and B respectively. Yellow ellipse shows location of the residue of the ancient Via Salaria. Pleiades data provided by the European Space Agency.

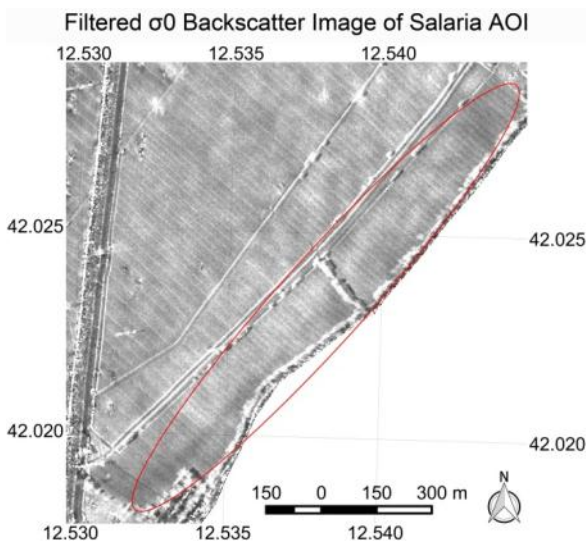


Figure 4.66 Image of filtered σ^0 backscatter over the Salaria AOI acquired on 7 April 2013. Red ellipse shows location of the residue of the ancient Via Salaria. COSMO SkyMed data provided by the Italian Space Agency.

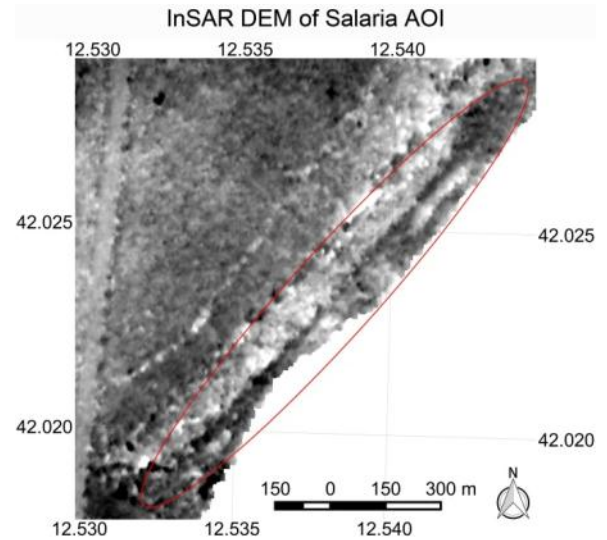


Figure 4.67 DEM over the Salaria AOI derived from InSAR using the CSK Stripmap image pair acquired on 10 and 26 August 2012. Red ellipse shows location of the residue of the ancient Via Salaria. The DEM is very noisy, but the residue of the ancient Via Salaria can clearly be seen.



Figure 4.68 Photo 9 acquired at the location of the residue of the ancient Via Salaria (see Figure 4.69 for location and direction of photo). Photo acquired on 1 October 2016 at 17.14. On this date, no trace is visible of the archaeological feature on the ground.

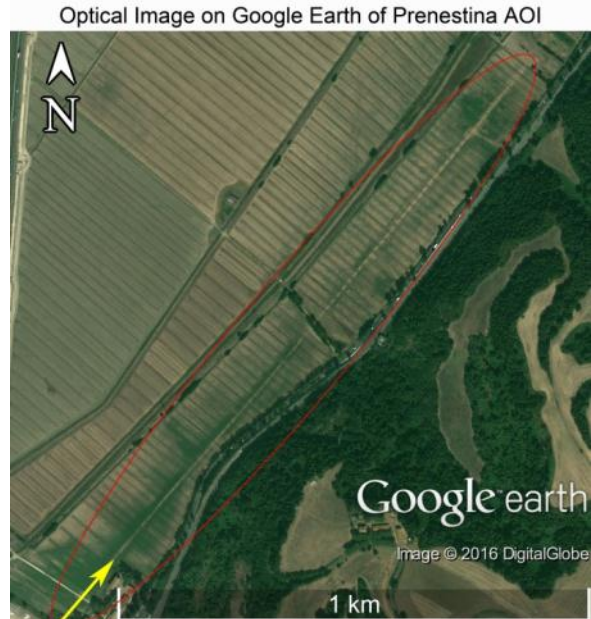


Figure 4.69 Optical image available on Google Earth, acquired on 11 September 2009. The ancient Via Salaria (highlighted by the red ellipse) is clearly visible as a negative crop mark with positive crop marks on either side along the southern part of the feature. Yellow arrow shows location and direction in which photo 9 was acquired (Figure 4.68). Courtesy of Google Earth.

4.4.4.1 Salaria features analysis

Figure 4.70 shows the subset areas over the ancient Via Salaria, and on either side of it, which were used to quantify the residue contrast in each of the σ^0 backscatter images. Figure 4.71 compares the σ^0 residue contrast of the Via Salaria over time and with PSMD. The graph shows no clear correspondence between PSMD and σ^0 residue contrast, although the times of highest contrast coincide with a period of high PSMS, which is not characteristic of crop marks.

Figure 4.72 shows σ^0 residue contrast with residue coherence. Throughout most of the time series there is no clear σ^0 residue contrast and coherence is consistently low. At the time of greatest σ^0 residue contrast, the coherence is at the same low value as throughout most of the time period.

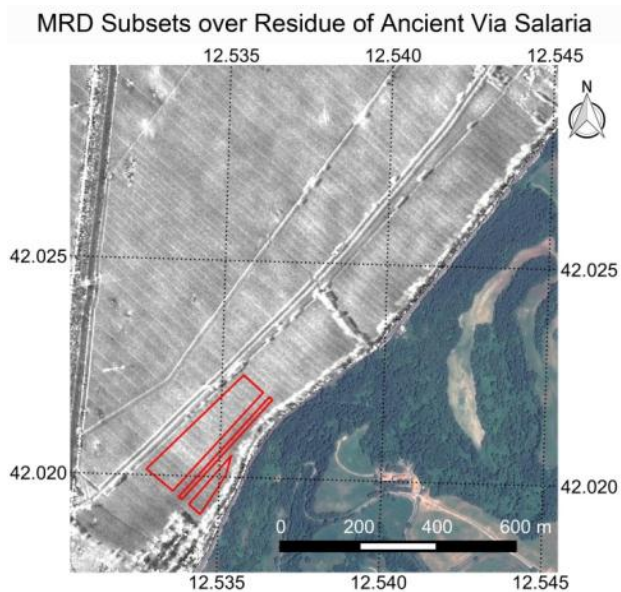


Figure 4.70 Subset areas used for MRD contrast analysis shown as red polygons over and outside of the Via Prenestina residue. Polygons are overlain on the image of filtered σ_0 backscatter acquired on 7 April 2013 and Pleiades image acquired on 22 May 2014. COSMO SkyMed data provided by the Italian Space Agency. Pleiades data provided by the European Space Agency.

4. Archaeological Prospection Using SAR in Agricultural Crop and Grassland Around Rome

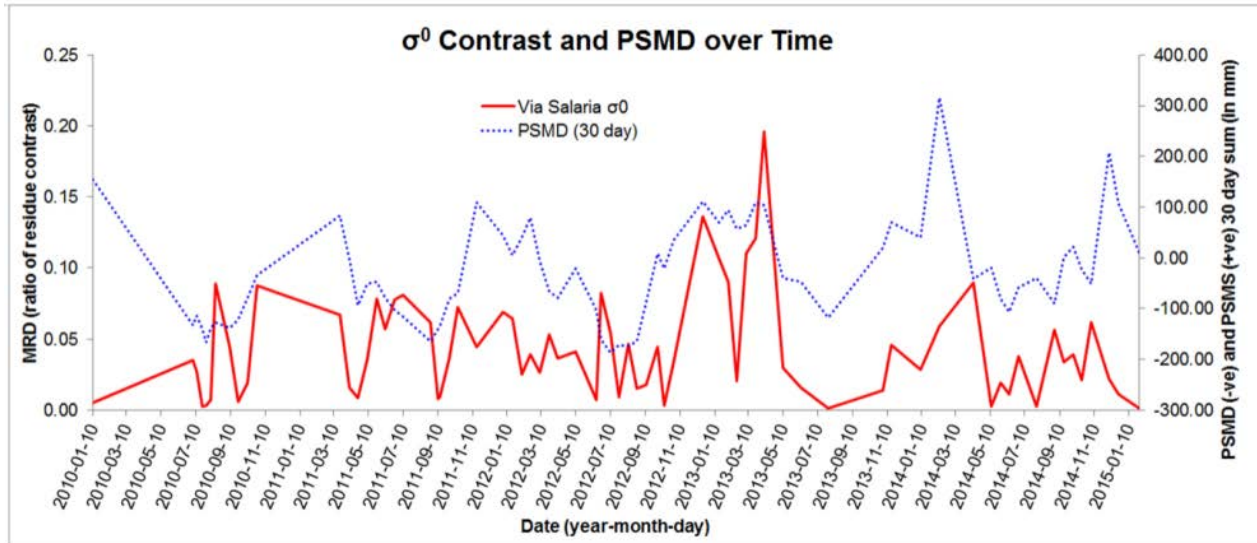


Figure 4.71. Graph showing clarity (contrast) of the residue of the ancient Via Salaria (in red), plotted over time and with PSMD (blue dotted line). The clarity of residues is quantified as a ratio (MRD). For the PSMD, negative values correspond to high PSMD (dry conditions), while positive values correspond to high PSMS (wet conditions).

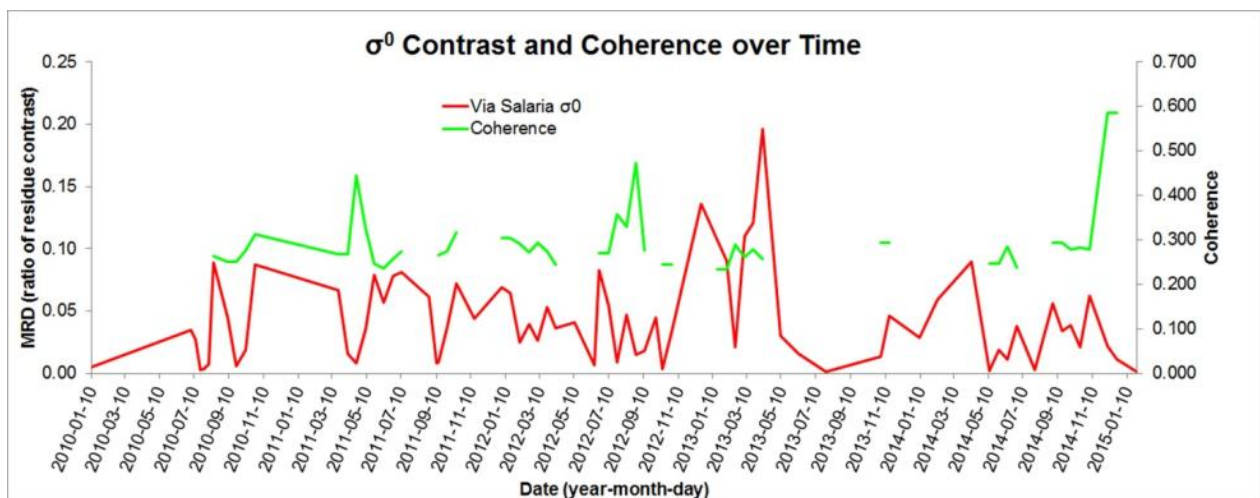


Figure 4.72. Graph showing clarity (contrast) of the residue of the ancient Via Salaria (in red), plotted over time and with residue coherence (in green). The clarity of residues is quantified as a ratio (MRD).

Given that the σ^0 residues appear as areas of lower relative backscatter, and given the low coherence in all images, it is likely that these residues are manifestations of negative crop marks, as is the case with the image on Google Earth. The presence of the topographic anomaly on the DEM indicates that there is still a slight topographic trace of the road. The photograph of the location of the residue on the ground shows that this is not visible at the surface (at least not at the time the photo was acquired). The negative crop mark along the buried road in the image on Google Earth is perhaps due to paving stones beneath the ground hindering crop growth. The positive crop marks on either side of the road in the same image may correspond with ancient drainage channels, but their broad and irregular nature, and the fact that they are mainly in the southern part of the road, suggests that they may instead be due to the accumulation of water within the slight valley causing enhanced crop growth where this is not

hindered by the ancient road. The presence of this slight valley may also be the reason why the σ^0 residue appears more clearly at a time of high PSMS, as high PSMS perhaps enhances the difference between abundant vegetation growth in the valley with stunted growth over the buried road. Although this is in contrast with the appearance of the residue in the available optical imagery of the area, on which it appears mainly in the hot summer months of July, August and early September, when the vegetation is parched. However, the appearance of crop marks in optical images is a result of colour differences, which is not the case for SAR.

The CSK Stripmap images used to produce the DEM were acquired on 10 and 26 August 2012. This does not coincide with high contrast of residues on the σ^0 backscatter, but it does coincide with high PSMD and high coherence. Perhaps the stunted and parched vegetation is less likely to contribute to temporal decorrelation than healthy, abundant growth. This may also be a time for the emergence of crop marks, as confirmed in the available optical images. It may be therefore that the topographic anomaly is due to differential crop growth. Perhaps not as enhanced as at other times, but possible to measure with InSAR due to the higher coherence.

4.5 Discussion

Archaeological residues in the CSK data were clearly visible in 3 out of the 6 AOIs. The AOIs situated in the flat alluvial Tiber river valley and delta were perhaps more successful at revealing residues: in both the Portus and Salaria AOIs, features were clearly visible. Even in the Ostia AOI some very faint traces were found. The AOIs situated over the pyroclastic deposits of the Albano and Sabatino volcano districts were a little less successful at revealing residues and these were only found in 1 of the 3 (Prenestina). Moreover, in the case of Prenestina, most (if not all) of the anomalies appeared to be of a topographic nature. In most areas the soil types were of class 2 and 3, in most cases limited by stoniness, shallow depth, poor texture or chemistry, and in others by excess water, either in the form of stagnant water in the soil or possible flooding. Residues were found on all these soil types. They were also present on both irrigated and non-irrigated agricultural land.

No clear correlation could be found between residue contrast and PSMD. The residue of Road 497 in the Prenestina AOI was most apparent at a time of high water stress, but this was not the case for the other residues. However, the other residues that were not of an obvious topographic nature were situated over the alluvial Tiber plain, in irrigated fields. Over these areas PSMD may have been less relevant.

Not all archaeological structures documented in each area left residues in the SAR data. Mainly linear features, such as roads and canals, were evident. This is perhaps due to the easy recognition of the shape of such features. Many of the archaeological structures identified in the various surveys that took place in the AOIs were interpreted from scant surface remains. This is particularly the case for the survey reported in Quilici, (Quilici 1974) over the Prenestina AOI. These structures may no longer have a coherent shape that would allow easy interpretation on remotely sensed data.

Where archaeological residues were found, they were present in either the filtered CSK σ^0 backscatter, the interferometric coherence (of 1 or 16 day temporal baseline), or the DEM (produced either by SBAS or InSAR). No residues were found in the PALSAR-1 or R2 data that could be clearly related to

archaeological structures. This is likely due to the coarseness of the spatial resolution of the data prohibiting resolving the small scale details of buried archaeological structures.

The sections below discuss the results of archaeological residue detection in each of the CSK SAR data products.

4.5.1 Filtered σ^0 backscatter

Multitemporal speckle filtering made a significant difference in the ability to distinguish archaeological residues in the CSK σ^0 backscatter. Figure 4.73 illustrates this by comparing an image of σ^0 backscatter acquired on 20 December 2012 over the Northern Canal residue of the Portus AOI (Figure 4.73a), with the same image after having applied De Grandi speckle filtering using only 10 images (Figure 4.73b), and using all 75 images of the time series (Figure 4.73c). The filtering preserves the spatial resolution and the details in the image become increasingly clear the more images are used in the filtering. With 10 images, and particularly with 75 images, it is possible even to detect plough lines in the fields.

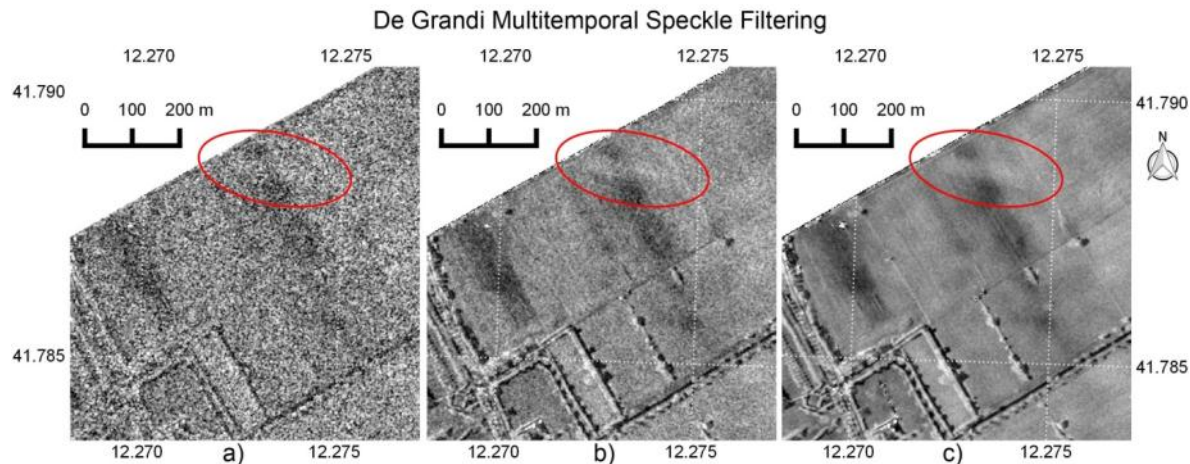


Figure 4.73 Examples of De Grandi multitemporal speckle filtering. a) σ^0 backscatter image over Northern Canal in Portus AOI, acquired on 20 December 2012. Location of Northern Canal shown in red ellipse. b) Same image as in a) but De Grandi speckle filtered with 9 additional images. The Northern Canal is now easier to distinguish. c) Same image as in a) but De Grandi filtered with all 75 images in Stripmap time series. The Northern Canal appears a lot clearer. COSMO SkyMed images provided by the Italian Space Agency.

Residues were found in the images of filtered σ^0 backscatter both from higher and lower backscatter relative to surrounding areas. Each is described in the subsections below:

4.5.1.1 Filtered σ^0 residues due to high relative backscatter

Over both the Northern Canal in the Portus AOI and Road 497 in the Prenestina AOI, residues were distinguished by high backscatter.

In the case of the Northern Canal, the peak residue contrast was observed during times of very high coherence. Given the rapid temporal decorrelation in X-band SAR coherence over vegetated areas (Zalite et al. , Zalite et al. 2014), it is unlikely that significant loose vegetation is present in areas where X-band coherence is high after a temporal baseline of 16 days. If coherence is high, it may be that the

fields are occupied by bare soil, or rigid vegetation (e.g. dried stumps or crops fixed to poles). If either is the case, it is suggested that it may be properties of the soil (differences in moisture or composition) that reveal the buried structures. The photograph of the residue revealed no topographic (or any other) trace. No correlation between the contrast of the Northern Canal residue and PSMD was observed, but if the residue is situated in irrigated fields, it may be less likely to be affected by external moisture conditions.

The residue of Road 497 in the filtered σ^0 backscatter in the Prenestina AOI is also distinguished by high relative backscatter. In this case the coherence is always low. The UAV DEM reveals the presence of a very slight topographic valley corresponding to this feature. It may be that the high relative backscatter is a result of increased scattering from more abundant vegetation growth (positive crop mark), or an increased moisture presence. Such vegetation or moisture differences may be a result of subtle differences in water drainage in the valley. The valley itself is not visible on the ground, nor is any trace of the residue. The residue of Road 497 appears clearly at times of high PSMD, which is known to provoke the appearance of negative crop marks (Jones and Evans 1975, Evans and Jones 1977).

4.5.1.2 Filtered σ^0 residues due to low relative backscatter

Over the built-up areas to the south of the Portus AOI, and over the AOI of the ancient Via Salaria, residues were distinguished by lower backscatter relative to surrounding areas. It is likely that these are both due to negative crop marks. In both cases low coherence is observed throughout the occurrence of residues, which may be a result of vegetation cover. The low backscatter may be indicative of shorter, stunted vegetation (smoother relative to the incident microwave signal), or it may be a result of a lower dielectric constant due to lower levels of moisture in parched vegetation, or shallower soil. These arguments are supported by the fact that both archaeological features causing the residues are objects made from construction material: confirmed by the magnetometer survey in the Portus AOI, and the negative crop mark in the optical image of the Via Salaria (probably due to basalt paving). No particular correlation was observed with PSMD, but this may again be expected if the residues in both AOIs are situated in irrigated fields.

The Portus AOI lies in the geologically flat area of the Tiber delta. Aside from on freely available topographic datasets from SRTM and ASTER GDEM, the topography of the Portus AOI was not measured at very high vertical accuracy. Moreover, the southern urban feature was not inspected, given access constraints. However, the nearby Northern Canal was possible to inspect, during which time no topographic trace was evident. When the area of the Via Salaria residue was inspected, it appeared flat, but the InSAR DEM revealed a clear low topographic anomaly over the Via Salaria itself. If this is due to stunted vegetation, it would support the interpretation of the low relative σ^0 backscatter residue as a negative crop mark.

4.5.2 Coherence

While the coherence was used throughout the AOIs to obtain additional surface information, the actual detection of residues on coherence images was limited to the Spotlight data over the Prenestina AOI. Here residues of lower relative coherence were identified that correspond to known archaeological

structures. These residues are interpreted as positive crop marks, given that more abundant vegetation is likely to reduce coherence (Engdahl et al. 2001, Zalite et al. 2014). In most cases the residues were in topographic valleys, and it is likely that the coherence anomalies are a result of topography induced moisture and soil differences resulting in differential vegetation growth. If this is the case with the residue of Road 497, it would suggest that even very subtle variations in the topography, not visible to the naked eye at the surface, are sufficient to cause coherence residues. Over the ancient Via Salaria, a topographic anomaly was detected, but this was not identified in any of the coherence images. However, low coherence was observed throughout most of the InSAR time series in this area, and the few occasions when coherence was not completely lost did not coincided with the appearance of σ^0 residues. It is likely therefore that the conditions for differential crop growth were not present when they may have been detected in the coherence.

The coherence residues occurred at times of peak PSMD (in dry periods). The peak residue occurred in a coherence image with a 16 day temporal baseline (between 9 and 25 July 2010). However, this happened to span the time of peak PSMD in the time series and in general the 1 day coherences yielded higher contrast residues.

4.5.3 DEM

The SBAS processing was successful only over 2 of the 6 AOIs using both Stripmap (Prenestina and Salaria) and Spotlight (Prenestina only) CSK data. However, over Salaria only a very noisy result with one interferometric pair was possible. In both cases topographic anomalies corresponding to locations of known archaeological structures were detected. In the case of Prenestina, these were visible on the ground as valleys of varying width, but in the case of Salaria, there was no topographic evidence on the ground. However, the area was not inspected at the same time as the acquisitions of the images with which the DEM was created. There may have been differential vegetation growth, in the form of a negative crop mark, sufficient to be detected on a DEM derived from Stripmap data, even if not on the σ^0 imagery. In the case of Prenestina, the topographical anomalies seemed permanent.

Repeat pass SAR interferometry may not be the most efficient technique for DEM generation over vegetated areas. Nonetheless, the results presented here show that it can in some cases be applied successfully. This may complement information provided by backscatter intensity and coherence derived from the same data. The vertical accuracy of spaceborne InSAR may not match that of airborne systems, but it may be sufficient to identify archaeological structures. Even if these are evident on the ground, the synoptic view enables a much better distinction between natural and artificially created topographic relief (such as that created by an ancient road).

4.6 Conclusions

In vegetated areas around the city of Rome, surface residues over buried archaeological features clearly appear in imagery derived from both the intensity and the phase of SAR data. This imagery includes multitemporal speckle filtered σ^0 backscatter, interferometric coherence, and DEMs derived from InSAR and SBAS. The clarity of residues in each of these types of SAR data often differs between features and over time. The application of both intensity and interferometric SAR processing therefore contributes to

increasing the probability of detecting traces of buried archaeological structures. It also combines to provide a better understanding of their underlying cause. Comparisons between σ^0 backscatter, coherence and DEMs have aided interpretation of trace features as manifestations of positive and negative crop marks, soil marks and topographic residues.

A large time series of SAR data greatly improves the quality of information and potential for extracting small scale features, such as buried structures. With such a time series the speckle in images of backscatter intensity can be greatly reduced while preserving spatial resolution if techniques such as De Grandi filtering are applied (De Grandi et al. 1997). The ability to derive topographic information using repeat pass interferometry is significantly limited in vegetated areas by temporal decorrelation. However, with a large time series, techniques such as SBAS can in some cases overcome such limitations. The interferometric coherence can be used to derive some information on surface characteristics, such as the fallow or vegetated state of a field. With a time series, such information can be derived with higher confidence if the measurements can be correlated with a possible crop cycle, or vegetation growth. Archaeological residues can be notoriously ephemeral, and their appearance depends on many factors, which are often very site specific. The higher the frequency of acquisition, the more likely an archaeological residue can be detected when it appears.

In practice a large time series may be difficult to acquire for archaeological analysis. Moreover, the processing techniques described are complex and time consuming, especially SBAS. However, the current trend in Earth Observation (EO) is characterized by an unprecedented rate of increase in the volume, variety and velocity of remotely sensed data, now coined as “Big Data”. This is becoming progressively available to users as access restrictions are lifted. Developments in EO closely accompany advances in IT, and complex data processing is increasingly automatized with the aid of cloud computing and big data analytics.

Fully polarimetric data can also yield more information about a target and its surrounding context. With the aid of polarimetric decompositions and through an analysis of the target scattering signature, the geometric nature of an object or a surface can be better understood. If a time series is available, further information may be derived of the permanence of a particular object, or the changing environmental context, such as an agricultural field undergoing a particular crop cycle. Through change of polarimetric bases, particular anomaly features may be enhanced, which may also facilitate the identification of similar features. Over the AOI selected for this study, this was applied theoretically. To assess its real utility for prospection of small scale archaeological structures in similar areas, it is suggested that higher resolution data would be needed than that used in this research, or that the technique is applied to detect residues of large features relative to the spatial resolution of the data.

5 ARCHAEOLOGICAL PROSPECTION USING SAR IN NORTH SINAI DESERT

Published in Papers 2 & 5 (See Appendix D.1)

This chapter assesses the potential of long wave SAR (PALSAR-1 and 2) to directly detect archaeological structures obscured by, or buried under, sand. It also describes novel approaches for anthropogenic feature extraction at various scales, and using both the phase and amplitude of the SAR signal. It is hoped that these feature extraction techniques may be modified to suit the needs of archaeological research.

Research on the feasibility of spaceborne SAR to carry out large scale, systematic archaeological surveys in the North Sinai is one of the objectives of the Satellite Remote Sensing in Support to Egyptological Research (SatER) team. SatER is a research group headed by the Institute for Ancient Mediterranean Studies (ISMA) of the Italian National Research Council (CNR), and coordinated by G. Capriotti Vittozzi. Its ultimate aim is to support the CNR Multidisciplinary Egyptological Mission (MEM). SatER seeks to apply innovative technologies that may increase the efficacy and efficiency of Egyptological research, drawing on a multidisciplinary team including remote sensing specialists, geophysical surveyors, geologists, and Egyptologists.

While the satellite data processing described in this chapter has been undertaken entirely in the framework of this PhD project, an initial analysis and interpretation of the results, and a discussion of its utility for archaeological research, has been carried out with the help of the multidisciplinary team of SatER specialists, who contributed their expertise in various fields ranging from geology to archaeology and Egyptology.

The satellite SAR data includes scenes acquired by the first and second generation Phased Array type L-band SAR (PALSAR-1 and 2) sensors carried on-board the Japanese Advanced Land Observing Satellites (ALOS-1 and 2). The PALSAR-1 data was acquired through an ESA Category-1 (research) project, while the PALSAR-2 data was obtained from the Japanese Space Agency (JAXA) via the fourth Research Agreement for ALOS-2.

The North Sinai area has been chosen as a suitable desert test area given the extent and homogeneity of its desert land cover, its lack of development, while still containing some infrastructure, and its archaeological significance as a land bridge between Egypt and the Levant.

5.1 Study Area

5.1.1 North Sinai Geography, Geology and Climate

The study area includes the arid, sand covered regions of North Sinai and is bounded by the Nile Delta in the northwest and Suez in the southwest, by the Negev Desert in the east, and the Mediterranean coast to the north (see Figure 5.1).

The climate of the study area is between hyperarid in the southwest, to arid in the northeast (Mohamed 2013). It is characterized by hot dry summers with a temperature average of 33° C in August to 10° C in January, and the temperature regimes have been defined as torric and thermic (El-Shazly and Abdel-Gaphour 1990). The average annual evapotranspiration is around 100 mm per year, and the average annual rainfall is about 140mm at El Arish (Gad et al. 2015). Elsewhere along the Mediterranean coast, annual averages are 67mm at Port Said, to the west of the study area (Tsoar 1995), and 200mm at Rafah, to the east of the study area (Abdel-Galil et al. 2000). At Gebel Maghara, further south, the mean annual rainfall drops to around 50mm (Ahmed 2010), and in the southernmost parts of the study area it drops further, and does not exceed 28 mm per year (Hermas et al. 2012).

The area is composed mainly of Aeolian sand dune fields and interdune areas. This is referred to as the northern Sinai dune field, or the Sinai-Negev erg (Muhs et al. 2013, Roskin et al. 2014). The sand dunes include barchans, transverse, and linear dunes. Linear dunes are the main Aeolian form in North Sinai (Hermas et al. 2012). Only in a small part of the study area, in the Negev Desert, are there vegetated linear dunes (Siegal et al. 2013). There are also some exposed rock formations including the Um Khushaib, El Maghara, and El Halal mountains. Figure 5.2 shows a DEM of the area from SRTM 3 arc-second (90m spatial resolution). Heights range from sea level, by the coast, to 900m in Gebel El Halal. Wadi El-Arish is the only wadi that dissects the northern Sinai dune field.

The northern Sinai dune field covers a substantial area from the east of the Nile Delta to the Negev in Israel, with dune heights sometimes exceeding 30m (Gad 2004). The dune crests extend in a general west-east orientation, apart from in the southwest, where dunes extend in an east-southeast orientation (Tsoar et al. 2004, Roskin et al. 2014). Measurements of wind and sand dune elongation, and the continuous availability of sand supply have been stated to imply that the dynamics of Sinai sand movement are mainly dependent on wind strength (Roskin et al. 2014). Strong south-eastern eolian sand transport drift potentials were calculated for the period 1987 to 1993 from meteorological measurements at Port Said airfield, and annual monthly average wind speeds of 7.4 to 10 ms⁻¹ were measured between the years 1989 to 1999 (Roskin et al. 2011). Measured winds from the central and eastern parts of north Sinai indicate that the strength of wind decreases to the east towards the Negev. These winds may be the cause for the presence of non-vegetated linear dunes in the western part of the northern Sinai dune field, which are elongating to the south-southeast by several meters per year (Tsoar et al. 2004). In the southwest of the study area dune migration rates have been measured to reach a maximum of 27.3 meters per year (Hermas et al. 2012). Elsewhere, elongation rates are generally in the range of 2 to 15 meters per year (Misak and Draz 1997, Tsoar et al. 2004) and tend to decrease from west to east (Roskin et al. 2014). Only limited sand is transported into the north-west Negev dune field (Allgaier 2008).

The coastal dunes are characterised by a lighter colour and a coarser grain size than the inland dunes in Sinai (Tsoar 1976). Many studies have been carried out to determine the origin of the northern Sinai dune field and most agree on a Nile source (Goring-Morris and Goldberg 1990, Amit et al. 2011, Roskin et al. 2011). While this has mainly been assumed from lack of other plausible evidence (Tsoar et al. 2008), recent empirical studies have shown evidence of a Nile origin, with a minor contribution from the Wadi El-Arish drainage system, through comparisons of the mineralogical composition of sands of the

5. Archaeological Prospection Using SAR in North Sinai Desert

Nile Delta, Wadi El-Arish, and Sinai-Negev erg. Both the Nile Delta and Sinai-Negev erg are rich in quartz, and contain similar small proportions of K-feldspar and plagioclase (Muhs et al. 2013). Stratigraphic studies show that dune incursions in the Sinai-Negev erg began in the Last Glacial period. At this time the Nile Delta area was a broad, sandy, sparsely vegetated plain, with seasonally dry anastomosing channels. These conditions were ideal for providing a ready source of sand, driven by glacial-age winds which were probably much stronger than the present. The Nile River began to aggrade with post-glacial rise in sea level, with sedimentation dominated by fine-grained silts and clays. This coincides with the timing of dune activity in the Sinai-Negev erg (Muhs et al. 2013). Studies using radiocarbon dating (Goring-Morris and Goldberg 1990), and optically stimulated luminescence (OSL) dating (Roskin et al. 2011), show that dunes of the Sinai-Negev erg were active during the Last Glacial period, the post-glacial period and the latest Holocene, but show little evidence of activity during the early-to mid-Holocene. This is similar to the history of other dunefields in the Sahara Desert-Arabian Peninsula region (Muhs et al. 2013).

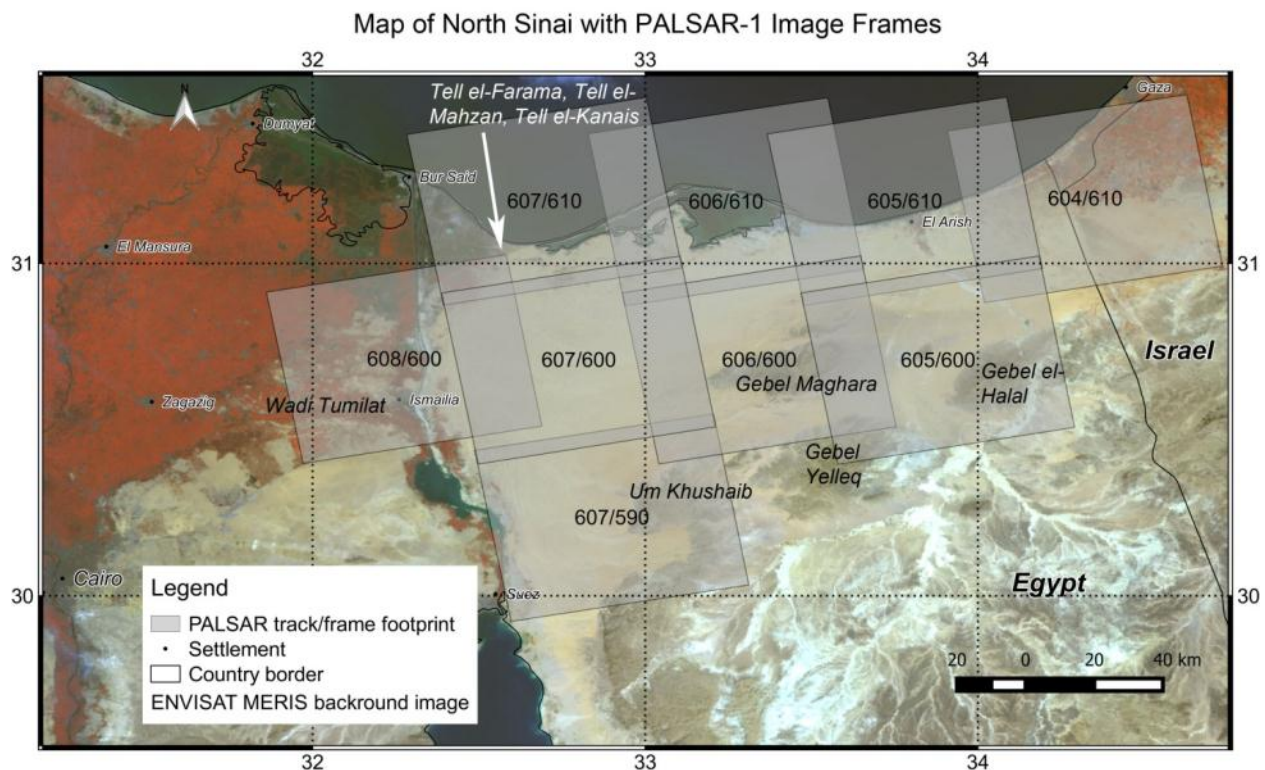


Figure 5.1. Map of the study area. Background image is a near-infrared and visible false colour composite of the ENVISAT Medium Resolution Imaging Spectrometer (MERIS). 300 m resolution. Band 10 (754 nm) displayed as red, band 5 (560 nm) as green, and band 2 (443 nm) as blue. Overlain on the MERIS image are the footprints of the PALSAR-1 images used for the mosaic, with their corresponding track/frame identification numbers. Data provided by ESA.

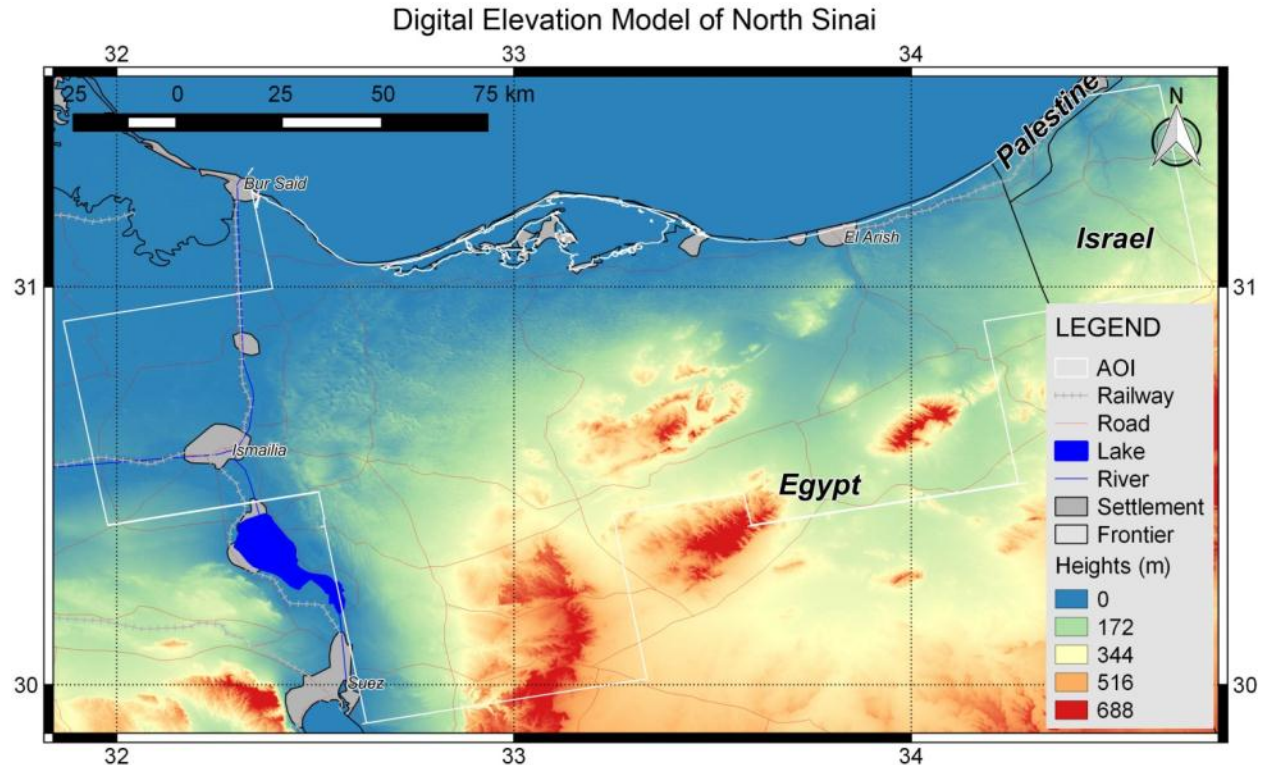


Figure 5.2 DEM of study area obtained from SRTM version 4, 3 arc-second (90m spatial resolution). Heights above sea level are shown in a colour scale from blue (0m above sea level) to red (maximum heights).

5.1.2 North Sinai Archaeology

As a land bridge connecting Africa and Western Asia, the Sinai Peninsula has been traversed and inhabited since prehistoric (Paleolithic) times (Mumford 2015).

Along the Mediterranean coast of Sinai a well-known land route existed as early as the mid-4th millennium BC (Oren 1989). Throughout the 2nd millennium BC, especially in the New Kingdom, this coastal route, known also as the “Way of Horus” or “Via Maris”, became the most travelled commercial and military road between Egypt and the Levant, with the erection of a series of forts along its course (Oren 1987, Hoffmeier and Moshier 2013). Many campsites and way stations from the 4th to 2nd millennium BC have been unearthed (Oren 1989), together with military fortifications from the New Kingdom to the Greco-Roman times. Towns, agricultural farmsteads, and irrigation canals continued to be developed in this region through later periods.

Ancient routes also existed further inland. An east–west route, the “Darb el-Hajj” or “Via Regia,” is known mostly from the Iron Age, but was possibly used since late prehistory for the exchange of copper ore from both the Wadi Arabah deposits (Timna and Faynan) and the Sinai desert to the Nile Valley (Abdel-Motelib et al. 2012). The present research team postulates, as suggested elsewhere (Hoffmeier 2012), that a route may have travelled from the Beersheba area in northern Negev, passed the limestone escarpments of Gebel Meghara and Gebel Halal, and continued along the Wadi Tumilat, a main entry point to Egypt (near the modern city of Ismailiya) (Tassie and van Wetering 2012). The

movement of Asiatics (the so-called Amw, ‘amu’) along these inland desert paths, and the consequent penetration of people from western Asia in the Nile Valley, are documented by both Egyptian literary (Hoffmeier 2014) and pictorial sources (Mourad 2014), and by the retrieval of Asiatic materials along the Wadi Tumilat. This way also represents the scenario of the biblical Exodus (it can be tentatively associated with the biblical “Way of Shur”) (Hoffmeier 2014). To this day, the route through North Sinai from the Wadi Tumilat to the south of Gebel Meghara constitutes one of the main alternatives to the coastal route.

In central-southern Sinai, mining sites related to the presence of copper and turquoise have been brought to light, as well as camps and villages from as early as the 4th millennium BC. Early settlement sites and ancient Sinaitic campsites of various periods have been found in this area. With dry masonry walls, and rooms, yards, and enclosures of varying circular forms, their shape resembles modern Bedouin camps in both the Negev and Sinai (Beit-Arieh 2003).

More modern structures exist in the form of roads, canals, powerlines, airfields, industrial, and residential centres. Much military hardware has been deposited in Sinai, particularly during contemporary period conflicts, such as the Six Day War (Dunstan 2012) and in more recent times (Gold 2014).

Despite the many surveys that have been carried out in the region, e.g., (Oren 1980, Valbelle 1989, Arthur and Oren 1998), systematic and large-scale surveys remain a challenge due mainly to the large extent of inhospitable and inaccessible terrain, and the frequent security threats (Gold 2014). Another challenge with archaeological survey throughout Egypt is that sites that have previously been surveyed and uncovered are sometimes lost again beneath the sand (Di Iorio et al. 2010). Sand drift and dune migration affect much of North Sinai. The burial of modern infrastructure is a common and serious problem (Misak and Draz 1997, Hermas et al. 2012). The use of spaceborne SAR to regularly survey large areas could potentially constitute a cost-effective technique, and given the transmissivity of dry sand to microwave wavelengths, may uniquely provide information on structures obscured by sand.

5.2 PALSAR-1 Data

A total of 74 PALSAR-1 images were procured for the analyses covering nine image tracks and frames in the PALSAR-1 Fine Beam (FB) mode (see Table 5-1, Figure 5.1, Table A-4 and Table A-5 in APPENDIX A). The imagery was obtained through an ESA Category-1 (research) project, with project ID: C1F11458. Given the image quotas, and the fact that the images covering frame 610 only included a small strip of coastline (the rest being over water), only two images were procured for each of the coastal frames, while over all other frames seven images were obtained to enable good multitemporal speckle filtering. The image mode chosen was Fine Beam Dual polarization mode (FBD) to benefit from both the Horizontal Transmit, Horizontal Receive (HH), and Horizontal Transmit, Vertical Receive (HV) polarisations. Due to the low signal to noise ratio of the HV polarization, the mosaic, and subsequent analysis, was done with the HH polarization. Once the subset areas were identified, further imagery was procured covering these areas in both FBD and Fine Beam Single (FBS) sensor modes. The FBS imagery included HH polarization only. The imagery of track 607, frame 590 was included towards the end of the

5. Archaeological Prospection Using SAR in North Sinai Desert

analysis, and comprised only FBS imagery, given that it was intended only for the mosaic in HH polarization. All images were acquired while the satellite was ascending, right looking, and all Fine Beam imagery with an incidence angle of 38.7 degrees. The PALSAR-1 Polarimetric image was acquired with an incidence angle of 23.9 degrees (see footprint in Figure 5.3). ALOS was launched in January 2006, and following a period of satellite commissioning, acquired data until April 2011 (JAXA 2011). Imagery over most tracks and frames were thus available from 2007 to 2010 or 2011.

Table 5-1. PALSAR-1 data characteristics. For the scene IDs of all data, see Table A-4 and Table A-5 in APPENDIX A

Number of scenes	Sensor mode and polarisation	Acquisition date range (yyyy/mm)	Scene Center Incidence Angle	Pass	Track/Frame (see Figure 1 for Location)
2	FBD (HH/HV)	2007/09 to 2010/06	38.7	Asc	604/610
7	FBD (HH/HV)	2007/06 to 2010/06	38.7	Asc	605/600
2	FBD (HH/HV)	2007/06 to 2010/05	38.7	Asc	605/610
7	FBD (HH/HV)	2007/06 to 2010/09	38.7	Asc	606/600
2	FBD (HH/HV)	2007/06 to 2010/06	38.7	Asc	606/610
8	FBS (HH)	2007/10 to 2011/02	38.7	Asc	607/590
21	10 FBS (HH), 11 FBD (HH/HV)	2007/06 to 2011/02	38.7	Asc	607/600
19	10 FBS (HH), 9 FBD (HH/HV)	2007/06 to 2011/02	38.7	Asc	607/610
7	FBD (HH/HV)	2007/11 to 2010/04	38.7	Asc	608/600
1	Polarimetric (HH/HV/VV/VH)	2009/04/08	23.9	Asc	See Figure 5.3

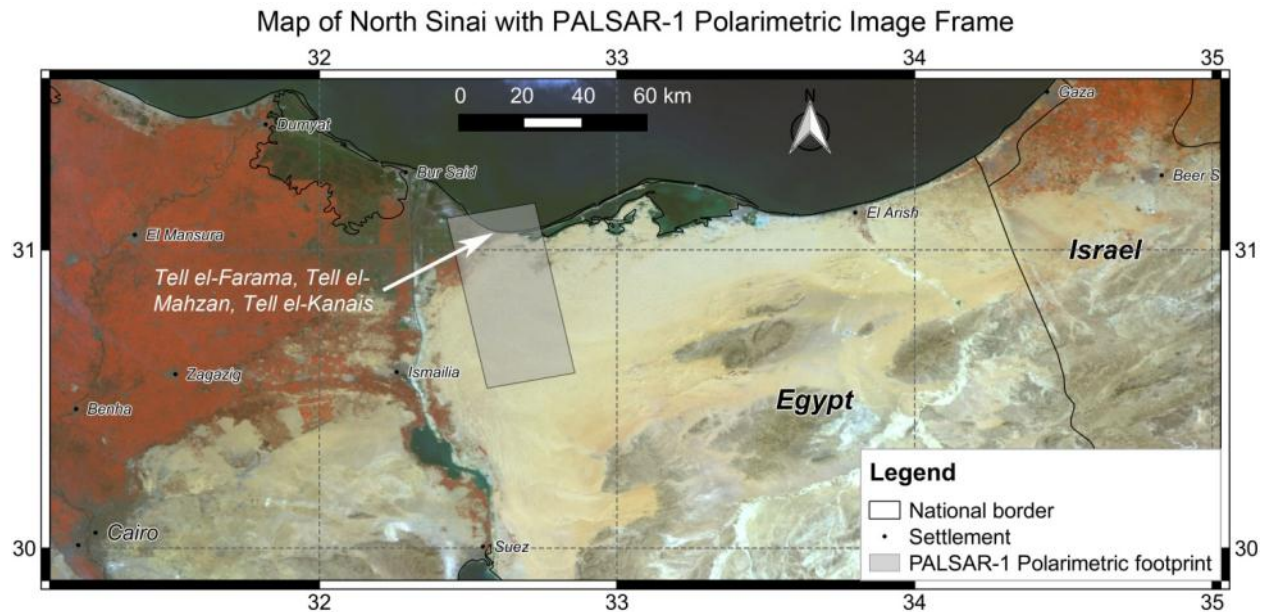


Figure 5.3 Map of the study area with PALSAR-1 Polarimetric image footprint overlain. Background image is the same MERIS NIR,R and G image as shown in Figure 5.1. MERIS data provided by European Space Agency (ESA).

5.3 PALSAR-2 Data

Eight new PALSAR-2 acquisitions were tasked on request to JAXA in the framework of the 4th JAXA Research Agreement for ALOS-2. Of these, seven were successfully acquired over Tell El-Farama, Tell El-Mahzan and Tell El-Kanais (see Figure 5.4) in August and September 2015 (see Table 5-2, and Table A-6 in APPENDIX A). Four of the images were acquired with an incidence angle of 49 degrees and three with an incidence angle of 40 degrees. All the images were acquired in descending node, right looking, and with HH polarization. The slant range pixel spacing of the images in Single Look Complex (SLC) format are 1.4 m in range and 0.9 m in azimuth.

Table 5-2 Acquisition dates and incidence angles of PALSAR-2 Spotlight images used for the analysis of Tell El-Farama, Tell El-Mahzan, and Tell El-Kanais. All were acquired in descending node, right looking, and with HH polarization. See and Table A-6 in APPENDIX A for the scene IDs of individual images.

Acquisition Date	Incidence Angle (Degrees)	Pass	Polarisation
5 August 2015	49	Des	HH
10 August 2015	40	Des	HH
19 August 2015	49	Des	HH
16 September 2015	49	Des	HH
21 September 2015	40	Des	HH
30 September 2015	49	Des	HH
5 October 2015	40	Des	HH

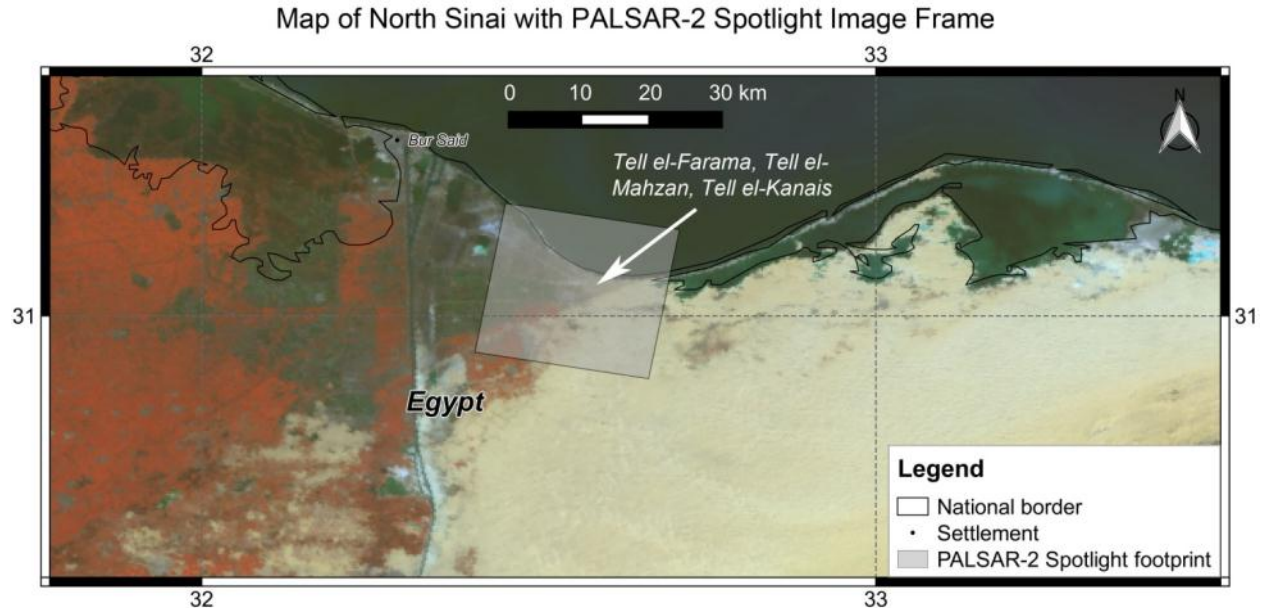


Figure 5.4 Map showing PALSAR-2 Spotlight image footprint. Background image is the same MERIS NIR,R and G image as shown in Figure 5.1. MERIS data provided by European Space Agency (ESA).

5.4 Methodology

Figure 5.5 is a diagram summarizing the methodology for anthropogenic feature extraction. The SAR satellite data processing involved first the creation of a mosaic of multitemporal speckle filtered PALSAR-1 backscatter intensity over the study area. The purpose of this was to obtain a synoptic view of the area and to select potential areas of interest to focus further research.

An interpretation of the mosaic was carried out by the SatER team through comparison with raster and vector information layers in a Geographic Information System (GIS). These layers included geological and archaeological charts, remotely sensed optical imagery and Web Map Service (WMS) vector layers of infrastructure (roads, railways, canals, etc.). The objective of this interpretation was to evaluate any features that were uniquely identified, or better highlighted, in the mosaic. Many seemingly man-made features were distinguished by abnormally high backscatter compared to the surrounding sand. A much smaller number of potential anthropogenic structures were characterised by lower backscatter relative to surrounding areas. These were mainly confined to an area near the eastern Nile Delta and Mediterranean coast, around the archaeological sites of Tell El-Farama, Tell El-Mahzan, and Tell El-Kanais (see Figure 5.1). It was decided therefore to focus further research on two Areas of Interest (AOIs):

- AOI 1: The region between the Wadi Tumilat and El Maghara Mountain (Gebel Maghara) (see Figure 5.1). This comprises an area of mobile sand dunes traversed, probably since antiquity (see Section 5.1.2) to the present. Many anomaly linear features of high relative backscatter were identified in this region.
- AOI 2: The area of Tell El-Farama, Tell El-Mahzan, and Tell El-Kanais. This is where features of low relative backscatter were found, which possibly correspond to archaeological structures.

Over AOI 1 a linear feature detection algorithm was designed and implemented to extract the abundant linear features of high backscatter. Conversion of these to vector format facilitated comparison and analysis with other layers in the GIS.

Over AOI 2, a time series of PALSAR-2 Spotlight imagery was procured to complement the existing data. Processing included a range of multitemporal techniques to better extract the low backscatter anomaly structures. These were then interpreted through comparison with other information layers, and with the results of previous archaeological survey in the area.

Methodology

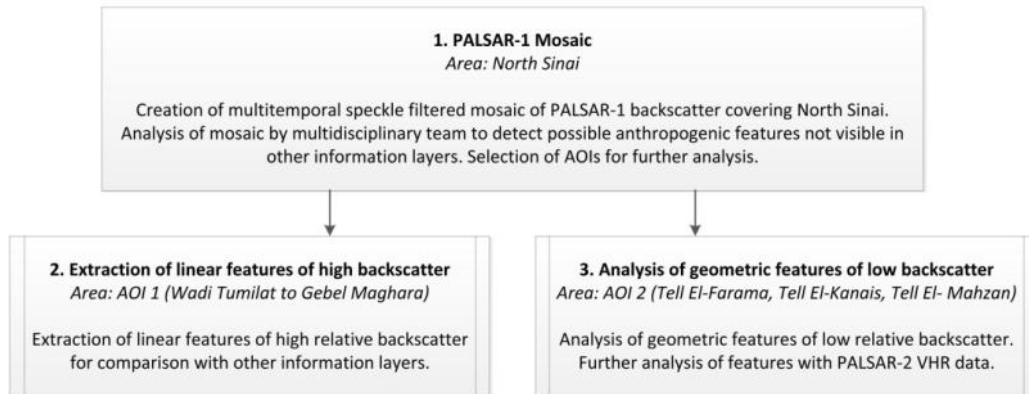


Figure 5.5 Diagram summarising methodological steps. Each step is described in a separate section: Step 1 in Section 5.4.1, Step 2 in Section 5.4.2, and Step 3 in Section 5.4.3.

The sections below describe the processing methodology for the mosaic and each of the two AOIs.

5.4.1 PALSAR-1 Mosaic of North Sinai

Figure 5.6 shows the processing chain used in the ENVI SARscape software to create the mosaic. Processing began with coregistration of Single Look Complex (SLC) data for each track/frame stack. Multilooking was then applied to produce square pixels: for FBS a multilooking of 3 in azimuth produced square pixels of approximately 10 m, for FBD a multilooking of 5 in azimuth produced square pixels of approximately 15 m.

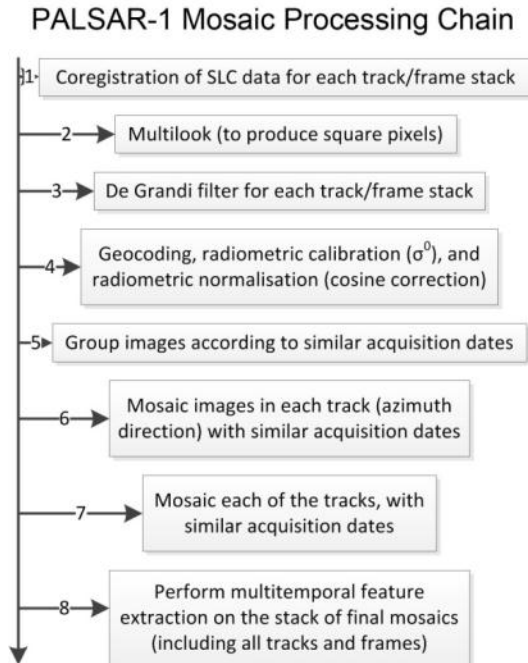


Figure 5.6 PALSAR-1 mosaic processing chain. The last step (8) included analysis of the mosaics and extraction of the mean mosaic backscatter.

De Grandi multitemporal speckle filtering (De Grandi et al. 1997) was then applied for each track/frame stack to reduce the image speckle without degrading spatial resolution. Conceptually, the De Grandi filter works by averaging in the temporal domain parts of images that are statistically homogenous. If such an area is interrupted by the appearance of a feature in one or more images, the areas to be averaged are divided to exclude this feature (De Grandi et al. 1997). The De Grandi filter is thus suitable for preserving small-scale structures in individual images, whilst averaging surrounding areas of homogenous backscatter. This filter was therefore chosen over various other filters which were attempted, including the Anisotropic Non-Linear Diffusion Filter (Aspert et al. 2007) and the multitemporal speckle filter described in (Quegan et al. 2000). The output of the De Grandi filtering process consists of the same number of images as the input.

Following De Grandi filtering, the imagery was geocoded and calibrated to σ^0 applying also radiometric normalisation (cosine correction).

The geocoding was done using the SRTM DEM version 4, at 3 arc second (90 m) resolution. Higher resolution DEMs could have been used. The Advanced Spaceborne Thermal Emission and Reflection Radiometer (ASTER) Global DEM (GDEM) is also freely available, and has a spatial resolution of 30 m (Tachikawa et al. 2011). However, it was found that the SRTM DEM was less noisy over this area. The 90 m SRTM was also favoured over the 1 arc second (30 m) SRTM, now freely available globally, given the issues with the accuracy and noise present in the 30 m SRTM (Mukul et al. 2016). Other DEMs could have been chosen, such as the TanDEM-X 12 m DEM, but this is not as accessible as the SRTM DEM, which was deemed sufficient for the purposes of the project.

The cosine correction was to compensate for near to far range backscatter variations. A correction factor, modified from (Ulaby and Dobson 1989), was applied in the SARscape software, according to,

$$\sigma_{norm}^0 = \sigma_{cal}^0 (\cos \theta_{norm} / \cos \theta_{inc})^2 \quad 5.1$$

where σ_{cal}^0 is the calibrated σ^0 , θ_{norm} is the incidence angle in the scene center, and θ_{inc} is the local incidence angle with reference to the ellipsoid.

The map system consisted in the Geographic Latitude/Longitude projection, with the WGS 84 datum. The pixel spacing was selected as 10m, to preserve the highest resolution FBS image details.

Mosaicking was then done first for each track (azimuth direction) with similar acquisition dates (the acquisition dates along the azimuth were not always identical given the varying amount of images procured for each track/frame stack). The mosaicked strips were in turn mosaicked together, again for similar dates, with mean values calculated over regions of track overlap. This resulted in a series of mosaics over the entire area for different date ranges. A final reference mosaic was created by averaging these mosaics and converting the mean backscatter to decibel.

Results of the mosaic processing, and a first interpretation by the SatER team are described in Section 5.5. The mosaic in ENVI format was imported into a GIS for comparison with a geological chart, DEMs, remotely sensed optical imagery, and WMS vector layers of infrastructure from Google Maps, Bing Maps Open Street Map and Apple iPhoto map. Export to Keyhole Markup Language (KML) format allowed overlay onto Google Earth. Using the history slider of Google Earth, it was possible to compare the mosaic with VHR optical imagery acquired, in most areas, in 2007 and 2010. This corresponded well with the PALSAR-1 time series used to create the mosaic, which included imagery acquired from 2007 to 2010/2011.

A number of features evident only in the PALSAR-1 mosaic were discovered following this initial analysis. These included two different types of anomaly: anomalies caused by low backscatter relative to the surroundings and by high relative backscatter. The anomalies of low relative backscatter were confined to a coastal region in the northwest of the study area, around the archaeological sites of Tell El-Farama, Tell El-Mahzan, and Tell El-Kanais. The anomalies caused by high relative backscatter can be seen throughout the mosaic, but are predominantly present in the region between the Wadi Tumilat and Gebel Maghara. This area is of particular interest given its strategic location, possibly since antiquity, as a southern route linking the Wadi Tumilat to Beersheba in northern Negev (see Section 5.1.2 above).

5.4.2 Extraction of Linear Features of High Backscatter over AOI 1

Many of the features of high relative backscatter in the area between the Wadi Tumilat and Gebel Maghara are in linear form. The backscatter properties of known natural linear objects (such as sand dune ridges) and artificial linear objects (such as roads and power cables) are very similar in the mosaic. A comparison of the mosaic with other information layers (optical imagery, geological charts, and WMS vector layers) revealed that many linear features correspond to roads or tracks. In some cases, these are very clearly visible in the optical remote sensing imagery and WMS vector layers. In other cases, they are

only barely visible in some of the available VHR optical remote sensing imagery, such as that provided by Google Earth, and do not appear in any of the other vector or raster layers procured for the analysis. Assuming a user would be interested in extracting traces of man-made features from SAR imagery, a method would be required to separate these from natural features of high backscatter. Not all linear features of high backscatter necessarily correspond with routes. They may equally well be objects such as pipelines, military structures, thin metal fences, or cables that do not appear on infrastructure maps. These may be buried or at the surface, but too small to be visible in VHR optical imagery, yet cause high backscatter due to their geometry or dielectric properties. To facilitate interpretation of these features, first the abundant linear features corresponding to natural objects need to be removed. Next a spatial analysis of the remaining linear features needs to be undertaken to better determine from their course, and from other information layers, what they are, and whether they are buried or still in use. Such filtering and analysis can be performed more easily if the linear features are in vector format. This can be achieved by manually digitizing the linear features, but given their abundance, a more feasible approach would be to extract and convert them automatically. An automatic algorithm was thus devised to extract anthropogenic linear features of interest from the SAR imagery and convert them from raster to vector format.

The concept of the linear feature extraction algorithm is to detect man-made features in a desert region characterized by a relatively large area with similar land cover (such as the case of North Sinai), but recognizing that parts of the feature may be buried, eroded or for any other reason no longer visible in the satellite imagery, and that they are likely to wind and deviate from a straight line.

The algorithm (implemented in IDL and Matlab) has, as its base, a simple mathematical morphological filter, such as the type described in (Quackenbush 2004). To detect long and possibly discontinuous linear features, a large kernel was used (31 x 31 pixels) without requiring all pixels in a particular orientation to detect the feature. Linear features, such as paths, clearly may not all follow a very straight line, but they are expected to cover distances beyond the length of the 31 pixel kernel. The basic filter functions as follows:

Pixels are compared iteratively along straight lines of all angles in a moving 31 × 31 pixel window with pixels outside each line in the same moving window. The pixel at the centre of this window is flagged as belonging to a line if two tests both result positive:

1. The mean value of pixels along a straight line of any orientation is greater than a threshold factor (1.6) multiplied by the mean value of pixels outside the line of the same orientation.
2. The standard deviation of pixels along a line of the same orientation is less than a second threshold (0.6).

Initially, the tests above were performed on the mosaic of average σ° backscatter. One problem encountered using this data as input was a difficulty in distinguishing the backscatter over apparently man-made linear features of interest from the backscatter over sand dunes. At small incidence angles, peak backscatter usually occurs at the incidence angle equal to the angle of repose of sand dunes (Blom

and Elachi 1987). Particularly for sand dunes oriented along the SAR azimuth direction, a line of bright pixels can be seen along the dunes. Having a line detection algorithm distinguish these from man-made linear features is particularly challenging. To overcome this problem, steep sand dunes were masked out by setting a threshold on the Local Incidence Angle variance over a moving window, calculated from the same SRTM DEM used for the terrain correction of the mosaic.

Results showed improved performance with the steep sand dunes masked out. In an attempt to improve further the results a different technique was attempted using interferometric coherence. Instead of taking the average σ° backscatter as input, the average interferometric coherence of all consecutive image acquisitions was used instead. The average coherence showed an even better distinction between bright linear features (high coherence) and surrounding sandy areas (low coherence). Moreover, the appearance of linear features over sand dunes was much less apparent. Consequently, the linear feature detection algorithm was applied instead to this dataset with greatly improved results, without the need for masking out sand dunes (Stewart et al. 2016a). Figure 5.7 summarises the initial method applied with the average σ° backscatter as input, while Figure 5.8 shows the algorithmic steps of the final approach with average coherence as input.

Automatic Linear Feature Extraction Algorithm with Average De Grandi Filtered σ^0 as Input

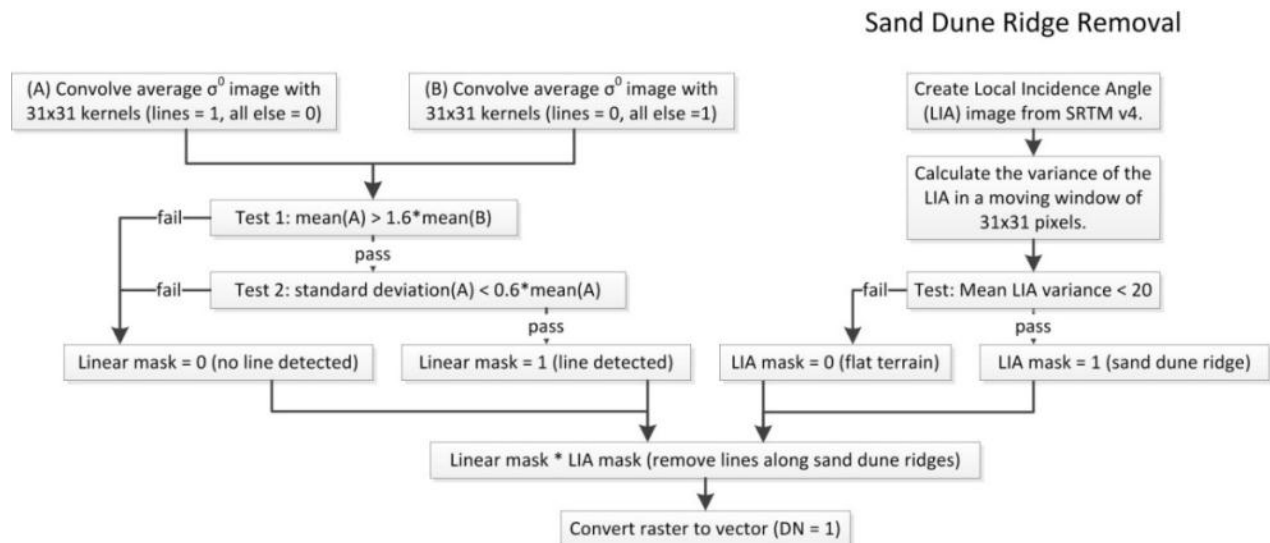


Figure 5.7 Linear feature detection algorithm with PALSAR-1 average, De Grandi filtered σ^0 as input and with local incidence angle mask from SRTM DEM

Automatic Linear Feature Extraction Algorithm with Average Coherence as Input

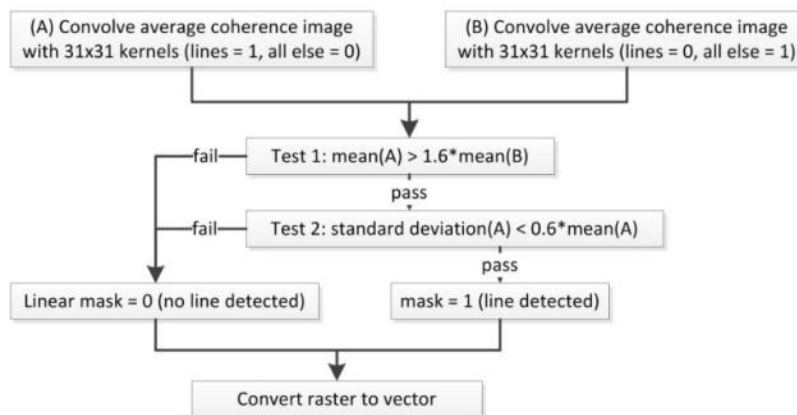


Figure 5.8 Linear feature detection algorithm with PALSAR-1 average coherence as input. With the average coherence as input there is no longer a need for the local incidence angle mask to remove sand dune ridges.

Various standard edge and line detection algorithms were applied initially, including those based on the Hough Transform, e.g., (Iisaka et al. 1995), and on template matching (Quackenbush 2004), but it was found that for this particular area and dataset, the custom approaches outlined above (particularly with average coherence as input) proved the most effective at extracting the linear features whilst avoiding false positives arising from natural features. A drawback of the algorithm is that it is quite computationally demanding. It requires convolution with the SAR coherence image of 2 (for line = 1 and line = 0) $\times 61$ (for all angles) $\times 31 \times 31$ pixel kernels.

5.4.3 Analysis of Geometric Features of Low Backscatter in AOI 2

5.4.3.1 Time series analysis on single polarisation images

The anomalies caused by low relative backscatter were confined to a relatively small area around the archaeological sites of Tell El-Farama, Tell El-Mahzan, and Tell El-Kanais (see Figure 5.1). Given the small scale of the features, it was considered appropriate to procure higher resolution datasets. A request was therefore made to the Japanese space agency (JAXA) to task acquisitions of PALSAR-2, in Spotlight mode, over the study area. Section 5.3 above describes this data.

The processing carried out on the time series of SLC imagery included the following:

1. Extraction of subset SLC images over the Tells
2. Multilooking: given the small variation in incidence angle, the same factor of 2 in azimuth could be applied to all images to produce a square ground range pixel spacing of approximately 2m
3. Coregistration
4. De Grandi multitemporal speckle filtering
5. Geometric correction and calibration: geometric correction to geographic latitude/longitude, WGS 84, with a pixel spacing of 1.5m. Calibration to σ^0 (in both dB and linear units)
6. Extraction of the following images calculated from the entire filtered time series (in both dB and linear):
 - a. Mean
 - b. Standard deviation
 - c. Gradient: maximum absolute variation between consecutive acquisition dates
 - d. Maximum
 - e. Minimum
 - f. Span difference: difference between the maximum value and the minimum value of all input data
 - g. Maximum increment between consecutive acquisition dates
 - h. Maximum decrement between consecutive acquisition dates
 - i. Span ratio: the ratio calculated between the maximum value and the minimum value of all input data
 - j. Maximum ratio: maximum value (max backscatter increment) among all ratios calculated between consecutive acquisition dates
 - k. Minimum ratio: minimum value (max backscatter decrement) among all ratios calculated between consecutive acquisition dates
 - l. Mu Sigma: mean/standard deviation ratio
 - m. Coefficient of variation: standard deviation/mean ratio
7. Average coherence generation (taking results of step 1 as input)
 - a. Coregistration of SLC data for each incidence angle separately
 - b. Coherence generation of consecutive acquisitions for each incidence angle stack
 - c. Multilooking by the same factor as above
 - d. Averaging multilooked coherence images within each stack

- e. Geometric correction to same map system as in step 5.

Steps 6 and 7 were also carried out on the PALSAR-1 FBS and FBD imagery, which had already been processed up to Step 5 for the mosaic. The purpose of Steps 6 and 7 was to determine whether any of these multitemporal techniques could enhance the visibility of features of low backscatter relative to surrounding areas. On the assumption that the low backscatter was caused by signal attenuation in sand, it was hoped that the contrast between volume scattering (over the low backscatter features) versus surface scattering (over surrounding areas) may be enhanced through time series analyses or through interferometric coherence.

All final imagery were analysed by the SatER team. Comparisons were made between the various results of the processing, together with optical remote sensing datasets (Pleiades, Kompsat-2, Sentinel-2, and imagery available on Google Earth). An interpretation of results has been provided, taking into account all previously published archaeological survey in the region. The archaeological chart produced by Jaritz, et al. (Jaritz et al. 1996) (see Section 5.5.3) was geocoded using a second-order polynomial, with manually collected Ground Control Points (GCPs) from the available geocoded EO imagery (Pleiades, Google Earth). The geocoded map could then be overlain onto the SAR and optical datasets. Results of the analysis and interpretation by the SatER team are provided in Section 5.5.3).

5.4.3.2 Polarimetric analysis

Polarimetric processing was undertaken on the PALSAR-1 Polarimetric image. This included calculation of the covariance matrix (see Equation 2.33) in the linear, horizontal and vertical basis. From this, various polarimetric target decompositions were extracted, including: Freeman 3 components (double bounce, odd bounce, volume scattering) (Freeman and Durden 1998), Krogager 3 components (diplane, helix, sphere) (Krogager 1990), Yamaguchi 4 components (double, helix, odd, volume) (Yamaguchi et al. 2005), and H/A/alpha (Cloude and Pottier 1997). Final images were subsetted and orthorectified using the same DEM and map system as for the imagery in single and dual pol PALSAR modes. At SLC the image has a slant range pixel spacing of 9.4m and an azimuth pixel spacing of 3.4m. The incidence angle was 23.9°, yielding a ground range pixel spacing of 23.2m. A multilook of 7 in azimuth was therefore applied after polarimetric processing to produce square pixels of approximately 23m.

5.5 Results

5.5.1 Mosaic

Figure 5.9 shows the final mosaic of multitemporal speckle filtered and averaged PALSAR-1 backscatter. The Aeolian sand dune fields are characterised by very low backscatter, while higher backscatter is observed over the irrigated fields of the Nile Delta and over the exposed rock formations of Um Khushaib, Gebel Maghara, and Gebel el-Halal. In between Gebel Maghara, el-Halal, and Yelleq, there is a flat plateau where greatly varying levels of SAR backscatter correspond to varying rock and sand formations. Anthropogenic features, such as power cables, roads, and buildings are clearly visible as highly reflective targets.

5. Archaeological Prospection Using SAR in North Sinai Desert

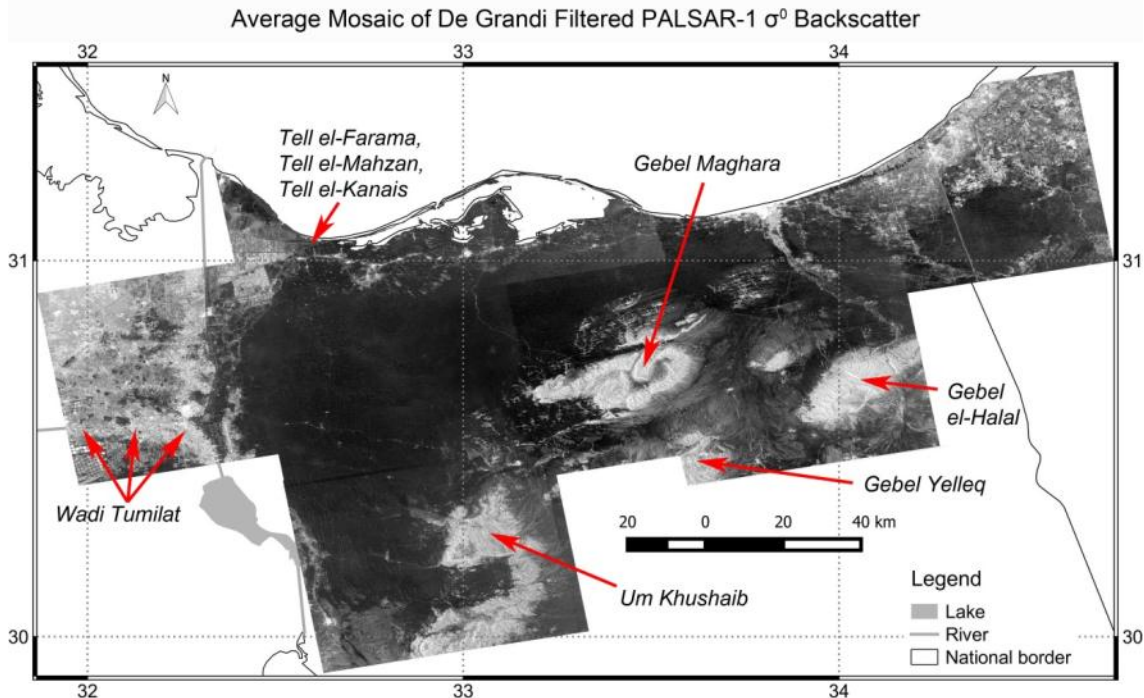


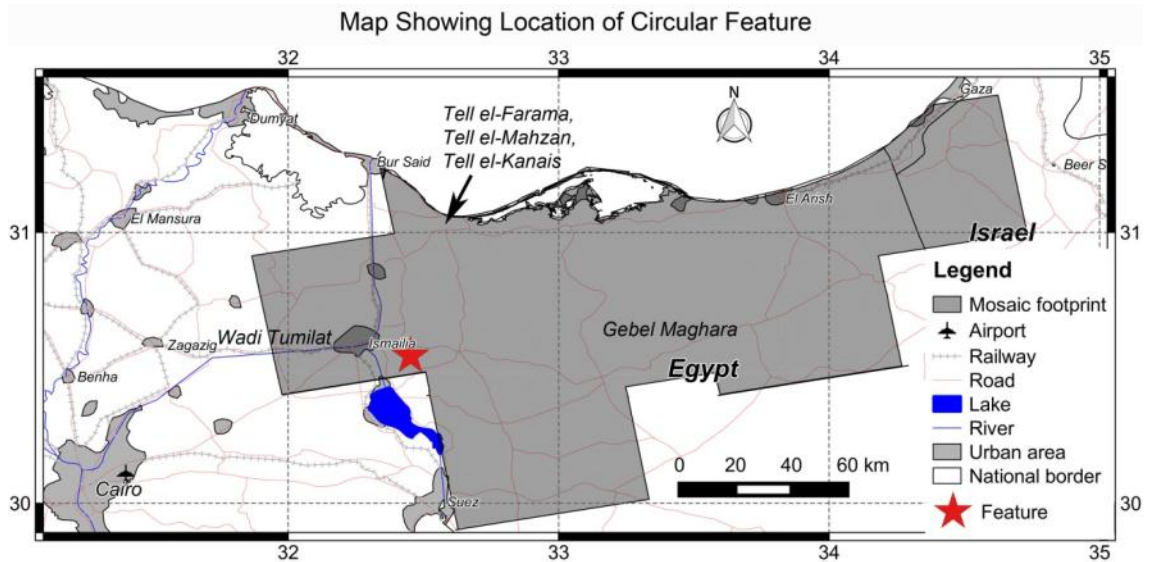
Figure 5.9 Final ALOS PALSAR-1 mosaic of North Sinai annotated with geographic features and showing the location of the Tells, where features of low relative backscatter were identified. PALSAR-1 data provided by ESA.

Analysis of the mosaic using the combined expertise of SAR remote sensing, geological, and archaeological interpretation revealed the presence of a number of features characterised by high backscatter relative to surrounding areas that were not visible in other information layers, but visible in all the intermediate PALSAR mosaics of different dates. In particular around Gebel Maghara, but also elsewhere, there are many isolated patches and patterns of bright backscatter that have been interpreted as exposed or partially buried rocks, the surfaces of which may be rough relative to the L-band (23 cm) PALSAR-1 wavelength. These are perhaps not visible in any of the available optical imagery either because they are partially buried, or because their spectral signature in the visible domain is the same as surrounding sand. They are too small to appear on the available geological chart.

Some features are in the form of concentric circles (see Figure 5.10). It is tempting to interpret these as Bronze Age structures given that their shape is very similar to early Bronze Age sites, such as those illustrated in (Arieh 1974). However, their scale in the SAR imagery is at least one order of magnitude larger (around 700 m while the early Bronze Age sites in (Arieh 1974) are from around 15 to 70 m), and therefore excludes this interpretation. They may be buried relics of military installations from past wars, such as the Six Day War (Dunstan 2012).

Many linear features of high backscatter are clearly visible. A detailed discussion of these over a subset region is provided in Section 0. In a small coastal region to the northwest of the mosaic, a few interesting features of low relative backscatter were identified. An in-depth analysis and interpretation of these is provided in Section 5.5.3. Throughout the mosaic there are also many features that are not

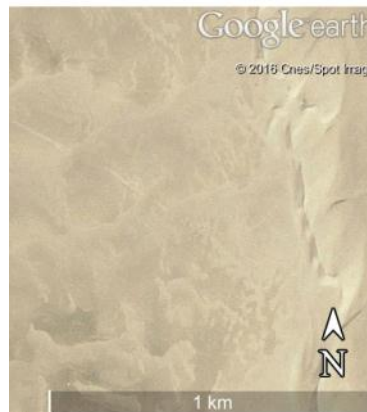
present in other information layers; these have been interpreted as image artefacts caused by sensor inconsistencies. They are discussed in Section 5.5.3.4.



(a) Circular Feature in PALSAR-1 Mosaic Circular Feature in 2007 Image on Google Earth Circular Feature in 2010 Image on Google Earth



(b)



(c)



(d)

Figure 5.10 (a) Map showing location of one of the circular features (as red star) in the context of the PALSAR-1 mosaic (grey filled polygon); (b) circular feature identified in PALSAR-1 mosaic of Average De Grandi filtered PALSAR-1 σ^0 backscatter. Feature is centred at 30.544° latitude and 32.452° longitude. PALSAR-1 data provided by ESA. (c) Optical image available on Google Earth acquired on 7 February 2007 and covering same extent as (b); (d) optical image available on Google Earth acquired on 5 May 2010 and covering same extent as (b).

5.5.2 Focus on AOI 1 (Region East of Wadi Tumilat and West of Gebel Maghara)

The desert region that lies between the Wadi Tumilat and Gebel Maghara (AOI 1) (see Figure 5.11) constitutes a sparsely developed hyperarid area, strategically located as a crossing point between routes and settlements that lie along the Wadi Tumilat and the plateau between the rock formations of Gebel Maghara and Gebel Yelleq. In this region the mosaic revealed many, particularly linear, anomaly features of higher backscatter than surrounding areas. These are in most cases identifiable in the

PALSAR-1 images only after multitemporal filtering. This is probably due to their small scale and the background of high speckle characterised by the low Signal to Noise Ratio (SNR) of the SAR backscatter over sand. Interpretation of these features is very difficult, especially lacking ground truth and the difficulty in identifying the same features in, even VHR, optical remote sensing imagery. The purpose of the linear feature extraction was to facilitate such interpretation through conversion of these features to vector format to enable easier comparison with other information layers.

Figure 5.12 shows the PALSAR-1 mosaic of average σ° backscatter over AOI 1 where many linear features are evident, this was the first input to the linear feature extraction algorithm. Figure 5.13 shows the average PALSAR-1 coherence image. Here linear features are also evident, but the sand dune crests are less sharply defined, hence constituting a better input to the feature detection algorithm.

Figure 5.14 shows vector layers from Google Maps, Bing Maps, Open Street Map, and Apple iPhoto Map overlain on a Sentinel-2 image of AOI 1. Figure 5.15 shows the extracted linear features overlain on the same Sentinel-2 image of AOI 1. A comparison of Figure 5.14 with Figure 5.15 shows that the majority of the WMS vectors correspond with extracted features. A few are very fragmented and some have not been extracted at all. Many more features have been extracted that do not correspond with any of the WMS vectors.

Using the history slider of Google Earth it was possible to view VHR optical imagery available in most of the area from both 2007 to 2010 (e.g. Figure 5.16), which corresponded well with the PALSAR-1 time series (also from 2007 to 2010). Careful comparison of the extracted features that are not present on any of the considered WMS layers with the available optical imagery reveals in many cases the presence of partially buried unpaved roads (e.g. Figure 5.16). Sand drift and dune migration covering infrastructure is a common problem throughout the region, e.g. (Misak and Draz 1997, Hermas et al. 2012). Dune migration has been studied and quantified in this area recently by Hermas, Leprince and El-Magd (Hermas et al. 2012), who detected lateral movements along the crest lines of linear dunes of up to 20 m per year. Often the extracted features do not correspond with any of the VHR optical or vector layers, despite their clear appearance in all multitemporal filtered PALSAR-1 images in the time series. In these cases the linear features may correspond with many objects that could produce a high backscatter in SAR data, but remain invisible in, even VHR, optical imagery. These could include, for example, buried or unburied metal cables, fences, pipelines, un-paved roads (with similar colour to surrounding sand), buried paved roads, and similar objects.

5. Archaeological Propection Using SAR in North Sinai Desert

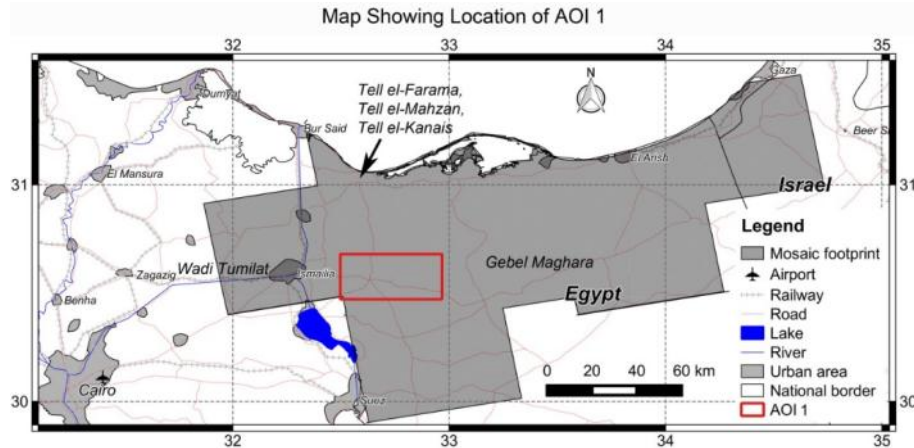


Figure 5.11 Map showing subset region (AOI 1), marked by red rectangle, east of the Wadi Tumilat and west of Gebel Maghara

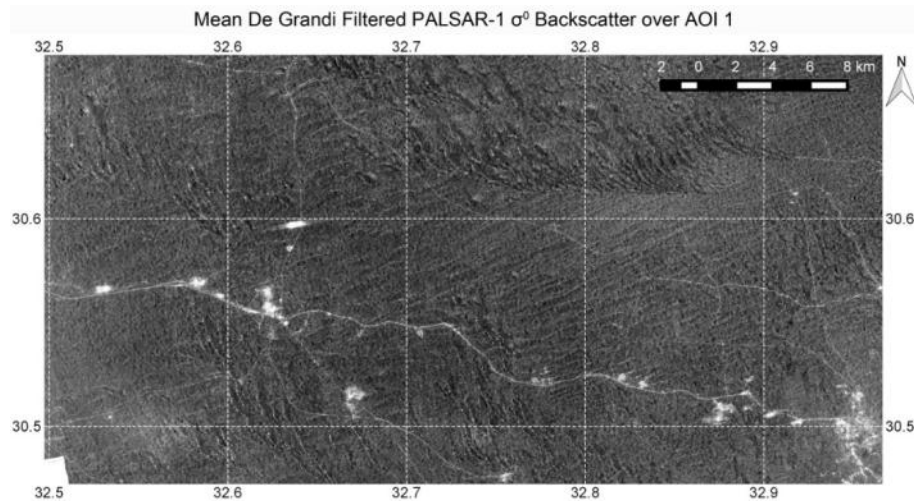


Figure 5.12 average De Grandi filtered PALSAR-1 σ° backscatter over AOI 1. This was initially used as input to the linear feature detection algorithm. PALSAR-1 data provided by ESA.

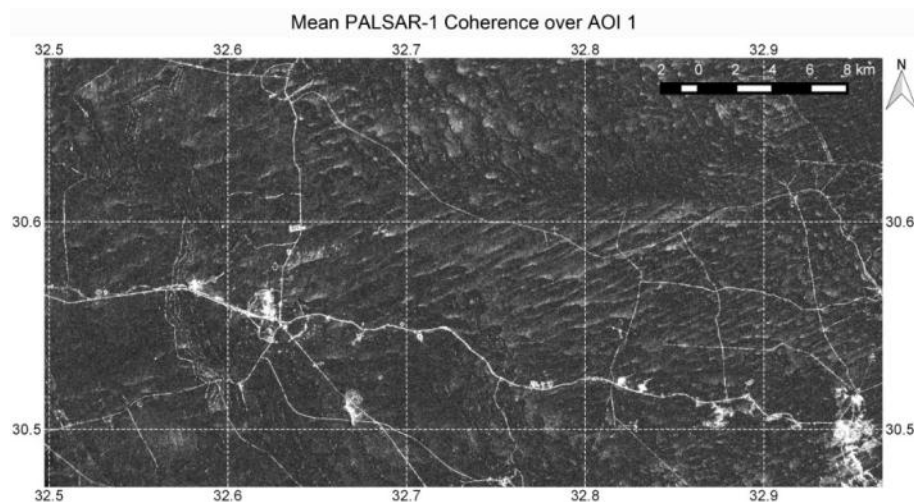


Figure 5.13 Average coherence of consecutive PALSAR-1 acquisitions over AOI 1. This was the final input to the linear feature detection algorithm. PALSAR-1 data provided by ESA.

5. Archaeological Propection Using SAR in North Sinai Desert

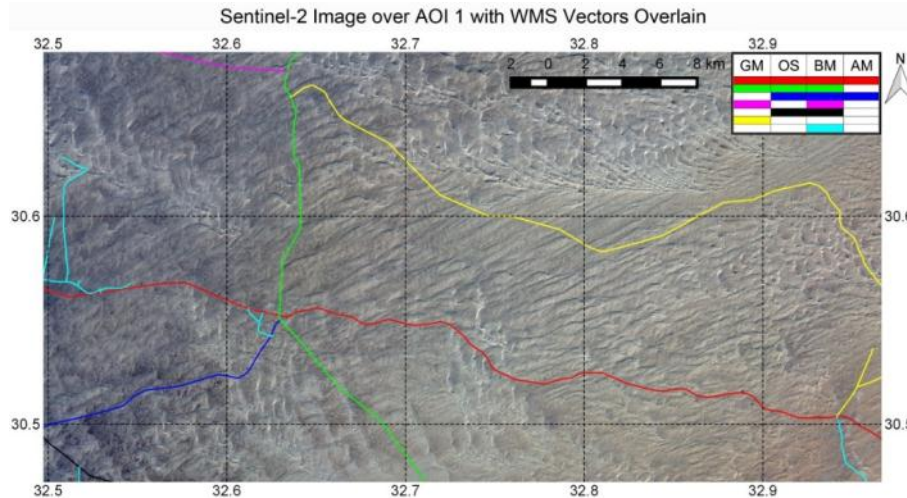


Figure 5.14 Sentinel-2 image over AOI 1 with WMS vectors (roads) overlain. Image acquired on 19 February 2016. Full resolution (10 m) true colour composite of band 4 (650 nm) displayed as red, band 3 (543 nm) displayed as green, and band 2 (458 nm) displayed as blue. All vectors correspond to roads. The only WMS vectors other than roads include an administrative boundary, but given that this does not correspond to a physical object on the ground, it is not shown here. The colour coding corresponds to the presence of the vectors on the various WMS': GM = Google Maps, OS = Open Street Map, BM = Bing Maps, AM = Apple iPhoto map. Contains modified Copernicus Sentinel data 2016.

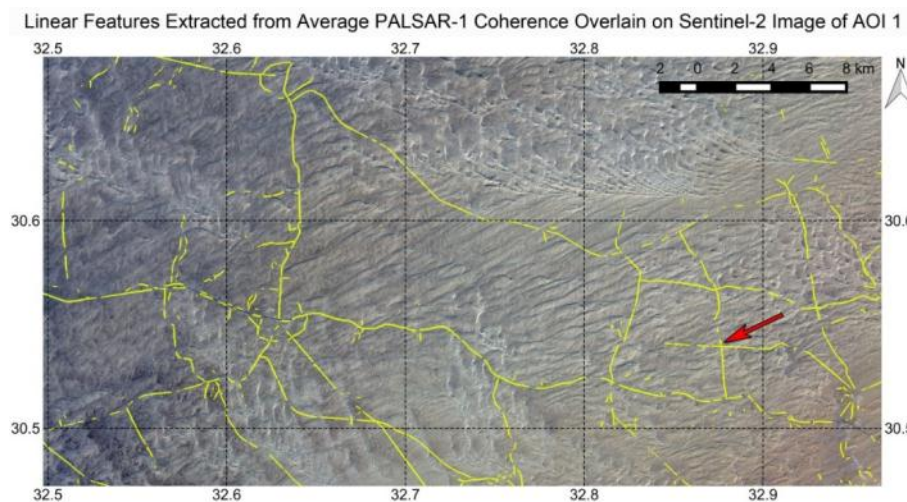


Figure 5.15 Lines extracted from average PALSAR-1 coherence (in yellow) overlain on same Sentinel-2 subset image as in Figure 5.14. Red arrow shows location of detail in Figure 5.16. Contains modified Copernicus Sentinel data 2016.

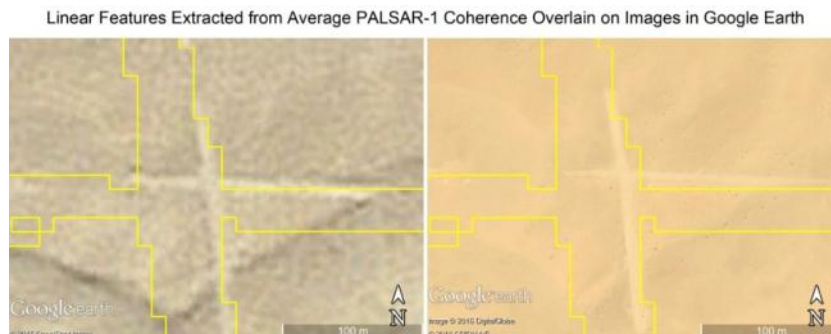


Figure 5.16 Detail of partially buried crossroads on optical remotely sensed images available on Google Earth acquired on 7 February 2007 (left) and 5 May 2010 (right). Lines extracted from average PALSAR-1 coherence overlain in

yellow. The centre of the crossroads, as identified in the SAR imagery, is located at 30.539° latitude and 32.877° longitude. The crossroads is an example of a feature not present on any of the available WSM vector layers. It appears unchanged from 2007 to 2010 and is visible in multitemporal speckle filtered PALSAR-1 imagery also from 2007 to 2010. The width of the vectors shows the coarse resolution of the PALSAR-1 average coherence image with respect to the VHR imagery on Google Earth. However, despite the PALSAR-1 coherence pixel spacing far exceeding the width of the roads, the crossroads nonetheless appears far more clearly on the PALSAR-1 average coherence than on any of the available optical layers.

5.5.3 Focus on AOI 2 (Area of Tell El-Farama, Tell El-Mahzan, and Tell El-Kanais)

Analysis of the mosaic revealed a number of anomaly features characterized by low backscatter relative to surrounding areas near the eastern Nile Delta and Mediterranean coast, around the archaeological sites of Tell El-Farama, Tell El-Mahzan, and Tell El-Kanais (see Figure 5.17 and Figure 5.18). As this area lies near the coast, and was covered only by a small part of frame 610, initially only two PALSAR-1 FBD images were procured for the mosaic (see Section 5.4.1). The anomalous features were already visible on these images. Once it was decided to focus analysis in this area, the remaining stack of PALSAR-1 FBS and FBD data over track 607 and frame 610, listed in Table 5-1, were obtained.

Tell El-Farama, Tell El-Mahzan, and Tell El-Kanais are situated along what used to be the ancient coastline and at the mouth of the now extinct Pelusiac Branch of the Nile, in the Plain of Tineh. After the stabilisation of the sea level, around 3000 BC, for several millennia the coastline followed the Pelusium Line (a transcontinental mega-shear suture) (see Figure 5.18). The Plain of Tineh was subsequently created by the seaward advance of the Pelusiac Nile Delta beyond the Pelusium Line, due to tectonic uplift (Stanley et al. 2008) around 1000 years BC (Moshier and El-Kalani 2008). Geoarchaeological studies confirm that the area evolved from an open shallow marine to a coastal setting around 1000 to 800 BC (Stanley et al. 2008). It has been stated by Moshier and El-Kalani (2008) that no archaeological sites older than Roman exist on the Plain of Tineh. The Pelusiac Branch was a distributary river in the Nile Delta that split from the main branch of the Nile (Quintanar et al. 2013). The silting up and blockage of the Pelusiac Branch has been attributed to a large and rapid influx of Nile River sediment in the early 9th century AD due to vertical tectonic motion of the lower delta plain (Stanley et al. 2008). This resulted in accretion of an extensive strand plain in the north-eastern Nile Delta margin (Goodfriend and Stanley 1999). The former Roman coastline and the ancient course of the Pelusiac Branch of the Nile have been delimited by Marcolongo (1992) (and see Figure 5.18).

Herodotus reported activity at Pelusium as early as the seventh century BC (Moshier and El-Kalani 2008). Tell El-Farama (also known by its Roman name of Pelusium) flourished in Ptolemaic and Greco-Roman times, during which it was the most important harbour in Egypt after Alexandria (Herbich 2009). Tell El-Kanais and Tell El-Mahzan were probably included in greater Pelusium. Tell El-Mahzan is located east of Tell El-Farama, at the south estuary of the Pelusiac Branch. Its height is around 7 meters. It has a circular form with a diameter of around 140m (Abd el-Samie 1992). Tell El-Kanais, which literally means “Tell of the Churches” in Bedouin, includes a series of tells east of Tell El-Mahzan. These extend several kilometres along an east-west direction (Carrez-Maratray and Wagner 1993).

The silting up of the Pelusiac Branch and the seaward migration of the coastline coincided with the decline and eventual abandonment of Pelusium, having been cut-off from the sea and the navigational

channel of the river. However, other factors have been attributed as having contributed to the decline of the city, including warfare with Persians and other invaders from the east, effects of plague, and diminished role of its commercial and trade activities following construction of Alexandria by the Greeks. After approximately 800–850 AD, Pelusium continued as a commercial center for an additional three to four centuries prior to its abandonment by the time of the Crusades (Stanley et al. 2008).

Submergence of the area by sea level rise has been counteracted by episodic fault-related uplift of this lower plain sector and continued subaerial exposure since Byzantine times (Stanley et al. 2008). The present geographical setting is that of a coastal desert with isolated sabkhas (mud flats). It is occupied by Quaternary deltaic sediments (Abu Al Izz 1977) and comprises silt and sand, covered in places with salt crusts (Jaritz et al. 1996). In most cases the climate is dry (El-Shazly and Abdel-Gaphour 1990), suggesting an aridic and torric soil moisture regime (Ibrahim et al. 1998). The preaquic moisture regime is associated with redistribution of salts and gypsum in soils formed on sabkhas characterised by an oscillating shallow water table (Ibrahim et al. 1998).

The first known archaeological study of the area was conducted in 1909, by the French Egyptologist Jean Clédat, who produced a sketch map of the area (Clédat 1913). Excavation began after Israel returned the Sinai to Egypt in 1982, under chief inspector for the North Sinai, Mohammed Abd El-Maksoud. More extensive excavation was carried out in the framework of the North Sinai Salvage Project for the el-Salaam Canal in the early 1990's (Marcolongo 1992, Stanley et al. 2008). The el-Salaam (Peace) Canal was constructed to transport Nile water to the Sinai. The canal and associated agricultural and urban development projects threatened archaeological sites in the area, as a consequence of which several rescue archaeological field expeditions were carried-out. Tell El-Farama, Tell El-Makhzan and Tell El-Kanais, were divided into concessions allocated to teams from Egypt, Canada, Switzerland, and Britain (Ibrahim et al. 1998). Since 2005, a joint Polish–Egyptian archaeology mission has been carrying out surveys in the area using geophysical prospection techniques (such as magnetometry and electrical resistivity) (Jakubiak 2012), some results of which are still unpublished. While these expeditions shed more light on the Ptolemaic, Roman, and Byzantine periods, which represent the golden age of the region, most of the area still remains unexcavated (Herbich 2009). The large extent of the area represents one challenge for archaeological surveying; another is the difficulty of access for security reasons, particularly in recent times.

Some studies have applied optical remote sensing techniques to study the wider context to aid archaeological research: for example, Marcolongo (Marcolongo 1992) used SPOT and SOYUZ satellite imagery to identify Holocene geomorphic features in the surrounding region related to archaeological sites, and Moshier and El-Kalani (Moshier and El-Kalani 2008) used CORONA optical satellite imagery to investigate the paleogeography of the region in relation to the ancient Ways of Horus. SAR analysis of the area has been undertaken for the first time by Stewart, Lasaponara and Schiavon (Stewart et al. 2013b), who interpreted a number of anomaly features as possible archaeological structures in PALSAR-1 Fine Beam and Polarimetric images. A further analysis of the area with both PALSAR-1 and 2 was published by (Stewart et al. 2016b). The work reported in these papers is the subject of the present chapter.

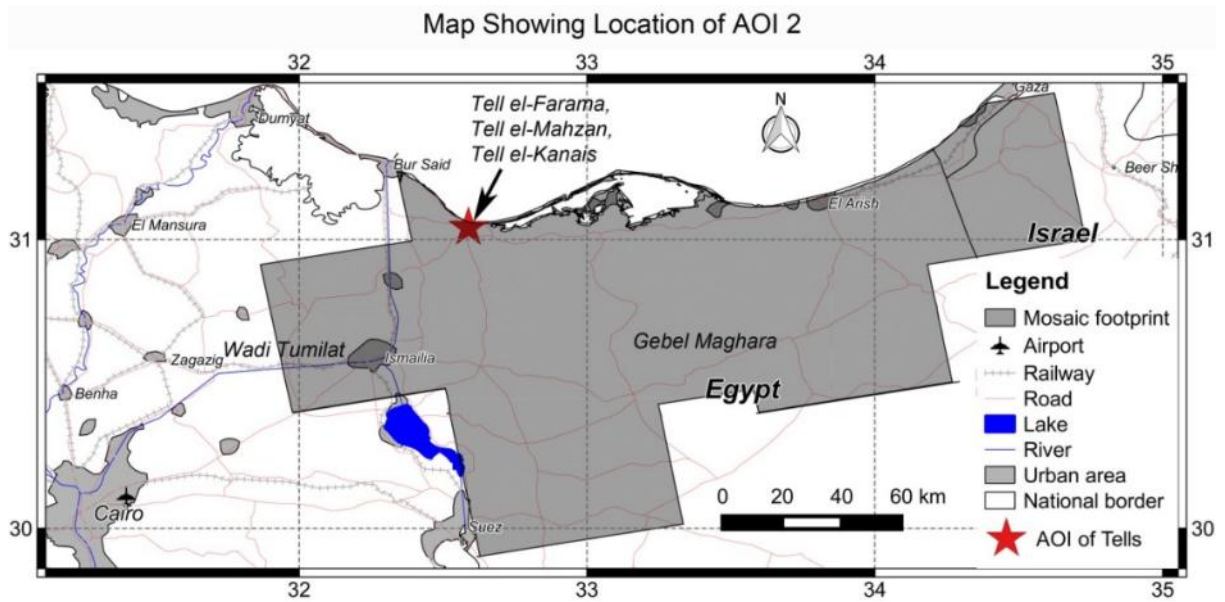


Figure 5.17 Map showing subset region of Tell el-Farama, Tell el-Mahzan, and Tell el-Kanais (AOI 2) marked by red star.

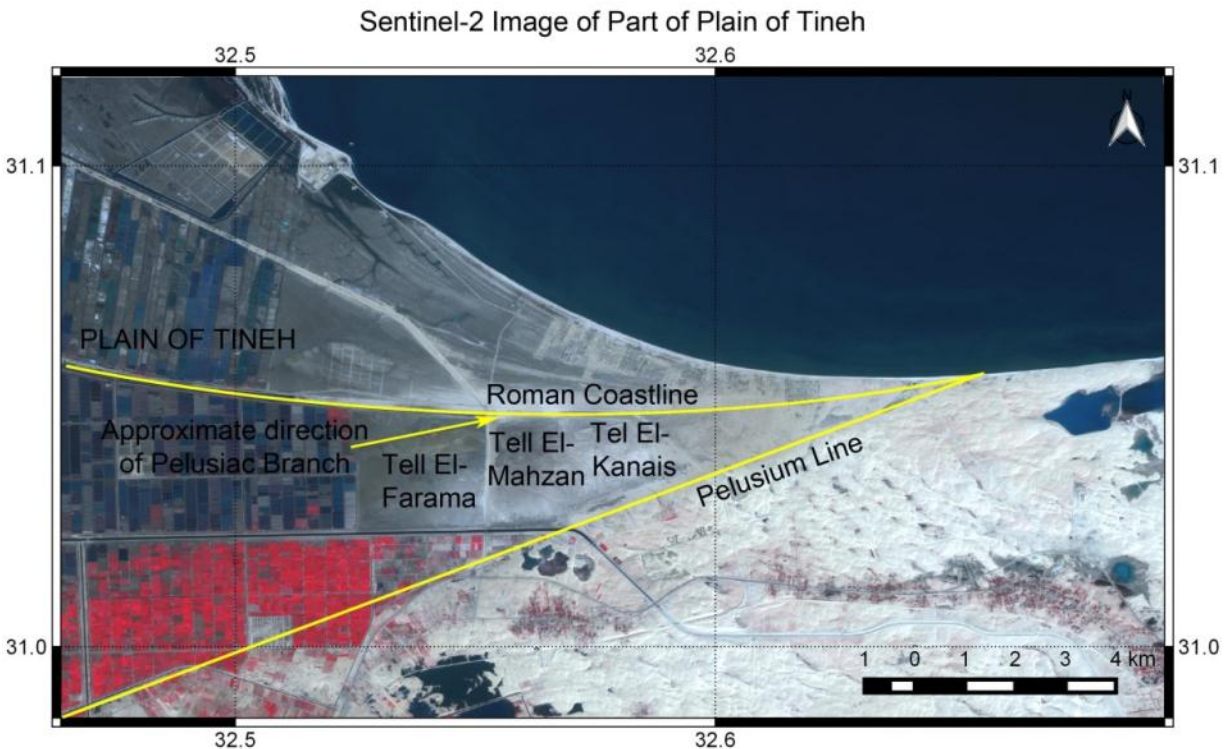


Figure 5.18 Sentinel-2 image showing the geographical context of AOI 2, which is situated in the Plain of Tineh at the Roman coastline. Image acquired on 19 February 2016. Displayed as full resolution (10 m) true colour composite of band 4 (650 nm) displayed as red, band 3 (543 nm) displayed as green, and band 2 (458 nm) displayed as blue.

In addition to the SAR data, remotely sensed optical data was used in the analysis described in the following sections. The characteristics of the optical data are shown in Table 5-3.

5. Archaeological Prospection Using SAR in North Sinai Desert

Table 5-3 Sensor names, acquisition dates, and characteristics of remotely sensed optical imagery used in the analysis of features over Tell el-Farama, Tell el-Mahzan, and Tell el-Kanais.

Sensor	Acquisition Date	Image Characteristics
Kompsat-2	11 July 2012	Four spectral bands from 450 to 900nm at 4m spatial resolution. One panchromatic band from 500 to 900nm at 1m spatial resolution (Yong and Ra 2004).
Sentinel-2	19 February 2016	13 spectral bands from 443 to 2190nm (Gascon et al. 2014), 4 of which (visible and near infrared) at 10m spatial resolution were used in the analysis.
Pleiades	24 November 2015	Four spectral bands from 430 to 950nm at 2.8m spatial resolution. One panchromatic band from 480 to 830nm at 0.7m spatial resolution (Gleyzes et al. 2012).
Imagery available on Google Earth (unknown sensor)	17 August 2003 7 February 2007 1 August 2009 26 July 2013 5 February 2016	True colour imagery

5.5.3.1 Features north of tells

Figure 5.19 is an image of the mean of all the De Grandi filtered σ^0 backscatter images of the PALSAR-1 FBD time series over the part of the Plain of Tineh where the tells are situated. A number of features of lower backscatter relative to surrounding areas are evident in this image. Some of these are in the form of geometric shapes which would suggest they are of anthropogenic origin. These are mainly situated in the area of the tells (shown on Figure 5.19). Other features appear to be of a more natural origin and may include palaeodrainage channels (such as “Fluvial Feature 1” on Figure 5.19). Figure 5.20 shows the same area on a coherence image calculated between the PALSAR-1 FBS images acquired on 19 December 2010 and 3 February 2011. The temporal baseline between these acquisitions is 46 days and the perpendicular baseline is 498m. Figure 5.21 is the same Sentinel-2 image over the area, with the same band combination, as in Figure 5.18.

One possible interpretation of Fluvial Feature 1 is that it is a palaeoriver channel. If this is the case, incident microwave radiation may interact differently with the infilled material with respect to the surrounding land cover (as described in Section 2.14.4, and illustrated in Figure 3.1). If this material has similar colour and interferometric decorrelation characteristics when compared to surrounding areas, it may not be as easy to distinguish in optical and SAR coherence images. However, palaeorivers may also be distinguished in coherence images if signal penetration is enough to cause volume decorrelation (see Section 2.13.6). In this case the infilled material may not be sufficiently dry and sandy to cause volume decorrelation. The description of the study area (see Section 5.5.3), would suggest that the infilled material may be moist and salty, thereby excluding signal penetration.

The feature labelled “Fluvial Feature 2” on Figure 5.18, Figure 5.19 and Figure 5.20 appears similar on both the Sentinel-2 and coherence images, while Fluvial Feature 1, so evident in the σ^0 backscatter image in Figure 5.19, is less visible. If the fluvial features further to the north contained water at the

5. Archaeological Prospection Using SAR in North Sinai Desert

time of image acquisitions, this would explain their clarity in both the optical and coherence images. In the coherence image it would likely be characterised by low coherence given the tendency for temporal decorrelation of water. Fluvial Feature 2 could therefore be interpreted as inundated areas.

The anomaly features situated in the area of the tells are described in more detail in the following sections.

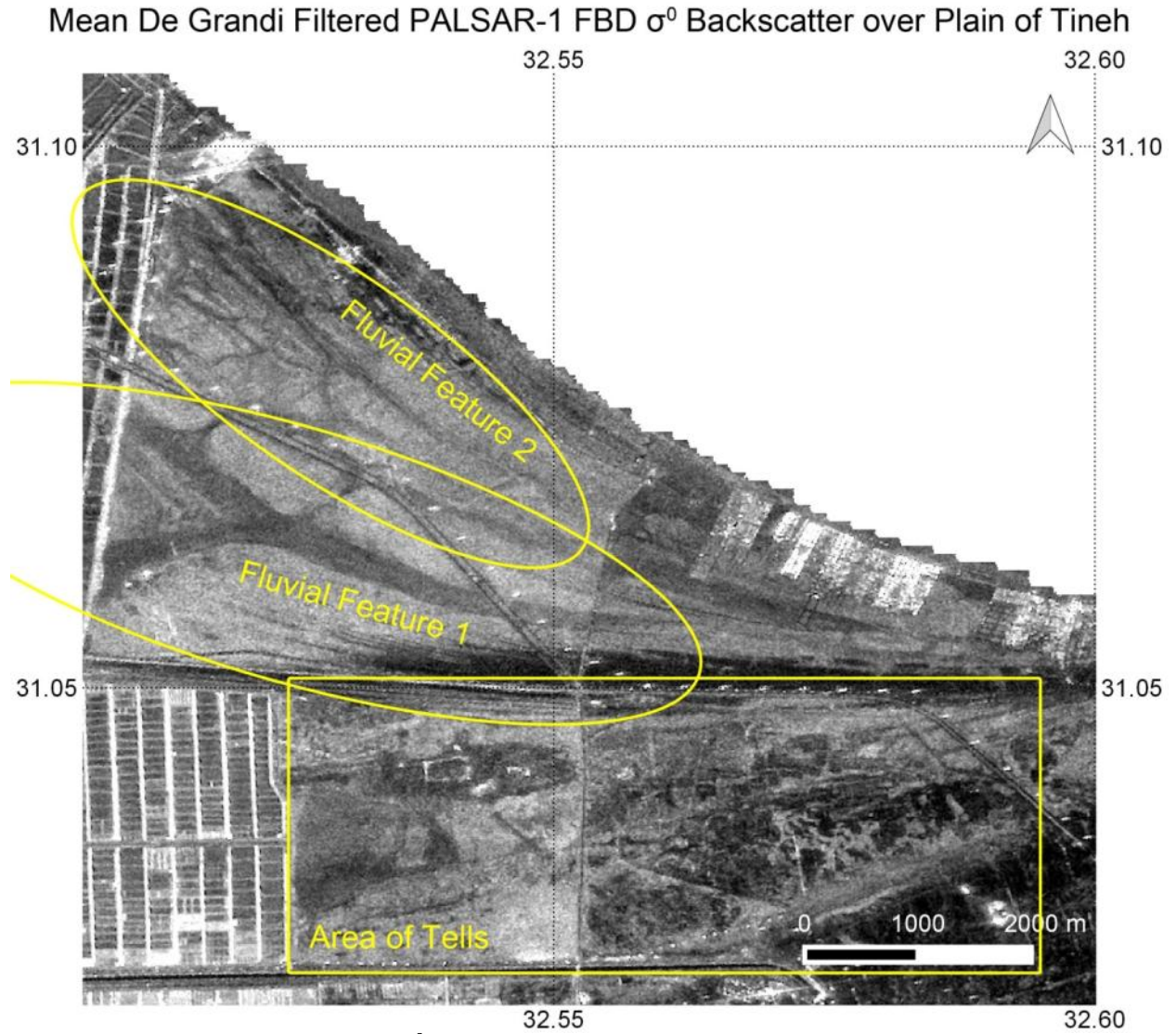


Figure 5.19 Mean of all De Grandi filtered σ^0 backscatter images of the PALSAR-1 FBD time series over part of Plain of Tineh. Anomaly features characterised by low relative backscatter are highlighted in yellow.

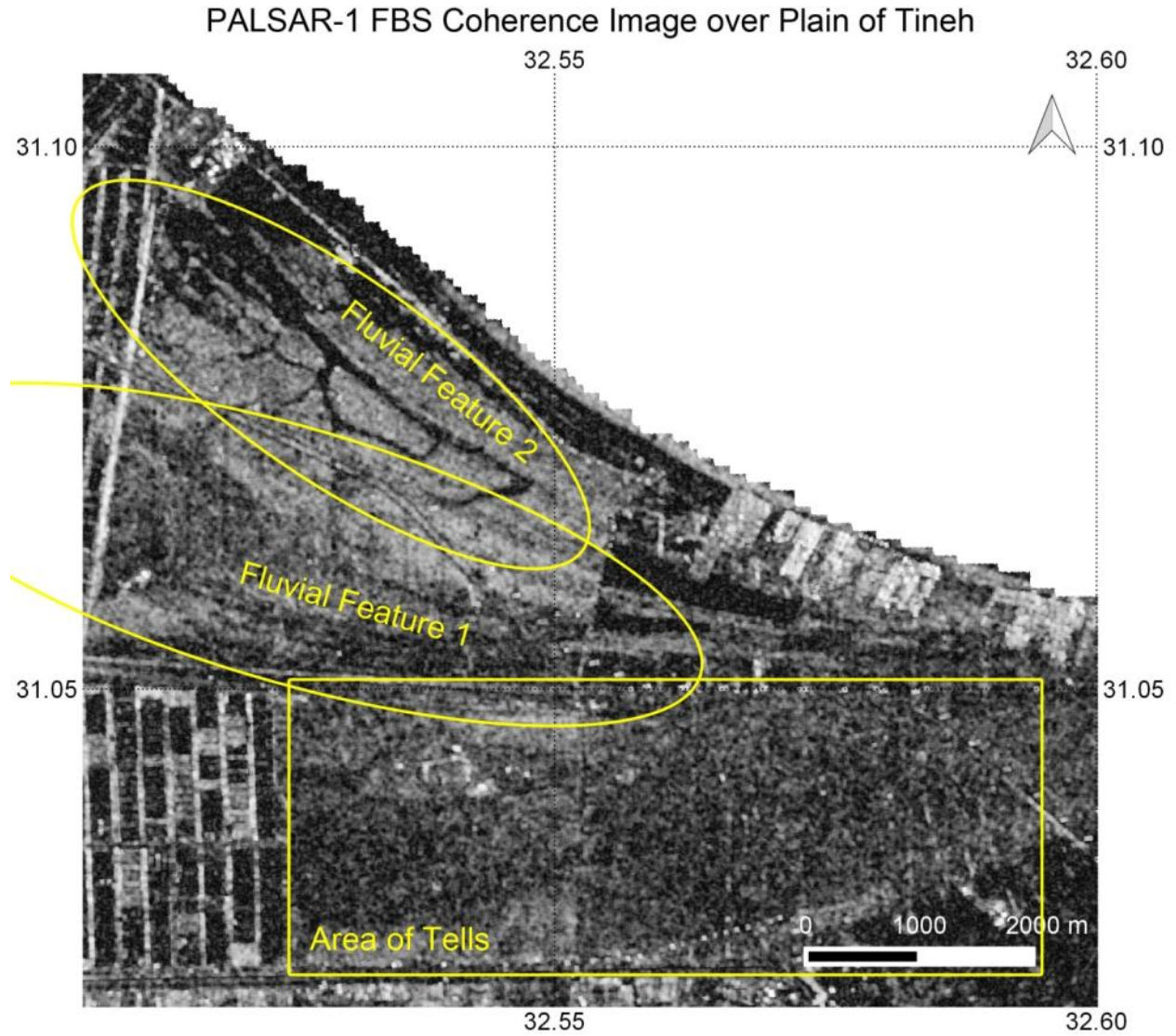


Figure 5.20 Coherence between two PALSAR-1 FBS images acquired on 19 December 2010 and 3 February 2011. The temporal baseline is 46 days and the perpendicular baseline 498m. Anomaly features identified in the filtered σ^0 backscatter images are highlighted in yellow.

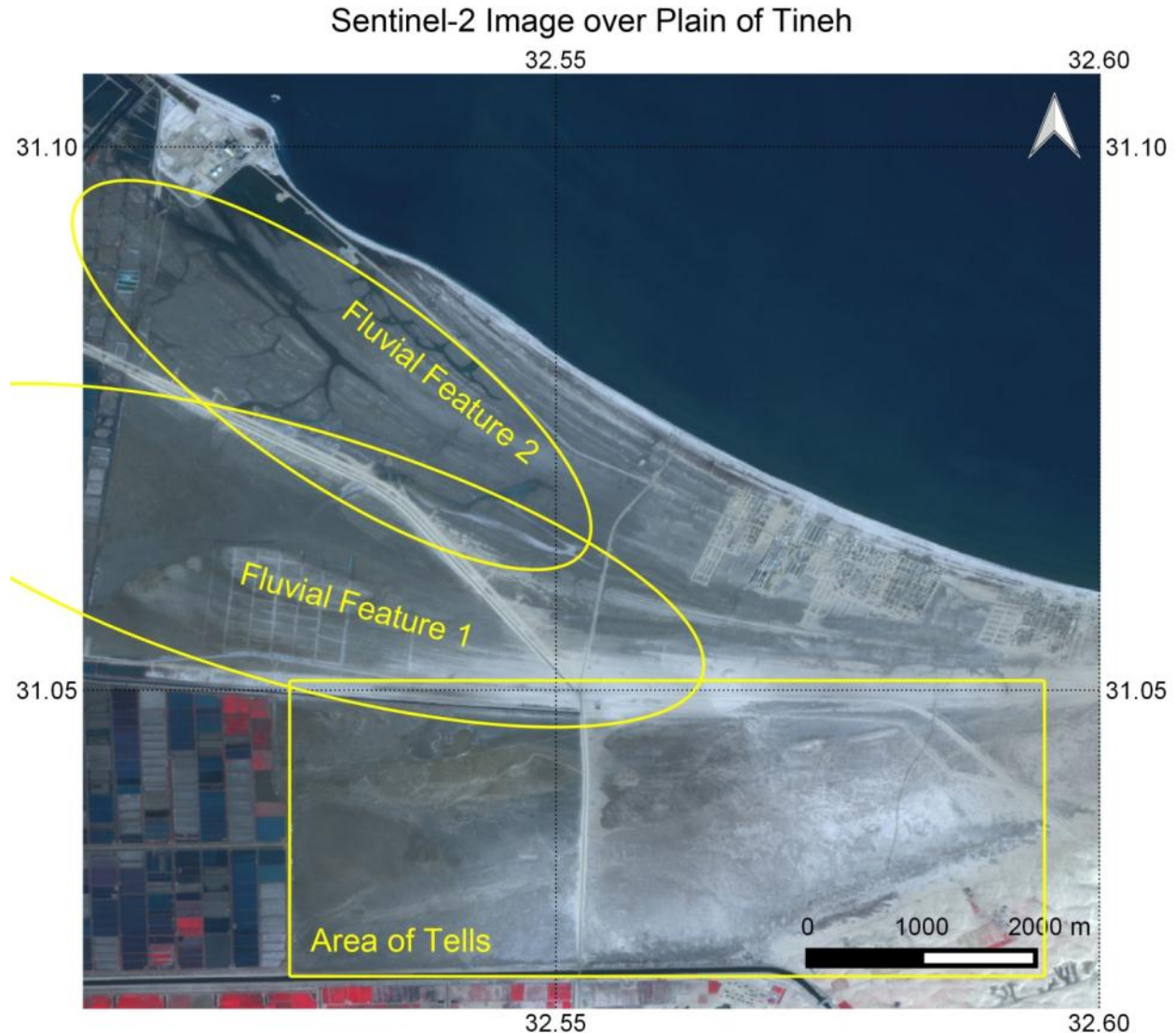


Figure 5.21 Same Sentinel-2 image, with the same band combination, as in Figure 5.18, covering the same extent and showing the same annotations as Figure 5.19 and Figure 5.20.

5.5.3.2 Tell El-Farama

Figure 5.22 shows the area of the tells on a pan-sharpened (0.5m spatial resolution) Pleiades image acquired on 24 November 2015 and displayed as an R, G, B colour combination of NIR, R and G respectively. Figure 5.23 and Figure 5.24 show the same area on an image of the mean of all the De Grandi filtered σ^0 backscatter images of the PALSAR-1 FBD time series (Figure 5.23) and the PALSAR-2 time series (Figure 5.24).

Some of the ancient ruins of Pelusium can still be seen in modern times, the most striking of which is a fortress with 36 towers and 3 gates. This has been dated to the late 6th century (el-Maksoud et al. 1994). Excavations have brought to light other significant structures, including the building of a bath complex and a well preserved theatre (Herbich 2009). These up-standing structures are clearly visible in the SAR

imagery as areas of high backscatter (see Figure 5.23 and Figure 5.24). Also visible in the SAR imagery are anomaly features of low backscatter, some of which do not correspond with known structures. These are highlighted by yellow ellipses in Figure 5.23 and Figure 5.24. These structures are visible in all the individual De Grandi filtered images in all the time series of PALSAR-1 FBS, FBD and PALSAR-2. They have greater contrast in the PALSAR-1 FBD imagery than in the FBS imagery. This seems to be due to the higher multilook factor in the FBD imagery (5 in azimuth for FBD as opposed to 3 for FBS, see Section 5.4) reducing further the image speckle. Increasing the multilook factor on the FBS imagery produced similar results. The HH polarisations yield much clearer results when compared to the HV. The improved visibility in HH is probably due to the dominance of single bounce scattering in the region causing only negligible depolarisation of the signal (see Section 5.5.3.4).

In addition to the mean of the De Grandi filtered stacks, also the standard deviation and Coefficient of Variation (CoV) of the filtered PALSAR-2 stack clearly showed the anomaly features. It would appear that the backscatter in the areas surrounding these features is not only higher, but also varies more than over the backscatter over the features. The standard deviation and CoV did not yield similarly good results in the PALSAR-1 time series, perhaps due to the presence of artefacts. Several of the images had a band of varying backscatter across the centre of the image, similar in width to the Radio Frequency Interference (RFI) patterns shown in Section 5.5.3.4. A number of bright linear features in all SAR images of the area are likely to be range ambiguities originating from the high backscatter of irrigated field boundaries to the west of the area of the Tells.

Two low backscatter anomaly features are highlighted in Figure 5.22, Figure 5.23 and Figure 5.24. The feature labelled on these figures as “Island Feature” surrounds a rectangular island. In the PALSAR-1 data the outlines of the island appear quite straight and sharp, while in the PALSAR-2 data they are less so. This maybe a former island of higher and dryer ground, surrounded by wetter areas in antiquity, as described in (Jaritz et al. 1996). The feature labelled on the same figures as “Linear Feature” is in the form of a straight line extending from the Roman bath complex towards the Pelusium Line. It is intersected by another linear feature of low relative backscatter, which traverses horizontally from east to west. One interpretation suggested in Stewart et al. (2013b) is that it may be the trace (such as an infilled ditch) of a former drainage feature connected to the ancient bath complex.

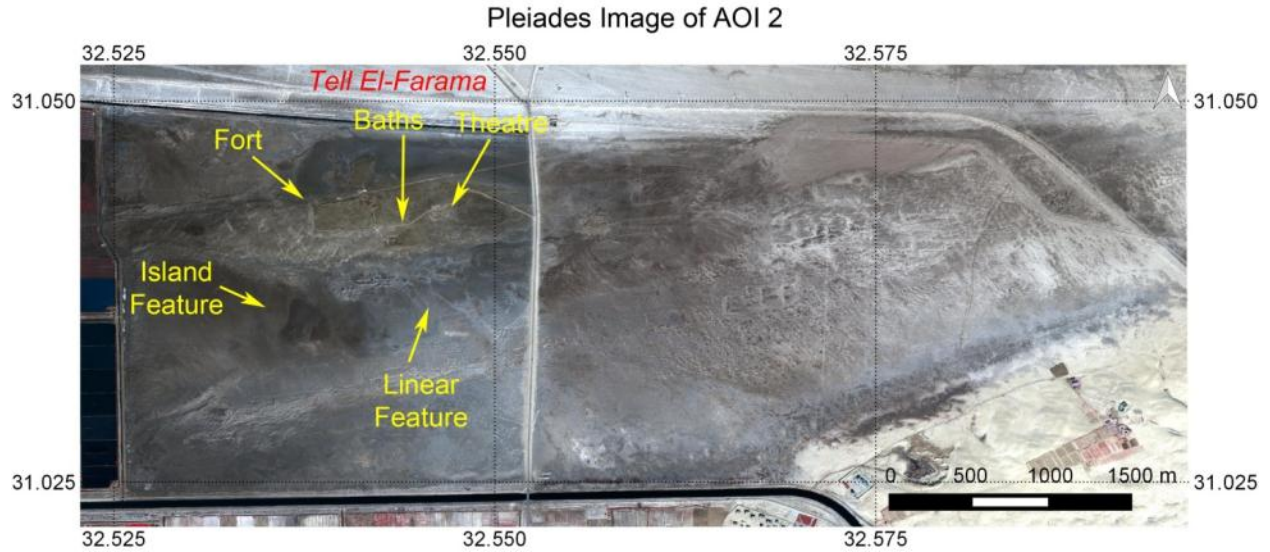


Figure 5.22 Pleiades image acquired on 24 November 2015, covering area of the tells. Pansharpned to 0.5 m pixel spacing. True colour composite of band 3 (660 nm) displayed as red, band 2 (550 nm) displayed as green, and band 1 (490 nm) displayed as blue. Pleiades data provided by ESA.

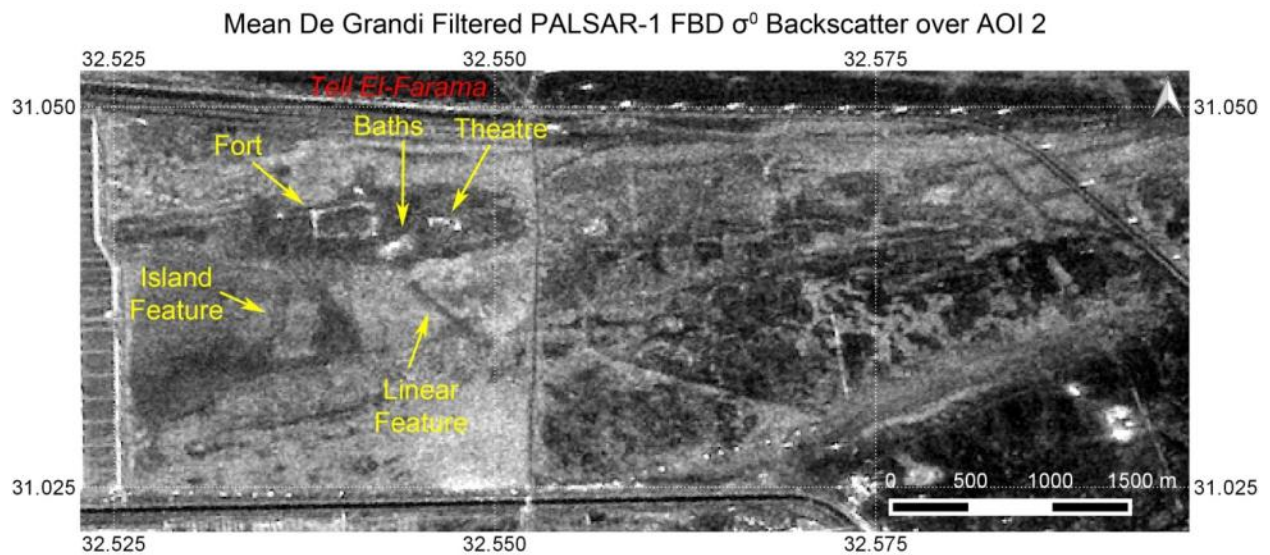


Figure 5.23 Average De Grandi filtered PALSAR-1 FBD σ^0 backscatter over subset region of tells.

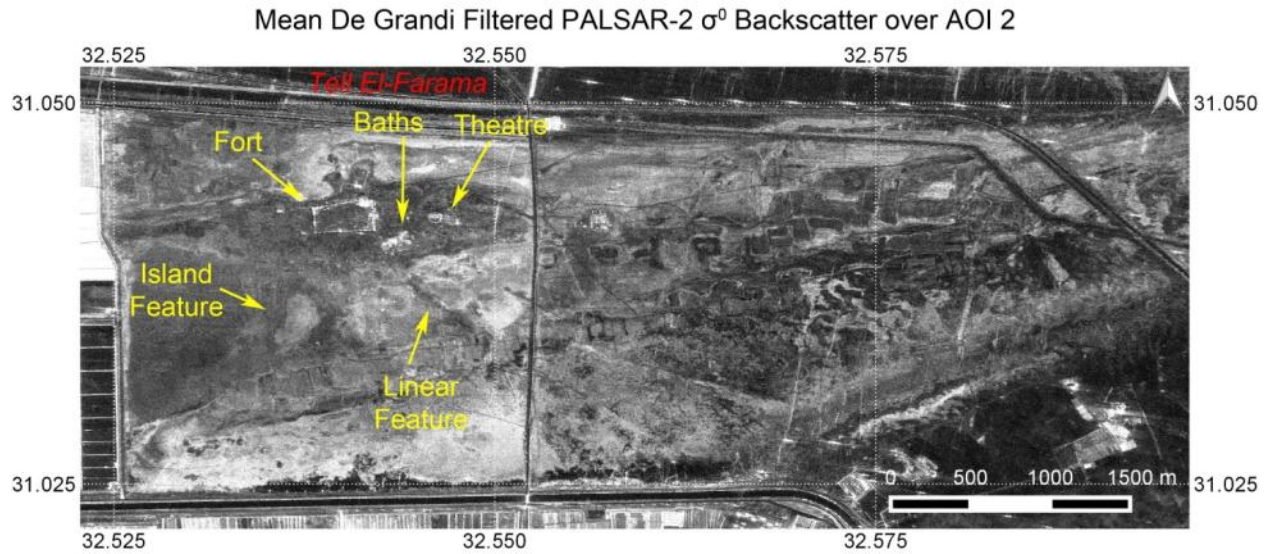


Figure 5.24 Average De Grandi filtered PALSAR-2 Spotlight σ^0 backscatter over subset region of tells.

5.5.3.3 Tell El-Mahzan and Tell El-Kanais

The anomalies visible in this region in the PALSAR-1 mosaic are in the form of patches of low backscatter (see ellipses in Figure 5.25), some of which seem to be arranged into geometric shapes (especially ellipses 1 and 2 of Figure 5.25). Out of the PALSAR-1 imagery, of all the processed images, the anomaly features were most clearly visible in the mean of the multitemporal De Grandi speckle filtered images, calibrated to σ^0 and converted to decibel (see Figure 5.25). Due to the small size of the features, they were easier to distinguish in the higher resolution FBS imagery than in the FBD. Out of the processed PALSAR-2 Spotlight imagery, the anomalous features were most clearly visible in the CoV of the multitemporal De Grandi speckle filtered images as areas of lower CoV (see Figure 5.26). The CoV did not yield good results in the PALSAR-1 time series perhaps for the same reasons as discussed in Section 5.5.3.2.

The anomalous features are less discernible in the optical remotely sensed imagery procured for the analysis (see Table 5-3, Figure 5.27 and Figure 5.28).

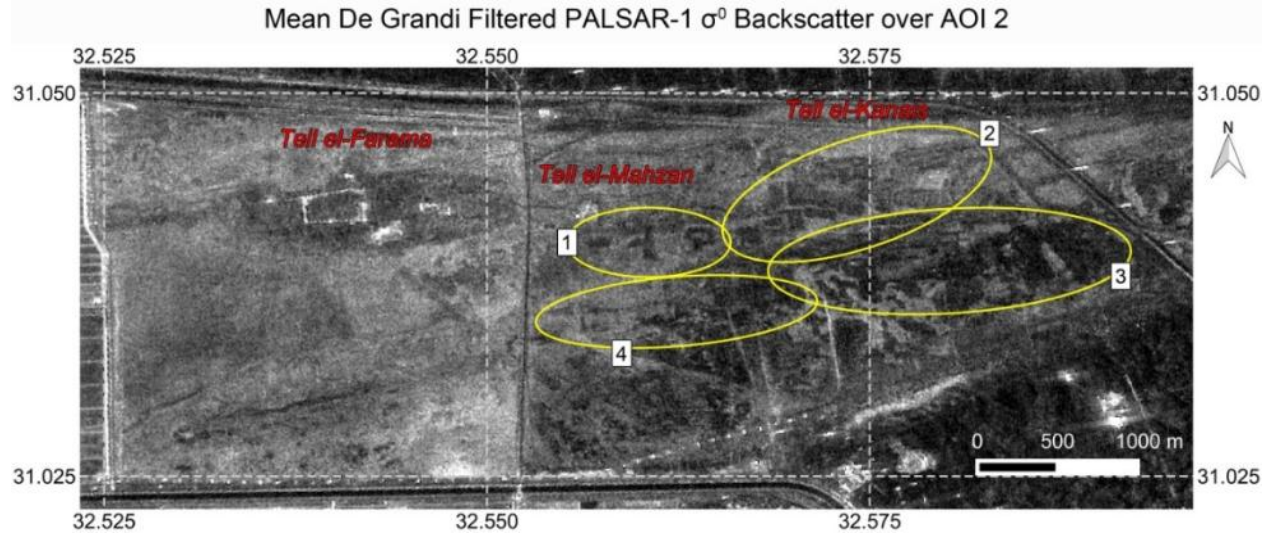


Figure 5.25 average De Grandi filtered PALSAR-1 FBS σ^0 backscatter over subset region of tells shown in Figure 5.17. Yellow ellipses highlight anomaly features. PALSAR-1 data provided by ESA.

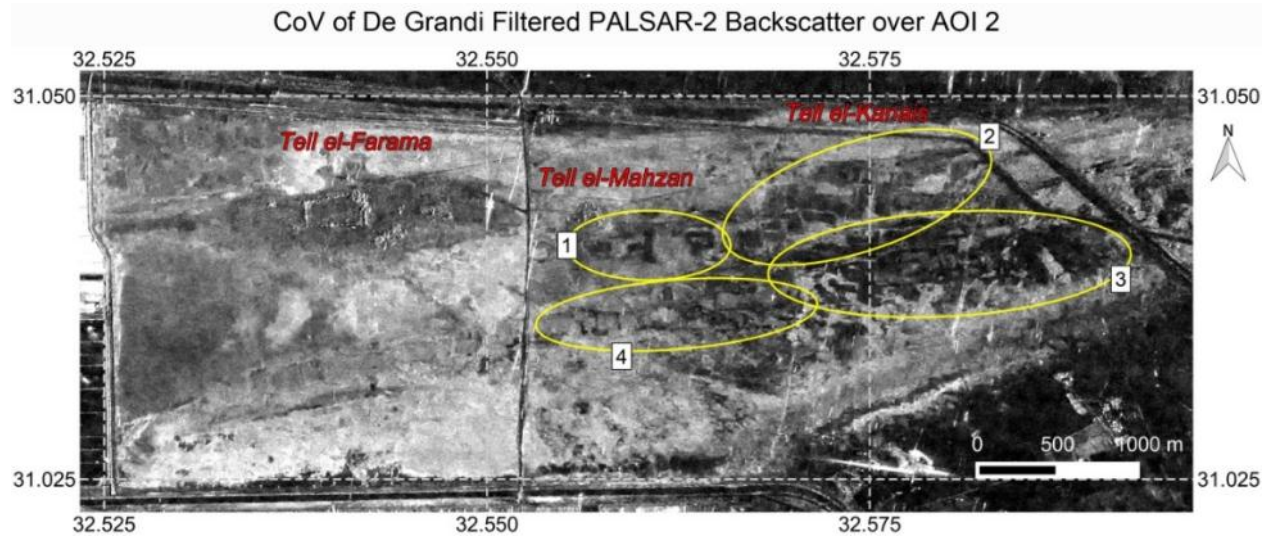


Figure 5.26 Coefficient of variation of seven PALSAR-2 Spotlight multitemporal De Grandi speckle filtered images over same subset region of tells. Yellow ellipses highlight anomaly features. PALSAR-2 data provided by JAXA.

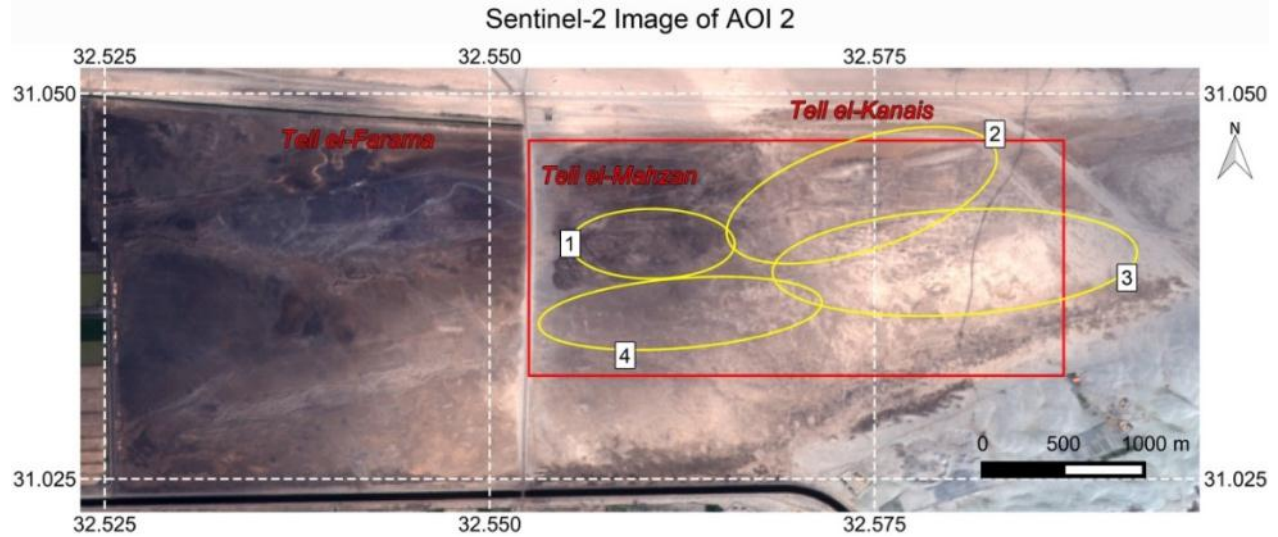


Figure 5.27 Sentinel-2 image over same subset region of tells, acquired on 19 February 2016. Full resolution (10 m) true colour composite of band 4 (650 nm) displayed as red, band 3 (543 nm) displayed as green, and band 2 (458 nm) displayed as blue. The red rectangle shows the coverage of an archaeological chart published by Jaritz, Favre, Nogara, Rodziewicz and Carrez-Maratray (Jaritz et al. 1996). Yellow ellipses show locations of anomalous features identified in the PALSAR-1 and PALSAR-2 processed imagery. Contains modified Copernicus Sentinel data 2016.

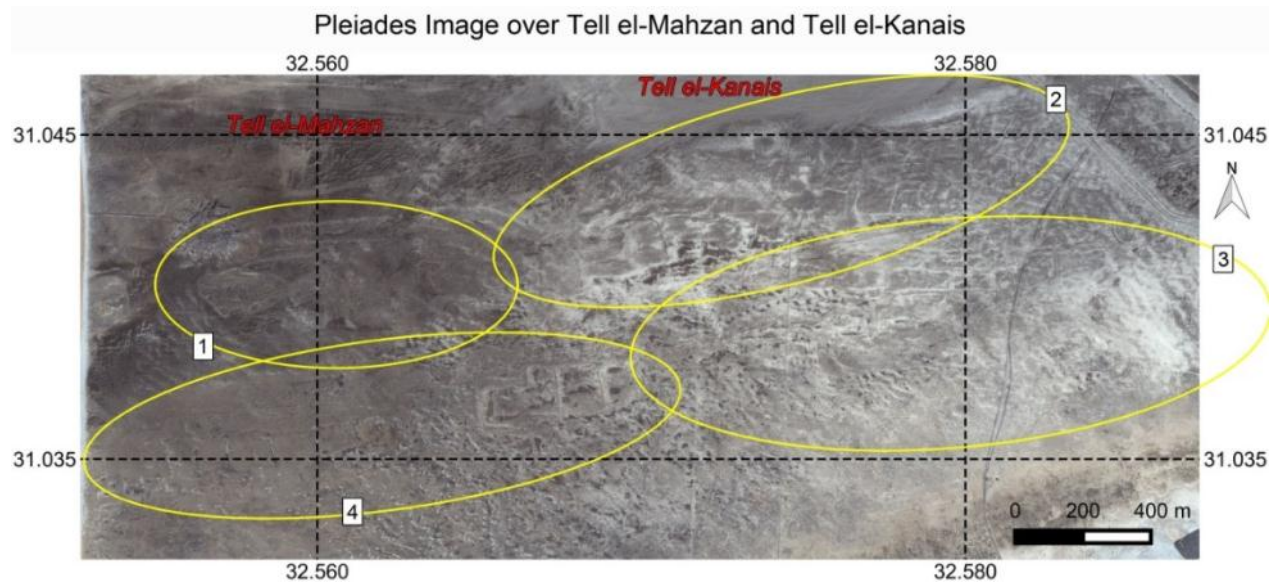


Figure 5.28 Pleiades image acquired on 24 November 2015, covering area included in the red rectangle in Figure 5.27. Pansharpned to 0.5 m pixel spacing. True colour composite of band 3 (660 nm) displayed as red, band 2 (550 nm) displayed as green, and band 1 (490 nm) displayed as blue. Yellow ellipses show locations of anomalous features identified in the PALSAR-1 and PALSAR-2 processed imagery. Pleiades data provided by ESA.

5. Archaeological Propection Using SAR in North Sinai Desert

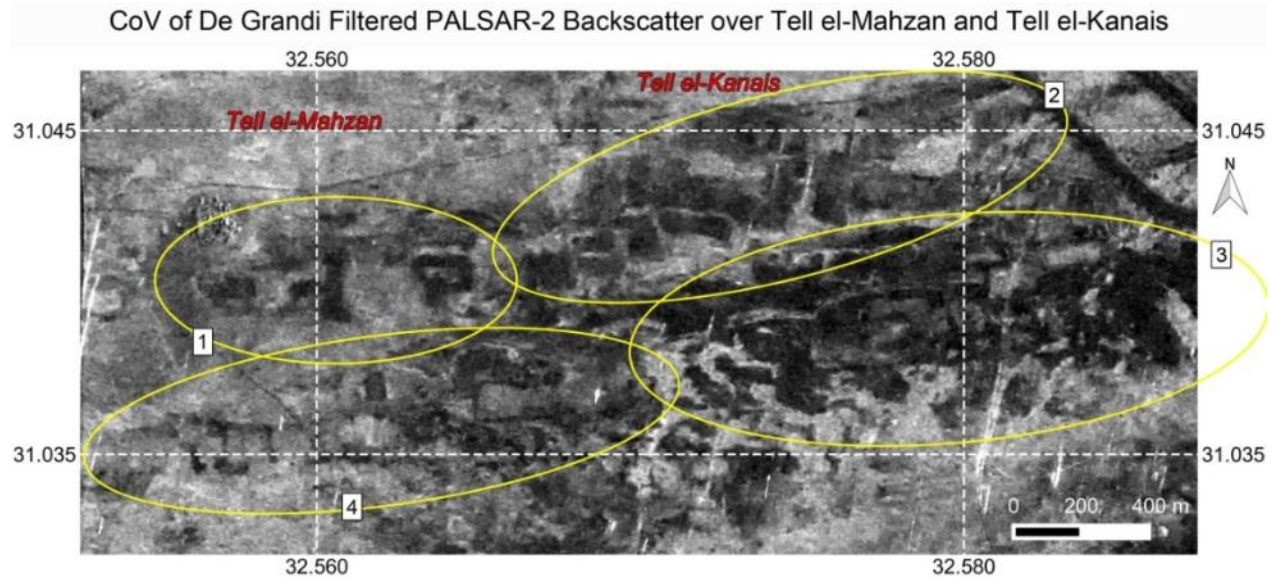


Figure 5.29 Coefficient of variation of 7 PALSAR-2 Spotlight multitemporal De Grandi speckle filtered images over same subset region as Figure 5.28. Yellow ellipses show locations of anomaly features. PALSAR-2 data provided by JAXA.

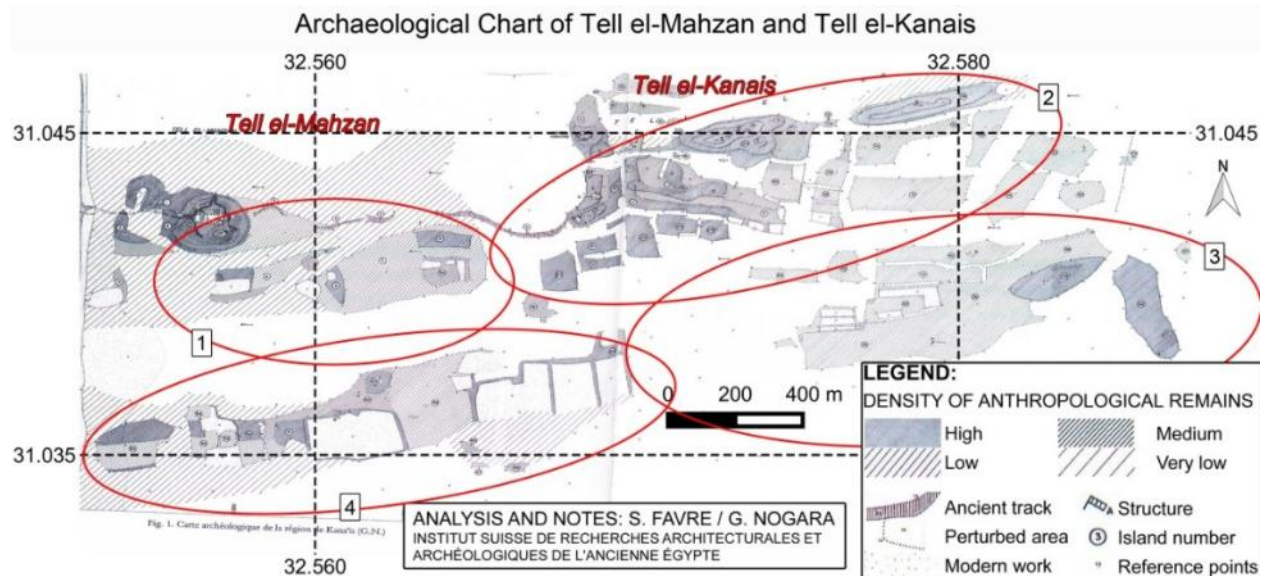


Figure 5.30 Archaeological chart published by Jaritz, Favre, Nogara, Rodziewicz and Carrez-Maratray (Jaritz et al. 1996) covering same area as in Figure 5.28 and Figure 5.29. Red ellipses show locations of anomalous features identified in the PALSAR-1 and PALSAR-2 processed imagery. Courtesy of Jaritz, Favre, Nogara, Rodziewicz and Carrez-Maratray (Jaritz et al. 1996).

Over the areas of Tell El-Mahzan and Tell El-Kanais, the SAR response was compared with the archaeological ground truth data published by (Jaritz et al. 1996). Continuing the work of others, in particular (Carrez-Maratray and Wagner 1993), Jaritz, Favre, Nogara, Rodziewicz and Carrez-Maratray (Jaritz et al. 1996) published a map showing the distribution of anthropogenic surface remains identified by field walking in the region of Tell el-Mahzan and Tell el-Kanais, east of Tell el-Farama. Figure 5.27 shows the coverage of this map overlain on a Sentinel-2 image. Figure 5.28, Figure 5.29 and Figure 5.30

show a Pleiades image covering the same area as the map, the CoV of the De Grandi filtered PALSAR-2 imagery also covering the same area, and the map itself, respectively. On this map, the density of anthropogenic material, including brick, ceramic, glass, metal, bone, etc. were divided into four classes of increasing density. Jaritz, Favre, Nogara, Rodziewicz and Carrez-Maratray (Jaritz et al. 1996) observed that one of the most interesting outcomes of the resulting map is that the density of anthropogenic material seems to be clustered in a number of islands. These islands have in some cases been tentatively classified according to the type of material found, such as a necropolis or a residential area. Some of the islands are connected, such as by an ancient road identified in the survey. A full description of each island is given in (Jaritz et al. 1996). A possible interpretation as to why anthropogenic remains seem to be clustered in these islands is also given by Jaritz, Favre, Nogara, Rodziewicz and Carrez-Maratray (Jaritz et al. 1996), who suggest the areas in between may have been ancient lagoons, swamps, and river branches, leaving patches of dry ground in between that were more attractive for human settlement.

Both the PALSAR-1 mean backscatter and PALSAR-2 CoV images largely show the same pattern of islands as in the archaeological chart, which in most cases appear darker than the spaces in between. If the interpretation of Jaritz, Favre, Nogara, Rodziewicz and Carrez-Maratray is correct, a possible reason for this may be that the former inundated areas in between the islands may still have moisture present beneath the surface. This moisture may cause a higher SAR backscatter response due to the increased relative permittivity (Ulaby et al. 1981) than the dryer areas apparently favoured by humans in antiquity and may explain the clarity of features in the PALSAR-1 mean backscatter. The dryer areas would attenuate the SAR backscatter and also reduce the backscatter variation, which may explain the clarity of features in the CoV of the PALSAR-2 imagery.

The interpretation by Jaritz, Favre, Nogara, Rodziewicz and Carrez-Maratray of the various islands of anthropogenic material mapped as a result of the field walking survey is summarised in the four ellipses highlighted in Figure 5.25 to Figure 5.30. Over the islands in ellipse 1 many surface remains of bricks have been found. The additional presence of slag and glass leads to the interpretation that some of these areas may have been occupied by craft workshops. Over the islands in ellipse 2, the strong concentration of fragmented building material may indicate that these were urban areas. The long feature in the top right of this area (island 28) may have been a necropolis, given the remains on the surface of offerings and human bones. The islands to the right of ellipse 3 are also likely to be necropoli, while to the left, modern works prior to the survey inhibited interpretation and only a low density of archaeological remains were found. The area in ellipse 4 was also seriously altered by works prior to the survey, in the form of modern terracing. However, the passage of water between the islands has been noted and interpreted as canals, which could have archaeological significance (Jaritz et al. 1996).

5.5.3.4 Polarimetric Analysis

Results of the polarimetric analysis undertaken on the quad pol image show that the VV power seems much greater than HH or HV (see Figure 5.31). The dominant scattering mechanism over the AOI is single bounce (see Figure 5.32), meaning that the incident SAR signal generally scatters once on the surface before returning to the sensor. It also means that the signal does not generally get depolarised. From a comparison with VHR optical data, it appears that this is the case primarily over the areas where

there does not appear to be very much sand cover. Over the sandy regions (e.g. around the fort) there is no clear dominant scattering mechanism and these areas are also characterised by high entropy (see Figure 5.33). The spatial resolution does not permit detailed polarimetric analysis of the smaller features identified in the higher resolution imagery acquired in single or dual polarisation modes, but it does show the behaviour of some larger features, such as those in Tell El-Farama. Here there is a clearly delineated rectangular feature where single bounce scattering dominates (characteristic of the non-sandy areas in this AOI), surrounded by an area of mixed scattering (more characteristic of the sandy areas). Also, the linear feature in Tell El-Farama is clearly distinguished as an area of uncertain scattering (perhaps due to more sand cover than surrounding areas) in an area characterised by single bounce. In the entropy image this feature cannot be clearly distinguished.

PALSAR-1 Polarimetric Image: Covariance Matrix

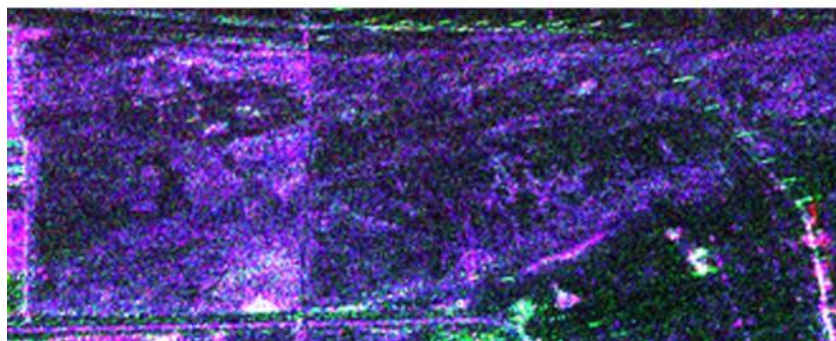


Figure 5.31 PALSAR-1 Quad Pol image of area of tells acquired on 8 April 2009. Colour combination of covariance matrix elements: C11 (corresponding to HH) as red, C22 (corresponding to HV) as green and C33 (corresponding to VV) as blue.

PALSAR-1 Polarimetric Image: Freeman Decomposition

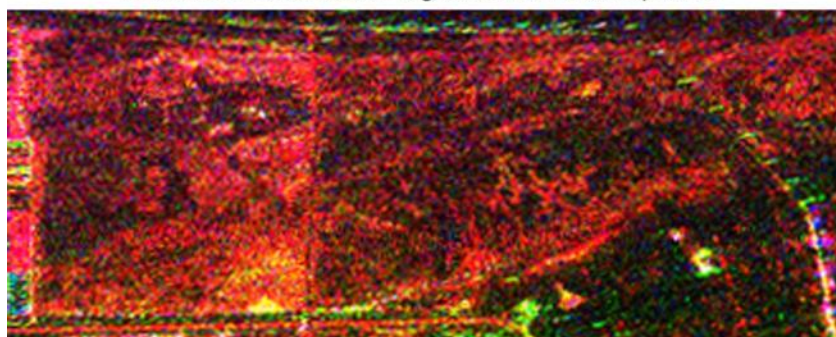


Figure 5.32 PALSAR-1 Quad Pol image of area of tells acquired on 8 April 2009. Colour combination of Freeman decomposition elements: Odd bounce (red), Volume scattering (green) and Double bounce (blue).

PALSAR-1 Polarimetric Image: Entropy

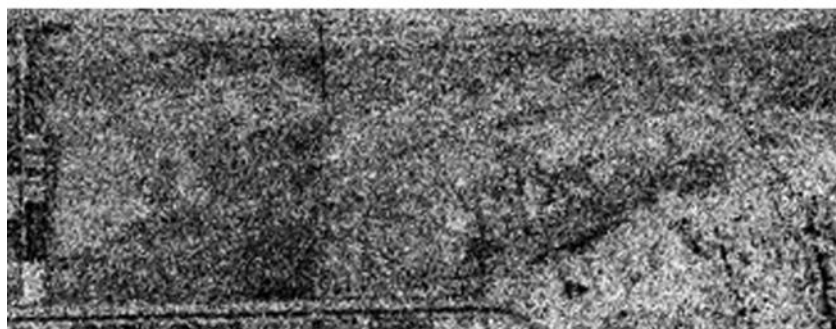


Figure 5.33 PALSAR Quad Pol image of area of tells acquired on 8 April 2009. Entropy image, showing degree of randomness of scattering.

5.5.4 Image Artefacts

Throughout the PALSAR-1 and PALSAR-2 imagery there are many features that are not present in other information layers; these have been interpreted as image artefacts. Most of these do not appear the same way in the individual PALSAR-1 and 2 images. Some of these artefacts are likely to be range or azimuth ambiguities (Li and Johnson 1983), while others may be due to Radio Frequency Interference (RFI) (Meyer et al. 2013). RFI is very high in this region (Rosen et al. 2008), and particularly affects long wavelength SAR (Meyer et al. 2013). A few scenes of PALSAR-1 and 2 polarimetric data were available

5. Archaeological Prospection Using SAR in North Sinai Desert

over some parts of the study area. In some cases, RFI can be identified in this polarimetric data as variations of backscatter in the two cross-polarised channels of Vertical transmit and Horizontal receive (VH) and Horizontal transmit and Vertical receive (HV). For monostatic SAR systems (such as PALSAR-1 and 2), where the transmitting and receiving antennas are collocated, the reciprocity constrains the scattering matrix to be symmetrical and the transmitted to received power ratios should be identical for HV and VH (Lee and Pottier 2009). If there is a difference in backscatter between the two, it means that polarised radiation is being received by the SAR antenna from an external source, which is the case with RFI. Figure 5.34 shows the probable presence of RFI in a region of the mosaic from the varying response in HV and VH backscatter. Figure 5.34a shows the location of a subsetting PALSAR-1 image in relation to the PALSAR-1 mosaic (note that it includes the subset of the Tells). Figure 5.34b is the backscatter amplitude in HV, while Figure 5.34c is the backscatter amplitude in VH. Note that the backscatter varies between the two images. This is likely due to RFI.

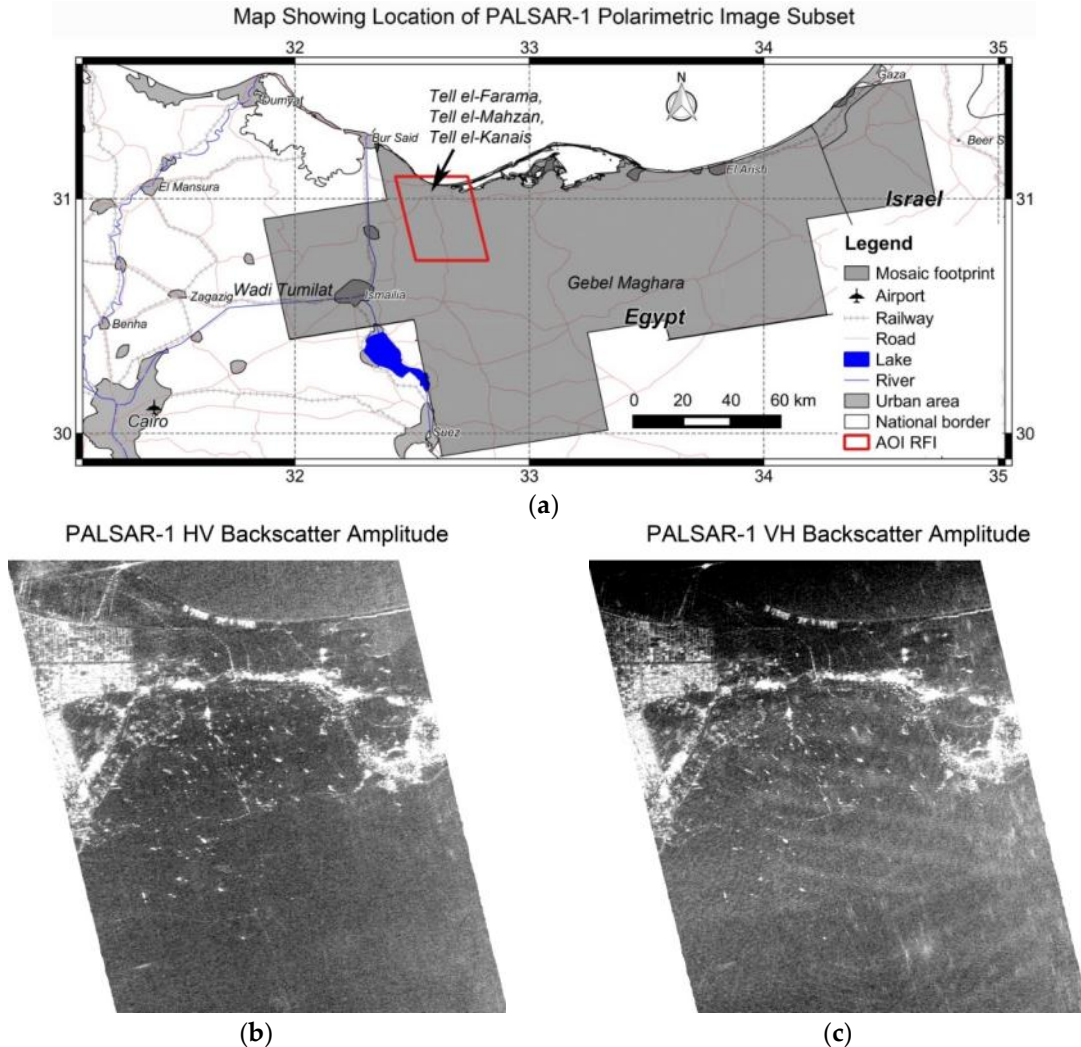


Figure 5.34 (a) Map showing subset region (as red polygon) where Radio Frequency Interference (RFI) has been detected on PALSAR-1 polarimetric data; (b) HV polarization backscatter amplitude of PALSAR-1 Polarimetric mode image subset acquired

over area shown in (a), on 8 April 2009. The image has a pixel spacing of 25 m and has been geocoded to geographic latitude/longitude, WGS84. PALSAR-1 data provided by ESA; (c) VH polarization backscatter amplitude of same PALSAR-1 Polarimetric image subset as in (b). PALSAR-1 data provided by ESA.

5.6 Conclusions

The sensitivity of microwave radiation to surface roughness and dielectric properties can be exploited to provide unique information about surface and subsurface objects in desert environments (Paillou et al. 2010). Longer wavelength SAR has increased penetration capability when compared to shorter wavelengths (Ulaby et al. 1981), and can thus provide information on subsurface features at greater depths. SAR can also provide a clear distinction of surface features if their roughness and composition causes a sufficiently high backscatter to contrast with the attenuated signal in the surrounding sand.

Techniques have been implemented to extract anthropogenic features in the desert region of North Sinai using PALSAR-1 and 2 data. To obtain a synoptic view over the study area, a mosaic of average De Grandi filtered PALSAR-1 σ° backscatter of North Sinai was produced. Many features of high relative backscatter in the desert sand were detected, while over a coastal mudflat, features of low relative backscatter were observed. The De Grandi speckle filtering made an enormous difference in the ability to distinguish features given the high amount of speckle due to the low signal to noise ratio of sand covered areas. Speckle filtering in the temporal domain reduced speckle while preserving spatial resolution. This is preferable when permanent, small-scale features are of interest in an area of largely homogeneous and unchanging land cover type. Two subset regions were selected for further analysis: The first included an area of abundant linear features of high relative backscatter in a strategic, but sparsely developed area between the Wadi Tumilat and Gebel Maghara. The second included an area of low backscatter anomaly features in a coastal sabkha around the archaeological sites of Tell el-Farama, Tell el-Mahzan, and Tell el-Kanais.

Over the subset region between the Wadi Tumilat and Gebel Maghara, algorithms were developed to extract linear features and convert them to vector format to facilitate interpretation. The algorithms were based on mathematical morphology, but to distinguish apparent man-made features from sand dunes, several techniques were applied. The first technique took as input the average σ° backscatter and used a DEM-derived LIA mask to exclude sand dune ridges. The second technique, which proved more effective, used the average interferometric coherence as input, no longer necessitating a mask given that there was no longer an ambiguity between sand dune ridges and anthropogenic linear features. Interpretation of extracted features revealed partially buried infrastructure that was not present in any of the available vector layers, and was difficult, and in some cases impossible, to distinguish in available optical imagery or any other non-SAR information layers obtained for the comparison.

Over the small coastal region including the archaeological sites of Tell El-Farama, Tell El-Mahzan, and Tell El-Kanais, some features of low relative backscatter were identified. To enable better distinction and interpretation of these, a time series of VHR PALSAR-2 Spotlight imagery was acquired with a ground range pixel spacing of 2m. Moreover, a comprehensive analysis was carried out with other VHR remote sensing datasets and results of ground surveys. Processing of the PALSAR-2 imagery revealed better

distinction of features in the CoV of De Grandi filtered backscatter intensity, while with the PALSAR-1 data, features were better revealed in the mean De Grandi filtered intensity. The reason for the difference may be due to image artefacts, including suspected range ambiguities in the PALSAR-2 data, and RFI in the PALSAR-1 data. It is suggested that the anomaly features are areas of greater signal attenuation, surrounded by land cover characterised by greater backscatter variability. A comparison of the SAR data was made with an archaeological chart of the same area produced by Jaritz, Favre, Nogara, Rodziewicz and Carrez-Maratray (Jaritz et al. 1996). A possible interpretation of the features is that they are local areas that in the past may have been islands of dry land surrounded by lagoons, rivers and swamplands. These areas may have been more favourable to settlement, which would explain the higher density of archaeological finds. It is suggested that there may still be a difference in soil moisture between the features and surrounding areas sufficient to be detected in processed SAR imagery, but not visible in optical remote sensing data. The areas of higher soil moisture may also be characterised by a greater variability in moisture, which would explain the high contrast of the features in the CoV and standard deviation images. Features were also identified in Tell El-Farama, which lay outside the coverage of the archaeological chart of Jaritz et al. (1996). Some of these are likely to be similar island features. One linear feature may possibly be an infilled ditch or drainage feature, originating at the Roman baths. However, this is just one interpretation. Ground survey may reveal more information about the origin of the feature.

Regular systematic and large scale survey of North Sinai remains a challenge. The inhospitable terrain and political instability (Gold 2014) hinders access. Moreover, sand drift and dune migration affecting much of North Sinai can rapidly bury modern structures (Misak and Draz 1997, Hermas et al. 2012) or ancient sites that may have been excavated in the past (Di Iorio et al. 2010). The use of long wavelength (L-band) spaceborne SAR could be a promising tool for regular survey of large areas for man-made structures. However, if it is to be applied operationally to extract specific features of interest, ground truth validation would be essential. Also, other datasets would likely be vital to aid interpretation. This is particularly in view of the many artefacts that can be present in SAR data, including range and azimuth ambiguities and RFI. The area of North Sinai is particularly prone to RFI (Rosen et al. 2008).

6 ARCHAEOLOGICAL PROSPECTION OF THE NORTH SEA PALAEOLANDSCAPE USING SAR

Published in Paper 3 (See Appendix D.1)

Shallow water regions, such as the North Sea, contain some of the best preserved palaeolandscapes, given that they have largely ceased to be modified by humankind since they were submerged by rising sea levels as a consequence of global warming following the last glacial maximum (Coles 1998). However, very little is known of these palaeolandscapes, partly due to their inaccessibility, and partly due to the sheer size of the areas. These regions are coming increasingly under threat due to activities such as mineral extraction, construction and commercial trawling (Westley et al. 2004). Mapping and monitoring of submerged palaeolandscapes is important to understand and preserve the underwater heritage. While bathymetry does not provide the full picture of past landscapes, due for instance to deposition or erosion induced changes, it nonetheless can support palaeolandscape analysis in conjunction with other techniques, such as seismic survey and coring (Gaffney et al. 2007).

The advantages of spaceborne bathymetry lie in its ability to cover large areas, at regular intervals and at low cost. A review of spaceborne bathymetry techniques is provided in Section 3.5.

The objectives of the research presented in this chapter are twofold. The first objective is to test on Sentinel-1 data and over the North Sea, the recently developed bathymetric retrieval algorithm of Renga et al. (2013, 2014), introduced in Section 3.5. It is worth recalling that this algorithm has been applied so far on the Mediterranean Sea, over a prevalently rocky floor, using COSMO-SkyMed X-band (Renga et al. 2014) and ALOS PALSAR L-band (Renga et al. 2013). To the best of the authors' knowledge, this is the first example of bathymetric data retrieval from Sentinel-1 C-band SAR data. Moreover, the algorithm has never been applied in the North Sea. The second objective is to determine how Sentinel-1 derived bathymetry could support the analysis and monitoring of submerged palaeolandscapes, through a comparison of the results of the Sentinel-1 bathymetry retrieval with palaeolandscape features mapped in the framework of the NSPP (Gaffney et al. 2007). The purpose is thus to determine to what extent the palaeolandscape features have a bathymetric signature identifiable in the Sentinel-1 derived water depth. This is essential because the systematic availability of high resolution SAR data acquired by Sentinel-1 could potentially support cost effective, regular monitoring of bathymetric features in extensive areas.

The chapter is structured as follows. Section 6.1 describes the submerged palaeolandscape of the North Sea. Section 6.2 describes in detail the methodology and results of the Sentinel-1 bathymetric retrieval. Section 6.3 compares the Sentinel-1 depth chart with the results of the NSPP. Section 6.4 provides a conclusion on Sentinel-1 derived bathymetry, and discusses its application for submerged palaeolandscape analysis.

6.1 The Palaeolandscape of the North Sea

Three simple criteria have been defined for the existence of submerged archaeological landscapes: the sea level must have been lower in the past, prehistoric humans must have been present and occupied the exposed land, and sedimentary processes during transgression must have preserved rather than eroded the landscape (Westley et al. 2011).

The North Sea, between the east coast of the United Kingdom, and west coast of mainland Europe, is one of the areas covered by sea as a consequence of global warming following the last glacial maximum (Coles 1998). During the Mesolithic (from around 12,000 to 6,000 years before present), the region was likely to have been a significant habitat for hunter-gatherer groups (Gaffney et al. 2007). The area contains one of the most extensive and probably best preserved prehistoric landscapes in Europe (Fitch et al. 2007).

From 2005 to 2006, the NSPP used existing data to provide information on the Mesolithic landscape of the Southern North Sea (approximately 23,000 km² from the Norfolk Coast to the Doggerbank). The project, headed by the University of Birmingham in the UK, used a variety of archive geophysical data sources and more traditional map data. The bulk of the data consisted of the 3D seismic 'Mega-Survey' produced by Petroleum Geo-Services and provided to the University of Birmingham for the project. This possibly represents one of the largest continuous areas of geophysical data ever used for archaeology. The NSPP focused on mapping the upper land-surfaces of the survey area, which relate to the Early Mesolithic. 13 landcover types were mapped during the project (Gaffney et al. 2007).

The results of the project have been made freely available in various formats, including an atlas in Portable Document Format (PDF), and geocoded vector files in Keyhole Markup Language (KML) format (University of Birmingham 2011) (see Figure 6.1). These vectors include the following:

- Early Holocene (around 11,600 to 9,600 years before present) Shorelines
- Location of Early Holocene Estuaries
- Location of Early Holocene Fluvially related features
- Location of possible Early Holocene lakes
- Relative Landscape Topography
- Location of possible Early Holocene Salt Marsh
- Location of possible Early Holocene Sand Banks

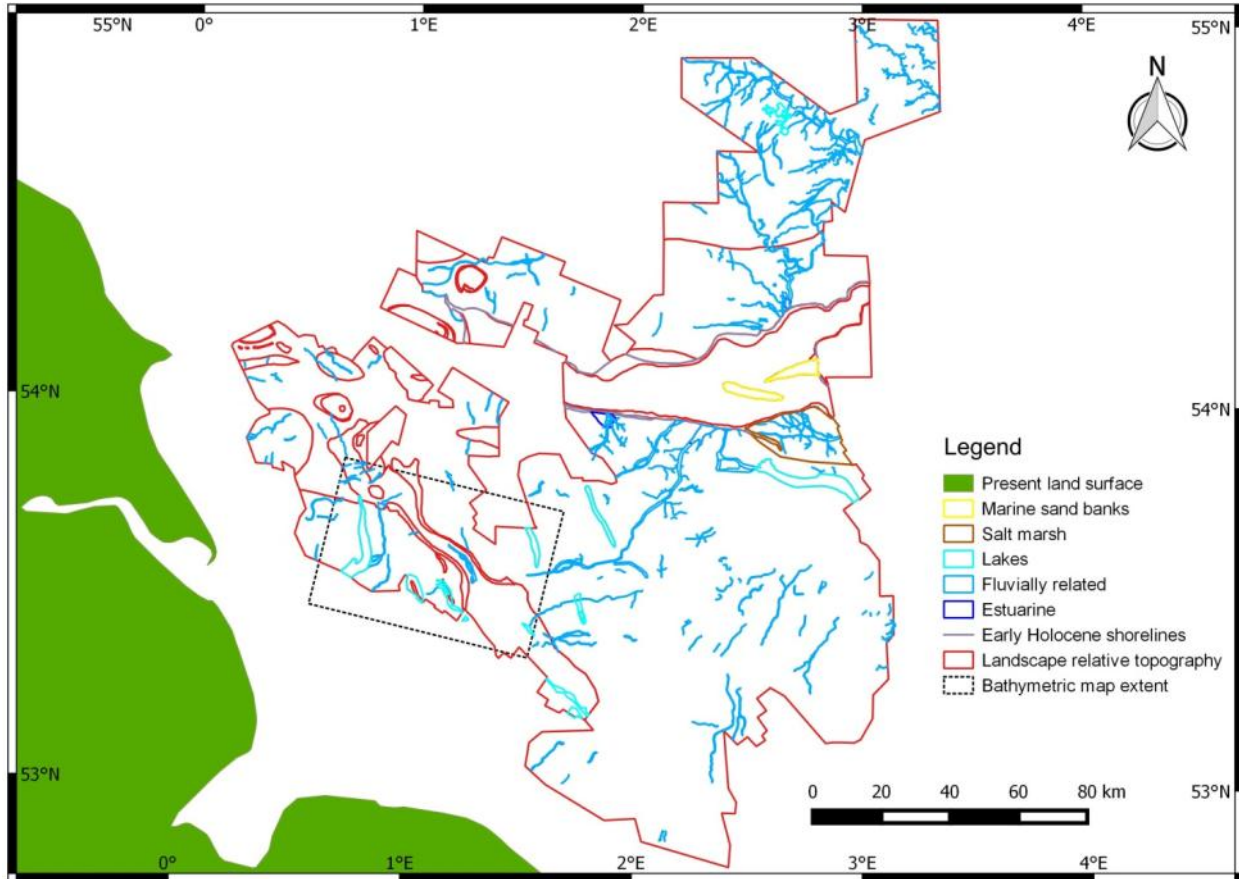


Figure 6.1 Map of the North Sea showing interpreted Early Holocene (around 11,600 to 9,600 years before present) features produced in the framework of the NSPP. The extent of the Sentinel-1 derived bathymetric map is shown by the black dashed rectangle. Data derived in part or whole from the North Sea Palaeolandscape Project: University of Birmingham. This project was funded by English Heritage, utilising funds made available by the Aggregates Levy Sustainability Fund (ALSF). Original Survey data for the project was provided courtesy of Petroleum Geo-Services (PGS) UK Ltd.

6.2 Sentinel-1 Bathymetry Retrieval

The methodology employed to derive the bathymetry from a Sentinel-1 image of SAR amplitude and the results of the retrieval are here described.

6.2.1 SAR data

The Southern North Sea is an area suitable for the application of current based bathymetric techniques due to the tidal currents, suitable winds and shallow water. Since the launch of Sentinel-1A on 3rd April 2014, until the end of 2014, certain regions were selected for intensive calibration and validation (cal/val) activities during which temporary disruptions to the delivery of imagery in consistent mode-polarization combinations were experienced. The region of the North Sea near the British coast, in which lies the region of interest of the NSPP, was one of these cal/val sites. During this period a Ground Range Detected SAR image acquired over part of the region of the NSPP was identified on the Sentinel-1 Data Hub (European Space Agency 2015), in which topographic features appeared to be evident in the image quicklook, confirming that during image acquisition the conditions for SAR bathymetry retrieval

were suitable. This is the image that was used for the bathymetry retrieval. Its characteristics are shown in Table 6-1.

Table 6-1 Characteristics of Sentinel-1 data used for the bathymetry retrieval.

Attribute	Value
Sensor Mode and Beam	S2 (Stripmap, Beam 2)
Product Type and Resolution Class	GRDH (Ground Range Detected, High resolution)
Processing Level	1 (focussed, detected, multi-looked, ground range projected)
Scene Center Incidence Angle (°)	26
Spatial Resolution (m)	23
Acquisition Date and Time	4 October 2014, 06:22 UTC (Universal Time Coordinated)
Pass	Descending
Polarisation	Single VV (Vertical transmit, Vertical receive)

6.2.2 Ancillary data for bathymetry retrieval

The selected algorithm requires only a-priori measurements of water depth along one range line, to tune the algorithm (Renga et al. 2014). This tuning is required to estimate the relaxation rate and the current velocity corresponding to “equilibrium” conditions (i.e. unperturbed current and flat topography), assuming they are not already known (see Section 6.2.3). However certain ancillary information was used to aid the bathymetry retrieval. This included current data, to facilitate estimation of current velocities at equilibrium, and bathymetric data, for algorithm tuning and evaluation of the final depth map.

6.2.2.1 EMODnet bathymetric chart

Reference depth data was obtained from the European Marine Observation and Data Network portal for bathymetry (EMODnet 2015). Initiated by the European Commission, the EMODnet portal provides a free service for viewing and downloading a harmonised Digital Terrain Model (DTM) for the European sea regions that is generated by the EMODnet Bathymetry partnership (an increasing number of data providers from government and research). Bathymetric data in American Standard Code for Information Interchange (ASCII) Grid format was downloaded over the area corresponding to the Sentinel-1 subsets. The data was converted from Geographic to Universal Transverse Mercator (UTM) Zone 31 North projection, with a sampling of 140m east/west and 230m north/south. Given the varied nature of the data sources, the accuracy of the EMODnet bathymetric data grid is difficult to determine. While the EMODnet data provides a useful source for comparison, it does not constitute a source for accurate quantitative validation.

The EMODnet bathymetry subset displays a mean water depth of approximately 25 meters. Within 2 standard deviations of the mean, the water depth values range from around -5 to -45 meters. This is within the feasible water depth range of SAR bathymetry. However, over the deep tunnel valleys, significantly greater water depths are recorded, up to a maximum of 97 m. In theory, topographic variations at this depth cannot realistically be mapped with SAR bathymetry techniques. Nonetheless, given that the available NSPP data shows only the location of these tunnel valleys, without providing

details on potential features within them, it is sufficient at this stage only to delimit the boundaries of these topographic features that reach water depths potentially beyond the limits of SAR bathymetry.

6.2.2.2 Current data

Although the algorithm used is able to function without a-priori current data, nonetheless, any information on currents facilitates the inversion given that the current velocity at equilibrium depth is required. If this is not known, it has to be determined through trial and error at the tuning stage (Renga et al. 2013).

Modelled, water depth averaged, current data produced by the Marine Data Products Team of the UK National Oceanography Centre (NOC) was thus obtained for the area covered by the Sentinel-1 image, and for the date and time of the image acquisition (4 October 2014, 06:22 UTC). The data was provided as an ASCII text file containing columns of latitude, longitude, speed in ms^{-1} and direction in degrees of the current.

The modelled current velocities over a part of the North Sea including the frame of the Sentinel-1 image acquired at 06:22 UTC on 4 October 2014 are shown in Figure 6.2. The figure shows that current speeds over the Sentinel-1 subset used for bathymetry retrieval vary from 0.3 to 0.9 ms^{-1} . The current directions are shown to flow towards the northwest throughout most of this subset area. In the southwesterly corner of the subset the currents appear to change east/west direction, and flow towards the northeast. Given that this area corresponds with a deep, tunnel valley, and that the modelled currents are water depth averaged, it is likely that the flow of water is forced in this direction by the channel. While the range component of the currents become progressively weaker from the east to the west of the subset, due to their tendency to flow in an increasingly northerly direction, this is partly compensated by an increase in total speed. The range velocity therefore varies little, and has been calculated to be from around 0.15 ms^{-1} in the east, to approximately 0.3 ms^{-1} in the west (apart from the area where the current changes east/west direction).

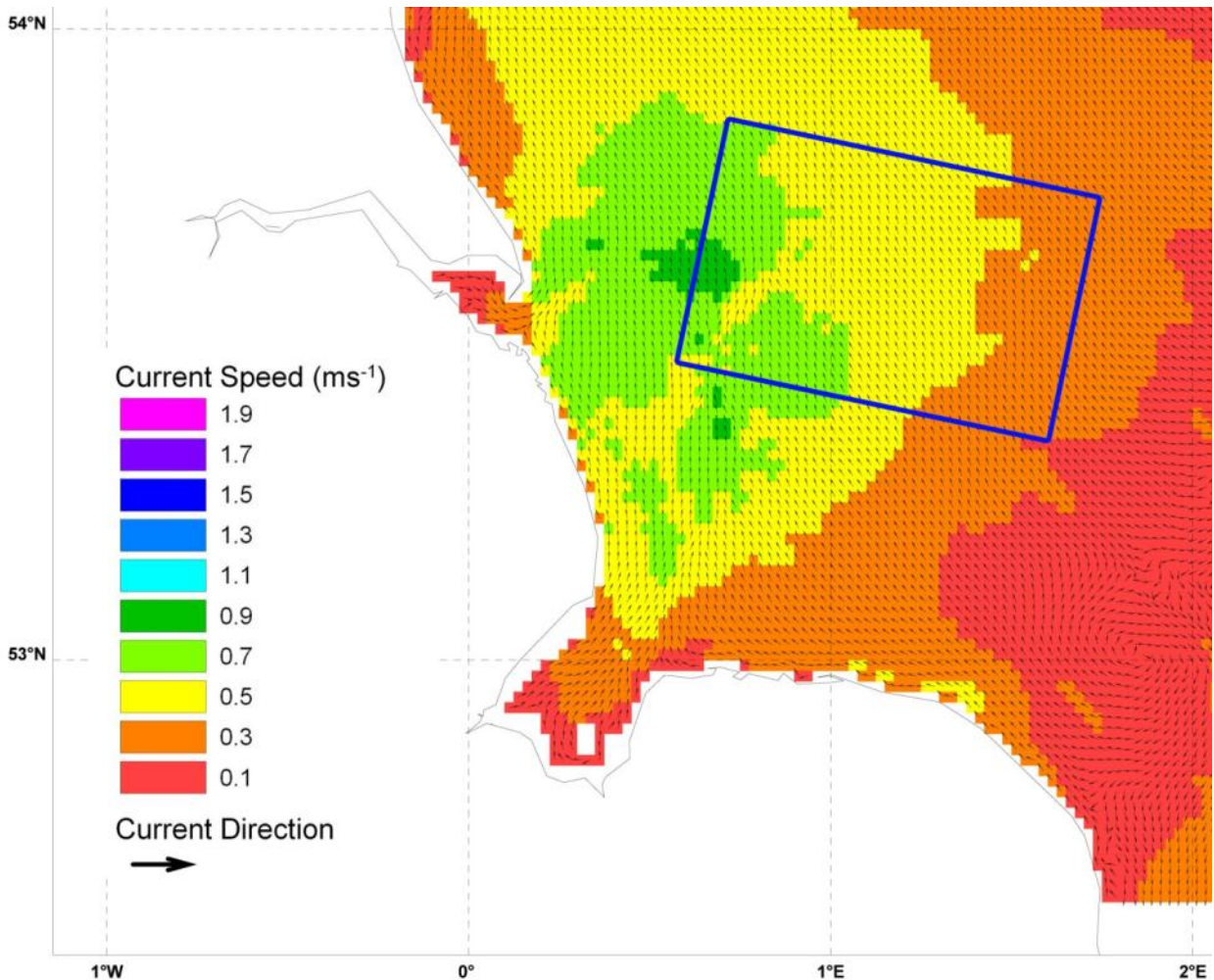


Figure 6.2 Modelled current data for 4 October 2014, 06:22 UTC (same date and time as Sentinel-1 image acquisition) produced by NOC using the Polpred software. The blue rectangle shows the Sentinel-1 image subset.

6.2.3 Methodology

To derive the bathymetry from the Sentinel-1 image scene, first some preprocessing steps had to be applied to ensure that the amplitude variations in the image were due only to influences of bathymetry. These steps were carried out using the programming language Python 2.7, and are described in sections 6.2.3.1 to 6.2.3.5. After preprocessing the inversion algorithm proposed by Renga and his team was applied to derive the bathymetry. This was undertaken in the programming language, Interactive Data Language (IDL), and is described in section 6.2.3.6. Finally, the bathymetric chart was geometrically corrected. This part, using the European Space Agency (ESA) Sentinel-1 Toolbox, is described in section 6.2.3.7. A flowchart showing the processing chain applied to the data to create a bathymetric map is shown in Figure 6.3.

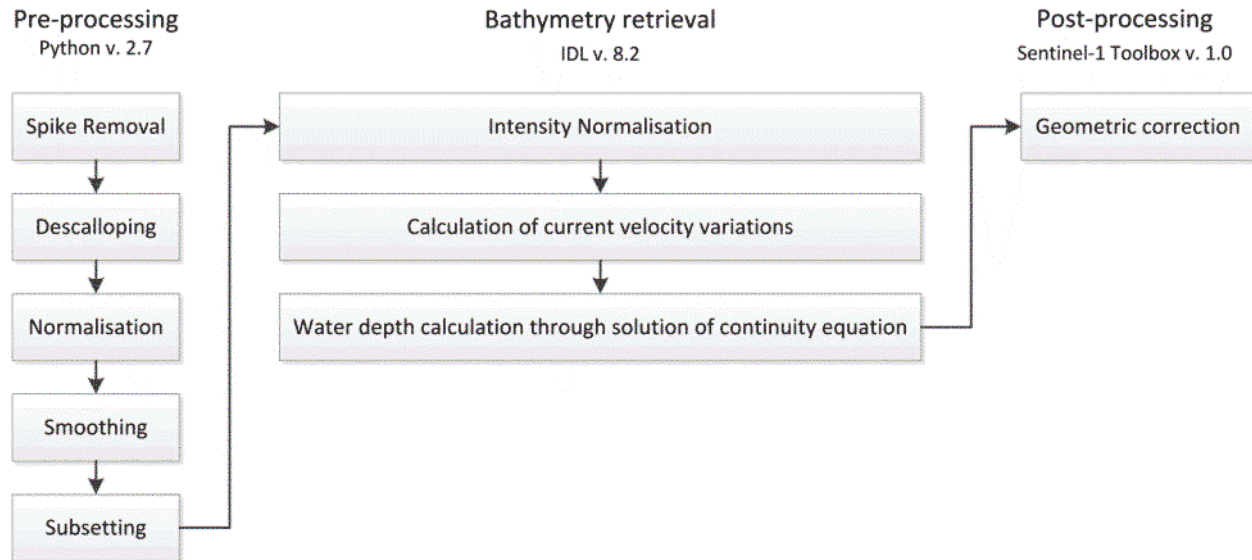


Figure 6.3 Sentinel-1 bathymetry processing chain.

6.2.3.1 Spike removal

This step included removal of small features of very high backscatter corresponding to ships, windmills, oil rigs and other objects that reflect strongly the SAR signal. Taking as input the full scene Sentinel-1 image of SAR amplitude in ground range geometry, the chosen method for spike removal is to replace with the column median those pixels that have a value higher than the column mean plus the column standard deviation multiplied by a threshold factor (see Equation 6.1).

$$\text{If, } i_o(x, y) > \bar{i}_o(y) + T \sigma_o(y), \text{ then } i_s(x, y) = \tilde{i}_o(y), \text{ otherwise } i_s(x, y) = i_o(x, y) \quad 6.1$$

where, for a pixel $i_o(x, y)$ in the original image, $\bar{i}_o(y)$ is the column mean, T is the threshold value, $\sigma_o(y)$ the column standard deviation, $\tilde{i}_o(y)$ the column median and $i_s(x, y)$ is the corresponding pixel in the spike removed image.

After several attempts with various threshold values, a value of 6 was deemed the most suitable in removing bright pixels corresponding to non-oceanic features of high backscatter, without modifying too many legitimate pixels of high backscatter. The implemented procedure for spike detection shows similarities with the standard approach for ship detection in SAR images in which adaptive threshold detectors are applied (Crisp 2004). It is worth noting that the value of the threshold typically ranges from 6 to 7 in those detectors. Careful scrutiny of the result revealed that the process performed well. Very few false positives were identified, and most features of high backscatter were removed. There were however still many residual pixels of high backscatter remaining around the edges of large and highly reflective non-oceanic features. An example of the spike removal procedure is shown in Figure 6.4.

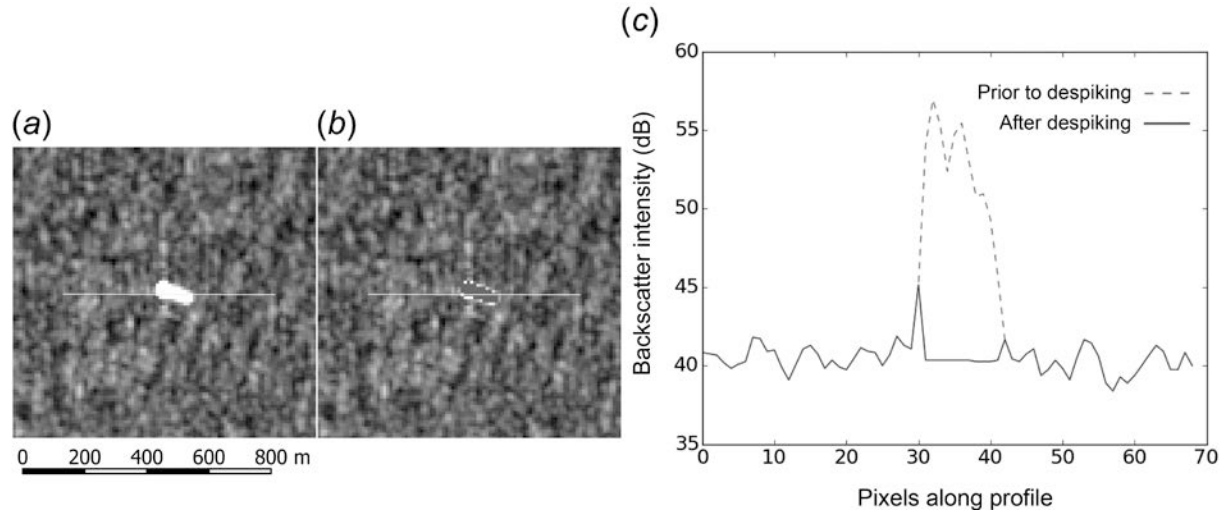


Figure 6.4 Example of spike removal: (a) Subset of Sentinel-1 image before spike removal. White line shows profile. (b) Same subset after spike removal, with same profile. (c) Comparison of backscatter intensity before and after spike removal along profile shown in (a) and (b). The profile runs from left to right.

6.2.3.2 Descalloping

Due to the Sentinel-1 cal-val activities, Sentinel-1 Stripmap images acquired early in the mission are affected by scalloping caused by periodic sensor calibration during image acquisition (see Figure 6.5(a) and Figure 6.6(a)). At the end of the cal-val activities, stripmap images will no longer be affected by this scalloping. For those images that are affected, such as in the case of the data used in this study, the scalloping pattern can easily be removed by post-processing, given that the pattern is regular and horizontally linear in range. To remove the pattern, the image was divided by the normalised mean azimuth profile (Equation 6.2).

The equation for descalloping reads,

$$i_d(x, y) = i_s(x, y) \bar{i}_s / \bar{i}_s(x) \quad 6.2$$

where $i_d(x, y)$ is the descalloped image pixel intensity, while \bar{i}_s and $\bar{i}_s(x)$ are the mean image pixel intensity and mean column pixel intensity respectively of the input spike removed image.

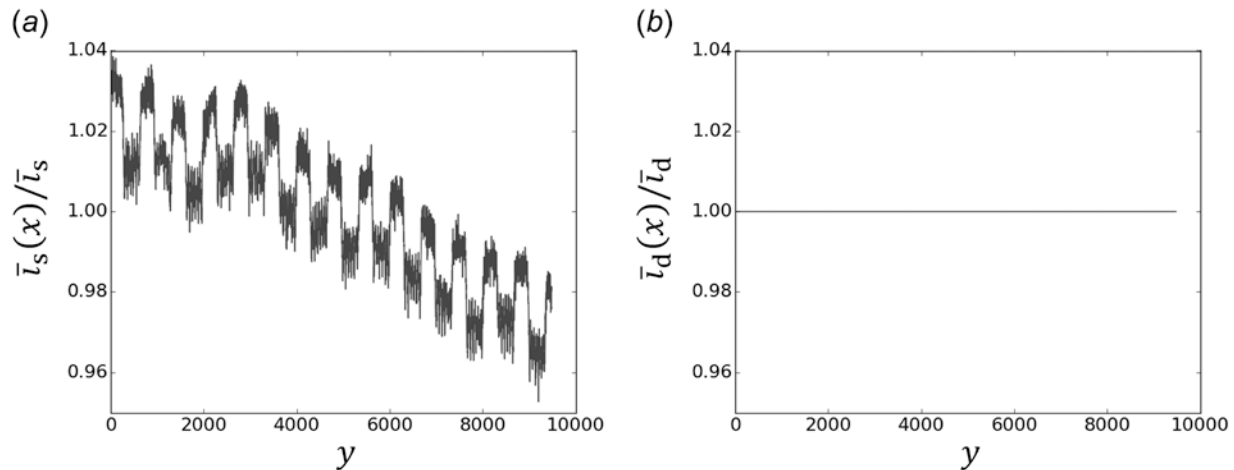


Figure 6.5 (a) Normalised mean azimuth profile prior to descalloping. (b) Normalised mean azimuth profile after descalloping.

6.2.3.3 Near to far range normalisation

A further pre-processing step involved removal of near to far range backscatter variation (see Figure 6.6(b) and Figure 6.6(c)), as these would be interpreted by the bathymetry algorithm as significant, steadily varying water depth in the form of a hill or a valley (depending on direction of current) with the peak or trough in the centre of the image. To remove this, normalisation was performed by dividing the entire image by a smoothed version of itself. Specifically a mean filter was applied with a 1500 by 1500 pixel kernel.

6.2.3.4 Smoothing

The purpose of this step was to smooth the image to remove SAR speckle. A moving mean filter of 15 by 15 pixels was applied to the entire image (see Figure 6.6(c)).

6.2.3.5 Subset selection

After the above pre-processing steps were applied to the entire image, subsets were extracted over areas covered by the NSPP on which to run the bathymetric retrieval algorithm. These subsets are grouped within one rectangular part of the Sentinel-1 image where the overall depth did not vary too greatly and where bathymetric features were clearly evident in the multilooked image of backscatter amplitude, suggesting that wind and current conditions were favourable for bathymetry retrieval. Within this rectangular area, further subsets were extracted to treat the deep tunnel valleys of the Inner Silver Pit and Sole Pit separately. The modelled current data produced by NOC showed a change in the east/west direction of the current flow over the Inner Silver Pit (see Section 6.2.2.2), and although the current data showed no change in the flow direction due to the presence of the Sole Pit, it was found that this area also had to be treated separately. Figure 6.6(c) shows the subsets which, in the original slant range geometry, were used as input to the bathymetry retrieval.

Given that geometric correction was performed only after the bathymetry retrieval (see Figure 6.3), the images provided as input to the bathymetric algorithm are in the original slant range geometry, with a

descending and right looking configuration. The images in Figure 6.6 therefore appear flipped horizontally and rotated with respect to the final geometrically corrected result (Figure 6.7).

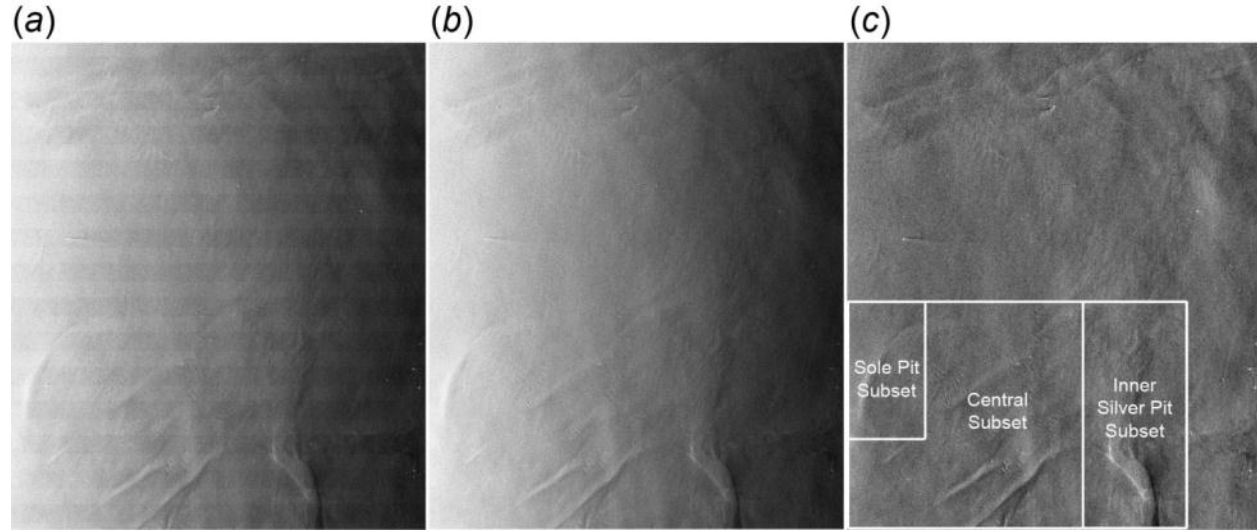


Figure 6.6 (a) Original Sentinel-1 image. The radar azimuth is the ordinate (vertical) and the radar range is the abscissa (horizontal). (b) Sentinel-1 image after spike removal and descalloping. (c) Final image after normalisation and smoothing. Subset areas are shown in white rectangles.

6.2.3.6 Bathymetry retrieval

The selected bathymetric algorithm was implemented in IDL version 8.2 and applied to the pre-processed subset image.

This technique is applied as follows (the interested reader is referred to (Renga et al. 2013, 2014) for further details about the algorithm). First, the image intensity is normalised (Eq. 6.3):

$$\frac{\Delta i(x, y)}{I_0} = \frac{i(x, y) - I_0}{I_0} \quad 6.3$$

where $i(x, y)$ is the image intensity for x and y pixel coordinates resulting from pre-processing, and I_0 is the image intensity at equilibrium. The normalised intensity is Fast Fourier Transformed (FFT) and the surface current velocity variations due to the current passing over varying seabed topography are calculated for each range line as follows (Eq. 6.4):

$$\Delta u_x(x, y) = \text{FFT}^{-1} \left[\frac{N_0}{G_{1x}(\mathbf{v})} \frac{\Delta I(\mathbf{v})}{I_0} \right] \quad 6.4$$

where FFT^{-1} is the inverse Fast Fourier Transform, N_0 is the action spectrum of surface short waves at equilibrium, G_{1x} is a kernel that can be calculated analytically by applying the theory of Volterra Series Expansion (VSE) (Inglada and Garello 2002) to solve the Action Balance Equation (ABE) (Alpers and Hennings 1984), $\mathbf{v} = (v_x, v_y)$ is the spatial wavenumber vector, and $\frac{\Delta I(\mathbf{v})}{I_0}$ is the Fast Fourier Transform of the normalised image intensity. With specific reference to the kernel G_{1x} , it can be calculated taking

into account relaxation only, or by including the contributions of advection and/or velocity bunching. The main term contributing to the kernel is relaxation (Alpers and Hennings 1984), while velocity bunching is up to several orders of magnitude lower than the relaxation and advection terms (Renga et al. 2014). In this case, the contributions of relaxation and advection were considered. One of the tuning parameters to be estimated at this stage includes the relaxation rate, μ . After some trial and error, this was chosen as $\mu = 0.00065 \text{ s}^{-1}$ in all subsets. The equation used to calculate the kernel G_{1x} for relaxation and advection is given below.

$$G_{1x}(\mathbf{v}_x) = -(4 + \gamma)N_0 \frac{c_g \mathbf{v}_x + j\mu}{(c_g \mathbf{v}_x)^2 + \mu^2} \mathbf{v}_x \quad 6.5$$

where j is the imaginary unit; analytical relations for the terms in Eq's. 6.4 to 6.5 are defined by:

$$N_0 = \frac{E_0}{\omega_0(k_x)} = \frac{k_x^{-4} a_p}{\omega_0(k_x)} \quad 6.6$$

$$\omega_0 = \sqrt{gk_x + \frac{\sigma_w}{\rho} k_x^3} \quad 6.7$$

$$k_x = \frac{4\pi \sin \theta}{\lambda} \quad 6.8$$

$$\gamma = \frac{gk_x}{2\omega_0^2} \left(1 + 3 \frac{\sigma_w}{\rho g} k_x^2 \right) \quad 6.9$$

$$c_g = \frac{g}{2\omega_0} \left(1 + \frac{3\sigma_w k_x^2}{\rho} \right) \quad 6.10$$

where ω_0 is the angular frequency of Bragg waves (Alpers and Hennings 1984), k_x is Bragg wavenumber, ρ is sea water density, g is the gravitational constant, σ_w is surface tension for the boundary between air and water, θ is the sensor incidence angle, λ is the radar wavelength, c_g is the group velocity of Bragg waves, γ is the group to phase velocity ratio and a_p is a constant (Phillips constant). Given that only normalized relative variations of the energy spectral density are of interest, a_p has no influence on bathymetric data retrieval and is therefore set to 1 (Alpers and Hennings 1984, Renga et al. 2014). Table 6-2 lists the values used for the parameters.

Table 6-2 Terms used to calculate the kernel G_{1x}

Term used in the calculation of the kernel G_{1x}	Value
ρ Sea water density	1025 kgm ⁻³
g Gravitational constant	9.807 ms ⁻²
σ_w Surface tension for the boundary between air and water	0.072 Nm ⁻¹
θ Sensor incidence angle	0.384 radians
λ Radar wavelength	0.056 m (C-band)
μ Relaxation rate	0.00065 s ⁻¹

Concerning the tuned value for the relaxation rate, past experimentations in C-Band (Calkoen et al. 2001), demonstrated that the adjusted values of the relaxation rate tend to be about one order of magnitude smaller than that typically expected from physical considerations. Hence, the tuned relaxation rate corresponds to a real relaxation rate in the order of $\mu = 0.0065 \text{ s}^{-1}$. This leads to a relaxation time of 153 s, which is in good agreement with that expected in C-band (Alpers and Hennings 1984).

Finally, the local water depth, $d(x)$, can be calculated by solving the continuity equation for one-dimensional stationary laminar flow as a first approximation defined by (Eq. 6.11):

$$d(x) = \frac{D_0 U_0}{U_0 + \Delta u_x} \quad 6.11$$

where D_0 and U_0 are respectively the water depth and current velocity at equilibrium. These are parameters to be estimated during the tuning phase, when the water depth is calculated for one range line with known a-priori water depth. Table 6-3 shows the estimated values of these parameters for the three subsets. Concerning Eq. 6.11 it is important to remark that, depending on the local bathymetry, conditions exist in which the assumption of one-dimensional laminar flow does not hold. In such cases more general models should be used (Baines 1998, Zheng et al. 2006, Zheng et al. 2012a, Zheng et al. 2012b).

Table 6-3 Estimated values for the equilibrium depth (D_0) and equilibrium current velocity (U_0) for each of the three subsets.

Subset	D_0 (m)	U_0 (ms^{-1})
Inner Silver Pit	-19	-0.1
Central	-20	0.1
Sole Pit	-23	-0.1

It was found at the tuning stage that increasing both the relaxation rate (μ) and the equilibrium current velocity (U_0) together produced similar results in terms of water depth values. Increasing μ acted as a smoothing filter in range, decreasing the detail, but also filtering out noise. Over the Central subset, in order to remain as close as possible to the modelled current data, but to retain as much detail as possible in the final bathymetric map, a value of U_0 was chosen slightly lower (0.1 ms^{-1}) than the estimated value from the modelled current data (around 0.25 ms^{-1}). Over the Inner Silver Pit subset, where the currents were shown to change east/west direction (see Fig. 2), a value of -0.1 ms^{-1} was chosen. This also appeared suitable for the Sole Pit subset (despite no apparent change in the modelled NOC current data revealed over the Sole Pit).

6.2.3.7 Geometric correction

The resulting depth maps of each subset were geometrically corrected to UTM zone 31 North with the reference ellipsoid World Geodetic System 1984 (WGS84), using the Range Doppler technique (Small and Schubert 2008). This process was performed fully automatically in the ESA Sentinel-1 toolbox,

without any need for manual selection of Ground Control Points (GCPs), using only the orbit ephemeris data associated with the Sentinel-1 image. The bathymetry retrieval process stripped the image subsets of all metadata. To enable automatic geometric correction therefore, the metadata of the processed subsets were replaced with the metadata of the subsets before preprocessing and bathymetry retrieval. The three subsets were finally combined into one map.

6.2.4 Results

The final bathymetric map (Figure 6.7) was compared with EMODnet bathymetric data of the same area (Figure 6.8) by overlaying the two geocoded datasets in QGIS (the Sentinel-1 map in Geotiff format and the EMODnet data in ASCII Grid format), and analysing profile plots. It is important to stress that, lacking information on the accuracy of the reference EMODnet data (given the multiple data sources), it is impossible to provide quantitative information on the accuracy of the Sentinel-1 derived bathymetric map. However, the EMODnet data provides a useful check.

Both maps show the same pattern of bathymetric features at various scales, from the large tunnel valleys of the Inner Silver Pit in the southwest corner of the map, and the Sole Pit in the northeast corner, to the small clusters of what appear to be sand banks and sand waves. However, there are also significant differences between the two maps. A number of narrow, deep trenches visible in the EMODnet chart are not visible in the Sentinel-1 map. Also, the Sole Pit, according to the EMODnet map, is a crescent shaped feature which curves around from the east (approximately aligned along the Sentinel-1 range direction) to the south (aligned roughly along the Sentinel-1 azimuth). Only the part aligned along the azimuth is visible in the Sentinel-1 map. Perhaps the reason for the partial mapping of the Sole Pit in the Sentinel-1 map is due to the ability of the retrieval algorithm to detect only depth variations in range (Alpers and Hennings 1984), and its inability to detect slowly varying water depth (Renga et al. 2013). There are other, more subtle, bathymetric features in the EMODnet map which are not present in the Sentinel-1 map. Assuming these are not artifacts in the EMODnet map, it may be that they are not present in the Sentinel-1 map due to unfavourable conditions for bathymetric retrieval, e.g. the height of the feature may be too short and the water depth too great to sufficiently modify current velocities, or there may have been non-uniform, or insufficient currents in the range direction, or unfavourable winds sufficient to produce small surface waves propagating along the range. There are also apparent bathymetric features in the Sentinel-1 map which are not in the EMODnet map. Again, assuming this is not due to an error in the EMODnet map, it may be due to other oceanic or atmospheric effects causing backscatter variation in the SAR image.

In terms of the water depth values, while the overall range of water depths recorded in both the EMODnet and Sentinel-1 depth charts are similar in most areas (approximately from 10 to 50 meters), there are large differences over some features, particularly the deep trenches, which are generally much deeper in the EMODnet map. This is probably due to current velocities within these features influencing the surface current velocities, which in turn influence the true calculation of the depth from the SAR backscatter. In fact, the maximum depth which can be sensed by SAR depends on local current and weather conditions and it is not expected to be significantly higher than 30-40 m.

Figure 6.9 compares the EMODnet and Sentinel-1 water depths over two transects: one crosses the Inner Silver Pit, the largest topographic feature (Figure 6.9(a)), the other crosses some of the smallest identified topographic features (Figure 6.9(b)). The locations of these profiles are shown in Figure 6.7 and Figure 6.8. The Sentinel-1 transects have been averaged by a moving filter of 21 points to attain approximately the same resolution (around 200m) as the EMODnet chart. Both transects are plotted from northwest to southeast.

The Inner Silver Pit transect (Figure 6.9(a)) shows roughly the same profile of the trench in both maps. However, the absolute values differ significantly. The Sentinel-1 map shows water depths from around 24 to 36 m over the trench, while according to the EMODnet map, the trench reaches a water depth of over 60 m along this transect, which is beyond the range of water depths SAR can sense, from an initial water depth of around 30 m.

The short transect (Figure 6.9(b)) shows better agreement in terms of the absolute water depths (only a few meters of difference between the two charts). However, the relative height difference of the peaks and troughs in both transects vary. This may in part be due to the heavy smoothing of the Sentinel-1 transect and the coarse sampling of the EMODnet map. There is also a phase shift between the two profiles at the second (rightmost) peak. Besides the consideration that the shift could be artificially generated by the coarse EMODnet map sampling, given that the size and proximity of these features are close to the limits possible with SAR bathymetry at these depths and current velocities, it is likely that there is not enough of a gap between features to allow sufficient time for the induced current perturbations to translate to surface wave modulations at the assumed relaxation rate. An alternative explanation is that the local flow direction does not match the assumption of one dimensional transverse flow (Baines 1998, Zheng et al. 2006, Zheng et al. 2012a, Zheng et al. 2012b).

6. Archaeological Prospection of the North Sea Palaeolandscape Using SAR

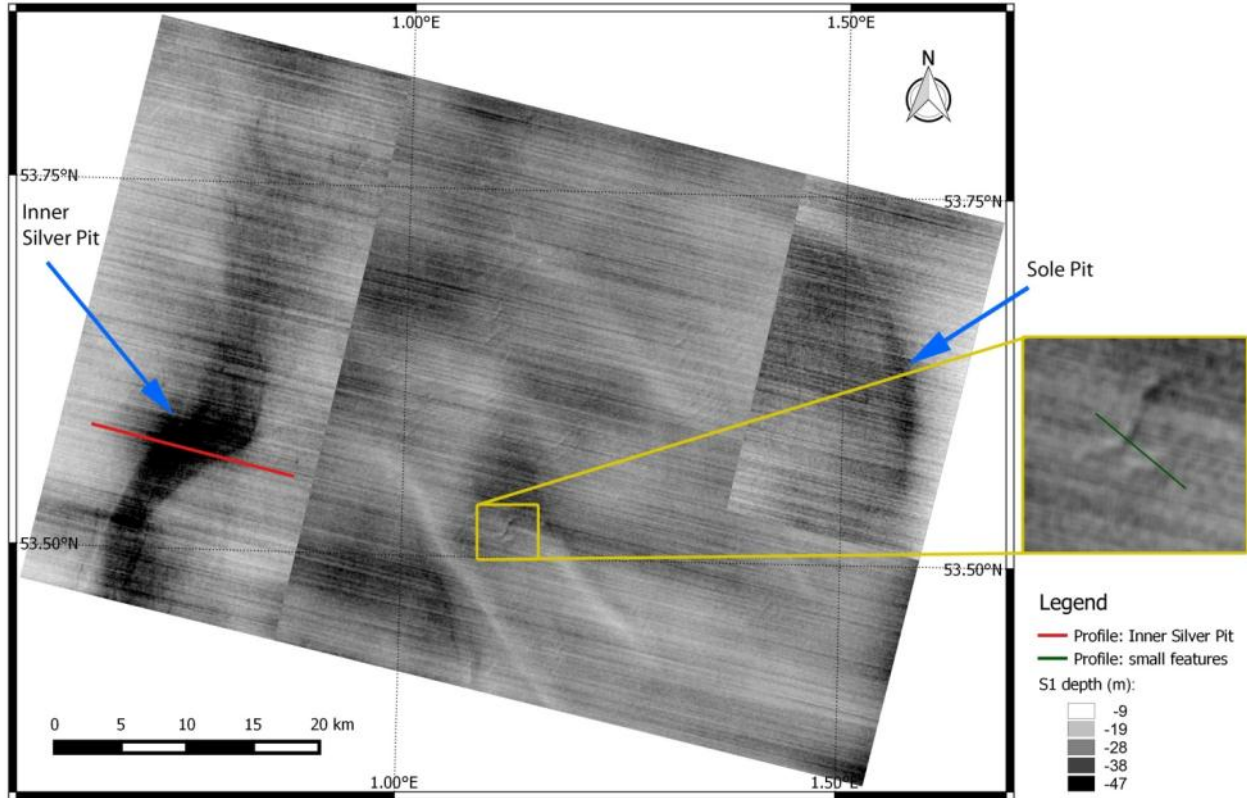


Figure 6.7 Sentinel-1 bathymetric chart. Profiles shown as red and green lines.

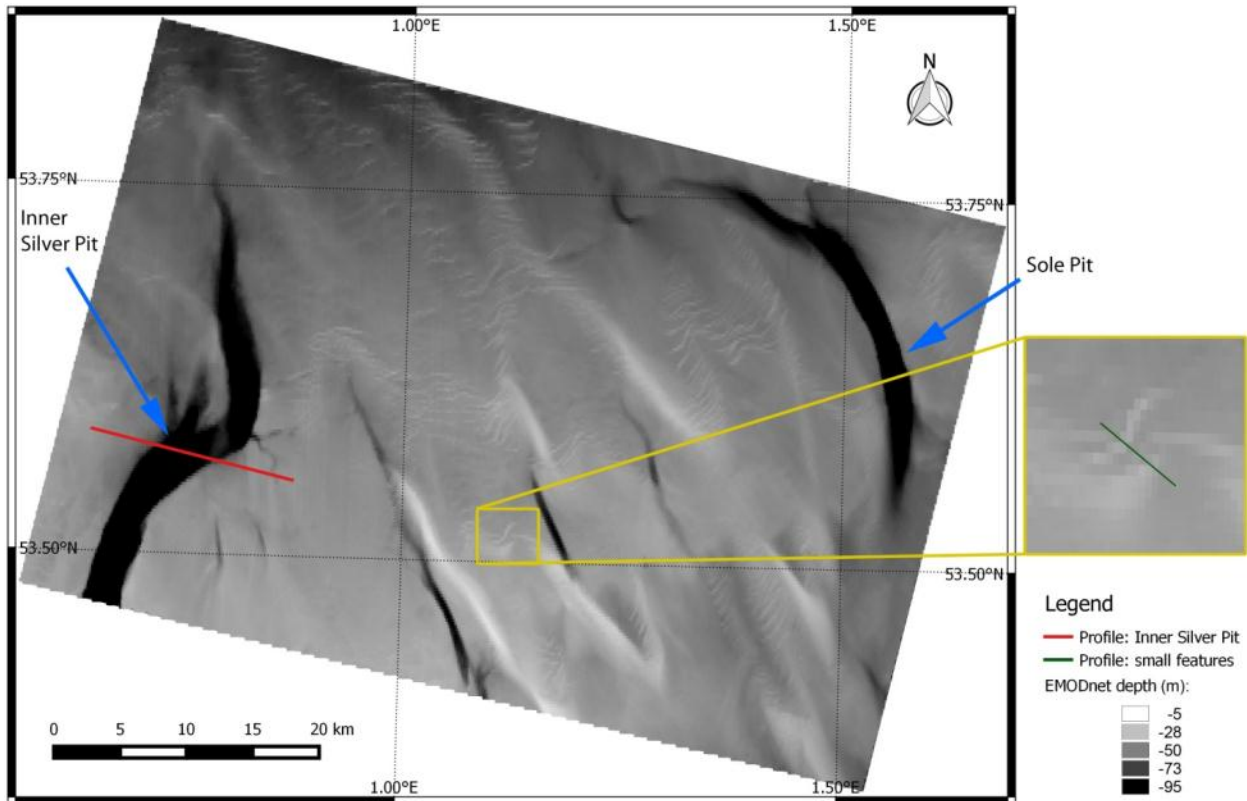


Figure 6.8 Extract of EMODnet depth chart covering same area as Sentinel-1 depth chart. Profiles shown as red and green lines.

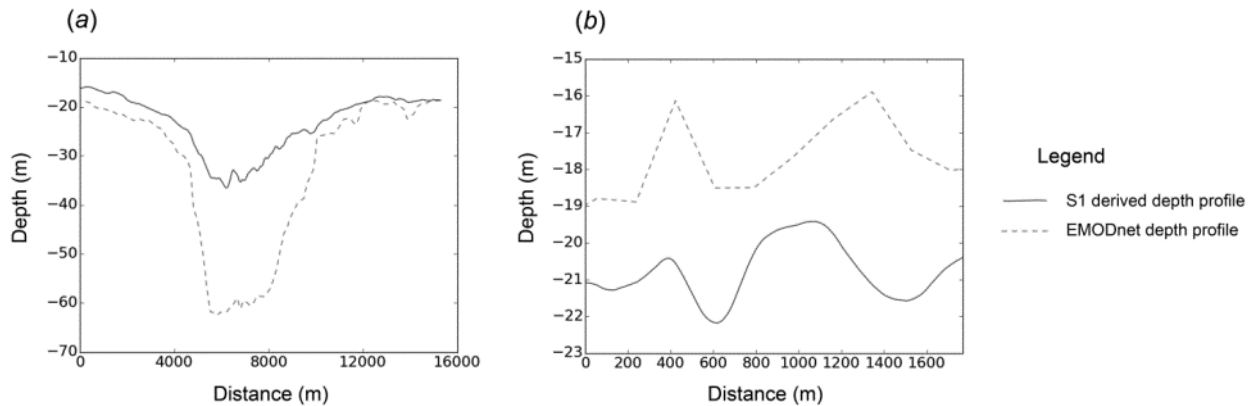


Figure 6.9 Profile plots of Sentinel-1 derived and EMODnet depths. (a) Depth profiles over Inner Silver Pit. (b) Depth profiles over small features.

6.3 SAR Support to the Mapping and Monitoring of Palaeolandscape Features

The Sentinel-1 chart has been compared with the atlas and vectors of palaeolandscape features of the Early Holocene produced by the NSPP (University of Birmingham 2011). The objective of this comparison is to see to what extent the datasets agree, and to determine the potential support that SAR bathymetry could provide for the analysis of such submerged palaeolandscapes.

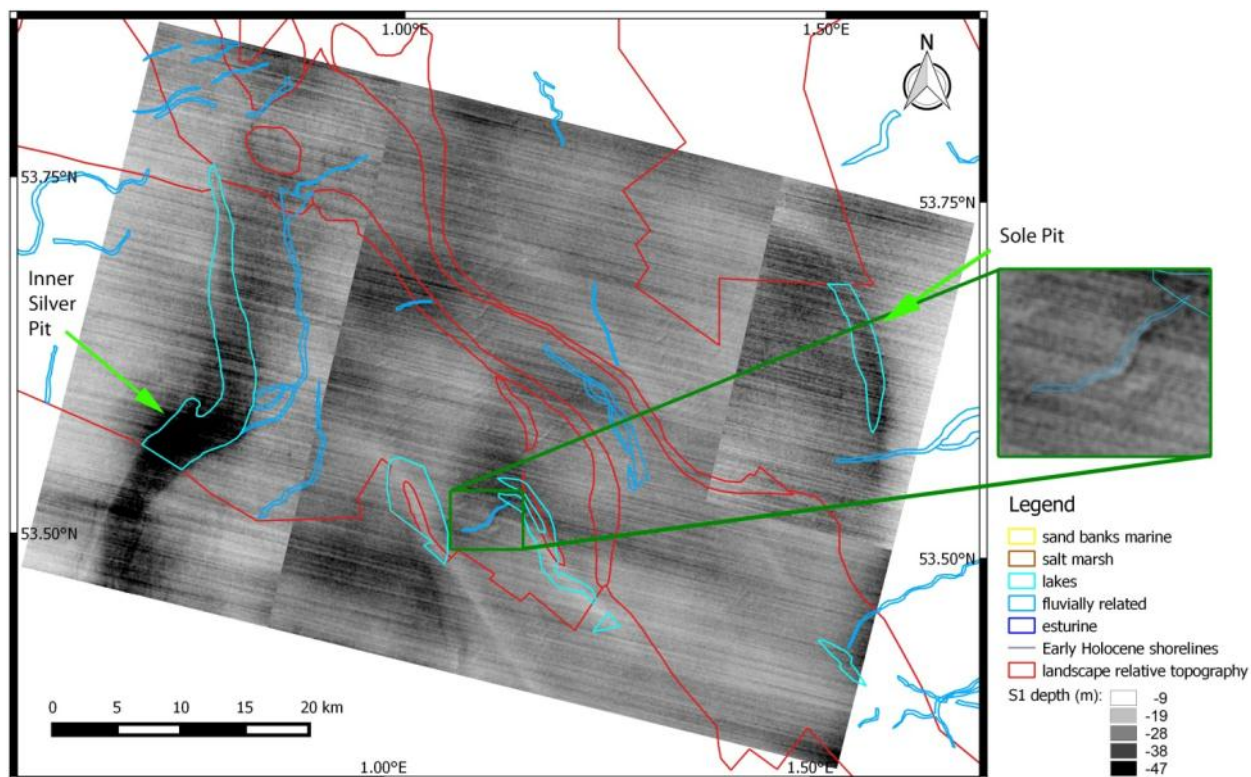
Figure 6.10 shows the vectors of Early Holocene features interpreted by the NSPP overlain on the Sentinel-1 chart. There is some agreement between the two datasets: The tunnel valleys of the Inner Silver Pit and Sole Pit mapped in the Sentinel-1 chart appear to correspond with lacustrine features in the Early Holocene landscape. Both features in the NSPP data are truncated, only because the limits of the project area have been reached. Two smaller features interpreted as Early Holocene lakes are also partially visible in the Sentinel-1 map. In between these there is a small and clearly delineated feature (see detail in Figure 6.10), interpreted as an Early Holocene riverine feature: perhaps an abandoned meander bend that once formed part of a larger fluvial system. Within one of the Early Holocene lakes, to the west of this riverine feature, there is a ridge of high ground (the relative height is given in the NSPP atlas), this corresponds with a ridge in the Sentinel-1 map.

There are also features mapped by the NSPP that are not in the Sentinel-1 map. These include a small lake and fluvial features. Also, there are some geological structures identified in the seismic data that would have influenced Early Holocene landscape features, including a broad, slight valley traversing the area from the southeast to northwest corners, some slight hills, and other small valleys and ridges. Apart from the small ridge mentioned above, these features have not been identified. However, the features are interpreted as Early Holocene landscape structures influenced by underlying geology, and they may no longer have a topographic signature on the modern seabed. The interpretation by the NSPP of the palaeolandscape structures may also need refinement.

Many topographic features are not present in the NSPP data, but are identified in both the Sentinel-1 and EMODnet depth maps (and can therefore be assumed to be seabed topography). These probably

6. Archaeological Prospection of the North Sea Palaeolandscape Using SAR

correspond with features that were not present in the Early Holocene landscape, such as modern sand banks. It was pointed out in the NSPP atlas (Gaffney et al. 2007) that modern sand banks have been identified in the seismic data during the palaeolandscape survey, but omitted from the atlas, given that they are recent structures. Many small features resembling sand banks can be seen in both the Sentinel-1 and EMODnet charts, only one of which corresponds with a palaeolandscape feature (Early Holocene riverine feature). From the Sentinel-1 chart alone, it would be difficult to distinguish this palaeolandscape feature from the many other similar features nearby, highlighting the need for datasets other than bathymetry for palaeolandscape studies. Palaeolandscape features that have a topographic expression may potentially be more static than modern structures with similar topographic characteristics. In this case, discrimination between the two could be aided by repeated mapping, which will be possible to achieve in a cost effective manner with the guaranteed, long term access to freely available Sentinel-1 data. It may of course be that the similar features in the Sentinel-1 chart are also palaeolandscape features, only not identified during the NSPP survey, but this is unlikely given that multiple high resolution datasets were used. Other features on both the Sentinel-1 and EMODnet charts, but not in the NSPP atlas, include larger structures, such as a large, but slight, ridge in the centre of the area. This may again be a modern feature. There are many mobile sand banks in the area, which may have moved between the acquisition times of the data used by the NSPP and the Sentinel-1 SAR sensor.



6.4 Conclusions

The results of applying a recently developed bathymetric retrieval algorithm to a subset of Sentinel-1 SAR data over the North Sea successfully demonstrate the suitability of the technique to work with C-band SAR data over a region very different from the Mediterranean. While an accurate scientific validation has not been carried out yet, a comparison of the resulting chart with data freely provided on the EMODnet bathymetry portal reveals the same pattern of bathymetric features. These features include underwater topographic structures at scales ranging from several hundred meters in the horizontal SAR range direction, and a few meters in altitude, to several kilometres in range and with an altitude (or water depth) of tens of meters. These features have been mapped at an initial water depth of around 15 to 25 meters.

While the chosen retrieval algorithm has the ability to perform direct inversion from image intensity to bathymetry without the need for *a-priori* information or in-situ measurements, nonetheless, certain limitations exist. The technique is only able to detect depth variations in the SAR range direction. This limitation may have resulted in incorrect mapping of the Sole Pit. Gradual depth variations are not easily detected. The retrieval algorithm exploits a one-dimensional fluid dynamics model which could potentially mask bathymetric features in areas of complex seabed topography. This limitation may have been the cause for the underestimation of the depths of deep trenches with respect to EMODnet, while over small features the depth variation appears similar. Perhaps there are current velocities within the trenches that alter the behaviour of overlying currents. Future developments of the algorithm shall therefore include a more general, multidimensional model (Baines 1998, Zheng et al. 2006, Zheng et al. 2012a, Zheng et al. 2012b), to relate seabed morphology with local current variations sensed by SAR. Moreover, additional effort shall be dedicated to the removal of all traces of oceanic and atmospheric phenomena influencing the SAR backscatter that are not due to bathymetry, as well as objects in the image scene, such as ships, oil-rigs, wind-farms, etc. This shall probably involve the assimilation in the algorithm of data from different sources, e.g. weather data, maritime traffic, database of known underwater or offshore man-made objects.

To gain an insight into the possible support that SAR bathymetry could provide for the study and monitoring of submerged palaeolandscapes, the Sentinel-1 derived bathymetric chart was compared with the vector data and atlas freely distributed by the NSPP. Several palaeolandscape features interpreted by the NSPP, at various scales, from a few hundred metres to a few kilometres, appear to correspond with bathymetric features detected on the Sentinel-1-bathymetric chart to a high geolocation accuracy (NSPP vectors overlain on the Sentinel-1 bathymetry match to within a few pixels, i.e. a few tens of meters). These include Early Holocene lakes, river segments, and landscape topography. There are NSPP mapped palaeolandscape features that do not appear to correspond with Sentinel-1-derived bathymetry. These features may no longer have a topographic signature, and can be detected only on other datasets, such as seismic data, or, if they do still have a topographic signature, the conditions may not have been sufficient for them to be detected on the Sentinel-1 data and with the chosen retrieval technique. There are also features on the Sentinel-1 bathymetry which do not correspond with NSPP features. These may be modern structures, such as sand banks, or artefacts caused by objects on the sea surface or by phenomena other than bathymetry.

Whilst bathymetry can provide a reasonable approximation of the land surface topography, it does not take into account possible burial of features that may have occurred during or after submersion (Cameron et al. 1992). However, bathymetry is nonetheless capable of providing detailed images of Late Quaternary and Holocene features that have a bathymetric expression (Gaffney et al. 2007). Submerged palaeolandscapes have received very little attention, despite the potentially enormous wealth of information they may be able to provide on an archaeological record kept from subsequent development and frozen in time since rising sea levels inundated the land. This lack of attention can lead to a complete disregard of possible threats to the palaeolandscape due to modern development activities. Mapping and regular monitoring of the submerged palaeolandscape would help to lift it from obscurity and deliver it to the public awareness as a resource to be preserved. The main challenge of such a task lies in the size and inaccessibility of the areas, and the cost involved, which may be very difficult to justify merely for the sake of preservation.

In this context SAR bathymetry could represent a useful tool for regular survey of large areas such as the North Sea, particularly with the advent of Sentinel-1. The Sentinel constellations provide unprecedented access to freely available data at a frequency of acquisition and long term continuity required to support operational services (European Space Agency 2016). The Sentinel-1 constellation comprises two satellites (Sentinel-1A and B), each carrying an imaging C-band SAR instrument. With two satellites in orbit, repeat acquisitions are possible every 6 days (Geudtner et al. 2014). The acquisition scenario envisages systematic acquisition in Interferometric Wide Swath (IW) mode over coastal areas, Extra Wide Swath (EW) over certain waters, and Wave Mode over the open ocean (Schmuck et al. 2014). The areas in which there are submerged palaeolandscapes will therefore be systematically and regularly imaged at either IW mode (20 m spatial resolution and 250 km swath width) or EW mode (50 m spatial resolution and 400 km swath width). The spatial resolution of the IW FR mode is identical to the SM HR mode of the image used in this study, but the swath is much wider.

Similar extensive areas of submerged, but previously inhabited landscapes also exist in the Black Sea (Ryan and Pitman 2000), the Florida Gulf (Faught 1988, Faught 2004), the Gulf of Arabia (Lambeck 1996) and a number of other parts of the world (Gaffney et al. 2007). While the SAR data may exist for these areas, the conditions for SAR bathymetry retrieval may not be suitable (currents, winds, etc.). However, the more imagery is available, the more likely it is that an image is acquired when the conditions are right, and at least for some of these areas it may be possible to carry out regular and cost effective bathymetric mapping to support the mapping, preservation and valorisation of the submerged palaeolandscape.

7 OVERALL CONCLUSIONS

Comparison of variously processed SAR data from a range of sensors with archaeological ground truth over a diversity of areas has demonstrated the capability and limitations of SAR to efficiently locate archaeological features which may otherwise go undetected. Three case studies were chosen in which different prospection techniques were applied over land and water surfaces. These include: archaeological prospection through vegetation and soil proxies in the temperate region of Rome in central Italy; prospection in sand covered parts of North Sinai in Egypt through signal penetration and surface roughness; and prospection underwater in a region of the North Sea through bathymetric mapping by detecting sea surface roughness alterations caused by sea bed topography modulated currents. In an attempt to assess the full capability of SAR for this application, the information content from both the phase and amplitude of the SAR signal was exploited. As much use as possible was made of the availability of large time series of data from sensors in various frequencies and acquisition modes. With this data, new and established techniques combining intensity time series, interferometric and polarimetric processing, and Fourier analysis, were attempted in order to test as far as possible the limits of current SAR capabilities for archaeological prospection.

Research results reveal a number of novelties: For the first time SAR coherence has been demonstrated to detect surface residues of buried archaeological structures in areas of crop or grassland. The use of an unprecedented time series length of VHR X-band SAR data (COSMO SkyMed) has been shown to greatly improve the detection capability of crop and soil marks through improved multitemporal filtering and SBAS DEM generation. It is also the first time that repeat pass InSAR has been shown to detect topographic anomalies of archaeological structures in vegetated regions. Novel techniques have been devised to extract for the first time in a systematic fashion anthropogenic structures in sand covered regions using both filtered intensity and average coherence of a time series of L-band SAR data. Finally, SAR bathymetry was applied for the first time for the mapping of a submerged palaeolandscape.

Results of the PhD research have been published in five peer reviewed publications, and have been presented at various workshops, conferences and symposia. During the course of the PhD, the author co-organised a conference on remote sensing for archaeology, and delivered training courses in Europe, Africa, Asia and South America.

The following sections summarise the main conclusions of each aspect of the research

7.1 Prospection over vegetated areas

An assessment was made of the utility of SAR to detect surface residues of buried archaeological features over vegetated areas in the temperate region surrounding Rome. Residues were identified in COSMO SkyMed Stripmap and Spotlight imagery. These were apparent in De Grandi multitemporal speckle filtered σ^0 backscatter, interferometric coherence and DEMs derived from InSAR and SBAS. The variously processed imagery helped to interpret the residues as manifestations of positive and negative crop marks, soil marks, and topographic traces marking the locations of archaeological structures. More residues were found in the area of the Tiber valley and delta, characterised by alluvial substrate and flat

7. Overall Conclusions

topography. Less residues were found in the volcanic districts on either side of the Tiber Valley, characterised by a volcanic substrate and undulating topography. However, some residues were found in these areas as well.

The large time series of data greatly aided speckle filtering in the temporal domain, while preserving spatial resolution. It also aided DEM generation, through use of the SBAS technique to minimise the limitations of loss in coherence over vegetated areas. Archaeological residues were in some cases identified in the coherence images. With a coherence time series, additional information on the state of the vegetation cover could be derived.

Polarimetric analysis was carried out over one subset area, near the Via Prenestina, near the Albano volcanic district. Polarimetric decompositions were extracted and analyses were made of the polarimetric signature over different areas. While the polarimetric processing yielded more information on the nature of the surface, it was not possible to unambiguously identify any traces of buried archaeological features. However, this may be primarily due to the coarse spatial resolution of the Radarsat-2 polarimetric data relative to the scale of the archaeological structures, many of which are likely to consist of fragmented and incoherent remains.

The research carried out in this case study have been published in two peer reviewed articles: The polarimetric analysis was published in the International Journal of Applied Earth Observation and Geoinformation (2015 IF: 3.8) (Stewart et al. 2014); the COSMO SkyMed analysis was published in the journal Remote Sensing (2015 IF: 3.036) (Stewart 2017).

7.2 Prospection over sand covered areas

The potential of L-band SAR to extract anthropogenic features in a desert region was assessed in the North Sinai Desert. To achieve this, a mosaic was first created of multitemporal speckle filtered σ^0 backscatter from single and dual polarised PALSAR-1 data covering the entire North Sinai region. A visual inspection of the mosaic and comparison with optical imagery of a similar acquisition date range revealed potential anthropogenic features characterised by higher backscatter relative to surrounding areas. Some apparent features of low relative backscatter were also identified in a coastal area in the northeastern Nile delta. Two case studies were selected for further analysis: one in the area between the Wadi Tumilat and Gebel Meghara, where seemingly anthropogenic features of higher backscatter than surroundings were apparent; the other over the region of the northeastern Nile delta, around the archaeological sites of Tell El-Farama, Tell El-Mahzan and Tell El-Kanais, where features of low relative backscatter, seemingly anthropogenic in nature, were identified.

Over the subset between the Wadi Tumilat and Gebel Meghara, an attempt was made to automatically extract features of high relative backscatter to facilitate further analysis with other available datasets in a GIS. Several attempts were made with algorithms based on mathematical morphology. Initially, the average multitemporal speckle filtered σ^0 backscatter of the PALSAR-1 data was used as input. The problem with this was that there was an ambiguity between the high backscatter of seemingly anthropogenic features and the similarly high backscatter occurring when the sensor incidence angle approached the angle of repose of sand dunes. A partially successful attempt to overcome this involved

use of a local incidence angle mask from a DEM. However, it was subsequently found that the average coherence between all consecutively acquired images in the time series clearly revealed the seemingly anthropogenic features without the ambiguity with sand dune ridges. The linear features were therefore extracted from this dataset. Extracted features were then analysed in a GIS with other available ground and remotely sensed data, and it was found that extracted features in some cases corresponded to seemingly abandoned, partially buried roads.

Over the subset area of Tell El-Farama, Tell El-Mahzan and Tell El-Kanais, a time series of PALSAR-2 Spotlight data were procured for analysis at a higher spatial resolution, given the small size of the features of low relative backscatter identified in the PALSAR-1 data. A number of multitemporal processing methods were applied using both the speckle filtered σ^0 backscatter and interferometric phase of both the PALSAR-1 and 2 data. It was found that the features of low relative backscatter were highlighted in the mean, standard deviation and coefficient of variation of the multitemporal speckle filtered σ^0 backscatter of both the PALSAR-1 and 2 datasets. The features corresponded largely with previous results of an archaeological survey over a part of the area carried out by field walking. The archaeologists who carried out the field walking survey interpreted the features as possible island areas of dry ground surrounded by water or by swampland. It is suggested that some traces of moisture may remain in between the island features sufficient to be detected in the SAR data, but not in optical imagery.

The utility of SAR for archaeological prospection through the direct detection of anthropogenic features appears promising and feasible, especially in the initial stages of large scale archaeological survey. However, the interpretation of features is challenging, particularly in view of the many artefacts that may be present, including radio frequency interference, range and azimuth ambiguities.

Interpretation of results was aided by a team of multi-disciplinary scientists, including geologists, Egyptologists, archaeologists, and remote sensing experts.

The results of the analyses in the North Sinai have been published in two peer reviewed articles. These have been published in the journal *Archaeological Prospection* (2015 IF: 1.327) (Stewart et al. 2013b) and *Remote Sensing* (2015 IF: 3.036) (Stewart et al. 2016b). Results have also been published in edited volumes of a *Progetto di Ricerca di Interesse Nazionale*, an Italian Research Project of National Interest (PRIN) (Stewart et al. 2015a, Stewart et al. 2016a), and in conference proceedings (Stewart et al. 2016a).

7.3 Prospection under water

Submerged palaeolandscapes potentially contain an enormous wealth of information given that they have been kept from subsequent development and frozen in time since they were inundated (Gaffney et al. 2007, Benjamin et al. 2011). Their vast extent poses significant challenges in their mapping and monitoring (Benjamin et al. 2011, Evans et al. 2014), and leaves them vulnerable to threats posed by activities such as mineral extraction, construction and commercial trawling (Westley et al. 2004). While bathymetry alone may not provide a complete picture of past landscapes, especially in areas of high deposition or erosion, it nonetheless can support palaeolandscape analysis in conjunction with other techniques, such as seismic survey and coring (Gaffney et al. 2007). In this context, the utility of SAR to

7. Overall Conclusions

map and monitor extensive submerged palaeolandscapes was tested over a region of the North Sea. This area contains one of the most extensive and probably best preserved prehistoric landscapes in Europe (Fitch et al. 2007).

The utility of SAR for bathymetric mapping has long been known and in some cases operationally applied, but it has always been challenging, requiring *a-priori* knowledge of water and atmospheric conditions, and has never been used for the detection or monitoring of underwater cultural heritage. The recently developed bathymetric retrieval algorithm developed by Renga et al. (2013, 2014) over coastal regions of the Mediterranean, was applied in this PhD research over the very different environment of the North Sea using Sentinel-1 SAR data. The ability of the inversion algorithm to retrieve bathymetry from image intensity without the need for *a-priori* information or in-situ measurements makes it potentially very promising as a cost effective technique for regular bathymetric mapping. A comparison of the results with the bathymetric chart on the EMODnet portal revealed the same pattern of bathymetric features. These include underwater topographic structures at scales ranging from several hundred meters in range, and a few meters in altitude, to several kilometres in range and with an altitude (or water depth) of tens of meters. These features were mapped at an initial water depth of around 15 to 25 meters. However, there were also significant discrepancies between the EMODnet and Sentinel-1 derived bathymetric maps. Limitations of the retrieval algorithm exist in its ability to detect depth variations only in the SAR range direction. The algorithm is based on a one-dimensional fluid dynamics model which may be insufficient to detect bathymetric features in areas of complex seabed topography. Limitations also exist in the dependence of the algorithm on particular conditions of current and wind velocity, which must be parallel to the SAR range direction. Finally, the sensitivity of the algorithm to other oceanic and atmospheric effects, as well as objects, such as ships, in the image scene, which must be removed to ensure successful bathymetric retrieval, is another significant limitation.

To assess the possible support that SAR bathymetry could provide for the study and monitoring of submerged palaeolandscapes, the Sentinel-1 derived bathymetric chart was compared with a map of the palaeolandscape of the same area produced by the North Sea Palaeolandscapes Project. Several palaeolandscape features mapped by the North Sea Palaeolandscapes Project, including Early Holocene lakes, river segments, and landscape topography, were apparent also in the Sentinel-1 bathymetric chart. Other mapped palaeolandscape features were not present in the S1 bathymetric map. These features may no longer have a surface topographic expression, or the conditions may not have been sufficient for them to be detected on the Sentinel-1 data with the retrieval technique. There were also features on the Sentinel-1 bathymetric chart which do not correspond with mapped palaeolandscape features. These may be modern structures, such as sand banks, or artefacts caused by objects on the sea surface or by phenomena other than bathymetry.

Bathymetric mapping with SAR is challenging, particularly given its dependence on water and atmospheric conditions. However, under favourable conditions, bathymetric features can be mapped, including topographic traces of palaeolandscape features. The wide swath and regular repeat pass of the Sentinel-1 constellation (European Space Agency 2016) increases the probability of image acquisitions

7. Overall Conclusions

occurring under conditions that favour bathymetric mapping, and may constitute a cost-effective technique for regular and large scale monitoring of extensive palaeolandscape regions.

The research on Sentinel-1 bathymetry for the mapping and monitoring of submerged palaeolandscapes has been published in an article in the *International Journal of Remote Sensing* (2015 IF: 1.640) (Stewart et al. 2016c). It has also been presented at various workshops and conferences (see Appendix C.4), and at several meetings of the ITACA project (see Appendix C.3.2).

7.4 PhD activities

Throughout the PhD research, the author has organised events and participated in many activities to disseminate the results of the research and collaborate with other scientists working in the field. Collaboration activities have included the co-organisation of a workshop, and participation in projects conferences and symposia; while the dissemination activities have included the organisation of training events, the publication of papers, and presentations given at a wide range of events.

Various projects have taken place during the course of the PhD which have focused on the use of remote sensing for archaeological prospection, and have been relevant to all three case studies chosen by the author. The ASI funded WHERE project (see Appendix C.3.1) contributed data and provided a platform in which to carry out research on the use of SAR for archaeological prospection in vegetated areas around Rome. The PRIN project (see Appendix C.3.3) provided essential expertise and guidance for the choice of area in which to undertake the research in the use of SAR for archaeological prospection in sand covered areas, and more importantly, contributed much needed expertise in the interpretation of results. The ITACA project (see Appendix C.3.2) enabled the author to regularly consult and compare notes with the only other experts working on SAR bathymetry for archaeological applications. The involvement of the author in projects has varied from supporting the technical officer with the project management and review of deliverables, which was the case of ArchEO (see Appendix C.3.4), to direct involvement as an active participant delivering project results, which was the case of WHERE and the PRIN project, to being a project spectator, attending and presenting at meetings and workshops, but not obliged to produce any project deliverables, which was the case with ITACA.

Results of the PhD have been presented in conferences, workshops and symposia. These range from small focused workshops with sessions dedicated to the application of SAR for specific types of archaeological prospection, such as in the case of the EARSeL, ITACA, or Aerial Archaeology workshops; to large conferences or symposia, such as EGU and the ESA Living Planet Symposia, where a very wide range of thematic areas are included. Both ends of the scale have been useful to promote results and collaborate with scientists, and such events have been attended in four continents, including Europe, South America, Africa and Asia. While the more focused workshops have provided the author with a better awareness of the activities and results of scientists working in the same field, the larger events with a more broader scope have provided the opportunity to promote the results to a wider audience and to seek advice from scientists in other disciplines, such as geologists, soil scientists, or agriculture experts, whose work has been relevant to the objectives of this PhD (see Appendix C.4).

Communication and dissemination of the work carried out during the PhD has also taken place through extensive training events, many of which have been organised or supported by ESA. The author is in full time employment as a consultant EO applications scientist providing support to EO training activities at ESA. In this context, the author has co-organised, or contributed training support, to a wide range of education, training and capacity building events to a diverse range of participants, from PhD students to service providers, to researchers in developing countries. Many of these training activities have focussed on the application of SAR for archaeological prospection and have been held in locations throughout Europe, South America, Africa and Asia (see Appendix C.2).

The research described in this PhD has been published in 5 peer reviewed papers, in journals including the International Journal of Applied Earth Observation and Geoinformation (2015 IF: 3.798), Remote Sensing (2015 IF: 3.036), the International Journal of Remote Sensing (2015 IF: 1.640) and Archaeological Prospection (2015 IF: 1.327) (see Appendix D.1). The author has also contributed to edited book chapters (see Appendix D.2), and published in conference proceedings (see Appendix D.3). Most publications have been placed in the context of remote sensing for archaeology: in some cases the context has focused more on archaeology, while in others it has been more centred on remote sensing science and engineering.

7.5 Final remarks

Materials interact with microwave radiation uniquely when compared to other parts of the electromagnetic spectrum. Consequently, exclusive information can be extracted by measuring the backscatter response from objects using SAR. This information can only be fully exploited if the measured backscatter is understood. The research carried out here demonstrates the merits and limitations of using SAR for archaeological prospection over water and land surfaces attempting to extract the maximum possible information from both the amplitude and phase of the microwave signal. The PhD has been undertaken at a time of unprecedented increase in the quantity and availability of data which is stimulating a complete transformation of both scientific and operational practice. These developments should be harnessed for the benefit of cultural heritage. Particularly given the increasing demand for resources fuelled by a growing population, the identification of archaeological structures is of paramount importance for their subsequent documentation, preservation and valorisation.

ACKNOWLEDGEMENTS

While a PhD should be the research of one individual, in reality it is very difficult to accomplish without the effort of many other individuals. In my case, the effort of others has been essential to obtain initial inspiration, guidance, opportunities, access to resources and moral support.

Colleagues and Peers

Firstly, I would like to extend an overwhelming thanks to Francesco Sarti at ESA. Not only did he stimulate me to undertake the PhD in the first place, but throughout has provided me with the most incredible opportunities and has demonstrated a patience, understanding and wisdom I have never seen before in a supervisor. As a consultant providing full time support to EO education, training and capacity building at ESA under the management of Francesco, thanks to him, I have been able to jointly organise workshops and training events, participate in conferences, make contacts and involve myself in projects that have been relevant to my research. Massive thanks also go to Kris Lemmens. While a trainee at ESA/ESRIN, he enthusiastically supported me with data processing, programming and event organisation. Everything was a lot more fun when Kris was around. Also from ESA I would like to thank Mike Rast and Gordon Campbell for providing me with the opportunity to follow projects or participate in events that have helped me with my research. I also must acknowledge countless other colleagues based at ESA/ESRIN who have continuously provided help and guidance throughout my PhD.

Huge thanks must be given to researchers at CNR. In particular, Rosa Lasaponara from CNR/IMAA and Nicola Masini from CNR/IBAM, with whom I have shared many adventures trespassing over fields, and organising workshops and training events worldwide. They have both been instrumental at almost every step of my PhD and have helped me in innumerable ways: from the procurement of satellite data, to the organisation of a ground data acquisition campaign halfway across Italy; from the invitation to training events in China and South America, to the co-organisation of a workshop at ESA/ESRIN. As leading experts in remote sensing for archaeology, they have always been super available to give me help and guidance in all aspects, to the point of driving four hours from Potenza when the situation demanded.

Much help and support came from colleagues in various institutes throughout Rome. Firstly I would like to thank Adriano La Regina, ex soprintendente of Rome (for almost 30 years) and now president of the National Institute for Archaeology and History of Art. Apart from advising me, and putting me in touch with various contacts, he allowed me to plunder his personal collection of Forma Italiae archaeological charts. Much support came from the various foreign academies based in Rome: Jeremia Pelgrom and Arthur Hamel at the Royal Netherlands Institute in Rome (KNIR) gave me much help with ground truth over the Via Appia, carried out in the framework of the Mapping the Via Appia project. They also helped maintain my motivation with their great presentations amid flowing prosecco at their wonderful KNIR summer “Porte Aperte” events. Support also came from the British School at Rome (BSR) and the Spanish School of History and Archaeology (CSIC).

A big thank you goes to Alfredo Renga, from the University of Naples. Having immersed myself in the murky depths of SAR bathymetry, I would certainly have drowned were it not for his patient support and detailed responses to my many long emails. Also fundamental to the bathymetry component of my research were: Gordon Campbell from ESA, for his mathematical genius and his help in getting my head around inversion algorithms; Roland Romeiser from the University of Miami, who promptly answered many questions regarding preprocessing steps; Amalia Castro Gomez, an ESA trainee who provided invaluable support with data acquisition and analysis; Vincent Gaffney from the University of Bradford, for his expertise in submerged palaeolandscape archaeology; Martin Gade and Werner Alpers, both from the University of Hamburg, who provided advice as SAR oceanographic experts.

Finally, I would like to thank and acknowledge the GeoInformation team of the Department of Civil Engineering and Computer Science at the Tor Vergata University of Rome. In particular, I would like to thank my supervisor, professor Giovanni Schiavon, for his advice, support and professionalism, which have been essential to the success of this PhD project. I would also like to thank professors Domenico Solimini, Fabio del Frate, and Dr Marco Fabbri, for their continuous help and support.

Software and Processing

I am hugely grateful to the team from Sarmap, in particular Paolo Riccardi (Paolino), Paolo Pasquali and Francesco Holecz. Most of the processing was carried out with the Sarscape software and I have never experienced a more efficient and helpful technical support from any other company. Moreover, I had the opportunity, on two separate occasions, to spend a week at their premises in Purasca in the Italian speaking Swiss Canton of Ticino, to work with the software under their guidance. During that time I had the opportunity to discover the secret ingredients for their brilliance, which must be a blend of Italian flexibility, Swiss efficiency, all in a beautiful and tranquil location of lush, forested mountains.

Many thanks go to Professor Eric Pottier, not only regarding the use of PolSARPro, but about SAR in general. He patiently provided me with essential help, in whichever part of the world I found him, and whatever time of the night or day. My work would have gone in a completely different direction were it not for Lt Col Stefano Gusmano from the Italian Ministry of Defence, who helped me with the selection of COSMO SkyMed data, and with whom many hours were spent discussing the technicalities of SAR and data processing. Michael Foumelis and Andrea Minchella, who both formerly worked at RSAC Ltd as consultants to ESA, provided me with much help on the use of the NEST and SNAP software, and in SAR processing in general. Also, many thanks must be extended to a large number of colleagues at ESA for their help with IDL, Matlab and Python programming.

Data Procurement

For the Rome analyses, the COSMO SkyMed SAR data was provided by the Italian Space Agency (ASI): 25 Stripmap and 8 Spotlight images for the WHERE project (see Appendix C.3.1), 52 Stripmap and 19 Spotlight images for the advanced SAR training event provided to the Italian Ministry of Defense and ASI (see Appendix C.2.1.3). Special thanks go to Alessandro Coletta and Maria Virelli from ASI for the data procured for the SAR training. PALSAR-1 SAR data, and VHR optical satellite data (Pleiades, Kompsat-2 and ALOS-1 PRISM) were provided by ESA via research project C1F.11458. Special thanks go to Lena

Stern from ESA for the prompt acceptance of my quota extensions for Third Party Mission data, and to Raffaele Rigoli, from EOPI at ESA, for his guidance through the various data request procedures and data access mechanisms of ESA. Sentinel-1 and 2 data were also provided by ESA. The Radarsat-2 Fine Quad images were procured via the SOAR (Science and Operational Application Research) project 1488 and the SOAR-EU project 6795 through the University of Tor Vergata. The PALSAR-2 data was obtained from JAXA via the 4th Research Announcement for ALOS-2. Special thanks go to Masanobu Shimada for programming 8 new acquisitions of PALSAR-2 Spotlight data (of which 7 were successful). Data for the project was also acquired by UAV. UAV flights (and an attempted magnetometry survey) were carried out by a team from CNR/IMAA and CNR/IBAM, including Rosa Lasaponara, Nicola Masini, Antonio Pecci, and Maria Sileo.

Project Participation

Very many thanks go to Alessio Di Iorio, an entrepreneurial genius who involved me in many exciting and relevant projects, including WHERE (see Appendix C.3.1) and ITACA (see Appendix C.3.2). In the context of WHERE, much help with data procurement for the experimental component I was undertaking was provided by Antonio Monteleone and others at NAIS.

Huge thanks go to Prof Giuseppina Capriotti Vittozzi, from CNR/ISMA. She was the driving force behind the research team within “The Seven Plagues” PRIN project, which evolved into the SatER team. She indulged my crazy ideas and stimulated frequent and lively debates amongst the “signori delle machine volanti”. With her endless energy and whirlwind drive she organised workshops and training events throughout Egypt and Italy. Also to thank in this context is Maurizio Fea, retired from ESA. I have to thank Maurizio especially for introducing me to the team in the first place, and for his frequent and perceptive advice. Maurizio has repeatedly saved me from the brink of disaster in the most diverse contexts and geographical locations: from the finding of additional funding in the organisation of a workshop in Europe, to the last minute preparation of an opening speech in Spanish at a symposium in South America.

Huge thanks also go to Rosanna Montanaro, from the University of Salento, and Maura Sala, a freelance Egyptological researcher. Their contribution was fundamental to the historical background research and interpretation of results of the SAR analysis in North Sinai.

Friends and Family

Finally, massive appreciation and gratitude go to my family and friends, for putting up with an increasingly stressed, irritable and unavailable human being. This was only possible thanks to their understanding, without which they would have long disowned me. An extra special thanks goes to my girlfriend, Sarah Barden. Her patience and support, especially in the last stages, which increased with decreasing reciprocity, makes her the person she is.

APPENDIX A IMAGE DATA SCENE IDS

Table A-1. Full list of COSMO SkyMed data used for the Rome analysis.

Sensor	Sensor Mode	Acquisition Date	Start Time	Stop Time	Polarisation	Pass	Scene Center Off-Nadir Angle	Antenna Point	Record Number
SAR3	SPOTLIGHT ENHANCED	2010-06-08	04:55:42	04:55:49	HH	A	23240	right	100622723
SAR2	SPOTLIGHT ENHANCED	2010-07-09	04:55:19	04:55:26	HH	A	23240	right	100626084
SAR2	SPOTLIGHT ENHANCED	2010-07-25	04:55:10	04:55:17	HH	A	23240	right	100627665
SAR3	SPOTLIGHT ENHANCED	2010-11-15	04:53:51	04:53:58	HH	A	23240	right	100642743
SAR2	SPOTLIGHT ENHANCED	2010-11-30	04:53:42	04:53:49	HH	A	23240	right	100644987
SAR2	SPOTLIGHT ENHANCED	2010-12-16	04:53:29	04:53:37	HH	A	23240	right	100648509
SAR2	SPOTLIGHT ENHANCED	2011-01-01	04:53:18	04:53:25	HH	A	23240	right	100652930
SAR3	SPOTLIGHT ENHANCED	2011-01-02	04:53:17	04:53:24	HH	A	23240	right	100653048
SAR2	SPOTLIGHT ENHANCED	2011-03-06	04:52:37	04:52:44	HH	A	23240	right	100661501
SAR3	SPOTLIGHT ENHANCED	2011-03-07	04:52:36	04:52:44	HH	A	23240	right	100661659
SAR2	SPOTLIGHT ENHANCED	2011-04-23	04:52:11	04:52:19	HH	A	23240	right	100670008
SAR3	SPOTLIGHT ENHANCED	2011-04-24	04:52:10	04:52:17	HH	A	23240	right	100670093
SAR2	SPOTLIGHT ENHANCED	2011-06-10	04:51:40	04:51:47	HH	A	23240	right	100678728
SAR3	SPOTLIGHT ENHANCED	2011-06-11	04:51:39	04:51:46	HH	A	23240	right	100679027
SAR4	SPOTLIGHT ENHANCED	2011-06-14	04:51:38	04:51:45	HH	A	23240	right	100679945
SAR1	SPOTLIGHT ENHANCED	2011-06-18	04:51:35	04:51:43	HH	A	23240	right	100681137
SAR1	SPOTLIGHT ENHANCED	2011-10-08	04:50:30	04:50:37	HH	A	23240	right	100719868
SAR3	SPOTLIGHT ENHANCED	2011-11-18	04:50:08	04:50:15	HH	A	23240	right	100735088
SAR2	SPOTLIGHT ENHANCED	2011-12-19	04:49:52	04:49:59	HH	A	22250	right	100744788
SAR2	SPOTLIGHT ENHANCED	2012-01-04	04:49:42	04:49:50	HH	A	23240	right	100749856
SAR2	SPOTLIGHT ENHANCED	2012-02-05	04:49:24	04:49:32	HH	A	23240	right	100760555
SAR2	SPOTLIGHT ENHANCED	2012-03-08	04:49:07	04:49:14	HH	A	23240	right	100771122
SAR3	SPOTLIGHT ENHANCED	2012-06-29	04:48:08	04:48:16	HH	A	23240	right	100811691
SAR3	SPOTLIGHT ENHANCED	2012-08-16	04:47:40	04:47:47	HH	A	23240	right	100829126

APPENDIX A Image Data Scene IDs

SAR2	SPOTLIGHT ENHANCED	2010-06-23	04:55:32	04:55:39	VV	A	23240	right	100624471
SAR3	SPOTLIGHT ENHANCED	2010-06-24	04:55:31	04:55:38	VV	A	23240	right	100624544
SAR3	SPOTLIGHT ENHANCED	2010-07-26	04:55:09	04:55:16	VV	A	23240	right	100627762
SAR3	STRIPMAP HIMAGE	2010-01-10	05:03:25	05:04:01	HH	A	30620	right	100606401
SAR2	STRIPMAP HIMAGE	2010-07-04	05:01:25	05:01:33	HH	A	30620	right	100625564
SAR1	STRIPMAP HIMAGE	2010-07-12	05:01:19	05:01:26	HH	A	30620	right	100626364
SAR3	STRIPMAP HIMAGE	2010-07-21	05:01:14	05:01:21	HH	A	30620	right	100627282
SAR1	STRIPMAP HIMAGE	2010-07-28	05:01:09	05:01:17	HH	A	30620	right	100627965
SAR2	STRIPMAP HIMAGE	2010-08-05	05:01:04	05:01:12	HH	A	30620	right	100628743
SAR1	STRIPMAP HIMAGE	2010-08-13	05:00:57	05:01:04	HH	A	30620	right	100629586
SAR3	STRIPMAP HIMAGE	2010-09-07	05:00:41	05:00:49	HH	A	30620	right	100632306
SAR2	STRIPMAP HIMAGE	2010-09-22	05:00:30	05:00:38	HH	A	30620	right	100635543
SAR3	STRIPMAP HIMAGE	2010-10-09	05:00:20	05:00:27	HH	A	30620	right	100637986
SAR3	STRIPMAP HIMAGE	2010-10-25	05:00:11	05:00:18	HH	A	30620	right	100639965
SAR4	STRIPMAP HIMAGE	2011-03-21	04:58:34	04:58:41	HH	A	30620	right	
SAR4	STRIPMAP HIMAGE	2011-04-06	04:58:25	04:58:32	HH	A	30620	right	
SAR4	STRIPMAP HIMAGE	2011-04-22	04:58:07	04:59:48	HH	A	30620	right	100669910
SAR4	STRIPMAP HIMAGE	2011-05-08	04:57:54	04:59:35	HH	A	30620	right	100671954
SAR4	STRIPMAP HIMAGE	2011-05-24	04:57:47	04:59:28	HH	A	30620	right	100674613
SAR4	STRIPMAP HIMAGE	2011-06-09	04:57:33	04:59:15	HH	A	30620	right	100678507
SAR4	STRIPMAP HIMAGE	2011-06-25	04:57:26	04:59:07	HH	A	30620	right	100683633
SAR4	STRIPMAP HIMAGE	2011-07-11	04:57:17	04:58:58	HH	A	30620	right	100688541
SAR4	STRIPMAP HIMAGE	2011-08-28	04:56:57	04:57:04	HH	A	30620	right	100705151
SAR3	STRIPMAP HIMAGE	2011-09-10	04:56:51	04:56:58	HH	A	30620	right	
SAR4	STRIPMAP HIMAGE	2011-09-13	04:56:46	04:56:53	HH	A	30620	right	100710891
SAR4	STRIPMAP HIMAGE	2011-09-29	04:56:37	04:56:44	HH	A	30620	right	100716702
SAR4	STRIPMAP HIMAGE	2011-10-15	04:56:21	04:58:02	HH	A	30620	right	100723007
SAR4	STRIPMAP HIMAGE	2011-11-16	04:56:11	04:56:19	HH	A	30620	right	100734549
SAR4	STRIPMAP	2012-01-03	04:55:44	04:55:52	HH	A	30620	right	100749475

APPENDIX A Image Data Scene IDs

	HIMAGE								
SAR4	STRIPMAP HIMAGE	2012-01-19	04:55:28	04:57:09	HH	A	30620	right	100755051
SAR4	STRIPMAP HIMAGE	2012-02-04	04:55:18	04:56:59	HH	A	30620	right	100760269
SAR4	STRIPMAP HIMAGE	2012-02-20	04:55:07	04:56:49	HH	A	30620	right	100765859
SAR4	STRIPMAP HIMAGE	2012-03-07	04:55:02	04:56:43	HH	A	30620	right	100770819
SAR4	STRIPMAP HIMAGE	2012-03-23	04:54:54	04:56:35	HH	A	30620	right	100776135
SAR4	STRIPMAP HIMAGE	2012-04-08	04:54:43	04:56:25	HH	A	30620	right	100781869
SAR4	STRIPMAP HIMAGE	2012-05-10	04:54:29	04:56:11	HH	A	30620	right	100793801
SAR1	STRIPMAP HIMAGE	2012-06-15	04:54:07	04:55:48	HH	A	30620	right	100806699
SAR2	STRIPMAP HIMAGE	2012-06-23	04:54:04	04:55:45	HH	A	30620	right	100809831
SAR2	STRIPMAP HIMAGE	2012-07-09	04:53:53	04:55:34	HH	A	30620	right	100815377
SAR2	STRIPMAP HIMAGE	2012-07-25	04:53:46	04:55:27	HH	A	30620	right	100821293
SAR2	STRIPMAP HIMAGE	2012-08-10	04:53:38	04:55:19	HH	A	30620	right	100827266
SAR2	STRIPMAP HIMAGE	2012-08-26	04:53:31	04:55:12	HH	A	30620	right	100833047
SAR2	STRIPMAP HIMAGE	2012-09-11	04:53:23	04:55:04	HH	A	30620	right	100838564
SAR4	STRIPMAP HIMAGE	2012-10-01	04:53:15	04:54:57	HH	A	30620	right	100845858
SAR2	STRIPMAP HIMAGE	2012-10-13	04:53:10	04:54:51	HH	A	30620	right	100850285
SAR2	STRIPMAP HIMAGE	2012-10-29	04:53:01	04:54:42	HH	A	30620	right	100858087
SAR4	STRIPMAP HIMAGE	2012-12-20	04:52:37	04:54:18	HH	A	30620	right	100876653
SAR2	STRIPMAP HIMAGE	2013-01-17	04:52:20	04:54:01	HH	A	30620	right	100886746
SAR2	STRIPMAP HIMAGE	2013-02-02	04:52:16	04:53:57	HH	A	30620	right	100893145
SAR2	STRIPMAP HIMAGE	2013-02-18	04:52:05	04:53:46	HH	A	30620	right	100899699
SAR2	STRIPMAP HIMAGE	2013-03-06	04:52:02	04:53:43	HH	A	30620	right	100906209
SAR2	STRIPMAP HIMAGE	2013-03-22	04:51:53	04:53:35	HH	A	30620	right	100913450
SAR2	STRIPMAP HIMAGE	2013-04-07	04:51:46	04:53:27	HH	A	30620	right	100920251
SAR2	STRIPMAP HIMAGE	2013-05-09	04:51:34	04:53:15	HH	A	30620	right	100934098
SAR2	STRIPMAP HIMAGE	2013-06-10	04:51:21	04:53:02	HH	A	30620	right	100946788
SAR2	STRIPMAP HIMAGE	2013-07-28	04:51:01	04:52:42	HH	A	30620	right	100966231
SAR2	STRIPMAP HIMAGE	2013-11-01	04:50:27	04:52:08	HH	A	30620	right	101009306

APPENDIX A Image Data Scene IDs

SAR2	STRIPMAP HIMAGE	2013-11-17	04:50:20	04:52:01	HH	A	30620	right	101016322
SAR4	STRIPMAP HIMAGE	2014-01-08	04:50:03	04:51:44	HH	A	30620	right	101038158
SAR2	STRIPMAP HIMAGE	2014-02-05	04:49:57	04:50:14	HH	A	30620	right	101050398
SAR4	STRIPMAP HIMAGE	2014-02-09	04:49:51	04:51:32	HH	A	30620	right	101051632
SAR4	STRIPMAP HIMAGE	2014-03-13	04:49:42	04:51:24	HH	A	30620	right	101064139
SAR2	STRIPMAP HIMAGE	2014-04-10	04:49:36	04:51:17	HH	A	30620	right	101074978
SAR2	STRIPMAP HIMAGE	2014-05-12	04:49:28	04:51:09	HH	A	30620	right	101087418
SAR2	STRIPMAP HIMAGE	2014-05-28	04:49:20	04:51:01	HH	A	30620	right	101092186
SAR2	STRIPMAP HIMAGE	2014-06-13	04:49:18	04:50:59	HH	A	30620	right	101096615
SAR2	STRIPMAP HIMAGE	2014-06-29	04:49:11	04:50:51	HH	A	30620	right	101101021
SAR2	STRIPMAP HIMAGE	2014-07-31	04:49:06	04:50:46	HH	A	30620	right	101111010
SAR2	STRIPMAP HIMAGE	2014-09-01	04:48:55	04:50:36	HH	A	30620	right	101121897
SAR2	STRIPMAP HIMAGE	2014-09-17	04:48:52	04:50:33	HH	A	30620	right	101126759
SAR2	STRIPMAP HIMAGE	2014-10-03	04:48:49	04:50:30	HH	A	30620	right	101132044
SAR2	STRIPMAP HIMAGE	2014-10-19	04:48:47	04:50:28	HH	A	30620	right	101136371
SAR2	STRIPMAP HIMAGE	2014-11-04	04:48:44	04:50:25	HH	A	30620	right	101140450
SAR2	STRIPMAP HIMAGE	2014-12-06	04:48:37	04:50:18	HH	A	30620	right	101150845
SAR2	STRIPMAP HIMAGE	2014-12-22	04:48:34	04:50:15	HH	A	30620	right	101155944
SAR4	STRIPMAP HIMAGE	2015-01-11	04:48:31	04:50:12	HH	A	30620	right	101161085
SAR4	STRIPMAP HIMAGE	2015-01-27	04:48:25	04:50:06	HH	A	30620	right	101166478
SAR4	STRIPMAP HIMAGE	2015-02-12	04:48:25	04:50:07	HH	A	30620	right	101175533
SAR4	STRIPMAP HIMAGE	2015-02-28	04:48:22	04:50:04	HH	A	30620	right	101187445
SAR4	STRIPMAP HIMAGE	2015-07-06	04:48:07	04:49:49	HH	A	30620	right	101246874

Table A-2. Full list of Radarsat-2 Fine Quad data used for the Rome analysis. (All data acquired in 2008.)

Radarsat-2 acquisition date (mm/dd)	Pass	Antenna beam number	Incidence angle at scene centre (degrees)	Nominal range resolution (m)	Nominal azimuth resolution (m)	Pixel spacing (after resampling) (m)
05/07	Asc	FQ2	20.9	14.6	7.6	14.6
05/31	Asc	FQ2	20.9	14.6	7.6	14.6
06/24	Asc	FQ2	20.9	14.6	7.6	14.6
07/18	Asc	FQ2	20.9	14.6	7.6	14.6

APPENDIX A Image Data Scene IDs

08/11	Asc	FQ2	20.9	14.6	7.6	14.6
09/04	Asc	FQ2	20.9	14.6	7.6	14.6
09/28	Asc	FQ2	20.9	14.6	7.6	14.6
10/22	Asc	FQ2	20.9	14.6	7.6	14.6
11/15	Asc	FQ2	20.9	14.6	7.6	14.6
12/09	Asc	FQ2	20.9	14.6	7.6	14.6
08/08	Desc	FQ9	28.9	10.8	7.6	7.5
08/25	Desc	FQ4	23.1	13.3	7.6	7.5
09/08	Desc	FQ14	34.3	9.3	7.6	7.5
09/15	Desc	FQ19	39.1	8.3	7.6	7.5
09/25	Desc	FQ9	28.9	10.8	7.6	7.5
10/02	Desc	FQ14	34.3	9.3	7.6	7.5
10/09	Desc	FQ19	39.1	8.3	7.6	7.5
10/19	Desc	FQ9	28.9	10.8	7.6	7.5
11/12	Desc	FQ9	28.9	10.8	7.6	7.5
12/13	Desc	FQ14	34.3	9.3	7.6	7.5

Table A-3. Full list of ALOS PALSAR data used for the Rome analysis. All acquisitions are ascending pass and with an scene centre incidence angle of 38.7 degrees (antenna beam number 7).

ALOS PALSAR acquisition date (yyyy/mm/dd)	Mode and polarisation	Nominal range resolution (m)	Nominal azimuth resolution (m)	Pixel spacing (after resampling) (m)
2007/06/19	FBD (HH/HV)	20	10 (2 looks)	15.9
2007/09/19	FBD (HH/HV)	20	10 (2 looks)	15.9
2008/05/06	FBD (HH/HV)	20	10 (2 looks)	15.9
2008/06/21	FBD (HH/HV)	20	10 (2 looks)	15.9
2008/08/06	FBD (HH/HV)	20	10 (2 looks)	15.9
2009/06/24	FBD (HH/HV)	20	10 (2 looks)	15.9
2009/09/24	FBD (HH/HV)	20	10 (2 looks)	15.9
2010/05/12	FBD (HH/HV)	20	10 (2 looks)	15.9
2010/06/27	FBD (HH/HV)	20	10 (2 looks)	15.9
2010/08/12	FBD (HH/HV)	20	10 (2 looks)	15.9
2007/12/20	FBS (HH)	10	10 (2 looks)	6.3
2010/03/27	FBS (HH)	10	10 (2 looks)	6.3
2010/12/28	FBS (HH)	10	10 (2 looks)	6.3

Table A-4 Scene IDs of PALSAR-1 FBD imagery used for the North Sinai analyses.

PALSAR-1 FBD Scene IDs (PSRPxxxxxxxx)							
604/610	605/600	605/610	606/600	606/610	607/600	607/610	608/600
233650610	182450600	229420610	084280600	231900610	073340600	194120610	223440600
086030610	075090600	075090610	245320600	077570610	086760600	133730610	095950600
	229420600		238610600		133730600	234380610	176470600
	236130600		184930600		247800600	227670610	163050600
	195870600		077570600		194120600	073340610	210020600
	142190600		124540600		227670600	080050610	156340600
	189160600		090990600		180700600	086760610	149630600
					080050600	120310610	
					234380600	180700610	
					127020600		
					120310600		

Table A-5 Scene IDs of PALSAR-1 FBS imagery used for the North Sinai analyses.

PALSAR-1 FBS Scene IDs (PSRPxxxxxxxx)		
607/590	607/600	607/610
106890590	106890600	106890610
106890590	093470600	207540610
267930590	100180600	214250610
261220590	207540600	261220610
093470590	214250600	267930610
220960590	220960600	093470610
160570590	267930600	100180610
153860590	261220600	153860610
	153860600	160570610
	160570600	220960610

The scene ID of the PALSAR-1 Polarimetric image used for the North Sinai analysis, and acquired on 8 April 2009, is **PSRP170780610**.

Table A-6 Scene IDs of PALSAR-2 imagery used for the North Sinai analyses.

PALSAR-2 (49° and 40° Incidence Angles) Scene IDs (ALOS2xxxxxxxx-xxxxxx)	
49°	40°
064802998-150805	065542993-150810
066872998-150819	071752993-150921
071012998-150916	073822993-151005
073082998-150930	

APPENDIX B CSK SBAS CONNECTIONS

Appendix B.1 Stripmap Prenestina AOI

number of images : [63]

[CSKS2_20100704_050126060_HIMAGE_A_HH_cut_slc]	ID : [1]
[CSKS1_20100712_050119737_HIMAGE_A_HH_cut_slc]	ID : [2]
[CSKS3_20100721_050114437_HIMAGE_A_HH_cut_slc]	ID : [3]
[CSKS1_20100728_050110037_HIMAGE_A_HH_cut_slc]	ID : [4]
[CSKS2_20100805_050105058_HIMAGE_A_HH_cut_slc]	ID : [5]
[CSKS1_20100813_050057540_HIMAGE_A_HH_cut_slc]	ID : [6]
[CSKS3_20100907_050041844_HIMAGE_A_HH_cut_slc]	ID : [7]
[CSKS2_20100922_050030854_HIMAGE_A_HH_cut_slc]	ID : [8]
[CSKS3_20101009_050020491_HIMAGE_A_HH_cut_slc]	ID : [9]
[CSKS3_20101025_050011170_HIMAGE_A_HH_cut_slc]	ID : [10]
[CSKS4_20110321_045834394_HIMAGE_A_HH_cut_slc]	ID : [11]
[CSKS4_20110406_045824660_HIMAGE_A_HH_cut_slc]	ID : [12]
[CSKS4_20110422_045815264_HIMAGE_A_HH_cut_slc]	ID : [13]
[CSKS4_20110508_045802368_HIMAGE_A_HH_cut_slc]	ID : [14]
[CSKS4_20110524_045755154_HIMAGE_A_HH_cut_slc]	ID : [15]
[CSKS4_20110609_045741526_HIMAGE_A_HH_cut_slc]	ID : [16]
[CSKS4_20110625_045733756_HIMAGE_A_HH_cut_slc]	ID : [17]
[CSKS4_20110711_045724570_HIMAGE_A_HH_cut_slc]	ID : [18]
[CSKS4_20110828_045657551_HIMAGE_A_HH_cut_slc]	ID : [19]
[CSKS3_20110910_045650866_HIMAGE_A_HH_cut_slc]	ID : [20]
[CSKS4_20110913_045646279_HIMAGE_A_HH_cut_slc]	ID : [21]
[CSKS4_20110929_045637571_HIMAGE_A_HH_cut_slc]	ID : [22]
[CSKS4_20111015_045628836_HIMAGE_A_HH_cut_slc]	ID : [23]
[CSKS4_20120103_045544958_HIMAGE_A_HH_cut_slc]	ID : [25]
[CSKS4_20120119_045536495_HIMAGE_A_HH_cut_slc]	ID : [26]
[CSKS4_20120204_045526147_HIMAGE_A_HH_cut_slc]	ID : [27]
[CSKS4_20120220_045515271_HIMAGE_A_HH_cut_slc]	ID : [28]
[CSKS4_20120307_045509771_HIMAGE_A_HH_cut_slc]	ID : [29]
[CSKS4_20120323_045502324_HIMAGE_A_HH_cut_slc]	ID : [30]
[CSKS4_20120408_045451678_HIMAGE_A_HH_cut_slc]	ID : [31]
[CSKS1_20120615_045414793_HIMAGE_A_HH_cut_slc]	ID : [33]
[CSKS2_20120623_045412276_HIMAGE_A_HH_cut_slc]	ID : [34]
[CSKS2_20120709_045400980_HIMAGE_A_HH_cut_slc]	ID : [35]
[CSKS2_20120725_045353794_HIMAGE_A_HH_cut_slc]	ID : [36]
[CSKS2_20120810_045346103_HIMAGE_A_HH_cut_slc]	ID : [37]

[CSKS2_20120826_045339398_HIMAGE_A_HH_cut_slc]	ID : [38]
[CSKS2_20120911_045330693_HIMAGE_A_HH_cut_slc]	ID : [39]
[CSKS4_20121001_045323392_HIMAGE_A_HH_cut_slc]	ID : [40]
[CSKS2_20121013_045318606_HIMAGE_A_HH_cut_slc]	ID : [41]
[CSKS2_20121029_045309385_HIMAGE_A_HH_cut_slc]	ID : [42]
[CSKS2_20130117_045228136_HIMAGE_A_HH_cut_slc]	ID : [44]
[CSKS2_20130202_045224300_HIMAGE_A_HH_cut_slc]	ID : [45]
[CSKS2_20130218_045213377_HIMAGE_A_HH_cut_slc]	ID : [46]
[CSKS2_20130306_045210182_HIMAGE_A_HH_cut_slc]	ID : [47]
[CSKS2_20130322_045201780_HIMAGE_A_HH_cut_slc]	ID : [48]
[CSKS2_20130407_045154408_HIMAGE_A_HH_cut_slc]	ID : [49]
[CSKS2_20131101_045035129_HIMAGE_A_HH_cut_slc]	ID : [53]
[CSKS2_20131117_045027967_HIMAGE_A_HH_cut_slc]	ID : [54]
[CSKS2_20140205_045001057_HIMAGE_A_HH_cut_slc]	ID : [56]
[CSKS4_20140209_044959156_HIMAGE_A_HH_cut_slc]	ID : [57]
[CSKS2_20140512_044936035_HIMAGE_A_HH_cut_slc]	ID : [60]
[CSKS2_20140528_044928437_HIMAGE_A_HH_cut_slc]	ID : [61]
[CSKS2_20140613_044926073_HIMAGE_A_HH_cut_slc]	ID : [62]
[CSKS2_20140629_044918810_HIMAGE_A_HH_cut_slc]	ID : [63]
[CSKS2_20140901_044903308_HIMAGE_A_HH_cut_slc]	ID : [65]
[CSKS2_20140917_044900160_HIMAGE_A_HH_cut_slc]	ID : [66]
[CSKS2_20141003_044857134_HIMAGE_A_HH_cut_slc]	ID : [67]
[CSKS2_20141019_044855156_HIMAGE_A_HH_cut_slc]	ID : [68]
[CSKS2_20141104_044852516_HIMAGE_A_HH_cut_slc]	ID : [69]
[CSKS2_20141206_044845523_HIMAGE_A_HH_cut_slc]	ID : [70]
[CSKS2_20141222_044841667_HIMAGE_A_HH_cut_slc]	ID : [71]
[CSKS4_20150111_044839021_HIMAGE_A_HH_cut_slc]	ID : [72]
[CSKS4_20150127_044833044_HIMAGE_A_HH_cut_slc]	ID : [73]

SUPER MASTER : [CSKS3_20100721_050114437_HIMAGE_A_HH_cut_slc] ID : [3]
number of masters : [31]

MASTER : 0 [CSKS3_20100721_050114437_HIMAGE_A_HH_cut_slc] ID : [3]
number of slaves : [4]

SLAVE : 0 [CSKS2_20100704_050126060_HIMAGE_A_HH_cut_slc] ID : [1]
NormalBaseline = [231.4766083] TemporalBaseline = [17] 2 Pi Ambiguity = [29.06435966]
Doppler Difference = [-757.7874146] Critical Baseline = [-4887.249959,4887.249959]

SLAVE : 1 [CSKS1_20100712_050119737_HIMAGE_A_HH_cut_slc] ID : [2]
NormalBaseline = [409.299408] TemporalBaseline = [9] 2 Pi Ambiguity = [16.42998314]
Doppler Difference = [-903.5560913] Critical Baseline = [-4884.470418,4884.470418]

SLAVE : 2 [CSKS1_20100728_050110037_HIMAGE_A_HH_cut_slc] ID : [4]
NormalBaseline = [-160.9055634] TemporalBaseline = [7] 2 Pi Ambiguity = [41.8387146]
Doppler Difference = [-1039.47522] Critical Baseline = [-4891.220407,4891.220407]

SLAVE : 3 [CSKS2_20100805_050105058_HIMAGE_A_HH_cut_slc] ID : [5]
NormalBaseline = [-228.4589844] TemporalBaseline = [15] 2 Pi Ambiguity = [29.46735573]
Doppler Difference = [-819.3861084] Critical Baseline = [-4891.220407,4891.220407]

MASTER : 1 [CSKS1_20100728_050110037_HIMAGE_A_HH_cut_slc] ID : [4]
number of slaves : [3]

SLAVE : 0 [CSKS1_20100712_050119737_HIMAGE_A_HH_cut_slc] ID : [2]
NormalBaseline = [569.9337158] TemporalBaseline = [16] 2 Pi Ambiguity = [11.7992363]
Doppler Difference = [135.9183502] Critical Baseline = [-4884.470418,4884.470418]

SLAVE : 1 [CSKS2_20100805_050105058_HIMAGE_A_HH_cut_slc] ID : [5]
NormalBaseline = [-68.82360077] TemporalBaseline = [8] 2 Pi Ambiguity = [97.8609848]
Doppler Difference = [220.0884399] Critical Baseline = [-4893.992103,4893.992103]

SLAVE : 2 [CSKS1_20100813_050057540_HIMAGE_A_HH_cut_slc] ID : [6]
NormalBaseline = [461.8630676] TemporalBaseline = [16] 2 Pi Ambiguity = [14.58255863]
Doppler Difference = [59.96373749] Critical Baseline = [-4893.992103,4893.992103]

MASTER : 2 [CSKS4_20110913_045646279_HIMAGE_A_HH_cut_slc] ID : [21]
number of slaves : [3]

SLAVE : 0 [CSKS4_20110828_045657551_HIMAGE_A_HH_cut_slc] ID : [19]
NormalBaseline = [-908.1816406] TemporalBaseline = [16] 2 Pi Ambiguity = [7.424568176]
Doppler Difference = [26.2723999] Critical Baseline = [-4901.104618,4901.104618]

SLAVE : 1 [CSKS3_20110910_045650866_HIMAGE_A_HH_cut_slc] ID : [20]
NormalBaseline = [-938.1237793] TemporalBaseline = [3] 2 Pi Ambiguity = [7.188072681]
Doppler Difference = [192.3855743] Critical Baseline = [-4901.546813,4901.546813]

SLAVE : 2 [CSKS4_20110929_045637571_HIMAGE_A_HH_cut_slc] ID : [22]
NormalBaseline = [74.66047668] TemporalBaseline = [16] 2 Pi Ambiguity = [90.09874725]
Doppler Difference = [-46.87347031] Critical Baseline = [-4886.226262,4886.226262]

MASTER : 3 [CSKS2_20100922_050030854_HIMAGE_A_HH_cut_slc] ID : [8]
number of slaves : [2]

SLAVE : 0 [CSKS3_20100907_050041844_HIMAGE_A_HH_cut_slc] ID : [7]
NormalBaseline = [-518.9039917] TemporalBaseline = [15] 2 Pi Ambiguity = [12.97079086]
Doppler Difference = [700.2961426] Critical Baseline = [-4889.773929,4889.773929]

SLAVE : 1 [CSKS3_20101009_050020491_HIMAGE_A_HH_cut_slc] ID : [9]
NormalBaseline = [-370.2346191] TemporalBaseline = [17] 2 Pi Ambiguity = [18.15400505]
Doppler Difference = [734.1065063] Critical Baseline = [-4881.162703,4881.162703]

MASTER : 4 [CSKS4_20110406_045824660_HIMAGE_A_HH_cut_slc] ID : [12]
number of slaves : [2]

SLAVE : 0 [CSKS4_20110321_045834394_HIMAGE_A_HH_cut_slc] ID : [11]
NormalBaseline = [512.5839233] TemporalBaseline = [16] 2 Pi Ambiguity = [13.10848713]
Doppler Difference = [35.35087204] Critical Baseline = [-4879.333222,4879.333222]

SLAVE : 1 [CSKS4_20110422_045815264_HIMAGE_A_HH_cut_slc] ID : [13]
NormalBaseline = [-846.0499878] TemporalBaseline = [16] 2 Pi Ambiguity = [7.95243454]
Doppler Difference = [61.7667923] Critical Baseline = [-4887.662105,4887.662105]
MASTER : 5 [CSKS4_20110508_045802368_HIMAGE_A_HH_cut_slc] ID : [14]
number of slaves : [2]
SLAVE : 0 [CSKS4_20110422_045815264_HIMAGE_A_HH_cut_slc] ID : [13]
NormalBaseline = [-431.6325073] TemporalBaseline = [16] 2 Pi Ambiguity = [15.62403393]
Doppler Difference = [43.07375336] Critical Baseline = [-4901.991872,4901.991872]
SLAVE : 1 [CSKS4_20110524_045755154_HIMAGE_A_HH_cut_slc] ID : [15]
NormalBaseline = [-768.3829346] TemporalBaseline = [16] 2 Pi Ambiguity = [8.766891479]
Doppler Difference = [114.2473068] Critical Baseline = [-4895.017625,4895.017625]
MASTER : 6 [CSKS4_20110609_045741526_HIMAGE_A_HH_cut_slc] ID : [16]
number of slaves : [2]
SLAVE : 0 [CSKS4_20110524_045755154_HIMAGE_A_HH_cut_slc] ID : [15]
NormalBaseline = [-1194.78064] TemporalBaseline = [16] 2 Pi Ambiguity = [5.650092602]
Doppler Difference = [33.38505936] Critical Baseline = [-4908.061028,4908.061028]
SLAVE : 1 [CSKS4_20110625_045733756_HIMAGE_A_HH_cut_slc] ID : [17]
NormalBaseline = [-659.2682495] TemporalBaseline = [16] 2 Pi Ambiguity = [10.20660591]
Doppler Difference = [39.77396393] Critical Baseline = [-4888.084195,4888.084195]
MASTER : 7 [CSKS4_20120119_045536495_HIMAGE_A_HH_cut_slc] ID : [26]
number of slaves : [2]
SLAVE : 0 [CSKS4_20120103_045544958_HIMAGE_A_HH_cut_slc] ID : [25]
NormalBaseline = [269.947937] TemporalBaseline = [16] 2 Pi Ambiguity = [24.96683693]
Doppler Difference = [-41.79135513] Critical Baseline = [-4897.929385,4897.929385]
SLAVE : 1 [CSKS4_20120204_045526147_HIMAGE_A_HH_cut_slc] ID : [27]
NormalBaseline = [388.3654785] TemporalBaseline = [16] 2 Pi Ambiguity = [17.36935997]
Doppler Difference = [-59.60748672] Critical Baseline = [-4903.075963,4903.075963]
MASTER : 8 [CSKS4_20120220_045515271_HIMAGE_A_HH_cut_slc] ID : [28]
number of slaves : [2]
SLAVE : 0 [CSKS4_20120204_045526147_HIMAGE_A_HH_cut_slc] ID : [27]
NormalBaseline = [-714.8231812] TemporalBaseline = [16] 2 Pi Ambiguity = [9.426342964]
Doppler Difference = [-42.70200348] Critical Baseline = [-4896.304983,4896.304983]
SLAVE : 1 [CSKS4_20120307_045509771_HIMAGE_A_HH_cut_slc] ID : [29]
NormalBaseline = [-980.9372559] TemporalBaseline = [16] 2 Pi Ambiguity = [6.855118752]
Doppler Difference = [86.62346649] Critical Baseline = [-4883.906514,4883.906514]
MASTER : 9 [CSKS4_20120323_045502324_HIMAGE_A_HH_cut_slc] ID : [30]
number of slaves : [2]
SLAVE : 0 [CSKS4_20120307_045509771_HIMAGE_A_HH_cut_slc] ID : [29]
NormalBaseline = [268.0273132] TemporalBaseline = [16] 2 Pi Ambiguity = [25.15223503]
Doppler Difference = [90.60635376] Critical Baseline = [-4899.793925,4899.793925]

SLAVE : 1 [CSKS4_20120408_045451678_HIMAGE_A_HH_cut_slc] ID : [31]
NormalBaseline = [823.5749512] TemporalBaseline = [16] 2 Pi Ambiguity = [8.190899849]
Doppler Difference = [297.20755] Critical Baseline = [-4903.932049,4903.932049]
MASTER : 10 [CSKS2_20120623_045412276_HIMAGE_A_HH_cut_slc] ID : [34]
number of slaves : [2]
SLAVE : 0 [CSKS1_20120615_045414793_HIMAGE_A_HH_cut_slc] ID : [33]
NormalBaseline = [534.163147] TemporalBaseline = [8] 2 Pi Ambiguity = [12.59900856]
Doppler Difference = [-104.0527573] Critical Baseline = [-4889.314012,4889.314012]
SLAVE : 1 [CSKS2_20120709_045400980_HIMAGE_A_HH_cut_slc] ID : [35]
NormalBaseline = [532.7244263] TemporalBaseline = [16] 2 Pi Ambiguity = [12.65211296]
Doppler Difference = [-133.2466431] Critical Baseline = [-4898.52557,4898.52557]
MASTER : 11 [CSKS2_20120725_045353794_HIMAGE_A_HH_cut_slc] ID : [36]
number of slaves : [2]
SLAVE : 0 [CSKS2_20120709_045400980_HIMAGE_A_HH_cut_slc] ID : [35]
NormalBaseline = [373.1782532] TemporalBaseline = [16] 2 Pi Ambiguity = [18.03552055]
Doppler Difference = [-191.8220825] Critical Baseline = [-4889.666894,4889.666894]
SLAVE : 1 [CSKS2_20120810_045346103_HIMAGE_A_HH_cut_slc] ID : [37]
NormalBaseline = [-76.57674408] TemporalBaseline = [16] 2 Pi Ambiguity = [87.98097992]
Doppler Difference = [-131.3443146] Critical Baseline = [-4895.9287,4895.9287]
MASTER : 12 [CSKS2_20120826_045339398_HIMAGE_A_HH_cut_slc] ID : [38]
number of slaves : [2]
SLAVE : 0 [CSKS2_20120810_045346103_HIMAGE_A_HH_cut_slc] ID : [37]
NormalBaseline = [306.8577881] TemporalBaseline = [16] 2 Pi Ambiguity = [21.96064568]
Doppler Difference = [-65.61766815] Critical Baseline = [-4897.281342,4897.281342]
SLAVE : 1 [CSKS2_20120911_045330693_HIMAGE_A_HH_cut_slc] ID : [39]
NormalBaseline = [411.3313599] TemporalBaseline = [16] 2 Pi Ambiguity = [16.39613914]
Doppler Difference = [41.04098892] Critical Baseline = [-4902.327891,4902.327891]
MASTER : 13 [CSKS2_20121013_045318606_HIMAGE_A_HH_cut_slc] ID : [41]
number of slaves : [2]
SLAVE : 0 [CSKS4_20121001_045323392_HIMAGE_A_HH_cut_slc] ID : [40]
NormalBaseline = [290.4906006] TemporalBaseline = [12] 2 Pi Ambiguity = [23.21279335]
Doppler Difference = [595.973999] Critical Baseline = [-4901.411965,4901.411965]
SLAVE : 1 [CSKS2_20121029_045309385_HIMAGE_A_HH_cut_slc] ID : [42]
NormalBaseline = [630.0336304] TemporalBaseline = [16] 2 Pi Ambiguity = [10.7118063]
Doppler Difference = [47.69557571] Critical Baseline = [-4906.540082,4906.540082]
MASTER : 14 [CSKS2_20130202_045224300_HIMAGE_A_HH_cut_slc] ID : [45]
number of slaves : [2]
SLAVE : 0 [CSKS2_20130117_045228136_HIMAGE_A_HH_cut_slc] ID : [44]
NormalBaseline = [1256.637817] TemporalBaseline = [16] 2 Pi Ambiguity = [5.35440731]
Doppler Difference = [-40.44261932] Critical Baseline = [-4887.854257,4887.854257]

SLAVE : 1 [CSKS2_20130218_045213377_HIMAGE_A_HH_cut_slc] ID : [46]
 NormalBaseline = [1198.960449] TemporalBaseline = [16] 2 Pi Ambiguity = [5.631186962]
 Doppler Difference = [-26.10747528] Critical Baseline = [-4908.968128,4908.968128]

MASTER : 15 [CSKS2_20130306_045210182_HIMAGE_A_HH_cut_slc] ID : [47]
 number of slaves : [2]

SLAVE : 0 [CSKS2_20130218_045213377_HIMAGE_A_HH_cut_slc] ID : [46]
 NormalBaseline = [1191.582153] TemporalBaseline = [16] 2 Pi Ambiguity = [5.647981167]
 Doppler Difference = [1.918840408] Critical Baseline = [-4889.091706,4889.091706]

SLAVE : 1 [CSKS2_20130322_045201780_HIMAGE_A_HH_cut_slc] ID : [48]
 NormalBaseline = [584.4118042] TemporalBaseline = [16] 2 Pi Ambiguity = [11.55391598]
 Doppler Difference = [21.83226204] Critical Baseline = [-4909.357412,4909.357412]

MASTER : 16 [CSKS2_20140528_044928437_HIMAGE_A_HH_cut_slc] ID : [61]
 number of slaves : [2]

SLAVE : 0 [CSKS2_20140512_044936035_HIMAGE_A_HH_cut_slc] ID : [60]
 NormalBaseline = [-913.8917847] TemporalBaseline = [16] 2 Pi Ambiguity = [7.399578094]
 Doppler Difference = [-106.9928818] Critical Baseline = [-4918.687278,4918.687278]

SLAVE : 1 [CSKS2_20140613_044926073_HIMAGE_A_HH_cut_slc] ID : [62]
 NormalBaseline = [-737.3830566] TemporalBaseline = [16] 2 Pi Ambiguity = [9.146738052]
 Doppler Difference = [-41.17012405] Critical Baseline = [-4902.658095,4902.658095]

MASTER : 17 [CSKS2_20140917_044900160_HIMAGE_A_HH_cut_slc] ID : [66]
 number of slaves : [2]

SLAVE : 0 [CSKS2_20140901_044903308_HIMAGE_A_HH_cut_slc] ID : [65]
 NormalBaseline = [44.01369858] TemporalBaseline = [16] 2 Pi Ambiguity = [153.2628937]
 Doppler Difference = [-199.7055206] Critical Baseline = [-4903.467911,4903.467911]

SLAVE : 1 [CSKS2_20141003_044857134_HIMAGE_A_HH_cut_slc] ID : [67]
 NormalBaseline = [-18.12529564] TemporalBaseline = [16] 2 Pi Ambiguity = [372.1530762]
 Doppler Difference = [-28.51423454] Critical Baseline = [-4903.517719,4903.517719]

MASTER : 18 [CSKS2_20141019_044855156_HIMAGE_A_HH_cut_slc] ID : [68]
 number of slaves : [2]

SLAVE : 0 [CSKS2_20141003_044857134_HIMAGE_A_HH_cut_slc] ID : [67]
 NormalBaseline = [258.9766846] TemporalBaseline = [16] 2 Pi Ambiguity = [26.04441452]
 Doppler Difference = [-33.75230789] Critical Baseline = [-4903.291337,4903.291337]

SLAVE : 1 [CSKS2_20141104_044852516_HIMAGE_A_HH_cut_slc] ID : [69]
 NormalBaseline = [-10.57188034] TemporalBaseline = [16] 2 Pi Ambiguity = [638.4907837]
 Doppler Difference = [-160.1797943] Critical Baseline = [-4907.901404,4907.901404]

MASTER : 19 [CSKS2_20100704_050126060_HIMAGE_A_HH_cut_slc] ID : [1]
 number of slaves : [1]

SLAVE : 0 [CSKS1_20100712_050119737_HIMAGE_A_HH_cut_slc] ID : [2]
 NormalBaseline = [178.1045227] TemporalBaseline = [8] 2 Pi Ambiguity = [37.77399826]
 Doppler Difference = [-145.7661896] Critical Baseline = [-4887.249959,4887.249959]

MASTER : 20 [CSKS2_20100805_050105058_HIMAGE_A_HH_cut_slc] ID : [5]
 number of slaves : [1]

SLAVE : 0 [CSKS1_20100813_050057540_HIMAGE_A_HH_cut_slc] ID : [6]
 NormalBaseline = [529.3901978] TemporalBaseline = [8] 2 Pi Ambiguity = [12.7240715]
 Doppler Difference = [-160.1243134] Critical Baseline = [-4894.8899,4894.8899]
 MASTER : 21 [CSKS3_20101009_050020491_HIMAGE_A_HH_cut_slc] ID : [9]
 number of slaves : [1]

SLAVE : 0 [CSKS3_20101025_050011170_HIMAGE_A_HH_cut_slc] ID : [10]
 NormalBaseline = [-463.1271667] TemporalBaseline = [16] 2 Pi Ambiguity = [14.52689838]
 Doppler Difference = [5.63949728] Critical Baseline = [-4887.233429,4887.233429]
 MASTER : 22 [CSKS4_20110625_045733756_HIMAGE_A_HH_cut_slc] ID : [17]
 number of slaves : [1]

SLAVE : 0 [CSKS4_20110711_045724570_HIMAGE_A_HH_cut_slc] ID : [18]
 NormalBaseline = [-118.2522278] TemporalBaseline = [16] 2 Pi Ambiguity = [56.99806976]
 Doppler Difference = [-32.36972046] Critical Baseline = [-4898.638293,4898.638293]
 MASTER : 23 [CSKS4_20110828_045657551_HIMAGE_A_HH_cut_slc] ID : [19]
 number of slaves : [1]

SLAVE : 0 [CSKS3_20110910_045650866_HIMAGE_A_HH_cut_slc] ID : [20]
 NormalBaseline = [-30.01248741] TemporalBaseline = [13] 2 Pi Ambiguity = [224.6683807]
 Doppler Difference = [166.1125793] Critical Baseline = [-4901.104618,4901.104618]
 MASTER : 24 [CSKS4_20110929_045637571_HIMAGE_A_HH_cut_slc] ID : [22]
 number of slaves : [1]

SLAVE : 0 [CSKS4_20111015_045628836_HIMAGE_A_HH_cut_slc] ID : [23]
 NormalBaseline = [-30.43380356] TemporalBaseline = [16] 2 Pi Ambiguity = [220.9693451]
 Doppler Difference = [37.78166962] Critical Baseline = [-4884.650835,4884.650835]
 MASTER : 25 [CSKS2_20130322_045201780_HIMAGE_A_HH_cut_slc] ID : [48]
 number of slaves : [1]

SLAVE : 0 [CSKS2_20130407_045154408_HIMAGE_A_HH_cut_slc] ID : [49]
 NormalBaseline = [306.4053955] TemporalBaseline = [16] 2 Pi Ambiguity = [22.00176048]
 Doppler Difference = [-94.80566406] Critical Baseline = [-4899.478953,4899.478953]
 MASTER : 26 [CSKS2_20131101_045035129_HIMAGE_A_HH_cut_slc] ID : [53]
 number of slaves : [1]

SLAVE : 0 [CSKS2_20131117_045027967_HIMAGE_A_HH_cut_slc] ID : [54]
 NormalBaseline = [491.8170776] TemporalBaseline = [16] 2 Pi Ambiguity = [13.71144772]
 Doppler Difference = [5.747022152] Critical Baseline = [-4901.559885,4901.559885]
 MASTER : 27 [CSKS2_20140205_045001057_HIMAGE_A_HH_cut_slc] ID : [56]
 number of slaves : [1]

SLAVE : 0 [CSKS4_20140209_044959156_HIMAGE_A_HH_cut_slc] ID : [57]
 NormalBaseline = [313.272522] TemporalBaseline = [4] 2 Pi Ambiguity = [21.54262352]
 Doppler Difference = [462.3518982] Critical Baseline = [-4906.111018,4906.111018]
 MASTER : 28 [CSKS2_20140613_044926073_HIMAGE_A_HH_cut_slc] ID : [62]
 number of slaves : [1]

SLAVE : 0 [CSKS2_20140629_044918810_HIMAGE_A_HH_cut_slc] ID : [63]
 NormalBaseline = [821.3265381] TemporalBaseline = [16] 2 Pi Ambiguity = [8.227842331]
 Doppler Difference = [-71.33869171] Critical Baseline = [-4914.801071,4914.801071]

MASTER : 29 [CSKS2_20141206_044845523_HIMAGE_A_HH_cut_slc] ID : [70]
 number of slaves : [1]

SLAVE : 0 [CSKS2_20141222_044841667_HIMAGE_A_HH_cut_slc] ID : [71]
 NormalBaseline = [83.00196075] TemporalBaseline = [16] 2 Pi Ambiguity = [81.30045319]
 Doppler Difference = [-50.71875381] Critical Baseline = [-4905.591136,4905.591136]

MASTER : 30 [CSKS4_20150111_044839021_HIMAGE_A_HH_cut_slc] ID : [72]
 number of slaves : [1]

SLAVE : 0 [CSKS4_20150127_044833044_HIMAGE_A_HH_cut_slc] ID : [73]
 NormalBaseline = [864.1117554] TemporalBaseline = [16] 2 Pi Ambiguity = [7.822984219]
 Doppler Difference = [-40.43447113] Critical Baseline = [-4916.495904,4916.495904]

number of pair to analyze : [54]
 4 Pi Lambda : [402.4022442]
 Max Doppler Difference Admitted : [2000]
 Mean Absolute Normal Baseline found: [488.8593712]
 Max Absolute Normal Baseline found: [1256.637817]
 Min Absolute Normal Baseline found: [10.57188034]
 Max Critical Baseline Percentage admitted: [35]
 Min Critical Baseline Percentage admitted: [0]
 Max Positive and Max Negative critical baseline : elements : [63]
 Mean Absolute Temporal Baseline found: [14.51851852]
 Max Temporal Baseline found: [17]
 Min Temporal Baseline found: [3]
 Max Temporal Baseline admitted: [17]
 Min Temporal Baseline admitted: [0]
 Mean Number of Connection per image : [1.714285714]
 Max Number of Connection per image : [4]
 Min Number of Connection per image : [1]
 number of discarded images : [11]

[CSKS3_20100110_050326090_HIMAGE_A_HH_cut_slc]	ID : [0]
[CSKS4_20111116_045611784_HIMAGE_A_HH_cut_slc]	ID : [24]
[CSKS4_20120510_045437524_HIMAGE_A_HH_cut_slc]	ID : [32]
[CSKS4_20121220_045245244_HIMAGE_A_HH_cut_slc]	ID : [43]
[CSKS2_20130509_045141791_HIMAGE_A_HH_cut_slc]	ID : [50]
[CSKS2_20130610_045129241_HIMAGE_A_HH_cut_slc]	ID : [51]
[CSKS2_20130728_045109316_HIMAGE_A_HH_cut_slc]	ID : [52]
[CSKS4_20140108_045010787_HIMAGE_A_HH_cut_slc]	ID : [55]
[CSKS4_20140313_044950983_HIMAGE_A_HH_cut_slc]	ID : [58]
[CSKS2_20140410_044944410_HIMAGE_A_HH_cut_slc]	ID : [59]

[CSKS2_20140731_044913814_HIMAGE_A_HH_cut_slc] ID : [64]

Appendix B.2 Spotlight Prenestina AOI

number of images : [17]

[CSKS2_SCS_B_S2_01_HH_RA_SF_20100709045519_20100709045527_hh_slc] ID : [1]
 [CSKS2_SCS_B_S2_01_HH_RA_SF_20100725045511_20100725045518_hh_slc] ID : [2]
 [CSKS3_SCS_B_S2_01_HH_RA_SF_20101115045351_20101115045359_hh_slc] ID : [3]
 [CSKS2_SCS_B_S2_01_HH_RA_SF_20101130045342_20101130045350_hh_slc] ID : [4]
 [CSKS2_SCS_B_S2_01_HH_RA_SF_20101216045330_20101216045337_hh_slc] ID : [5]
 [CSKS2_SCS_B_S2_01_HH_RA_SF_20110101045318_20110101045325_hh_slc] ID : [6]
 [CSKS3_SCS_B_S2_01_HH_RA_SF_20110102045317_20110102045325_hh_slc] ID : [7]
 [CSKS2_SCS_B_S2_01_HH_RA_SF_20110306045237_20110306045245_hh_slc] ID : [8]
 [CSKS3_SCS_B_S2_01_HH_RA_SF_20110307045237_20110307045244_hh_slc] ID : [9]
 [CSKS2_SCS_B_S2_01_HH_RA_SF_20110423045212_20110423045219_hh_slc] ID : [10]
 [CSKS3_SCS_B_S2_01_HH_RA_SF_20110424045211_20110424045218_hh_slc] ID : [11]
 [CSKS2_SCS_B_S2_01_HH_RA_SF_20110610045140_20110610045147_hh_slc] ID : [12]
 [CSKS3_SCS_B_S2_01_HH_RA_SF_20110611045139_20110611045147_hh_slc] ID : [13]
 [CSKS4_SCS_B_S2_01_HH_RA_SF_20110614045138_20110614045145_hh_slc] ID : [14]
 [CSKS1_SCS_B_S2_01_HH_RA_SF_20110618045136_20110618045143_hh_slc] ID : [15]
 [CSKS2_SCS_B_S2_0D_HH_RA_SF_20111219044953_20111219045000_hh_slc] ID : [18]
 [CSKS2_SCS_B_S2_01_HH_RA_SF_20120104044943_20120104044950_hh_slc] ID : [19]

SUPER MASTER : [CSKS2_SCS_B_S2_01_HH_RA_SF_20101216045330_20101216045337_hh_slc] ID : [5]

number of masters : [10]

MASTER : 0 [CSKS2_SCS_B_S2_01_HH_RA_SF_20101216045330_20101216045337_hh_slc]
 ID : [5] number of slaves : [3]

SLAVE : 0 [CSKS2_SCS_B_S2_01_HH_RA_SF_20101130045342_20101130045350_hh_slc]
 ID : [4] NormalBaseline = [-327.136322] TemporalBaseline = [16] 2 Pi Ambiguity =
 [14.03836823] Doppler Difference = [35.13415146] Critical Baseline = [-
 12029.30434,12029.30434]

SLAVE : 1 [CSKS2_SCS_B_S2_01_HH_RA_SF_20110101045318_20110101045325_hh_slc]
 ID : [6] NormalBaseline = [-30.80691719] TemporalBaseline = [16] 2 Pi Ambiguity =
 [148.8270721] Doppler Difference = [-108.3288803] Critical Baseline = [-
 12006.42349,12006.42349]

SLAVE : 2 [CSKS3_SCS_B_S2_01_HH_RA_SF_20110102045317_20110102045325_hh_slc]
 ID : [7] NormalBaseline = [-79.22516632] TemporalBaseline = [17] 2 Pi Ambiguity =

[57.87179947] Doppler Difference = [926.0366211] Critical Baseline = [-12006.42349,12006.42349]
MASTER : 1 [CSKS2_SCS_B_S2_01_HH_RA_SF_20110610045140_20110610045147_hh_slc]
ID : [12] number of slaves : [3]
SLAVE : 0 [CSKS3_SCS_B_S2_01_HH_RA_SF_20110611045139_20110611045147_hh_slc]
ID : [13] NormalBaseline = [-18.54505348] TemporalBaseline = [1] 2 Pi Ambiguity = [246.3049164] Doppler Difference = [902.5050659] Critical Baseline = [-11955.11772,11955.11772]
SLAVE : 1 [CSKS4_SCS_B_S2_01_HH_RA_SF_20110614045138_20110614045145_hh_slc]
ID : [14] NormalBaseline = [-147.2059631] TemporalBaseline = [4] 2 Pi Ambiguity = [31.02956963] Doppler Difference = [609.1749268] Critical Baseline = [-11955.11772,11955.11772]
SLAVE : 2 [CSKS1_SCS_B_S2_01_HH_RA_SF_20110618045136_20110618045143_hh_slc]
ID : [15] NormalBaseline = [-415.6147461] TemporalBaseline = [8] 2 Pi Ambiguity = [10.99031639] Doppler Difference = [-199.5983887] Critical Baseline = [-11955.11772,11955.11772]
MASTER : 2 [CSKS3_SCS_B_S2_01_HH_RA_SF_20110611045139_20110611045147_hh_slc]
ID : [13] number of slaves : [2]
SLAVE : 0 [CSKS4_SCS_B_S2_01_HH_RA_SF_20110614045138_20110614045145_hh_slc]
ID : [14] NormalBaseline = [-129.4454498] TemporalBaseline = [3] 2 Pi Ambiguity = [35.28761673] Doppler Difference = [-358.8591309] Critical Baseline = [-11955.59871,11955.59871]
SLAVE : 1 [CSKS1_SCS_B_S2_01_HH_RA_SF_20110618045136_20110618045143_hh_slc]
ID : [15] NormalBaseline = [-397.5046082] TemporalBaseline = [7] 2 Pi Ambiguity = [11.4912405] Doppler Difference = [-1201.122559] Critical Baseline = [-11955.59871,11955.59871]
MASTER : 3 [CSKS2_SCS_B_S2_01_HH_RA_SF_20100709045519_20100709045527_hh_slc]
ID : [1] number of slaves : [1]
SLAVE : 0 [CSKS2_SCS_B_S2_01_HH_RA_SF_20100725045511_20100725045518_hh_slc]
ID : [2] NormalBaseline = [-903.3471069] TemporalBaseline = [16] 2 Pi Ambiguity = [5.049755573] Doppler Difference = [-5.129265308] Critical Baseline = [-11936.98155,11936.98155]
MASTER : 4 [CSKS3_SCS_B_S2_01_HH_RA_SF_20101115045351_20101115045359_hh_slc]
ID : [3] number of slaves : [1]
SLAVE : 0 [CSKS2_SCS_B_S2_01_HH_RA_SF_20101130045342_20101130045350_hh_slc]
ID : [4] NormalBaseline = [-599.5754395] TemporalBaseline = [15] 2 Pi Ambiguity = [7.641210079] Doppler Difference = [-970.7128296] Critical Baseline = [-11996.33133,11996.33133]
MASTER : 5 [CSKS2_SCS_B_S2_01_HH_RA_SF_20110101045318_20110101045325_hh_slc]
ID : [6] number of slaves : [1]
SLAVE : 0 [CSKS3_SCS_B_S2_01_HH_RA_SF_20110102045317_20110102045325_hh_slc]
ID : [7] NormalBaseline = [-48.53982162] TemporalBaseline = [1] 2 Pi Ambiguity = [94.4705658] Doppler Difference = [1034.433594] Critical Baseline = [-12008.34616,12008.34616]

MASTER : 6 [CSKS2_SCS_B_S2_01_HH_RA_SF_20110306045237_20110306045245_hh_slc]
 ID : [8] number of slaves : [1]
 SLAVE : 0 [CSKS3_SCS_B_S2_01_HH_RA_SF_20110307045237_20110307045244_hh_slc]
 ID : [9] NormalBaseline = [-108.6615524] TemporalBaseline = [1] 2 Pi Ambiguity =
 [42.33830261] Doppler Difference = [943.0652466] Critical Baseline = [-
 12053.65502,12053.65502]
 MASTER : 7 [CSKS2_SCS_B_S2_01_HH_RA_SF_20110423045212_20110423045219_hh_slc]
 ID : [10] number of slaves : [1]
 SLAVE : 0 [CSKS3_SCS_B_S2_01_HH_RA_SF_20110424045211_20110424045218_hh_slc]
 ID : [11] NormalBaseline = [133.8237915] TemporalBaseline = [1] 2 Pi Ambiguity =
 [34.29808807] Doppler Difference = [1080.831665] Critical Baseline = [-
 12021.69114,12021.69114]
 MASTER : 8 [CSKS4_SCS_B_S2_01_HH_RA_SF_20110614045138_20110614045145_hh_slc]
 ID : [14] number of slaves : [1]
 SLAVE : 0 [CSKS1_SCS_B_S2_01_HH_RA_SF_20110618045136_20110618045143_hh_slc]
 ID : [15] NormalBaseline = [-269.111145] TemporalBaseline = [4] 2 Pi Ambiguity =
 [17.01931] Doppler Difference = [-842.0564575] Critical Baseline = [-11992.15614,11992.15614]
 MASTER : 9 [CSKS2_SCS_B_S2_0D_HH_RA_SF_20111219044953_20111219045000_hh_slc]
 ID : [18] number of slaves : [1]
 SLAVE : 0 [CSKS2_SCS_B_S2_01_HH_RA_SF_20120104044943_20120104044950_hh_slc]
 ID : [19] NormalBaseline = [129.918396] TemporalBaseline = [16] 2 Pi Ambiguity =
 [35.3043251] Doppler Difference = [-44.35052872] Critical Baseline = [-12052.03159,12052.03159]

number of pair to analyze : [15]
 4 Pi Lambda : [402.4022442]
 Max Doppler Difference Admitted : [5913.021207]
 Mean Absolute Normal Baseline found: [249.2307653]
 Max Absolute Normal Baseline found: [903.3471069]
 Min Absolute Normal Baseline found: [18.54505348]
 Max Critical Baseline Percentage admitted: [35]
 Min Critical Baseline Percentage admitted: [0]
 Max Positive and Max Negative critical baseline : elements : [17]
 Mean Absolute Temporal Baseline found: [8.4]
 Max Temporal Baseline found: [17]
 Min Temporal Baseline found: [1]
 Max Temporal Baseline admitted: [17]
 Min Temporal Baseline admitted: [0]
 Mean Number of Connection per image : [1.764705882]
 Max Number of Connection per image : [3]
 Min Number of Connection per image : [1]
 number of discarded images : [7]
 [CSKS3_SCS_B_S2_01_HH_RA_SF_20100608045543_20100608045550_hh_slc] ID : [0]

APPENDIX B CSK SBAS Connections

[CSKS1_SCS_B_S2_01_HH_RA_SF_20111008045031_20111008045038_hh_slc]	ID : [16]
[CSKS3_SCS_B_S2_01_HH_RA_SF_20111118045009_20111118045016_hh_slc]	ID : [17]
[CSKS2_SCS_B_S2_01_HH_RA_SF_20120205044925_20120205044932_hh_slc]	ID : [20]
[CSKS2_SCS_B_S2_01_HH_RA_SF_20120308044907_20120308044914_hh_slc]	ID : [21]
[CSKS3_SCS_B_S2_01_HH_RA_SF_20120629044809_20120629044816_hh_slc]	ID : [22]
[CSKS3_SCS_B_S2_01_HH_RA_SF_20120816044740_20120816044748_hh_slc]	ID : [23]

APPENDIX C COMMUNICATION AND DISSEMINATION ACTIVITIES

Aside from the actual research, an essential component of the PhD was collaboration with other researchers through project participation, the joint organisation of a workshop and attendance at other workshops, conferences and symposia. Continuous communication of results, and awareness of the work of my peers, helped to channel the research in the right direction. Moreover, as a full time consultant supporting training activities for ESA, the author has been able to further disseminate results of the research in numerous training events focussed on the use of SAR for archaeological prospection. These communication and dissemination activities are described in this section.

Appendix C.1 Workshop: Advances in Remote Sensing for Cultural Heritage

On the 12th and 13th of November 2015 an international workshop was organised at ESA/ESRIN on the Advances in Remote Sensing for Cultural Heritage: From Site Detection, to Documentation and Risk Monitoring. The aim was to bring together experts in remote-sensing, archaeologists and cultural heritage specialists to address the key strategic issues of knowledge improvement and the sustainable management of cultural resources. The workshop was organised jointly between ESA and CNR (Department of Earth and Environment). It was carried out in the framework of the European Association of Remote Sensing Laboratories (EARSeL), and was the fifth of a series of such workshops, the previous having taken place in 2008, 2011, 2012 and 2013. Most of the organisation on behalf of ESA was carried out by the author of this PhD, while Rosa Lasaponara was the main organiser on behalf of CNR.



Figure C-1 Front cover of programme flyer.

The themes of the workshop were related to the cultural and practical interconnections between environment, culture, territory and climate change. The organising committee selected some priority subjects related to:

- SAR for palaeoenvironmental applications, site detection, risk monitoring
- From aerial photo to declassified satellite images: the study of landscape over time using historical data sources
- From visual data interpretation to semiautomatic and automatic procedures in an archaeological perspective
- Remote Sensing, GIS and Geospatial analysis for risk monitoring and the management of cultural resources
- Integration of space/air borne and ground remote sensing in archaeogeophysics
- The “LiDAR revolution” for site discovery and the reconstruction of historical landscapes
- Remote sensing methods for studying past human-environment interactions?
- Tools and ideas for creating a platform to share knowledge and data.

In total, 89 participants attended the workshop. These were from 17 countries throughout Europe, Asia, Africa, Australasia, North and South America. 36 oral presentations were held in 7 sessions, and there were 24 poster presentations. The full workshop programme is shown in Table C-1.

Following the workshop, selected papers were published in a Special Issue of the Journal Remote Sensing (IF 3.036). The title of the Special Issue is “Remote Sensing for Cultural Heritage”.

Prior to the workshop, a 3-day training course was organised on the use of SAR for archaeological prospection and monitoring. This is described in Appendix C.2.1.

More information about the workshop, together with all oral and poster presentations freely available to download in PDF format, are available through the website which can be found at the following URL: <http://earth.esa.int/heritage/2015-events/15m38/>.

Table C-1. Advances in Remote Sensing for Cultural Heritage Workshop programme.

12 November 2015	
08:30 – 09:00	Registration
09:00 – 10:00	<p style="text-align: center;">Opening Ceremony:</p> <p>Michael Rast, Head of Science Strategy, Coordination and Planning Office, Earth Observation Programmes, ESA</p> <p>Riccardo Pozzo, Director, Department of Social Sciences, Cultural Heritage, CNR</p> <p>Rosa Lasaponara, Institute of Methodologies for Environmental Analysis, CNR. EARSeL chair of SIG - RS for Cultural and Natural Heritage.</p> <p>Enrico Flamini, Chief Scientist, ASI</p>

	Antonia La Recchia , Director General, MiBACT
10:00 – 12:00	Plenary Session Invited Keynotes
10:00 – 10:20	Application of InSAR for Cultural Heritage Risk Monitoring <i>Diane Evans and Thomas Farr</i>
10:20 – 10:40	Prayers and aqueducts: the response of Ancient Nasca to water shortages <i>Nicola Masini and Rosa Lasaponara</i>
10:40 – 11:00	Coffee Break
11:00 – 11:20	A Report from ICOMOS: The Emerging Role of Satellite and Aerial Remote Sensing in Managing Archaeological World Heritage Sites <i>Douglas Comer</i>
11:20 – 11:40	Innovation for Cultural Heritage <i>Riccardo Pozzo</i>
11:40 – 12:00	Discussion
12:00 – 13:00	Session Mapping, Documentation and Monitoring of Cultural Heritage along Silk Road <i>Chair: D. Evans</i>
12:00 – 12:15	Mission of HIST and its International Projects Along the Silk Road <i>T. Hong</i>
12:15 – 12:30	Silk Road : remote sensing for a smart management of cultural heritage from site detection to monitoring and documentation <i>N. Masini; F. Chen, R. Lasaponara</i>
12:30 – 12:45	On the use of historical archive of aerial photographs for the discovery and interpretation of ancient hidden linear cultural relics in the alluvial plain of eastern Henan, China <i>P. Lu; R. Yang; P. Chen; Y. Guo; F. Chen; N. Masini; R. Lasaponara</i>
12:45 – 13:00	Satellite X-, C- and L-band radar data to image the cultural heritage and landscape of the Yumen Frontier Pass and Niya ruins in the Western Regions of the Silk Road Corridor <i>F. Chen; N. Masini; J. Liu; J. You; R. Lasaponara</i>
13:00 – 14:00	Discussion and Lunch Break
14:00 – 17:00	Session Historical Landscapes and Environmental Analysis <i>Chair: Rosa Lasaponara (CNR/IMAA, Italy)</i>
14:00 – 14:15 Invited	Remote Sensing For Cultural Heritage Documentation and Risk Monitoring <i>Enrico Brugnoli</i>
14:15 – 14:30	Multi-temporal archaeological and environmental prospection in Nasca (Peru) with ERS-1/2, ENVISAT and Sentinel-1A C-band SAR data <i>F. Cigna; D. Tapete; R. Lasaponara; N. Masini</i>
14:30 – 14:45	A multi-disciplinary approach for monitoring cultural heritage: the satellite-based SAR technique integrated with structural models and geo-hazard maps. <i>M. Marsella, P. J. V. D'Aranno, S. Scifoni, M. Scutti, A. Sonnessa</i>
14:45 – 15:00	Submerged Palaeolandscape Monitoring with Sentinel-1 <i>C. Stewart</i>
15:00 – 15:30	Coffee Break
15:30 – 15:45	Remote Sensing for Archaeological Research in the Province of Santa Cruz, Argentina <i>D. Marchionni; R. Goñi; G. Cassiodoro; F. Guichón; A. R. J. Dellepiane; J. F. Coni; S. G. Guraieb</i>
15:45 – 16:00	Combined Use of High-Resolution Satellite Imagery and Ground Data for Research on

	the Original Inhabitants of Patagonia, Argentina <i>G. S. de Salmuni; D. Marchionni; R. Lasaponara</i>
16:00 – 16:15	A Cross-Comparative Study for the use of CORONA Satellite Imagery in Diverse Archaeological Landscapes <i>T. Kalayci</i>
16:15 – 16:30	The Territory of Ancient Caere <i>P. Tartara</i>
16:30 – 17:00	Discussion
17:00 – 18:00	Poster Session and Ice Breaker
13 November 2015	
09:00 – 10:30	Session Techniques for Archaeological Prospection <i>Chair: Chris Stewart (RSAC c/o ESA)</i>
09:00 – 09:15	World Heritage observation and education by using Remote Sensing and digital Geomedia <i>S. Naumann; N. Wolf; A. Siegmund</i>
09:15 – 09:30	Analysis of SAR Sensitivity to Archaeological Proxy Indicators <i>C. Stewart</i>
09:30 – 09:45	The potential of airborne LiDAR for detection of new archaeological sites in Romania <i>I. Pavel; P. Anca; L. Zavate; B. S. Stefan</i>
09:45 – 10:00	Overview of Remote Sensing applications for Cultural Heritage in Cyprus in the “Pre-ESA” era. <i>A. Agapiou; V. Lysandrou; B. Cuca; D. Hadjimitsis</i>
10:00 – 10:15	Remote sensing for archaeological studies and territory management: case study of the roman city of Lucus Asturum (Asturias, Spain) <i>O. R. Pagés; J. F. Calleja</i>
10:15 – 10:30	Discussion
10:30 – 11:00	Coffee Break
11:00 – 12:30	Session Applications of SAR for Cultural Heritage Risk Monitoring <i>Chair: Francesco Sarti (ESA)</i>
11:00 – 11:15	Surveying and monitoring of cultural heritage: the role of the COSMO-SkyMed mission <i>P. Sacco; M. L. Battagliere; M. G. Daraio; A. Coletta</i>
11:15 – 11:30	Supporting hazard assessment of the Italian cultural heritage using the satellite active A-DInSAR/PSInSAR remote sensing techniques <i>G. Avanzi; M. Morigi; N. Straccia</i>
11:30 – 11:45	Radar remote sensing of the Angkor World Heritage site <i>F. Chen</i>
11:45 – 12:00	A novel VHR SAR solution to monitor archaeological looting from space <i>D. Tapete; F. Cigna</i>
12:00 – 12:15	TerraSAR-X and Sentinel-1A change detection in historic urban settings: an example in the Middle East <i>D. Tapete; F. Cigna</i>
12:15 – 12:30	Discussion
12:30 – 13:30	Lunch Break

13:30 – 15:15	<p style="text-align: center;">Session</p> <p style="text-align: center;">Integrated monitoring systems for the preservation of cultural heritage <i>Chair: Nicola Masini (CNR/IBAM, Italy)</i></p>
13:30 – 13:45	Remote Sensing Analysis for the Study of Cultural Heritage in the Mesoamerican Corridor <i>J. G. Rejas; M.C. Pineda; J. Bonatti</i>
13:45 – 14:00	Cultural Landscape risk Identification, Management and Assessment (CLIMA) <i>A. Di Iorio; S. De Angeli; J. Patruno</i>
14:00 – 14:15	An Integrated, Open-Source Set of Tools for Urban Risk Monitoring Using Earth Observation Data in a Context of Cultural Heritage Preservation <i>D. De Vecchi; M. Harb; D. A. Galeazzo; F. Dell'Acqua</i>
14:15 – 14:30	Innovative Technologies and Applications for Coastal Archaeological sites FP7 - ITACA <i>A. Di Iorio, S. Bollandos, L. B. Hansen, M. Bagni</i>
14:30 – 14:45	Impact map of natural hazards <i>M. B. Dan; C. O. Gociman</i>
14:45 – 15:00	VIDEOR: Cultural Heritage risk assessment and monitoring on the Web <i>A. Monteleone</i>
15:00 – 15:30	Discussion
15:30 – 16:00	Coffee Break
16:00 – 17:30	<p style="text-align: center;">Session</p> <p style="text-align: center;">Remote Sensing Data Integration for Cultural Heritage Management <i>Chair: Douglas C. Comer (CRSM, USA)</i></p>
16:00 – 16:15	3D settlement model generation and landscape change: contributions to image-based digital retrospection of the demolished village of Breginj, Slovenia <i>T. Veljanovski; Ž. Kokalj</i>
16:15 – 16:30	Open data integration: from satellite to UAV for protection of built environments. The San Clemente archaeological site inside the Centa River bed in Albenga <i>L. Barazzetti; R. Brumana; B. Cuca; M. Previtali; R. Valente</i>
16:30 – 16:45	Inaccessible and Remote Archaeological Landscapes. Earth Observation to explore late Holocene human-environment interactions in the central Sahara <i>F. C. Conesa; S. Biagetti and S. Merlo</i>
16:45 – 17:00	Applications of Synthetic Aperture Radar for Archaeological Documentation in North Sinai <i>C. Stewart</i>
17:00	Discussion and Closing Ceremony
Poster Session 12 November	
Number	Poster
1	Natural heritage sites from space: Monitoring the National Park of Iguazú, Argentina-Brazil <i>M. Presutti; G. S. De Salmuni</i>
2	Spatial analysis for the study of environmental settlement patterns: the archaeological sites of the Santa Cruz County <i>M. Danese; N. Masini; R. Goñi ; G. Cassiodoro; F. Guichón; R. Lasaponara</i>
3	Multi-temporal data fusion techniques for archaeological prospection in Poland (Sławsko case study)

	<i>D. Ruciński; S. Królewicz; Ł. Banaszek; W. Rączkowski</i>
4	Early Medieval Stronghold in Sławsko from a remote sensing perspective: Adding New Fragments to an Old Puzzle <i>Ł. Banaszek; W. Rączkowski; D. Ruciński</i>
5	Challenging mountainous landscapes: the stratified cultural heritage of Crete from the Air <i>G. Cantoro</i>
6	UAV proximal remote sensing for the 3D documentation of complex ancient quarries. <i>S. Cara; C. Matzuzzi</i>
7	Numidian Burial Landscapes: Analysing the Archaeological Record and its Changing Conditions with Remote Sensing Techniques. <i>I. Cruz-Folch; D. Montanero; J. Campillo; J. Sanmartí</i>
8	Detecting traces of Roman Centuriation in large-scale, old aerial photos: a case study of Pavia, Italy <i>F. Dell'Acqua; M. E. Gorrini; G. Lisini; G. C. Iannelli; C. Mussi; N. Ricardi; M. T.A. Robino</i>
9	Airborne Monitoring: case study of Abruzzo <i>P. Tartara</i>
10	Satellite archaeological surveys through "Bing Maps" satellite images: a new perspective <i>D. Mastroianni</i>
11	Remote sensing and ground truth comparison for the analysis of crop-marks in Capitanata - Italy. <i>C. A. Sabia</i>
12	Sensing patterns: unveiling archaeological landscapes through Pattern Recognition in Remote Sensing. <i>A. Traviglia; A. Torsello</i>
13	Extracting ancient irrigation canals from Chinese GF-1 VHR panchromatic imagery: a case study of the Milan archaeological site on the Silk Road <i>L. Luo; X. Wang; J. Liu; H. Guo; R. Lasaponara</i>
14	Space Archaeology: disciplinary attributes, research objects, methods and tasks <i>X. Wang; H. Guo; L. Luo; L. Zhu</i>
15	Deciphering palimpsests. Satellite images and non-invasive archaeology in favor of tracing changes in the rural landscapes in Poland. <i>M. Kostyrko; D. Ruciński; A. Wilgocka</i>
16	Structural health monitoring of the natural bridge, Puente del Inca, Mendoza, Argentina <i>E. Lannutti; M. G. Lenzano; J. Barón; L. Lenzano</i>
17	Trace of the ancient Via Salaria in the Lower Tiber Valley as seen by Landsat <i>MA Panu Hyppönen</i>
18	Cultural Landscape risk Identification, Management and Assessment (CLIMA) <i>A. Di Iorio; S. De Angeli; J. Patruno; M.C. Salvi</i>
19	Remote Sensing and UNESCO European Heritage sites affected by geo-hazard : PROTHEGO project proposal. <i>Claudio Margottini, Daniele Spizzichino, Francesca Cigna, Giovanni B. Crosta, Paolo Frattini, Kyriacos Themistocleous and José Antonio Fernandez Merodo.</i>
20	Mapping of pre-Columbian Settlement Topography through UAS Photogrammetry <i>T. Sonnemann</i>
21	Cultural Heritage management and GIS: cataloguing "Specchia" in the territory of Manduria (Taranto, Southern Italy). <i>Maurizio Delli santi</i>

22	Application of remote sensing techniques combined to identify and delineate the archaeological heritage of the valley of the White River in Écija, Sevilla <i>D.V. Torres</i>
23	Monitoring the ground stability of the World Heritage Cultural Site of the Giza Pyramids and surroundings using persistent scatterers interferometry from 1992 to 2010. <i>J. M. Delgado Blasco</i>
24	Using remote sensing and GIS techniques for monitoring the environmental status The problems and solutions around the Esna temple at luxor, Egypt <i>Abdel Aziz Fathi Abdel Aziz Elfadaly</i>

Appendix C.2 Training Courses

Throughout the duration of the PhD, the author carried out many training activities based on the on-going research. This involved the organisation of courses on behalf of ESA, or contributing to courses organised by other establishments. A complete list of training events, in reverse chronological order, is provided in this section.

Appendix C.2.1 Co-organised training events

Appendix C.2.1.1 Training on remote sensing for heritage management

From 22 June to 7 July 2016 the 3rd International Training Workshop on Space Technologies for Management and Conservation of World Heritage Sites was organised at the International Centre on Space Technologies for Natural and Cultural Heritage (HIST) in Beijing, China. The training was jointly organised by EARSeL, CNR, ESA and HIST. The participants included 25 professionals from 12 Asian, African and East European developing countries. The author organised 3 days of the training, from 27 to 29 July. The programme of these days is shown in Table C-2. Figure C-2 and Figure C-3 are photos acquired during the training.



Figure C-2. Photo acquired of the author at the 3rd International Training Workshop on Space Technologies for Management and Conservation of World Heritage Sites, held in Beijing, China.



Figure C-3. Photo acquired of the participants of the 3rd International Training Workshop on Space Technologies for Management and Conservation of World Heritage Sites.

Table C-2. Programme of 3 day contribution of the author to training on remote sensing for heritage management.

27 June 2016	
09:00 – 11:00	ESA presentation Earth Observation (EO) Principles and Applications EO programme of ESA <i>Chris Stewart</i>
11:00 – 11:30	<i>Discussion</i>
11:30 – 12:30	<i>Lunch Break</i>
12:30 – 14:00	Fundamentals of SAR SAR sensors and data access <i>Chris Stewart</i>
14:00 – 14:30	<i>Discussion and Coffee Break</i>
12:30 – 13:30	<i>Lunch Break</i>
13:30 – 15:30	SAR Applications in Archaeology Demonstration of data catalogue and software tools for SAR processing <i>Chris Stewart</i>
15:30 – 16:00	<i>Coffee Break</i>
16:00– 17:00	Exercise: Basic SAR processing: from data download to processing and analysis <i>Chris Stewart</i>
28 June 2016	
09:00 – 11:00	Exercise: Multisensor, Rome <i>Chris Stewart</i>
11:00 – 11:30	<i>Discussion</i>
11:30 – 12:30	<i>Lunch Break</i>
12:30 – 14:00	Risk estimation for natural and cultural heritage <i>Rosa Lasaponara & Nicola Masini</i>
14:00 – 14:30	<i>Discussion and Coffee Break</i>
14:00 – 14:30	<i>Coffee Break</i>
14:30 – 16:30	Exercise: Intensity and interferometric analysis for archeological research, Sahara <i>Chris Stewart</i>
29 June 2016	
09:00 – 11:00	Exercise: Change Detection, Beijing <i>Chris Stewart</i>
11:00 – 11:30	<i>Discussion</i>
11:30 – 12:30	<i>Lunch Break</i>
12:30 – 14:00	Exercise: Flood Mapping <i>Chris Stewart</i>
14:00 – 14:30	<i>Discussion and Coffee Break</i>

12:30 – 13:30	<i>Lunch Break</i>
13:30 – 15:30	Exercise: DInSAR <i>Chris Stewart</i>
15:30 – 16:00	<i>Coffee Break</i>
16:00– 17:30	Exercise: DInSAR <i>Chris Stewart</i>

Appendix C.2.1.2 Training on remote sensing for archaeology

Associated with the International Workshop on the Advances in Remote Sensing for Cultural Heritage (Appendix C.1) was a training course on remote sensing for archaeology. The course took place from the 9th to 11th of November 2015 at ESA/ESRIN. The training was organised jointly between ESA and CNR. It was carried out in the framework of EARSeL, and was the third of a series of such training courses. The main focus of the course was on the use of SAR for both archaeological prospection (over vegetated and sand surfaces) and structural monitoring, although the last half day was dedicated to the theory and application of Structure from Motion (SfM) through the use of UAVs. For each topic covered, theoretical lectures were followed by practical exercises on computers. Data from a range of SAR sensors were used, including Sentinel-1, COSMO SkyMed, ALOS PALSAR-1 and ENVISAT ASAR. Optical satellite and UAV imagery were also used in the exercises. The software used for processing included OS toolboxes, mainly SNAP and QGIS. The full programme of the course is shown in Table C-3.

The training was carried out by 12 trainers, including the author. The affiliation of the trainers included: the British Geological Survey (BGS), UK; the International Council on Monuments and Sites (ICOMOS), USA; the International Centre on Space Technologies for Natural and Cultural Heritage (HIST) of the Chinese Academy of Sciences (CAS), China; ASI, Italy; the CNR institutes of Methodologies for Environmental Analysis (CNR/IMAA) and Archaeological and Monumental Heritage (CNR/IBAM), Italy; The Argentinian Space Agency (CONAE), Argentina; and ESA.

There were 24 participants from 8 countries, mainly in Europe, but there were also participants from Argentina, China and the USA. Most participants had a background in archaeology and were mainly from academia, at the PhD and post-doc level. Some participants were archaeologists from the private sector, and a few others were engineering students.

The last afternoon of the course focused on the Structure from Motion (SfM) technique using UAV data. Following this, a UAV flight was demonstrated on the roof of the ESRIN sports facilities building, during which time an optical group photo was acquired by the UAV (Figure C-4) of the participants (Figure C-5).

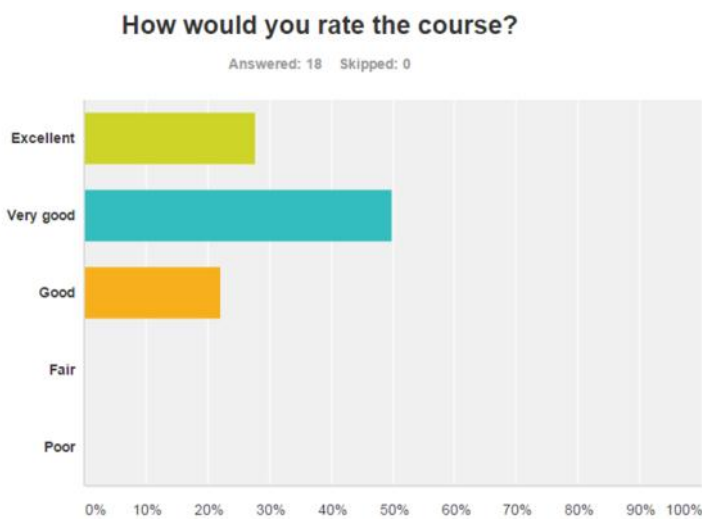


Figure C-4. UAV used in the demonstration during the 3rd ESA, EARSeL course on remote sensing for archaeology.



Figure C-5. Group photo of the participants of the 3rd ESA, EARSeL course on remote sensing for archaeology, acquired by the UAV shown in Figure C-4.

At the end of the training participants were asked to complete an anonymous online evaluation questionnaire with 10 questions. The response to the first question (overall evaluation) is shown in Figure C-6.



Answer Choices	Responses
Excellent	27.78% 5
Very good	50.00% 9
Good	22.22% 4
Fair	0.00% 0
Poor	0.00% 0
Total	18

Figure C-6. Overall evaluation of participants of the 3rd ESA, EARSeL course on remote sensing for archaeology.

Table C-3. Training on remote sensing for archaeology programme.

9 November 2015

08:30 – 09:00	Registration
09:00 – 09:30	Opening ceremony ESA-EARSeL-CNR
09.30 – 09.45	HIST: International Center on Space Technologies for Natural and Cultural Heritage, under the Auspices of UNESCO, Beijing, China <i>Tianhua Hong, HIST, China</i>
09.45 – 10.00	The COSMO SkyMed Satellite Constellation <i>Alessandro Coletta, ASI, Italy</i>
10.00 – 11.00	An Overview of remote sensing for Cultural Heritage: from site detection, to documentation and risk monitoring <i>Rosa Lasaponara, CNR, Italy</i>
11:00 – 11.30	<i>Discussion and Coffee Break</i>
11:30 – 12:00	Fundamentals of SAR <i>Chris Stewart, RSAC c/o ESA, Italy</i>
12:00 – 12:30	Fundamentals of InSAR <i>Jose Manuel Delgado Blasco, CGI-Serco c/o ESA</i>
12:30 – 13:00	SAR sensors and data access <i>Chris Stewart</i>
13:00 – 14:00	<i>Lunch Break</i>
14:00 – 15:00	Demonstration of data catalogue and software tools for SAR processing <i>Chris Stewart</i>
15:00 – 15.30	<i>Discussion and coffee break</i>
15:30 – 17:30	Exercise: Basic SAR processing: from data download to processing and analysis: Italy <i>Chris Stewart</i>
10 November 2015	
09:00 – 10:30	Exercise: Intensity and interferometric analysis for archeological research: Sahara <i>Chris Stewart</i>
10:30 – 11.00	<i>Coffee Break</i>
11:00 – 12:30	Exercise: Intensity and interferometric analysis for archeological research: Sahara <i>Chris Stewart</i>
12:30 – 13:30	<i>Lunch Break</i>
13:30 – 15:00	Exercise: Archaeological analysis in Pagatonia using SAR: Argentina <i>Daniela Marchionni, CONAE, Argentina</i>
15:00 – 15:30	<i>Coffee Break</i>
15:30 – 17:30	Exercise: Archaeological analysis in Pagatonia using SAR: Argentina <i>Daniela Marchionni</i>
11 November 2015	
09:00 – 09:20	Change detection in cultural landscapes <i>Deodato Tapete & Francesca Cigna, BGS, UK</i>
09:20 – 10:30	Exercise: Intensity change detection analysis
10:30 – 11:00	<i>Coffee Break</i>

11:00 – 11:20	Multi-temporal InSAR for structural monitoring and condition assessment <i>Deodato Tapete & Francesca Cigna</i>
11:20 – 12:30	Exercise: InSAR for structural monitoring <i>Deodato Tapete & Francesca Cigna</i>
12:30 – 13:30	<i>Lunch Break</i>
13:30 – 14:00	Remote Sensing for Cultural heritage monitoring and preservation <i>Douglas Comer, ICOMOS, USA</i>
14:00 – 14:30	SfM theoretical approach <i>Nicola Masini, CNR, Italy</i>
14:30 – 16:00	SfM Practical exercise <i>Antonio Pecci, CNR, Italy</i>
16:00 – 16:30	<i>Coffee Break</i>
16:30 – 17:30	SfM Practical exercise <i>Antonio Pecci & Nicola Masini</i>

Appendix C.2.1.3 Advanced SAR training for Italian MoD and ASI

A two week advanced SAR training course was organised from 9 to 20 November 2015 for the Italian Ministry of Defence (MoD) and for ASI. The course was hosted at ESA ESRIN but organised primarily by the Italian “Scuola di Aerocooperazione” (SAC) of the MoD. In addition to 3 internal trainers from ESA/ESRIN, 10 leading experts were invited to contribute to the training from both public and private sector organisations. These organisations included the Italian Istituto Nazionale di Geofisica e Vulcanologia (INGV), Sarmap, Planetek, E-geos, Thales Alenia Space, EU Satellite Center (SatCen), the University of Rome “Tor Vergata”, and the Politecnica di Milano (POLIMI). The programme of the training is shown in Table C-4.

30 participants from the Italian Air Force, Army and Navy and 7 participants from ASI attended the training.

Given that the COSMO SkyMed SAR satellite constellation is a joint Italian military and civilian system, it was of particular interest and relevance to the Italian MoD and ASI participants. For the purposes of the training, 52 CSK Stripmap and 19 CSK Spotlight images were provided by ASI. Much of the results reported in Chapter 4 were derived by the author for the purpose of the training using this data.

Figure C-7 and Figure C-8 show photos acquired of the training in the ESA/ESRIN Big Hall. Figure C-9 shows the results of the first question of an evaluation questionnaire the participants were asked to complete following the training.



Figure C-7. Photo acquired during the Advanced SAR training for the Italian MoD and ASI.



Figure C-8. Photo of some of the participants of the Advanced SAR training for the Italian MoD and ASI.

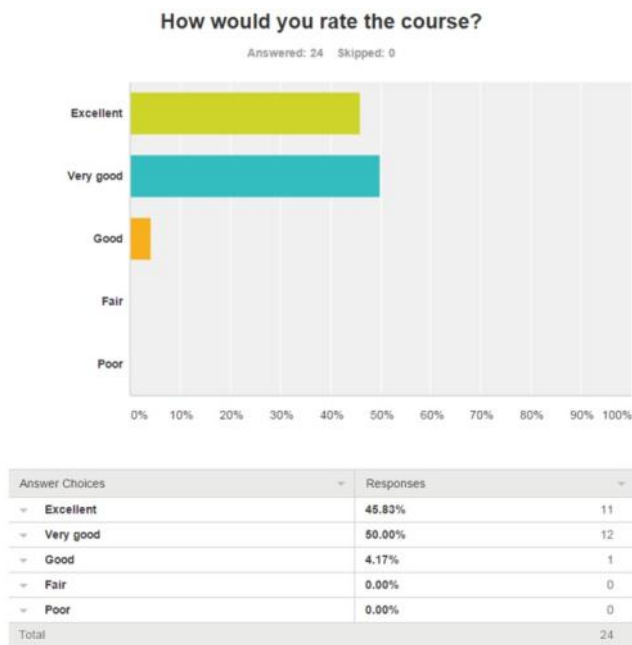


Figure C-9. Results of the first question of an evaluation questionnaire completed by participants of the Advanced SAR training for the Italian MoD and ASI.

APPENDIX C Communication and Dissemination Activities

Table C-4. Programme of advanced SAR training for Italian MoD and ASI.

Ora	09-Nov Lunedì	10-Nov Martedì	11-Nov Mercoledì	12-Nov Giovedì	Ora	13-Nov Venerdì
09.00 - 10.00	Presentazione Workshop ESRIN-SAC	DEM da riprese TanDEM e DEM da small baseline SARMAP	DEM da dati SAR: tecniche di radargrammetria e sinergia con tecniche interferometriche PLANETEK	Change detection (coerente e incoerente) EGEOS	09.00 - 10.00	Tecniche di analisi a sub-apertura e applicazioni (moving target, target complessi, detection delle ambiguità) - Teoria EGEOS
10.00 - 10.30*	Interferometria differenziale, subsidenza e tecniche PS INGV	Esercizi estrazione DEM da small baseline SARMAP	GCP Estrazione di GCP da immagini SAR e creazione di monografie PLANETEK	Coerenza EGEOS	10.00 - 10.30*	
11.00 - 12.00				Combinazioni CD, Coerenza e parametri statistici (MTC, ILLI, CoVAnCoh) EGEOS	11.00 - 12.00	
12.00 - 13.00				EGEOS	12.00 - 13.00	
13.00 - 14.00	PAUSA PRANZO				13.00 - 14.00	PAUSA PRANZO
14.00 - 15.00*	Interferometria differenziale, subsidenza e tecniche PS INGV	Filtraggio nel tempo di De Grandi SARMAP	Battle Damage Assessment mediante CCD e interpretazione con dati ottici. Data fusion SAR-ottico. PLANETEK	Multi-coerenza EGEOS	14.00 - 15.00*	Tecniche di analisi a sub-apertura e applicazioni (moving target, target complessi, detection delle ambiguità) - Esercizi EGEOS
15.30 - 16.00			Esempio di applicazioni SAR: aree allagate e ship/oil spill detection PLANETEK	Prodotti derivati (activity maps, proxy damage maps...) EGEOS	15.30 - 16.00	
16.00 - 17.00	Scelta delle coppie interferometriche, creazione/collezione di GCP INGV	Scelta coppie e creazione di GCP; estrazione coordinate e nuvole di punti SARMAP	Processi speditivi per l'applicazione di tecniche interferometriche per la mappatura del cambiamento e dei movimenti del terreno. PLANETEK	Applicazioni EGEOS		

*= Dalle 10:30 alle 11:00 e dalle 15:00 alle 15:30 Coffee Break

Ora	16-Nov Lunedì	17-Nov Martedì	18-Nov Mercoledì	19-Nov Giovedì	Ora	20-Nov Venerdì
09.00 - 10.00	Super/Ultra High Resolution SAR Images THALES ALENIA SPACEITALIA	Keynote Speech Prof. ROCCA	Esercizio con SNAP: uso del suolo / monitoraggio copertura del suolo ESA	SBAS with StaMPS ESA	09.00 - 10.00	Estrazione automatica feature da immagini radar, tecniche varie con Python ESA
10.00 - 10.30*	Super/Ultra High Resolution SAR Images THALES ALENIA SPACEITALIA				10.00 - 10.30*	
11.00 - 12.00	Elaborazione immagini SAR modalità banda allargata THALES ALENIA SPACEITALIA	La costellazione SENTINEL ESA	Esercizio con SNAP: InSAR monitoraggio delle deformazioni ESA	SBAS with StaMPS ESA	11.00 - 12.00	Chiusura Corso Direttore ESRIN Comandante SAC
12.00 - 13.00	Rifocalizzazione di immagini da dati raw THALES ALENIA SPACEITALIA	Presentazione di STEP e dimostrazione di SNAP ESA				
13.00 - 14.00	PAUSA PRANZO					
14.00 - 15.00*	Utilizzo di immagini SAR al EU SatCen SATCEN	Esercizio con SNAP: creazione di mosaico ESA	Research & Service Support presentation ESA	Presentazione e dimostrazione di PoISARPro ESA		
15.30 - 16.00			Software per applicazioni marittime UNIVERSITA' TOR VERGATA	Esercizio con PoISARPro e SNAP ESA		
16.00 - 17.00						

*= Dalle 10:30 alle 11:00 e dalle 15:00 alle 15:30 Coffee Break

Appendix C.2.1.4 SAR training in Malta

From the 10th to the 14th of November 2014 a SAR training course was organised by ESA to participants from Malta. The aim was to build capacity in SAR theory and applications in the country, which may potentially become a new member state of ESA. The training was hosted by the Malta Council for Science and Technology (MCST) and held in Kalkara, Malta. 31 Maltese participants from universities, research institutes and public authorities attended the training. The author provided support to the organisation of the course and delivered the last afternoon of training on the use of SAR for archaeological applications. The programme of the training is shown in Table C-5.

Table C-5. Programme of SAR training in Malta.

Day 1	Monday 10th November 2014
Target	All entities requiring an introduction to SAR and Earth Observation
08:15	Registration and Welcome Coffee
08:30	Welcome Address by Dr. James Foden, MCST
08:40	SAR Introduction Theory <ul style="list-style-type: none"> • Introduction and familiarisation with Synthetic Aperture Radar (SAR) data and understanding what the data can tell a user, as well as what can be done with SAR data in practice • Examples of visual interpretation of some SAR images Basic principles and theory to enable understanding of the SAR data characteristics
11.00	Coffee break
11.15	SAR Introduction Theory (continued)
13.00	Lunch break
14.00	Keynote Speech by Dr. Jeffrey Pullicino Orlando, Executive Chairman, MCST
14.10	SAR Introduction Theory (continued)
15.30	Coffee break
15.45	SAR Introduction: Practical <ul style="list-style-type: none"> • NEST exercise demonstrating the pre-processing of SAR data
Lecturer	Dr. Christian Thiel
Day 2	Tuesday 11th November 2014
Target	Higher education institutions, academia, public planning authorities, SMEs, heritage, environmental agencies and public entities
08:15	Registration and Welcome Coffee
08:30	SAR Polarimetry/Interferometry Introduction <ul style="list-style-type: none"> • Differentiating between both techniques and discussing the potential and fields of application of PolSAR and InSAR
11.00	Coffee break
11.15	SAR vegetation applications <ul style="list-style-type: none"> • Applications of SAR data with respect to forestry and agriculture (e.g. biomass mapping etc.)
13.00	Lunch break
14.00	SAR vegetation applications (continued)
15.30	Coffee break

15.45	SAR vegetation applications (continued)
Lecturer Dr. Christian Thiel	
Day 3	Wednesday 12th November 2014
Target	Higher education institutions, academia, public planning authorities, SMEs, heritage, environmental agencies and public entities, homeland security, water policy and energy divisions, transport authorities
08.15	<ul style="list-style-type: none"> • Registration and Welcome Coffee
08.30	<ul style="list-style-type: none"> • Land Cover Applications and Mapping • Basic SAR data processing, in essence from SLC to σ_0 & coherence data • The use of multi-temporal SAR data • The use of different frequencies and polarizations • Multi-temporal multi-sensor SAR and optical data • Several examples in particular agriculture, forestry, land cover changes • Ev. SAR and optical data fusion for DEM generation.
11.00	Coffee break
11.15	Land Cover Applications and Mapping (continued)
13.00	Lunch break
14.00	Land Cover Applications and Mapping (continued)
15.30	Coffee break
15.45	Land Cover Applications and Mapping (continued)
Lecturer Dr. Francesco Holecz	
Day 4	Thursday 13th November 2014
Target	The morning session addresses all entities with interest in the complementarity of geographic information systems (GIS) and GPS, and their integration. The afternoon session focused on marine applications, with specific interest expected from Energy and Environmental entities, transport authorities, homeland security and others.
08.15	<ul style="list-style-type: none"> • Registration and Welcome Coffee
08.30	<ul style="list-style-type: none"> • GIS/GPS Integration <p><u>Theory</u></p> <ul style="list-style-type: none"> - Global Navigation Satellite Systems (GNSS) (GPS, GLONASS, Galileo...) - Geographical Information Systems (GIS) - Integration of GNSS and GIS with Earth Observation (EO) data <p><u>Applications</u></p> <ul style="list-style-type: none"> - Geological mapping (lineaments, faults) with Earth observation data (SAR and optical) - Coastal erosion monitoring with EO data, GNSS and GIS - Change detection by means of coherence estimation (SAR interferometry) - Flash-flood mapping with SAR data and GIS - Earth observation digital elevation models production, validation and applications (in geomorphology, morphotectonics, seismotectonics) - Subsidence monitoring with SAR Interferometry and GNSS
11.00	Coffee break

11.15	GIS/GPS integration Practical: - Coherence change detection and flash-flood mapping (using NEST) - Coastal erosion monitoring (would preferably require dedicated GIS software, such as ArcGIS, QGIS etc.). If participants are already using a particular GIS they are more than welcomed to use it. If not, it would be advisable to install Quantum GIS (QGIS): http://www.qgis.org/en/site/forusers/download.html	
13.00	Lunch break	
14.00	Maritime applications <ul style="list-style-type: none"> • -Historical Background • -Basics of Radar Remote Sensing of the Ocean Surface • -Wind Fields • -Storms and Tropical Cyclones • -Oceanic Internal Waves • -Marine Surface Films • -Ocean Surface Currents • -Sea Bottom Topography • -Ship Detection • -Oil Pollution Monitoring • -Intertidal Flats • -Exercises 	
15.30	Coffee break	
15.45	Maritime applications (continued)	
Lecturer	GIS/GPS integration	Dr. Antonios Mouratidis
Lecturer	Marine Applications	Dr. Martin Grade
Day 5	Friday 14th November 2014	
Target	Higher education institutions, academia, public planning authorities, SMEs, heritage, environmental agencies and public entities, homeland security, water policy and energy divisions, transport authorities	
08.15	Registration and Welcome Coffee	
08.30	Maritime applications (continued)	
11.00	Coffee break	
11.15	Maritime applications (continued)	
13.00	Lunch break	
14.00	<ul style="list-style-type: none"> • Archaeology Applications <ul style="list-style-type: none"> ○ Archaeological Propection: <ul style="list-style-type: none"> ▪ Indirect: (soil and vegetation proxies) ▪ Direct: (under sand) ▪ Topographic signature ○ <i>Palaeolandscape Studies:</i> <ul style="list-style-type: none"> ▪ Land (e.g. DEM analysis) ▪ Underwater (indirect, through analysis of surface waves) ○ <i>Cultural Heritage Management and Monitoring:</i> 	

	<ul style="list-style-type: none"> ▪ Monitoring of structural integrity of sites (applications of DInSAR, PSI, SBAS) ▪ Change detection (looting, dumping, vandalism, etc.) 	
15.30	Coffee break	
15.45	Archaeology Applications (continued)	
Lecturer	Marine Applications	Dr. Martin Grade
Lecturer	Archaeology applications	Chris Stewart

Appendix C.2.1.5 Remote sensing for archaeology video training

From the 25th to the 28th of November 2014 a training course was held on the use of spaceborne SAR for natural and cultural heritage. The training was organised jointly by the Argentinian Space Agency (CONAE), CNR and ESA, with the support also of the Italian Ministry of Foreign Affairs. It was held via videoconference from ESA/ESRIN to participants in Buenos Aires, Argentina, at the headquarters of CONAE, and also to participants in Potenza, Italy, at one of the institutes of CNR. The participants included researchers working in the field of natural and cultural heritage and practicing archaeologists. Around 20 participants attended in Buenos Aires, and around 7 attended in Potenza. The programme of the training, which was held partly in Spanish, Italian and English, is shown in Table C-6.

Table C-6. Remote sensing for archaeology video training programme.

Martes, 25 de noviembre de 2014	
	SESIÓN I: Introducción A TELEDETECCION SAR
09:00-09:45	Conceptos básicos de la Teledetección SAR. Sistemas de radar pasivo y radar activo. Geometría de las imágenes SAR: Desplazamiento del terreno: acortamiento de pendientes, inversión de relieve y efecto de sombras. Radiometría de las imágenes de RADAR. <i>Daniela Marchionni.</i>
09:45-10:15	Procesamiento de las imágenes de RADAR. Interpretación de las imágenes SAR: Mecanismos de reflexión de las microondas. Percepción Remota del relieve, suelo, vegetación, agua, humedad. <i>Graciela Salinas de Salmuni.</i>
10:15-10:30	<i>Pausa-café</i>
	SESIÓN II: USO DE TELEDETECCIÓN SAR EN PATRIMONIO NATURAL Y CULTURAL (Teleconferencia con ESRIN, Frascati, Italia) (10:30-12:30 hs)
10:30-11:30	Introducción a las misiones SAR (Desde las misiones históricas al presente, incluyendo Sentinel-1). Introducción al catálogo para acceder a los datos Sentinel-1. <i>Francesco Sarti.</i>
11:30-12:30	Introducción a SNAP y Sentinel-1 SAR processing toolboxes. <i>Fabiano Costantini, Chris Stewart.</i>

12.30-13:00	<p>Parámetros de adquisición de datos SAR: frecuencia, polarización, Resolución, ángulos de adquisición, fecha de adquisición y otros. <i>Daniela Marchionni</i>.</p> <p>Formato de datos (nivel de procesamiento, metadatos). Centrado en los diferentes tipos de imágenes SAR que se usarán: COSMO SkyMed, RADARSAT-1, Selección de imágenes en los catálogos. <i>Graciela Salinas de Salmuni</i>.</p> <p>Selección de datos para procesamientos específicos en estudios de Patrimonio Cultural y Natural. (diapositivas preparadas por ESA)</p>
13:00-14:00	<i>Almuerzo</i>
	SESIÓN III: PRACTICA I: INSTALACION DE SOFTWARE Y CARGA DE IMAGENES
14:00-15:30	Instalación del software NEST. Visita al sitio web de ESA y NEST. Introducción a los manuales de NEST y tutoriales. Introducción a los manuales de los datos SAR: COSMO SkyMed y otros. <i>Graciela Salinas de Salmuni</i>
15:30-15:45	<i>Pausa-café</i>
15:45-17:00	Apertura y visualización de imágenes SAR de distintos sensores - Análisis de sus propiedades. <i>Daniela Marchionni</i>
Miércoles, 26 de noviembre de 2014	
	SESIÓN IV: INTRODUCCIÓN AL SOFTWARE NEST (teleconferencia con ESRIN, Frascati, Italia) (10:30-13:30 hs)
09.00-10:30	Presentación de los ejercicios 1 y 2: “Detección de Paleocausas en las arenas de Selima, Sudan” y “Detección de Palaeocausas en Bir Safsaf. Enumeración de los procesamientos digitales a realizar en las prácticas de los días miércoles, jueves y viernes. <i>Chris Stewart</i> .
10:30-11:00	<i>Pausa-café</i>
10:30-11:00	Preguntas y discusión en vivo sobre SAR processing toolboxes de ESA.
11:00-13.00	<p>Ejercicios prácticos con SNAP (funciones básicas) <i>Fabiano Costantini</i>.</p> <p>Fundamentos básicos de las imágenes SAR usando el software SNAP, los pre-procesamiento (calibración, corrección, eliminación de los valores extremos y atípicos, moteado, multilooking). Seguir paso a paso ejercicios prácticos sobre los materiales didácticos. Y finalmente la visualización de los resultados.</p>
13:00-13.30	Ejemplos de SAR Remote Sensing en Estudios de Patrimonio Cultural y Natural. <i>Chris Stewart</i> .
13:30-14:30	<i>Almuerzo</i>
	SESIÓN V: Práctica II: visualización de imágenes SAR y comparación con imágenes ópticas.

14:30-15:30	Observación e Interpretación de imágenes SAR de distintos ambientes - Comparación e interpretación de imágenes ópticas versus radar. Análisis de la matriz de dispersión. <i>Daniela Marchionni.</i>
15:30-15:45	<i>Pausa-café</i>
15:45-17:00	Uso del software SNAP para calibrar, corregistrar, aplicación de filtros para el efecto speckle y aplicar multilooking. Uso de datos ASAR del Ejercicio 1: "Detección de Paleocauces en las arenas de Selima, Sudan" Parte 1. <i>Chris Stewart.</i>
Jueves, 27 de noviembre de 2014	
	SESIÓN VI: CONCEPTOS Y HERRAMIENTAS SAR (teleconferencia con ESRIN, Frascati, Italia) (10:30-13:30 hs)
09:00-10:00	Continuación del Ejercicio 1: View DEM. Change the DEM Look Up Table (LUT). Compare SAR with DEM. Open Landsat Selima. Contrast Stretch. Layer stack. Reproject (change projection to that of SAR (Geographic Lat/Lon, WGS84)). View RGB. Compare ASAR with Landsat and DEM. Parte 2. <i>Chris Stewart.</i>
10:00-10:30	<i>Pausa-café</i>
10:30-12:00	Uso de Datos Polarimétricos en Estudios de Patrimonio Cultural y Natural.
12:00 – 13:30	– Ejercicios prácticos con POLSARPRO. <i>Jolanda Patruno y Nicole Doré.</i>
13:30 – 14:30	- <i>Almuerzo</i>
	SESIÓN VII: PRACTICA III: calibración, coregistración, Aplicación de filtros para efecto speckle y uso del multilooking
14:30-15:30	Ejercicio 2: Detección de Paleocauces en Bir Safsaf, Egipto. En este ejercicio se realizarán los mismos pasos del ejercicio 1 pero en forma automática, usando la construcción con gráficos de la cadena de procesamiento (batch processing). Parte 1. <i>Chris Stewart.</i>
15:30-15:45	<i>Pausa-café</i>
15:50-17:00	Análisis del área Bir Safsaf usando datos satelitales. Repetir los pasos del Ejercicio 1, usando el procedimiento batch con las imágenes SAR y Landsat de Bir Safsaf. <i>Chris Stewart.</i>
Viernes, 28 de noviembre de 2014	
	SESIÓN VII: CONCEPTOS AVANZADOS DE SAR Y PROCESAMIENTOS ESPECÍFICOS (teleconferencia con ESRIN, Frascati, Italia) (09:00-13:00 hs)
09:00-10:30	Continuación del Ejercicio 2 "Detección de Paleocauces en Bir Safsaf, Egipto", Análisis de Coherencia de paleocauces. Corregistración las dos imágenes SAR. <i>Chris Stewart.</i>
10:30-11:00	<i>Pausa-café</i>

10:30-12:45	Calculo de la Coherencia interferométrica, Coherencia interferométrica Multilook, Ortorectificación de coherencias. Comparación de las Amplitudes SAR, coherencia y reflectancia óptica (Landsat),. Extraer una ventana del área sobre el área de los ríos., Estimar valores de backscatter sobre “ríos radar”, Enmascarar “ríos radar. <i>Chris Stewart</i> .
12:45-13:30	Resultados de la interferometría en Estudios de Patrimonio Cultural y Natural. <i>Jose. Manuel. Delgado Blasco</i> .
13:00-14:00	<i>Almuerzo</i>
	SESIÓN IX: Practica iv: Procesamiento avanzados de Teledetección.
14:00-15:30	Continuación del Ejercicio 2 Calculo de la Coherencia interferométrica, Crear un stack de las multilooks, calibradas y geocodificadas imágenes SAR de Bir Safsaf. Filtrado de speckle Multitemporal, Exportar a Google Earth, Ver “radar rios” en Google Earth. ”, Filtrado para suavisar las máscaras, Exportar las coberturas a geotiff. <i>Chris Stewart</i> .
15:30-15:45	<i>Pausa-café</i>
15:50-17:00	Creación Mapa: crear un mapa de las capas vectoriales (ríos extraídos automáticamente, coberturas y contornos) que no se observaban en los datos Landsat, utilizando QGIS. Redacción de informe final. <i>Chris Stewart</i> .

Appendix C.2.1.6 SAR archaeology training to Egyptologists

On the 29th of May 2014 a training was held at ESA/ESRIN on Satellite Remote Sensing for Archaeological Research. The training formed a part of a wider multi-disciplinary education programme of the CNR and Italian Ministry of Foreign Affairs called “DIPLOMAzia”, the purpose of which is to deliver training to young graduates and administrators from Mediterranean countries in a number of application areas, including cultural heritage. The cultural heritage component was organised by the CNR Institute for Ancient Mediterranean Studies (CNR/ISMA). This component included a series of training events held in various organisations, one of which comprised the one day training organised by the author at ESA/ESRIN. The participants included 5 researchers from various Mediterranean countries and 2 participants from CNR/ISMA. The programme of the training is shown in Table C-7.

Table C-7. Programme of SAR archaeology training to Egyptologists.

29th May 2014	
<i>Trainer: Chris Stewart</i>	
09:30	Introduction to ESA
10:00	Satellite Remote Sensing for Archaeological Research
11:00	<i>Coffee</i>
11:30	Case Studies of Satellite Remote Sensing for Archaeological Research in Egypt
12:30	<i>Lunch</i>
13:30	Practical Exercise on Image Processing for Archaeological Analysis in Egypt (using ESA NEST software toolbox, ALOS PALSAR and Kompsat-2 data)
15:30	Wrap up and closure

Appendix C.2.2 Externally organised training

In addition to the training courses described in Appendix C.2.1, which were co-organised by the author, a number of other training events related to the subject of the PhD took place in which the author contributed training on behalf of ESA. These are described, in reverse chronological order, in Table C-8.

Table C-8. List of externally organised training events in which the author contributed training.

Training Event	Date	Location	Description of contribution
Curso "Uso de Imagenes Opticas y SAR en Estudios de Patrimonio: Yacimientos Arqueológicos y Areas Protegidas"	2016/11/09-10	Iguazu, Argentina	Practical training sessions provided on SAR data processing for archaeological applications using SNAP
Greek Space Week	2015/12/07-09	Athens, Greece	Theoretical and practical training sessions provided on the use of SNAP for SAR data processing for various applications, including archaeology
ENEA Summer School	2014/09/10	Rome, Italy	Presentation on satellite remote sensing for archaeological research
Training at ISPRS Young Scientist Days 2014	2014/06/17-20	Warsaw, Poland	Practical training sessions on remote sensing techniques for classification, feature extraction and change detection
Training during 4 th EARSeL Workshop on Education and Training	2013/06/04	Matera, Italy	Practical training sessions on the use of the ESA OS software LEOWorks 4 for classification, feature extraction and change detection using remotely sensed data.
EGU Geoscience Information for Teachers (GIFT) Workshop on Natural Disasters, Global Change, and the Preservation of World Heritage Sites	2012/11/15-16	Cuzco, Peru	Practical training sessions on the use of ESA OS software for EO data processing for applications related to natural disasters and World Heritage site preservation.
1 st EARSeL Course on Remote Sensing and Cultural Heritage "Radar remote sensing applications for the study and observation of archaeological sites"	2012/09/17-18	Ghent, Belgium	Presentation on EO data access.
SANSA-COSPAR Capacity Building Workshop on Advanced Land Surface Characterisation from Space	2011/10/10-21	Cape Town, South Africa	Theoretical and practical sessions provided on spaceborne optical and SAR remote sensing techniques for various applications, and data access.
"Taller Internacional sobre las Aplicaciones Integradas de la Tecnología Espacial para el Desarrollo Sostenible en las	2010/10/25-29	Cochabamba, Bolivia	Practical sessions provided on spaceborne optical and SAR remote sensing techniques for various applications.

Appendix C.3 Project participation

Appendix C.3.1 WHERE

The project World HERitage monitoring by Remote sEnsing (WHERE) aimed to develop and demonstrate an operational and cost effective service based on remote sensing to monitor UNESCO sites in urban areas. The project was co-funded by ASI and was devised in response to an ASI call for innovative projects in Earth Observation targeted to Italian Small and Medium Enterprises (SMEs). The project kicked off in February 2012 and ended in November 2013. It was carried out by a small consortium of Italian SMEs headed by NEXTANT SpA and including also ALMA Sistemi sas, A&C2000 Srl, MEE0 Srl and SurveyLab Srl. The author was involved in the project as an affiliate of ALMA Sistemi sas.

Three types of monitoring were foreseen in the project:

- Urbanization and human activities (e.g. looting and urban expansion)
- Small scale meteorological and climate change impacts, including pollution
- Geotechnical and structural stability of monuments and the geological substrate

The monitoring of human activities was carried out using spaceborne HR and VHR optical and SAR data, the meteorological monitoring with spaceborne atmospheric data, and the geotechnical monitoring with spaceborne VHR SAR using Persistent Scatterers Interferometry (PSI). These monitoring processing chains were integrated into a webGIS. A fourth experimental component included research on the possibility to carry out archaeological prospection using SAR data over vegetated, temperate areas. This component was carried out by the author (Di Iorio and Straccia 2013, Stewart et al. 2013a).

The project test areas included the following:

- Historical centre of Rome
- The "Sassi e il Parco delle Chiese Rupestri di Matera"
- Ancient Harbor of Ostia.
- Eastern outskirts of Rome, near Torre Gaia

The centre of Rome and Matera were chosen for the monitoring services, while Ostia and the eastern outskirts of Rome were chosen by the author for the experimental component.

ASI provided 25 CSK Stripmap images and 9 CSK Spotlight images for the purposes of the project. Results of the analysis by the author using this data are published by Stewart et al. (2013a), and results including this, and other data, are soon to be published in the journal Remote Sensing.

Appendix C.3.2 ITACA

From 2013-12-12 to 2016-08-01 a project was carried out called ITACA (Innovation Technologies and Applications for Coastal Archaeological sites). This project was initiated in response to the EU FP7-SPACE call for proposals. The project aimed to demonstrate a management system for underwater archaeological sites in coastal regions. It comprised a discovering and monitoring service using innovative satellite remote sensing techniques combined with image processing algorithms. The project developed a set of applications integrated in a system that pursued the following objectives:

- Search and location of ancient ship wrecks.
- Monitoring of ship wrecks, ruins and historical artefacts that are now submerged.
- Integration of resulting search and monitoring data with onsite data into a management tool for underwater sites.
- Demonstration of the system's suitability for a service.

The search, location and monitoring was carried out with VHR SAR data (TerraSAR-X and COSMO-SkyMed) and multispectral satellite data (WorldView-2). An extensive on-ground (sea) campaign carried out with side-scan sonar, multi beam echo sounder, and submarine exploration with professional scuba divers was carried out for validation purposes.

The total budget of the project was 2 219 580,78 euros, and was mainly funded by the EU. The project involved many organisations from the public and private sector and was headed by Planetek Hellas, from Athens, Greece. The test sites of the project included coastal areas around Italy and Greece.

The technique applied for the detection and monitoring of submerged structures using SAR data included the same bathymetric algorithm of Renga et al. (2013, 2014), which was also used by Stewart et al. (2016c) to assess its utility for the monitoring of the submerged palaeolandscape of the North Sea (see Chapter 6). However, given the weak currents of the Mediterranean and the small scale of the structures that the project hoped to detect (sunken ships), the technique proved largely unsuccessful (Tusa 2016).

The author contributed to many of the project meetings and workshops as an interested participant, often presenting results of the research described in Chapter 6.

Appendix C.3.3 PRIN “The Seven Plagues”

The Italian Ministry of Education, Universities and Research (MIUR) periodically announces calls for proposals for funding, on a three-year basis, of research projects of national interest (PRIN). One such project kicked off in 2009 with the title “The Seven Plagues”. It included various components of research related to historical catastrophes, and attempted to verify historical sources of ancient calamities through archaeological and geological evidence (Capriotti Vittozzi 2015b).

The author became involved in this project, contributing satellite radar remote sensing expertise, and worked closely with an element of the PRIN research team. The team included Italian experts in Egyptology, archaeology, geology and remote sensing. The help and guidance of this multidisciplinary

team was essential throughout the research carried out by the author on the use of SAR for archaeological prospection in the desert region of North Sinai, reported in Chapter 5 of this thesis. The choice to focus the research in the North Sinai region was made largely on the recommendation of the PRIN research team. The team was also indispensable for the interpretation of the results of the analysis (Stewart et al. 2015a, Stewart et al. 2016b).

When the 3 year project ended in 2012, the team involved in remote sensing analysis continued through the creation of a follow-on group called “Satellite remote sensing in support to Egyptological Research” (SatER). This team is headed by Prof. Giuseppina Capriotti Vittozzi, an Egyptologist of CNR/ISMA, and includes also: Dr Maurizio Fea, a remote sensing specialist from the Associazione Geofisica Italiana; Lt. Col. Stefano Gusmano, also a remote sensing expert from the Italian Ministry of Defence; Dr Andrea Angelini, an archaeologist from CNR/ITABC; Dr Marina Baldi, a climatologist from CNR/IBIMET; Dr Paola Falcioni, a geographer from the University of Rome “Roma Tre”; and the author, who contributed expertise in satellite remote sensing (Capriotti Vittozzi 2015a).

Several publications, dissemination events and training activities resulting from work carried out by the author were within the framework of the PRIN project, or of follow-on activities of the SatER team. This included publications in journals and edited books (see APPENDIX D), presentations at various workshops and conferences (see Appendix C.4), and training provided by the author at ESA/ESRIN for a team of researchers from various Mediterranean countries (see Appendix C.2.1.6).

Appendix C.3.4 ArchEO

From January 2014 to September 2016 an ESA funded project called ArchEO took place, the main objective of which was to assess the potential of satellite remote sensing for archaeological prospection. The project was proposed by a Polish consortium in response to an open call in the framework of an ESA Polish industry incentive scheme, when Poland became a new member state of ESA. The consortium included the private company Wasat Sp. z o.o. (specialised in remote sensing) and the Institute of Prehistory at the Adam Mickiewicz University in Poznań (specialised in aerial archaeology and archaeological interpretation). The project budget was 180,000 euros (Stewart et al. 2015b).

The main technical objectives of ArchEO were the following:

- The practical assessment of the suitability of optical satellite EO methods for archaeological survey;
- Selection and algorithm development of EO methods best adopted to the specific environmental and cultural conditions of Central Europe;
- Comparison of optical satellite EO capabilities with other non-destructive archaeological techniques;
- The promotion of satellite EO data and techniques in the archaeological community.

A number of test areas around Poland were selected where buried archaeological structures (from Neolithic to medieval) are known to exist. An attempt was made also to apply the techniques to areas

where buried archaeological structures are not known to exist. Validation was carried out with other non-invasive techniques involving geophysical ground survey.

Results were generally positive, highlighting the potential of VHR optical techniques to detect crop marks of various structures in a range of ground conditions. However, it was found that the various processing techniques applied did not significantly differ in their ability to detect archaeological residues. More important was the spatial resolution of the imagery, for which pan-sharpening proved the most effective technique (Ruciński et al. 2015, Stewart et al. 2015b, Wilgocka et al. 2016).

The author supported the ESA technical officer, Gordon Campbell, with the review of the project deliverables.

Appendix C.4 Conference, symposium and workshop presentations

Throughout the PhD, on-going research was presented at many workshops, conferences and symposia. Either on behalf of the Tor Vergata University of Rome, or on behalf of ESA. These are listed in reverse chronological order in Table C-9.

Table C-9. List of workshops, conferences and symposia at which PhD work was presented.

Event	Date	Location	Title of presentation and type (oral or poster)
Italian - Egyptian Workshop on Sciences and Technologies applied to Cultural Heritage I (STACH 1)	2016/12/11-13	Cairo, Egypt	Application of Synthetic Aperture Radar (SAR) for archaeological research in Egypt ORAL
2 nd International Conference on Aerial Archaeology	2016/02/03-05	Rome, Italy	Applications of Synthetic Aperture Radar for Archaeological Documentation in North Sinai ORAL
5 th International Workshop: Advances in Remote Sensing for Cultural Heritage: From Site Detection, to Documentation and Risk Monitoring	2015/11/12-13	Frascati, Italy	1. Submerged Palaeolandscape Monitoring with Sentinel-1 ORAL 2. Applications of Synthetic Aperture Radar for Archaeological Documentation in North Sinai ORAL 3. Analysis of SAR Sensitivity to Archaeological Proxy Indicators ORAL
ENVI and SARscape User Group Workshop	2015/10/08	Rome, Italy	L'Elaborazione dei Dati SAR con ENVI, Sarscape e IDL per la Ricerca Archeologica ORAL
Workshop "Tecnologie Applicative e servizi AeroSpaziali a supporto del Patrimonio Culturale"	2015/09/15	Rome, Italy	1. ESA Activities in Earth Observation for Cultural Heritage Applications

			ORAL 2. Perspectives on big data management at ESA ORAL
Workshop on Remote Sensing for Cultural Heritage and Landscape - Euromed2014	2014/11/03-08	Limassol, Cyprus	ESA Activities in Earth Observation for Cultural Heritage Applications ORAL
34 th EARSeL Symposium	2014/06/16-19	Warsaw, Poland	Assessment of SAR Configurations for Archaeological Survey in Desert Regions ORAL
European Geosciences Union (EGU) 2014	2014/04/27-05/02	Vienna, Austria	Satellite time series analysis to study the ephemeral nature of archaeological marks POSTER (see Figure D-1)
Second International Conference on Remote Sensing and Geo-information of Environment (RSCy2014)	2014/04/07-10	Pathos, Cyprus	Satellite SAR remote sensing for archaeological prospection ORAL
ITACA Preliminary Design Review and End Users Workshop	2014/03/27-28	Palermo, Italy	<i>No presentation given</i>
"Piaghe d'Egitto: Disastri Ambientali dalle Fonti Documentarie dell'Egitto Antico" workshop in the framework of the project PRIN 2009 "Le sette piaghe. Cataclismi e distruzioni tra Palestina ed Egitto in epoca preclassica".	2013/12/06	Rome, Italy	Earth Observation: Case Studies in Egypt ORAL
WHERE Final Workshop	2013/11/29	Rome, Italy	Prospezioni archeologiche mediante dati satellitari ORAL
"Italian Days in Aswan" workshop	2013/11/15-18	Aswan, Egypt	Satellite information in support to archaeological research in Egypt ORAL
ESA Living Planet Symposium 2013	2013/09/09-13	Edinburgh, UK	Satellite Remote Sensing for Archaeological Applications POSTER (see Figure D-2)
European Space Expo Photographic Exhibition: Sensing the Past: COSMO SkyMed and radar technologies for archaeology	2013/08/26-09/02	Rome, Italy	ALOS PALSAR and COSMO SkyMed Prospection in Pelusium POSTER (see Figure D-3)
4 th EARSeL Workshop on Remote Sensing for Cultural and Natural Heritage	2013/06/06-07	Matera, Italy	1. ALOS PALSAR in desert regions of North Sinai: the case study of Pelusium ORAL 2. Analysis of the utility of Cosmo Skymed stripmap for archaeological prospection in the region of Rome

				ORAL
The 6 th International Workshop on Science and Applications of SAR Polarimetry and Polarimetric Interferometry (POLinSAR) 2013	2013/01/ 28-02/01	Frascati, Italy	An Analysis of the Application of PolSAR, at Multiple Frequencies, for Archaeological Prospection POSTER (see Figure D-4)	
International Conference "Reading Catastrophes"	2012/12/ 03-04	Rome, Italy	SAR Archaeological Analysis in Egypt ORAL	
8 th EGU Alexander von Humboldt (AvH) International Conference on Natural Disasters, Global Change, and the Preservation of World Heritage Sites	2012/11/ 12-16	Cuzco, Peru	An overview of Earth Observation (EO) programmes of the European Space Agency (ESA) for applications in disaster monitoring, global change and the preservation of world heritage sites ORAL	
22 nd UN/IAF International Workshop on Space Technologies Applied to the Needs of Humanity: Experience from Cases in the Mediterranean Area	2012/09/ 28-30	Naples, Italy	Satellite Remote Sensing in Support to Archaeological Investigation in Egypt: Some Methodological Remarks ORAL	
3rd EARSeL Workshop Advances in Remote Sensing for Archaeology and Cultural Heritage Management	2012/09/ 19-22	Ghent, Belgium	Potential of quad pol c-band, single and dual pol l-band SAR to identify buried archaeological features ORAL	
European Geosciences Union (EGU) 2012	2012/04/ 22-27	Vienna, Austria	Seasonal and yearly polarimetric time series analysis of Radarsat 2 quad pol data over the area around Rome ORAL	

APPENDIX D PUBLICATIONS

Appendix D.1 Peer Reviewed Journal Articles

Appendix D.1.1 Paper 1

Title: Detection of Archaeological Residues in Vegetated Areas Using Satellite Synthetic Aperture Radar
Author: Christopher Stewart
Pages: 45
Journal: Remote Sensing (Open Access)
Impact Factor: 3.036
Publication date: Received: 3 November 2016. Accepted: 22 January 2017. Published: 30 January 2017
URL: <http://www.mdpi.com/2072-4292/9/2/118>

Abstract: Buried archaeological structures, such as earthworks and buildings, often leave traces at the surface by altering the properties of overlying material, such as soil and vegetation. These traces may be better visible from a remote perspective than on the surface. Active and passive airborne and spaceborne sensors acquiring imagery from the ultraviolet to infrared have been shown to reveal these archaeological residues following the application of various processing techniques. While the active microwave region of the spectrum, in the form of Synthetic Aperture Radar (SAR) has been used for archaeological prospection in desert regions, it has yet to be fully exploited to detect buried structures indirectly through proxy indicators in overlying materials in vegetated areas. Some studies have used polarimetric SAR, but no studies have applied coherence or interferometric SAR for this application. This paper demonstrates that SAR backscatter intensity, coherence and interferometry can be used to identify archaeological residues over a number of study areas in the vicinity of Rome, Italy. 77 COSMO SkyMed images in Stripmap mode and 27 in Spotlight mode have been used for the analysis. Processing included multitemporal speckle filtering, coherence generation and Digital Elevation Model (DEM) creation from Small Baseline Subsets (SBAS). Comparison of these datasets with archaeological, geological, soil, vegetation and meteorological data reveal that different types of SAR data can expose various types of archaeological residues under different environmental conditions.

Appendix D.1.2 Paper 2

Title: Feature Extraction in the North Sinai Desert Using Spaceborne Synthetic Aperture Radar: Potential Archaeological Applications
Author: Christopher Stewart
Co-authors:

1. Rosanna Montanaro, Department of Cultural Heritage, University of Salento, Lecce 73100, Italy
2. Dr. Maura Sala, Freelance Consultant, Rome 00183, Italy
3. Dr. Paolo Riccardi, Sarmap SA, Purasca 6989, Switzerland

Pages: 27

Journal: Remote Sensing (Open Access)
Impact Factor: 3.036 (2015)
Publication date: Received: 14 July 2016. Accepted: 27 September. Published: 7 October 2016
URL: <http://www.mdpi.com/2072-4292/8/10/825>

Abstract: Techniques were implemented to extract anthropogenic features in the desert region of North Sinai using data from the first- and second-generation Phased Array type L-band Synthetic Aperture Radar (PALSAR-1 and 2). To obtain a synoptic view over the study area, a mosaic of average, multitemporal (De Grandi) filtered PALSAR-1 σ° backscatter of North Sinai was produced. Two subset regions were selected for further analysis. The first included an area of abundant linear features of high relative backscatter in a strategic, but sparsely developed area between the Wadi Tumilat and Gebel Maghara. The second included an area of low backscatter anomaly features in a coastal sabkha around the archaeological sites of Tell el-Farama, Tell el-Mahzan, and Tell el-Kanais. Over the subset region between the Wadi Tumilat and Gebel Maghara, algorithms were developed to extract linear features and convert them to vector format to facilitate interpretation. The algorithms were based on mathematical morphology, but to distinguish apparent man-made features from sand dune ridges, several techniques were applied. The first technique took as input the average σ° backscatter and used a Digital Elevation Model (DEM) derived Local Incidence Angle (LIA) mask to exclude sand dune ridges. The second technique, which proved more effective, used the average interferometric coherence as input. Extracted features were compared with other available information layers and in some cases revealed partially buried roads. Over the coastal subset region a time series of PALSAR-2 spotlight data were processed. The coefficient of variation (CoV) of De Grandi filtered imagery clearly revealed anomaly features of low CoV. These were compared with the results of an archaeological field walking survey carried out previously. The features generally correspond with isolated areas identified in the field survey as having a higher density of archaeological finds, and interpreted as possible islands of dry land, which may have been surrounded by lagoons, rivers, and swamplands in antiquity. It is suggested that these surrounding areas may still have a higher water content, sufficient to be detected in processed Synthetic Aperture Radar (SAR) imagery.

Appendix D.1.3 Paper 3

Title: Sentinel-1 bathymetry for North Sea palaeolandscape analysis
Author: Christopher Stewart
Co-authors: 1. Dr. Alfredo Renga, University of Naples, Italy
2. Prof. Vincent Gaffney, University of Bradford, UK
3. Prof. Giovanni Schiavon, Tor Vergata University of Rome, Italy
Pages: 22
Journal: International Journal of Remote Sensing
Impact Factor: 1.640 (2015)
Publication date: Received: 14 July 2015. Accepted: 4 November 2015. Published online: 21 Jan 2016
URL: <http://www.tandfonline.com/doi/full/10.1080/01431161.2015.1129563>

Abstract: Submerged palaeolandscapes can contain pristine underwater heritage. Regular monitoring of these areas is essential to assess and mitigate threats from development including construction, mining and commercial trawling. While bathymetry alone may be insufficient to detect submerged palaeolandscape features, it can nonetheless recognise previously mapped structures that have a topographic expression. The Sentinel-1 constellation will provide unprecedented access to freely available, high resolution Synthetic Aperture Radar (SAR) data, acquired systematically and with a long term continuity, and may constitute a cost effective solution for the monitoring of submerged palaeolandscapes. The paper shows the application of a recently developed bathymetric algorithm on Sentinel-1 SAR data over a region of the Southern North Sea. Results show general agreement with water depth data obtained from the European Marine Observation and Data Network portal for bathymetry (EMODnet). To assess the support that SAR bathymetry can provide to the analysis of submerged palaeolandscapes, the Sentinel-1 derived water depths have been compared with a palaeolandscape map of the same area produced by the North Sea Palaeolandscapes Project (NSPP). Results show a clear correspondence between some topographic structures identified in the Sentinel-1 water depth map and features interpreted by the NSPP as Early Holocene lakes, rivers and landscape topography.

Appendix D.1.4 Paper 4

Title: Multi-frequency, polarimetric SAR analysis for archaeological prospection
Author: Christopher Stewart
Co-authors: 1. Dr. Rosa Lasaponara, CNR IMAA, Potenza, Italy
2. Prof. Giovanni Schiavon, Tor Vergata University of Rome, Italy
Pages: 10
Journal: International Journal of Applied Earth Observation and Geoinformation
Impact Factor: 3.798 (2015)
Publication date: Received: 18 March 2013. Accepted: 13 November 2013. Published: May 2014
URL: <http://www.sciencedirect.com/science/article/pii/S0303243413001542>

Abstract: The aim of this study is to assess the sensitivity to buried archaeological structures of C and L band Synthetic Aperture Radar (SAR) in various polarisations. In particular, single and dual polarised data from the Phased Array type L-band SAR (PALSAR) sensor on-board the Advanced Land Observing Satellite (ALOS) is used, together with quadruple polarised (quad pol) data from the SAR sensor on Radarsat-2. The study region includes an isolated area of open fields in the eastern outskirts of Rome where buried structures are documented to exist. Processing of the SAR data involved multitemporal averaging, analysis of target decompositions, study of the polarimetric signatures over areas of suspected buried structures and changes of the polarimetric bases in an attempt to enhance their visibility. Various ancillary datasets were obtained for the analysis, including geological and lithological charts, meteorological data, Digital Elevation Models (DEMs), optical imagery and an archaeological chart.

For the Radarsat-2 data analysis, results show that the technique of identifying the polarimetric bases that yield greatest backscatter over anomaly features, and subsequently changing the polarimetric bases

of the time series, succeeded in highlighting features of interest in the study area. It appeared possible that some of the features could correspond with structures documented on the reference archaeological chart, but there was not a clear match between the chart and the results of the Radarsat-2 analysis. A similar conclusion was reached for the PALSAR data analysis. For the PALSAR data, the volcanic nature of the soil may have hindered the visibility of traces of buried features. Given the limitations of the accuracy of the archaeological chart and the spatial resolution of both the SAR datasets, further validation would be required to draw any precise conclusions on the sensitivity of the SAR data to buried structures. Such a validation could include geophysical prospection or excavation.

Appendix D.1.5 Paper 5

Title: ALOS PALSAR Analysis of the Archaeological Site of Pelusium
Author: Christopher Stewart
Co-authors: 1. Dr. Rosa Lasaponara, CNR IMAA, Potenza, Italy
2. Prof. Giovanni Schiavon, Tor Vergata University of Rome, Italy
Pages: 8
Journal: Archaeological Prospection
Impact Factor: 1.327 (2015)
Publication date: Received: 14 February 2013. Accepted: 4 April 2013. Published online: 15 May 2013
URL: <http://onlinelibrary.wiley.com/doi/10.1002/arp.1447/abstract>

Abstract: An analysis of the archaeological site of Pelusium in the north-eastern edge of the Nile Delta, Egypt, is carried out with PALSAR data. The aim is to assess the potential of PALSAR to identify buried archaeological structures. 18 PALSAR images acquired in various polarimetric modes have been obtained for the analysis through an ESA Category-1 project. Processing included coregistration and summation of images for each polarimetric mode to reduce speckle. The summed images were then compared with each other and with optical imagery to identify any features that may be of archaeological interest. Features identified on the summed images were also viewed in the individual images to assess their ephemeral nature. One image was available in quad pol mode with which polarimetric analysis was undertaken, including extraction of target decompositions and analysis of the scattering characteristics of the study area. Linear and geometric features that may be archaeological structures are visible in the processed SAR imagery. Possible palaeolandscape features are also identified. Some of these are visible in the optical imagery, but not clearly delineated. The results of the polarimetric analysis show that single bounce scattering dominates over the study area, and that over the sandy regions the signal is much weaker in all polarisations, with mixed scattering. While the spatial resolution does not enable clear identification and characterisation of the physical scattering properties of small scale features, the PALSAR data demonstrates the capability to highlight features which become almost invisible on optical imagery at the synoptic scale (even if they are visible up-close) leading to the conclusion that PALSAR may be a useful tool in the first stages of archaeological surveys to analyse the spatial pattern of features, and identify where to focus smaller scale surveys in areas with land cover similar to that of the study area.

Appendix D.2 Edited Book Chapters

Appendix D.2.1 AHMES Volume 2, Chapter 14

Chapter 14 title	Satellite Radar in Support to Archaeological Research in Egypt: Tracing Ancient Tracks Between Egypt and Southern Levant Across North Sinai
Book title	Archaeological Heritage & Multidisciplinary Egyptological Studies (AHMES) Volume 2 EGYPTIAN CURSES 2 A Research on Ancient Catastrophes
Publisher	CNR, Roma
Book Editor	Giuseppina Capriotti Vittozzi, CNR ISMA
Chapter Author	Christopher Stewart, Tor Vergata University of Rome
Chapter Co-author 1	Kris Lemmens, Department of Earth and Environmental Sciences, University of Leuven, Leuven
Chapter Co-author 2	Maura Sala, Rome
Date published	2015
Pages	25

Abstract: Preliminary research results are presented on the application of long wave (L-band) spaceborne Synthetic Aperture Radar (SAR) remote sensing for the identification of ancient tracks in North Sinai. The work is undertaken with data obtained from the European Space Agency (ESA) to support the Italian Ministry of Education, Universities and Research (MUIR) project, “The Seven Plagues”. One objective of this project is to carry out archaeological surveys in areas of historical interest in Egypt. North Sinai has long represented a key bridge between Egypt and the Southern Levant, where land routes were followed and raw materials transported since the 5th millennium BC. 74 SAR images have been obtained over the North Sinai region. These have been acquired by the Phased Array type L-band Synthetic Aperture Radar (PALSAR) sensor on-board the Japanese Advanced Land Observing Satellite (ALOS). Processing includes multitemporal speckle filtering, mosaicking and automatic feature extraction. Results obtained so far have shown that PALSAR is capable of identifying roads and partially buried tracks, which produce a higher backscatter and a higher interferometric coherence than the surrounding sand. In addition, over parts of North Sinai not covered by sand dunes, features of lower backscatter that may be of archaeological interest have also been identified. Interpretation of features is still ongoing.

Appendix D.2.2 AHMES Volume 2, Chapter 13

Chapter 13 title	Possibili vie tra Nilo e Mar Rosso. Rapporto preliminare di un caso di studio interdisciplinare
Book title	Archaeological Heritage & Multidisciplinary Egyptological Studies (AHMES) Volume 2 EGYPTIAN CURSES 2 A Research on Ancient Catastrophes

Publisher	CNR, Roma
Book Editor	Giuseppina Capriotti Vittozzi, CNR ISMA
Chapter Author	Giuseppina Capriotti Vittozzi, CNR ISMA
Chapter Co-author 1	Christopher Stewart, Tor Vergata University of Rome
Chapter Co-author 2	Kris Lemmens, Department of Earth and Environmental Sciences, University of Leuven, Leuven
Chapter Co-author 3	Bruno Marcolongo, IRPI - CNR, Padova
Date published	2015
Pages	22

Abstract: The SatER team is working on the ancient ways through the Eastern Desert to the Red Sea. C. Stewart has underlined the existence of a linear feature between the Dashur area and Port Suez. A lively debate developed about this fact and a preliminary report is presented here. Our goal is to show the first results as much as to present an interdisciplinary case study and its methodological work. Recent archaeological discoveries have demonstrated the importance of the Red Sea coast in the Pharaonic time. In particular, the French excavations in the sites of Ayn Sukhna and Wadi el-Jarf have revealed the role of the northern part of the Red Sea in relation with the Sinai mines and the royal necropolis areas. Even in later periods, such as the Ramesside Era, a connection between the Memphite area and the region of Port Suez was important. The research of ancient ways through the desert must consider the ability of the ancient Egyptians to optimise the geographical situation (ground, accessibility, security, water supply, winds etc.) and the availability of resources.

Appendix D.2.3 AHMES Volume 2, Chapter 12

Chapter 12 title	Satellite Radar Remote Sensing in Support to Archaeological Research in Egypt
Book title	Archaeological Heritage & Multidisciplinary Egyptological Studies (AHMES) Volume 2 EGYPTIAN CURSES 2 A Research on Ancient Catastrophes
Publisher	CNR, Roma
Book Editor	Giuseppina Capriotti Vittozzi, CNR ISMA
Chapter Author	Stefano Gusmano, Department of Remote Sensing Courses, Scuola di Aerocooperazione, Guidonia
Chapter Co-author 1	Christopher Stewart, Tor Vergata University of Rome
Chapter Co-author 2	Maurizio Fea, Italian Geophysical Association (AGI)
Date published	2015
Pages	10

Abstract: Remote sensing has become an established discipline providing support for analysis in the field of archaeology. In this study the approach chosen was to reinterpret some techniques of feature extraction normally applied with optical images, through satellite image exploitation in the microwave spectral domain. In this regard, a pair of interferometric images of the Italian Space Agency (ASI) satellite

constellation Cosmo-SkyMed has been used, with data obtained through a Category-1 (research) project of the European Space Agency (ESA). The methodological process includes the production of a Digital Elevation Model (DEM) through an interferometric processing and hillshade analysis. The results obtained confirm the utility of the process and the need for further investigations with images at higher resolution.

Appendix D.2.4 Remote Sensing Survey of Saddina

Chapter 13 title	Remote Sensing Survey of Saddina
Book title	La Ville Médiévale de Saddina un Site Archéologique a Valoriser dans le Prérif au Nord de Fès
Publisher	Une publication de la Faculté des Lettres et des Sciences Humaines Saïs, Université Sidi Mohamed Ben Abdellah
Book Editor	Brahim Akdim, Virgilio Martinez Enamorado and Grigori Lazarev, Université Sidi Mohamed Ben Abdellah
Chapter Author	Christopher Stewart, Tor Vergata University of Rome
Chapter Co-author	Grigori Lazarev, Université Sidi Mohamed Ben Abdellah
Date published	2014
Pages	12

Appendix D.3 Conference Proceedings

Appendix D.3.1 Proceedings: 2nd International Conference of Aerial Archaeology

Title:	A Review of the Subsurface Mapping Capability of SAR in Desert Regions, Bir Safsaf Revisited with Sentinel-1A and ENVISAT ASAR
Author:	Christopher Stewart, Tor Vergata University of Rome, Department of Civil Engineering and Computer Science, Rome, Italy
Co-author 1	Stefano Gusmano, Department of Remote Sensing Courses, Scuola di Aerocooperazione, Guidonia
Co-author 2	Maurizio Fea, Italian Geophysical Association (AGI)
Co-author 3	Giuseppina Capriotti Vittozzi, CNR ISMA
Co-author 4	Maura Sala, Freelance Consultant, Rome
Co-author 5	Rosanna Montanaro, Department of Cultural Heritage, University of Salento, Lecce, Italy
Conference:	2 nd International Conference of Aerial Archaeology
Conference Date:	3-5 February 2016
Conference Location	Rome, Italy
Publisher:	Proceedings of 2 nd International Conference of Aerial Archaeology
Publication date:	In review process
URL:	
Pages:	14

Abstract: A review of the main principles and techniques of satellite Synthetic Aperture Radar (SAR) remote sensing for subsurface mapping in desert regions is presented here. Its application over the well-

studied region of Bir Safsaf in south-central Egypt is demonstrated with Copernicus Sentinel and European Space Agency (ESA) ENVISAT Advanced SAR data. The analysis has been undertaken in the wider scope of the Italian Research Project of Particular National Interest (PRIN), “AHMES” (Archaeological Heritage & Multidisciplinary Egyptological Studies). This is an interdisciplinary project which brings together experts in remote sensing, GIS, geology, archaeology and Egyptology to seek further information on certain historical events in the Mediterranean region through convergence of evidence.

Appendix D.3.2 Proceedings: International Workshop “Italian Days in Aswan”

Title: A Contribution of Satellite Radar to Archaeological Research in North Sinai, Egypt
Author: Christopher Stewart, Tor Vergata University of Rome, Department of Civil Engineering and Computer Science, Rome, Italy
Co-author 1 Kris Lemmens, Department of Earth and Environmental Sciences, University of Leuven, Leuven
Co-author 2 Maura Sala, Rome
Co-author 3 Giuseppina Capriotti Vittozzi, ISMA-CNR, Rome
Conference: International Workshop “Italian Days in Aswan”
Conference Date: 16-18 November 2013
Conference Location Aswan, Egypt
Publisher: Archaeological Heritage & Multidisciplinary Egyptological Studies (AHMES)
 Volume 3
 ARCHAEOLOGY AND ENVIRONMENT
 Understanding the Past to Design the Future: A Multidisciplinary Approach
 Proceedings of the International Workshop “Italian Days in Aswan”, 16th-18th November 2013
 Edited by Giuseppina Capriotti Vittozzi and Francesco Porcelli CNR, Roma
Publication date: 2016
URL: http://www.academia.edu/23689019/A_Contribution_of_Satellite_Radar_to_Archaeological_Research_in_North_Sinai_Egypt
Pages: 11

Abstract: Initial research results are presented on the application of long wave (L-band) spaceborne Synthetic Aperture Radar (SAR) remote sensing for the detection of possible ancient routes traversing the desert region of North Sinai. The work is undertaken with data obtained from the European Space Agency (ESA) to support the Research Program PRIN 2009 “The Seven Plagues”, one objective of which is to carry out archaeological survey using innovative techniques. Processing has been carried out on 74 SAR images of the area to produce a seamless multitemporal averaged mosaic of calibrated SAR backscatter. An automatic feature detection algorithm has then been applied to extract linear features. Extracted features are in the process of being interpreted together with other datasets to verify their archaeological significance.

Appendix D.3.3 Proceedings: Cultural Heritage Workshop – Euromed2014

Title: ESA activities in Earth Observation for Cultural Heritage applications

Author: Christopher Stewart, RSAC c/o ESA, Earth Observation Programmes, ESA EOP-SA, 00044 Frascati, Italy

Co-author 1 Michael Rast, ESA, Earth Observation Programmes, ESA EOP-SA, 00044 Frascati, Italy

Co-author 2 Francesco Sarti, ESA, Earth Observation Programmes, ESA EOP-SA, 00044 Frascati, Italy

Co-author 3 Olivier Arino, ESA, Earth Observation Programmes, ESA EOP-SE, 00044 Frascati, Italy

Conference: Workshop on REMOTE SENSING FOR CULTURAL HERITAGE AND LANDSCAPE - Euromed2014

Conference Date: 7 November, 2014

Conference Location Limassol, Cyprus

Publisher: International Journal of Heritage in the Digital Era
volume 4 number 3+4 2015

Publication date: 2015

URL: https://www.researchgate.net/publication/286510131_ESA_activities_in_Earth_Observation_for_Cultural_Heritage_applications

Pages: 15

Abstract: An overview is provided of the activities of the European Space Agency, ESA, to support the documentation, monitoring and management of Cultural Heritage through the use of Earth Observation, EO. These activities include: participation in international agreements; funding of service demonstration projects and support to researchers through the provision of data, training courses and the hosting of research students at the ESA European Space Research Institute, ESRIN, establishment. Since ESA and the United Nations Educational, Scientific and Cultural Organisation, UNESCO, signed the “Open Initiative on the Use of Space Technologies to Support the World Heritage Convention”, world heritage has become increasingly prominent in ESA as an emerging application area. Various demonstration projects have successfully revealed the potential to bridge the gap between research and operational service delivery. These projects include Heritage Observation and Retrieval Under Sand, HORUS, which used radar to document archaeological structures buried beneath the sand in Egypt, and ArchEO, a project recently kicked-off, aimed at demonstrating optical Earth observation techniques for the detection of archaeological structures in Poland. An increasing number of research projects are exploiting ESA and Third Party Mission, TPM, data for cultural heritage applications. Some of these include a project using radar remote sensing for subsurface archaeological feature detection, a project focussing on monitoring land subsidence over Syrian archaeological sites using Interferometric Synthetic Aperture Radar, InSAR, and a project documenting archaeological structures over the Silk Road in China. In addition to the provision of data and processing tools, ESA supports the heritage research and user community through training courses that focus on the application of EO for cultural heritage. Finally, ESA contributes to workshops to provide a forum for the heritage and remote sensing communities to exchange ideas, and provide insights into evolving user needs and technological achievements. ESA activities are driven by user requirements. The increasing involvement of ESA in EO related activities in cultural heritage is indicative of the emerging awareness of the benefits of EO on the part of the heritage community, and their growing interest in its integration into their activities. In order to most

efficiently channel resources and plan future EO developments to meet this increased demand, interdisciplinary dialogue is essential between the heritage and remote sensing communities.

Appendix D.3.4 Proceedings: 4th EARSeL Workshop on Cultural and Natural Heritage

Title: Analysis of the Utility of COSMO SkyMed Stripmap to Detect Buried Archaeological Features in the Region of Rome.
Experimental Component of WHERE Project

Author: Christopher Stewart, Tor Vergata University of Rome, Department of Civil Engineering and Computer Science, Rome, Italy

Co-author 1 Alessio Di Iorio, ALMA Sistemi sas, Rome, Italy

Co-author 2 Giovanni Schiavon, Tor Vergata University of Rome, Department of Civil Engineering and Computer Science, Rome, Italy

Conference: 4th EARSeL Workshop on Cultural and Natural Heritage

Conference Date: 6-7 June 2013

Conference Location Matera, Italy

Publisher: Proceedings of the 4th EARSeL Workshop on Cultural and Natural Heritage

Publication date: 2013

URL: http://www.earsel.org/SIG/NCH/4th-workshop/pdf_proceedings/4.4.pdf

Pages: 10

Abstract: Buried features often leave traces in the overlying soil and vegetation. These traces can be in the form of differences in soil moisture or vegetation growth caused for example by increased soil water retention over a buried ditch, or by insufficient soil depth over a buried wall for vegetation to place deep roots. The aim of this research is to determine whether Cosmo Skymed (CSK) Stripmap imagery can be used to detect traces of buried archaeological features taking advantage of the sensitivity of SAR to soil moisture and surface roughness. The research forms a part of the World HERitage monitoring by Remote sEnsing (WHERE) project, the primary objective of which is to develop and demonstrate a pre-operational system and a cost effective service based on remote sensing data to monitor UNESCO sites in urban areas.

The focus of the analysis is in two areas of interest (AOIs), one of which includes a region east of Portus, the ancient port of Rome, located at the delta of the Tiber River, and the other a region in the eastern outskirts of Rome, where there is an isolated area of agricultural fields surrounded by urban development. 23 CSK Stripmap images, provided by the Italian Space Agency (ASI), have been acquired in Single Look Complex (SLC) format, HH polarization, from July 2011 to October 2012. Processing is carried out to enhance the visibility of buried archaeological features identified in the imagery. Analysis is then undertaken to determine the reason for the appearance of such features in the data. In both regions archaeological ground truth is available. Over the Portus AOI this includes results of a geophysical magnetometry survey published by Keay et al., 2005. Over the Eastern Rome AOI the ground truth data includes the Forma Italiae archaeological chart published by Quilici, 1974, which was digitized and geocoded by the main author. Optical imagery from various sensors has been available to

compare the visibility of features in both SAR and optical data over both AOIs. These include ALOS PRISM and Kompsat-2 data obtained through an ESA Category 1 (research) project, and a time series of optical imagery available in Google Earth. For the research into the cause of buried archaeological features appearing in the data, surface soil moisture data from the Technical University of Vienna and meteorological data from local private weather stations was obtained.

Results show that CSK data is sensitive to both crop and soil marks and a processing chain has been developed to improve their visibility in the data. Research on the underlying cause of these features appearing in the imagery tends to the conclusion that buried structures are more evident in vegetated fields, as opposed to bare soil, and in conditions of less than average soil moisture. It is hoped to continue the analyses with more ancillary data to obtain better statistical estimates to support these conclusions.

Appendix D.4 Poster Presentations

Satellite time series analysis to study the ephemeral nature of archaeological marks

Time series of spaceborne Synthetic Aperture Radar (SAR) images (COSMO SkyMed) are analysed to extract traces of buried archaeological structures. The SAR techniques are compared with more conventional methods using optical multispectral satellite images (Kompsat 2) and geophysical survey data (magnetometry). Given the wavelength of the SAR sensor (X-band, 3.1 cm) and the characteristics of the surface that inhibits direct penetration of the SAR signal into the soil medium, features are identified indirectly through the analysis of vegetation, soil and topographic anomalies. Research is carried out on the optimal conditions for detection of such archaeological features in the study areas. The COSMO SkyMed data was obtained in both Stripmap HIMAGE and Enhanced Spotlight modes from the Italian Space Agency (ASI) in the framework of the WHERE project (World Heritage Monitoring by Remote Sensing). All other satellite data was obtained through a European Space Agency (ESA) Category 1 project (C1F.11458). The areas of interest include sites near the city of Rome, Italy.

Christopher Stewart (1), Giovanni Schiavon (2)
 (1) Virginia University, Department of Civil Engineering and Computer Science, Rome, Italy
 (2) Research Institute for Cultural Heritage, Rome, Italy

Archaeological Crop and Soil Marks

Features buried beneath the ground can affect the characteristics of the overlying soil, including its depth, composition and ability to retain moisture. This in turn can alter the properties of vegetation that may grow on the surface. If the differences in the soil and vegetation over buried features are sufficient to render them visible to the human eye, they are termed soil and crop marks respectively (see Fig. 1).

Crop marks are visible at certain times on remotely sensed optical imagery when conditions are right, usually in dry periods when vegetation is parched.



Figure 1: Diagram showing soil and crop marks. Figure 2: 3D visualization of a crop mark. Figure 3: Photograph of a field with a crop mark.

In the framework of the WHERE project, a time series of 25 COSMO SkyMed (CSK) Stripmap images acquired in HH polarization, according east, at intervals of approximately 16 days from June 2011 to October 2012, and with perpendicular baselines to allow interferometric processing, were obtained for the analysis in Portus. A processing chain was developed to identify potential crop and soil marks, to be verified with the magnetometry data, optical imagery and field visits. A further processing chain was then elaborated to determine whether any identified features in the acquired imagery were crop marks or soil marks.

CSK processing chain – visualisation of crop/soil marks



CSK processing chain – crop mark or soil mark?

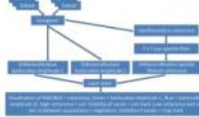


Figure 4: Result of processing chain to visualize archaeological crop and soil marks in the CSK images. Portus, Italy. Images provided by the Italian Space Agency.

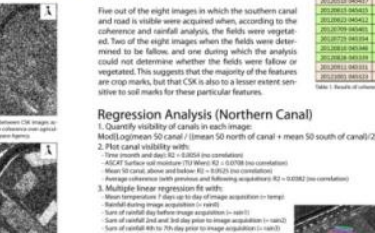


Figure 5: Comparison of the results of the CSK processing chain with the magnetometry data. Portus, Italy. Images provided by the Italian Space Agency.

CSK Acquisition Date Time	Canal/Field Visibility (1=yes, 0=no)	Interferometric Coherence (1=yes, 0=no)	Canal/Field Visibility (1=yes, 0=no)	Interferometric Coherence (1=yes, 0=no)
20110711 045700	0	0	0	0
20110728 045700	0	0	0	0
20110814 045700	0	0	0	0
20110830 045700	0	0	0	0
20110915 045700	0	0	0	0
20110930 045700	0	0	0	0
20111015 045700	0	0	0	0
20111030 045700	0	0	0	0
20111114 045700	0	0	0	0
20111129 045700	0	0	0	0
20111214 045700	0	0	0	0
20111229 045700	0	0	0	0
20120113 045700	0	0	0	0
20120128 045700	0	0	0	0
20120212 045700	0	0	0	0
20120227 045700	0	0	0	0
20120313 045700	0	0	0	0
20120328 045700	0	0	0	0
20120412 045700	0	0	0	0
20120427 045700	0	0	0	0
20120513 045700	0	0	0	0
20120528 045700	0	0	0	0
20120612 045700	0	0	0	0
20120627 045700	0	0	0	0
20120713 045700	0	0	0	0
20120728 045700	0	0	0	0
20120812 045700	0	0	0	0
20120827 045700	0	0	0	0
20120912 045700	0	0	0	0
20120927 045700	0	0	0	0
20121012 045700	0	0	0	0
20121027 045700	0	0	0	0

Table 1: Results of coherence analysis.

Regression Analysis (Northern Canal)

- Quantity visibility of canal (1=visible, 0=invisible) vs mean south of canal (20)
- Plot canal visibility with:
 - Three month and day (2 - 3/2012 (no correlation))
 - ASCI Factor and moisture (7/1/2012 (no correlation))
 - Mean 50 canal, above and below (81 - 7/1/2012 (no correlation))
 - Average linear regression fit results
 - Multiple linear regression fit results
 - Mean temperature 7 days up to day of image acquisition (no temp)
 - Rainfall during image acquisition (no rain)
 - Sum of rainfall day before image acquisition (no sum)
 - Sum of rainfall day and day prior to image acquisition (no sum)
 - Sum of rainfall to 10h day prior to image acquisition (no sum)
- Fit function:

$$\text{Canal visibility} = 0.497 \sin(\pi t) + 0.27 \sin(2\pi t) + 0.27 \sin(3\pi t) + 0.27 \sin(4\pi t) + 0.27 \sin(5\pi t)$$

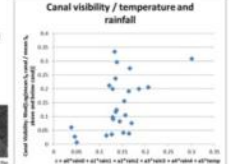


Figure 6: Scatter plot showing the relationship between canal visibility and temperature and rainfall.

Archaeological Shadow Marks

Buried features are often distinguished by subtle topographic differences on the surface. When the sun is low in the sky, these differences are visibly enhanced by shadows and reflection. Archaeological shadow marks can be rendered visible by artificially illuminating Digital Elevation Models (DEMs) produced for example by LiDAR, photogrammetry or interferometric SAR (InSAR). This technique is called "shading analysis".

A second study area includes a region in the eastern outskirts of Rome, south of the Via Peninsulare and east of the Grande Rocce di Aniene, the main ring road around Rome (Fig. 14). This is an isolated area of open fields surrounded by urban development in which there is a high density of archaeological sites both at the surface and buried beneath the ground, documented on the Forma Urbis archaeological chart (Quilici, 1974) (Fig. 17). Traces of buried structures are visible on optical imagery (Fig. 15). The same processing chain for the identification of archaeological marks using SAR was applied to a time series of CSK Enhanced Spotlight images, acquired from June 2011 to June 2012 by ASI and obtained in the framework of the WHERE project (Fig. 16). The archaeological feature identified in Fig. 16 is a topographic mark. An interferometric DEM was produced from two of the CSK images, and subsequently an image of shaded relief, to see to what extent the feature can be identified in the SAR data as a shadow mark.



Figure 14: Diagram showing the location of the study area in the eastern outskirts of Rome.

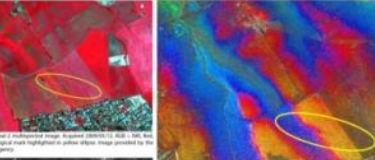


Figure 15: Optical imagery showing traces of buried structures.

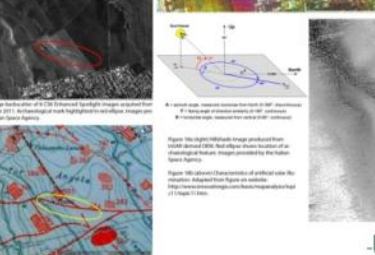


Figure 16: SAR data showing a topographic mark.

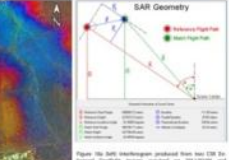


Figure 17: SAR Geometry diagram showing the geometry of the SAR sensor and the resulting image.

Figure D-1. Poster presented at EGU 2014 (see Appendix C.4).

Satellite Remote Sensing for Archaeological Applications

The research presented here applies existing satellite remote sensing techniques to the documentation of buried archaeological features and attempts to develop new techniques with sensors that have previously been underutilised for this application. Satellite sensors used for the analysis include optical (Komsat-2, ALOS PRISM) and SAR (Envisat ASAR, ALOS PALSAR and COSMO Skymed). The COSMO Skymed data was obtained from the Italian Space Agency (ASI) in the framework of the WHERE project (World Heritage Monitoring by Remote Sensing). All other data was obtained through a European Space Agency (ESA) Category 1 project (C1F.11458). The processing applied to the data takes advantage of the various different sensor characteristics to detect directly, or indirectly via proxies, evidence of buried archaeological features. Results show that SAR sensors can be utilised to detect archaeological features conventionally identified with optical sensors. The application of various techniques for archaeological prospection are demonstrated over sites in Italy and Egypt.

Christopher Stewart
 Tor Vergata University, Department of Civil Engineering and Computer Science
 Rome, Italy
 stewartc@roma2.infn.it

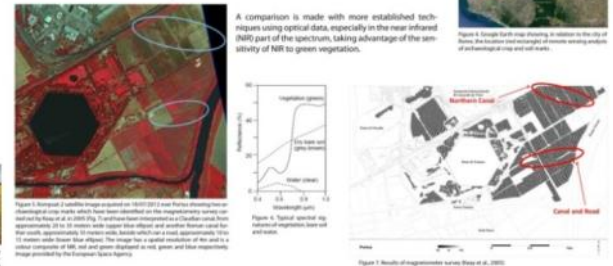
Archaeological Crop and Soil Marks

Features buried beneath the ground can affect the characteristics of the overlying soil, including its depth, composition and ability to retain moisture. This in turn can alter the properties of vegetation that may grow on the surface. If the differences in the soil and vegetation over buried features are sufficient to render them visible to the human eye, they are termed soil and crop marks respectively (see Fig. 1).

Crop marks are visible at certain times on remotely sensed optical imagery when conditions are right, usually in dry periods when vegetation is parched.



An analysis has been carried out on the visibility of archaeological crop and soil marks in remotely sensed data in an area between the hexagonal lake of Portus (the ancient port of Rome) and the Tiber river (see Fig. 4). The region was chosen for its flat and open landscape, the abundance of buried archaeological features, and good ground truth in the form of magnetometry survey data, published by Kay et al. in 2005. The analysis aimed at determining whether SAR is capable of distinguishing crop and soil marks, taking advantage of its sensitivity to surface roughness to detect differences in vegetation growth, and its sensitivity to the dielectric properties of materials to detect differences in the moisture content of soils over archaeological features.



In the framework of the WHERE project, a time series of 23 COSMO Skymed (CSK) Stripmap images acquired in HH polarisation, ascending pass, at intervals of approximately 16 days from July 2011 to October 2012, and with perpendicular baselines to allow interferometric processing, were obtained for the analysis in Portus. A processing chain was developed to identify potential crop and soil marks, to be verified with the magnetometry data, optical imagery and field visits. A further processing chain was then elaborated to determine whether any identified features in the acquired imagery were crop marks or soil marks.

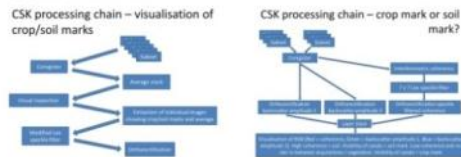


Table 1 shows the results of the interferometric analysis to determine whether archaeological crop and soil marks are visible in conditions of bare soil or vegetation. The outcome reveals that there is a period of the year from 28 August 2011 to 7 March 2012 in which coherence is very high (see Fig. 11), apart from an occasion when there was (at least) more than 1.56 cm of rainfall between these acquisitions. In the period from 10 Aug to 28 Aug 2012 there is partial coherence, but from 26 Aug to the last image acquisition date (1 Oct 2012) coherence is low, but the rainfall between acquisition dates in this period exceeds the maximum measured at which coherence is still high (1.56cm), so it is difficult to say whether in this period the fields were fallow or vegetated.

CSK Acquisition Date Time	Coherence (0-1)	CSK Rain (mm)	Coherence Class (0-1)	CSK Rain Class (0-1)
20110728 045725	0	0	0	0
20110805 045809	0	0	0	0
20110812 045811	0	0	0	0
20110819 045809	0	0	0	0
20110826 045812	0	0	0	0
20110902 045819	0	0	0	0
20110909 045812	0	0	0	0
20110916 045812	0	0	0	0
20110923 045812	0	0	0	0
20110930 045812	0	0	0	0
20111007 045812	0	0	0	0
20111014 045812	0	0	0	0
20111021 045812	0	0	0	0
20111028 045812	0	0	0	0
20111104 045812	0	0	0	0
20111111 045812	0	0	0	0
20111118 045812	0	0	0	0
20111125 045812	0	0	0	0
20111202 045812	0	0	0	0
20111209 045812	0	0	0	0
20111216 045812	0	0	0	0
20111223 045812	0	0	0	0
20120106 045812	0	0	0	0
20120113 045812	0	0	0	0
20120120 045812	0	0	0	0
20120127 045812	0	0	0	0
20120203 045812	0	0	0	0
20120210 045812	0	0	0	0
20120217 045812	0	0	0	0
20120224 045812	0	0	0	0
20120303 045812	0	0	0	0
20120310 045812	0	0	0	0
20120317 045812	0	0	0	0
20120324 045812	0	0	0	0
20120331 045812	0	0	0	0
20120407 045812	0	0	0	0
20120414 045812	0	0	0	0
20120421 045812	0	0	0	0
20120428 045812	0	0	0	0
20120505 045812	0	0	0	0
20120512 045812	0	0	0	0
20120519 045812	0	0	0	0
20120526 045812	0	0	0	0
20120602 045812	0	0	0	0
20120609 045812	0	0	0	0
20120616 045812	0	0	0	0
20120623 045812	0	0	0	0
20120630 045812	0	0	0	0
20120707 045812	0	0	0	0
20120714 045812	0	0	0	0
20120721 045812	0	0	0	0
20120728 045812	0	0	0	0
20120804 045812	0	0	0	0
20120811 045812	0	0	0	0
20120818 045812	0	0	0	0
20120825 045812	0	0	0	0
20120901 045812	0	0	0	0
20120908 045812	0	0	0	0
20120915 045812	0	0	0	0
20120922 045812	0	0	0	0
20120929 045812	0	0	0	0
20121006 045812	0	0	0	0
20121013 045812	0	0	0	0
20121020 045812	0	0	0	0
20121027 045812	0	0	0	0
20121103 045812	0	0	0	0
20121110 045812	0	0	0	0
20121117 045812	0	0	0	0
20121124 045812	0	0	0	0
20121201 045812	0	0	0	0
20121208 045812	0	0	0	0
20121215 045812	0	0	0	0
20121222 045812	0	0	0	0
20130105 045812	0	0	0	0
20130112 045812	0	0	0	0
20130119 045812	0	0	0	0
20130126 045812	0	0	0	0
20130202 045812	0	0	0	0
20130209 045812	0	0	0	0
20130216 045812	0	0	0	0
20130223 045812	0	0	0	0
20130301 045812	0	0	0	0
20130308 045812	0	0	0	0
20130315 045812	0	0	0	0
20130322 045812	0	0	0	0
20130329 045812	0	0	0	0
20130405 045812	0	0	0	0
20130412 045812	0	0	0	0
20130419 045812	0	0	0	0
20130426 045812	0	0	0	0
20130503 045812	0	0	0	0
20130510 045812	0	0	0	0
20130517 045812	0	0	0	0
20130524 045812	0	0	0	0
20130601 045812	0	0	0	0
20130608 045812	0	0	0	0
20130615 045812	0	0	0	0
20130622 045812	0	0	0	0
20130629 045812	0	0	0	0
20130706 045812	0	0	0	0
20130713 045812	0	0	0	0
20130720 045812	0	0	0	0
20130727 045812	0	0	0	0
20130803 045812	0	0	0	0
20130810 045812	0	0	0	0
20130817 045812	0	0	0	0
20130824 045812	0	0	0	0
20130831 045812	0	0	0	0
20130907 045812	0	0	0	0
20130914 045812	0	0	0	0
20130921 045812	0	0	0	0
20130928 045812	0	0	0	0
20131005 045812	0	0	0	0
20131012 045812	0	0	0	0
20131019 045812	0	0	0	0
20131026 045812	0	0	0	0
20131102 045812	0	0	0	0
20131109 045812	0	0	0	0
20131116 045812	0	0	0	0
20131123 045812	0	0	0	0
20131130 045812	0	0	0	0
20131207 045812	0	0	0	0
20131214 045812	0	0	0	0
20131221 045812	0	0	0	0
20140104 045812	0	0	0	0
20140111 045812	0	0	0	0
20140118 045812	0	0	0	0
20140125 045812	0	0	0	0
20140201 045812	0	0	0	0
20140208 045812	0	0	0	0
20140215 045812	0	0	0	0
20140222 045812	0	0	0	0
20140301 045812	0	0	0	0
20140308 045812	0	0	0	0
20140315 045812	0	0	0	0
20140322 045812	0	0	0	0
20140329 045812	0	0	0	0
20140405 045812	0	0	0	0
20140412 045812	0	0	0	0
20140419 045812	0	0	0	0
20140426 045812	0	0	0	0
20140503 045812	0	0	0	0
20140510 045812	0	0	0	0
20140517 045812	0	0	0	0
20140524 045812	0	0	0	0
20140601 045812	0	0	0	0
20140608 045812	0	0	0	0
20140615 045812	0	0	0	0
20140622 045812	0	0	0	0
20140629 045812	0	0	0	0
20140706 045812	0	0	0	0
20140713 045812	0	0	0	0
20140720 045812	0	0	0	0
20140727 045812	0	0	0	0
20140803 045812	0	0	0	0
20140810 045812	0	0	0	0
20140817 045812	0	0	0	0
20140824 045812	0	0	0	0
20140831 045812	0	0	0	0
20140907 045812	0	0	0	0
20140914 045812	0	0	0	0
20140921 045812	0	0	0	0
20140928 045812	0	0	0	0
20141005 045812	0	0	0	0
20141012 045812	0	0	0	0
20141019 045812	0	0	0	0
20141026 045812	0	0	0	0
20141102 045812	0	0	0	0
20141109 045812	0	0	0	0
20141116 045812	0	0	0	0
20141123 045812	0	0	0	0
20141130 045812	0	0	0	0
20141207 045812	0	0	0	0
20141214 045812	0	0	0	0
20141221 045812	0	0	0	0
20150104 045812	0	0	0	0
20150111 045812	0	0	0	0
20150118 045812	0	0	0	0
20150125 045812	0	0	0	0
20150201 045812	0	0	0	0
20150208 045812	0	0	0	0
20150215 045812	0	0	0	0
20150222 045812	0	0	0	0
20150301 045812	0	0	0	0
20150308 045812	0	0	0	0
20150315 045812	0	0	0	0
20150322 045812	0	0	0	0
20150329 045812	0	0	0	0
20150405 045812	0	0	0	0
20150412 045812	0	0	0	0
20150419 045812	0	0	0	0
20150426 045812	0	0	0	0
20150503 045812	0	0	0	0
20150510 045812	0	0	0	0
20150517 045812	0	0	0	0
20150524 045812	0	0	0	0
20150601 045812	0	0	0	0
20150608 045812	0	0	0	0
20150615 045812	0	0	0	0
20150622 045812	0	0	0	0
20150629 045812	0	0	0	0
20150706 045812	0	0	0	0
20150713 045812	0	0	0	0
20150720 045812	0	0	0	0
20150727 045812	0	0	0	0
20150803 045812	0	0	0	0
20150810 045812	0	0	0	0
20150817 045812	0	0	0	0
20150824 045812	0	0	0	0
20150831 045812	0	0	0	0
20150907 045812	0	0	0	0
20150914 045812	0	0	0	0
20150921 045812	0	0	0	0
20150928 045812	0	0	0	0
20151005 045812	0	0	0	0
20151012 045812	0	0	0	0
20151019 045812	0	0	0	0
20151026 045812	0	0	0	0



Figure D-3. Poster presented at the European Space Expo 2013 Photographic Exhibition: Sensing the Past: COSMO SkyMed and radar technologies for archaeology (see Appendix C.4).

REFERENCES

Abd el-Samie, M. (1992). "Preliminary Report on the Excavations at Tell el-Makhzan (Pelusium)." Cahiers de Recherches de L'Institut de Papyrologie et d'Egyptologie de Lille **14**: 6.

Abdel-Galil, M., M. Hereher and H. El-Etr (2000). Study of movement of sand dunes of Northern Sinai and their potential impact on regional development. 2nd International Conference on Earth Observation and Environmental Information, Cairo, Egypt.

Abdel-Motelib, A., M. Bode, R. Hartmann, U. Hartung, A. Hauptmann and K. Pfeiffer (2012). "Archaeometallurgical expeditions to the Sinai Peninsula and the Eastern Desert of Egypt (2006, 2008)." Metalla (Bochum) **19**(1.2): 56.

Abdelsalam, M. G., C. Robinson, F. El-Baz and R. J. Stern (2000). "Applications of orbital imaging radar for geologic studies in arid regions: the Saharan Testimony." Photogrammetric Engineering and Remote Sensing **66**(6): 717-726.

Abdelsalam, M. G. and R. J. Stern (1996). "Mapping Precambrian structures in the Sahara Desert with SIR-C/X-SAR radar: The Neoproterozoic Kerf Suture, NE Sudan." Journal of Geophysical Research: Planets **101**(E10): 23063-23076.

Abu Al Izz, M. S. (1977). Landforms of Egypt. Cairo, The American University Press.

Adams, R. E. (1980). "Swamps, canals, and the locations of ancient Maya cities." Antiquity **54**(212): 206-214.

Adams, R. E. (1982). "Ancient Maya Canals: Grids and Lattices in the Maya Jungle." Archaeology New York, NY **35**(6): 28-35.

Agapiou, A., D. D. Alexakis and D. G. Hadjimitsis (2014). "Spectral sensitivity of ALOS, ASTER, IKONOS, LANDSAT and SPOT satellite imagery intended for the detection of archaeological crop marks." International Journal of Digital Earth **7**(5): 351-372.

Agapiou, A., D. G. Hadjimitsis, A. Sarris, A. Georgopoulos and D. D. Alexakis (2013). "Optimum temporal and spectral window for monitoring crop marks over archaeological remains in the Mediterranean region." Journal of Archaeological Science **40**(3): 1479-1492.

Ahmed, M. T. (2010). Ecosystems and Human Well-being: El Maghara, Northern Sinai, Egypt, UNEP/Earthprint.

References

- Allgaier, A. (2008). Aeolian sand transport and vegetation cover. Arid Dune Ecosystems, Springer: 211-224.
- Alpers, W. and I. Hennings (1984). "A theory of the imaging mechanism of underwater bottom topography by real and synthetic aperture radar." Journal of Geophysical Research **89**(C6): 10529-10546.
- Amit, R., Y. Enzel, O. Crouvi, O. Simhai, A. Matmon, N. Porat, E. McDonald and A. R. Gillespie (2011). "The role of the Nile in initiating a massive dust influx to the Negev late in the middle Pleistocene." Geological Society of America Bulletin **123**(5-6): 873-889.
- Arieh, I. B. (1974). "An Early Bronze Age II Site at Nabi Salah in Southern Sinai." Tel Aviv **1**(4): 144-156.
- Arikawa, Y., H. Saruwatari, Y. Hatooka and S. Suzuki (2014). ALOS-2 launch and early orbit operation result. IGARSS.
- Arthur, P. and E. D. Oren (1998). "The North Sinai survey and the evidence of transport amphorae for Roman and Byzantine trading patterns." Journal of Roman Archaeology **11**: 193-212.
- Aschbacher, J. and M. P. Milagro Perez (2014). Sentinel-1A-Launching the first satellite and launching the operational Copernicus programme. EGU General Assembly Conference Abstracts.
- Aspert, F., M. Bach-Cuadra, A. Cantone, F. Holecz and J.-P. Thiran (2007). Time-varying segmentation for mapping of land cover changes. ENVISAT Symposium.
- Baines, P. G. (1998). Topographic effects in stratified flows, Cambridge University Press.
- Barnes, I. (2003). "Aerial remote-sensing techniques used in the management of archaeological monuments on the British Army's Salisbury Plain Training Area, Wiltshire, UK." Archaeological prospection **10**(2): 83-90.
- Barnes, R. M. (1988). Roll-invariant decompositions for the polarization covariance matrix. Polarimetry Technology Workshop. REDSTONE Arsenal, AL.
- Bartalis, Z., W. Wagner, V. Naeimi, S. Hasenauer, K. Scipal, H. Bonekamp, J. Figa and C. Anderson (2007). "Initial soil moisture retrievals from the METOP-A Advanced Scatterometer (ASCAT)." Geophysical Research Letters **34**(20).

References

Beck, A. (2007). Archaeological site detection: the importance of contrast. Proceedings of the 2007 Annual Conference of the Remote Sensing and Photogrammetry Society, Newcastle University.

Becker, H. (2015). "Prospecting in Ostia Antica (Italy) and the Discovery of the Basilica of Constantinus I. in 1996." ICOMOS–Hefte des Deutschen Nationalkomitees **33**: 139-143.

Beit-Arieh, I. (2003). Archaeology of Sinai: the Ophir expedition, Emery and Claire Yass publications in archaeology.

Bellotti, P., G. Calderoni, F. Di Rita, M. D'Orefice, C. D'amico, D. Esu, D. Magri, M. P. Martinez, P. Tortora and P. Valeri (2011). "The Tiber river delta plain (central Italy): coastal evolution and implications for the ancient Ostia Roman settlement." The Holocene **21**(7): 1105-1116.

Ben-Dor, E., J. Portugali, M. Kochavi, M. Shimoni and L. Vinitzky (2013). "Airborne thermal video radiometry and excavation planning at Tel Leviah, Golan Heights, Israel." Journal of field archaeology.

Benjamin, J., C. Bonsall, C. Pickard and A. Fischer (2011). Submerged prehistory, Oxbow Books Oxford.

Berardino, P., G. Fornaro, R. Lanari and E. Sansosti (2002). "A new algorithm for surface deformation monitoring based on small baseline differential SAR interferograms." IEEE Transactions on Geoscience and Remote Sensing **40**(11): 2375-2383.

Berlin, G. L., M. A. Tarabzouni, A. H. Al-naser, K. M. Sheikho and R. W. Larson (1986). "SIR-B subsurface imaging of a sand-buried landscape: Al Labbah Plateau, Saudi Arabia." Geoscience and Remote Sensing, IEEE Transactions on(4): 595-602.

Berry, J. A. and W. J. S. Downton (1982). "Environmental regulation of photosynthesis." Photosynthesis **2**: 263-343.

Bingham, J. (1966). "Varietal response in wheat to water supply in the field, and male sterility caused by a period of drought in a glasshouse experiment." Annals of Applied Biology **57**(3): 365-377.

Blom, R. and C. Elachi (1987). "Multifrequency and multipolarization radar scatterometry of sand dunes and comparison with spaceborne and airborne radar images." Journal of Geophysical Research B **92**(B8): 7877-7889.

Blom, R. and G. Hedges (1997). Space technology and the discovery of the lost city of Ubar. Aerospace Conference, 1997. Proceedings., IEEE, IEEE.

References

Blom, R. G., R. E. Crippen and C. Elachi (1984). "Detection of subsurface features in SEASAT radar images of Means Valley, Mojave Desert, California." Geology **12**(6): 346-349.

Brabham, D. C. (2013). Crowdsourcing, Mit Press.

Brusch, S., P. Held, S. Lehner, W. Rosenthal and A. Pleskachevsky (2011). "Underwater bottom topography in coastal areas from TerraSAR-X data." International Journal of Remote Sensing **32**(16): 4527-4543.

Calkoen, C., G. Hesselmann, G. Wensink and J. Vogelzang (2001). "The bathymetry assessment system: efficient depth mapping in shallow seas using radar images." International Journal of Remote Sensing **22**(15): 2973-2998.

Calkoen, C. J., C. F. De Valk, G. J. Wensink, C. Vernemmen and J. Verstraeten (2000). Towards the Operational Use of ERS SAR for bathymetry mapping in Belgium using the advanced Bathymetry Assessment System: BABEL2. Frascati, Italy, European Space Agency: 55.

Cameron, T. D. J., A. Crosby, P. S. Balson, D. H. Jeffery, G. K. Lott, J. Bulat and D. J. Harrison (1992). United Kingdom offshore regional report: the geology of the Southern North Sea. HMSO for the British Geological Survey: 1-150.

Cameron, W. L. and L. K. Leung (1990). Feature motivated polarization scattering matrix decomposition. IEEE 1990 International Radar Conference.

Campana, S. (2016). Filling gaps in space and time at Veii. 'Emptyscapes' project. Veii – An Etruscan City. O. Cerasuolo and J. Tabolli. Texas, USA, University of Texas Press.

Cannell, R. and M. Drew (1973). "Plant root systems and crop growth." SPAN Shell Publ Health Agr News(16): 4.

Capriotti Vittozzi, G. (2015a). ...Con l'occhio del satellite. Egyptian Curses 2. A Research on Ancient Catastrophes. G. Capriotti Vittozzi. Rome, Consiglio Nazionale Delle Ricerche (CNR), Istituto Di Studi Sul Mediterraneo Antico (ISMA): 161-164.

Capriotti Vittozzi, G., Ed. (2015b). Egyptian Curses 2. A Research on Ancient Catastrophes. Archaeological Heritage & Multidisciplinary Egyptological Studies (AHMES). Rome.

Carrez-Maratray, J.-Y. and G. Wagner (1993). "Tell el-Kanais." Cahiers de recherches de l'Institut de Papyrologie et d'Égyptologie de Lille(15): 6.

References

Catalao, J., G. Nico and V. Conde (2011). Detection of ground subsidence in the city of Lisbon: comparison of InSAR and topographic measurements. 2011 Joint Urban Remote Sensing Event, IEEE.

Chapoulie, R., M. Martinaud, P. Paillou, D. Barraud and P. Dreuillet (2002). The airborne ramses radar experiment for archaeological prospecting in a temperate climate region. 8th EEGS-ES Meeting.

Chen, F., N. Masini, R. Yang, P. Milillo, D. Feng and R. Lasaponara (2015). "A space view of radar archaeological marks: First applications of COSMO-SkyMed X-band data." Remote Sensing **7**(1): 24-50.

Cigna, F., R. Lasaponara, N. Masini, P. Milillo and D. Tapete (2014). "Persistent scatterer interferometry processing of COSMO-SkyMed StripMap HIMAGE time series to depict deformation of the historic centre of Rome, Italy." Remote Sensing **6**(12): 12593-12618.

Clédat, J. (1913). "Le temple de Zeus Casios à Péluse." ASAE **13**: 79-85.

Cloude, S. R. and E. Pottier (1996). "A review of target decomposition theorems in radar polarimetry." IEEE Transactions on Geoscience and Remote Sensing **34**(2): 498-518.

Cloude, S. R. and E. Pottier (1997). "An entropy based classification scheme for land applications of polarimetric SAR." IEEE Transactions on Geoscience and Remote Sensing **35**(1): 68-78.

Coles, B. J. (1998). "Doggerland: a Speculative Survey." Proceedings of the Prehistoric Society **64**: 45-81.

Comer, D. C. and R. G. Blom (2006). Detection and identification of archaeological sites and features using synthetic aperture radar (SAR) data collected from airborne platforms. Remote sensing in archaeology. Berlin/Heidelberg, Germany, Springer: 103-136.

Conesa, F. C., N. Devanthery, A. L. Balbo, M. Madella and O. Monserrat (2014). "Use of satellite SAR for understanding long-term human occupation dynamics in the monsoonal semi-arid plains of North Gujarat, India." Remote Sensing **6**(11): 11420-11443.

Constable, S. (2013). "Review paper: Instrumentation for marine magnetotelluric and controlled source electromagnetic sounding." Geophysical Prospecting **61**(s1): 505-532.

Constable, S. and L. J. Srnka (2007). "An introduction to marine controlled-source electromagnetic methods for hydrocarbon exploration." Geophysics **72**(2): WA3-WA12.

References

Cooper, A., S. Chubb, F. Askari, G. Valenzuela, J. Bennett and W. Keller (1994). "Radar surface signatures for the two-dimensional tidal circulation over Phelps Bank, Nantucket shoals: A comparison between theory and experiment." Journal of Geophysical Research: Oceans **99**(C4): 7865-7883.

Corte, A. E. (1966). "Particle sorting by repeated freezing and thawing." Biuletyn Peryglacialny **15**: 175-240.

Covello, F., F. Battazza, A. Coletta, E. Lopinto, C. Fiorentino, L. Pietranera, G. Valentini and S. Zoffoli (2010). "COSMO-SkyMed an existing opportunity for observing the Earth." Journal of Geodynamics **49**(3): 171-180.

Crawford, O. G. S. (1923). "Air Survey and Archaeology." Geographical Journal: 324-366.

Crisp, D. J. (2004). The state-of-the-art in ship detection in synthetic aperture radar imagery, DEFENCE SCIENCE AND TECHNOLOGY ORGANISATION SALISBURY (AUSTRALIA) INFO SCIENCES LAB: 1-136.

Czajlik, Z. (2009). "The role of efficiency in aerial archaeological research of Hungary." AARGnews: 10.

Dabbagh, A. E., K. G. Al-Hinai and M. A. Khan (1997). "Detection of sand-covered geologic features in the Arabian Peninsula using SIR-C/X-SAR data." Remote Sensing of Environment **59**(2): 375-382.

De Franceschini, M. (2005). Ville dell'Agro romano. Rome, L'ERMA di BRETSCHEIDER.

De Grandi, G., M. Leysen, J. Lee and D. Schuler (1997). Radar reflectivity estimation using multiple SAR scenes of the same target: technique and applications. Geoscience and Remote Sensing, 1997. IGARSS'97. Remote Sensing-A Scientific Vision for Sustainable Development., 1997 IEEE International, IEEE.

De Loo, G. (1981). "The observation of tidal patterns, currents, and bathymetry with SLAR imagery of the sea." IEEE Journal of Oceanic Engineering **6**(4): 124-129.

Della Portella, I., G. P. Sartorio and F. Ventre (2004). The Appian Way: from its foundation to the Middle Ages, Getty Publications.

Di Iorio, A., D. Biliouris, R. Guzinski, L. B. Hansen and M. Bagni (2015). Innovation Technologies and Applications for Coastal Archaeological sites FP7 - ITACA. 36th International Symposium on Remote Sensing of Environment, 11-15 May 2015. Berlin, Germany, The International Archives of the Photogrammetry, Remote Sensing and Spatial Information Sciences. **XL-7/W3**: 1367 to 1373.

References

Di Iorio, A. and N. Straccia (2013). World HERitage monitoring by Remote sEnsing (WHERE) The SAR simulator. 4th EARSeL Workshop on Cultural and Natural Heritage, Matera, Italy, European Association of Remote Sensing Laboratories (EARSeL).

Di Iorio, A., N. Straccia and R. Carlucci (2010). Advancement in automatic monitoring and detection of archaeological sites using a hybrid process of remote sensing, GIS techniques and a shape detection algorithm. Proceedings of the 30th EARSeL Symposium, Paris, France.

Doneus, M., N. Doneus, C. Briese, M. Pregebauer, G. Mandlbauer and G. Verhoeven (2013). "Airborne laser bathymetry—detecting and recording submerged archaeological sites from the air." Journal of Archaeological Science **40**(4): 2136-2151.

Dore, N., J. Patruno, E. Pottier and M. Crespi (2013). "New research in polarimetric SAR technique for archaeological purposes using ALOS PALSAR data." Archaeological Prospection **20**(2): 79-87.

Dore, N., J. Patruno, F. Sarti, A. B. Ruescas and M. Hernandez (2010). Applications of Remote Sensing in Archaeology: Surface and sub-surface feature detection over UNESCO World Heritage sites and archaeological sites in Italy using optical and radar data. Proceedings of the 29th Symposium of the European Association of Remote Sensing Laboratories, Chania, Greece, IOS Press.

Dunstan, S. (2012). The Six Day War 1967: Sinai, Bloomsbury Publishing.

Edeine, B. (1956). "Une méthode pratique pour la détection aérienne des sites archéologiques, en particulier par la photographie sur films en couleurs et sur films infra-rouges." Bulletin de la Société préhistorique de France **53**(Fasc. 9): 540-546.

El-Baz, F. (1999). "Groundwater Concentration beneath Sand Fields in the Western Desert of Egypt: Indications by Radar Images from Space." Egyptian Journal of Remote Sensing and Space Sciences **1**: 1-24.

el-Maksoud, M. A., A. EL-TABA and P. Grossmann (1994). "The Late Roman army castrum at Pelusium (Tall al-Faramā)." Cahier de recherches de l'Institut de papyrologie et d'égyptologie de Lille(16): 95-103.

El-Shazly, M. and E. Abdel-Gaphour (1990). "Genesis, formation and classification of soils of the coastal plain of Sinai Peninsula, Egypt." Egyptian Journal of Soil Science **30**(1-2): 59-72.

Elachi, C., L. E. Roth and G. G. Schaber (1984). "Spaceborne radar subsurface imaging in hyperarid regions." IEEE Transactions on Geoscience and Remote Sensing(4): 383-388.

References

EMODnet. (2015). "Portal for Bathymetry." Retrieved 10 May, 2015, from <http://portal.emodnet-bathymetry.eu/>.

Engdahl, M. E., M. Borgeaud and M. Rast (2001). "The use of ERS-1/2 tandem interferometric coherence in the estimation of agricultural crop heights." IEEE transactions on geoscience and remote sensing **39**(8): 1799-1806.

Erasmi, S., R. Rosenbauer, R. Buchbach, T. Busche and S. Rutishauser (2014). "Evaluating the quality and accuracy of TanDEM-X digital elevation models at archaeological sites in the Cilician Plain, Turkey." Remote sensing **6**(10): 9475-9493.

Estes, J. E., J. R. Jensen and L. R. Tinney (1977). "The use of historical photography for mapping archaeological sites." Journal of Field Archaeology **4**(4): 441-447.

European Space Agency. (2015). "Sentinel-1 Scientific Data Hub." Retrieved 10 May, 2015, from <https://scihub.esa.int/>.

European Space Agency. (2016). "Sentinels Scientific Data Hub." Retrieved April 25, 2016, from <https://scihub.copernicus.eu/>.

Evans, A. M., J. Flatman and N. Flemming (2014). Prehistoric Archaeology on the Continental Shelf, Springer.

Evans, D. L. and T. G. Farr (2006). The use of Interferometric Synthetic Aperture Radar (InSAR) in archaeological investigations and cultural heritage preservation. Remote sensing in archaeology, Springer: 89-102.

Evans, D. L., E. R. Stofan, T. D. Jones and L. M. Godwin (1994). "Earth from sky." Scientific American **271** (6): 6.

Evans, R. (2007). "The weather and other factors controlling the appearance of crop marks on clay and 'difficult' soils." Populating clay landscapes: 16-27.

Evans, R. and R. Jones (1977). "Crop marks and soils at two archaeological sites in Britain." Journal of Archaeological Science **4**(1): 63-76.

Fan, K., W. Huang, B. Fu and M. He (2008a). Simulation Study on the Optimal Conditions for Shallow Water Bathymetry Observation by SAR. IGARSS 2008-2008 IEEE International Geoscience and Remote Sensing Symposium, IEEE.

References

Fan, K., W. Huang, M. He and B. FU (2008b). "Progress on remote sensing of the shallow sea bottom topography by SAR." Remote Sensing of Technology and Application **23**(4): 479-485.

Fanti, R., G. Gigli, D. Tapete, F. Mugnai and N. Casagli (2013). Monitoring and modelling slope instability in cultural heritage sites. Landslide Science and Practice, Springer: 467-473.

Farr, T. G., C. Elachi, P. Hartl and K. Chowdhury (1986). "Microwave penetration and attenuation in desert soil-A field experiment with the Shuttle Imaging Radar."

Faught, M. (1988). "Inundated sites in the Apalachee Bay area of the eastern Gulf of Mexico." Florida Anthropologist **41**(1): 1-5.

Faught, M. K. (2004). "The underwater archaeology of paleolandscapes, Apalachee Bay, Florida." American Antiquity: 275-289.

Ferretti, A., A. Monti-Guarnieri, C. Prati, F. Rocca and D. Massonnet (2007). InSAR principles: guidelines for SAR interferometry processing and interpretation. The Netherlands, ESA Publications Division, ESTEC, Noordwijk, the Netherlands.

Feynman, R. P. (2005). The Feynman Lectures on Physics 2, Addison-Wesley.

Fitch, S., V. Gaffney and K. Thomson (2007). "In Sight of Doggerland: From speculative survey to landscape exploration." Internet Archaeology(22): 1-20.

Folegani, M., S. Mantovani, S. Natali and M. G. Veratelli (2013). WHERE - World HEritage monitoring by Remote sEnsing: the role of the Microclimate processing chain for monitoring the UNESCO sites. 4th EARSeL Workshop on Cultural and Natural Heritage, Matera, Italy, European Association of Remote Sensing Laboratories (EARSeL).

Freeman, A. and S. L. Durden (1998). "A three-component scattering model for polarimetric SAR data." IEEE Transactions on Geoscience and Remote Sensing **36**(3): 963-973.

Funciello, R., G. Heiken and D. De Rita (2006). I sette colli: guida geologica a una Roma mai vista. Milano, Italy, R. Cortina.

Gaber, A., M. Koch, M. H. Griesh, M. Sato and F. El-Baz (2013). "Near-surface imaging of a buried foundation in the Western Desert, Egypt, using space-borne and ground penetrating radar." Journal of Archaeological Science **40**(4): 1946-1955.

References

Gad, A. (2004). A Parametric Approach in Assessment of Soil Degradation Using Remote Sensing and GIS. A Case Study in North Sinai. presentation for the United Nations Office for Outer Space Affairs, National Authority for Remote Sensing and Space Sciences, Egypt: 30.

Gad, M., S. Zeid, S. Khalaf, A. Abdel-Hamid, E. Seleem and A. El Feki (2015). "Optimal Management of Groundwater Resources in Arid Areas Case Study: North Sinai, Egypt."

Gade, M. and J. Kohlus (2015). Radar Imaging of Archaeological Sites on Intertidal Flats. 12th International Conference on the Mediterranean Coastal Environment MEDCOAST 2015, Varna, Bulgaria.

Gaffney, V. L., K. Thomson, S. Fitch, A. L. S. Fund and E. Heritage (2007). Mapping Doggerland: The Mesolithic Landscapes of the Southern North Sea, Archaeopress.

Gallagher, J. M. and R. L. Josephs (2008). "Using LiDAR to detect cultural resources in a forested environment: an example from Isle Royale National Park, Michigan, USA." Archaeological Prospection **15**(3): 187-206.

Gao, J. (2009). "Bathymetric mapping by means of remote sensing: methods, accuracy and limitations." Progress in Physical Geography **33**(1): 103-116.

Garrison, T. G., B. Chapman, S. Houston, E. Román and J. L. G. López (2011). "Discovering ancient Maya settlements using airborne radar elevation data." Journal of Archaeological Science **38**(7): 1655-1662.

Gascon, F., E. Cadau, O. Colin, B. Hoersch, C. Isola, B. L. Fernández and P. Martimort (2014). Copernicus Sentinel-2 mission: products, algorithms and Cal/Val. SPIE Earth Observing Systems XIX, San Diego, California, Proc. SPIE (International Society for Optics and Photonics).

Geudtner, D., R. Torres, P. Snoeij, D. Bibby and B. Rommen (2014). Sentinel-1 System. EUSAR 2014; 10th European Conference on Synthetic Aperture Radar; Proceedings of, VDE.

Gibson, C. (2016). "Rescue Archaeology: Foundations for the Future." European Journal of Archaeology **19**(2): 393-397.

Gleyzes, M.-A., L. Perret and P. Kubik (2012). "Pleiades system architecture and main performances." International Archives of the Photogrammetry, Remote Sensing and Spatial Information Sciences **39**: B1.

Gojda, M. and M. Hejcman (2012). "Cropmarks in main field crops enable the identification of a wide spectrum of buried features on archaeological sites in Central Europe." Journal of Archaeological Science **39**(6): 1655-1664.

References

Gold, Z. (2014). "Security in the Sinai: Present and Future." ICCT Research Paper, March.

Goodfriend, G. A. and D. J. Stanley (1999). "Rapid strand-plain accretion in the northeastern Nile Delta in the 9th century AD and the demise of the port of Pelusium." Geology **27**(2): 147-150.

Goring-Morris, A. N. and P. Goldberg (1990). "Late Quaternary dune incursions in the southern Levant: archaeology, chronology and palaeoenvironments." Quaternary International **5**: 115-137.

Grandjean, G., P. Paillou, P. Dubois-Fernandez, T. August-Bernex, N. N. Baghdadi and J. Achache (2001). "Subsurface structures detection by combining L-band polarimetric SAR and GPR data: Example of the Pyla Dune (France)." IEEE Transactions on Geoscience and Remote Sensing **39**(6): 1245-1258.

Greidanus, H., C. Calkoen, I. Hennings, R. Romeiser, J. Vogelzang and G. Wensink (1997). Intercomparison and validation of bathymetry radar imaging models. Geoscience and Remote Sensing, 1997. IGARSS'97. Remote Sensing-A Scientific Vision for Sustainable Development., 1997 IEEE International, IEEE.

Gubbi, J., R. Buyya, S. Marusic and M. Palaniswami (2013). "Internet of Things (IoT): A vision, architectural elements, and future directions." Future Generation Computer Systems **29**(7): 1645-1660.

Gumerman, G. J. and T. R. Lyons (1971). "Archaeological methodology and remote sensing." Science **172**(3979): 126-132.

Han, J., J. Pei and M. Kamber (2011). Data mining: concepts and techniques, Elsevier.

Harris, R. and I. Baumann (2015). "Open data policies and satellite Earth observation." Space Policy **32**: 44-53.

Hashem, I. A. T., I. Yaqoob, N. B. Anuar, S. Mokhtar, A. Gani and S. U. Khan (2015). "The rise of "big data" on cloud computing: Review and open research issues." Information Systems **47**: 98-115.

Heliere, F., C. Lin, F. Fois, M. Davidson, A. Thompson and P. Bensi (2009). BIOMASS: a P-band SAR earth explorer core mission candidate. 2009 IEEE Radar Conference, IEEE.

Henderson, F. M. and A. J. Lewis (1998). Principles and applications of imaging radar. Manual of remote sensing, volume 2, John Wiley and sons.

References

Hennings, I. (1990). "Radar imaging of submarine sand waves in tidal channels." Journal of Geophysical Research: Oceans **95**(C6): 9713-9721.

Hennings, I. (1998). "An historical overview of radar imagery of sea bottom topography." International Journal of Remote Sensing **19**(7): 1447-1454.

Hennings, I. and D. Herbers (2007). "The expected potential of TerraSAR-X high resolution spotlight mode data for shallow sea bottom topography imaging: a preview." EARSeL eProceedings **6**(2): 67-81.

Hennings, I., B. Lurin and N. Didden (2001). "Radar imaging mechanism of the seabed: Results of the C-STAR experiment in 1996 with special emphasis on the relaxation rate of short waves due to current variations." Journal of Physical Oceanography **31**(7): 1807-1827.

Herbich, T. (2009). Reconstructing the layout of Pelusium. Newsletter of the Polish Centre of Mediterranean Archaeology of the University of Warsaw. Warsaw, Polish Centre of Mediterranean Archaeology of the University of Warsaw: 4.

Hermas, E., S. Leprince and I. A. El-Magd (2012). "Retrieving sand dune movements using sub-pixel correlation of multi-temporal optical remote sensing imagery, northwest Sinai Peninsula, Egypt." Remote Sensing of Environment **121**: 51-60.

Hesselmans, G. H. F. M., G. J. Wensink and C. J. Calkoen (1995). The use of ERS-1 SAR data to support bathymetric surveys. EARSeL Workshop on Remote Sensing and GIS for Coastal Zone Management, Delft.

Hightet, G. (1949). The Classical Tradition: Greek and Roman Influences on Western Literature: Greek and Roman Influences on Western Literature, Oxford University Press, USA.

Hoffmeier, J. K. (2012). Sinai in Egyptian, Levantine and Hebrew (Biblical) Perspectives. The History of the Peoples of the Eastern Desert. H. Barnard and K. Duistermaat. Los Angeles, Cotsen Institute of Archaeology. **Monograph 73**: 105-124.

Hoffmeier, J. K. (2014). The Exodus and Wilderness Narratives. Ancient Israel's history: an introduction to issues and sources. B. T. Arnold and R. S. Hess. Michigan, Grand Rapids: 46-90.

Hoffmeier, J. K. and S. O. Moshier (2013). "A highway out of Egypt": The main road from Egypt to Canaan. Desert road archaeology in ancient Egypt and beyond. H. Riemer and F. Förster. Köln, Heinrich-Barth-Institut: 485-510.

References

Hogg, W. H. (1971). Regional and local environments. Potential Crop Production. P. F. Wareing, and Cooper, J. P. London: 6-22.

Holcomb, D. W. (1991). "Shuttle imaging radar and archaeological survey in China's Taklamakan Desert." Journal of Field Archaeology **19**(1): 129-138.

Holcomb, D. W. (2001). "Imaging radar and archaeological survey: An example from the Gobi Desert of Southern Mongolia." Journal of field archaeology **28**(1-2): 131-141.

Holliday, D., G. St-Cyr and N. E. Woods (1986). "A radar ocean imaging model for small to moderate incidence angles." International Journal of Remote Sensing **7**(12): 1809-1834.

Holliday, D., G. St-Cyr and N. E. Woods (1987). "Comparison of a new radar ocean imaging model with SARSEX internal wave image data." International Journal of Remote Sensing **8**(9): 1423-1430.

Holt, B. (2004). SAR Imaging of the Ocean Surface. NOAA SAR Marine User's Manual. C. R. Jackson and J. R. Apel. Washington DC, U.S. Department of Commerce, National Oceanic and Atmospheric Administration (NOAA): 55.

Hritz, C. (2010). "Tracing settlement patterns and channel systems in southern Mesopotamia using remote sensing." Journal of Field Archaeology **35**(2): 184-203.

Hritz, C. (2014). "Contributions of GIS and satellite-based remote sensing to landscape archaeology in the Middle East." Journal of Archaeological Research **22**(3): 229-276.

Hritz, C. and T. Wilkinson (2006). "Using Shuttle Radar Topography to map ancient water channels in Mesopotamia." antiquity **80**(308): 415-424.

Huadong, G. (1997). "Spaceborne Multifrequency, Polarametric and Interferometric Radar for Detection of the Targets on Earth Surface and Subsurface [J]." Journal of Remote Sensing **1**(1): 32-39.

Huadong, G., G. Schaber, C. Breed and A. Lewis (1986). Shuttle imaging radar response from sand dunes and subsurface rocks of Alashan Plateau in north-central China. Remote sensing for resources development and environmental management. International symposium. 7.

Huang, W., B. Fu, C. Zhou, J. Yang, A. Shi and D. Li (2000). "Simulation study on optimal currents and winds for the spaceborne SAR mapping of sea bottom topography." Progress in natural science **10**(11): 859-866.

References

Huang, W., B. Fu, C. Zhou, J. Yang, A. Shi and D. Li (2001). Shallow water bathymetric surveys by spaceborne synthetic aperture radar. Geoscience and Remote Sensing Symposium, 2001. IGARSS'01. IEEE 2001 International, IEEE.

Huynen, J. R. (1982). A revisit of the phenomenological approach with applications to radar target decomposition. Chicago, Dept. of Electrical Engineering and Computer Sciences, University of Illinois at Chicago.

Hyppönen, P. (2014). Salaria via usque ad lapidem XVIII, a reconstruction of the ancient road line between Porta Collina and the 18th milestone of the road. Master's thesis in Archaeology, University of Oulu.

Ibrahim, E., M. Sherief and A. Al-Metwally (1998). "Shallow geophysical investigations on Tell el Farama, Northwest Sinai, Egypt." Archaeological Prospection 5(2): 91-100.

Iisaka, J., T. Sakurai-Amano and T. I. Lukowski (1995). Automated detection of road intersections from ERS-1 SAR imagery. Geoscience and Remote Sensing Symposium, 1995. IGARSS'95. 'Quantitative Remote Sensing for Science and Applications', International, IEEE.

Inglada, J. and R. Garello (1999a). Depth estimation and 3D topography reconstruction from SAR images showing underwater bottom topography signatures. Geoscience and Remote Sensing Symposium, 1999. IGARSS'99 Proceedings. IEEE 1999 International, IEEE.

Inglada, J. and R. Garello (1999b). Volterra model for the imaging mechanism of ocean surface currents by synthetic aperture radar. Geoscience and Remote Sensing Symposium, 1999. IGARSS'99 Proceedings. IEEE 1999 International, IEEE.

Inglada, J. and R. Garello (2002). "On rewriting the imaging mechanism of underwater bottom topography by synthetic aperture radar as a volterra series expansion." IEEE Journal of Oceanic Engineering 27(3): 665-674.

Inglada, J. and G. Mercier (2007). "A new statistical similarity measure for change detection in multitemporal SAR images and its extension to multiscale change analysis." IEEE transactions on geoscience and remote sensing 45(5): 1432-1445.

Jakubiak, K. (2012). Tell Farama (Pelusium). The city on Sinai - where Egypt and Middle East meet. Identity and Connectivity, Florence, Italy, BAR International Series 2581 (I).

References

Jaritz, H., S. Favre, G. Nogara, M. Rodziewicz and J.-Y. Carrez-Maratray (1996). "Pelusium. prospection archéologique et topographique de la région de Tell el-Kana'is 1993 et 1994." Beiträge zur ägyptischen Bauforschung und Altertumskunde **12**: 29.

JAXA. (2011). "DAICHI (ALOS) Operation Completion." Retrieved 2 June, 2016, from http://global.jaxa.jp/press/2011/05/20110512_daichi_e.html.

Jensen, D. L. (1992). Renaissance Europe: age of recovery and reconciliation, Wadsworth Publishing Company.

Jin, M.-B. and Y. Yuan (1997a). "Formulation and solution to the mathematical and physical inverse problem of detecting sea topography by SAR image." Oceanologia et Limnologia Sinica **XXIX**: 5.

Jin, M.-B. and Y. Yuan (1997b). "Simulation and analysis of the visibility of sea topography on SAR image." Oceanologia et Limnologia Sinica **XXIX**: 6.

Jones, B. (1984). Past imperfect. The story of rescue archaeology, Heinemann.

Jones, G. (2008). "Geophysical mapping of historic cemeteries." Technical Briefs in Historical Archaeology **3**: 25-38.

Jones, R. and R. Evans (1975). "Soil and crop marks in the recognition of archaeological sites by air photography." Aerial reconnaissance for archaeology: 1-11.

Kaimaris, D., P. Patias and M. Tsakiri (2012). "Best period for high spatial resolution satellite images for the detection of marks of buried structures." The Egyptian Journal of Remote Sensing and Space Science **15**(1): 9-18.

Kankaku, Y., M. Sagisaka and S. Suzuki (2014). PALSAR-2 launch and early orbit status. 2014 IEEE Geoscience and Remote Sensing Symposium, IEEE.

Keay, S., M. Millett, L. Paroli and K. Strutt (2005). Portus: an Archaeological Survey of the Port of Imperial Rome. London, British School at Rome.

Keay, S. J., S. H. Parcak and K. D. Strutt (2014). "High resolution space and ground-based remote sensing and implications for landscape archaeology: the case from Portus, Italy." Journal of Archaeological Science **52**: 277-292.

Keller, G. V. and F. C. Frischknecht (1966). "Electrical methods in geophysical prospecting."

References

Kerr, Y. H., P. Waldteufel, J.-P. Wigneron, J. Martinuzzi, J. Font and M. Berger (2001). "Soil moisture retrieval from space: The Soil Moisture and Ocean Salinity (SMOS) mission." IEEE transactions on Geoscience and remote sensing **39**(8): 1729-1735.

Klemas, V. (2011). "Beach profiling and LIDAR bathymetry: An overview with case studies." Journal of Coastal Research **27**(6): 1019-1028.

Knipling, E. B. (1970). "Physical and physiological basis for the reflectance of visible and near-infrared radiation from vegetation." Remote Sensing of Environment **1**(3): 155-159.

Kooij, M. v. d., J. Vogelzang and C. Calcoen (1995). "A simple analytical model for brightness modulations caused by submarine sand waves in radar imagery." Journal of Geophysical Research: Oceans **100**(C4): 7069-7082.

Kramer, B. (2012). Electrocommunication in teleost fishes: behavior and experiments, Springer Science & Business Media.

Krieger, G., A. Moreira, H. Fiedler, I. Hajnsek, M. Werner, M. Younis and M. Zink (2007). "TanDEM-X: A satellite formation for high-resolution SAR interferometry." IEEE Transactions on Geoscience and Remote Sensing **45**(11): 3317-3341.

Kristeller, P. O. (1979). Renaissance thought and its sources, Columbia University Press.

Krogager, E. (1990). "New decomposition of the radar target scattering matrix." Electronics Letters **26**(18): 1525-1527.

Lambeck, K. (1996). "Shoreline reconstructions for the Persian Gulf since the last glacial maximum." Earth and Planetary Science Letters **142**(1): 43-57.

Lambers, H., F. S. Chapin III and T. L. Pons (2008). Photosynthesis. Plant physiological ecology, Springer: 11-99.

Lanari, R., F. Casu, M. Manzo, G. Zeni, P. Berardino, M. Manunta and A. Pepe (2007). "An overview of the small baseline subset algorithm: A DInSAR technique for surface deformation analysis." Pure and Applied Geophysics **164**(4): 637-661.

Lanciani, R. (1868). "Ricerche topografiche sulla città di Porto." Annali dell'Istituto di Corrispondenza Archeologica, Rome: 51.

References

Lasaponara, R., G. Leucci, N. Masini and R. Persico (2014). "Investigating archaeological looting using satellite images and GEORADAR: the experience in Lambayeque in North Peru." Journal of Archaeological Science **42**: 216-230.

Lasaponara, R. and N. Masini (2007). "Detection of archaeological crop marks by using satellite QuickBird multispectral imagery." Journal of archaeological science **34**(2): 214-221.

Lasaponara, R. and N. Masini (2012a). Remote sensing in archaeology: From visual data interpretation to digital data manipulation. Satellite Remote Sensing. Berlin/Heidelberg, Germany, Springer: 3-16.

Lasaponara, R. and N. Masini (2012b). Satellite remote sensing: A new tool for archaeology. New York, NY, USA, Springer Science & Business Media.

Lee, J.-S. and E. Pottier (2009). Polarimetric radar imaging: from basics to applications, CRC press.

Lehner, M. (1992). "Reconstructing the Sphinx." Cambridge Archaeological Journal **2**(01): 3-26.

Leyshon, A. and R. Sheard (1974). "Influence of short-term flooding on the growth and plant nutrient composition of barley." Canadian journal of soil science **54**(4): 463-473.

Li, F. and W. Johnson (1983). "Ambiguities in Spaceborne Synthetic Aperture Radar Systems." Aerospace and Electronic Systems, IEEE Transactions on(3): 389-397.

Li, X., C. Li, Q. Xu and W. G. Pichel (2009). "Sea surface manifestation of along-tidal-channel underwater ridges imaged by SAR." IEEE Transactions on Geoscience and Remote Sensing **47**(8): 2467-2477.

Lin, A. Y.-M., A. Novo, S. Har-Noy, N. D. Ricklin and K. Stamatiou (2011). "Combining GeoEye-1 satellite remote sensing, UAV aerial imaging, and geophysical surveys in anomaly detection applied to archaeology." IEEE Journal Of Selected Topics In Applied Earth Observations And Remote Sensing **4**(4): 870-876.

Linck, R., T. Busche and S. Buckreuss (2013a). POSSIBILITIES OF TERRASAR-X DATA FOR THE PROSPECTION OF ARCHAEOLOGICAL SITES BY SAR. 5th TerraSAR-X / 4th TanDEM-X Science Team Meeting, 10-14 June 2013, German Aerospace Center (DLR), Oberpfaffenhofen.

Linck, R., T. Busche, S. Buckreuss, J. Fassbinder and S. Seren (2013b). "Possibilities of Archaeological Prospection by High-resolution X-band Satellite Radar—a Case Study from Syria." Archaeological Prospection **20**(2): 97-108.

References

Linck, R., J. W. Fassbinder, K. Papathanassiou and R. Křivánek (2011). "Multipol-SAR-Survey of the UNESCO World Heritage Site Palmyra (Syria)." Archaeological prospection, Archaeology and art publications: 21-24.

Lozny, L. R. (2006). Landscapes under pressure: Theory and practice of cultural heritage research and preservation, Springer Science & Business Media.

Lugli, G. and G. Filibeck (1935). Il porto di Roma imperiale e l'Agro Portuense. Bergamo, Officine dell'Istituto Italiano d'Arti Grafiche.

Lyzenga, D. R., N. P. Malinas and F. J. Tanis (2006). "Multispectral bathymetry using a simple physically based algorithm." IEEE Transactions on Geoscience and Remote Sensing **44**(8): 2251.

Manyika, J., M. Chui, B. Brown, J. Bughin, R. Dobbs, C. Roxburgh and A. H. Byers (2011). "Big data: The next frontier for innovation, competition, and productivity."

Marcolongo, B. (1992). "Evolution du paléo-environnement dans la partie orientale du delta du Nil depuis la transgression flandrienne (8000 BP)." Cahiers de Recherches de l'Institut de Papyrologie et d'Égyptologie de Lille **14**: 23-31.

Massonnet, D. and J.-C. Souyris (2008). Imaging with synthetic aperture radar, CRC Press.

Matzler, C. (1998). "Microwave permittivity of dry sand." IEEE Trans. Geosci. Remote Sens. **36**: 3.

Maxwell, J. C. (1865). "A dynamical theory of the electromagnetic field." Philosophical transactions of the Royal Society of London **155**: 459-512.

Maxwell, J. C. (1881). A treatise on electricity and magnetism, Clarendon press.

May, L. H. and F. L. Milthorpe (1962). "Drought resistance of crop plants." Field Crop Abstracts **15**: 9.

McCauley, J. F., C. S. Breed, G. G. Schaber, W. P. McHugh, B. Issawi, C. V. Haynes, M. J. Grolier and A. E. Kilani (1986). "Paleodrainages of the Eastern Sahara-The Radar Rivers Revisited (SIR-A/B Implications for a Mid-Tertiary Trans-African Drainage System)." Geoscience and Remote Sensing, IEEE Transactions on(4): 624-648.

References

McCauley, J. F., G. G. Schaber, C. S. Breed, M. J. Grolier, C. V. Haynes, B. Issawi, C. Elachi and R. Blom (1982). "Subsurface valleys and geoarchaeology of the eastern Sahara revealed by shuttle radar." Science **218**(4576): 1004-1020.

McHugh, W. P., C. S. Breed, G. G. Schabers, J. F. McCauley and B. J. Szabo (1988a). "Acheulian sites along the "radar rivers," southern Egyptian Sahara." Journal of Field Archaeology **15**(4): 361-379.

McHugh, W. P., J. F. McCauley, C. V. Haynes, C. S. Breed and G. G. Schaber (1988b). "Paleorivers and geoarchaeology in the southern Egyptian Sahara." Geoarchaeology **3**(1): 1-40.

McHugh, W. P., G. G. Schaber, C. S. Breed and J. F. McCauley (1989). "Neolithic adaptation and the Holocene functioning of Tertiary palaeodrainages in southern Egypt and northern Sudan." Antiquity **63**(239): 320-336.

McManus, K. and D. Donoghue (2002). Airborne thermography of the vegetation-soil interface for detecting shallow ground disturbance. Space Applications for Heritage Conservation.

Meehl, G. A., T. F. Stocker, W. D. Collins, P. Friedlingstein, A. T. Gaye, J. M. Gregory, A. Kitoh, R. Knutti, J. M. Murphy and A. Noda (2007). "Global climate projections." Climate change **3495**: 747-845.

Mei-bing, J., Z. Jie and Y. Ye-li (1998). "Analysis of bathymetric features using sar image: An example from the southern North Sea." Chinese Journal of Oceanology and Limnology **16**(2): 128-136.

Meiggs, R. (1973). Roman Ostia. Oxford, Oxford University Press.

Menze, B. H. and J. A. Ur (2012). "Mapping patterns of long-term settlement in Northern Mesopotamia at a large scale." Proceedings of the National Academy of Sciences **109**(14): E778-E787.

Menze, B. H., J. A. Ur and A. G. Sherratt (2006). "Detection of Ancient Settlement Mounds." Photogrammetric Engineering & Remote Sensing **72**(3): 321-327.

Meyer, F. J., J. B. Nicoll and A. P. Doulgeris (2013). "Correction and characterization of radio frequency interference signatures in L-band synthetic aperture radar data." Geoscience and Remote Sensing, IEEE Transactions on **51**(10): 4961-4972.

Misak, R. and M. Draz (1997). "Sand drift control of selected coastal and desert dunes in Egypt: case studies." Journal of Arid Environments **35**(1): 17-28.

References

Missiaen, T. (2015). Efficiency of marine acoustic techniques for the archaeological prospection of intertidal areas: Results from a test study on the Belgian coast (Ostend-Raversijde). 2015 IEEE/OES Acoustics in Underwater Geosciences Symposium (RIO Acoustics), IEEE.

Modigliani, D. (2008a). Carta agropedologica del territorio comunale. PIANO REGOLATORE GENERALE. Rome, Comune di Roma.

Modigliani, D. (2008b). Carta dell'uso del suolo e delle fisionomie vegetazionali del territorio comunale. PIANO REGOLATORE GENERALE. Rome, Comune di Roma.

Modigliani, D. (2008c). Carta delle serie di vegetazione del territorio comunale. PIANO REGOLATORE GENERALE. Rome, Comune di Roma.

Modigliani, D. (2008d). Carta geolitologica del territorio comunale. PIANO REGOLATORE GENERALE. Rome, Comune di Roma.

Mohamed, E. S. (2013). "Spatial assessment of desertification in north Sinai using modified MEDLAUS model." Arabian Journal of Geosciences **6**(12): 4647-4659.

Mols, S. (2014). "Mapping the Via Appia." Forma Urbis **XIX**(9): 4.

Monteith, J. and M. Unsworth (2007). Principles of environmental physics. New York, NY, USA, Academic Press.

Moore, E., T. Freeman and S. Hensley (2007). Spaceborne and airborne radar at Angkor: introducing new technology to the ancient site. Remote sensing in archaeology. Berlin/Heidelberg, Germany, Springer: 185-216.

Moreira, A., P. Prats-Iraola, M. Younis, G. Krieger, I. Hajnsek and K. P. Papathanassiou (2013). "A tutorial on synthetic aperture radar." Geoscience and Remote Sensing Magazine, IEEE **1**(1): 6-43.

Morrison, K. (2013). "Mapping subsurface archaeology with SAR." Archaeological Prospection **20**(2): 149-160.

Moshier, S. O. and A. El-Kalani (2008). "Late Bronze Age paleogeography along the ancient ways of Horus in Northwest Sinai, Egypt." Geoarchaeology **23**(4): 450-473.

Mott, H. (1992). Antennas for radar and communications: a polarimetric approach, Wiley.

References

Mourad, A. L. (2014). The Procession of Asiatics. Beni Hassan. Volume I: The Tomb of Khnumhotep II. N. Kanawati and L. Evans. Oxford, Oxford. **Australian Centre for Egyptology: Reports 36**: 72-78.

Muhs, D. R., J. Roskin, H. Tsoar, G. Skipp, J. R. Budahn, A. Sneh, N. Porat, J.-D. Stanley, I. Katra and D. G. Blumberg (2013). "Origin of the Sinai–Negev erg, Egypt and Israel: mineralogical and geochemical evidence for the importance of the Nile and sea level history." Quaternary Science Reviews **69**: 28-48.

Mukul, M., V. Srivastava and M. Mukul (2016). "Accuracy analysis of the 2014–2015 Global Shuttle Radar Topography Mission (SRTM) 1 arc-sec C-Band height model using International Global Navigation Satellite System Service (IGS) Network." Journal of Earth System Science **125**(5): 909-917.

Mumford, G. (2015). "The Sinai Peninsula and its Environs: Our Changing Perceptions of a Pivotal Land Bridge Between Egypt, the Levant, and Arabia." Journal of Ancient Egyptian Interconnections **7**(1): 1-24.

NASA, J. (2016, 6 July 2016). "SRTM Mission Statistics." Retrieved 6 July, 2016, from <http://www2.jpl.nasa.gov/srtm/statistics.html>.

Nisio, S. and G. Ciotoli (2016). Rome: sinkhole events and network of underground cavities (Italy). EGU General Assembly Conference Abstracts.

Oh, Y., K. Sarabandi and F. Ulaby (1993). An empirical model for phase difference statistics of rough surfaces. Geoscience and Remote Sensing Symposium, 1993. IGARSS'93. Better Understanding of Earth Environment., International, IEEE.

Oliver, C. and S. Quegan (1998). "Understanding synthetic aperture radar images. Artech House." INC. Boston. London: 451-461.

Oren, E. D. (1980). "North Sinai Survey 1972-1978." Sinai in Antiquity, eds. Z. Meshel and I. Finkelstein. Tel Aviv: Hakkibutz Hameu-chad (Hebrew): 101-158.

Oren, E. D. (1987). The 'Ways of Horus' in North Sinai. Egypt, Israel, Sinai: Archaeological and Historical Relationships in the Biblical Period. A. F. Rainey. Tel Aviv: 69-119.

Oren, E. D. (1989). Early Bronze Age Settlement on Northern Sinai: A Model for Egypto-Canaanite Interconnections. L'urbanisation de la Palestine à l'âge du Bronze ancien. Bilan et perspectives des recherches actuelles. Actes du Colloque d'Emmaüs (20-24 octobre 1986). P. de Miroshedji. Oxford, BAR IS. **527**: 389-405.

References

Paillou, P., T. August, Y. Lasne, G. Grandjean and G. Ruffie (2003). A phase signature for detecting subsurface moisture using polarimetric L-band SAR: example of the Pyla dune-France. Geoscience and Remote Sensing Symposium, 2003. IGARSS'03. Proceedings. 2003 IEEE International, IEEE.

Paillou, P., S. Lopez, T. Farr and A. Rosenqvist (2010). "Mapping subsurface geology in Sahara using L-Band SAR: first results from the ALOS/PALSAR imaging radar." IEEE Journal of Selected Topics in Applied Earth Observations and Remote Sensing **3**(4): 632.

Paillou, P. and A. Rosenqvist (2003). A JERS-1 radar mosaic for subsurface geology mapping in East Sahara. Geoscience and Remote Sensing Symposium, 2003. IGARSS'03. Proceedings. 2003 IEEE International, IEEE.

Parcak, S. H. (2009). Satellite remote sensing for archaeology, Routledge.

Pathe, C., W. Wagner, D. Sabel, M. Doubkova and J. B. Basara (2009). "Using ENVISAT ASAR global mode data for surface soil moisture retrieval over Oklahoma, USA." IEEE Transactions on Geoscience and Remote Sensing **47**(2): 468-480.

Patruno, J., N. Dore, M. Crespi and E. Pottier (2013). "Polarimetric Multifrequency and Multi-incidence SAR Sensors Analysis for Archaeological Purposes." Archaeological Prospection **20**(2): 89-96.

Patruno, J., N. Dore, A. Ruescas, M. Lavallo, C. Putignano, A. Jaia, G. Galdieri, E. Loret and F. Sarti (2009). Preliminary results of Alos Palsar imaging for investigation of archaeological underground marks. 4th Int. Workshop on Science and Applications of SAR Polarimetry and Polarimetric Interferometry – PolInSAR 2009, Frascati, Italy, ESA.

Penman, H. (1970a). "Woburn irrigation, 1960–8: IV. Design and interpretation." The Journal of Agricultural Science **75**(01): 69-73.

Penman, H. (1970b). "Woburn irrigation, 1960–8: V. Results for leys." The Journal of Agricultural Science **75**(01): 75-88.

Penman, H. (1970c). "Woburn irrigation, 1960–8: VI. Results for rotation crops." The Journal of Agricultural Science **75**(01): 89-102.

Penman, H. L. (1948). Natural evaporation from open water, bare soil and grass. Proceedings of the Royal Society of London A: Mathematical, Physical and Engineering Sciences, The Royal Society.

Piggott, S. (1937). "Prehistory and the romantic movement." Antiquity **11**(41): 31-38.

References

Pleskachevsky, A., S. Lehner, T. Heege and C. Mott (2011). "Synergy and fusion of optical and synthetic aperture radar satellite data for underwater topography estimation in coastal areas." Ocean Dynamics **61**(12): 2099-2120.

Poortinga, W., A. Spence, L. Whitmarsh, S. Capstick and N. F. Pidgeon (2011). "Uncertain climate: An investigation into public scepticism about anthropogenic climate change." Global environmental change **21**(3): 1015-1024.

Pope, K. O. and B. H. Dahlin (1989). "Ancient Maya wetland agriculture: New insights from ecological and remote sensing research." Journal of Field Archaeology **16**(1): 87-106.

Quackenbush, L. J. (2004). "A review of techniques for extracting linear features from imagery." Photogrammetric Engineering & Remote Sensing **70**(12): 1383-1392.

Quegan, S., T. Le Toan, J. J. Yu, F. Ribbes and N. Floury (2000). "Multitemporal ERS SAR analysis applied to forest mapping." Geoscience and Remote Sensing, IEEE Transactions on **38**(2): 741-753.

Quilici, L. (1974). Collatia. Rome, De Luca Editore.

Quilici, L. (1992). "Evoluzione della tecnica stradale nell'Italia centrale." Atlante tematico di topografia antica 1. Tecnica stradale romana, Roma: 13.

Quilici, L. and S. Q. Gigli (1980). Crustumerium. Rome, Italy, Consiglio nazionale delle ricerche, Centro di studio per l'archeologia etrusco-italica.

Quintanar, J., S. D. Khan, M. S. Fathy and A.-F. A. Zalat (2013). "Remote sensing, planform, and facies analysis of the Plain of Tineh, Egypt for the remains of the defunct Pelusiac River." Sedimentary Geology **297**: 16-30.

Rackham, O. (1972). Responses of the barley crop to soil water stress. Crop processes in controlled environments. A. R. Rees, Cockshull, K. E., Hand, D. W., and Hurd, R. G., Academic Press London, New York: 127-138.

Rączkowski, W. (2011). "Cropmarks 2011 in Poland—is there a need for further discussion?" AARGnews **43**: 37-42.

Regione Lazio. (2016). "Centro Funzionale Regionale." Retrieved 20 October, 2016, from <http://www.idrografico.roma.it/>.

References

Renga, A., V. Boccia, M. D'Errico, G. Rufino, A. Moccia, C. Aragno and S. Zoffoli (2012). Analysis of SAR monitoring capabilities in coastal areas. IET Conference Proceedings, The Institution of Engineering & Technology.

Renga, A., G. Rufino, M. D'Errico, A. Moccia, V. Boccia, M. D. Graziano, C. Aragno and S. Zoffoli (2013). "Analysis of spaceborne SAR monitoring capabilities for coastal areas bathymetry with COSMO-SkyMed and ALOS data." Proceedings of SPIE - The International Society for Optical Engineering **8888**: 88808-88801 to 88808-88815.

Renga, A., G. Rufino, M. D'Errico, A. Moccia, V. Boccia, M. D. Graziano, C. Aragno and S. Zoffoli (2014). "SAR bathymetry in the Tyrrhenian sea by COSMO-SkyMed data: A novel approach." IEEE Journal of Selected Topics in Applied Earth Observations and Remote Sensing **7**(7): 2834-2847.

Rignot, E., K. Echelmeyer and W. Krabill (2001). "Penetration depth of interferometric synthetic-aperture radar signals in snow and ice." Geophysical Research Letters **28**(18): 3501-3504.

Riley, D. (1979). "Factors in the development of crop marks." Aerial Archaeology **4**: 28-32.

Robinson, C., F. El-Baz and V. Singhroy (1999). "Subsurface imaging by RADARSAT: comparison with Landsat TM data and implications for ground water in the Selima area, northwestern Sudan." Canadian Journal of Remote Sensing **25**(3): 268-277.

Rodriguez, E. and J. Martin (1992). Theory and design of interferometric synthetic aperture radars. IEE Proceedings F-Radar and Signal Processing, IET.

Romeiser, R. and W. Alpers (1997). "An improved composite surface model for the radar backscattering cross section of the ocean surface, 2. Model response to surface roughness variations and the radar imaging of underwater bottom topography." Journal of Geophysical Research-Part C-Oceans-Printed Edition **102**(11): 25251-25267.

Romeiser, R., W. Alpers and V. Wismann (1997). "An improved composite surface model for the radar backscattering cross section of the ocean surface: 1. Theory of the model and optimization/validation by scatterometer data." Journal of Geophysical Research: Oceans **102**(C11): 25237-25250.

Rosa, P. (1870). Carta topografica del Lazio. Rome, Soprintendenza di Roma: Archaeological chart of Lazio, Italy, at a scale of 1:20,000.

Rosen, P. A., S. Hensley and C. Le (2008). Observations and mitigation of RFI in ALOS PALSAR SAR data: Implications for the DESDynI mission. Radar Conference, 2008. RADAR'08. IEEE, IEEE.

References

Roskin, J., I. Katra and D. G. Blumberg (2014). "Particle-size fractionation of eolian sand along the Sinai-Negev erg of Egypt and Israel." Geological Society of America Bulletin **126**(1-2): 47-65.

Roskin, J., N. Porat, H. Tsoar, D. G. Blumberg and A. M. Zander (2011). "Age, origin and climatic controls on vegetated linear dunes in the northwestern Negev Desert (Israel)." Quaternary Science Reviews **30**(13): 1649-1674.

Roth, L. E. and C. Elachi (1975). "Coherent electromagnetic losses by scattering from volume inhomogeneities." IEEE Transactions on Antennas and Propagation **23**: 674.

Ruciński, D., W. Rączkowski and J. Niedzielko (2015). A Polish perspective on optical satellite data and methods for archaeological sites prospection. Third International Conference on Remote Sensing and Geoinformation of the Environment, International Society for Optics and Photonics.

Russell, E. W. (1961). Soil conditions and plant growth. London.

Ryan, W. and W. Pitman (2000). Noah's Flood: The new scientific discoveries about the event that changed history, Simon and Schuster.

Salmon, R. (1963). "Magnesium relationships in soils and plants." Journal of the Science of Food and Agriculture **14**(9): 605-610.

Salter, P. and F. Haworth (1961). "THE AVAILABLE-WATER CAPACITY OF A SANDY LOAM SOIL." Journal of Soil Science **12**(2): 326-334.

Sandidge, J. C. and R. J. Holyer (1998). "Coastal bathymetry from hyperspectral observations of water radiance." Remote Sensing of Environment **65**(3): 341-352.

Saturno, W., T. L. Sever, D. E. Irwin, B. F. Howell and T. G. Garrison (2006). Putting us on the map: remote sensing investigation of the ancient Maya landscape. Remote sensing in archaeology, Springer: 137-160.

Schaber, G. G. (1999). "SAR studies in the Yuma Desert, Arizona: sand penetration, geology, and the detection of military ordnance debris." Remote sensing of environment **67**(3): 320-347.

Schaber, G. G. and C. S. Breed (1999). "The importance of SAR wavelength in penetrating blow sand in northern Arizona." Remote sensing of environment **69**(2): 87-104.

References

Schaber, G. G., J. F. McCauley and C. S. Breed (1997). "The use of multifrequency and polarimetric SIR-C/X-SAR data in geologic studies of Bir Safsaf, Egypt." Remote Sensing of Environment **59**(2): 337-363.

Schaber, G. G., J. F. McCauley, C. S. Breed and G. R. Olhoeft (1986). "Shuttle imaging radar: physical controls on signal penetration and subsurface scattering in the eastern sahara." Geoscience and Remote Sensing, IEEE Transactions on(4): 603-623.

Schmuck, S., J. Roeder and P. Potin (2014). Sentinel-1A observation scenario simulations—Initial operations phase. Geoscience and Remote Sensing Symposium (IGARSS), 2014 IEEE International, IEEE.

Scollar, I., A. Tabbagh, A. Hesse and I. Herzog (1990). Archaeological prospecting and remote sensing, Cambridge University Press.

Sever, T. L. and D. E. Irwin (2003). "Landscape archaeology: Remote-sensing investigation of the ancient Maya in the Peten rainforest of northern Guatemala." Ancient Mesoamerica **14**(01): 113-122.

Sheets, P. and T. L. Sever (2006). Creating and perpetuating social memory across the ancient Costa Rican Landscape. Remote Sensing in Archaeology. Berlin/Heidelberg, Germany, Springer: 161-184.

Shuchman, R., D. Lyzenga and G. Meadows (1985). "Synthetic aperture radar imaging of ocean-bottom topography via tidal-current interactions: theory and observations." International Journal of Remote Sensing **6**(7): 1179-1200.

Siegal, Z., H. Tsoar and A. Karnieli (2013). "Effects of prolonged drought on the vegetation cover of sand dunes in the NW Negev Desert: Field survey, remote sensing and conceptual modeling." Aeolian Research **9**: 161-173.

Small, D. (2011). "Flattening gamma: Radiometric terrain correction for SAR imagery." Geoscience and Remote Sensing, IEEE Transactions on **49**(8): 3081-3093.

Small, D. and A. Schubert (2008). "Guide to ASAR geocoding." 36.

Snoeij, P., N. van der Valk, E. Boom and D. Hoekman (2001). Effect of the ionosphere on P-band spaceborne SAR images. Geoscience and Remote Sensing Symposium, 2001. IGARSS'01. IEEE 2001 International, IEEE.

Stanjek, H. and J. Fassbinder (1995). "Soil aspects affecting archaeological details in aerial photographs." Archaeological Prospection **2**: 91-102.

References

Stanley, J.-D., M. P. Bernasconi and T. F. Jorstad (2008). "Pelusium, an ancient port fortress on Egypt's Nile Delta coast: its evolving environmental setting from foundation to demise." Journal of Coastal Research: 451-462.

Stern, R. J. and M. G. Abdelsalam (1996). "The origin of the great bend of the Nile from SIR-C/X-SAR imagery." Science **274**(5293): 1696-1698.

Stewart, C. (2017). "Detection of Archaeological Residues in Vegetated Areas Using Satellite Synthetic Aperture Radar." Remote Sensing **9**(2): 118.

Stewart, C., A. Di Iorio and G. Schiavon (2013a). Analysis of the Utility of Cosmo Skymed Stripmap to Detect Buried Archaeological Features in the Region of Rome. 4th EARSeL Workshop on Cultural and Natural Heritage, Matera, Italy, European Association of Remote Sensing Laboratories (EARSeL).

Stewart, C., R. Lasaponara and G. Schiavon (2013b). "ALOS PALSAR analysis of the archaeological site of Pelusium." Archaeological Prospection **20**(2): 109-116.

Stewart, C., R. Lasaponara and G. Schiavon (2014). "Multi-frequency, polarimetric SAR analysis for archaeological prospection." International Journal of Applied Earth Observation and Geoinformation **28**: 211-219.

Stewart, C., K. Lemmens and M. Sala (2015a). Satellite Radar in Support to Archaeological Research in Egypt: Tracing Ancient Tracks Between Egypt and Southern Levant Across North Sinai. Egyptian Curses 2. A Research on Ancient Catastrophes. G. Capriotti Vittozzi. Rome, Consiglio Nazionale Delle Ricerche (CNR), Istituto Di Studi Sul Mediterraneo Antico (ISMA): 197-221.

Stewart, C., K. Lemmens, M. Sala and G. C. Vittozzi (2016a). "A Contribution of Satellite Radar to Archaeological Research in North Sinai, Egypt." Archaeological Heritage & Multidisciplinary Egyptological Studies (AHMES) **3**: 11.

Stewart, C., R. Montanaro, M. Sala and P. Riccardi (2016b). "Feature Extraction in the North Sinai Desert Using Spaceborne Synthetic Aperture Radar: Potential Archaeological Applications." Remote Sensing **8**(10): 825.

Stewart, C., M. Rast, F. Sarti and O. Arino (2015b). "ESA activities in Earth Observation for Cultural Heritage applications." International Journal of Heritage in the Digital Era **4**(3-4): 325-338.

Stewart, C., A. Renga, V. Gaffney and G. Schiavon (2016c). "Sentinel-1 bathymetry for North Sea palaeolandscape analysis." International Journal of Remote Sensing **37**(3): 471-491.

References

- Stiebing, W. H. (1993). Uncovering the past: a history of archaeology, Oxford University Press on Demand.
- Stubbs, J. H. and K. L. McKee (2006). Applications of remote sensing to the understanding and management of cultural heritage sites. Remote Sensing in Archaeology, Springer: 515-540.
- Tachikawa, T., M. Kaku, A. Iwasaki, D. B. Gesch, M. J. Oimoen, Z. Zhang, J. J. Danielson, T. Krieger, B. Curtis and J. Haase (2011). ASTER global digital elevation model version 2-summary of validation results. Sioux Falls, USA, NASA Land Processes Distributed Active Archive Center.
- Tapete, D., F. Cigna and D. N. Donoghue (2016). "'Looting marks' in space-borne SAR imagery: Measuring rates of archaeological looting in Apamea (Syria) with TerraSAR-X Staring Spotlight." Remote Sensing of Environment **178**: 42-58.
- Tapete, D., F. Cigna, N. Masini and R. Lasaponara (2013). "Prospection and monitoring of the archaeological heritage of Nasca, Peru, with ENVISAT ASAR." Archaeological Prospection **20**(2): 133-147.
- Tapete, D., R. Fanti, R. Cecchi, P. Petrangeli and N. Casagli (2012). "Satellite radar interferometry for monitoring and early-stage warning of structural instability in archaeological sites." Journal of Geophysics and Engineering **9**(4): S10.
- Tassie, G. J. and J. F. L. van Wetering (2012). The Wadi Tumulat. Encyclopedia of Ancient History. R. S. Bagnall, K. Brodersen, C. B. Champion, A. Erskine and S. R. Huebner. Oxford, Wiley-Blackwell: 7035-7036.
- Testaguzza, O. (1970). Portus: illustrazione dei Porti di Claudio e Traiano e della città di Porto a Fiumicino. Rome, Julia Editrice.
- Timothy, D. J. (2007). Managing heritage and cultural tourism resources, Ashgate.
- Touzi, R. and F. Charbonneau (2002). "Characterization of target symmetric scattering using polarimetric SARs." IEEE Transactions on Geoscience and Remote Sensing **40**(11): 2507-2516.
- Trabant, P. K. (2013). Applied high-resolution geophysical methods: offshore geoengineering hazards, Springer Science & Business Media.
- Tsoar, H. (1976). "Characterization of sand dune environments by their grain-size, mineralogy and surface texture." Geography in Israel: Jerusalem, Israel National Committee, International Geographical Union: 327-343.

References

- Tsoar, H. (1995). "Desertification in northern Sinai in the eighteenth century." Climatic change **29**(4): 429-438.
- Tsoar, H., D. Blumberg and R. Wenkart (2008). Formation and geomorphology of the North-Western Negev sand dunes. Arid dune ecosystems, Springer: 25-48.
- Tsoar, H., D. G. Blumberg and Y. Stoler (2004). "Elongation and migration of sand dunes." Geomorphology **57**(3): 293-302.
- Tusa, S. (2016). Innovation Technologies and Applications for Coastal Archaeological sites, ITACA. D25.1 Final Results of Project ITACA.
- Ulaby, F. T. and M. C. Dobson (1989). "Handbook of Radar Scattering Statistics for Terrain." ARTECH HOUSE, 685 CANTON STREET, NORWOOD, MA 02062(USA), 1989, 500.
- Ulaby, T., K. Moore and K. Fung (1981). Microwave remote sensing. Volume I: Microwave Remote Sensing Fundamentals and Radiometry. Norwood, Artech House.
- Ulaby, T., K. Moore and K. Fung (1982). Microwave remote sensing. Volume II : Radar Remote Sensing and surface Scattering and Emission Theory. New York, Addison Wesley.
- University of Birmingham. (2011). "North Sea Palaeolandscape Project." Retrieved 26 May, 2015, from http://archaeologydataservice.ac.uk/archives/view/nspp_eh_2011/downloads.cfm.
- Valbelle, D. (1989). "Recherches archéologiques récentes dans le Nord-Sinai." Comptes rendus des séances de l'Académie des Inscriptions et Belles-Lettres **133**(3): 594-607.
- Verhoeven, G. J. and K. D. Schmitt (2010). "An attempt to push back frontiers—digital near-ultraviolet aerial archaeology." Journal of Archaeological Science **37**(4): 833-845.
- Viets, F. (1972). "Water deficits and nutrient availability." Water deficits and plant growth **3**: 217-239.
- Vogelzang, J. (1989). "A comparison of the hydrodynamic modulation in some existing models." International Journal of Remote Sensing **10**(9): 1503-1518.
- Vogelzang, J. (1997). "Mapping submarine sand waves with multiband imaging radar: 1. Model development and sensitivity analysis." Journal of Geophysical Research: Oceans **102**(C1): 1163-1181.

References

Vogelzang, J. (2001). "A model comparison study to the imaging of submarine reefs with synthetic aperture radar." International Journal of Remote Sensing **22**(13): 2509-2536.

Vogelzang, J., G. Wensink, C. Calkoen and M. Van der Kooij (1997). "Mapping submarine sand waves with multiband imaging radar 2. Experimental results and model comparison." J. Geophys. Res **102**: 1163-1192.

Vogelzang, J., G. Wensink, G. De Loor, H. Peters and H. Pouwels (1992). "Sea bottom topography with X-band SLAR: The relation between radar imagery and bathymetry." International Journal of Remote Sensing **13**(10): 1943-1958.

Wackerman, C., D. Lyzenga, E. Ericson and D. Walker (1998). Estimating near-shore bathymetry using SAR. International Geoscience and Remote Sensing Symposium (IGARSS), IEEE International.

Waldrop, M. M. (2008). "Science 2.0." Scientific American **298**(5): 68-73.

Walker, A., J. W. Olsen and Bagen (1987). "The Badain Jaran Desert: Remote Sensing Investigations." Geographical Journal: 205-210.

Ward-Perkins, J. B. (1961). "Veii: the historical topography of the ancient city." Papers of the British School at Rome **29**: 1-119.

Wendorf, F., A. E. Close and R. Schild (1987). "A survey of the Egyptian radar channels: An example of applied archaeology." Journal of Field Archaeology **14**(1): 43-63.

Westley, K., J. Dix and R. Quinn (2004). "A re-assessment of the archaeological potential of continental shelves." English Heritage Aggregates Levy Sustainability Fund Project **3362**.

Westley, K., R. Quinn, W. Forsythe, R. Plets, T. Bell, S. Benetti, F. McGrath and R. Robinson (2011). "Mapping submerged landscapes using multibeam bathymetric data: a case study from the north coast of Ireland." International Journal of Nautical Archaeology **40**(1): 99-112.

Wilgocka, A., W. Rączkowski, M. Kostyrko and D. Ruciński (2016). Sherlock Holmes' or Don Quixote's certainty? Interpretations of cropmarks on satellite imageries in archaeological investigation. Fourth International Conference on Remote Sensing and Geoinformation of the Environment, International Society for Optics and Photonics.

Wilson, D. R. (2000). Air Photo Interpretation for Archaeologists. Stroud Gloucestershire United Kingdom, Tempus Publishing.

References

Wiseman, J. and F. El-Baz (2007). Remote sensing in archaeology. Interdisciplinary contributions to archaeology, Springer.

Wiseman, T. (1970). "Roman Republican Road Building." Papers of the British School at Rome **38**: 30.

Woodhouse, I. H. (2005). Introduction to microwave remote sensing. Boca Raton, FL, USA, CRC press.

Wright, S. T. C. (1972). Physiological and biochemical responses to wilting and other stress conditions. Crop processes in controlled environments. A. R. Rees, Cockshull, K. E., Hand, D. W., and Hurd, R. E.: 349-361.

Wynn, J. C. (1986). "A review of geophysical methods used in archaeology." Geoarchaeology **1**(3): 245-257.

Xia, C. and Y. Yuan (2002). "Simulation and Inversion Study on the Submarine Topography in the Tangu Sea Area Using SAR images." Advances in Marine Science **21**(4): 437-445.

Yakam-Simen, F., E. Nezry, J. J. Ewing and T. Maschal (1998). Legendary lost city Ciudad Blanca found under tropical forest in Honduras, using ERS-2 and JERS-1 SAR imagery. Remote Sensing, International Society for Optics and Photonics.

Yamaguchi, Y., T. Moriyama, M. Ishido and H. Yamada (2005). "Four-component scattering model for polarimetric SAR image decomposition." IEEE Transactions on Geoscience and Remote Sensing **43**(8): 1699-1706.

Yong, S.-S. and S.-W. Ra (2004). The design of MSC (multi-spectral camera) system operation. Geoscience and Remote Sensing Symposium, 2004. IGARSS'04. Proceedings. 2004 IEEE International, IEEE.

Zalite, K., O. Antropov, J. Praks, K. Voormansik and M. Noorma "Monitoring of Agricultural Grasslands With Time Series of X-Band Repeat-Pass Interferometric SAR."

Zalite, K., K. Voormansik, J. Praks, O. Antropov and M. Noorma (2014). Towards detecting mowing of agricultural grasslands from multi-temporal COSMO-SkyMed data. 2014 IEEE Geoscience and Remote Sensing Symposium, IEEE.

Zheng, Q., B. Holt, X. Li, X. Liu, Q. Zhao, Y. Yuan and X. Yang (2012a). "Deep-water seamount wakes on SEASAT SAR image in the Gulf Stream region." Geophysical Research Letters **39**(16).

References

Zheng, Q., L. Li, X. Guo, Y. Ge, D. Zhu and C. Li (2006). "SAR imaging and hydrodynamic analysis of ocean bottom topographic waves." Journal of Geophysical Research: Oceans (1978–2012) **111**(C9).

Zheng, Q., Q. Zhao, Y. Yuan, X. Liu, J. Hu, X. Liu, L. Yin and X. Ye (2012b). "Shear-flow induced secondary circulation in parallel underwater topographic corrugation and its application to satellite image interpretation." Journal of Ocean University of China **11**(4): 427-435.